Springer Proceedings in Physics 276

Alon Gany
Xiaolong Fu *Editors*

2021 International Conference on Development and Application of Carbon Nanomaterials in Energetic Materials

Springer

Springer Proceedings in Physics

Volume 276

Indexed by Scopus

The series Springer Proceedings in Physics, founded in 1984, is devoted to timely reports of state-of-the-art developments in physics and related sciences. Typically based on material presented at conferences, workshops and similar scientific meetings, volumes published in this series will constitute a comprehensive up-to-date source of reference on a field or subfield of relevance in contemporary physics. Proposals must include the following:

- name, place and date of the scientific meeting
- a link to the committees (local organization, international advisors etc.)
- scientific description of the meeting
- list of invited/plenary speakers
- an estimate of the planned proceedings book parameters (number of pages/articles, requested number of bulk copies, submission deadline).

Please contact:

For Americas and Europe: Dr. Zachary Evenson; zachary.evenson@springer.com
For Asia, Australia and New Zealand: Dr. Loyola DSilva; loyola.dsilva@springer.com

More information about this series at https://link.springer.com/bookseries/361

Alon Gany · Xiaolong Fu
Editors

2021 International Conference on Development and Application of Carbon Nanomaterials in Energetic Materials

中国兵工学会
China Ordnance Society

Springer

Editors
Alon Gany
Faculty of Aerospace Engineering
Technion—Israel Institute of Technology
Haifa, Israel

Xiaolong Fu
Xi'an Modern Chemistry Research Institute
Xi'an, China

ISSN 0930-8989 ISSN 1867-4941 (electronic)
Springer Proceedings in Physics
ISBN 978-981-19-1773-8 ISBN 978-981-19-1774-5 (eBook)
https://doi.org/10.1007/978-981-19-1774-5

Jointly published with China Ordnance Society
The print edition is not for sale in China (Mainland). Customers from China (Mainland) please order the print book from: China Ordnance Society.

This Springer imprint is published by the registered company Springer Nature Singapore Pte Ltd.
The registered company address is: 152 Beach Road, #21-01/04 Gateway East, Singapore 189721, Singapore

Preface

I am hugely delighted and excited to be writing this preface to the Proceedings Preface of the 2021 International Conference on Development and Application of Carbon Nanomaterials in Energetic Materials (ICCN). This is the second ICCN and is intended to be one in a long series of International Conference, taking place at intervals of approximately 20 months. The 2021 ICCN is co-chaired by Prof. Alon Gany and myself and supported by the China Ordnance Society and Xi'an Modern Chemistry Research Institute.

Due to circumstances beyond our control, the ICCN was postponed from 18–21 August 2021 to 2022. We recognised it was important to many authors that their papers were published in August, as originally scheduled. Therefore, with the kind agreement of the publisher (Springer Proceedings in Physics), it might be publishing the 2021 ICCN Proceedings in April 2022.

The ICCN provides a platform for the international experts and the participants to discuss advanced carbon nanomaterials of energetic materials. Advanced carbon nanomaterials are widely used in aviation, aerospace, energy, medical treatment, etc. In energetic materials field, the advanced carbon nanomaterials are an important matter to enhance performance and decrease sensitivity. This forum is mainly about the new technology and development of advanced carbon nanomaterials in energetic materials by international experts.

The main topics of ICCN Proceedings are about development trend of carbon nanomaterials, the research on design technology of carbon nanomaterials, preparation and process of carbon nanomaterials, the research on properties of carbon nanomaterials and application of carbon nanomaterials in energetic materials.

This is the first ICCN Proceedings to be published by Springer Proceedings in Physics. The Proceedings were enabled by the good cooperation between the ICCN and Defence Technology journal, which is sponsored by the China Ordnance Society and published by KeAi Publishing Communications Ltd. I would like to thank the China Ordnance Society, the Editors and the Editorial Office, Ms. Ying Li, Ms. Xin Ma, Ms. Yanhong Ma and Ms. Liu Li, for their dedicated, hard and expeditious work in producing this issue. I also thank the technical reviewers of the papers contained

in these Proceedings and the sponsors of the ICCN who have helped to make the ICCN possible.

I hope you will find these Proceedings stimulating and very interesting. ICCN provides an opportunity to develop an understanding of the carbon nanomaterials of energetic materials outside of the reader's specialist area. I, therefore, highly commend these Proceedings to you.

Xi'an, China

Xiaolong Fu
2021 ICCN Co-chair

Haifa, Israel

Alon Gany
Clive Woodley
Institute of Shock Physics
Imperial College
London, UK

Contents

Contributors

Chaofei Bai School of Materials Science and Engineering, Beijing Institute of Technology, Beijing, China

Tao Bowen Science and Technology on Aerospace Chemical Power Laboratory, Xiangyang, PR China;
Hubei Institute of Aerospace Chemotechnology, Xiangyang, PR China

Yufan Bu Xi'an Modern Chemistry Research Institute, Xi'an, P.R. China

Xiaoya Chang State Key Laboratory of Explosion Science and Technology, Beijing Institute of Technology, Beijing, China

Chunyan Chen Xi'an Modern Chemistry Research Institute, Xi'an, P.R. China

Dong Chen State Key Laboratory of Fluorine and Nitrogen Chemicals, Xi'an Modern Chemistry Research Institute, Xi'an, Shaanxi, P.R. China

Dongping Chen State Key Laboratory of Explosion Science and Technology, Beijing Institute of Technology, Beijing, China

Fuyao Chen School of Chemistry and Chemical Engineering, Nanjing University of Science and Technology, Nanjing, Jiangsu, China

Guohui Chen Xi'an Modern Chemistry Research Institute, Xi'an, China

Hao Chen Xi'an Modern Chemistry Research Institute, Xi'an, China

Jianhua Chen Science and Technology on Applied Physical Chemistry Laboratory, Shaanxi Applied Physics-Chemistry Research Institute, Xi'an, Shaanxi, China

Jing Chen Xi'an Modern Chemistry Research Institute, Xi'an, PR China

Jun-bo Chen Xi'an Modern Chemistry Research Institute, Xi'an, China

Tao Chen Xi'an Modern Chemistry Research Institute Xi'an, Shaanxi, China

Yu Cheng Shanghai Space Propulsion Technology Research Institute, Huzhou, China

Zhiyuan Cong State Key Laboratory of Fluorine and Nitrogen Chemicals, Xi'an Modern Chemistry Research Institute, Xi'an, Shaanxi, P.R. China

Qingzhong Cui State Key Laboratory of Explosion Science and Technology, Beijing Institute of Technology, Beijing, China

Zenghui Cui No. 66109 Troops of PLA, Qinhuangdao, China

Huang Danchun Science and Technology on Aerospace Chemical Power Laboratory, Xiangyang, PR China;
Hubei Institute of Aerospace Chemotechnology, Xiangyang, PR China

Xiaoqiang Diao Xi'an Modern Chemistry Research Institute, Xi'an, China

Shanjun Ding State Key Laboratory of Explosion Science and Technology, Beijing Institute of Technology, Beijing, China

Jun Dong Naval University of Engineering, Wuhan, China;
Xi'an Modern Chemistry Research Institute, Xi'an, China

Mao-hua Du Naval University of Engineering, Wuhan, China

Shiguo Du Department of Ammunition Engineering, Army Engineering University, Shijiazhuang, China

Xuekun Fan Academy of Ordnance Science, Beijing, China

Xuezhong Fan Xi'an Modern Chemistry Research Institute, Xi'an, China

D. U. Fang Science and Technology on Aerospace Chemical Power Laboratory, Xiangyang, PR China;
Hubei Institute of Aerospace Chemotechnology, Xiangyang, PR China

Muhua Feng National Key Laboratory of Transient Physics, Nanjing University of Science and Technology, Nanjing, Jiangsu, China

Xiaojun Feng Xi'an Modern Chemistry Research Institute, Xi'an, Shanxi, PR China

Xiaolong Fu Xi'an Modern Chemistry Research Institute, Xi'an, China

You Fu School of Chemistry and Engineering, Nanjing University of Science and Technology, Nanjing, China

Chao Gao State Key Laboratory of Fluorine and Nitrogen Chemicals, Xi'an Modern Chemistry Research Institute, Xi'an, Shaanxi, P.R. China

Zhengming Gao School of Computer Engineering, Jingchu University of Technology, Jingmen, China

Jian Guan National Key Laboratory of Transient Physics, Nanjing University of Science and Technology, Nanjing, Jiangsu, China

Guojian Guo Shandong Non-Metallic Materials Institute, Jinan, Shandong, China

Rongjun Guo National Key Laboratory of Transient Physics, Nanjing University of Science and Technology, Jiangsu, China

Zhaoqi Guo School of Chemical Engineering/Xi'an Key, Laboratory of Special Energy Materials, Northwest University, Xi'an, China

Zhiming Guo School of Mechatronics Engineering, North University of China, Taiyuan, Shanxi, China

Ruishan Han Science and Technology on Applied Physical Chemistry Laboratory, Shaanxi Applied Physics-Chemistry Research Institute, Xi'an, Shaanxi, China

Gazi Hao School of Chemistry and Chemical Engineering, National Special Superfine Powder Engineering Research Center of China, Nanjing University of Science and Technology, Nanjing, China

Aifeng He Science and Technology on Applied Physical Chemistry Laboratory, Shaanxi Applied Physics-Chemistry Research Institute, Shaanxi, China

Qiwen He Xi'an Modern Chemistry Research Institute, Shaanxi, Xi'an, People's Republic of China

Chen Hong Science and Technology on Aerospace Chemical Power Laboratory, Xiangyang, PR China;
Hubei Institute of Aerospace Chemotechnology, Xiangyang, PR China

Dou Hong School of Mechanical Engineering, Nanjing University of Science and Technology, Nanjing, Jiangsu, China

Xiaoting Hou Science and Technology on Combustion and Explosion Laboratory, Xi'an Modern Chemistry Research Institute, Xi'an, China;
Shanxi North Xing'an Chemical Industry Co, Ltd., Taiyuan, China

Yan Hu School of Chemistry and Chemical Engineering, Nanjing University of Science and Technology, Nanjing, China

Yi-wen Hu Xi'an Modern Chemistry Research Institute, Xi'an, China

Yubing Hu School of Chemistry and Chemical Engineering, Nanjing University of Science and Technology, Nanjing, Jiangsu, China

Wang Huisi Science and Technology on Aerospace Chemical Power Laboratory, Xiangyang, PR China;
Hubei Institute of Aerospace Chemotechnology, Xiangyang, PR China

Xianzhen Jia Xi'an Modern Chemistry Research Institute, Xi'an, Shaanxi, China

Gu Jian Science and Technology on Aerospace Chemical Power Laboratory, Xiangyang, PR China;
Hubei Institute of Aerospace Chemotechnology, Xiangyang, PR China;
Laboratory of Emergency Safety and Rescue Technology, Xiangyang, PR China

Fan Jiang Xi'an Modern Chemistry Research Institute, Xi'an, Shanxi, PR China

Liping Jiang Xi'an Modern Chemistry Research Institute, Xi'an, China

Ning Jiang School of Mechanical Engineering, Nanjing University of Science and Technology, Nanjing, Jiangsu, China

Wei Jiang School of Chemistry and Chemical Engineering, National Special Superfine Powder Engineering Research Center of China, Nanjing University of Science and Technology, Nanjing, China

Yuke Jiao School of Materials Science and Engineering, Beijing Institute of Technology, Beijing, China

Tian Jin National Key Laboratory of Transient Physics, Nanjing University of Science and Technology, Nanjing, Jiangsu, China

Haibo Ke School of Chemistry and Chemical Engineering, National Special Superfine Powder Engineering Research Center of China, Nanjing University of Science and Technology, Nanjing, China

Junli Kong Liaoning Qingyang Chemical Industry Corporation, Liaoyang, Liaoning, China

Hongbing Lei Shanxi North Xing'an Chemical Industry Co., Ltd., Taiyuan, China

Li Lei Science and Technology on Aerospace Chemical Power Laboratory, Xiangyang, PR China;
Hubei Institute of Aerospace Chemotechnology, Xiangyang, PR China

Ruiqin Li Science and Technology on Combustion and Explosion Laboratory, Xi'an Modern Chemistry Research Institute, Xi'an, China;
Shanxi North Xing'an Chemical Industry Co, Ltd., Taiyuan, China

J. N. Liang Institute for Frontier Technologies of Low-Carbon Steelmaking, School of Metallurgy, Northeastern University, Shenyang, China

Xin Liao School of Chemistry and Engineering, Nanjing University of Science and Technology, Nanjing, China

Da Li Xi'an Modern Chemistry Research Institute, Xi'an, China

Dayong Li China North Chemical Research Academy Group Co., Ltd., Beijing, People's Republic of China

Fengsheng Li School of Chemistry and Chemical Engineering, National Special Superfine Powder Engineering Research Center of China, Nanjing University of Science and Technology, Nanjing, China

Guoping Li School of Materials Science and Engineering, Beijing Institute of Technology, Beijing, China;
Key Laboratory for Ministry of Education of High Energy Density Materials, Beijing Institute of Technology, Beijing, China

Hui Li Science and Technology on Combustion and Explosion Laboratory, Xi'an Modern Chemistry Research Institute, Xi'an, China

Jiankang Li Xi'an Modern Chemistry Research Institute, Xi'an, People's Republic of China

Jizhen Li Xi'an Modern Chemistry Research Institute, Xi'an, China

Qiang Li Shanxi North Xing'an Chemical Industry Co., Ltd., Taiyuan, China

Shaojie Li Department of Ammunition Engineering, Army Engineering University, Shijiazhuang, China

Shenghua Li School of Materials Science and Engineering, Beijing Institute of Technology, Beijing, China

Shengnan Li School of Materials Science and Engineering, Beijing Institute of Technology, Beijing, China

Weihang Li School of Mechanical Engineering, Nanjing University of Science and Technology, Nanjing, Jiangsu, China

Wenbin Li School of Mechanical Engineering, Nanjing University of Science and Technology, Nanjing, Jiangsu, China

Xiaojiang Li Xi'an Modern Chemistry Research Institute, Xi'an, PR China

Yang Li Xi'an Modern Chemistry Research Institute, Xi'an, China

Dongqi Liu School of Chemistry and Chemical Engineering, National Special Superfine Powder Engineering Research Center of China, Nanjing University of Science and Technology, Nanjing, China

Jianqun Liu State Key Laboratory of Fluorine and Nitrogen Chemicals, Xi'an Modern Chemistry Research Institute, Xi'an, Shaanxi, P.R. China

Jianxia Liu Xi'an Modern Chemistry Research Institute, Xi'an, China

Jiaran Liu School of Materials Science and Engineering, Beijing Institute of Technology, Beijing, China

Jie Liu School of Chemistry and Chemical Engineering, National Special Superfine Powder Engineering Research Center of China, Nanjing University of Science and Technology, Nanjing, China

Meng Liu Xi'an Modern Chemistry Research Institute, Xi'an, PR China

Xia Liu Shandong Non-Metallic Materials Institute, Jinan, Shandong, China

Xiang Liu National Key Laboratory of Transient Physics, Nanjing University of Science and Technology, Jiangsu, China

Xuwen Liu School of Chemistry and Chemical Engineering, Nanjing University of Science and Technology, Nanjing, China;

Micro-Nano Energetic Devices Key Laboratory, Ministry of Industry and Information Technology, Nanjing, China

Yingzhe Liu Xi'an Modern Chemistry Research Institute, Xi'an, People's Republic of China

Yucun Liu School of Safety and Environmental Engineering, Central North University, Shanxi, Taiyuan, China

Zesheng Liu PLA, Baicheng, Jilin, China

Feipeng Lu Science and Technology on Applied Physical Chemistry Laboratory, Shaanxi Applied Physics-Chemistry Research Institute, Xi'an, Shaanxi, China

Qiangqiang Lu School of Chemistry and Chemical Engineering, National Special Superfine Powder Engineering Research Center of China, Nanjing University of Science and Technology, Nanjing, China

Yi Lu Shandong Non-Metallic Materials Institute, Jinan, Shandong, China

Yunjun Luo School of Materials Science and Engineering, Beijing Institute of Technology, Beijing, China;
Key Laboratory for Ministry of Education of High Energy Density Materials, Beijing Institute of Technology, Beijing, China

Haixia Ma School of Chemical Engineering/Xi'an Key, Laboratory of Special Energy Materials, Northwest University, Xi'an, China

Liang Ma Xi'an Modern Chemistry Research Institute, Xi'an, China

Shunnian Ma Xi'an Modern Control Technology Research Institute, Xi'an, China

Yiding Ma Xi'an Modern Chemistry Research Institute, Xi'an, People's Republic of China

Saiqin Meng Xi'an Modern Chemistry Research Institute, Xi'an, China

Shenghao Meng High-Tech Institute, Qingzhou, China

Hai Nan High-Tech Institute of Xi'an, Xi'an, P.R. China;
Xi'an Modern Chemistry Research Institute, Xi'an, P.R. China

Xinyao Nie Liaoning Qingyang Chemical Industry Corporation, Liaoyang, Liaoning, China

Yan-li Ning Xi'an Modern Chemistry Research Institute, Xi'an, China

Yulei Niu Xi'an Modern Chemistry Research Institute, Xi'an, P.R. China

Ziteng Niu School of Materials Science and Engineering, Beijing Institute of Technology, Beijing, China

Yan Qi Xi'an Modern Chemistry Research Institute, Xi'an, China

Zhenyu Qi Beijing Institute of Technology, Beijing, China

Bei Qu Xi'an Modern Chemistry Research Institute, Xi'an, China

Yinghui Ren School of Chemical Engineering/Xi'an Key, Laboratory of Special Energy Materials, Northwest University, Xi'an, China

Zhi Ren Xi'an Modern Chemistry Research Institute, Xi'an, PR China

Yuling Shao China North Chemical Research Academy Group Co., Ltd., Beijing, China

Ruiqi Shen School of Chemistry and Chemical Engineering, Nanjing University of Science and Technology, Nanjing, China;
Micro-Nano Energetic Devices Key Laboratory, Ministry of Industry and Information Technology, Nanjing, China

Aijuan Shi Xi'an Modern Chemistry Research Institute, Xi'an, China

La Shi Xi'an Modern Chemistry Research Institute, Xi'an, China

Ying Shi Junior Middle School of Henglin, Hubei, Tianmen, China

Jiaxin Su School of Chemistry and Chemical Engineering, Nanjing University of Science and Technology, Nanjing, China

Yuxin Sun National Key Laboratory of Transient Physics, Nanjing University of Science and Technology, Nanjing, Jiangsu, China

Bo Tan Naval University of Engineering, Wuhan, China

Cun-quan Wang Xi'an Modern Chemistry Research Institute, Xi'an, China

Deqi Wang School of Chemistry and Chemical Engineering, National Special Superfine Powder Engineering Research Center of China, Nanjing University of Science and Technology, Nanjing, China

Guanyi Wang State Key Laboratory of Explosion Science and Technology, Beijing Institute of Technology, Beijing, China

Jiangning Wang Xi'an Modern Chemistry Research Institute, Xi'an, China

Jinpin Wang School of Ordance Engineering, Naval Engineering University, Hubei, Wuhan, China

Min-chang Wang Xi'an Modern Chemistry Research Institute, Xi'an, China

Wang Wang School of Chemistry and Chemical Engineering, National Special Superfine Powder Engineering Research Center of China, Nanjing University of Science and Technology, Nanjing, China

Wei-li Wang Naval University of Engineering, Wuhan, China

Xiaofeng Wang Xi'an Modern Chemistry Research Institute, Xi'an, Shanxi, PR China

Xuanjun Wang High-Tech Institute of Xi'an, Xi'an, P.R. China

Yanlan Wang Science and Technology on Applied Physical Chemistry Laboratory, Shaanxi Applied Physics-Chemistry Research Institute, Xi'an, Shaanxi, China

Yin Wang Science and Technology On Applied Physical Chemistry Laboratory, Shaanxi Applied Physics-Chemistry Research Institute, Shaanxi, China

Yuan-jing Wang China Academy of Ordnance Science, Beijing, China

Zhenghong Wang Liaoning Qingyang Chemical Industry Corporation, Liaoyang, Liaoning, China

Zihao Wang State Key Laboratory of Explosion Science and Technology, Beijing Institute of Technology, Beijing, China

Ding Wei Xi'an Modern Chemistry Research Institute, Xi'an, China

Lijun Wu Shandong Non-Metallic Materials Institute, Jinan, Shandong, China

Lizhi Wu School of Chemistry and Chemical Engineering, Nanjing University of Science and Technology, Nanjing, China

Qingpo Wu School of Ordance Engineering, Naval Engineering University, Hubei, Wuhan, China

Shuxin Wu Xi'an Modern Chemistry Research Institute, Xi'an, China

Xiong-Gang Wu Xi'an Modern Chemistry Research Institute, Xi'an, PR China

Haijun Xi Liaoning Qingyang Chemical Industry Corporation, Liaoyang, Liaoning, China

Min Xia Beijing Institute of Technology, Beijing, China

Lei Xiao School of Chemistry and Chemical Engineering, National Special Superfine Powder Engineering Research Center of China, Nanjing University of Science and Technology, Nanjing, China

Xiao Xiao Xi'an Modern Chemistry Research Institute, Xi'an, China

Linsheng Xie East China University of Science and Technology, Shanghai, People's Republic of China

Wuxi Xie Xi'an Modern Chemistry Research Institute Xi'an, Shaanxi, China

Xiaoling Xing Xi'an Modern Chemistry Research Institute, Xi'an, China

Bin Xu School of Chemistry and Engineering, Nanjing University of Science and Technology, Nanjing, China

Hong-tao Xu Xi'an Modern Chemistry Research Institute, Xi'an, China

Min Xu Xi'an Modern Chemistry Research Institute, Xi'an, China

Xinying Xue Xi'an Modern Control Technology Research Institute, Xi'an, China

Qining Xun Shandong Non-Metallic Materials Institute, Jinan, Shandong, China

Caimin Yang School of Chemistry and Chemical Engineering, Nanjing University of Science and Technology, Nanjing, China;
Micro-Nano Energetic Devices Key Laboratory, Ministry of Industry and Information Technology, Nanjing, China

Desheng Yang School of Materials Science and Engineering, Beijing Institute of Technology, Beijing, China

Hongtao Yang Xi'an Modern Chemistry Research Institute Xi'an, Shaanxi, China

Li-bo Yang Xi'an Modern Chemistry Research Institute, Xi'an, China

Lilong Yang Xi'an Modern Chemistry Research Institute Xi'an, Shaanxi, China

Shishan Yang Xi'an Modern Chemistry Research Institute, Xi'an, China

X. H. Yang Institute for Frontier Technologies of Low-Carbon Steelmaking, School of Metallurgy, Northeastern University, Shenyang, China

Xiurong Yang School of Chemical Engineering/Xi'an Key, Laboratory of Special Energy Materials, Northwest University, Xi'an, China

Ding Yanqing Science and Technology on Aerospace Chemical Power Laboratory, Xiangyang, PR China;
Hubei Institute of Aerospace Chemotechnology, Xiangyang, PR China

Wang Yanwei Science and Technology on Aerospace Chemical Power Laboratory, Xiangyang, PR China;
Hubei Institute of Aerospace Chemotechnology, Xiangyang, PR China

Tian-le Yao Naval University of Engineering, Wuhan, China

Yinghua Ye School of Chemistry and Chemical Engineering, Nanjing University of Science and Technology, Nanjing, China;
Micro-Nano Energetic Devices Key Laboratory, Ministry of Industry and Information Technology, Nanjing, China

Xinran You Shandong Non-Metallic Materials Institute, Jinan, Shandong, China

Huipeng Zeng School of Chemistry and Chemical Engineering, Nanjing University of Science and Technology, Nanjing, China;
Micro-Nano Energetic Devices Key Laboratory, Ministry of Industry and Information Technology, Nanjing, China

Jianyou Zeng School of Chemical Engineering/Xi'an Key, Laboratory of Special Energy Materials, Northwest University, Xi'an, China

Chao Zhang Xi'an Modern Chemistry Research Institute, Xi'an, China

Chi Zhang School of Chemical Engineering/Xi'an Key, Laboratory of Special Energy Materials, Northwest University, Xi'an, China

Fang Zhang Science and Technology on Applied Physical Chemistry Laboratory, Shaanxi Applied Physics-Chemistry Research Institute, Xi'an, Shaanxi, China

Guangpu Zhang School of Chemistry and Chemical Engineering, Nanjing University of Science and Technology, Nanjing, Jiangsu, China

Hengning Zhang Xi'an Modern Chemistry Research Institute Xi'an, Shaanxi, China

Jun Zhang School of Ordance Engineering, Naval Engineering University, Hubei, Wuhan, China

Kun Zhang Xi'an Modern Chemistry Research Institute, Xi'an, Shanxi, PR China

Lei Zhang Science and Technology on Applied Physical Chemistry Laboratory, Shaanxi Applied Physics-Chemistry Research Institute, Xi'an, Shaanxi, China

Ming Zhang Science and Technology on Combustion and Explosion Laboratory, Xi'an Modern Chemistry Research Institute, Xi'an, China

Minghao Zhang Beijing Institute of Technology, Beijing, China

Rui Zhang Science and Technology on Applied Physical Chemistry Laboratory, Shaanxi Applied Physics-Chemistry Research Institute, Xi'an, Shaanxi, China

Siwei Zhang State Key Laboratory of Explosion Science and Technology, Beijing Institute of Technology, Beijing, China

Teng-yue Zhang China Academy of Ordnance Science, Beijing, China

Xi Zhang Xi'an Modern Chemistry Research Institute, Shaanxi, Xi'an, People's Republic of China

Xiaoxiao Zhang School of Chemistry and Engineering, Nanjing University of Science and Technology, Nanjing, China

Xiaozhi Zhang China North Chemical Research Academy Group Co., Ltd., Beijing, China

Yuling Zhang Department of Ammunition Engineering, Army Engineering University, Shijiazhuang, China

Zhe Zhang Shanghai Space Propulsion Technology Research Institute, Huzhou, China

Zhixiang Zhang Xi'an Modern Chemistry Research Institute, Xi'an, People's Republic of China

Fengqi Zhao Science and Technology on Combustion and Explosion Laboratory, Xi'an Modern Chemistry Research Institute, Xi'an, China

Juan Zhao Xi'an Modern Chemistry Research Institute, Xi'an, China

Wenhui Zhao National Key Laboratory of Transient Physics, Nanjing University of Science and Technology, Nanjing, Jiangsu, China

Xitong Zhao Xi'an Modern Chemistry Research Institute, Xi'an, China

Yayun Zhao Hubei Aerospace Vehicle Research Institute, Wuhan, Hubei, China

Chuiqi Zhong National Key Laboratory of Transient Physics, Nanjing University of Science and Technology, Nanjing, Jiangsu, China

Jing Zhou Xi'an Modern Chemistry Research Institute, Xi'an, China

Lisheng Zhou Xi'an Modern Chemistry Research Institute, Xi'an, China

Wen-jing Zhou Xi'an Modern Chemistry Research Institute, Xi'an, China

Sihua Zhu School of Ordance Engineering, Naval Engineering University, Hubei, Wuhan, China

Yi-ju Zhu Xi'an Modern Chemistry Research Institute, Xi'an, China

Yonghu Zhu School of Chemistry and Chemical Engineering, Nanjing University of Science and Technology, Nanjing, China

Yingying Zuo Shanxi North Xing'an Chemical Industry Co, Ltd., Taiyuan, China

Chapter 1
Carbon Nanodots Doped Graphite Carbon Nitride Towards Highly Efficient Visible Light Driven-Photocatalytic Hydrogen Evolution

J. N. Liang and X. H. Yang

Abstract Graphite carbon nitride (g-C_3N_4), as one of the promising candidates for photocatalytic hydrogen evolution, owns the advantages of visible light response, good stability, and no harm to the environment. However, the photocatalytic water splitting of g-C_3N_4 has been limited due to its slow photocarrier transfer rate and insufficient light absorption. Herein, carbon dots (CDs) were prepared by a hydrothermal method using ginkgo biloba leaves as the raw material. Afterwards, the g-C_3N_4 nanosheets decorated with CDs were obtained by a thermal polymerization method. CDs have unique way of light-induced charge transfer and special heterogeneous interface. The reservoir characteristics of the composite enable to greatly reduce the recombination of photo-generated carriers and significantly improve the hydrogen evolution efficiency. In this work, we found that g-C_3N_4 decorated with 1.0 wt% CDs achieved the highest hydrogen evolution rate (2878.2 μmol/h/g) under visible light ($\lambda > 420$ nm), which was about 5 times higher than that of pristine g-C_3N_4 (582.2 μmol/h/g). Schematic illustration of the separation and transfer of photo-generated charge carriers of CDs-g-C_3N_4 nanoparticles under visible light irradiation.

J. N. Liang · X. H. Yang (✉)
Institute for Frontier Technologies of Low-Carbon Steelmaking, School of Metallurgy, Northeastern University, Shenyang 110819, China
e-mail: yangxh@mail.neu.edu.cn

J. N. Liang
e-mail: 1971364@stu.neu.edu.cn

A. Gany and X. Fu (eds.), *2021 International Conference on Development and Application of Carbon Nanomaterials in Energetic Materials*, Springer Proceedings in Physics 276,
https://doi.org/10.1007/978-981-19-1774-5_1

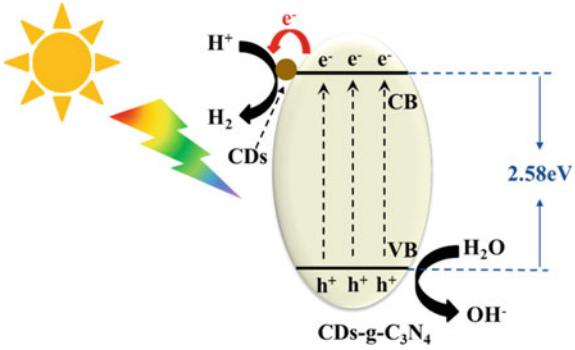

1.1 Introduction

Converting inexhaustible solar energy into clean hydrogen energy is considered as one of the most important strategies to solve environmental pollution and energy consumption problems [1–3]. In this scenario, exploring sustainable and efficient photocatalysts have attracted tremendous attention of scientific researchers. As a typical organic polymer semiconductor, widely studied g-C_3N_4 has a planar two-dimensional layered structure similar to graphite, and the layers are connected through van der Waals forces. Due to its visible light absorption, suitable band gap, chemical stability, large specific surface area and low production cost, it is considered to be one of the most promising photocatalyst for solar to hydrogen conversion [4–6]. On the other hand, the photocatalytic performance of pristine g-C_3N_4 is normally limited by its fast recombination of photo-generated holes and electrons and low quantum efficiency. In order to overcome these issues and improve the over photocatalytic water splitting performance, researchers have carried out a series of exploration, including morphology control (nanosheets [7], nanotubes [8], nanospheres [9], nanorods [10], etc.), atomic doping (such as gold [11], silver [12], platinum [13], phosphorus [14], sulfur [15], etc.) and the construction of heterojunctions (metal oxides [16, 17], sulfides [18, 19], organics [20, 21], etc.). Among the modification strategies mentioned above, carbon dots (CDs) incorporation with g-C_3N_4 was a competitive alternative due to the resulting unique light-induced charge transfer and special coupling heterogeneous interface.

Compared with metal quantum dot materials, CDs have higher biocompatibility and lower cytotoxicity, excellent optical properties, good water solubility, abundant sources of raw material, and low preparation cost. Furthermore, they are less harmful to the environment. So far, CDs have been widely used in many fields such as bioimaging [22], drug delivery monitoring [23], chemical analysis [24], and energy development [25]. Therefore, convenient, simple and efficient synthesis methods of CDs could facilitate their transition from research laboratories to practical applications. In this work, we used autumn ginkgo leaves as raw materials and successfully

prepared CDs by one-step hydrothermal method, which provides a green, efficient and renewable way for mass production of high-quality CDs for versatile application in various fields.

Herein, we successfully prepared the CDs decorated g-C_3N_4 by a thermal polymerization method to improve the visible light induced water splitting H_2 evolution. The morphology and composition of the as-prepared composites were characterized by several analytical techniques, such as transmission electron microscopy (TEM), X-ray diffraction (XRD), ultraviolet-visible absorption spectroscopy (UV spectroscopy). The photo induced charge transfer was investigated by electrochemical workstation facilitated with simulated sun light irritation electrochemical workstation, etc. The photocatalytic water splitting performance of a set of CDs-g-C_3N_4 composites were measured and evaluated under visible light irradiation. We found that the hydrogen evolution capacity of CDs decorated g-C_3N_4 under visible light ($\lambda > 420$ nm) has been significantly improved compared with the pristine g-C_3N_4 under the same condition ($\lambda > 420$ nm visible light). Among them, 1.0 wt% of CDs can achieve the highest hydrogen evolution rate as high as 2878.2 μmol/h/g, about 5 times higher than pristine g-C_3N_4 (582.2 μmol/h/g).

1.2 Experimental Method

1.2.1 Synthesis of CDs-Doped g-C_3N_4 Nanosheets

1.2.1.1 Synthesis of CDs

The ginkgo leaves were collected and washed several times with deionized water and then put in an oven to dry 5 g of ginkgo leaves were added into 15 mL deionized water. Then the mixture was transferred into a 30 mL PTFE hydrothermal reactor and held at 200 °C for 24 h. After naturally cooled to room temperature, the resultant is suction filtered to obtain a brownish-yellow filtrate. The product CDs was collected after rotary evaporation.

1.2.1.2 Synthesis of CDs-Doped g-C_3N_4

CDs-doped g-C_3N_4 was synthesized by a typical thermal polymerization method. 10 g urea was dissolved in 10 mL deionized water. Then a certain quality of CDs was added (m_{CDs}: $m_{g\text{-}C3N4=}$0, 0.5 wt%, 1.0 wt%, 1.5 wt% and 2.0 wt%) into the above solution under stirring. The resultant was transferred into a covered alumina crucible, and calcined in a muffle furnace at 550 °C for 3 h in air at a speed of 5 °Cmin^{-1}. After naturally cooled to room temperature, the product was collected and ground into powder. It can be observed that the colour of the product gradually darkens from light yellow to brown.

1.2.2 Characterization

Powder X-ray diffraction (XRD) studies were performed by Phillips X′ pert Multipurpose X-ray Diffraction System (Philip MPD diffractometer) with Cu-Kα radiation ($\lambda = 1.54$ Å) at a setting of 40 kV and 40 mA. In the 2θ rang of 5°–90° at a scan rate of 0.13° s^{-1} to observe the phase composition and purity of the synthesized nanoparticles. The UV-vis diffuse reflectance spectroscopy (DRS) was carried out on Shimazu UV-2600 spectrophotometer to test the optical properties. The photoelectrochemical measurements were carried out with a CHI660E electrochemical workstation (Shanghai, China) by a three-electrode method. An Ag/AgCl electrode and a Pt wire electrode were employed as the reference electrode and counter electrode, respectively. ITO glass with a fixed area of 3 × 1 cm covered with the as-prepared photocatalysts was used as the working electrode. 0.5 M of Na_2SO_4 solution was used as the electrolyte and the whole three-electrode system was placed in a 100 ml Quartz electrolytic cell. A 300 W Xenon lamp (PLS-SXE300C) was used as the light source to test the photocurrent measurements (it curves) at a bias potential of 0.5 V and the electrochemical impedance spectroscopy (EIS) with a range of 0.01–10^5 Hz.

1.2.3 The Construction and Measurements of Photocatalytic Hydrogen Evolution

Specifically, the photocatalytic hydrogen production equipment consists of two main parts. They are a vacuum system and a meteorological chromatograph (GC7900, TCD detector, 5A° molecular sieve column and Ar_2 carrier), respectively. The photocatalytic reaction of the composite photocatalyst is carried out in an externally illuminated photoreactor (Pyrex glass) connected to a closed circulation system. 20 mg of photocatalyst was dispersed in 100 mL ultrapure water containing 10 vol% TEOA sacrificial agent and 3 wt% Pt co-catalyst by a magnetic stirrer. Purge with argon for half an hour before the reaction to remove residual air. In the experiment, the circulating water pump controlled the temperature of the reactor to stabilize at 5 °C. A 300 W Xe lamp (PLS-SXE300, Perfect Light) equipped with cut-off filters (AM 1.5G; $\lambda > 420$ nm) was used to irradiate for hydrogen production as the light source. The product is sent to the gas chromatograph for production analysis.

1.3 Results and Discussion

1.3.1 Morphology and Characterization of the Physical Structure of the Pristine g-C_3N_4 and CDs Decorated g-C_3N_4

The functional groups exited on the surface of CDs (such as –OH, –NH_2, –COOH) own excellent optical properties and high conductivity, which can provide a number of active sites for the reaction of catalysts. Arising from these good properties, a set of CDs-g-C_3N_4 composites were synthesized in this work. The pristine g-C_3N_4 and CDs-g-C_3N_4 composites were characterized by transmission electron microscopy (TEM), respectively. Figure 1.1a shows the morphology of the as-prepared g-C_3N_4, the layered nanosheet structure is consistent with the previous report. In Fig. 1.1b, c, it is noted that the CDs particles (about 2–3 nm in diameter) were successfully embedded in the g-C_3N_4, but the distribution of the CDs is relatively uneven. The CDs tend to be embedded in the larger mesopores of g-C_3N_4. The structure and the composition of CDs-g-C_3N_4 was analyzed by XRD. As shown in Fig. 1.1c, the peak at 13.0° is attributed to the (100) plane of g-C_3N_4, and the peak at 27.3° corresponds

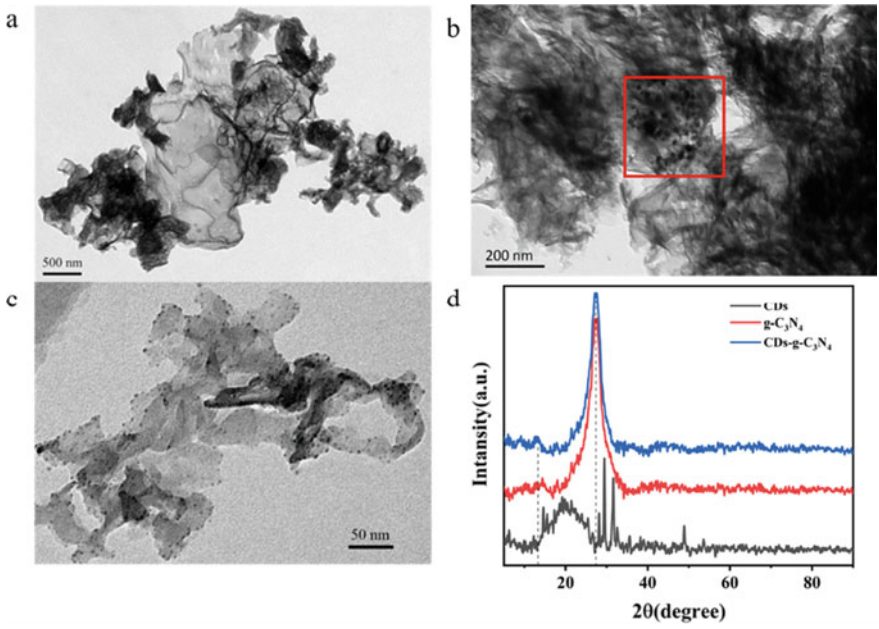

Fig. 1.1 Morphology and composition of the as-prepared photocatalyst. **a** TEM image of pristine g-C_3N_4; **b**, **c** Magnified TEM image of the CDs-g-C_3N_4 composites; **d** XRD patterns of pristine g-C_3N_4 and CDs-g-C_3N_4 composites

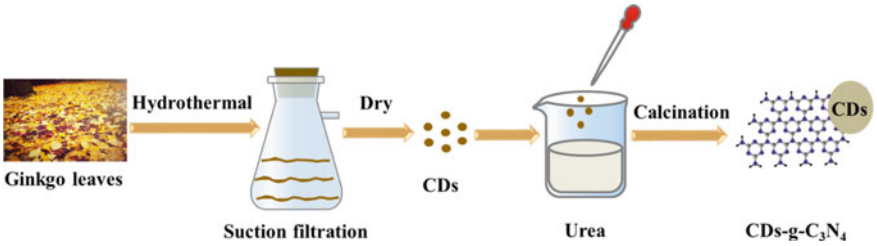

Scheme 1.1 Schematic illustration of the preparation of CDs and CDs-g-C_3N_4 nanoparticles

to the (002) crystal plane, which correspond to the repeating unit in-plane of tri-s-triazine and the stacked sandwich of conjugated aromatic structure, respectively. The XRD pattern showed the same peaks which confirmed that the intrinsic layer graphite structure was retained. The CDs are in amorphous state, and there are miscellaneous peaks nearby, which corresponds to the existence of chlorophyll and other biomass in the ginkgo leaves. The XRD of the CDs-g-C_3N_4 composite material did not change much compared with pristine g-C_3N_4 indicating that the interlayer spacing of the two samples is the same due to the extremely small amount of CDs doping (Scheme 1.1).

1.3.2 The Optical Properties of the Pure g-C_3N_4 and Composite Catalyst

The UV-vis spectra of g-C_3N_4 and CDs-g-C_3N_4 was collected and compared in Fig. 1.2. It can be found that the ability of g-C_3N_4 to absorb light changes after the

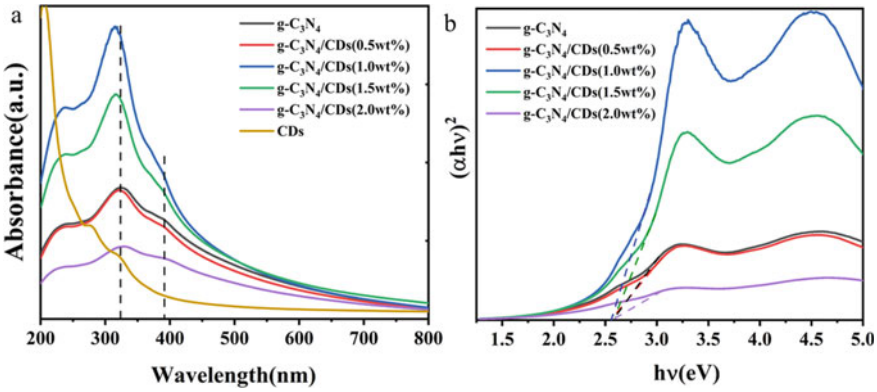

Fig. 1.2 Optical properties of the as-prepared photocatalyst. **a** UV-vis spectra of the pristine g-C_3N_4 and CDs-g-C_3N_4 composites; **b** Tauc plot curve of the pristine g-C_3N_4 and CDs-g-C_3N_4 composites

CDs decoration. The UV spectrum of carbon dots has a strong absorption peak near 200 nm and a long tail in the ultraviolet (Fig. 1.2b). 1.0 wt% CDs-g-C_3N_4 provides a greatly enhanced light-absorbing ability and 1.5 wt% CDs-g-C_3N_4 provides a strong light-absorbing ability. The light absorption capacity of 0.5 wt% CDs-g-C_3N_4 was almost the same as that of pristine g-C_3N_4, while the light absorption ability of g-C_3N_4 doped with 2.0 wt% carbon dots is significantly reduced. At the same time, the Tauc plot was used to estimate the band gap of the semiconductor (convert the UV-vis spectrum to an αhv^2 vs hv curve, where a, h and v refer to the absorption coefficient, Planck's constant and the speed of light, respectively. Besides, $r = 2$ for direct band gap materials, $r = 1/2$ for indirect band gap materials). Figure 1.2b shows a good linear fit with $r = 2$, the absorption edge of g-C_3N_4 is about 460 nm, which corresponds to a band gap of 2.73 eV. It can be observed that the band gap of CDs-g-C_3N_4 dots composites does not change significantly, which remains around 2.58 eV.

1.3.3 Specific Surface Area of the Pure g-C_3N_4 and CDs-g-C_3N_4 Nanoparticles

The surface area plays a crucial role in determining the efficiency of photocatalytic reaction. Brunauer-Emmett-Teller (BET) surface area of the pristine g-C_3N_4 and CDs-g-C_3N_4 nanocomposites were measured, respectively. The typical characteristic of nitrogen adsorption and desorption curve produced by mesoporous solids is that the adsorption and desorption curves of isotherms are inconsistent, and hysteresis loops appear shown in Fig. 1.3a–c. The specific surface area of the pristine g-C_3N_4 reached to 82.8 m^2/g, which was consistent with previous reports that g-C_3N_4 nanosheets exhibit a higher specific surface area. As shown in Fig. 1.3, the specific surface area of the CDs-g-C_3N_4 was improved to varying degrees. Specifically, 1.0 wt% CDs-g-C_3N_4 has the largest specific surface area, reaching to 212.3 m^2/g, which is about 3 times that of g-C_3N_4. According to the pore size distribution diagram, the pore size distribution of g-C_3N_4 is relatively uniform, concentrates below 20 nm. As the carbon content increased, the diameter of the mesopores gradually decreases. When 1.0 wt% carbon dots are doped, the mesopore diameter is mainly concentrated around 2.6 nm. As the carbon content continues to increase, the mesopore diameter distribution increases. When doped with 2.0 wt% carbon dots, the mesopore diameter is mainly concentrated in the part larger than 10 nm. The doping of CDs enables to generate smaller mesopores, thereby increasing the specific surface area of the composite and providing more reactive sites. However, when the amount of CDs was excessive, the original pores of g-C_3N_4 would be fully covered, which may reduce the amount of reactive sites. Therefore, it is very important to choose the suit doping quantity of CDs for photocatalytic hydrogen evolution (Table 1.1).

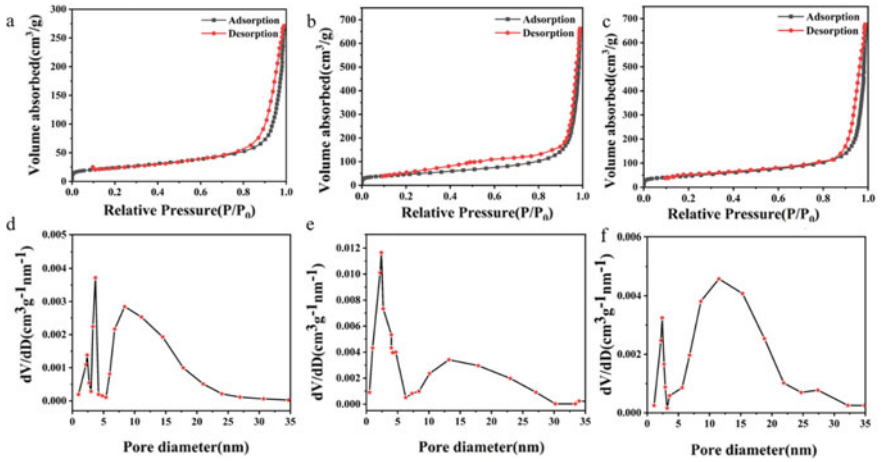

Fig. 1.3 BET analysis of CDs-g-C_3N_4.N_2 sorption isotherms and the corresponding pore distribution plot of the pristine g-C_3N_4, 1.0 wt% CDs-g-C_3N_4 and 2.0 wt% CDs-g-C_3N_4nanoparticles

1.3.4 Photocatalytic Hydrogen Evolution Performance

In order to evaluate the behavior of the charge transfer (CDs-g-C_3N_4), electrochemical impedance spectroscopy (EIS) and optical transient current tests were carried out conducted beforehand. As shown in Fig. 1.4a, it can be inferred that the g-C_3N_4 nanosheets has a large resistance, and the resistance had been reduced to some extent after the decoration of CDs. Among the samples, the resistance of 1.0 wt% CDs-g-C_3N_4 resistance is the smallest. However, the resistance of composite is still larger, indicating that the transfer rate of photogenerated carriers in the catalyst is relatively slow, and the CDs played a minor role in the transport process. In the corresponding photocurrent test, the current value of 1.0 wt% CDs-g-C_3N_4 current was proved to be the largest one, which was about 2 times higher than that of pristine g-C_3N_4. On the other hand, the transient currents of both pristine g-C_3N_4 and CDs-g-C_3N_4 were smaller, indicating that the separation and transfer of photogenerated hole-electron pairs carriers is not sufficient in this scenario (Fig. 1.4b). In the meanwhile, we carried out the photocatalytic hydrogen evolution test for pristine g-C_3N_4 and CDs-g-C_3N_4 under visible light irradiation ($\lambda > 420$ nm). As shown in Fig. 1.4c, d, the hydrogen evolution volume and the hydrogen evolution rate wewe improved obviously with the incorporation of CDs. The hydrogen evolution rate of pristine g-C_3N_4 was maintained at 582.2 μmol/h/g, and the volume of hydrogen production reached 2.985 mmol/g within 4 h. With the addition of CDs, the hydrogen evolution rate of CDs-g-C_3N_4 reached to the highest at 1.0 wt% CDs-g-C_3N_4. The volume of hydrogen evolution reached 12.475 mmol/g within 4 h. Compared with pristine g-C_3N_4, the 1.0 wt% CDs-g-C_3N_4 exhibited the highest hydrogen evolution rate (2878.2 μmol/h/g), which is 5 times higher than that of g-C_3N_4 (582.2 μmol/h/g).

Table 1.1 The specific surface area and pore distribution of the nanocomposites

	$g\text{-}C_3N_4$	0.5 wt%CDs-g-C_3N_4	1.0 wt%CDs-g-C_3N_4	1.5 wt%CDs-g-C_3N_4	2.0 wt%CDs-g-C_3N_4
Isotherm type	IV	IV	IV	IV	IV
Hysteresis loop type	H_3	H_3	H_3	H_3	H_3
BET (m^2/g)	82.8	115.9	212.3	173.0	189.6
Main pore diameter (nm)	3.6	5.6	2.6	2.0	11.6

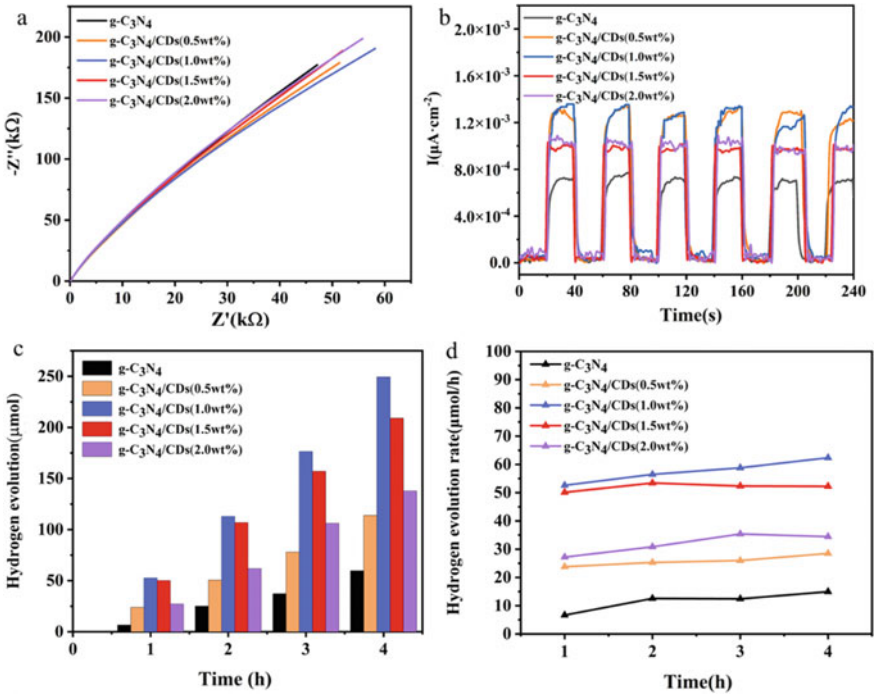

Fig. 1.4 The charge transfer properties and hydrogen production performance of CDs-g-C_3N_4. **a** electrochemical impedance spectra; **b** transient photocurrent response of the pristine g-C_3N_4 and CDs-g-C_3N_4 nanoparticles; **c**, **d** the hydrogen production and hydrogen evolution rate of pristine g-C_3N_4 and CDs-g-C_3N_4 nanoparticles under visible light ($\lambda > 420$ nm)

But keep increasing the CDs amount to 2.0 wt%, the hydrogen evolution rate dropped greatly.

1.4 Conclusions

In this work, a facile synthetic strategy of preparing CDs-g-C_3N_4 nanosheets from ginkgo biloba and urea was demonstrated by the combination of hydrothermal method and thermal shrinkage method. Under the reported conditions, CDs-g-C_3N_4 composite with CDs of about 2–3 nm were successfully obtained. The visible light response was greatly enhanced by incorporating CDs with g-C_3N_4. Based on the photocatalytic water splitting test of a series of CDs-g-C_3N_4 composites, 1.0 wt% CDs-g-C_3N_4 were found to have the best hydrogen evolution performance (2878.2 μmol/h/g), which is about 5 times that of pristine g-C_3N_4 (582.2 μmol/h/g) under visible light irradiation ($\lambda > 420$ nm). This is due to the special heterogeneous interface formed by the introduction of CDs increases the specific surface area of

g-C_3N_4 and provides more reactive sites for hydrogen production. The results of this work may shed light on the multifunctional application of CDs in a greener and environmentally friendly way, especially in energy conversion and environmental remediation fields.

Acknowledgements The authors are grateful for the financial support by the National Natural Science Foundation of China (No. 51901038 and No. 51974086), and the Fundamental Research Funds for the Central Universities (N2125027). Special thanks are due to the instrumental or data analysis from Analytical and Testing Center, Northeastern University.

References

1. J.H. Kim, D. Hansora, P. Sharma, J.-W. Jang, J.S. Lee, Toward practical solar hydrogen production—an artificial photosynthetic leaf-to-farm challenge. Chem. Soc. Rev. **48**, 1908–1971 (2019)
2. Z. Wang, C. Li, K. Domen, Recent developments in heterogeneous photocatalysts for solar-driven overall water splitting. Chem. Soc. Rev. **48**, 2109–2125 (2019)
3. L. Chen, G. Chen, C.-F. Leung, C. Cometto, M. Robert, T.-C. Lau, Molecular quaterpyridine-based metal complexes for small molecule activation: water splitting and CO_2 reduction. Chem. Soc. Rev. **49**, 7271–7283 (2020)
4. W. Wang, Y. Huang, Z.Y. Wang, Defect engineering in two-dimensional graphitic carbon nitride and application to photocatalytic air purification. Acta Phys.-Chim. Sin. **37**, 13 (2021)
5. S. Asadzadeh-Khaneghah, A. Habibi-Yangjeh, g-C_3N_4/carbon dot-based nanocomposites serve as efficacious photocatalysts for environmental purification and energy generation: a review. J. Clean Prod. **276**, 19 (2020)
6. Y.F. Li, M.H. Zhou, B. Cheng, Y. Shao, Recent advances in g-C_3N_4-based heterojunction photocatalysts. J. Mater. Sci. Technol. **56**, 1–17 (2020)
7. C. Han, Y.D. Wang, Y.P. Lei, B. Wang, N. Wu, Q. Shi, Q. Li, In situ synthesis of graphitic-C_3N_4 nanosheet hybridized N-doped TiO_2 nanofibers for efficient photocatalytic H-2 production and degradation. Nano Res. **8**, 1199–1209 (2015)
8. M. Faraji, M. Yousefi, S. Yousefzadeh, M. Zirak, N. Naseri, T.H. Jeon, W. Choi, A.Z. Moshfegh, Two-dimensional materials in semiconductor photoelectrocatalytic systems for water splitting. Energy Environ. Sci. **12**, 59–95 (2019)
9. Y.J. Zou, J.W. Shi, D.D. Ma, Z.Y. Fan, L. Lu, C.M. Niu, In situ synthesis of C-doped TiO_2@g-C_3N_4 core-shell hollow nanospheres with enhanced visible-light photocatalytic activity for H-2 evolution. Chem. Eng. J. **322**, 435–444 (2017)
10. A.K. Rathi, H. Kmentova, A. Naldoni, A. Goswami, M.B. Gawande, R.S. Varma, S. Kment, R. Zboril, Significant enhancement of photoactivity in hybrid TiO_2/g-C_3N_4 nanorod catalysts modified with Cu Ni-based nanostructures. ACS Appl. Nano Mater. **1**, 2526–2535 (2018)
11. M. Caux, H. Menard, Y.M. AlSalik, J.T.S. Irvine, H. Idriss, Photo-catalytic hydrogen production over Au/g-C_3N_4: effect of gold particle dispersion and morphology. Phys. Chem. Chem. Phys. **21**, 15974–15987 (2019)
12. Q. Zhang, Y.Y. Chai, M.T. Cao, F.L. Yang, L. Zhang, W.L. Dai, Facile synthesis of ultra-small Ag decorated g-C_3N_4 photocatalyst via strong interaction between Ag^+ and cyano group in monocyanamide. Appl. Surf. Sci. **503**, 8 (2020)
13. G.G. Zhang, Z.A. Lan, L.H. Lin, S. Lin, X.C. Wang, Overall water splitting by Pt/g-C_3N_4 photocatalysts without using sacrificial agents. Chem. Sci. **7**, 3062–3066 (2016)
14. M. Wu, J. Zhang, B.B. He, H.W. Wang, R. Wang, Y.S. Gong, In-situ construction of coral-like porous P-doped g-C3N4 tubes with hybrid 1D/2D architecture and high efficient photocatalytic hydrogen evolution. Appl. Catal. B-Environ. **241**, 159–166 (2019)

15. M.H. Vu, M. Sakar, C.C. Nguyen, T.O. Do, Chemically bonded Ni cocatalyst onto the S doped g-C_3N_4 nanosheets and their synergistic enhancement in H_2 production under sunlight irradiation. Acs Sustain. Chem. Eng. **6**, 4194–4203 (2018)
16. P. Karthik, T.R.N. Kumar, B. Neppolian, Redox couple mediated charge carrier separation in g-C_3N_4/CuO photocatalyst for enhanced photocatalytic H_2 production. Int. J. Hydrog. Energy **45**, 7541–7551 (2020)
17. D. Kim, K. Yong, Boron doping induced charge transfer switching of a C_3N_4/ZnO photocatalyst from Z-scheme to type II to enhance photocatalytic hydrogen production. Appl. Catal. B-Environ. **282**, 10 (2021)
18. R. Rameshbabu, P. Ravi, M. Sathish, Cauliflower-like CuS/ZnS nanocomposites decorated g-C_3N_4 nanosheets as noble metal-free photocatalyst for superior photocatalytic water splitting. Chem. Eng. J. **360**, 1277–1286 (2019)
19. E.D. Koutsouroubi, I. Vamvasakis, I.T. Papadas, C. Drivas, S.A. Choulis, S. Kennou, G.S. Armatas, Interface engineering of MoS_2-modified graphitic carbon nitride nano-photocatalysts for an efficient hydrogen evolution reaction. ChemPlusChem **85**, 1379–1388 (2020)
20. Y. Wang, F. Silveri, M.K. Bayazit, Q. Ruan, Y.M. Li, J.J. Xie, C.R.A. Catlow, J.W. Tang, Bandgap engineering of organic semiconductors for highly efficient photocatalytic water splitting. Adv. Energy Mater. **8**, 10 (2018)
21. C.P. Bai, J.C. Bi, J.B. Wu, H. Meng, Y. Xu, Y.D. Han, X. Zhang, Fabrication of noble-metal-free g-C_3N_4-MIL-53(Fe) composite for enhanced photocatalytic H-2-generation performance. Appl. Organomet. Chem. **32**, 7 (2018)
22. H.Q. Tao, K. Yang, Z. Ma, J.M. Wan, Y.J. Zhang, Z.H. Kang, Z. Liu, In vivo NIR fluorescence imaging, biodistribution, and toxicology of photoluminescent carbon dots produced from carbon nanotubes and graphite. Small **8**, 281–290 (2012)
23. M. Tuerhong, Y. Xu, X.B. Yin, Review on carbon dots and their applications. Chin. J. Anal. Chem. **45**, 139–149 (2017)
24. P. Zhang, T. Wang, X.X. Chang, L. Zhang, J.L. Gong, Synergistic cocatalytic effect of carbon nanodots and Co_3O_4 nanoclusters for the photoelectrochemical water oxidation on hematite. Angew. Chem.-Int. Edit. **55**, 5851–5855 (2016)
25. W.D. Li, Y. Liu, B.Y. Wang, H.Q. Song, Z.Y. Liu, S.Y. Lu, B. Yang, Kilogram-scale synthesis of carbon quantum dots for hydrogen evolution, sensing and bioimaging. Chin. Chem. Lett. **30**, 2323–2327 (2019)

Chapter 2
Effects of Carbon Nanofibers (CNFs) on Combustion and Mechanical Properties of RDX-Based Modified Single Base Propellant

Xiaoxiao Zhang, Xuekun Fan, You Fu, Bin Xu, and Xin Liao

Abstract To improve the properties of the modified single base propellant with RDX, propellant samples with different mass fractions of carbon nanofibers (CNFs) (0, 0.2, 0.4, 0.6, 0.8%) were prepared. The combustion performance of modified single base propellant samples were studied by closed bomb test and the mechanical properties were tested by universal material testing machine and beam impact testing machine. In addition, the microstructure was observed by SEM. Results show that agglomeration occurs when the CNFs content is greater than 0.2%. And the burning rate of the modified single base propellant increases after adding CNFs. The mechanical properties of single base propellant were improved after adding CNFs content of 0.2%, in which the tensile strength increased by 63%, 11.25%, 18% at −40 °C, 20 °C and 50 °C, respectively. The addition of CNFs can improve the stability of modified single base propellant.

2.1 Introduction

The single base propellant mainly consisting of nitrocellulose is widely used in the barrel weapons [1]. The history of the single base propellant is so long that its

X. Zhang · Y. Fu · B. Xu (✉) · X. Liao
School of Chemistry and Engineering, Nanjing University of Science and Technology, Nanjing 210094, China
e-mail: windieed@126.com

X. Zhang
e-mail: zxx18njust@163.com

Y. Fu
e-mail: nanligongzhuangyao@163.com

X. Liao
e-mail: liaoxin331@163.com

X. Fan
Academy of Ordnance Science, Beijing 100089, China
e-mail: fansnowsky@163.com

A. Gany and X. Fu (eds.), *2021 International Conference on Development and Application of Carbon Nanomaterials in Energetic Materials*, Springer Proceedings in Physics 276,
https://doi.org/10.1007/978-981-19-1774-5_2

manufacturing technology is mature. It also has excellent mechanical properties, high combustion stability and low ablation. However, its energy is too low to meet the requirement of modern army for the long range power of weapons. RDX is a high energy density substance, which can effectively improve the energy of the propellant [2]. Nevertheless, the addition of RDX has influence on the mechanical properties, combustion properties and thermal decomposition properties of the single base propellant, thus the ballistic and safety properties of the weapon will be affected [3].

Carbon nanofibers (CNFs) are a kind of discontinuous graphite fibers, which are obtained by cracking gas phase hydrocarbons [4]. Carbon nanofibers have many advantages such as large aspect ratio, massive specific surface area and so on. And CNFs also performance well at mechanical strength [5], thermal conductivity and electrical conductivity [6]. CNFs now are widely used in composite materials, energetic materials and other fields. For example, Daniel B. Nileson and Dean M. Lester added carbon nanofibers of different mass fractions to a variety of energetic materials. It is found that the combustion performance of gun propellant and propellant was improved [7]. Zhao Fengqi, Chen Pei and others adding carbon fibers into RDX/AP/HTPB propellant as a kind of burning rate regulator. As a result, the decomposition peak temperature of AP decreases. The initial partial liberation heat of the propellant increases. The peak of liberation heat and the burning rate is increased [8]. Hence CNFs has performed well in improving the properties of energetic materials, but the current researches focus more on combustion performance. While after using RDX to modify the single base propellant, the mechanical properties, combustion properties and thermal decomposition properties of the propellant are affected to some extent. In particular, mechanical properties of the single base propellant will decline. Hence, in this study, different content of CNFs was added to the modified single base propellant to explore its influence on combustion properties and mechanical properties.

2.2 Experimental

2.2.1 Meterials Preparation

The modified single base gun propellants were composed of Nitrocellulose (NC, 12.6 nitrogen percent) from Luzhou Northern Chemical Industry Co., Ltd. (Sichuan, China), RDX from Gansu Yinguang Chemical Industry Co., Ltd. (Gansu, China), 2,4-dinitrotoluene(DNT) and diphenylamine (DPA) from Guoyao Group Chemical Reagent Co., Ltd. (Shanghai, China).

Table 2.1 Formula of modified single base gun propellant with different mass fraction of carbon nanofibers (CNFs)

Sample	*w* (%)				
	CNFs	NC	RDX	DNT	DPA
1#	0	81.0	10	8	1
2#	0.2	80.8	10	8	1
3#	0.4	80.6	10	8	1
4#	0.6	80.4	10	8	1
5#	0.8	80.2	10	8	1

2.2.2 Sample Preparation

Table 2.1 is the formulation of modified single base propellant with different content of CNFs (Aladdin Chemical Reagent Co., Ltd., Shanghai, China). The formulation of total solid mass is 350 g. And the plasticization was dissolved with acetone and ethanol (the volume ratio is 1:1) equivalent to 51% of the total mass of the sample solid. First, CNFs and a certain amount of acetone were mixed (The volume is 40 mL when the CNFs content is 0%. While for every 0.2% increase in CNFs content, acetone volume increased by 5 mL). Second, adding a small amount of OP-10 emulsifier (1/1000 of the volume of the solution) to increase decentralization with magnetic stirring of 30 min and ultrasonic treatment of 30 min to disperse the CNFs. Third, the nitrocellulose, DNT, DPA, RDX, ethanol and acetone were added to the kneading machine to be knead for 30 min. And adding CNFs-acetone mixed solvent to knead for 3 h. Then two different extrusion dies (dumbbell mould and single hole mould) and hydraulic press were used to get the propellant samples. Finally, all the samples put into fume hood to volatilize the solvent for 7 days, then were dried in a wet oven at 40 °C for 3 days and drying oven at 45 °C for 3 days to remove the solvent completely.

2.2.3 Combustion Performance

The closed bomb were tested at 20 °C. And the volume of the closed explosive is 104.97 cm^3 with the ignition pressure of 10.98 MPa. The filling density is 0.12 $g{\cdot}cm^{-3}$ and 0.20 $g{\cdot}cm^{-3}$, respectively. While the length of the samples are 40.00 mm.

2.2.4 Mechanical Properties

The impact strength, tensile strength and compression strength are tested according to the GJB 770B-2005 gunpowder test method. The experimental temperature is 20 °C.

The impact strength is tested by se2 simply supported beam pendulum impact tester and the length of the samples are 60.00 mm. The tensile strength and compression strength are tested by instron3367 universal material testing machine and the tensile sample was dumbbell type with the length of 40.00 mm. The ratio of length to diameter of the compression is 1:1.

2.2.5 Microstructure Test

The microstructure was tested by Quanta FEG 250 scanning electron microscope of American FEI company.

2.2.6 DSC Test

The thermal decomposition performance experiment was carried out with differential scanning calorimeter of HPDSC 827 produced by Mettler Toledo company. The samples were tested from 50 to 350 °C with the weight of 1.10 ± 0.02 mg. And the heating rate is 15 °C·min^{-1}.

2.3 Results and Discussion

2.3.1 Microstructure

Figure 2.1a shows the SEM images of carbon nanofibers (CNFs). As you can see, the diameter of the CNFs is at the nanometer level and the length is about 2 μm with a phenomenon of mutual entanglement. Figure 2.1b is a cross-sectional view of the single base propellant. It can be seen from the picture that the nitrocellulose is

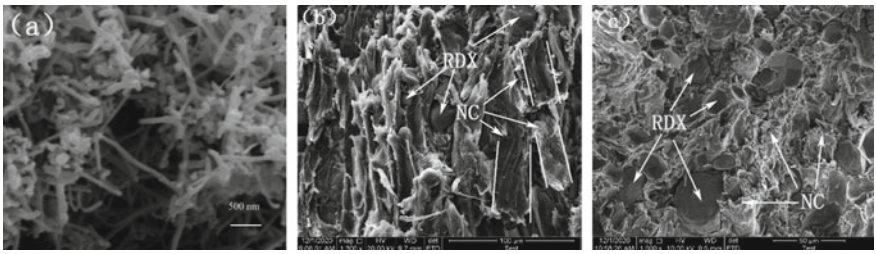

Fig. 2.1 SEM images of carbon nano fibers, modified single base propellant tear and fracture surfaces

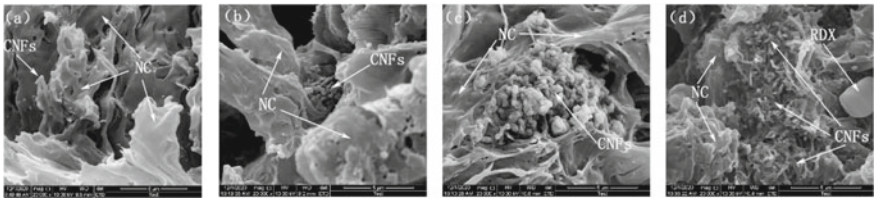

（a）0.2%　（b）0.4%　（c）0.6%　（d）0.8%

Fig. 2.2 SEM images of modified single base propellants with different mass fraction of CNFs

fibrous and twining and the diameter is between 10 and 50 μm. The nitrocellulose still maintains the basic skeleton after a series of processes. Figure 2.1c is a longitudinal fracture surface diagram of a single base propellant. It can be seen from the diagram that the RDX is ellipsoid with a diameter between 2 and 30 μm.

Figure 2.2 is the SEM images of modified single base propellant with different content of CNFs. It can be seen from the images that when the CNFs content is less, CNFs can be "inlaid" in nitrocellulose matrix. While agglomeration occurs when the CNFs content continues to increase.

2.3.2 Combustion Performance

For the purpose of studying the effect of CNFs on the combustion performance of modified single base propellant, the closed bomb was tested at 20 °C. The *u-p* curve was gotten from the closed bomb test, in which *u* is the firing rate of the propellant and *p* is the pressure measured by the closed bomb. It can be seen from the Fig. 2.3 that *u-p* curves were smooth, which shows that the stability of combustion is good. The burning rate of the modified single base propellant with CNFs was higher than that without CNFs, which is due to the good thermal conductivity of the CNFs in the combustion process of modified single base propellant [9]. But the burning rate decreases when the CNFs content is more than 0.2%. The reason is that excessive

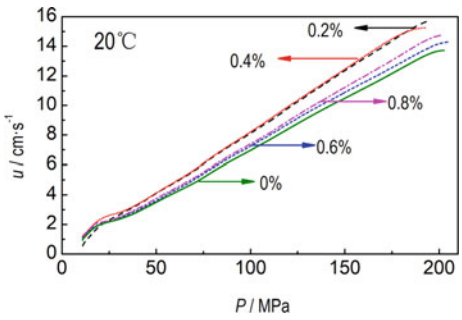

Fig. 2.3 *u-p* curves of modified single based gun propellant with different mass fraction of CNFs

Table 2.2 Combustion performance parameters of modified single base propellant with different content of CNFs

Sample	Parameter	P (MPa)				
		50–100	100–150	150-p_{dpm}	50-p_{dpm}	p_{dpm}
1#	u_1	0.0665	0.0610	0.0645	0.0671	203.04
	n	1.0118	1.0306	1.0165	1.0098	
2#	u_1	0.0809	0.0628	0.0869	0.0768	199.13
	n	1.0024	1.0570	0.9905	1.0148	
3#	u_1	0.0787	0.0673	0.0778	0.0756	193.10
	n	1.0105	1.0446	1.0141	1.0199	
4#	u_1	0.0675	0.0664	0.0854	0.0724	205.46
	n	1.0180	1.0209	0.9685	1.0017	
5#	u_1	0.0769	0.0589	0.0680	0.0719	203.37
	n	0.9934	1.0509	1.0200	1.0092	

Note u_1 is the burning rate coefficient, n is the burning rate pressure exponent, p_{dpm} is the pressure when dp/dt reaches its maximum value

CNFs can cause agglomeration [10], which cause that the contact area between the CNFs and the propellant matrix does not increase linearly with the increase of CNFs content. It can be confirmed from Fig. 2.2 that the agglomeration does exist.

Table 2.2 shows the combustion performance parameters of modified single base propellant with different content of CNFs. As can be seen from Table 2.2, the burning rate pressure exponent of the modified single base propellant with a CNFs content of 0.8% is less than 1 when the pressure is from 50 to 100 MPa. While the rest of the propellant are greater than 1. The burning rate pressure exponent of the modified single base propellants are greater than 1 when the pressure is from 100 to 150 MPa. The burning rate pressure exponent of the modified single base propellant with a CNFs content of 0.2% and 0.6% is less than 1 when the pressure is from 150 MPa to p_{dpm} MPa. Considering the whole pressure range (50 ~ p_{dpm} MPa), the burning rate pressure exponent of the sample is more than 1.

2.3.3 Energy Performance

The energy characteristic parameters of propellant are the basic index of propellant design and the important standard to evaluate the work ability of propellant. For the purpose of investigating the effect of CNFs content on the energy performance of the modified single base propellant, 15/1 single-hole tubular propellants were tested with the closed bomb to obtain propellant force (f) and covolume (a). Table 2.3 is the propellant force and covolume data of the samples. It can be seen from the table that propellant force of the samples basically remain unchanged, which indicates that the

Table 2.3 Energy properties of modified single base propellant

Sample	CNFs content (%)	f (kJ kg^{-1})	a (L kg^{-1})
1#	0	997.31	0.78
2#	0.2	997.68	0.80
3#	0.4	980.76	0.76
4#	0.6	989.42	0.75
5#	0.8	986.38	0.75

Note f is the propellant force, a is the covolume

addition of a small amount of CNFs has little effect on the energy performance of the modified single base propellant.

2.3.4 Mechanical Properties

The mechanical properties of the modified single base propellant were tested at different temperatures (−40, 20 and 50 °C). The results show in Table 2.4. As can be seen from Table 2.4, the mechanical properties all show increase first and then decrease as the CNFs content increases. The mechanical properties reach the maximum value at 0.2%. And the impact strength of 2# increases 21% from

Table 2.4 Effects of CNFs on the mechanical properties of modified single base propellant

Sample	T (°C)	α_k (kJ m^{-2})	σ_m (MPa)	δ_m (MPa)
1#	−40	11.10 ± 2.47	102.72 ± 2.73	58.59 ± 1.47
	20	18.18 ± 2.70	91.56 ± 2.53	54.44 ± 1.78
	50	27.05 ± 2.73	87.55 ± 3.09	39.28 ± 2.53
2#	−40	11.40 ± 1.60	104.13 ± 4.42	95.36 ± 1.55
	20	22.00 ± 2.35	99.01 ± 4.73	60.55 ± 1.68
	50	28.92 ± 2.71	96.81 ± 3.95	46.16 ± 1.17
3#	−40	10.00 ± 2.09	99.39 ± 3.58	80.52 ± 0.67
	20	18.16 ± 2.86	97.67 ± 5.78	59.24 ± 2.41
	50	25.78 ± 1.53	91.04 ± 1.61	40.93 ± 2.41
4#	−40	9.30 ± 1.76	98.43 ± 3.04	74.50 ± 2.43
	20	18.06 ± 1.94	94.59 ± 5.63	59.07 ± 2.73
	50	22.69 ± 2.38	90.07 ± 3.66	40.02 ± 2.89
5#	−40	8.64 ± 1.71	97.78 ± 4.87	64.84 ± 1.28
	20	12.78 ± 2.67	93.76 ± 2.76	57.21 ± 2.29
	50	22.44 ± 2.66	87.00 ± 1.78	39.21 ± 1.58

Note α_k is the impact strength, σ_m is the compressive strength, δ_m is the tensile strength

18.18 kJ·m^{-2} to 22.00 kJ·m^{-2} at 20 °C. While at −40 °C and 50 °C, it only increased by 3% and 7%, respectively. Compressive strength increased by 8% over 1# at 20 °C, 1.4% at −40 °C and 10.6% at 50 °C. The tensile strength increases by 11.2% at 20 °C, 63% at 40 °C and 18% at 50 °C, respectively.

Above all, when the content of CNFs is 0.2%, the mechanical properties of the modified single base propellant reach the maximum value, in which the impact strength, tensile strength and compressive strength are greatly improved at 20 °C, the impact strength changes little at 50 and 40 °C. And the tensile strength is greatly improved at −40 °C. The reason is that the CNFs and nitrocellulose matrix become a more uniform mixture after mixing (Fig. 2.2). When the external stress propagates in the propellant, the structure composed of nitrocellulose and CNFs can improve the effect of stress transfer. So the nitrocellulose matrix were strengthened to enhance the mechanical properties.

2.4 Thermal Decomposition Performance

The thermal decomposition performance at the heating rate of 5 °C·min^{-1}, 10 °C·min^{-1}, 15 °C·min^{-1} and 20 °C·min^{-1} are shown in Table 2.5 and Fig. 2.4. As can be seen from Table 2.5 and Fig. 2.4, the initial decomposition temperature and the exothermic peak temperature are basically unchanged after adding CNFs. While the exothermic heat increases first and then decreases with the increase of CNFs content and reaches the maximum when the CNFs content is 0.2%. The main reasons caused the decreasing trends are catalytic effect and high thermal conductivity of CNFs [7].

The activation energy of thermal decomposition kinetic parameters is obtained by using the Kissinger Eq. (2.4.1) through DSC experiments at the heating rate of 5 °C·min^{-1}, 10 °C·min^{-1}, 15 °C·min^{-1} and 20 °C·min^{-1}, respectively. The results of the temperature of the exothermic peak are shown in Table 2.6.

Table 2.5 Summarized results for DSC experiments of modified single base propellant with different mass fraction of CNFs at 5 °C·min^{-1}

Sample	CNFs content (%)	Tonset (°C)	T_{exo} (°C)	ΔH (J g^{-1})
1#	0	187.80	195.61	1933.02
2#	0.2	187.40	195.89	2008.24
3#	0.4	187.65	195.84	1940.87
4#	0.6	187.99	195.29	1910.05
5#	0.8	188.23	195.09	1922.37

Note T_{onset} is the temperature of the exothermic peak, T_{exo} is the temperature of the exothermic peak, ΔH is the enthalpy of decomposition

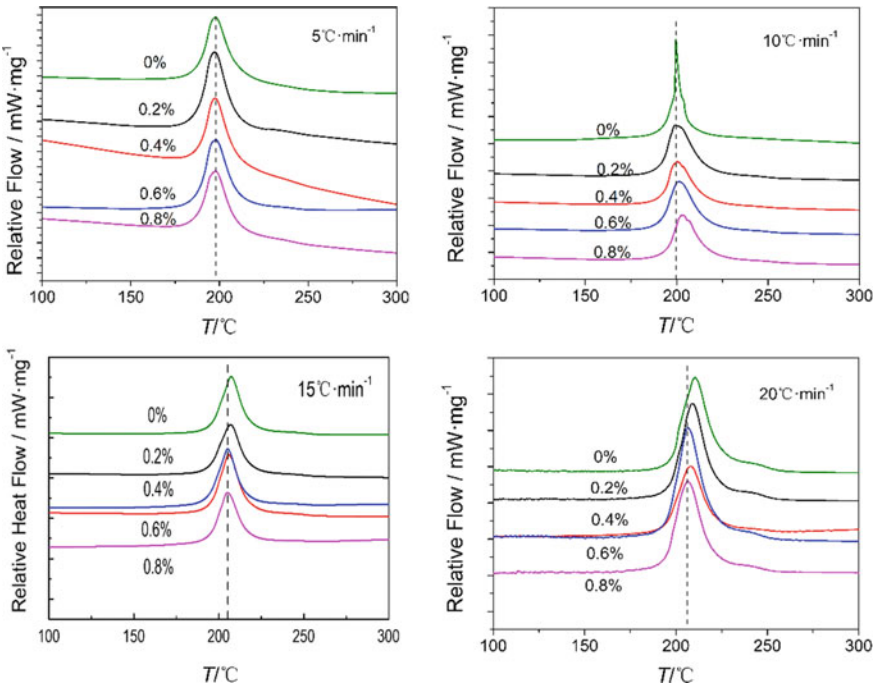

Fig. 2.4 DSC images of modified single base propellant with different mass fraction of CNFs at 5 °C·min^{-1}, 10 °C·min^{-1}, 15 °C·min^{-1} and 20 °C·min^{-1}, respectively

Table 2.6 Results of the temperature of the exothermic peak at the heating rate of 5 °C·min^{-1}, 10 °C·min^{-1}, 15 °C·min^{-1}, 20 °C·min^{-1}, respectively

Sample	CNFs content (%)	T_{exo} (°C)			
		5 °C·min^{-1}	10 °C·min^{-1}	15 °C·min^{-1}	20 °C·min^{-1}
1#	0	195.61	202.19	207.20	210.53
2#	0.2	195.89	201.99	206.90	210.12
3#	0.4	195.84	203.72	205.85	209.40
4#	0.6	195.29	201.43	205.33	208.44
5#	0.8	195.09	203.15	205.17	207.98

$$\ln\left(\frac{\beta}{T_p^2}\right) = \ln\frac{AR}{E_a} - \frac{E_a}{RT_p} \tag{2.4.1}$$

A is the preexponential, s^{-1}. R is the molar gas constant, 8.314 J·mol^{-1}·K^{-1}. β is the heating rate, K·min^{-1}. T_p is the temperature of the exothermic peak, K. Ea is the activation energy, kJ·mol^{-1}.The Ozawa equation is also a method of calculating kinetic parameters that can be used to verify the accuracy of the data obtained by the

Table 2.7 Results of activation energy of samples with different CNFs contents

Sample	CNFs content (%)	E_a/kJ·mol^{-1}	
		Ozawa equation	Kissinger equation
1#	0	177.34	174.29
2#	0.2	184.98	182.25
3#	0.4	187.39	187.09
4#	0.6	190.22	190.80
5#	0.8	191.37	192.65

Note E_a is the activation energy

Kissinger equation, as shown in (2.4.2)

$$\lg\beta = \lg\left(\frac{AE_a}{RG(a)}\right) - 2.315 - 0.4567\frac{E_a}{RT} \tag{2.4.2}$$

In the formula, G(a) is the function of conversion rate. The activation energy data obtained by Kissinger equation and Ozawa equation are shown in Table 2.7. It can be seen from the table that the activation energy data obtained by Kissinger equation and Ozawa equation are similar and can be considered to be accurate. After the addition of CNFs, the activation energy of the modified single base propellant increase with the increase of CNFs content. The activation energy was 175.82 kJ·mol^{-1} without CNFs, and 192.01 kJ·mol^{-1} with 0.8% CNFs. It shows that the addition of CNFs improves the stability of modified single base propellant. In conclusion, the addition of CNFs has little effect on the decomposition peak temperature of nitrocellulose and RDX, but it can improve the activation energy of propellant combustion process which shows the improvement of the thermal stability of modified single base propellant.

2.5 Conclusion

The burning rate of the modified single base propellant is increased with the addition of the CNFs. And the burning rate pressure exponent of the sample is greater than 1 in the whole pressure range (50 ~ p_{dpm} MPa). The propellant force basically decreases with the increase of CNFs content, but the variation range is little. The propellant force is basically unchanged when the CNFs content is 0.2%. With the increase of CNFs content, the mechanical properties of the modified single base propellant samples increase first but then decrease, and reach the maximum value when the CNFs content is 0.2%. The impact strength increases 21% at 20 °C and the tensile strength increases 63% at −40 °C. And the addition of CNFs can improves the stability of modified single base propellant.

References

1. Z. Wang, Prospect of propellant technology. J. North China Inst. Technol. (Soc. Sci. Ed.) **2001**(S1): 36–40+103
2. J. Shen, Z. Liu, B. Xu et al., Influence of carbon nanofibers on thermal and mechanical properties of NC-TEGDN-RDX triple-base gun propellants. Propellant Explos. Pyrotech. **44**(3), 355–361 (2019)
3. Y. Fu, B. Wang, X. Liao, et al., Influence of RDX on thermal property of modified single base propellant. Chin. J. Energ. Mater. (Hanneng Cailiao) **25**(02), 161–166 (2017)
4. D. Su, X. Chen, W. Gisela, et al., Hierarchically structured carbon: synthesis of carbon nanofibers nested inside or immobilized onto modified activated carbon. Angew. Chem. (Int. ed. in English) **44**(34), 5488–5492 (2005)
5. K. Shimoda, T. Hinoki, A. Kohyama, Effect of carbon nanofibers (CNFs) content on thermal and mechanical properties of CNFs/SiC nanocomposites. Compos. Sci. Technol. **70**, 387–392 (2010)
6. C. Xi, B. Jia, B. Cai, et al., Graphenized carbon nanofiber: a novel light-trapping and conductive material to achieve an efficiency breakthrough in silicon solar cells. Adv. Mater. **27**(5), 849–855 (2015)
7. B. Nielson Daniel, M. Lester Dean, Use of carbon fibrils to enhanced burn rate of pyrotechnics and gas generants. US5470408 (1995)
8. F. Zhao, P. Chen, S. Li, et al., Effect of burning rate regulator on thermal decomposition of RDX /AP/HTPB propellant. J. Propul. Technol. **4**(1), 80–82 (2003)
9. Q. Yan, F. Zhao, K.K. Kuo, et al., Catalytic effects of nano additives on decomposition and combustion of RDX-, HMX-, and AP-based energetic compositions. Prog. Energy Combust. Sci. **57** (2016)
10. F. Zhao, G. Tan, B. Cai, Application and development of nanomaterials in explosive and propellant. Chin. J. Explos. Propellants (04), 61–65 (2001)

Chapter 3
Preparation and Performance Characterization of CNTs/KNO_3 Composite Materials

Guanyi Wang, Zihao Wang, Siwei Zhang, and Qingzhong Cui

Abstract The presence of impurities such as amorphous carbon, carbon nanoparticles and catalyst particles in the crude products of carbon nanotubes is not conducive to the systematic study of the intrinsic physical and chemical properties of carbon nanotubes, and the purification of CNTs is required necessarily. In this paper, the CNTs/KNO_3 was purified by neutralisation method to increase their surface area for effective loading, and fully characterized. The results indicated the fractal dimension of the prepared CNTs/KNO_3 was increased, and the decomposition temperature and activation energy of CNTs/KNO_3 was elevated effectively compared with unloaded CNTs.

3.1 Introduction

The ignition transfer mechanism is the first element in the sequence of ammunition fire and explosion transfer [1], which is directly related to the ability of the ammunition to act reliably in a timely manner [2]. Due to the characteristics of modern warfare with fast manoeuvring and long-range strikes [3], the overload resistance of ammunition has raised higher requirements, even up to 2.4×10^5 g [4]. The traditional point-transmission pyrotechnics have defects such as poor ignition safety/transmission reliability at high loading densities [5], unstable combustion after long standing and poorly adjustable energy output, which can no longer guarantee the role reliability and use safety requirements of the munitions in complex environments [6]. The essence of the defects of the traditional ignition technology is that the heat transfer process is disturbed by the outside world and causes the energy release process to be shifted [7]. By reducing the binding scale of each component of the agent and realizing the nano-scale assembly of the agent components [8], the influence of the heat transfer process on the performance can be effectively reduced and the controlled output of energy can be further realized [9]. For solid oxidant/combustible agent systems

G. Wang · Z. Wang · S. Zhang · Q. Cui (✉)
State Key Laboratory of Explosion Science and Technology, Beijing Institute of Technology, Beijing 100081, China
e-mail: cqz1969@bit.edu.cn

A. Gany and X. Fu (eds.), *2021 International Conference on Development and Application of Carbon Nanomaterials in Energetic Materials*, Springer Proceedings in Physics 276,
https://doi.org/10.1007/978-981-19-1774-5_3

[10], carbon nanotubes are used as templates and artificial assembly techniques [11] are employed to assemble nanoscale oxidant/combustible agent particles onto their surfaces to achieve the ordered assembly of particle components [12].

The assembly of ordered nanostructured materials has been successfully applied in the fields of synthetic polymers [13], encapsulated nanomaterials [14], and multilayer functional material films [15] through weak intermolecular interactions such as electrostatic interactions [16], hydrogen bonding [17], coordination bonding [18], and charge transfer, but basic and applied research work on ordered nanostructured point-transmitting pyrotechnics is uncommon and needs to be broadened to explore the scope [19]. In this paper, a CNTs/KNO_3 composite was prepared by the reaction method approach and orthogonal experiments were applied to select and optimize the process parameters [20].

3.2 Process Conditions for the Preparation of CNTs/KNO_3 Composites Materials

In this paper, a composite material CNTs/KNO_3 synthesized by neutralisation method was presented and its raw material is shown in Table 3.1.

The process parameters of the CNTs/KNO_3 composite materials was selected and optimized by the orthogonal experiments. The factors of the orthogonal test were designed, and the mass ratio of folded KNO_3 to CNTs (A), mass of active agent (B), specific surface area of CNTs (C), reaction temperature (D), reaction time (E), stirring rate (F), titration rate of KOH (G), and addition time of KOH (H) were selected. A mixed orthogonal table L18 (2×3^7) was chosen and the levels of each factor are shown in Table 3.2

Among them, the carbon nanotubes were 100mesh sieve offsets with a mass of 1 g. The sonication dispersion time was 30 min, and the titration of potassium hydroxide solution to neutral was started at a fixed titration rate after 30 min of stirring, and then the titration was continued with heating and stirring for a specified time.

The amount of carbon nanotubes added in the test was 1 g, and the actual loading (weight gain) of the composite was used as the evaluation index, and the results were processed in Table 3.3.

Table 3.1 Raw materials and reagents

Number	Category	Specification	Place of product
1	CNTs	L-1020, L-2040, S-60100	Shenzhen Nanoport Co.
3	KOH	Analytically pure	Beijing Yili Fine Chemical Co., Ltd.
4	HNO_3	Analytically pure	Beijing Yili Fine Chemical Co., Ltd.
5	SDBS	Analytically pure	Tianjin Yaohua Chemical Reagent Co., Ltd.

Table 3.2 The orthogonal experimental factor level table for the preparation of CNTs/KNO_3 composite materials by reaction method L_{18} (2×3^7)

Leves	Factors							
	A (g)	B (%)	C ($m^2\ g^{-1}$)	D (°C)	E (h)	F ($r\ min^{-1}$)	G ($d\ min^{-1}$)	H (min)
1	2:1	0	160–180	65	2.0	300	60	30
2	5:1	0.001	60–70	75	2.5	400	90	45
3	10:1	0.002	55–65	85	3.0	–	120	60

Table 3.3 Orthogonalization of results

Orthogonalization		Factors							
		A	B	C	D	E	F	G	H
Reaction method	$\overline{K}_1$	1.02	1.15	1.23	1.12	1.09	1.05	1.24	1.14
	$\overline{K}_2$	0.96	1.31	0.94	1.28	1.27	1.75	1.19	1.34
	$\overline{K}_3$	1.32	1.28	0.81	1.47	1.36		1.32	1.29
	R_j	0.36	0.16	0.42	0.35	0.27	0.30	0.13	1.20

In Table 3.2, $\overline{K}_j$ indicates the j-th level orthogonalization treatment mean, the term with the largest value indicates the factor with the greatest influence, and the R_j indicates the importance data of the influencing factor. The degree of influence of each factor is C > A > D > F > E > H > B > G. It has been concluded that the optimal optimization of experimental conditions of CNTs/KNO_3 composite materials was that the mass ratio of potassium nitrate to CNTs was 10:1, the amount of sodium dodecylbenzene sulfonate was 0.001% of CNTs, the specific surface area of CNTs was 160–180m^2/g, the reaction temperature was 85 °C, the reaction time was 3.0 h and the stirring speed was 300 r/min.

3.3 Characterization of Composite Material Properties

The structural and morphological properties of the CNTs/KNO_3 were fully characterized by SEM, XPS, and DSC/TG.

As seen from Fig. 3.1, compared with the unloaded carbon nanotubes, the material prepared by the reaction method has a layer of covering on the surface and ends, and the tube diameter ranges from 50 to 80 nm, and the loading effect of the reaction method is more uniform.

As seen in the above Fig. 3.2, the main components of the carbon nanotube surface coverings are K, N, and O. The spectral peak of C1s are between 285.0 and 289.5 eV, and judging from the binding ability of the 1 s electrons and nuclei of C atoms, the spectral peaks refer to the energy level spectrum of carbon in benzene and thick ring carbon atoms (≈285.0 eV-286.4 eV), —CH_2O— (≈286.3 eV), $\rangle$C=O (≈288.5 eV),

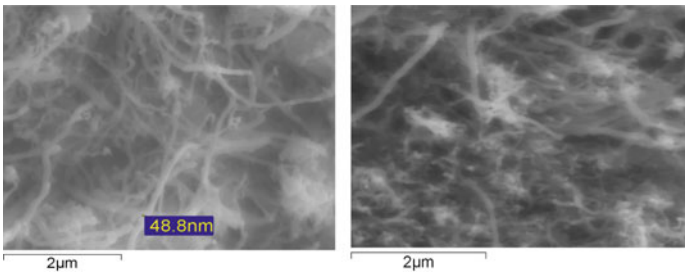

(a) KNO_3 (b) CNTs/KNO_3

Fig. 3.1 SEM of CNTs/KNO_3 composite

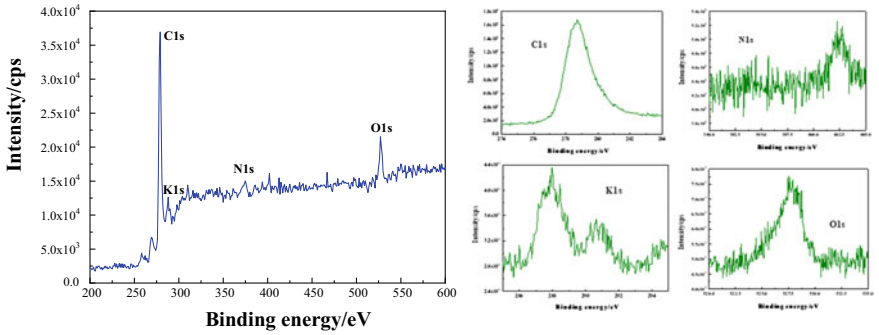

Fig. 3.2 XPS spectra of CNTs/KNO_3 composites prepared by reaction method

$\overset{O}{\overset{\|}{—C}}—O—$ (≈289.3 eV), and the spectral peak of o1s is at (≈532.0 eV). The XPS results further confirm that KNO_3 is attached to the surface of carbon nanotubes.

The thermal decomposition curves of the KNO_3 and the CNTs/KNO_3 composites prepared by the reaction methods were measured separately and the results are shown in Fig. 3.3.

As seen in Fig. 3.3, the thermal decomposition of pure KNO_3 consists of two heat-absorbing peaks and one exothermic peak. The absorbing peak corresponds to a peak top temperature of 133.17 and 331.09 °C. There is no loss of weight in the TG-DSC recording graph, which can be judged as the crystalline transformation peak and melting peak of KNO_3, and the exothermic peak is the decomposition peak of KNO_3 in the molten state, which corresponds to a peak top temperature of 429.26 °C. The thermal decomposition process can be described as:

① Crystallographic transformation: $KNO_3(r\,\mathrm{hom}\,bic) \rightarrow KNO_3(trigonal)$;

② Melting: $KNO_3(s) \rightarrow KNO_3(l)$;

③ Decomposition: $2KNO_3(l) \rightarrow 2KNO_2(l) + O_2$.

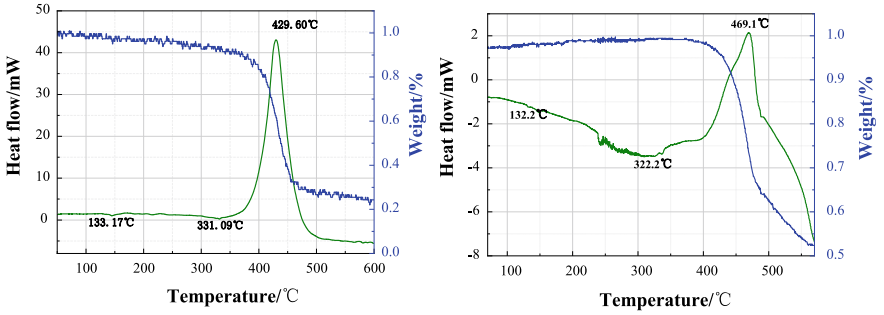

(a) KNO_3 (b) $CNTs/KNO_3$

Fig. 3.3 TG-DSC curves of $CNTs/KNO_3$ composites

Table 3.4 Calculation results of kinetic parameters of thermal decomposition

Material categories	Decomposition peak temperature (°C)	Kissinger methods			Ozawa methods	
		E_a (kJ mol^{-1})	lgA	γ	E_a (kJ mol^{-1})	γ
KNO_3	429.26	109.2	11.30	0.992	110.8	0.993
$CNTs/KNO_3$	469.10	188.7	19.67	0.994	187.0	0.992

The decomposition activation energies of KNO_3 and $CNTs/KNO_3$ composites were solved by the Kissinger and Ozawa methods (Table 3.4) on the basis of DSC/TG, respectively.

The results indicated that the addition of CNTs increased the decomposition peak temperature and drove the thermal decomposition of KNO_3 more difficult to occur.

3.4 Conclusion

In this paper, the functionalisation of carbon nanotubes, the preparation, characterisation and thermal decomposition patterns of $CNTs/KNO_3$ composites were investigated and the following conclusions were obtained.

The state of existence of KNO_3 crystals on CNTs as well as their content were demonstrated by the characterisation of the elemental composition, functional group structure and micro/nano scale surface interface of the composites using SEM, XPS and TG-DSC. The analysis of the thermal decomposition process of the materials showed that the thermal decomposition temperature and activation energy of the composites were elevated.

References

1. C. Huiqun, Z. Meifang, L. Yaogang, Novel carbon nanotube iron oxide magnetic nanocomposites. J. Magn. Magn. Mater. **305**(2), 321–324 (2006)
2. C. Mocella, J.A. Conkling, *Chemistry of pyrotechnics* (Taylor & Francis Group, New York, 2010)
3. F. Lupo, R. Kamalakaran, C. Scheu et al., Microstructural investigations on zirconium oxide–carbon nanotube composites synthesized by hydrothermal crystallization. Carbon **42**(10), 1995–1999 (2004)
4. J.A. Miller, C.T. Bowman, Mechanism and modeling of nitrogen chemistry in combustion. Prog. Energy Combust. Sci. **15**(4), 287–338 (1989)
5. H. Yoshida, T. Uchiyama, J. Kikkawa et al., Growth of single-walled carbon nanotubes on silicon nanowires. Solid State Commun. **141**(11), 632–634 (2007)
6. P.J.F. Harris, Solid state growth mechanisms for carbon nanotubes. Carbon **45**(2), 229–239 (2007)
7. D. Jain, R. Wilhelm, An easy way to produce α-iron filled multiwalled carbon nanotubes. Carbon **45**(3), 602–606 (2007)
8. J.S. Lee, B. Min, K. Cho et al., Al2O3 nanotubes and nanorods fabricated by coating and filling of carbon nanotubes with atomic-layer deposition. J. Cryst. Growth **254**(3–4), 443–448 (2003)
9. S.H. Lee, P.S. Alegaonkar, U.-H. Lee et al., Formation of buried-layer CNTs in porous SiO_2 templates. Diam. Relat. Mater. **16**(2), 326–333 (2007)
10. A.V. Krasheninnikov, K. Nordlund, Irradiation effects in carbon nanotubes. Nucl. Instrum. Methods Phys. Res., Sect. B **216**, 355–366 (2004)
11. M.K. Shukla, J. Leszczynski, A density functional theory study on the effect of shape and size on the ionization potential and electron affinity of different carbon nanostructures. Chem. Phys. Lett. **428**(4–6), 317–320 (2006)
12. W. Brenner, Environmental protection of pyrotechnic products and devices. AD-A034818/5 GA (1983)
13. S.C. Tsang, Y.K. Chen, A simple chemical method of opening and filling carbon nanotubes. Nature **372**(6502), 159 (1994)
14. S.T. Oyama, *Chemistry of Transition Metal Carbides and Nitrides* (Blackie Academic & Professional, London, 1997)
15. A. Esawi, K. Morsi, Dispersion of carbon nanotubes (CNTs) in aluminum powder. Compos. Part A: Appl. Sci. Manuf. **38**(2), 646–650 (2007)
16. D. Yang, L. Li, D. Yang, L. Li, The application of nano-oxide in nitramine propellant. Proc. Int. Pyrotech. Semin. **26**, 622–626 (1999)
17. T. Griffiths, et al., Dynamic vapour sorption studies of pyrotechnics. Int. Annu. Conf. ICT 32 (2001)
18. B. D'Andrea, F. Lillo, A. Faure et al., A new generation of solid propellants for space launchers. Acta Astronaut. **47**(2–9), 103–112 (2000)
19. X. Huang, C. Pan, X. Huang, Preparation and characterization of γ-MnO_2/CNTs nanocomposite. Mater. Lett. **61**(4–5), 934–936 (2007)
20. T.M. Tillotson, A.E. Gash, R.L. Simpson et al., Nanostructured energetic materials using sol–gel methodologies. J. Non-Cryst. Solids **285**(1–3), 338–345 (2001)

Chapter 4
Research on the Shock Ignition of CL-20 and HMX Based Explosives

Xiaoqiang Diao, Xiaoling Xing, Shunnian Ma, Xinying Xue, and Yan Qi

Abstract The shock sensitivities of HMX and CL-20 based explosives were obtained by shock initiation experiment, and the shock pressure of initiation were calculated, respectively. The results show that the critical initiation pressure of HMX based and CL-20 based explosive is 3.02 and 2.64GPa. The power work of the ignition process is analyzed intensively to establish an ignition criterion, and the difference of the two samples is quantized expressed as $\frac{W_{HMX}}{W_{CL-20}} = 1.145\frac{v_{CL-20Ds}}{v_{HMXDs}}$. The slab flyer test was simulated by using the explicit software, and the results show that the value of $\frac{v_{CL-20Ds}}{v_{HMXDs}}$ is between 1.08 and 1.12 with the different experimental conditions for the flyer.

4.1 Introduction

Semennov theory is a famous theory on the self-catalysis explosive reaction. Generally, one of the most important premises of the theory is that the temperature and the substance are well-distributed in the whole system. Actually the produced heat of the explosive sample is asymmetrical and the hot spot model is introduced to illustrate the initiation of the explosive samples under different conditions. The hot spot theory can be accepted and applied to describe the initiation of different explosives. Under shock conditions, the heat effect is reflected by the density of the explosive samples, and the microscopic structure is also embodied in the macroscopic test data. In this paper, the shock sensitivities of HMX and CL-20 based explosive samples

X. Diao · X. Xing (✉) · Y. Qi
Xi'an Modern Chemistry Research Institute, Xi'an 710065, China

X. Diao
e-mail: dxq312@163.com

Y. Qi
e-mail: qy8031@163.com

S. Ma · X. Xue
Xi'an Modern Control Technology Research Institute, Xi'an 710065, China
e-mail: xinying_xue@163.com

A. Gany and X. Fu (eds.), *2021 International Conference on Development and Application of Carbon Nanomaterials in Energetic Materials*, Springer Proceedings in Physics 276,
https://doi.org/10.1007/978-981-19-1774-5_4

were obtained by shock initiation experiment, and the shock pressure of initiation were calculated, respectively. The critical initiation pressure of HMX based explosive is much higher than CL-20 based explosives. The power work of the ignition process is analyzed intensively to establish an ignition criterion, and the difference of the two shock ignition processes is quantized expressed. The slab flyer test was simulated by using the explicit software FEA and AUTODYN, the difference of the shock energy for initiation of HMX-based and CL-20 based explosives was obtained in the research.

4.2 Experiment

4.2.1 Sample Preparation

The original HMX and CL-20 particles were refining by mechanical milling and the diameters of the particles between 85 and 95 um were selected by screening method. The energetic binder ETPE was selected and the compatibility of them was sufficient good. The mass ratio of main explosives and binder was 96:4.

The aqueous suspension method was employed to ensure the system uniformity of the binder coated HMX or CL-20. The particles obtained were dried and the crystal form of CL-20 was detected by FTIR. The particles were put into cylinder mould of 40 mm diameter and stressed under a pressure of 10 MPa.

4.3 The Experiments of Critical Initial Pressures for HMX and CL-20 Based Explosives

The certain RDX based explosive ($\Phi 40 \times 30$, $\rho = 1.675\ \mathrm{gcm}^{-3}$) was used to produce shock waves and the waves were transmitted in organic glass. The manganin pressure transducers were placed per 10 mm during the whole length of 55 mm. The pressure of the shock waves was determined and the reduction regulation of its transition in organic glass was obtained.

The critical initial pressures of shock experiments for HMX and CL-20 based explosives were carried under the same conditions, respectively.

4.4 Results and Discussions

1. The FTIR spectrum of CL-20 raw material and CL-20explosive

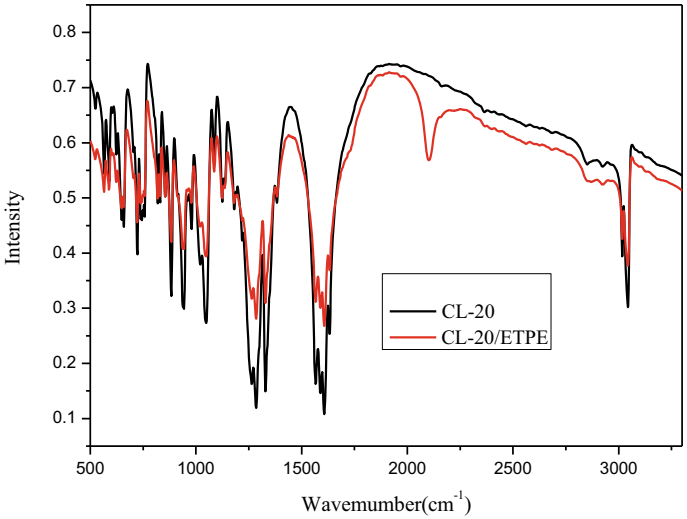

Fig. 4.1 The FTIR spectrum chart of CL-20 and CL-20 with binder

The crystal form was studied particularly after the whole dealing process. The spectrum was shown in Fig. 4.1. One can see that there is no phase transition takes place and the crystal form was not change after the coating process. The 2100 cm^{-1} can be attributed to the strong absorption of $-N_3$ from the binder structure. The results show that the ε-CL-20 phase was controlled well during the whole process.

2. The shock sensitivities of HMX and CL-20 based explosives

Generally, the shock sensitivity of explosives is measured by gap test method. The thickness of the clap board when 50% explosive explodes is regarded as the expression of the shock sensitivity. The pressure decay process of shock waves in organic glass was determined by the test point assemble per 10 mm during the whole length of the gap was 55 mm. and the relationship of the initiation pressure and thickness was shown in Fig. 4.2.

The decay tendency of shock waves pressure in dense medium can be expressed by exponential equation. The relationship between the imitation pressure and gap thickness of organic glass is fitted as Eq. 4.1:

$$p = 2.243 + 15.72\exp\left(\frac{-x}{13.48}\right) \tag{4.1}$$

where p is the pressure of shock waves in the organic glass, x is the thickness of the organic glass gap.

The thickness of the organic glass gap and the correspondingly pressure of shock wave values of different explosives are shown in Table 4.1.

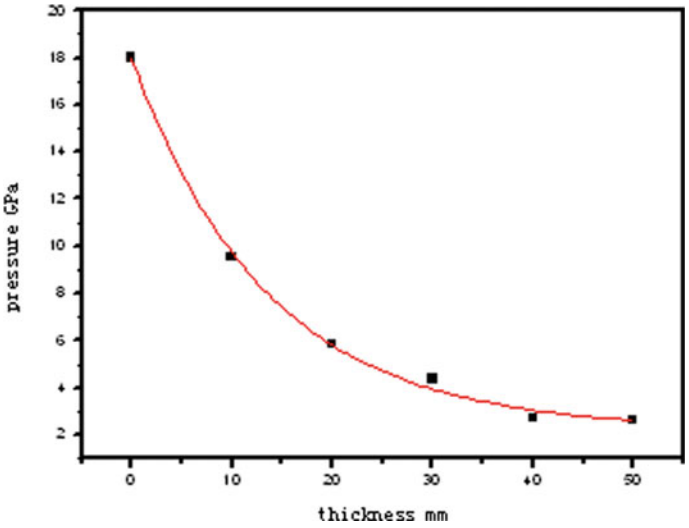

Fig. 4.2 The relationship between the imitation pressure and gap thickness of organic glass

Table 4.1 The thickness of the organic glass gap and the correspondingly pressure of shock wave values of HMX and CL-20 based explosives

Explosives	Thickness (mm)	Pressure (GPa)
HMX based	40.50	3.02
CL-20 based	49.51	2.64

The obtained pressure of shock wave values can be regard as the critical initiation pressures of HMX and CL-20 based explosives. The different values represent the shock sensitivity differences of different explosives. From Table 4.1, one can see that the critical initiation pressure of HMX based explosive is much higher than CL-20 based explosives, which means that the shock sensitivity of HMX based explosive is apparently lower than the other one.

3. The ignition criterion

The ignition process is not only determined by the ignition pressure, but also related to the sustaining time of the pressure. This can be expressed by Eq. (4.2).

$$p^2\tau = C \tag{4.2}$$

In which, C is constant and τ is the sustaining time of the pressure.

The physical signification of Eq. (4.2) is the absorbent energy of the certain explosives for the ignition. The unit area power work to the ignition process is expressed by Eq. (4.3), where u the velocity of the particle.

$$W = \int_{v}^{\tau} pud\tau = pu\tau = \frac{p^2\tau}{\rho_{mo} v_{D_s}} \tag{4.3}$$

$\rho_{mo} v_{D_s}$ keeps as the same value B for a certain explosive sample, and then Eq. (4.4) is obtained.

$$W = \frac{C}{B} = A \tag{4.4}$$

From Eq. (4.4), one can see that the unit area power is constant under the same sustaining time of the pressure for a certain explosive sample. This constant connects to the response characteristics of the sample for the shock waves. The shock wave with same intense for different explosive samples to the detonation, the time of duration is very different. The shock wave intense here cannot be lower than the critical pressure and the work can be employed as a criterion. The criterion work is the expression of the absorbent or storage energy by the explosive sample under the critical condition.

The value of B is constant as above mentioned for CL-20 or HMX based explosives, then Eq. (4.5) is obtained.

$$\frac{W_{HMX}}{W_{CL-20}} = \frac{C_{HMX}B_{CL-20}}{C_{CL-20}B_{HMX}} = \frac{\rho_{CL-20}}{\rho_{HMX}} \frac{v_{CL-20Ds}}{v_{HMXDs}} \frac{p_{HMX}^2 \tau_{HMX}}{p_{CL-20}^2 \tau_{CL-20}} \tag{4.5}$$

The distance of the shock wave in the organic glasses for HMX and CL-20 based explosives is 40.50 and 49.51 cm, respectively. The value of $\frac{\tau_{HMX}}{\tau_{CL-20}}$ is 0.818, and $\frac{p_{HMX}^2}{p_{CL-20}^2}$ is 1.308 under the shock ignition condition. The $\frac{\rho_{CL-20}}{\rho_{HMX}} = \frac{2.035}{1.900} = 1.07$ is assumed and Eq. (4.6) can be given from Eq. (4.5).

$$\frac{W_{HMX}}{W_{CL-20}} = 1.145 \frac{v_{CL-20Ds}}{v_{HMXDs}} \tag{4.6}$$

4. The simulation of the flyer velocity

The slab flyer test was simulated by using the explicit software FEA and AUTODYN, the value of v_{HMXDs} is from Ref. [1], and the value of $v_{CL-20Ds}$ is obtained with the same software method to insure the same setting. The parameters needed in the simulation of CL-20 is from Ref. [2]. The values of v_{HMXDs} and $v_{CL-20Ds}$ are listed in Table 4.2.

Table 4.2 The needed values of v_{HMXDs} and $v_{CL-20Ds}$

Sample	Velocity km s^{-1}			
HMX based	3.59	3.66	3.76	3.88
CL-20 based	3.88	3.99	4.14	4.34

One can see that the value of $\frac{v_{CL-20Ds}}{v_{HMXDs}}$ is between 1.08 and 1.12 with the different experimental conditions for the flyer by the CL-20 or HMX based explosive samples. Then Eq. (4.6) can be expressed as Eq. (4.7) here. Which means that the shock energy for initiation of HMX-based explosive is 23–28% higher than that of CL-20 based explosives.

$$1.23 \leq \frac{W_{HMX}}{W_{CL-20}} \leq 1.28 \tag{4.7}$$

4.5 Conclusion

1. The HMX and CL-20 based explosive samples are prepared for the shock sensitivity research. The crystal of CL-20 does not change from the FTIR determination.
2. The critical initiation pressure of HMX based explosive is much higher than CL-20 based explosives. The power work of the ignition process is analyzed intensively to establish an ignition criterion, and the difference of the two shock ignition processes is quantized expressed as $\frac{W_{HMX}}{W_{CL-20}} = 1.145\frac{v_{CL-20Ds}}{v_{HMXDs}}$.
3. The slab flyer test was simulated by using the explicit software, and the results show that the shock energy for initiation of HMX-based explosive is 23–28% higher than that of CL-20 based explosives.

References

1. D.E. Lambert, D.S. Stewart, S. Yoo, Experimental validation of detonation shock dynamics in condensed explosives. J. Fluid Mech. **546**, 227–253 (2006)
2. C.H.E.N. Wen, H.U. Xiaodong, Experimental study on impact initiation characteristics of a new explosive. Initiat. Pyrotech. **2**, 5–9 (2009)
3. H. Junming, C. Tianyun, *Explosion Theory* (Jiansu Science Technology Press, 1994)
4. S. Quancai, Y. Chonghui, J. Shaohua, *Theory* (Weapons Technology Press, 1997)
5. Z. Lin, *Basic Explosive Chemistry* (Beijing Institute of Technology Press, 2005)
6. W. Kicinski, W.A. Trzcinski, Calorimetry studies of explosion heat of non-ideal explosives. J. Therm. Anal. Calorim. **96**, 623 (2009)
7. A. Elbeih, A. Husarov, S. Zeman, Path to ε-HNIW with reduced impact sensitivity. Cent. Eur. J. Energ. Mater. **8**, 173–182 (2011)
8. M. Xiang, G. Rao, J. Peng, The numerical simulation on driven metallic flyer plate rule for the composite charge structure. Initiat. Pyrotech. **6**, 1–4 (2010)
9. B.M. Dobratz, LLNL Explosives Handbook: Properties of Chemical Explosives and Explosive Simulants, Lawrence Livermore National Laboratory, Rept. UCRL-52997, 1981
10. Y. Nan, J. Jiang, S. Wang, D. Chen, Z. Sun, X. Liu, JWL equation of state of detonation product for CL-20 based pressed composite explosive. Chin. J. Energ. Mater. **23**(6), 516–522 (2015)

Chapter 5
Molecular Dynamics Study of the Structure and Properties for CL-20/Graphene Composite

Lilong Yang, Tao Chen, Hengning Zhang, Hongtao Yang, and Wuxi Xie

Abstract Molecular dynamics was applied to study the famous high-energy density compound ε-CL-20 (hexanitro hexaazaisowurtzitane) crystal and ε-CL-20/graphene composite. Graphene was added into the three separate crystalline surfaces of CL-20 to build the CL-20/graphene composite. The vibrational mode, phonon density of states (DOS), binding energy, initiation bond length and elastic coefficient, isotropic mechanical properties (Young's modulus, bulk modulus, shear modulus, Poisson's ratio, Cauchy pressures and K/G) were studied for CL-20 crystals and CL-20/graphene composite. It turned out that the region of 1450–1750 cm^{-1} and 600–900 cm^{-1} corresponded to the main vibrational features of ε-CL-20. The ability of graphene to decrease the DOS of CL-20 at different crystalline surfaces was (100) > (001) ≈ (010). The interaction between an individual crystalline surface of CL-20 and graphene was different, and the binding energy of the three crystalline surfaces was ordered as (100) > (001) > (010). A study on the initiation bond length showed that the probable bond length (L_{prob}) of N–NO_2 increased in different extent and it was related to the sensitivity of the CL-20. By adding a little graphene, the mechanical properties of CL-20 could be efficiently enhanced, and the (100) crystalline surface exhibited better overall mechanical properties than the other crystalline surfaces. These findings have guided further studies on the application of CL-20 and its composite.

L. Yang (✉) · T. Chen · H. Zhang · H. Yang · W. Xie
Xi'an Modern Chemistry Research Institute Xi'an, Shaanxi 710065, China
e-mail: yanglilong.1988@163.com

H. Zhang
e-mail: zhanghn1985@aliyun.com

H. Yang
e-mail: yht540@163.com

W. Xie
e-mail: xiewuxi@163.com

A. Gany and X. Fu (eds.), *2021 International Conference on Development and Application of Carbon Nanomaterials in Energetic Materials*, Springer Proceedings in Physics 276,
https://doi.org/10.1007/978-981-19-1774-5_5

5.1 Introduction

Energy-rich materials are extensively applied in military and civilian areas, including propellants, explosives and pyrotechnics, etc. [1–3]. The traditional nitramines 1,3,5-trinitroperhydro-1,3,5-triazine (RDX) and octahydro-1,3,5,7-tetranitro-1,3,5,7-tetrazocine (HMX) are popular as explosives. However, it is less energetic and therefore unable to be extensively utilized in high-energy explosives and long-range weapons. To pursue higher chemical energies, a lot of effort has been devoted to design and synthesis of new energy-containing compounds [4]. According to the study, new high-energy polycyclic nitramine, 2,4,6,8,10,12-hexanitro-2,4,6,8,10,12-hexaazaisowurtzitane (CL-20) has a high density (approximately 2.0 g cm^{-3}), energy, and excellent detonation properties (velocity detonation is 9762 m s^{-1}, exceeding HMX by about 7%) [5–7]. Extensive research has been conducted to improve the decomposition and combustion performance of energy-containing composites, which include polymer bonded explosive [7] and propellant [8, 9]. CL-20 has attracted interest as a prospective candidate to replace energy-containing compounds like RDX, HMX and ammonium perchlorate (AP) used for future missile and space missions in order to achieve environmentally friendliness, high performances, high specific impulse (Isp) and low signature of propellant [10, 11]. However, due to many technical bottlenecks such as chemical compatibility, thermal and mechanical stability, high sensitivity to impact, friction, shock wave, thermal and electric spark, CL-20 is not yet a complete replacement for the commonly used explosives in most cases [12–14]. The development of effective methods to reduce CL-20 sensitivities is essential and has proven to be a challenging task.

In order to solve the problem of balancing high energy and low sensibility, some strategies have been conducted to lower sensitivities of high energetic materials. These approaches include modification of the particle surface by coating [15, 16], preparation of microcapsules by in situ polymerization [17], and exploration of high-energy cocrystals [18–20]. The coating method is the most effective way to reduce the sensibility of energy-containing materials [21]. In particular, the use of nanosized materials has attracted more and more attention [22]. Zhang et al. [13] investigated the phase transitions, thermal behavior, friction and impact sensitivity for ε-CL-20 coated in desensitizers (paraffin wax, microcrystal wax, graphite, molybdenum disulfide, tungsten disulfide, and graphite fluoride). It is shown as graphite lowered the phase transition critical temperature. The molybdenum disulfide/paraffin wax composite system decreased the friction and impact sensitivity for ε-CL-20. Li et al. [23] prepared nanocomposite with a lamellar arrangement structure using a simple and rapid anti-solvent crystallization method, which consisted of nanosheets comprising CL-20 and 1,3,5-triamino-2,4,6-trinitrobenzene (TATB), and further covered with dendritic nano-scale TATB. Owing to the multiple desensitization effect of this structure, the sensitivity of this nanocomposite is much lower and approximately comparable to that of the insensitive explosive LLM-105.

Graphene has been investigated as a desensitizing component for energy-containing materials because of its ultra-low mass density, excellent thermal and

electrical conductivity, good lubricity and superior mechanical performance [24–28]. Wang et al. [21] obtained a superior insensitive HMX/Viton/GO composite applied to the booster explosives by water suspension method using graphene oxide to decrease the sensitivity of the impact and shock wave. Li et al. [29] prepared an outstanding antistatic graphene nanoplates/lead styphnate composite with resistance to electrostatic spark sensitivity and static electricity accumulation for igniter applications using 2D graphene nanoplate (1 wt%) for minimizing the electrostatic hazard of explosive.

It is well known, that the conventional approach to study the energetic materials is experimental research [30–32]. Force field methods, particularly molecular dynamics, are currently an essential and excellent method for studying the structure and properties of material. MD simulations have been extensively used in the study of high-energy explosives and the results are well in accordance with experimental findings [33–36]. In this paper, graphene was added into the three separate crystalline surfaces for ε-CL-20 to build the CL-20/graphene composites. By using MD method the relationships among structure, energy, mechanical properties and sensitivity of three separate crystalline surfaces for CL-20 and CL-20/graphene composite were investigated. It is hoped that this study will contribute some basic data and direction to the further application research of CL-20 and its composite.

5.2 Model and Method

5.2.1 Construction of Models

The crystallographic parameters of ε-CL-20 are obtained by X-ray diffraction. The single cell parameters of ε-CL-20 are as follows: a = 8.852 Å, b = 12.556 Å, c = 13.386 Å, $\alpha = \gamma = 90°$, $\beta = 111.18°$. To begin with, a 2 × 3 × 3 supercell was built with Super cell using Material Studio software (MS) 8.0. The CL-20 crystals were cleaved along the different crystalline surface (001), (010), (100) using the cleave surface approach and then 10 Å vacuum layer was put in the periodic cells along the c direction. A new periodic 3D cell containing 72 ε-CL-20 molecules was constructed. Moreover, the model of single-layer graphene with 256 carbon atoms was also constructed. A after CL-20/graphene composite systems was built by adding graphene into the vacuum layer. The single molecular, single crystal, 2 × 3 × 3 supercell structures for ε-CL-20 and ε-CL-20(001)/graphene composites were shown in Fig. 5.1.

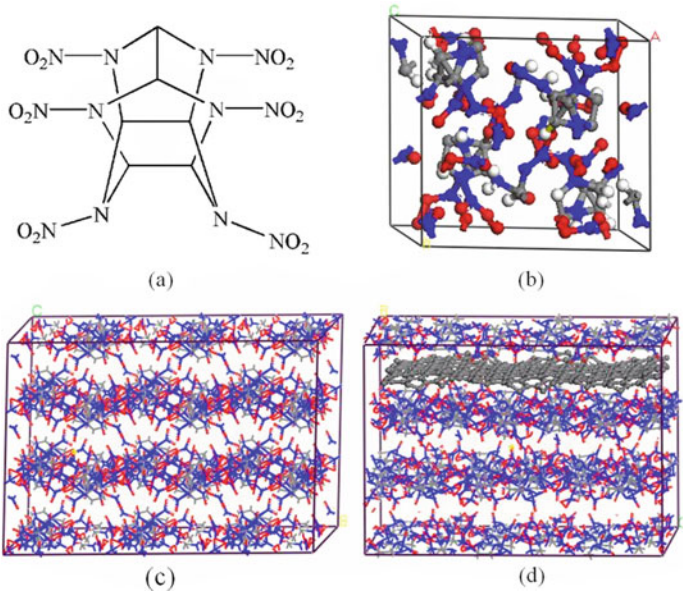

Fig. 5.1 Single molecular (**a**), single crystal (**b**), 2 × 3 × 3 supercell (**c**) of ε-CL-20 and ε-CL-20(001)/graphene composite (**d**). Color code: C, gray; O, red; N, blue; H, white

5.2.2 MD Simulation Method

Simulation has been carried out using Forcite module under COMPASS force field. First step was geometry optimization of CL-20 and CL-20/graphene composite. The quality of geometry optimization is "Fine". Algorithm is "Smart". The final structure with minimum energy is obtained through geometry optimization with 10,000 steps. The CL-20 structure was optimized and performed a vibrational analysis to obtain the vibrational intensities of the IR spectral bands. Hessian was generated by single-point energy calculation to visualize the normal vibrational modes. The Hessian matrix is the second order derivative matrix of energy and is employed to determine the normal mode of vibration. The next was executing dynamics of CL-20/graphene composite to get the equilibrium conformations, MD simulation with 1000 ps was performed under NPT ensemble, time step was 1 fs. The atom-based methods and Ewald summation are employed for van der Waals and electrostatic interactions. The Andersen thermostat temperature (298 K) and Berendsen barostat pressure (1.0×10^5 Pa) control algorithms were used throughout. The MD simulation system is in equilibrium when the temperature fluctuates within 10 k or when the energy fluctuates less near the average energy value. Finally, the effect of graphene on the structure, energy and mechanical properties of different crystalline surfaces for CL-20 was investigated. Phonon density of states simulation was conducted by Gulp module under Dreiding force field. Optimized structure was analyzed to get the state density of phonon.

5.3 Results and Discussionn

5.3.1 Structure of CL-20 and CL-20/graphene Composite

5.3.1.1 Vibrational Modes

Vibrational spectra are generated due to atoms vibrating around their average position. The frequency of the atomic vibrations depends on the environment in which the atom is located and its elemental type. There are several different methods of calculating vibrational spectra, which include molecular mechanics, semi-empirical and ab initio quantum mechanics methods. The frequencies calculated using molecular mechanics methods are highly related to the force field applied. The Forcite module combined with the COMPASS forcefield gives a good prediction of the vibrational frequencies because the force constants are well specified. Figure 5.2 showed the representative vibration mode of ε-CL-20 at frequency 1517 cm^{-1}. Table 5.1 showed the theoretical simulation along with the experimental infrared frequencies as reported in the literature [30] of ε-CL-20 and the vibrational mode assignment. The range 1450–1750 cm^{-1} corresponded to the NO_2 stretching vibration and the range 600–900 cm^{-1} corresponded to most bending and deformation (NNO bending, ring deformation, NO out of plane bending and ONO bending) vibration. Figure 5.2 displayed the major vibrational characteristics of ε-CL-20 appearing at 1517 cm^{-1}, that were consistent with ε-CL-20 published in the literatures [30, 37].

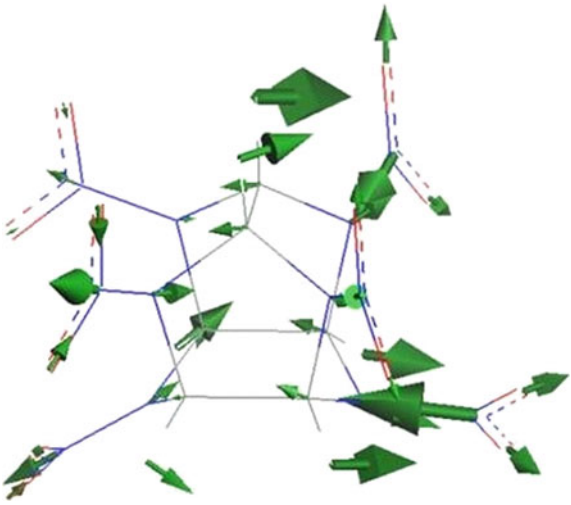

Fig. 5.2 Simulation vibrational mode of ε-CL-20 at 1517 cm^{-1} (the arrow indicates the vibration intensity)

Table 5.1 The theoretical simulation and experimental infrared [30] frequencies of ε-CL-20

Simulation (cm^{-1})	Literature (cm^{-1})	Vibrational mode assignment
380 vw, 402 w	445 vw	NNO bend
556 w	567 w	NNO bend
576 w	590 w	Ring def
708 s	705 vw	NO bend
722 s, 734 s, 743 s	723 w, 738 w, 744 w	NO bend; NNO_2 bend
776 s,781 w	750 w, 758 w	ONO bend; NO bend
836 vw, 858 vw, 891 w	820 w, 831 w,854 w,883 m	ONO bend; NO bend
908 w, 983 w	912 w, 980 w	Ring str; NN str
1101 m, 1144 w	1124 w, 1136 w	Ring str
1169 m	1182 w, 1191 w	CH bend; NO str sym
1280 m, 1302 m, 1329 m, 1337 m	1285 vs, 1298 vs, 1329 vs, 1338 vs	CH bend; NO str sym
1517 vs, 1525 s, 1536 m, 1545 m	1568 vs	Ring str; NN str, NO str sym
1706s, 1718 vs	1632 m	NO str asym
2951 vw	3017 m	CH str

vs very strong; *s* strong; *m* medium; *w* weak; *vw* very weak

5.3.1.2 Phonon Density of States

Atoms must be in constant motion due to the Heisenberg uncertainty principle, which is achieved by vibrations. At low temperature, the vibration corresponds to simple harmonic motion at the position of minimal energy, and with increasing temperature, it becomes more and more inharmonic vibration. For molecules, it will have 3 N-6 vibrational modes (or 3 N-5 for linear systems). With an infinite perfect three-dimensional solid, it will have a correspondence of an unlimited number of phonons. To characterize these phonons is done by calculating their values at points in reciprocal space, normally in the first Brillouin zone. Phonon density of states (DOS) of a solid, i.e., the number of frequency to frequency values, is a continual function when integrated over the entire Brillouin zone [38]. Although the complete integration of the Brillouin zone is not easy to achieve, this integration is approximated through numerical integration. To execute these integrals, the GULP module is applied. It is based on three known shrinking factors, n1, n2, and n3, each reciprocal to the lattice vector. The phonon density of states of the different crystalline surface for CL-20 crystal and CL-20/graphene composite was shown in Fig. 5.3. As shown in Fig. 5.3, the 200–2000 cm^{-1} range of frequencies contained the slow collective modes of the structure, which corresponded to the largest fluctuations of

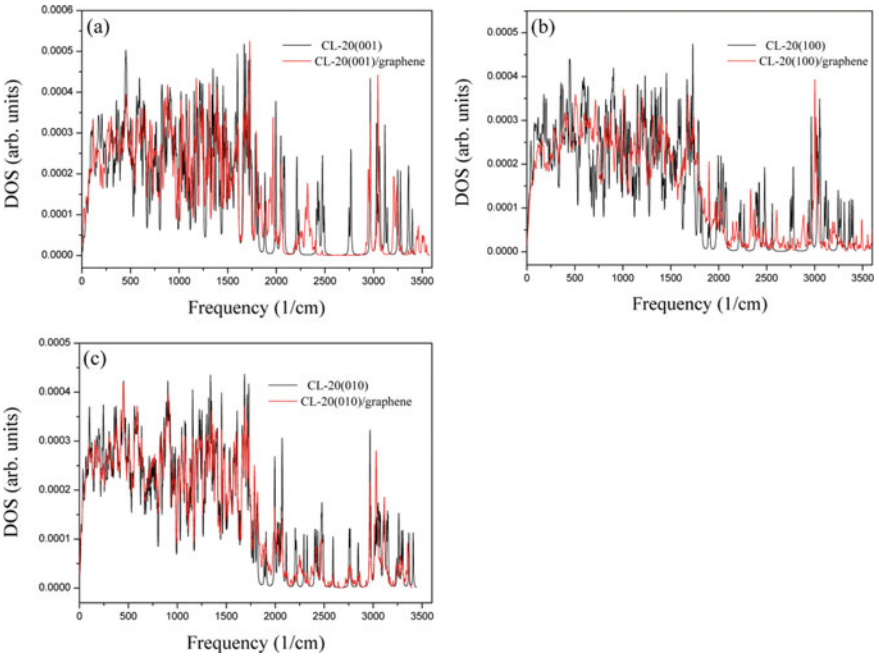

Fig. 5.3 Phonon density of states of different crystalline surface for CL-20 and CL-20/graphene composite. **a** 001, **b** 100, **c** 010 crystalline surface, respectively

the system. The DOS of different crystalline surface for CL-20 and CL-20/graphene composite showed a stronger peak within a range of 1550–1750 cm^{-1} frequencies, which was attributed to the stretching modes of ring, NN bonds, NO bonds symmetry and asymmetry. By comparing the total DOS of different crystalline surface for CL-20 and CL-20/graphene composite, it was observed that as the DOS of CL-20/graphene composite was lower than of CL-20, which can be attributed to the interaction or combine between sp^2 bonding networks stretching of graphene and vibration modes of CL-20. The intermolecular interaction between (100) crystalline surfaces of CL-20 and graphene was strongest. This feature can be attributed to the van der Waal's forces and electrostatic interactions. The ability of graphene to decrease the DOS of CL-20 at different crystalline surfaces was (100) > (001) ≈ (010).

5.3.1.3 Initiation Bond Length

An initiating bond is a chemical bond with minimal energy in a high-energy material. The initiating bonds are easily triggered by external influences and then explosion occurs. Therefore, it is important to study the changes of the initiating bonds. According to the study of CL-20, it was known that the initiating bond is N-NO_2 [34, 35]. Analysis of the N-NO_2 change for CL-20 contributes in investigating the

influence of graphene on the sensitivity for CL-20. The radial distribution function g(r) is applied to weigh the possibility of another atom appearing at the distance r to an assigned atom. The most probable bond length (L_{prob}) and the interactions between between the components are determined by radial distribution function. In general, chemical bond interactions are the most powerful forces. Intermolecular action consists of hydrogen bonds and van der Waals (vdW) forces, which in turn include dipole-dipole, induction, and dispersion interaction forces. Hydrogen bond, strong vdW, and weak vdW interaction forces correspond to the distance of 2.6–3.1 Å, 3.1–5.0 Å or above 5.0 Å between atoms, respectively [39]. From Fig. 5.4, it was found that the most probability between N–N atom pair in CL-20 to simultaneously arised in the distance of 1.15–1.60 Å and peak value in the g(r) curves was high to 6–14, illustrated that the strong chemical bond interaction was formed, and most probable bond length was determined in Table 5.2. The incorporation of

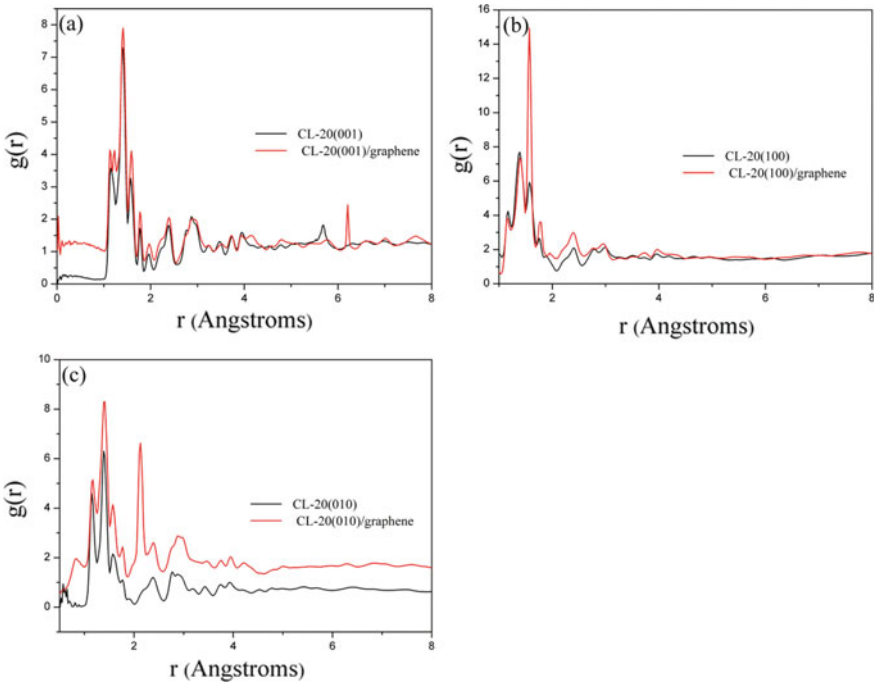

Fig. 5.4 Radial distribution function between N–N atom pair on three different crystalline surfaces of CL-20 and CL-20/graphene composite. **a** 001, **b** 100, **c** 010 crystalline surface, respectively

Table 5.2 Probable bond length L_{prob} of different crystalline surfaces of CL-20 and CL-20/graphene composite

Lprob (Å)	(0 0 1)	(1 0 0)	(0 1 0)
CL-20	1.39	1.39	1.39
CL-20/graphene	1.41	1.57	1.41

graphene modified the distribution width for N-NO_2 and slightly enhanced the probability for L_{prob}. Meanwhile, a peaks arised again in the 2.10–2.90 Å region, demonstrated there was strong intramolecular interaction. In the region of above 3.5 Å, a comparative high peak arised, predicted that some van der Waals interactions existed between them. In all, the interactions between N–N atom pairs in CL-20 are mainly intramolecular and chemical bonds. The study of the distribution for the initiation bond length indicated that there was a different increase in the L_{prob} of N–NO_2, which was associated with the sensitivity of CL-20. The order of L_{prob} was (100) > (001) = (010), which indicated that the (100) crystalline surface of CL-20/graphene composite owned higher sensitivity.

5.3.2 Binding Energy of CL-20 with Graphene

The equilibrium configuration of the model can be obtained by MD simulation. The binding energy ($E_{binding}$) can be used to evaluate the compatibilities of two components in a blends. It is determined in terms of the negative value of the intermolecular interaction energy (E_{inter}), i.e. $E_{binding} = -E_{inter}$. The E_{inter} is calculated from the total energy of the blend and the energy of the individual components at equilibrium condition. The $E_{binding}$ between CL-20 and graphene is calculated by the following formula.

$$E_{\text{binding}} = -E_{\text{inter}} = -\left(E_{\text{total}} - E_{\text{CL-20}} - E_{\text{graphene}}\right) \tag{5.1}$$

where E_{total} is the total energy for the CL-20/graphene hybrid system. $E_{CL\text{-}20}$ and $E_{graphene}$ are the total energy for CL-20 and graphene, respectively.

For comparison, the E_{total}, $E_{CL\text{-}20}$, $E_{graphene}$ and $E_{binding}$ of different crystalline surface were listed in Table 5.3. The results show that the binding energy of CL-20 (100) surface to graphene is stronger than that of (001) and (010) surfaces. That is, when graphene is added to CL-20 crystals, graphene is inclined to concentrate on the CL-20 (100) surface because of the higher intermolecular interaction. The interaction between separate crystal surfaces for CL-20 and graphene is distinct, and the binding energy order is (100) > (001) > (010).

Table 5.3 Binding energies (kcal mol^{-1}) for CL-20/graphene with graphene on three separate crystalline surfaces of CL-20 at 298 K

CL-20/graphene	Etotal	ECL-20	Egraphene	Ebinding
(0 0 1)	199,370.218	190,076.862	9609.182	315.826
(1 0 0)	203,473.862	194,241.571	9662.952	430.661
(0 1 0)	197,464.904	188,027.604	9679.403	242.103

5.3.3 Mechanical Properties

The mechanical properties of explosive have an essential impact on the performance of energetic materials in formation and safety in application. The relationship of stress and strain for material abides by the universal Hooke's law, and the equation is as below.

$$\sigma_i = C_{ij}\varepsilon_j \tag{5.2}$$

where C_{ij} (i,j = 1–6) is (6 × 6) a matrix of elastic coefficient. By considering the strain energy, the matrix of elastic coefficient is symmetrical, that is, $C_{ij} = C_{ji}$. Consequently, it has 21 elastic coefficients to express the relationship between stress and strain of anisotropic material. With regard to most commonly used anisotropic material, the 21 elastic coefficients C_{ij} are independent of each to other. The isotropic material has only two independent elastic coefficients, which are called Lame coefficients (λ and μ). Using λ and μ, the tensile modulus E, shear modulus G, bulk modulus K and Poisson's ratio γ is calculated by the following Eq. (5.3) [40]. The program supposes that the material is isotropic, and the computational isotropic mechanical characteristics of material are obtained.

$$E = \frac{\mu(3\lambda + 2\mu)}{\lambda + \mu}$$

$$K = \lambda + \frac{2}{3\mu}$$

$$G = \mu$$

$$\gamma = \frac{\lambda}{2(\lambda + \mu)} \tag{5.3}$$

Poisson's ratio (γ) is often used to assess the plasticity of materials. There is the relation between Poisson's ratio and different moduli as below.

$$E = 3K(1 - 2\gamma) = 2G(1 + \gamma) \tag{5.4}$$

Due to that matrix of elastic coefficients is symmetric, in Table 5.4 only were listed partial coefficients of three separate crystalline surfaces for CL-20 and CL-20/graphene composites. The differences in elastic coefficients of the separate crystalline surfaces for CL-20 and CL-20/graphene composite revealed that the analyzed CL-20 crystals have anisotropic properties in a certain degree. From Table 5.4, it could be seen that most of the elasticity coefficients of CL-20/graphene composite were reduced in comparison with pure CL-20 crystal, indicated that the stresses

Table 5.4 The elasticity coefficients and moduli of CL-20 and CL-20/graphene composite on different crystalline surfaces (in GPa)

Name	CL-20(001)	CL-20(001)/graphene	CL-20(100)	CL-20(100)/graphene	CL-20(010)	CL-20(010)/graphene
C11	13.32	9.94	7.35	5.18	10.68	8.59
C22	18.45	14.97	8.47	9.43	3.82	5.93
C33	10.25	6.97	7.00	5.36	4.97	6.57
C44	2.81	1.23	3.26	0.43	2.20	1.08
C55	3.60	2.63	0.95	0.20	1.49	1.01
C66	3.87	2.87	1.88	0.20	0.76	0.13
C12	4.08	3.99	12.89	11.17	10.05	17.74
C13	7.61	5.34	14.25	13.64	7.97	9.78
C23	4.55	4.31	12.68	10.13	15.70	11.17
E	9.18	7.63	1.85	0.83	2.13	1.90
K	7.34	5.04	9.92	9.59	8.86	9.36
G	3.43	2.91	0.63	0.28	0.73	0.65
C12- C44	1.27	2.76	9.63	10.74	7.85	16.66
Poisson's ratio	0.34	0.31	0.47	0.48	0.46	0.46
K/G	2.14	1.73	15.75	34.25	12.14	14.40

required to produce the same strain are reduced, i.e., the elasticity of CL-20/graphene composites was improved.

Cauchy pressure (C_{12}–C_{44}), which is a measure of ductility and brittleness for materials, with positive values indicating ductile and negative values indicating brittle. The data of the Table 5.4 predicted that compared to pure CL-20, all (C_{12}–C_{44}) values for CL-20/graphene composite with different crystalline surfaces were increased with a different extent, and the percentage increase of ductility of the different crystalline surfaces for CL-20 was (001) > (010) > (100). When graphene was placed on the (010) crystalline surface for CL-20, the obtained CL-20/graphene composite at 298 K had the best ductility, and the (C_{12}–C_{44}) value was 16.66.

Tensile modulus (E), bulk modulus (K), and shear modulus (G) are applied to evaluate the capacity of a materials to withstand elastic deformation. Toughness is the deformation capacity of a materials after absorption of energy and is determined from the ratio (K/G). The higher the K/G value, the stronger the toughness of the material. It was thus clear in Table 5.4 that the E, K, and G moduli of different crystalline surfaces for CL-20/graphene composite were reduced in comparison with pure CL-20 crystal, predicted that the stiffness and brittleness of the system were decreased, but the flexibility and plasticity were increased. Whereas the little increase of K for (010) crystalline surfaces of CL-20/graphene composite predicted the decreasing tendency of elasticity. According to the K/G values in Table 5.4, it is noticed that the CL-20/graphene composite with graphene on a crystalline surface (100) for CL-20 was regarded to obtain optimal toughness. In summary, there are still some differences in the ability of graphene to enhance the mechanical properties of CL-20 on different crystalline surfaces, and the ranking is (100) > (001) > (010). The Poisson's ratio of different crystalline surface for CL-20 and CL-20/graphene composite ranged from 0.31 to 0.48, showed the better plasticity. The order of increase of Poisson's ratio on different crystalline surfaces was (100) > (010) > (001).

In comparison of pure CL-20, the elastic coefficient and elastic modulus of CL-20/graphene composites with different crystalline surfaces in Table 5.4 decreased, and the Cauchy pressure (C_{12}–C_{44}) and K/G increased, indicating that the addition of graphene improved the elasticity, ductility and toughness of CL-20. Graphene on the (100) crystalline surface of CL-20 has the greatest influence on the mechanical properties of CL-20. This may be attributed to the flexibility and good ductility for graphene. So, it covered the explosives excellently and acted as a shock and heat absorption. Therefore, coating graphene on the surface of explosives is an effective way to achieve higher stability of explosives.

5.4 Conclusion

In this paper, the structure, energetic and mechanical properties of different crystal surfaces of ε-CL-20 and ε-CL-20/graphene composite were studied using molecular dynamics simulation. The vibrational mode, phonon density of states, binding energy, initiation bond length and elastic coefficient, isotropic mechanical properties (such as

Young's modulus, bulk modulus, shear modulus, Poisson's ratio, Cauchy pressures and K/G) for CL-20 crystals and CL-20/graphene composite were analyzed. The conclusions were as shown below.

1. The zones of 1450–1750 cm^{-1} and 600–900 cm^{-1} corresponded to major vibrational features for ε-CL-20. In comparison with CL-20, the DOS of three separate crystalline surfaces of CL-20/graphene composite decreased, which meant that the stability of them became better when graphene was added into the crystalline surfaces of CL-20. The ability of graphene to decrease the DOS of CL-20 was (100) > (001) ≈ (010).
2. In addition, adding graphene into the different crystalline surface of CL-20 changed the value of initiation bond length. Then the order of L_{prob} was (100) > (001) = (010). This was consistent with the maximum binding energy between graphene and (100) crystalline surface of CL-20.
3. In comparison with pure CL-20, the elastic coefficient and elastic modulus of CL-20/graphene composites with different crystalline surfaces decreased, and the Cauchy pressure (C_{12}–C_{44}) and K/G increased, indicating that the addition of graphene improved the elasticity, ductility, and toughness for CL-20. Graphene showed the most effective improvement in the overall mechanical performance of CL-20 when it is positioned on (100) crystalline surface of CL-20.

To summarize, MD simulation investigations of ε-CL-20 crystal and ε-CL-20/graphene composites have provided valuable knowledge about their structural, energetic and mechanical properties. Hopefully, this work is meaningful to further research on the application of CL-20 and its composite.

References

1. A.K. Sikder, N. Sikder, A review of advanced high performance, insensitive and thermally stable energetic materials emerging for military and space applications. J. Hazard. Mater. **112**(1–2), 1–15 (2004)
2. D.M. Badgujar, M.B. Talawar, S.N. Asthana, P.P. Mahulikar, Advances in science and technology of modern energetic materials: an overview. J. Hazard. Mater. **151**(2–3), 289–305 (2008)
3. I.V. Kuchurov, M.N. Zharkov, L.L. Fershtat, N.N. Makhova, S.G. Zlotin, Prospective symbiosis of green chemistry and energetic materials. Chem. Sus. Chem. **10**(20), 3914–3946 (2017)
4. J. Yang, G. Wang, X. Gong, J. Zhang, Y.A. Wang, High-energy nitramine explosives: a design strategy from linear to cyclic to caged molecules. ACS Omega **3**(8), 9739–9745 (2018)
5. Q. Jiang, J. Yang, G. Song, Feng-sheng, Study of nano-nitramine explosive preparation, sensitivity and application. Defence Technol. **10**(2), 184–189 (2014)
6. A.K. Hussein, A. Elbeih, S. Zeman, The effect of glycidyl azide polymer on the stability and explosive properties of different interesting nitramines. Rsc Adv. **8**(31), 17272–17278 (2018)
7. H.M. Zou, S.S. Chen, X. Li, S.H. Jin, Q.H. Shu, Preparation, thermal investigation and detonation properties of ε-CL-20-based polymer-bonded explosives with high energy and reduced sensitivity. Mater. Express **7**(3), 199–208 (2017)
8. Y.E. Bao-Yun, J.Y. Wang, A.N. Chong-Wei, Y.U. Bin-Shuo, J.I. Wei, L.I. He-Qun, Preparation and properties of CL-20 based composite energetic material. J. Solid Rocket Technol. **40**(2), 199–203 (2017)

9. S.M. Aldoshin, D.B. Lempert, T.K. Goncharov, A.I. Kazakov, S.I. Soglasnova, E.M. Dorofeenko, N.A. Plishkin, Energetic potential of solid composite propellants based on CL-20-containing bimolecular crystals. Russ. Chem. Bull. **65**(8), 2018–2024 (2016)
10. M. Ghosh, S. Banerjee, M.A. Shafeeuulla Khan, N. Sikder, A.K. Sikder, Understanding metastable phase transformation during crystallization of RDX, HMX and CL-20: experimental and DFT studies. Phys. Chem. Chem. Phys. **18**(34), 23554–23571 (2016)
11. J. Chen, S. He, B. Huang, P. Wu, Z. Qiao, J. Wang, L. Zhang, G. Yang, H. Huang, Enhanced thermal decomposition properties of CL-20 through space-confining in three-dimensional hierarchically ordered porous carbon. ACS Appl. Mater. Interfaces **9**(12), 10684–10691 (2017)
12. X. Li, Y.-Y. Qin, L.-l. Zhu, B.-l. Wang, Investigation on compatibility and thermal stability of CL-20 with several plasticizers. Int. J. Energy Mater. Chem. Propul. **16**(4), 359–366 (2017)
13. J. Zhang, X. Guo, Q. Jiao, H. Zhang, H. Li, Effects of desensitizers on phase transitions, thermal behavior, and sensitivity of ε-CL-20. J. Energy Mater. **36**(1), 111–120 (2018)
14. J. Yue, Z. Liu, W. Zhu, Searching for a new family of modified CL-20 cage derivatives with high energy and low sensitivity. Struct. Chem. **29**(3), 837–845 (2018)
15. B. Ye, C. An, J. Wang, H. Li, J. Wei, G. Kang, Preparation and characterization of RDX-based composite with glycidyl azide polymers and nitrocellulose. J. Propul. Power **32**(4), 1035–1039 (2016)
16. B.Y. Ye, C.W. An, J.Y. Wang, X.H. Geng, Formation and properties of HMX-based microspheres via spray drying. Rsc Adv. **7**(56), 35411–35416 (2017)
17. Z. Yang, D. Ling, W. Peng, Y. Liu, F. Nie, F. Huang, Fabrication of RDX, HMX and CL-20 based microcapsules via in situ polymerization of melaminea.formaldehyde resins with reduced sensitivity. Chem. Eng. J. **268**, 60–66 (2015)
18. H. Li, C. An, W. Guo, X. Geng, J. Wang, W. Xu, Preparation and performance of nano HMX/TNT cocrystals. Propell. Explos. Pyrot. **40**(5), 652–658 (2015)
19. B. Duan, Y. Shu, N. Liu, B. Wang, Y. Lu, Direct insight into the formation driving force, sensitivity and detonation performance of the observed CL-20-based energetic cocrystals. Cryst. Eng. Comm. **20**(38), 5790–5800 (2018)
20. X.Q. Zhang, J.N. Yuan, G. Selvaraj, G. Ji, X.R. Chen, D.Q. Wei, Toward low-sensitive and high-energetic cocrystal explosive CL-20/TNT: from intermolecular interactions to structures and properties. Phys. Chem. Chem. Phys. **20**(25), 17253–17261 (2018)
21. J. Wang, B. Ye, C. An, B. Wu, H. Li, Y. Wei, Preparation and properties of surface-coated HMX with viton and graphene oxide. J. Energy Mater. **34**(4), 235–245 (2016)
22. S. Wang, C. An, J. Wang, B. Ye, Reduce the sensitivity of CL-20 by improving thermal conductivity through carbon nanomaterials. Nanoscale Res. Lett. **13**(1), 85–92 (2018)
23. P. Li, K. Liu, D. Ao, X. Liu, C. Pei, A low-sensitivity nanocomposite of CL-20 and TATB. Cryst. Res. Technol. **53**(11), 1800189–1800196 (2018)
24. Y. Li, W.Y. Zhao, Z.H. Mi, L. Yang, Z.N. Zhou, T.L. Zhang, Graphene-modified explosive lead styphnate composites. J Ther. Anal. Calorim. **124**(2), 683–691 (2016)
25. Z. Li, W. Yu, Y. Zhang, L. Long, S. Zhang, CL-20 hosted in graphene foam as high energy materials with low sensitivity. Rsc Adv. **5**(120), 98925–98928 (2015)
26. L. Rui, J. Wang, P.S. Jin, H. Cheng, G.C. Yang, Preparation and characterization of insensitive HMX/graphene oxide composites. Propell. Explos. Pyrot. **38**(6), 798–804 (2013)
27. Y. Lan, X. Wang, Y. Luo, Preparation and characterization of GA/RDX nanostructured energetic composites. Bull. Mater. Sci. **39**(7), 1701–1707 (2016)
28. G. He, Z. Yang, X. Zhou, J. Zhang, L. Pan, S. Liu, Polymer bonded explosives (PBXs) with reduced thermal stress and sensitivity by thermal conductivity enhancement with graphene nanoplatelets. Compos. Sci. Technol. **131**, 22–31 (2016)
29. Z.M. Li, M.R. Zhou, T.L. Zhang, J.G. Zhang, Z.N. Zhou, The facile synthesis of graphene nanoplate lead styphnate composites and their depressed electrostatic hazards. J. Mater. Chem. A **1**(41), 12710–12714 (2013)
30. M. Ghosh, V. Venkatesan, A. Sikder, N. Sikder, Preparation and characterisation of ε-CL-20 by solvent evaporation and precipitation methods. Defence Sci. J. **62**(6), 390–398 (2012)

31. B. Gao, D. Wang, J. Zhang, Y. Hu, G. Yang, Facile, continuous and large-scale synthesis of CL-20/HMX nano co-crystals with high performance by ultrasonic spray-assisted electrostatic adsorption method. J. Mater. Chem. A **2**(47), 19969–19974 (2014)
32. S. Jinpeng, S. Weimei, W. Jun, G. Bing, Q. Zhiqiang, H. Hui, N. Fude, L. Rui, L. Zhaoqian, L. Yu, Facile fabrication of porous CL-20 for low sensitivity high explosives. Phys. Chem. Chem. Phys. **16**(43), 23540–23543 (2014)
33. X. Wei, J. Xu, H. Li, X. Long, C. Zhang, Comparative study of experiments and calculations on the polymorphisms of 2,4,6,8,10,12- hexanitro-2,4,6,8,10,12-hexaazaisowurtzitane (CL-20) precipitated by solvent/antisolvent method. J. Phys. Chem. C **120**(9), 5042–5051 (2016)
34. T. Sun, J.J. Xiao, Q. Liu, F. Zhao, H.M. Xiao, Comparative study on structure, energetic and mechanical properties of a ε-CL-20/HMX cocrystal and its composite with molecular dynamics simulation. J. Mater. Chem. A **2**(34), 13898–13904 (2014)
35. F. Wang, L. Chen, D. Geng, J. Lu, J. Wu, Effect of density on the thermal decomposition mechanism of ε-CL-20: a reaxff reactive molecular dynamics simulation study. Phys. Chem. Chem. Phys. **20**(35), 22600–22609 (2018)
36. G.Y. Hang, W.L. Yu, T. Wang, J.T. Wang, Theoretical investigations into effects of adulteration crystal defect on properties of CL-20/TNT cocrystal explosive. Comp. Mater. Sci. **156**, 77–83 (2019)
37. Y. Kholod, S. Okovytyy, G. Kuramshina, M. Qasim, L. Gorb, J. Leszczynski, An analysis of stable forms of CL-20: A DFT study of conformational transitions, infrared and Raman spectra. J. Mol. Struct. **843**(1–3), 14–25 (2007)
38. Y. Hong, M.G. Ju, J. Zhang, X.C. Zeng, Phonon thermal transport in a graphene/$MoSe_2$ van der waals heterobilayer. Phys. Chem. Chem. Phys. **4**(20), 2637–2645 (2018)
39. G.Y. Hang, W.L. Yu, T. Wang, Z. Li, Theoretical investigation of the structures and properties of CL-20/DNB cocrystal and associated PBXs by molecular dynamics simulation. J. Mol. Model. **24**(4), 97–105 (2018)
40. B. Duan, Y. Shu, N. Liu, Y. Lu, B. Wang, X. Lu, J. Zhang, Comparative studies on structure, sensitivity and mechanical properties of CL-20/DNDAP cocrystal and composite by molecular dynamics simulation. Rsc Adv. **8**(60), 34690–34698 (2018)

Chapter 6
Stabilization of Energetic Compounds into the Nanoscale Carbon Materials: Insights from Computational Simulations

Jiankang Li, Zhixiang Zhang, Yiding Ma, Dayong Li, and Yingzhe Liu

Abstract Carbon materials, such as carbon nanotube and graphene, are promising candidates for the stabilization of energetic compounds by inducing certain arrangements of energetic molecules through confinement. We studied the structure rearrangements of NM confined in single-walled carbon nanotube (SWNT) and graphene (GRA), and its reaction activities. The investigations show that the NM tends to align head-to-tail when confined. The structures depend on the radius of SWNTs and the distance between GRA bilayers, and the energy surfaces of initial reaction of NM alters when attached to GRA surface. Moreover, the binding energy of C-N bond increases, suggesting better thermal stability when confined in SWNT.

6.1 Introduction

Developing new energetic materials has been a challenge because of the contradiction between the performance of power and safety. Researchers have made great process in discovering high-energy-density materials (HEDMs), for example, all-nitrogen compounds [1], which are expected to be several times as powerful as the general energetic materials. However, the stability of such HEDMs stands in the way of

J. Li · Z. Zhang · Y. Ma (✉) · Y. Liu
Xi'an Modern Chemistry Research Institute, Xi'an 710065, People's Republic of China
e-mail: yiding@mail.ustc.edu.cn

J. Li
e-mail: lqk0369@126.com

Z. Zhang
e-mail: zhangzx13@mails.jlu.edu.cn

Y. Liu
e-mail: liuyz_204@163.com

D. Li
China North Chemical Research Academy Group Co., Ltd, Beijing 100089, People's Republic of China

A. Gany and X. Fu (eds.), *2021 International Conference on Development and Application of Carbon Nanomaterials in Energetic Materials*, Springer Proceedings in Physics 276,
https://doi.org/10.1007/978-981-19-1774-5_6

the fabrication, application, storage, and so on. Thus, it calls for effective ways to promote the safety performances of new HEDMs.

The confinement of energetic molecules in carbon-based backbones is a promising way for the stabilization of HEDMs. There is evidence that the carbon-based confinements such as graphene (GRA) and carbon nanotubes (CNT) can alter the chemical reactivity and dynamics of molecules [2–4]. Theoretical studies have shown that the thermal stabilities of typical energetic molecules such as HMX (octahydro-1,3,5,7-tetranitro-1,3,5,7-tetrazocine), FOX-7(1,1-diamino-2,2-dinitroethylene), RDX(hexahydro-1,3,5-trinitro-striazine) are improved when confined in CNT and double-layered GRA. For novel HEDMs such as polymeric nitrogen, it is also proved that the stability is governed by the charge transfer between polymeric nitrogen and carbon nanostructures when confined in a CNT or a graphene matrix [5–8]. Furthermore, functionalized GRA sheets can enhance the thermal decomposition of organic explosives [9]. As one of the simplest energetic molecules, nitromethane (NM) has been intensively employed as a prototype system to study the features in theory of structure [10–16], melting, crystallization [17, 18], and thermal decomposition [9, 19–21]. Its thermal decomposition mechanism is rather complex and the preference of the several elementary reactions are closely relevant to the environmental conditions, which can be representative in the study on the stabilization of energetic compounds into the nanoscale carbon materials. At nanoscale tubular or planar confinements in CNT or GRA, the orientation and arrangement of NM molecules are expected to be different from that in bulk, and quantum mechanics study has shown that the thermal decomposition of NM is accelerated when confined in (5,5) CNT [22]. In summary, the theoretical and computational research on NM in confined environments will help us understand the structural rearrangement, reaction activities, and the stabilization of nanostructured energetic materials.

6.2 Methods

6.2.1 Quantum Mechanics Calculation

For the reaction activity calculation of NM in confined system, the ONIOM method [23] was employed, where the system is divided into two layers and energy is calculated separately. The inner layer including NM molecules is calculated with high-precision density functional theory B3LYP/6-31 + G** [24, 25], and the outer layer include GRA is calculated with UFF force field [26]. The vibrational frequency was calculated at the ONIOM (B3LYP/6-31 + G**:UFF) level to find the most stable geometry of ground state and to identify the transition state of reaction. The reaction paths were double-checked using intrinsic reaction coordinate method [27]. The electronic structure calculations were carried out with Gaussian09 series of programs to quantify the interaction of molecules in the system [28].

6.2.2 Molecular Dynamics Simulations

The CHARMM36 general force field [29] was employed to describe the NM molecules. All the SWNT and GRA atoms were described by means of the sp2 aromatic carbon parameters of CHARMM27 force field [30] devoid of the net atomic charge. The CHARMM potential energy functions used to calculate the potential energy, V(r), is given by the following equation:

$$
\begin{aligned}
V(r) = & \sum_{\text{bonds}} K_b(b - b_0)^2 + \sum_{\text{angles}} K_\theta(\theta - \theta_0)^2 \\
& + \sum_{\text{dihedras}} K_\phi(1 + \cos(n\phi - \delta)) \\
& + \sum_{\text{improper}} K_\varphi(\varphi - \varphi_0)^2 + \sum_{\text{Urey - Bradtey}} K_{\text{UB}}(r_{1,3} - r_{1,3;0})^2 \\
& + \sum_{\text{nonbonded}} \varepsilon_{ij}\left[\left(\frac{R_{\min,ij}}{r_{ij}}\right)^{12} - 2\left(\frac{R_{\min,ij}}{r_{ij}}\right)^{6}\right] + \frac{q_i q_j}{4\pi D r_{ij}}
\end{aligned}
$$

where r represents the Cartesian coordinated of the system. b_0, θ_0, φ_0, and $r_{1,3;0}$ are the bond, angle, improper, and Urey-Bradley equilibrium terms, respectively. n and δ are the dihedral multiplicity and phase. Ks are the respective force constants. ε_{ij}, $R_{\text{min,ij}}$, and r_{ij} are the Lennard-Jones well depth, the minimum interaction radius, and the distance between atom i and j, respectively. q_{i} and q_{j} are the partial atomic charge of atom i and j that is obtained from the quantum mechanics calculations. D is the dielectric constant.

All the MD simulations were performed using the program NAMD2.9 [31] in the isobaric-isothermal ensemble with periodic boundary conditions applied in three directions of Cartesian space. The temperature and the pressure were maintained at 300 K and 1 bar, respectively, employing Langevin dynamics and Langevin piston pressure control [32]. The equations of motion were integrated using the multiple time step Verlet r-RESPA algorithm [33] with the time steps of 2 and 4 fs for short- and long-range interactions, respectively. Covalent bonds involving hydrogen atoms were constrained to their equilibrium lengths by means of the SHAKE/RATTLE algorithms [34, 35]. A smoothed of 1.2 nm spherical cutoff was used to truncate van der Waals interactions, and long-range electrostatic forces were evaluated employing the particle mesh Ewald approach [36].

6.3 Results

6.3.1 Structural Rearrangement

6.3.1.1 NM Confined in SWNT

To investigate the characteristics of NM confined in tubular cavities, undecorated and ideal SWNTs of the armchair type with (n,n) indices (Table 6.1) were immersed into NM solvents [37, 38]. Simulations show that NM molecules spontaneously enter the nanotube and rearrange into ordered fashion, except the (5,5) SWNT, into which the NMs need extra energy to encapsulate (Fig. 6.1). As the radius of the SWNTs increase, NMs form linear structure in (6,6) and (7,7) SWNTs, double and triple

Table 6.1 Parameters of NM-SWNT system for molecular dynamics simulation

(n, n)	r_0 (nm)	N_C	N_{NM}	N_{in}
(5, 5)	0.339	260	1135	0.00
(6, 6)	0.407	312	1121	3.86
(7, 7)	0.475	364	1111	5.43
(8, 8)	0.542	416	1097	7.71
(9, 9)	0.610	468	1243	11.71
(10, 10)	0.678	520	1227	15.29
(11, 11)	0.746	572	1209	21.29
(12, 12)	0.814	624	1208	27.00
(13, 13)	0.881	676	1305	32.71
(14, 14)	0.949	728	1292	40.14
(15, 15)	1.017	780	1274	48.86
(16, 16)	1.085	832	1261	55.43

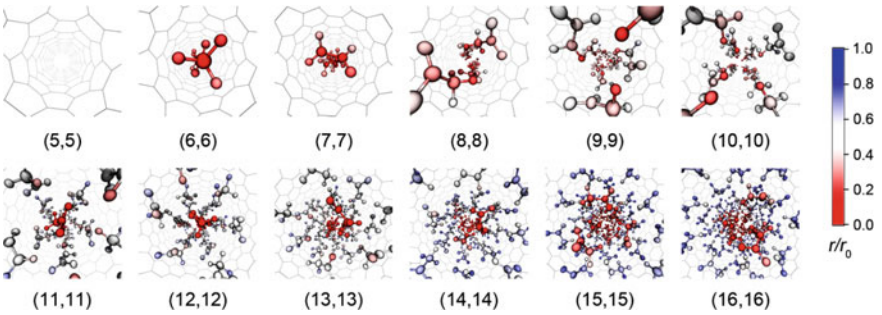

Fig. 6.1 Illustration of NM molecules confined in SWNTs, the color of atoms depends on the distance to the central axis. r is the distance to the central axis of SWNTs, r_0 is the radius of SWNTs

helix of NM arrangements are formed in (8,8) and (9,9) SWNTs. Furthermore, a quadrangular structure is formed in the (10,10) SWNTs. For the (11,11) (12,12) and (13,13) SWNTs, the NMs inside exhibit a two-layered structures: the outer layers which contacts with the SWNT form pentagonal, hexagonal, and a blurry hepta helix structures, respectively, and the inner ones form linear structure emerges. For larger SWNTs, the two-layered structure of NM is maintained except that both the inner and outer layers become less ordered when the radius of SWNT increase. It is evident that the arrangement of NM is highly dependent on the SWNT radius, and we can reasonably infer that there will be a critical radius in which the structure of confined NM is almost the same as that in bulk.

In correspondence of the linear or layered distribution of NM in tubular confinement, the radial mass densities of NM in SWNTs shows accumulations in certain regions (Fig. 6.2). For cavities from (6,6) to (10,10) the single-peak mass distribution shows the NM is displaced isometrically in the confined space. For cavities from (11,11) to (16,16), the double-peak distributions are consistent with the two-layered NM structure in SWNTs, the densities of inner layers decrease with the increasing SWNT radius, while the densities of outer layers keep stable, which may be due to the van der Waals attraction that drags outer NM to the nanotube wall. When the SWNT is larger than (10,10), the NM attracted to the nanotube wall saturates and the densities of the outer layer become constant.

Another obvious feature of NM confined in SWNTs is the preferred orientations of the molecular dipole moments. The orientation angle θ between the dipole moment of NM and the axis of SWNTs is closely relevant to the ordered structure of confined

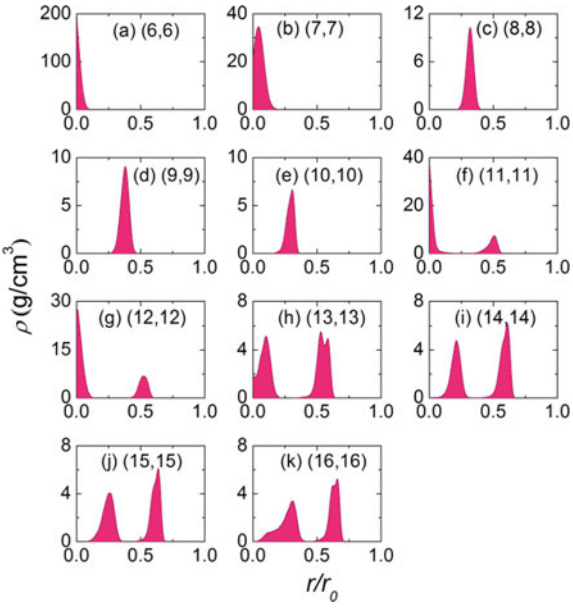

Fig. 6.2 Radial mass density of NM in SWNTs. r is the distance to the central axis of SWNTs. r_0 is the radius of SWNTs

NM. We investigated the distribution of cos θ and compared to that in bulk NM, and found that the more concentrated the distribution, the more ordered the structure.

As displayed in Fig. 6.3, the distribution of cos θ is uniform in bulk NM, indicative of random distribution of the molecular dipole moments. In contrast, the tubular confinement induced an oriented molecular dipole moment distribution of NM. For (6,6), (10,10), (13,13) and (15,15) SWNTs, cos θ distribution exhibits a single-peak distribution at 1 or -1, suggesting that the NM dipole aligns in the direction of the SWNT axis. For (8,8), (9,9), (11,11), (12,12) and (14,14) SWNTs, the curve exhibits double peaks located at the value of both 1 and -1, indicative of two preferred directions which are opposite and parallel to the SWNT axis. For larger SWNTs such as (15,15) and (16,16), the percentage of the two peaks decrease, showing a less ordered arrangement of NM molecules. Specially, for (7,7) SWNT, the distribution concentrates around 0, suggesting that the dipole is arranged perpendicular to the SWNT axis.

Figure 6.4 delineates the dipole orientation of NM in SWNTs. For (7,7) SWNT, the dipole vectors displaces shoulder-to-shoulder along the tubular axis, which may result from the compromise of the dipole–dipole interactions of NM to maximize the number of NM in SWNT. For other SWNTs the dipoles align head-to-tail in the nanotube, in some cases there are two opposite orientations of NM vectors, which may be relevant with the initial orientation on the first NM entering the SWNTs. From (13,13) to (16,16) SWNT, the van der Waals attraction between NM and SWNT weakens, so that the orientations of NM dipole vectors become less ordered.

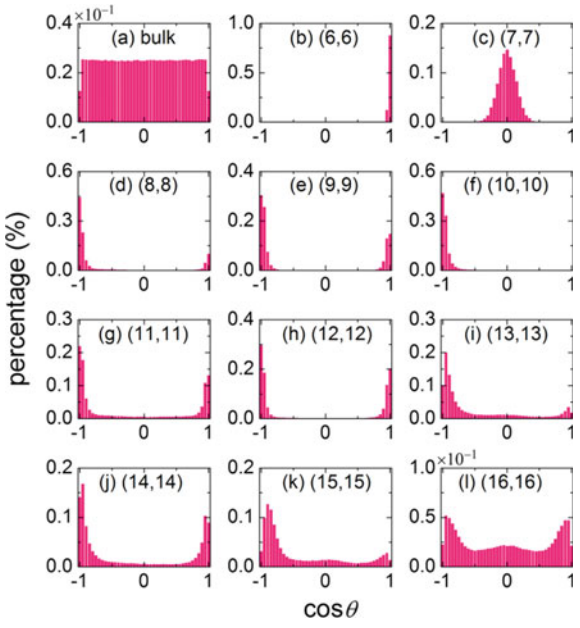

Fig. 6.3 The distribution of the orientation of NM dipole. θ is the orientation angle between the dipole moment of NM and the axis of SWNTs

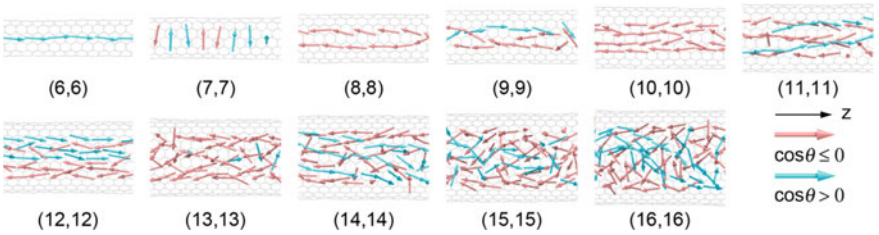

Fig. 6.4 Configurations of NM dipole vectors in SWNT confinements. The pink and blue vectors represent the dipole vectors of different directions

6.3.1.2 NM Confined in Graphene

To study the structure rearrangement of NM on the planar surfaces, a 25 Å × 25 Å single-layer armchair graphene is immersed in the NM solven [39]. Carbon atoms on GRA are restrained at initial positions by a weak harmonic potential of 1.0 kcal/mol/Å^2.

Figure 6.5 shows the density distribution of NM along the normal axis of GRA after thermal equilibrium. The distribution exhibits to 4 peaks when the distance to the GRA surface increases, indicating that the NM rearranges into lamellar form near the surface. The according regimes are labeled as L1(2.0–5.9 Å), L2(5.9–9.8 Å), L3(9.8–13.7 Å) and L4(13.7–17.6 Å), respectively. The density from L1 to L4 regime decreases. L1 owns the highest value of 3.0 g/cm^3, almost 2.5 times of the density in the NM bulk. It is most likely that the NM is attracted by the van der Waals interactions and concentrates around the GRA surface. When the distance to the GRA surface increases, the attraction becomes weaker which results in the lower densities of L2, L3, and L4. For L3 and L4, the density is close to that in bulk NM. Interestingly, there are two peaks of $–NO_2$ group in L1 regime, suggesting two configurations of NM. Here we label the configuration where H-C-N-O dihedral is 0°–15° to be the

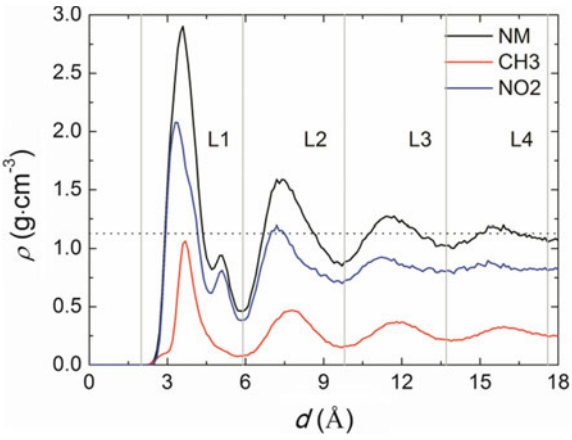

Fig. 6.5 The density distributions of NM and constituent groups. *d* is the distance to the GRA surface. Dashed line represents the average density of NM in bulk

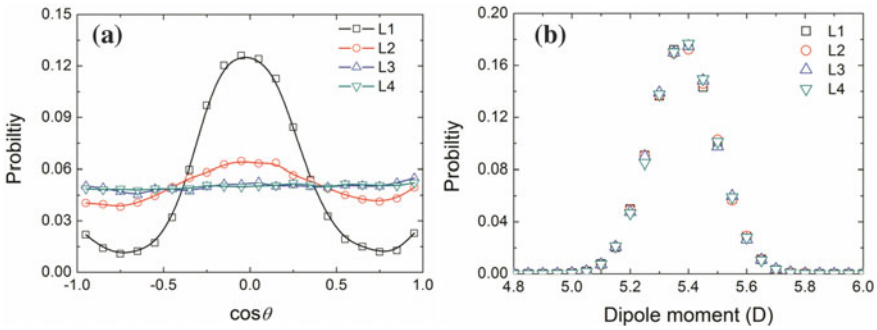

Fig. 6.6 The probability distribution of **a** cos θ and **b** amplitude of dipole moment of NM

staggered configuration and 15˚-30˚ to be the eclipsed configuration. The probability ratio of staggered and eclipsed NM in L1 to L4 regime is calculated and shown in Fig. 6.6a. In L1 regime, the staggered configuration is 2 times of that of eclipsed configuration, while in L2 to L4 regimes the probability of two configurations are almost equal, indicating that the attraction between GRA surface and NM induces the transformation from the eclipsed to the staggered configuration, which would finally result in the reaction activity of NM, as discussed in the following section.

The high local density and preferred configuration of NM in L1 suggest that the NM is likely to be oriented. The distribution of angle θ between NM dipole moment and the normal axis of GRA surface has also been investigated (Fig. 6.6a). The results show that cos θ exhibit single-peak distribution in L1 and L2, especially in L1 where the probability of cos $\theta = 0$ dominates, indicating that NM tends to point to the perpendicular direction of the normal axis of the GRA surface. In L3 and L4 NM distributes randomly. The amplitude of NM dipole, on the other hand, is not influenced in the system (Fig. 6.6b), suggesting that the interactions between NM and GRA are nonpolar thus it does not induce the change of NM dipole.

Since the NM can regularly rearrange on the surface of GRA, one could be curious about characteristics of NM confined between GRA bilayer. We modeled parallel sheets of GRA with edge length of 25 Å × 25 Å and immersed into NM solvents. The influence of the distance d between the GRA sheets on the characteristics of NM is studied.

Not surprisingly, NM can spontaneously enter the gap between GRA sheets when d is larger than 7 Å. The mass density profile (Fig. 6.7) shows that when d increases, NM first arrange into single-layer structure on $d = 7$ Å, and evolve to double-layer on $d = 10$ Å, finally form triple-layer structure on $d = 14$ Å. This is a relatively dense accumulation where the interlayer distance of NM is about 3 Å, considering the first neighbor shell of NM in bulk is about 6 Å, and the peak value of ρ/ρ_0 curve is about 5.

To understand the orientations of NM encapsulated in the GRA bilayer, the distribution of cos θ is displayed in Fig. 6.8 where θ is the angle between NM dipole moment and the normal axis of GRA bilayer. NM dipole prefers to be parallel with

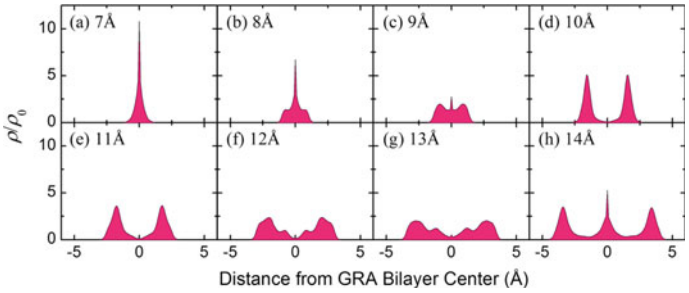

Fig. 6.7 Mass density profile of NM in GRA bilayers of different width. ρ_0 is the density of NM in bulk

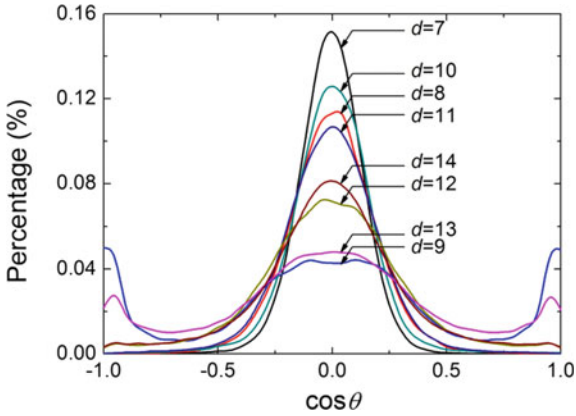

Fig. 6.8 Probability distributions of cos θ in GRA bilayers of different width

GRA bilayer, and the distribution depends strongly on the distance between GRA bilayers. Notably, the peak height near $\cos\theta = 0$ shows a somewhat periodic feature rather than decreasing monotonously as the bilayer distance increases. When $d = 7$, 10, and 14 Å the peak height reaches an extreme value, where the single-, double- and triple-layer structures are completely formed. Moreover, there is another preferred orientation when d = 9 Å, i.e., the dipole is perpendicular to the GRA bilayers.

Detailed pictures of the arrangement and dipole orientations of NM are displayed in Fig. 6.9. The NM molecules form highly regular arrangements and the dipoles tend to array head-to-tail parallel to GRA sheets. For d = 9 Å, NM molecules arrange shoulder-to-shoulder and the dipole is perpendicular to the GRA sheets in certain region. With the distance between GRA bilayers increases, the arrangement become less ordered due to the weakened interaction between GRA and NM.

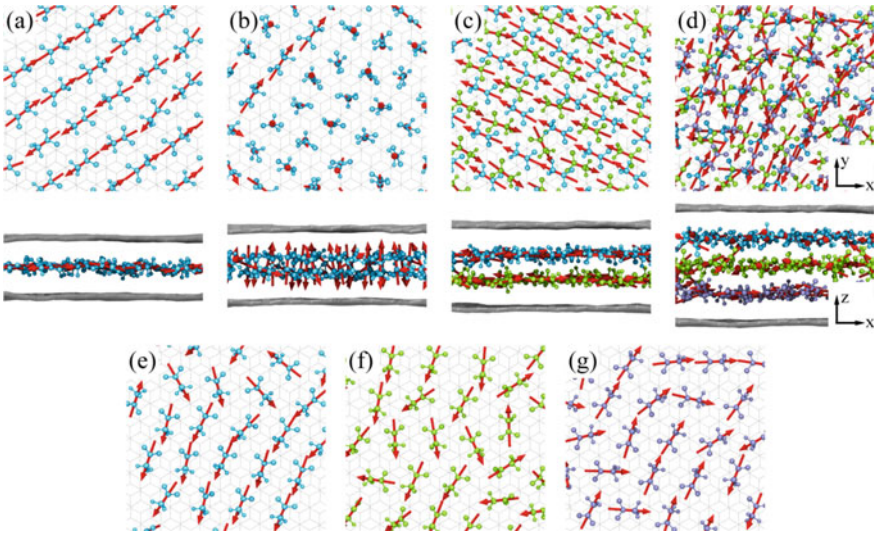

Fig. 6.9 **a–g** Illustrations of structures of NM confined within GRA bilayers. Bilayers distance in a-d is 7 Å, 9 Å, 10 Å, 14 Å, respectively. **e–g** Represents the three layers in **d**

6.3.2 Reaction Activity

The confinement of energetic molecules could remarkably influence the intra- and intermolecular structures, thus it is expected such confinements could change thermal stability, reaction activity, and so on. The initial reactions of NM mainly include the nitromethane-methyl nitrite (NM-MN) rearrangement reaction, hydrogen transfer reaction, and C-N bond homolysis reaction:

$$CH_3NO_2 \rightarrow CH_3ONO$$
$$CH_3NO_2 \rightarrow CH_2NOOH$$
$$CH_3NO_2 \rightarrow \cdot CH_3 + \cdot NO_2$$

As mentioned above, GRA surface could induce the transformation of NM from the eclipsed to the staggered configuration, we thus studied the influence to NM initial reactions when adsorbed on GRA surface using quantum chemistry methods. Single NM molecule is adsorbed onto 20 Å × 20 Å GRA surface and geometrically optimized at ONIOM (B3LYP/6–31 + G**:UFF) level. Structure of NM in vacuum coincides with experimental results, proving the accuracy of the calculation method. Quantum chemistry calculations also show that the optimal geometry of NM is the staggered structure on GRA, which it can fully contact with GRA surface.

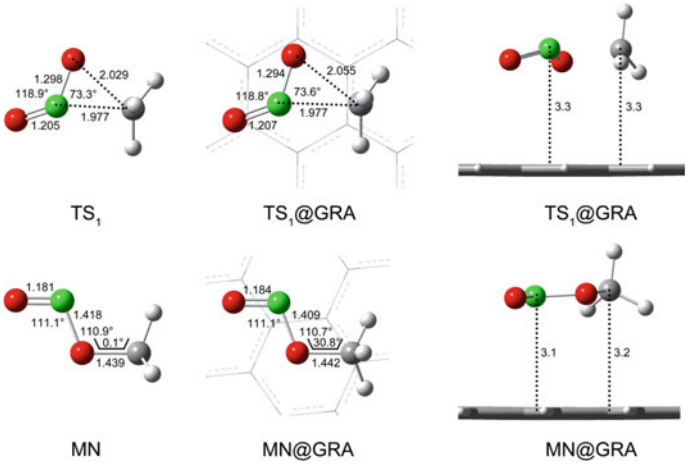

Fig. 6.10 Optimized structures of the transition states and products in the NM-MN rearrangement reactions for NM and NM@GRA

6.3.2.1 NM-MN Rearrangement Reaction

The transition state of NM and NM@GRA in NM-MN rearrangement reaction, labeled as TS_1 and TS_1@GRA, are calculated on B3LYP/6-31 + G** and ONIOM (B3LYP/6-31 + G**:UFF) level, respectively. The structure of the transition states are illustrated in Fig. 6.10, the energies and frequencies are shown in Table 6.2.

The bond length of C-N and C-O is 1.977 and 2.029 Å, similar to the results of Nguyen et al. (1.9 Å for C-N and 2.0 Å for C-O) [40]. The C●●●O distance of TS_1@GRA increases from 2.029 to 2.055 Å, and the imaginary frequency reduces by 27.1 cm^{-1}. The relative energy of TS_1-NM is 270.7 kJ/mol, which is 13.4 kJ/mol higher to the relative energy of TS_1@GRA-NM@GRA (257.3 kJ/mol), indicating that the NM-MN rearrangement reaction would be easier on GRA surface than in pure NM. On the other hand, the energy of MN is 10.9 kJ/mol higher than NM, while the energy of MN@GRA is 13.8 kJ/mol higher than NM@GRA. The activation energies of the positive and reverse reaction of NM-MN rearrangement reactions are similar, indicating that the NM-MN rearrangement reaction is reversible.

6.3.2.2 Hydrogen Transfer Reaction

With the same level of basis, the hydrogen transfer reaction of NM and NM@GRA, labeled as TS_2 and TS_2@GRA, are also calculated. Shown in Fig. 6.11, the structure of TS_2 and TS_2@GRA has no significant difference. In contrast, GRA has greater influence on the product of the reaction CH2NOOH. In isolated CH2NOOH, the hydrogen atom in adjacent of oxygen atom is not coplanar with other atoms, H-O-N-C dihedral is 38.4°, while it is 178.4° in CH_2NOOH@GRA. Furthermore, the

Table 6.2 Energies and vibrational frequencies of NM and NM@GRA systems

	Total energy (a.u)	ZPE (kJ mol^{-1})	Relative energy (kJ·mol^{-1})	Imaginary frequency (cm^{-1})
NM	−245.02873	131.0	0.0 [a]	
MN	−245.02285	126.4	10.9 [a]	
CH2NOOH	−244.99423	126.4	85.8 [a]	
(•CH3 + •NO2)	–	–	254.8 [a]	
TS_1	−244.92111	118.8	270.7 [a]	−820.34
TS_2	−244.92446	116.3	259.0 [a]	−2111.78
NM@GRA	−243.89364	4926.2	0.0 [b]	
MN@GRA	−243.88663	4921.6	13.8 [b]	
CH2NOOH@GRA	−243.87395	4923.7	49.4 [b]	
(•CH3 + •NO2)@GRA	–	–	260.2 [b]	
TS_1@GRA	−243.79102	4914.5	257.3 [b]	−793.24
TS_2@GRA	−243.78779	4911.2	262.8 [b]	−2136.62

[a] Relative to the NM calculated at the B3LYP/6–31 + G** level of theory
[b] Relative to the NM@GRA calculated at the ONIOM (B3LYP/6–31 + G**:UFF) level of theory

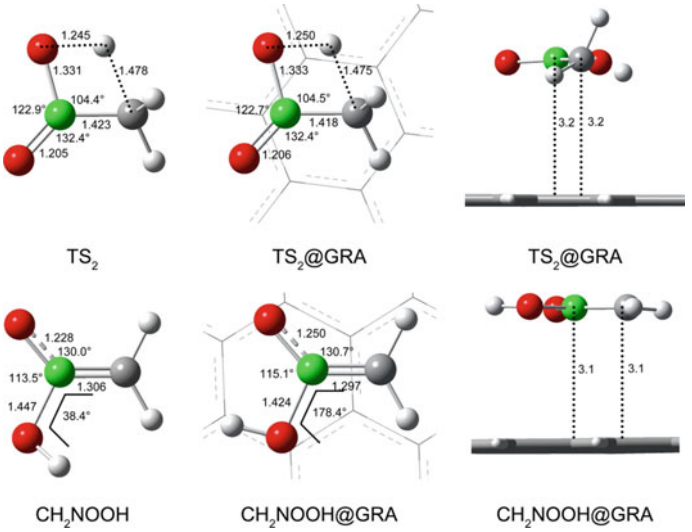

Fig. 6.11 Optimized structures of the transition states and products in the hydrogen transfer reactions for NM and NM@GRA

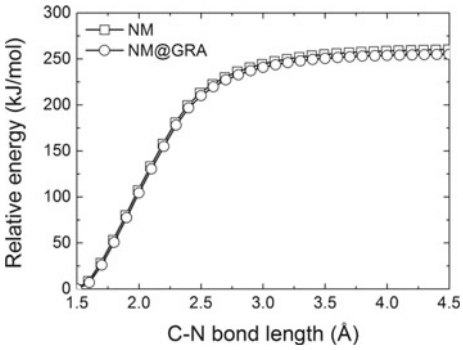

Fig. 6.12 Potential energy of NM and NM@GRA in the C-N bond homolysis reactions

N-O bond length increases by 0.022 Å and N–OH bond length decreases by 0.023 Å induced by GRA.

6.3.2.3 C-N Bond Homolysis Reaction

The potential energy curves of NM and NM@GRA C-N bond homolysis reaction are scanned under ONIOM(B3LYP/6–31 + G**:UFF) level, during which the NM structure is optimized in the process. As displayed in Fig. 6.12, the energy of NM and NM@GRA both increase with increasing C-N bond length, the energy barrier of C-N bond homolysis reaction of NM and NM@GRA are 254.8 kJ/mol and 260.2 kJ/mol, respectively, indicating a slight increase of C-N bond homolysis of NM on GRA.

6.3.2.4 Potential Energy Surface of NM Initial Reactions

The Potential energy surfaces of NM and NM@GRA initial reactions are shown in Fig. 6.13. Due to the activation energy change of NM initial reactions on GRA surface, the sequence of the activation energy of NM@GRA is "NM-MN rearrangement < C-N bond homolysis < hydrogen transfer reaction", which is different than that of NM "C-N bond homolysis < hydrogen transfer reaction < NM-MN rearrangement". Such activation energy change may be relative to the experimental data that GRA enhances the NM combustion [41].

6.3.2.5 Thermal Stability in GRA Bilayers

The thermal stability of NM confined in GRA bilayers was evaluated by the bond dissociation energy (BDE) in different structures of its dimer. The BDE, EBD (CH_3NO_2), was calculated by the equation:

$$\mathrm{EBD}(CH_3NO_2) = \mathrm{E}(\cdot CH_3) + \mathrm{E}(\cdot NO_2) - \mathrm{E}(CH_3NO_2)$$

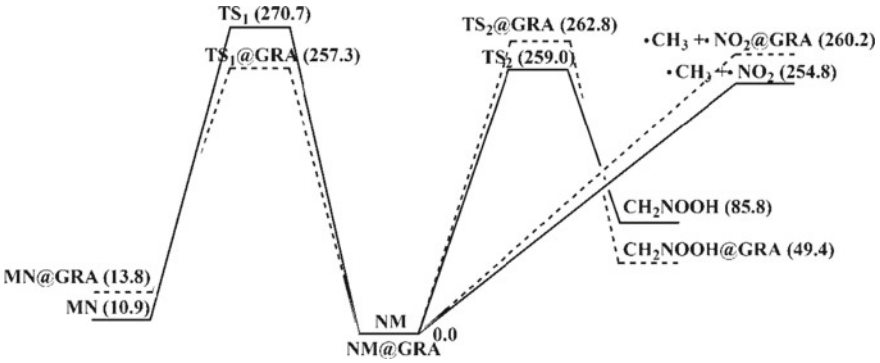

Fig. 6.13 Potential energy surfaces in the initial reactions of NM (solid line) and NM@GRA (dotted line). Relative energies are given in kJ/mol

where E(•CH_3), E(•NO_2), and E(CH_3NO_2) stands for the electronic energies of corresponding molecules or groups. The electronic energy was calculated at the B3LYP/6-31G* level.

Shown in Fig. 6.14, for the linear dimer, the head-to-tail arrangement has the highest BDE, while the head-to-head structure is the most activate structure (Fig. 6.14a), for parallel NM dimer, the staggered arrangement has higher stability than the eclipsed arrangement (Fig. 6.14b). As investigated in previous section, the most stable arrangements and orientations in two typical structural motifs can be induced by the confinement of GRA bilayer compared with the random displacement in bulk NM. Therefore, it is reasonable to believe that the NM is more stable in the confinement of GRA bilayer than in bulk.

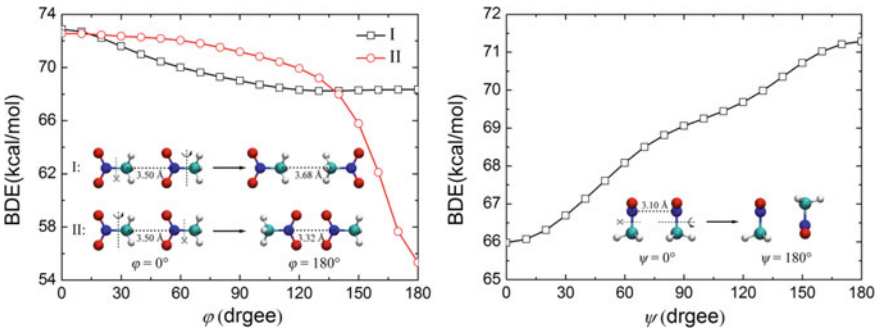

Fig. 6.14 BDE profile of **a** the linear dimer of NM as a function of rotation degree (φ) of the dipole vectors. **b** Parallel NM dimer as a function of rotation degree (ψ) of eclipsed-staggered transform

6.4 Conclusions

The structural rearrangement and the reaction activity of NM confine in carbon nanotube and graphene surface are investigated using computational methods to discover the influence of 1D and 2D confinement on characteristics of energetic materials. Our study shows that NM can spontaneously diffuse into the carbon nanotubes and graphene bilayers. In most cases, the NM molecules align head-to-tail, forming linear structures in 1D confinement and planar structures in 2D confinement. As the radius of tubular radius increases, the linear structures of NM tangles into multiple helix, while multiple layered structures are formed when the distance of planar confinement increases. In rare cases, NM molecules displace shoulder-to-shoulder, most likely to maximize the number of NM molecules in the confinement, due to the attraction between NM and carbon-based confinements.

Moreover, the structures in confinement are relevant to the changes of NM reaction activity, since the staggered conformation and heat-to-tail arrangements of NM are dominant when confined on GRA surface, leading to the increase of the C-N bond dissociation energy, and the favor of NM initial reactions. Those changes in the NM characteristics are likely to influence its thermo stability and the reaction rate of combustion.

Further studies could focus on the dynamics of the spontaneous entering of energetic molecules into confinement for effective self-assembly of energetic materials and confinement backbones, and/or on the decoration of carbon nanotubes and graphene, to improve the comprehensive performance of the complex.

References

1. M.I. Eremets, A.G. Gavriliuk, I.A. Trojan, D.A. Dzivenko, R. Boehler, Nat. Mater. **3**, 558 (2004)
2. A.N. Khlobystov, D.A. Britz, G.A.D. Briggs, Acc. Chem. Res. **38**, 901 (2005)
3. B. Jin, R. Peng, S.J. Chu et al., Prop. Explo. Pyrotech. **33**, 454 (2008)
4. R. Li, J. Wang, J.P. Shen et al., Prop. Explo. Pyrotech. **38**, 798 (2013)
5. M. Smeu, F. Zahid, W. Ji et al., J. Phy. Chem. C **115**, 10985 (2011)
6. H. Abou-Rachid, A. Hu, V. Timoshevskii, Y. Song, L.S. Lussier, Phys. Rev. Lett. **100**, 196401 (2008)
7. W. Ji, V. Timoshevskii, H. Guo, H. Abou-Rachid, L.S. Lussier, Appl. Phys. Lett. **95**, 021904 (2009)
8. V. Timoshevskii, W. Ji, H. Abou-Rachid, L.S. Lussier, H. Guo, Phys. Rev. B **80**, 115409 (2009)
9. L.M. Liu, R. Car, A. Selloni, D.M. Dabbs, I.A. Aksay, R.A. Yetter, J. Am. Chem. Soc. **134**, 19011 (2012)
10. V.N. Kabadi, B.M. Rice, J. Phys. Chem. A **108**, 532 (2004)
11. T. Megyes, S. Bálint, T. Grósz, T. Radnai, I. Bakó, L. Almásy, J. Chem. Phys. **126**, 164507 (2007)
12. S. Appalakondaiah, G. Vaitheeswaran, S. Lebègue, J. Chem. Phys. **138**, 184705 (2013)
13. H.E. Alper, F. Abu-Awwad, P. Politzer, J. Phys. Chem. B **103**, 9738 (1999)
14. D.C. Sorescu, B.M. Rice, D.L. Thompson, J. Phys. Chem. B **104**, 8406 (2000)
15. D.C. Sorescu, B.M. Rice, D.L. Thompson, J. Phys. Chem. A **105**, 9336 (2001)

16. S. Alavi, D.L. Thompson, J. Chem. Phys. **120**, 10231 (2004)
17. A. Siavosh-Haghighi, D.L. Thompson, J. Chem. Phys. **125**, 184711 (2006)
18. A. Siavosh-Haghighi, T.D. Sewell, D.L. Thompson, J. Chem. Phys. **133**, 194501 (2010)
19. N. Rom, S.V. Zybin, A.C.T. van Duin, W.A. Goddard, Y. Zeiri, G. Katz, R. Kosloff, J. Phys. Chem. A **115**, 10181 (2011)
20. F. Guo, X.L. Cheng, H. Zhang, J. Phys. Chem. A **116**, 3514 (2012)
21. J. Chang, P. Lian, D.Q. Wei, X.R. Chen, Q.M. Zhang, Z.Z. Gong, Phys. Rev. Lett. **105**, 188302 (2010)
22. L.X. Wang, C.H. Yi, H.T. Zou, J. Xu, W.L. Wu, Chem. Phys. **367**, 120 (2010)
23. T. Vreven, K.S. Byun, I. Komáromi et al., J. Chem. Theo. Comp. **2**, 815 (2006)
24. A.D. Becke, J. Chem. Phys. **98**, 5648 (1993)
25. C. Lee, W. Yang, R.G. Parr, Phys. Rev. B **37**, 785 (1988)
26. A.K. Rappé, C.K. Casewit, K.S. Colwell et al., J. Am. Chem. Soc. **95**, 3358 (1992)
27. K. Fukui, Acc. Chem. Res. **14**, 363 (1984)
28. M.J. Frisch, G.W. Truck, H.B. Schlegel, et al. (Gaussian, Inc., Wallingford, CT, 2009)
29. K. Vanommeslaeghe, E. Hatcher, C. Acharya, S. Kundu, S. Zhong, J. Shim, E. Darian, O. Guvench, P. Lopes, I. Vorobyov, A.D. Mackerell, J. Comput. Chem. **31**, 671 (2010)
30. A.D. MacKerell, D. Bashford, M. Bellott, R.L. Dunbrack et al., J. Phys. Chem. B **102**, 3586 (1998)
31. J.C. Phillips, R. Braun, W. Wang, J. Gumbart, E. Tajkhorshid et al., J. Comput. Chem. **26**, 1781 (2005)
32. S.E. Feller, Y. Zhang, R.W. Pastor, B.R. Brooks, J. Chem. Phys. **103**, 4613 (1995)
33. M. Tuckerman, B.J. Berne, G.J. Martyna, J. Chem. Phys. **97**, 1990 (1992)
34. J.P. Ryckaert, G. Ciccotti, H.J.C. Berendsen, J. Comput. Phys. **23**, 327 (1977)
35. H.C. Andersen, J. Comput. Phys. **52**, 24 (1983)
36. T. Darden, D. York, L. Pedersen, J. Chem. Phys. **98**, 10089 (1993)
37. Y.Z. Liu, W.P. Lai, T. Yu, Z.X. Ge, Y. Kang, J. Mol. Model. **20**, 2459 (2014)
38. Y.Z. Liu, W.P. Lai, T. Yu, Z.X. Ge, Y. Kang, Phys. Chem. Chem. Phys. **17**, 6995 (2015)
39. Y.Z. Liu, T. Yu, W.P. Lai, Y. Kang, Z.X. Ge, J. Mol. Model. **21**, 40 (2015)
40. Y.Z. Liu, Y. Kang, W.P. Lai, T. Yu, Z.X. Ge, Chin. J. Energy Mater. 1006–9941 09–0871–06 (2015)
41. Y.Z. Liu, W.P. Lai, Y. Wang, T. Yu, G. Ren, Z.X. Ge, Y. Kang, Chin. J. Energy Mater. 1006–9941 07–0639–05 (2016)

Chapter 7
Preparation and Characterization of CNTs@SiO_2 Nano-composites

Shaojie Li, Shenghao Meng, Shiguo Du, Zenghui Cui, and Yuling Zhang

Abstract To achieve expected dispersion of carbon nanotubes (CNTs) and improve interfacial characteristics between CNTs and matrix in composites, a simple and effective method for preparation of CNTs@SiO_2 nano-composites were put forward using polyvinyl pyrrolidone (PVP) as a surfactant. The morphology, microstructure and chemical composition of CNTs@SiO_2 nano-composites were characterized by transmission electron microscopy (TEM), Fourier transform infrared spectroscopy (FTIR), X-ray diffraction (XRD), thermogravimetric analysis (TGA_DSC) and BET test. It was found that amorphous nano-SiO_2 uniformly and densely grown on the surface of CNTs, forming a rougher film, and the modification process didn't destroy the surface structure of CNTs. The specific surface area of CNTs@SiO_2 was approximately two times larger than that of pristine CNTs, which can be promising candidates for application in nano-composite energetic materials.

S. Li · S. Du · Y. Zhang (✉)
Department of Ammunition Engineering, Army Engineering University, Shijiazhuang 050003, China
e-mail: zhangyuling2009@163.com

S. Li
e-mail: l13057698021@163.com

S. Du
e-mail: shiguoduaeu@163.com

S. Meng
High-Tech Institute, Qingzhou 262500, China
e-mail: 1019754117@qq.com

Z. Cui
No. 66109 Troops of PLA, Qinhuangdao 066000, China
e-mail: lgdsxqli@aliyun.com

A. Gany and X. Fu (eds.), *2021 International Conference on Development and Application of Carbon Nanomaterials in Energetic Materials*, Springer Proceedings in Physics 276,
https://doi.org/10.1007/978-981-19-1774-5_7

7.1 Introduction

Carbon nanotubes (CNTs) have aroused wide interests of researchers as excellent nano-materials [1]. The unique mechanical, electrical and thermal properties of CNTs render them attractive in nano-reinforcement, catalytic reactions, hydrogen storage and other fields. In recent years, many studies have been reported about incorporating CNTs into energetic materials to achieve the desired performances [2–4]. In terms of the latest research results, to further improve combustion performance and mechanical properties of energetic matrix, CNTs can be mixed with other energetic materials to prepare nano-composite energetic materials. The introduction of CNTs can greatly increase the contact area between energy-containing components and improve the catalytic effect [5–7]. Especially, for composite solid propellants, the addition of CNTs can significantly improve its mechanical properties. But like other nanomaterials, dispersion and interfacial bonding greatly limit excellent performance of CNTs in composites [8, 9]. Therefore, it's necessary to carry out related research on surface modification of CNTs to expand application of CNTs in energetic materials.

Nano-SiO_2 possesses excellent properties such as high specific surface area, high chemical activity and simple preparation process, and has wide application prospects in many fields. Moreover, a large number of hydroxyl active groups exist on surface of nano-SiO_2, which are beneficial for the combination with other materials to prepare nanocomposites, such as polymers, ceramics and other materials. Researchers have prepared high-energy explosive/silica composite system to reduce explosive sensitivity and improve combustion performance by sol_gel method. Therefore, it can be considered to explore surface modification of CNTs with nano-SiO_2 to improve their surface chemical activity, maintain their nano-skeleton structure while increasing the surface roughness, which is valuable and innovative research work to promote CNTs dispersion and enhance interfacial adhesion between CNTs and energetic matrix.

In this paper, the CNTs coated by nano-SiO_2 (CNTs@SiO_2) were successfully prepared and characterized. Effects of different kinds of surfactants on CNTs dispersion were evaluated. Noticeably, the sol–gel method employed in this paper is simple in operation and easy to control, and it is also the ideal method for preparing nano-composite energetic materials at present, which provides possibility for the direct preparation of nano-composite energetic materials from the modified CNTs in the future. It also can be believed that the research is beneficial to improve dispersion and interfacial microstructure between CNTs and energetic matrix, and provides an alternative candidate for the application of CNTs in energetic composites.

7.2 Experiment

7.2.1 Materials

The physical properties of the used CNTs were presented in Table 7.1. The other

Table 7.1 Properties of CNTs used in the experiment

Diameter (nm)	Length (μm)	Purity (wt%)	Ash (wt%)	Specific surface area (m^2/g)
30–50	<10	>98%	<1.5	>100

chemical reagents used in the preparation process include ethyl orthosilicate (TEOS), anhydrous ethanol, concentrated hydrochloric acid, and deionized water. These are all commercially available without further purification. The surfactants used for dispersing CNTs include sodium dodecyl sulfate (SDS), sodium dodecyl benzene sulfonate (SDBS), hexadecyl trimethyl ammonium bromide (CTAB), dodecyl dimethyl betaine (BS-12), Triton X-100 (Triton), Tween 60 (Tween) and polyvinyl pyrrolidone (PVP).

7.2.2 Preparation of Surfactant Treated CNTs Dispersion

All surfactants were first diluted in water followed by mild sonication with CNTs at the weight ratio (dispersant: CNTs = 2:1) to achieve homogenized suspension. The dispersion status was observed after one month. The plain CNTs water dispersion without additive was also observed for contrast.

7.2.3 Preparation of CNTs@SiO_2 Nano-composites

The modified sol–gel method was used in the preparation process of CNTs@SiO_2 nano-composites. At first, 14 ml ethyl silicate was mixed with 20 ml absolute ethanol, and appropriate amount of nitric acid was added dropwise to the solution under vigorous agitation. The solution was stirred for 2 h at about 60 °C to obtain liquid A. Subsequently, 0.2 g CNTs, deionized water and PVP were added to a three-necked flask, and mixed thoroughly, followed by 10 min sonication. Then solution A was slowly added in the solution under stirring, and undergone reflux process for 50 min. The upper liquid was separated by centrifugation, and washed several times with anhydrous ethanol and deionized water in turn. After dried at constant 50 °C for 1 h and calcined at 400 °C for 3 h, CNTs@SiO_2 nano-composites were obtained.

7.2.4 Characterization

The transmission electron microscope (TEM) micrographs were examined with FEI TalosF200x. Fourier transform infrared (FTIR) spectra of samples was recorded on the Bruker TENSOR II instrument. X-ray diffraction measurement (XRD) were

carried out on the Bruker D8 Advance. Thermal gravimetric analysis was measured with SDT Q600 thermal analyzer (TGA–DSC, TA Instrument) under air atmosphere at the gas flow of 100 mL/min, and the heating rate was 10 °C/min. BET test (BET, Quantachrome NOVA4000e) was carried out to study the specific surface area and porosity of samples.

7.3 Results and Discussion

7.3.1 The Stability of CNTs Dispersion

The good dispersion of CNTs is the key to achieve its excellent performance. Typical surfactants were selected to study dispersion effects on CNTs. To be specific, SDS and SDBS are anionic surfactants, while CTAB is cationic surfactant, respectively. Triton, Tween and PVP are used as non-ionic surfactants, with BS-12 used as zwitterionic surfactant. As shown in Fig. 7.1a, CNTs can be dispersed uniformly in each tube and keep stable in a short time after ultrasonication. However, the dispersion of CNTs after one month was shown in Fig. 7.1b. CNTs without any additive were difficult to disperse in water, and agglomerated at the bottom. Three kinds of nonionic surfactants, i.e., Triton, Tween and PVP, make CNTs disperse uniformly in

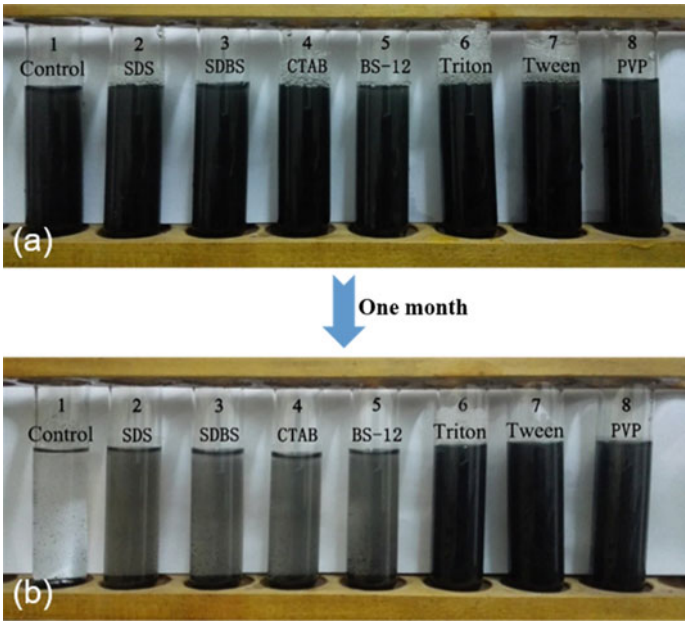

Fig. 7.1 CNTs dispersion with various surfactants: **a** after immediate sonication; **b** standing for one month

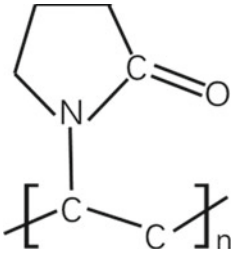

Fig. 7.2 Molecular structure of PVP

water, which are ideal dispersants for CNTs. Both Triton and Tween contain cyclic structures, which is similar to the graphite structure of CNTs. Especially for PVP (Fig. 7.2), the long carbon chain tends to be tightly wound with the out walls of CNTs, and the hydrophilic ring structure hinder the agglomeration of CNTs by the steric hindrance, which might be responsible for the excellent dispersion effect [10, 11]. Therefore, PVP was used as the dispersant in the preparation of CNTs@SiO_2 nano-composites in next step.

7.3.2 Characterization of Surface Morphology

The surface morphologies of pristine CNTs and CNTs@SiO_2 were observed by TEM, as shown in Fig. 7.3. The pristine CNTs possess multilayer structure of tube walls with a neat and smooth surface. The multilayer tube walls are regularly spaced, and the space was about 0.4 nm. Compared to that, a thin SiO_2 film was observed around the surface of CNTs@SiO_2. The average thickness of the film was about 3–5 nm. The internal microstructure of CNTs after modification showed no obvious changes, as the surface roughness was evidently improved. More importantly, the SiO_2 nanoparticles uniformly nucleated and grown on surface of CNTs, and no single nucleated SiO_2 aggregates were found. This indicates that the preparation conditions used in the experiment is favorable and controllable, which is beneficial for the design of nano-composites containing CNTs.

7.3.3 Chemical Composition Analysis

In order to investigate functional groups changes of samples surface, CNTs (a) and CNTs@SiO_2 (b) composites were studied by FTIR, as shown in Fig. 7.4. The spectra curve of CNTs (a) was smooth and there was no sharp absorption peak. The bending vibration peak of H–O-H at 1640 cm^{-1} and the stretching vibration peak of H–O-H at 3440 cm^{-1} were very weak, which may be associated with the physically absorbed H_2O. It can be seen from the curve B that there were obvious absorption peaks at 1640 and 3440 cm^{-1}, indicating that there are a lot of hydroxyl groups and adsorbed

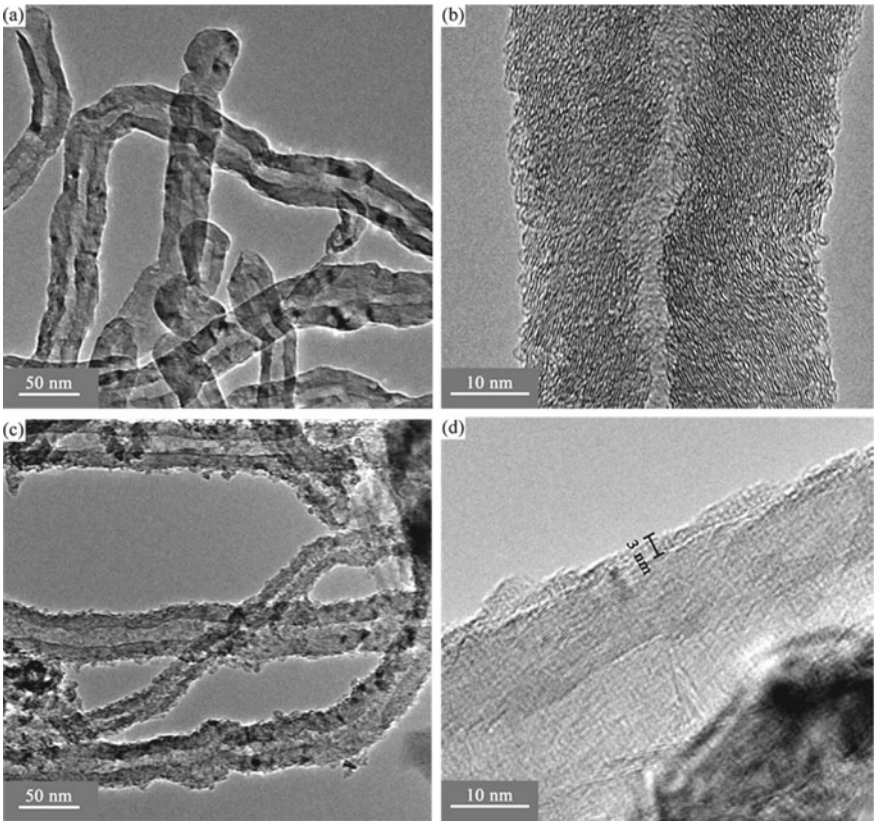

Fig. 7.3 TEM micrographs of pristine CNTs (**a**, **b**) and CNTs@SiO_2 (**c**, **d**)

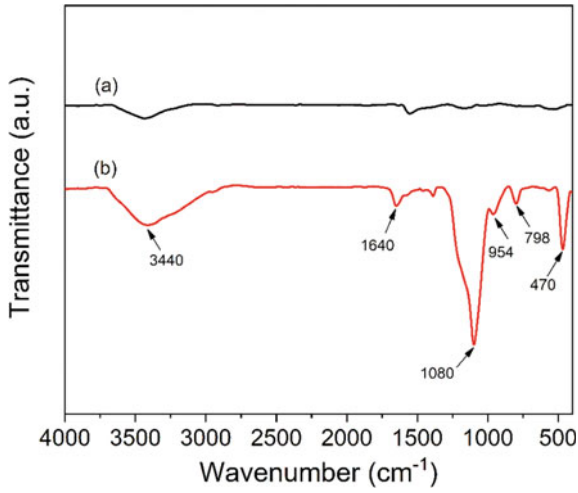

Fig. 7.4 FTIR spectra of CNTs (**a**) and CNTs@SiO_2 (**b**)

water on the surface of CNTs@SiO_2 nano-composites, which may be due to the porous structure of CNTs@SiO_2 composite particles, leading to the adsorption of a lot of water molecules. The spectra of CNTs@SiO_2 also exhibited characteristic absorption peaks at 1080 and 798 cm^{-1} due to the stretching vibration modes of Si–O–Si groups. Additionally, the emerging peaks at 954 and 470 cm^{-1} can be attributed to Si–O–Si blending vibration in absorption spectra [12, 13]. From analysis above, it can be identified that nano-SiO_2 exists in the film structure of CNTs@SiO_2.

The XRD patterns of CNTs@SiO_2 composite particles was shown in Fig. 7.5. It can be seen from Fig. 7.5a that CNTs@SiO_2 showed characteristic diffraction peaks at 26°, 43° and 54°, corresponding to (002), (100) and (004) reflections of the hexagonal graphitic structure, respectively [14–16]. Furthermore, the peak separation and fitting result of 2θ from 15° to 35° was presented in Fig. 7.5b. It can be found that in there was a steamed bread peak appearing at about 22°, with no diffraction peak of SiO_2 at other positions, indicating that SiO_2 possessed amorphous structure.

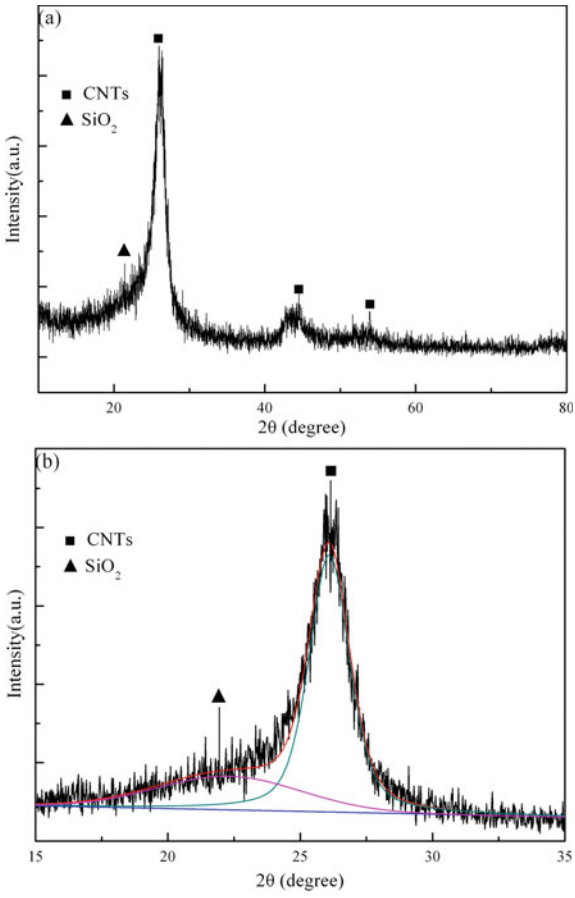

Fig. 7.5 **a** XRD pattern of CNTs@SiO_2; **b** The fitting results of characteristic peak for CNTs@SiO_2

Amorphous SiO_2 has the porous and loose characteristics, featuring strong adsorption capacity. These results indicate that the original crystal structure of CNTs was maintained well instead of being destroyed after surface modification [17].

Figure 7.6 shows the TGA–DSC curves of original CNTs and CNTs@SiO_2 in air flow. As shown in Fig. 7.6a, the CNTs mass didn't change basically before 500 °C. At about 500 °C, the CNTs began to oxidize and the sample mass began to decrease rapidly. The maximum exothermic peak appeared approximately at 613 °C, and oxidation reaction completed at 650 °C. After that, the system mass remained unchanged, with the mass of the remaining solid being about 2.1%. The thermal analysis curve of CNTs@SiO_2 in Fig. 7.6b shows that there was obvious weight loss about 1.9% at about 100 °C, which can be attributed to water evaporation absorbed in CNTs@SiO_2 surface, and this was consistent with the previous FTIR results. The significant weight loss corresponding to 500~650 °C was allotted to the oxidative decomposition of CNTs in air, and the system mass didn't change after that. The oxidation temperature of CNTs in CNTs@SiO_2 nano-composites was basically the same as that of the original CNTs in air, with 11.95% of the residual solid content.

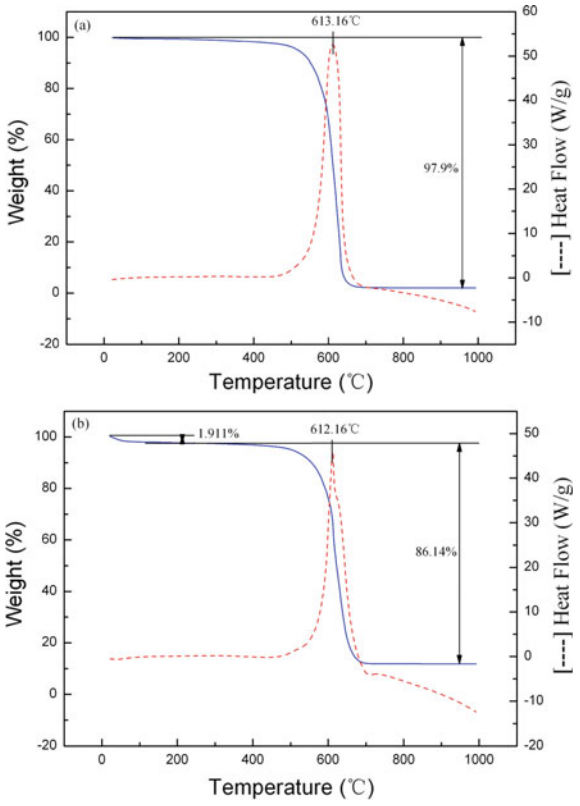

Fig. 7.6 TGA–DSC curves of pristine CNTs (**a**) and CNTs@SiO_2 (**b**)

Table 7.2 Specific surface and porosity of pristine CNTs and CNTs@SiO_2 nano-composites

Samples	SSA (m^2/g)	Pore volume (cc/g)	Pore size (nm)
CNTs	108.263	0.321	3.745
CNTs@SiO_2	196.812	0.329	3.785

This can be considered as SiO_2 coating on surface of CNTs, indicating approximate mass fraction of SiO_2 in composites.

The specific surface area (SSA) and porosity of the original CNTs and CNTs@SiO_2 were tested respectively, and the results were shown in Table 7.2. It can be seen that the SSA of original CNTs and CNTs@SiO_2 nano-composites are 108.263 and 196.812 m^2/g, respectively. After coated with SiO_2 particles, the SSA of CNTs was approximately two times larger than that of original CNTs, and the pore volume and pore size remained basically unchanged. The SSA is one of the important parameters of the doped particles, which determines the size of the contact area between the doped particles and matrix. The larger the SSA is, the larger the contact area between the doped particles and the matrix is, which is more beneficial for the catalytic reaction. In addition, CNTs@SiO_2 nano-composites have larger SSA, and the pore volume and pore size remain unchanged, indicating that the CNTs@SiO_2 nano-composites have stronger adsorption capacity, which can be rather attractive in the research of adsorption, catalysis and other aspects.

7.3.4 Mechanism Analysis

The preparation of nano-SiO_2 sol from ethyl silicate is a complex hydrolysis condensation process. The main reactions are as follows:

$$\mathrm{Si(OC_2H_5)_4} + x\mathrm{H_2O} \rightarrow \mathrm{Si(OH)}_x\mathrm{(OC_2H_5)}_{4-x} + x\mathrm{C_2H_5OH}$$
$$\equiv \mathrm{Si-OH} + \mathrm{Si-OH} \equiv\!\!\rightarrow \equiv \mathrm{Si-O-Si} \equiv + \mathrm{H_2O}$$
$$\equiv \mathrm{Si-OH} + \mathrm{Si-OC_2H_5} \equiv\!\!\rightarrow \equiv \mathrm{Si-O-Si} \equiv + \mathrm{C_2H_5OH}$$

The ratio of raw materials in the reaction exerts important influence on the reaction process and the final products. Ethanol, the reaction solvent, is also one of the reaction products. When the ethanol content is less, the concentration of the reaction system is large, and the reaction is less full. When the ethanol content is more, the reaction rate is mild, and it also hinders the hydrolysis reaction. Water is not only a reactant of hydrolysis reaction but also a product of condensation reaction. When the water quantity is less, the system concentration is large, leading to the insufficient reaction. When water amount increases to a certain extent, it also acts as a solvent. More importantly, inorganic acid plays an important role in promoting the formation of Si–OH and accelerating the reaction process. PVP, used as the dispersant, can significantly improve the dispersibility of CNTs in water. Due to steric hindrance

effect, PVP can slow down the contact opportunities of different intermolecular reactive groups, and control the deposition rate of SiO_2 nano-particles on the surface of CNTs, thus promoting the uniform growth of SiO_2 on CNTs surface [18].

7.4 Conclusion

In this paper, CNTs@SiO_2 nano-composites were prepared and characterized. The dispersion test revealed that the nonionic surfactants, represented by PVP, showed excellent dispersion effect on CNTs, which might be attributed to the steric hindrance of the cyclic structure. On the premise that CNTs were not treated by strong acid oxidation, SiO_2 nanoparticles uniformly deposited on the surface of CNTs by the sol-reflux method, forming CNTs@SiO_2 nano-composites. Analysis showed that the nano-SiO_2 were amorphous, and the nano-SiO_2 film greatly expanded surface roughness of CNTs. The specific surface area of CNTs@SiO_2 was about 2.18 times higher than that of pristine CNTs, which will be conducive to the doping of CNTs into other oxide matrices, thus forming composites with high bonding strength and excellent comprehensive properties. More importantly, the modification process is simple and practicable, without destroying the surface structure of CNTs. Further study will focus on the application of CNTs@SiO_2 nano-composites in energetic materials.

References

1. I. Kinloch, J. Suhr, J. Lou, R. Young, P. Ajayan, Composites with carbon nanotubes and graphene: an outlook. Science **362**, 547–553 (2018)
2. M. Rehwoldt, D. Kline, M. Zachariah, Numerically evaluating energetic composite flame propagation with thermally conductive, high aspect ratio fillers. Chem. Eng. Sci. **229**, 116087 (2020)
3. G. Zhang, J. Han, L. Yang, T. Zhang, Theoretical study of the reduction in s ensitivity of copper azide following encapsulation in carbon nanotubes. J. Mol. Model. **26**, 1–8 (2020)
4. J. Abrahamson, C. Song, J. Hu, J. Forman, S. Mahajan, N. Nair, W. Choi, E. Lee, M. Strano, Synthesis and energy release of nitrobenzene-functionalized single-walled carbon nanotubes. Chem. Mater. **23**, 4557–4562 (2011)
5. K. Gu, X. Li, R. Yang, Catalytic action on combustion and decomposition of AP with CNTs. Chin. J. Explos. Propellants **29**, 48–51 (2006)
6. Y. Liu, W. Jiang, J. Liu, The catalytic study of nano Cu/CNTs on the thermal decomposition and combustion of AP/HTPB propellant. Acta Armamentarii **29**, 1029–1033 (2008)
7. X. Yu, Effect of carbon nanotubes on thermal decomposition properties of CL-20. Chin. J. Explos. Propellants **27**, 78–80 (2004)
8. H. Yuan, C. Wang, S. Zhang, X. Lin, Effect of surface modification on carbon fiber and its reinforced phenolic matrix composite. Appl. Surf. Sci. **259**, 288–293 (2012)
9. Y. Pan, S. Xiao, X. Lu, C. Zhou, Y. Li, Z. Liu, B. Liu, W. Xu, C. Jia, X. Qu, Fabrication, mechanical properties and electrical conductivity of Al_2O_3 reinforced Cu/CNTs composites. J. Alloys Compd. **782**, 1015–1023 (2018)

10. K.M. Koczkur, S. Mourdikoudis, L. Polavarapu, S. Skrabalak, Polyvinylyrr-olidone (PVP) in nanoparticle synthesis. Dalt. Trans. **44**, 17883–17905 (2015)
11. W. Rieter, K. Taylor, W. Lin, Surface modification and functionalization of nanoscale metal-organic frameworks for controlled release and luminescence sensing. J. Am. Chem. Soc. **129**, 9852–9853 (2007)
12. G. Wu, L. Ma, H. Jiang, L. Liu, Y. Huang, Improving the interfacial strength of silicone resin composites by chemically grafting silica nanoparticles on carbon fiber. Compos. Technol. **153**, 160–167 (2017)
13. M. Lu, H. Xiao, M. Liu, X. Li, H. Li, L. Sun, Improved interfacial strength of SiO_2 coated carbon fiber in cement matrix. Cem. Concr. Compos. **91**, 21–28 (2018)
14. N. Wang, S. Pandit, L. Ye, M. Edwards, V. Mokkapati, M. Murugesan, V. Kuzmenko, C. Zhao, F. Westerlund, I. Mijakovic, J. Liu, Efficient surface modification of carbon nanotubes for fabricating high performance CNT based hybrid nanostructures. Carbon **111**, 402–410 (2017)
15. M. Dresselhaus, G. Dresselhaus, R. Saito, A. Jorio, Raman spectroscopy of carbon nanotubes. Phys. Rep. **409**, 47–99 (2005)
16. A. Jorio, M. Pimenta, A. Filho, R. Saito, G. Dresselhaus, M. Dresselhaus, Characterizing carbon nanotube samples with resonance Raman scattering. New J. Phys. **5**, 139 (2003)
17. X. Ling, Y. Wei, L. Zou, S. Xu, The effect of different order of purification treatments on the purity of multiwalled carbon nanotubes. Appl. Surf. Sci. **276**, 159–166 (2013)
18. S.J. Cho, S.M. Jung, M. Kang, H.S. Shin, J.H. Youk, Preparation of hydrophilic PCL nanofiber scaffolds via electrospinning of PCL/PVP-b-PCL block copolymers for enhanced cell biocompatibility. Polymer **69**, 95–102 (2015)

Chapter 8
Study on Mechanical Properties of Carbon Nano-titanium Composites by Prefabricated Fragments

Ning Jiang, Wenbin Li, Weihang Li, and Dou Hong

Abstract Carbon Nanomaterials have excellent mechanical, thermal and electrical properties, and their strength, modulus and thermal conductivity are much higher than those of existing metal materials. It is one of the best choices for metal-matrix composites. By adjusting the content and distribution of carbon nanomaterials reinforced with titanium alloy and titanium aluminum alloy, it is expected that the mechanical strength, electrical conductivity and thermal conductivity of titanium matrix will be greatly improved, and excellent integrated materials with structure and function will be obtained. Based on this, using powder metallurgy are reviewed in this paper the preparation of carbon nanotube reinforced titanium matrix composites research progress at home and abroad, this paper introduces the preparation of nano carbon—titanium composites molding process, and finally through the simulation analysis of prefabricated fragment on carbon mickey target wear properties of composite materials, thus analysis summarized the titanium nanometer carbon—the mechanical properties of composite materials, This study provides a basis for the protection research of carbon—titanium nanocomposites in the future.

N. Jiang (✉) · W. Li · W. Li · D. Hong
School of Mechanical Engineering, Nanjing University of Science and Technology, Nanjing 210094, Jiangsu, China
e-mail: njustjn@163.com

W. Li
e-mail: lwb2000cn@njust.edu.cn

W. Li
e-mail: 992190035@qq.com

D. Hong
e-mail: 875854607@qq.com

A. Gany and X. Fu (eds.), *2021 International Conference on Development and Application of Carbon Nanomaterials in Energetic Materials*, Springer Proceedings in Physics 276,
https://doi.org/10.1007/978-981-19-1774-5_8

8.1 Introduction

Titanium and its alloys have the advantages of light weight, high strength (density 4.5 g/cm^3, strength up to more than 1 GP), good corrosion resistance and biocompatibility, etc., and have been widely used in functional structural components in aerospace, automotive, medical and other fields [1–3]. Titanium matrixcomposites (TMCs) with excellent properties such as high strength, heat resistance, corrosion resistance and high specific modulus have rapidly entered people's vision, and have been widely used, with the proportion increasing year by year [4–6]. The forming processes of titanium matrix composites include solid state method, liquid state method and surface compound method [7]. Powder metallurgy (PM) is a technology method to compound matrix and reinforcement in the form of solid powder to form new materials, which is generally applicable to carbon nanomaterials and titanium composites. Titanium matrix composites can be divided into in-situ and non-in-situ autogenous titanium matrix composites according to their reinforcement forming process [8–11]. Since the emergence of ultra-high strength carbon nanomaterials represented by carbon nanotubes (CNTs) at the end of the twentieth century, the use of CNTs to strengthen metal matrix composites has always been one of the research hotspots of ultra-high strength composites [12–14]. CNTs are composed of carbon atom faces with hexagonal "honeycomb" structure curled into cylindrical fibers, and their length-diameter ratio can reach about 105. According to the number of layers of carbon atom curled faces, CNTs can be divided into single-walled carbonnanotubes (SWCNTs) and multi-walled carbonnanotubes (MWCNTs). CNTs are characterized by light weight and high strength, with a density slightly higher than that of water, Young's modulus up to about 1 tPa, yield strength up to about 110 GPa, and thermal expansion coefficient almost zero [15–17]. Graphene (Graphene, GR) and CNTs have the same elemental composition, which can be regarded as the "isomer" of CNTs. Although the two have the same "honeycomb" lattice structure, GR is in the form of non-closed curved lamellae. Studies have shown that CNTs can be dissociated along their height to obtain lamellar GR [18]. GR has ultra-high specific surface area (about 2600 m2/g), as well as light weight, high strength (about 1.2–2 g/cm^3, yield strength about 130 GPa), ultra-high room temperature thermal conductivity (3000–5000 W/(m K) and other properties [19–24]. Other carbon nanomaterials, such as nano-diamonds (NDS) with diamond-shaped cube structure [25], also have much higher strength and hardness than existing metals [26].

Although some studies have shown that the composite interface of titanium and carbon nanomaterials is in a thermodynamic stable state at a certain temperature [27], the chemical compatibility and wettability of metal materials and carbon nanomaterials are very poor [28, 29], and it is easy to react with many defects of carbon nanomaterials to form TiCx [30–34]. It can be seen from Table 8.1 that the interface reaction between carbon and titanium in a wide temperature range (373–1223 K) ΔG is about −180 kJ/mol, indicating that the reaction can be spontaneous and has a large reaction tendency [35, 36]. Moreover, the large difference in thermal expansion coefficient between carbon nanomaterials and titanium and its alloys is likely to lead

Table 8.1 Simulation conditions

No	Fracture size of tungsten sphere, D/mm	The target plate material	The target plate thickness, H/mm
S-1	3	CNTs-Ti	5
S-2	5	CNTs-Ti	10
S-3	8	CNTs-Ti	15

to thermodynamic mismatch at the composite interface, resulting in stress concentration, resulting in cracks or gaps in the interface [37], which leads to a serious decline in the performance of carbon nanomaterials and titanium composites. Therefore, how to control the interfacial reaction and form strong interfacial bonding becomes one of the key factors to improve the properties of carbon nanomaterials and titanium composites.

8.2 Preparation of Carbon Nanomaterial—Titanium Composite Material

Metal matrix composites prepared by powder metallurgy have a long history and a mature process [38], and the process mainly includes two parts: powder homogenization and solid sintering forming. In the process of preparing carbon nanomaterials and titanium composites, powder homogenization is a process of pretreatment powder, whose main purpose is to distribute carbon nanomaterials uniformly in the titanium matrix powder. However, due to the strong van der Waals force (about − 100 eV) between CNTs and GR and other carbon nanomaterials [39], these carbon nanomaterials are attracted to each other and tend to generate cluster aggregation [40–44]. The agglomerated carbon nanomaterials cannot form a strong bond with the matrix during the forming process, which will result in the uneven distribution of carbon nanomaterials in the matrix, poor interfacial bonding force and the existence of voids, which will seriously affect the properties of the composites. At present, the commonly used pretreatment processes to solve the problem of powder dispersion mainly include ultrasonic-assisted dispersion method, ball milling method, etc., but these processes can only solve the dispersibility problem of carbon nanomaterials in titanium matrix with low content (mass fraction less than 2%, not described below). When the mass fraction of CNTs and GR exceeds 2%, the aggregation phenomenon also appears in the microstructure of carbon nanomaterials and titanium composites to varying degrees [45].

The density of titanium and its alloys differs greatly from that of carbon nanomaterials, and there is a strong van der Waals force interaction between CNTs and GR. Ultrasonic auxiliary dispersion method can be a small amount of carbon nanotubes reinforcing evenly dispersed in the alcohol and deionized water in the solution, stirring and ultrasonic stirring technology can cooperate solution to evenly dispersed

into the matrix powder carbon nano materials, but it is difficult to achieve high quality score (0.5%) carbon nano materials evenly dispersed in titanium matrix powder, In addition, due to van der Waals force, carbon nanomaterials may re-aggregate in local areas during the desolution and drying process. For non-in-situ self-generated CNTs and other nanomaterials with large aspect ratios or width-to-thickness ratios, the materials themselves will entangle each other and form mechanical interlocking agglomeration [46–48]. Ultrasound-assisted dispersion cannot be uniformly dispersed in advance, and subsequent mixing processes cannot perfectly solve the agglomeration problem. At present, high energyball milling (HEBM) method is often used in powder metallurgy to solve the problem of poor dispersion of carbon nanomaterials. The clusters between carbon nanomaterials are peeledby the effects of high speed rotation of the ball mill, high speed impact between the powder and the grinding ball, convection and impact between the powder, etc. The ball milling energy can be improved by increasing the mass of the grinding ball and the difference between the inner diameter of the grinding tank and the diameter of the grinding ball, so as to peel off the agglomeration of carbon nanomaterials caused by van der Waals force and solve the aggregation problem. However, carbon nanomaterials will be deformed or even broken in high-speed rotation and collision with the grinding ball, leading to a large number of defects, as shown in Fig. 8.1. Due to the high-speed impact of the grinding ball, CNTs and GR are likely to be broken, as shown in Fig. 8.1a, b. A large number of defects such as unshaped carbon and non-hexagonal carbon rings may occur at the end of the fracture. These defects have strong chemical activity and are easy to react with titanium matrix or cold welding at high temperature. Cold welding refers to the instantaneous impact of GR and other carbon nanomaterials on Ti matrix by high-speed grinding ball, and the two achieve atomic level bonding at the same time (as shown in Fig. 8.1c). In addition, another problem in the high-energy ball milling process is heat accumulation, that is, the poor heat dissipation in the ball milling process is easy to cause energy accumulation, the

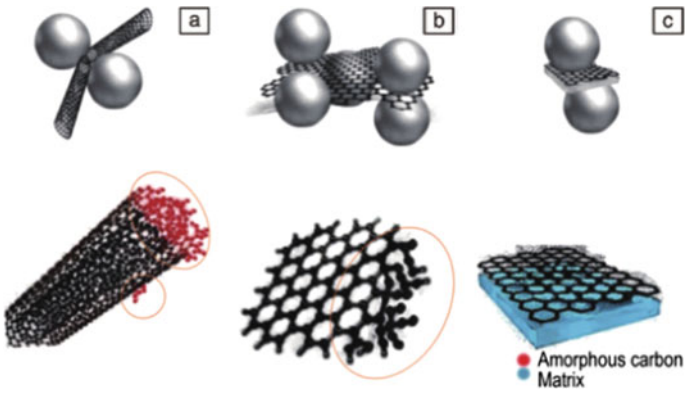

Fig. 8.1 Schematic diagrams of the defects during ball milling: **a** deformed and broken CNTs, **b** fractured graphene, c old welding

temperature in the ball milling tank rises, carbon and titanium may occur mechanical alloying, in-situ formation of TiCx.

8.3 Properties of Carbon Nanomaterials and Titanium Composites

8.3.1 Mechanical Property Analysis

Figure 8.2 shows the strengthening effect of carbon nanomaterials (CNTs, GR) content on titanium matrix. It can be seen that carbon nanomaterials with mass fraction less than 0.5% can greatly improve the yield strength of the composites, and the processing technology after molding has a significant effect on the mechanical properties of the composites. For example, Gr/Ti composites with 0.1% Gr content were hot-rolled at 823 K (black box in Fig. 8.2) and 1223 K (light blue triangle in Fig. 8.2) respectively after forming, and their yield strength increased by 57.12% and 97.91%, respectively. Compared with the unmolded carbon nanomaterials and titanium composites, their strength is also greatly improved [49–53]. In composite materials, factors such as large modulus difference and strength difference between matrix and reinforcement should be taken into account, so the formula is as follows:

$$\tau_{O\text{rowan}} = \frac{\alpha M G \mathrm{b}}{\pi\sqrt{1-\Upsilon}} \cdot \frac{\ln(\frac{d_p}{b})}{\lambda - \mathrm{d_p}} \tag{8.1}$$

where, α is the material dependent constant, M is the Taylor factor dependent on the lattice type, Dp is the diameter of the nanometer reinforcing phase, and γ is

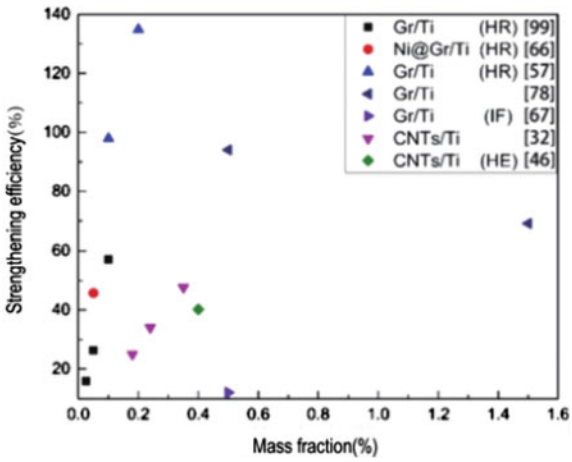

Fig. 8.2 The strengthening status of the contents of carbon nanomaterials to different composites

the Poisson's ratio of the titanium matrix. Second, the high temperature processing promotes the interface reaction, which makes the interface of TiC transition layer widen, interface strength increase, and the efficiency of load transfer increase. For CNTs and GR carbon nanomaterials with two-dimensional dimensions, the interfacial strength is also related to the length of the carbon nanomaterials along the stress direction [54]. When the length of carbon nanomaterials is small, the total area of the interface is small, and the total strength of the interface is not enough to transfer all the load on the matrix to the reinforcing body, so the interface fails first, and the carbon nanomaterials are pullout state. When carbon nano material is longer than the total area of the interface, the interface can make the base load intensity is passed on to the enhancement of body, reinforced cause stress concentration, so the carbon nanotubes reinforced body first, that there is a critical length lc for load transfer efficiency, lc can be represented by the Eq. (8.3):

$$\mathrm{l_c} = \sigma_\mathrm{y} \frac{A\mathrm{l}}{\tau S} \tag{8.2}$$

where, σ_y is the yield strength of graphene, A is the longitudinal cross-sectional area of carbon nanomaterials, L is the radial length of carbon nanomaterials, τ is the interfacial shear stress, and S is the effective interfacial area of composites. When the average length of carbon nanomaterials is greater than LC, the load transfer mechanism plays a dominant role. Combined with Eq. (8.1) and (8.2), it can be seen that the approximate strength of composites, σc, can be expressed by Eq. (8.3) [55]:

$$\sigma_\mathrm{c} = \sigma_\mathrm{y} V_G \left(1 - \frac{A\sigma_\mathrm{y}}{2\tau S}\right) + \sigma_\mathrm{m}\left(1 - \sigma_\mathrm{y} V_G\right) \tag{8.3}$$

where, V_g is the mass fraction of carbon nanotitanium matrix composites, and σm is the yield strength of matrix.

When the content of carbon nanomaterials is lower than 0.5%, the yield strength of the material increases with the increase of the content of carbon nanomaterials, as shown in Fig. 8.2. In the rolled Gr/Ti composites, when the content of graphene is low, the contribution of texture strengthening, load transfer and fine grain strengthening to the material strength has little difference, and the texture strengthening is dominant. When the volume fraction of graphene exceeds 0. 05%, the texture strengthening curve rises rapidly, followed by the load transfer curve, and the fine grain strengthening curve tends to be stable. This is because the volume fraction of graphene is too low compared with the whole composite material, so the fine grain strengthening and load transfer are not obvious. When the volume fraction of graphene exceeds 0. 11%, the texture strengthening curve increases rapidly, and the slope of the load transfer curve also increases, but the fine grain strengthening curve still tends to be stable. At this point, the texture strengthening is dominant, so the subsequent processing has a relative advantage in improving the material strength. In addition, the yield strength of 0.05% Gr/Ti composite (red dots in Fig. 8.2) is higher than that of 0.05% Gr/Ti composite, which indicates that the surface modification of graphene further

improves the yield strength of the composite. At present, there are few reports on surface modified carbon nanomateries-titanium composites. Here, this paper intends to study the penetration of carbon nanomateries-titanium matrix composites through prefabricated fragments.

8.3.2 The Simulation Analysis

8.3.2.1 Finite Element Model

For the purpose of engineering application and further study on the penetration performance of carbon nanotitanium matrix composites with shaped prefabricated fragments of different sizes, the Lagrange algorithm in AutoDyn was used to simulate the penetration performance of carbon nanotitanium matrix composites with different thickness and different target materials. The simulation conditions are shown in Tables 8.1 and 8.2. Based on the simulation results, the relationship between prefabricated fragments and mechanical properties of carbon nanomaterials was explored under a series of different influencing factors and conditions, as shown in Table 8.3.

The algorithm is used to simulate the interaction between the target material and the prefabricated fragments. The mesh size is 2 mm. The rigid model of the prefabricated fragments is adopted, which ignores the deformation and mass loss of the fragments under the penetration of the target material. Table 8.3 lists the main simulation parameters. The discrete computing domain is shown in Fig. 8.3 (taking s-1 as an example).

Table 8.2 Additional simulation conditions

No.	Fracture size of tungsten sphere, D/mm	The target plate material	The target plate thickness, H/mm
S-4	3	Cu	5
S-5	5	Cu	10
S-6	8	Cu	15
S-7	3	1006Steel	5
S-8	5	1006Steel	10
S-9	8	1006Steel	15
S-10	3	Ti–Al	5
S-11	5	Ti–Al	10
S-12	8	Ti–Al	15

Table 8.3 Numerical simulation parameters

Material	Simulation parameters			
Tungsten ball	ρ/g/cm^3	G	C1/m/s	S1
	17.6	1.54	4.092e+3	1.237
CNTs-Ti	ρ/g/cm^3	G	C1/m/s	S1
	4.51	1.23	5.02e+3	1.536
Cu	ρ/g/cm^3	BM/Kpa		
	8.96	1.29e+8		
1006Steel	ρ/g/cm^3	G	C1/m/s	S1
	7.896	2.17	4.569e+3	1.49
Ti–Al	ρ/g/cm^3	G	C1/m/s	S1
	4.419	1.23	5.13e+3	1.028

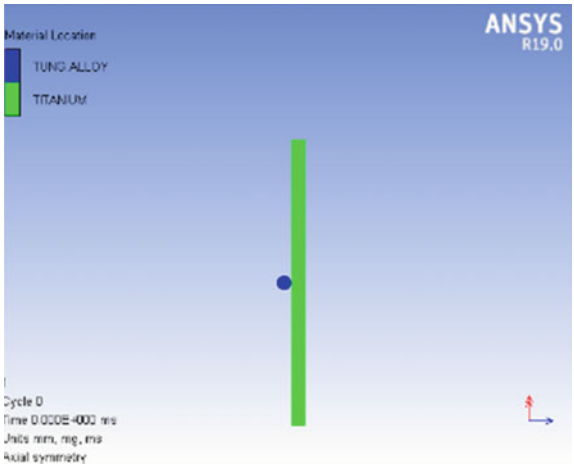

Fig. 8.3 Discrete computing domain

8.3.2.2 The Simulation Results

In this study, considering the symmetry of the simulation model, a two-dimensional symmetric model was adopted. Figure 8.4 is the target penetration process diagram of the tungsten spherical fragment on carbon nanotitanium matrix composites under the condition of S-3. The simulation can well predict the process of fragments passing through the target, so as to explore the mechanical properties of carbon nanotitanium matrix composites.

The simulation results of the downpassing target limit speed are shown in Table 8.4. Figure 8.5 shows the limit penetration velocity of the fragment under the condition of S1-3 penetrating the target; Fig. 8.6 shows the limit penetration velocity of the 5 mm tungsten spherical fragment against 10 mm target of different materials; Fig. 8.7 shows the limit penetration velocity of the tungsten spherical fragment

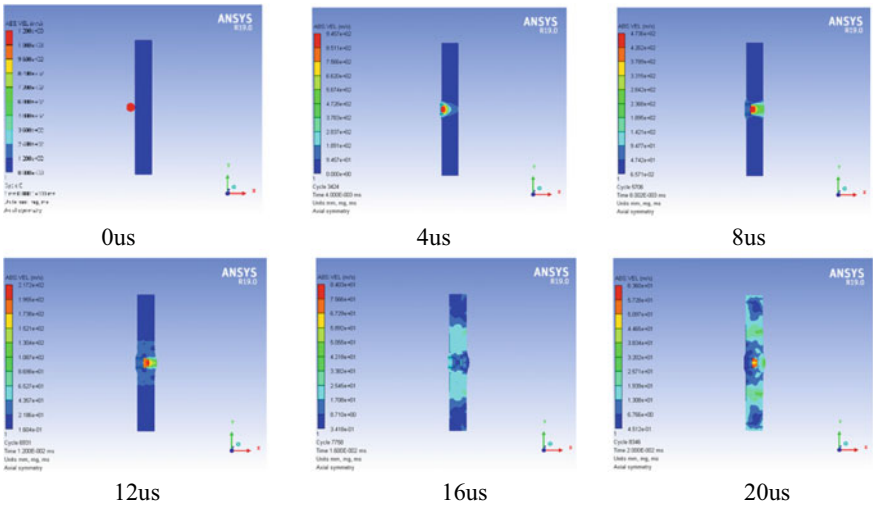

Fig. 8.4 Diagram of the penetration process of prefabricated fragments to carbon nanotitanium matrix composites under S-3 condition

Table 8.4 Statistics of the ultimate velocity of target penetration

Target/mm	Fragment/mm					
	3	5	8	3	5	8
1006 Steel				Cu		
5	1275	663	421	1223	573	375
10	2586	1376	723	2251	1273	641
15	4735	2064	1168	4166	1976	1074
CNTs–Ti				Ti–Al		
5	1375	821	567	1435	924	617
10	2636	1468	873	2675	1534	1042
15	4872	2163	1275	5075	2311	1367

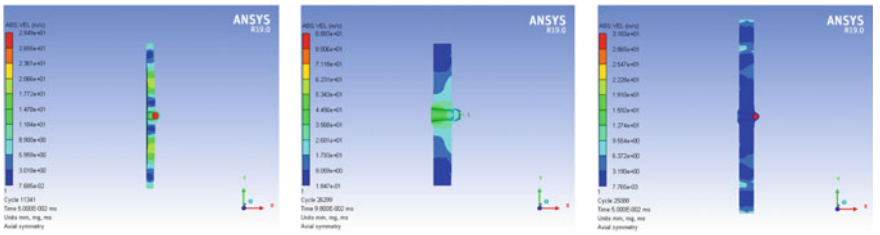

Fig. 8.5 Limit fragment penetration velocity under target penetration condition of S1-3

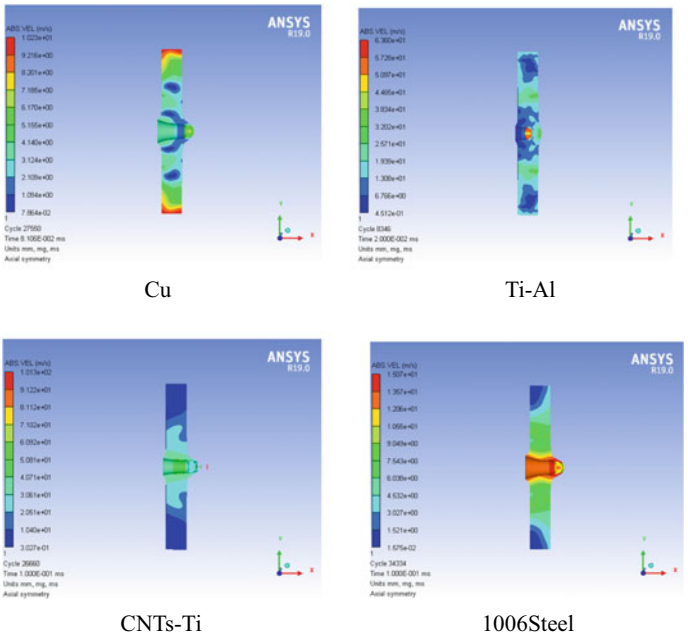

Fig. 8.6 Limit penetration velocity of 5 mm tungsten ball fragments against 10 mm targets of different materials

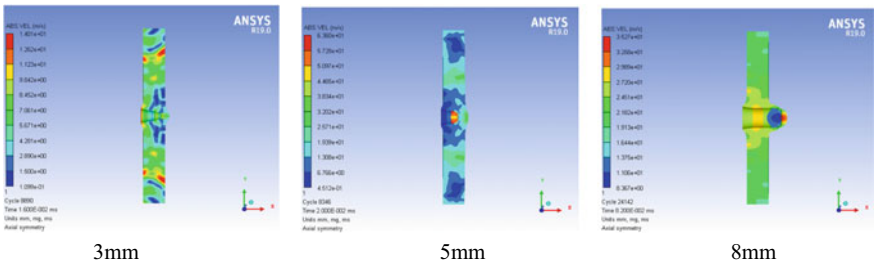

Fig. 8.7 Limit penetration velocities of tungsten ball fragments at different sizes against Ti–Al 10 mm targets

against Ti-Al10mm target of different sizes.

According to the statistical analysis in Table 8.4, under the condition of the same fragment size, CNTS-Ti material has higher strength than commonly used Cu and 1006Steel, but lower strength than carbon nano-Ti–Al material. The kinetic energy consumed by penetrating CNTS-Ti with the same thickness is equivalent to that consumed by penetrating 1006Steel at about 1.523 times, and equivalent to that consumed by penetrating 1006 Steel at about 1.876 times. The kinetic energy

consumed by penetrating the same thickness of carbon nano-Ti–Al material is equivalent to about 1.785 times of the kinetic energy consumed by penetrating 1006 Steel and 2.23 times of the kinetic energy consumed by penetrating 1006 Steel. The kinetic energy consumed by penetrating the same thickness of carbon nano-Ti–Al material is about 1.18 times that of penetrating carbon nano-titanium and materials. This provides a foundation for the subsequent study of mechanical properties of carbon nanomaterials.

8.4 Conclusion

At present, the research work of carbon nanomaterials and titanium composites is not perfect, and a complete system has not been formed, and a lot of research work is still needed to enrich and support to promote its development and industrial application. How to extend the strengthening effect of carbon nanomaterials in pure titanium matrix to other high strength titanium alloy systems, and then study the strengthening effect of carbon nanomaterials in titanium alloy matrix composites is also a direction that needs to be developed. Based on the research of carbon nanomaterials reinforced metal matrix composites in recent years, the influence of carbon nanomaterials and titanium composites on the material mechanical properties under prefabricated fragments was studied by simulation. The research results are as follows.

1. Under the condition of the same fragment size, CNTS-Ti material has higher strength than commonly used Cu and 1006Steel, but lower strength than carbon nano-Ti–Al material.
2. The kinetic energy consumed by penetrating CNTS-Ti with the same thickness is equivalent to that consumed by penetrating 1006 Steel at about 1.523 times, and equivalent to that consumed by penetrating 1006 Steel at about 1.876 times
3. The kinetic energy consumed through the same thickness of carbon nano-Ti–Al material is equivalent to about 1.785 times of the kinetic energy consumed through 1006Steel, which is equivalent to about 2.23 times of the kinetic energy consumed through 1006Steel.
4. The kinetic energy consumed by penetrating the same thickness of carbon nano Ti–Al material is about 1.18 times that of penetrating carbon nano titanium and materials.

References

1. K. Kondoh, J. Umeda, R. Soba et al., *Titanium in medical and dental applications* (Woodhead Publishing, UK, 2018), pp. 583–590
2. Q. Yu, L. Q , T. Tsuru, et al., *Science* **347**(6222), 635–639 (2015)
3. S. Guo, Q.K. Meng, X.Q. Zhao, et al., Sci. Rep. **5**, 14688 (2015)
4. Z.L. Ding, Y.C. Fan, H.B. Qi et al., Int. J. Automot. Mech. Eng. **4**(4), 974–980 (2011)

5. S.C. Tjong, Y.W. Mai, Compos. Sci. Technol. **68**(3/4), 583–601 (2008)
6. L.J. Huang, S. Wang, L. Geng et al., Compos. Sci. Technol. **82**, 23–28 (2013)
7. L.J. Huang, L. Geng, H.X. Peng, Prog. Mater. Sci. **71**, 93–168 (2015)
8. F. Ma, T. Wang, P. Liu, et al., Mater. Sci. Eng. A 654, 352–358 (2016)
9. K. Vasanthakumar, N.S. Karthiselva, N.M. Chawake et al., J. Alloys Compounds **709**, 829–841 (2017)
10. H. Feng, Y. Zhou, D. Jia, et al., Crystal Growth De. **6**(7), 1626–1630 (2006)
11. H. Feng, Y. Zhou, D. Jia, et al., Compos. Sci. Technol. **64**(16), 2495–2500 (2004)
12. S. Li, K. Kondoh, H. Imai, et al., Mater. Sci. Eng. A. **628**, 75–83 (2015)
13. X. Guo, L. Wang, M. Wang, et al., Acta Materialia **60**(6/7), 2656–2667 (2012)
14. L. Huang, L. Wang, M. Qian, et al., Scripta Materialia. **141**, 133–137 (2017)
15. H. Zheng, K. Jaganandham, J. Heat Transfer. **136**(6), 061301 (2014)
16. W.Z. Yang, W.M. Huang, Z. Wang, et al., Acta Metallurgica Sinica (English Letters) **29**(8), 707–713 (2016)
17. K. Chu, X.H. Wang, F. Wang et al., Carbon **133**, 127–139 (2018)
18. K. Yang, X. Shi, W. Zhai, et al., RSC Adv. **5**(55), 44618–44625 (2015)
19. T.R. Tamilarasan, U. Sanjith, M. Siva Shankar, et al., Wear **390/391**, 385–391 (2017)
20. S. Stankovich, D.A. Dikin, G.H. Dommett et al., Nature **442**(7100), 282–286 (2006)
21. F. Saba, S.A. Sajjadi, M. Haddad-Sabzevar, et al. Diamond Rel. Mater. **89**, 180–189 (2018)
22. K. Kondoh, T. Threrujirapapong, H. Imai, et al., Compos. Sci. Technol. **69**(7), 1077–1081 (2009)
23. S. Iijima, Nature **354**(6348), 56–58 (1991)
24. P.V. Kamat, Cheminform **41**(13), 520–527 (2010)
25. Q. Zeng, J. Luna, Y. Bayazitoglu, et al., Mater. Sci. Forum. **561–565**, 655–658 (2007)
26. S.C. Tjong, Mater. Sci. Eng. R **74**(10), 281–350 (2013)
27. M. Yang, L. Weng, H. Zhu, et al., Scripta Materialia **138**, 17–21 (2017)
28. H.G.P. Kumar, M.A. Xavior, Procedia Eng. **97**, 1033–1040 (2014)
29. N. Nunn, M. Torelli, G. Mcguire, et al., Curr. Opin. Solid State Mater. Sci. **21**(1), 1–9 (2017)
30. F. Zhang, P. Zhao, T. Liu, et al., Diamond Relat. Mater. **83**, 60–66 (2018)
31. K.P. So, J.C. Jeong, J.G. Park et al., Compos. Sci. Technol. **74**, 6–13 (2013)
32. S.I. Oh, J.Y. Lim, Y.C. Kim et al., J. Alloy. Compd. **542**(1), 111–117 (2012)
33. K. Chu, F. Wang, X.H. Wang et al., Mater. Des. **144**, 290–303 (2018)
34. N. Xiong, R. Bao, J. Yi, et al., J. Alloys Compounds **770**, 204–213 (2019)
35. A.F. Fonseca, T. Liang, D. Zhang et al., ACS Appl. Mater. Interfaces **9**(38), 33288–33297 (2017)
36. X. Sun, Y. Han, S. Cao, et al. J. Mater. Sci. Technol. **33**(10), 1165–1171 (2017)
37. B. Cheng, R. Bao, J. Yi, et al., J. Alloys Compounds **722**, 852–858 (2017)
38. S. Li, B. Sun, H. Imai, et al., Compos. Part A: Appl. Sci. Manuf. **48**, 57–66 (2013)
39. X. Zhang, F. Song, Z. Wei, et al., Mater. Sci. Eng. A **705**, 153–159 (2017)
40. K.S. Munir, Y. Li, J. Lin et al., Materialia **3**, 122–138 (2018)
41. K. Kondoh, T. Threrujirapapong, J. Umeda, et al., Compos. Sci. Technol. **72**(11), 1291–1297 (2012)
42. C. Ke, Jia C. Physica Status Solidi [J] **211**(1), 184–190 (2014)
43. Z. Hu, G. Tong, Q. Nian, et al., Compos. Part B: Eng. **93**, 352–359 (2016)
44. B. Chen, S. Li, H. Imai, et al., Mater. Des. **72**, 1–8 (2015)
45. B. Guo, B. Chen, X. Zhang, et al., Carbon **135**, 224–235 (2018)
46. B. Guo, X. Zhang, X. Cen, et al., Carbon **139**, 459–471 (2018)
47. Z. Yang, W. Lu, J. Qin, et al., Mater. Sci. Eng. A **425**(1/2), 185–191 (2006)
48. K. Kondoh, *Titanium Powder Metallurgy* (Butterworth-Heinemann, Boston, 2015)
49. S.F. Bartolucci, J. Paras, M.A. Rafiee et al., Mater. Sci. Eng. **528**(27), 7933–7937 (2011)
50. P. Shao, W. Yang, Q. Zhang, et al., Compos. Part A: Appl. Sci. Manuf. **109**, 151–162 (2018)
51. M. Rashad, F. Pan, M. Asif, et al., J. Ind. Eng. Chem. **20**(6), 4250–4255 (2014)
52. M. Yang, L. Weng, H. Zhu, et al., Carbon **118**, 250–260 (2017)
53. X.N. Mu, H.N. Cai, H.M. Zhang et al., Carbon **137**, 146–155 (2018)

54. Z. Cao, X. Wang, J. Li, et al., J. Alloys Compounds **696**, 498–502 (696)
55. K.S. Munir, Y. Li, D. Liang et al., Mater. Des. **88**, 138–148 (2015)
56. K.S. Munir, Y. Zheng, D. Zhang et al., Mater. Sci. Eng. A **688**, 505–523 (2017)
57. K.S. Munir, P. Kingshott, C. Wen, Crit. Rev. Solid State Mater. Sci. **40**(1), 38–55 (2015)
58. X.N. Mu, H.N. Cai, H.M. Zhang et al., Mater. Des. **140**, 431–441 (2018)
59. K.S. Munir, Y. Li, M. Qian et al., Carbon **99**, 384–397 (2016)

Chapter 9
Preparation, Structure and Performance of TKX-50/AP/GO Composite

Kun Zhang, Fan Jiang, Xiaofeng Wang, and Xiaojun Feng

Abstract Graphene oxide (GO) is a commonly used energetic additive in explosive and propellants systems. In order to study the effect of GO on the performance of TKX-50/AP blends, TKX-50/GO, AP/GO, TKX-50/AP/GO composites were prepared by solvent method. Then the structure was characterized by scanning electron microscope (SEM), fourier infrared technology (FT-IR), powder X-ray (XRD). Differential scanning calorimetry (DSC) was used to compare and study the thermal performance changes of TKX-50, AP and the two after being loaded by GO. Finally, the mechanical sensitivity of them was tested by the national military standard method. The results show that GO can be better loaded on the surface of TKX-50 and AP, and there is no chemical change during the loading process, only the combination of physical adsorption force. DSC shows that in the two-component system, GO can reduce the thermal decomposition peak temperature of TKX-50 and AP by 8.86°C and 40.16°C; but in the TKX-50/AP/GO three-component system, GO only significantly reduces the thermal decomposition peak temperature of TKX-50, and hardly changes the decomposition temperature of AP. In addition, after loading GO, the impact and friction sensitivity of TKX-50 and AP have been significantly reduced, and the safety has been improved.

K. Zhang · F. Jiang · X. Wang · X. Feng (✉)
Xi'an Modern Chemistry Research Institute, Xi'an Zhangbadong Road 168, Xi'an 710065, Shanxi, PR China
e-mail: bingqi204suo@163.com

K. Zhang
e-mail: zhangkun204@163.com

F. Jiang
e-mail: jiangfan9101@163.com

X. Wang
e-mail: wangxf_204@163.com

A. Gany and X. Fu (eds.), *2021 International Conference on Development and Application of Carbon Nanomaterials in Energetic Materials*, Springer Proceedings in Physics 276,
https://doi.org/10.1007/978-981-19-1774-5_9

9.1 Introduction

Lightweight carbon materials such as carbon black, fullerenes, carbon nanotubes, and graphene have certain application value in explosives. Among them, graphene is a two-dimensional material with a six-element honeycomb structure composed of carbon atoms, which can be used as the basic unit of carbon materials [1–4]. Graphene oxide (GO) is obtained by oxidation of graphene in concentrated acid by a strong oxidant. It has a two-dimensional planar structure with a large π bond in the molecule and a carboxyl group at the edge [5, 6]. GO only has the thickness of one atomic layer, but the width can reach tens of microns, which makes it have a large specific surface area [7]. GO has the characteristics of high energy and thermal instability. It is prone to exothermic disproportionation reaction under mild heating conditions. A certain amount of chemical energy can be released during the decomposition reaction, which can be regarded as a potential energetic material. Moreover, the unique structure gives GO excellent physical and chemical properties (excellent electrical conductivity, thermal conductivity, mechanical properties and huge theoretical specific surface area), making it a better application advantage in the field of energetic materials than other materials [8–14].

Nitrogen-rich energetic compounds, not only have high energy density, good safety, but also are environmentally friendly. It is a new type of energetic material integrating high energy, safety and greenness [15]. In 2012, Fischer et al. [16] designed and synthesized a new type of nitrogen-rich energetic ion salt, 5,5'-bitetrazole-1,1'-dioxodihydroxy (TKX-50), which belongs to this material. The theoretical density of TKX-50 is 1.918 g cm^{-3}, the detonation velocity is 9699 m s^{-1}, and the standard enthalpy of formation is 446.6 kJ mol^{-1}. Calculations show that its energy is equivalent to CL-20, and the production and preparation process is simpler, and the gas production is large. Therefore, TKX-50 is an energetic ionic salt compound with high energy, insensitivity and excellent comprehensive performance [17, 18]. However, Sinditskii [19] found that its heat of combustion is (2054 ± 6) kJ mol^{-1}, and the calculated generation of TKX-50 is only (111 ± 16) kJ mol^{-1}, which is much lower than the Fischer report. Xing and Yang [20, 21] measured the explosion heat value of TKX-50 by experiments to be only 4650, the explosion pressure is 26.4 GPa, and the working power is 1.377 kJ g^{-1}, which is significantly lower than the calculated energy value. Therefore, TKX-50 is a serious negative oxygen energetic material (oxygen balance is −27.1%), and it is necessary to explore the effect of oxidants on its performance. Ammonium perchlorate (AP) is a commonly used oxidant with a high positive oxygen balance value and is often used to adjust negative oxygen energetic materials (such as RDX[22], HMX[23], CL-20[24] etc.). In addition, studies have found that GO can significantly reduce the high and low temperature decomposition peak temperatures of AP, and even make the low temperature decomposition heat peak disappear [9, 25–27]. By loading GO with TKX-50/AP blends, it is expected to improve the oxygen balance of TKX-50 and improve its reaction characteristics,

which has certain application value and theoretical significance. However, the preparation and performance study of the TKX-50/AP/GO three-component composite has not been reported yet.

For this reason, in this paper, TKX-50/GO, AP/GO, TKX-50/AP/GO composites were prepared separately by using a solvent method. Then the structure was characterized by scanning electron microscope (SEM), Fourier infrared technology (FT-IR), powder X-ray (XRD). Differential scanning calorimetry (DSC) was used to compare and study the thermal performance changes of TKX-50, AP and the two after being loaded by GO. Finally, the impact sensitivity of them was tested by the national military standard method [28].

9.2 Experimental

9.2.1 Samples

TKX-50, white powder, particle size 200 μm, AP, white powder, particle size 360 μm, all made by Xi'an Modern Chemistry Research Institute. GO, gray black powder, produced by Suzhou Tanfeng Technology Co., Ltd. TKX-50/GO, AP/GO, TKX-50/AP/GO composites: Weigh a certain amount of GO, TKX-50, AP, add it to the ethyl acetate solution, stir, filter, and dry to obtain the product. Among them, the component systems in the TKX-50/GO and AP/GO composites are 80% and 20%; the component systems in the TKX-50/AP/GO composites are 40, 40, and 20% (Fig. 9.1).

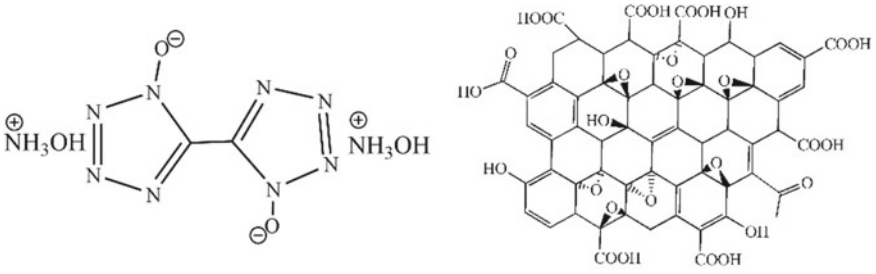

a. TKX-50 b. GO

Fig. 9.1 Molecular structure of TKX-50 and GO

9.2.2 Instrument

DSC, NETZSCH DSC 204 HP; FT-IR, NEXUS 870 Fourier Transform Infrared Spectrometer, Thermo-Fisher Company, USA; PXRD, D/MAX-2400 XRD analyzer, Rigaku Corporation.

9.2.3 Experimental Conditions

DSC experiment: Atmosphere is dynamic high-purity nitrogen, flow rate is 50 mL·min^{-1}, pressure is 0.1 MPa, heating rate is 10 °C·min^{-1}, sample mass is 1.0 mg, container is aluminum crucible.

Mechanical sensitivity: impact sensitivity, using GJB772A-97 method 601.1, sample conditions are drop weight 10 kg, drop height 25 cm, and drug amount 50 mg; friction sensitivity, using GJB772A-97 method 602.1, sample conditions are drop gauge pressure 3.92 MPa, pendulum The angle is 90°, and the dose is 20 mg [28].

9.3 Results and Discussion

9.3.1 Structural Analysis

9.3.1.1 SEM Analysis

SEM pictures can intuitively compare the changes in the crystal morphology of energetic materials before and after processing, and can see the physical state and diffusion distance of the composite material. Figure 9.2 is the SEM images of AP, TKX-50, TKX-50/AP blends raw materials and after being loaded by GO. It can be seen from the Fig. 9.2 that the AP crystal is elliptical, TKX-50 is nearly hexahedron, the surface is smooth, and the GO is an agglomerated layered structure. After loading, the crystal morphology of AP and TKX-50 did not change, and GO was adsorbed on the crystal surface, indicating that AP, TKX-50 and GO may have a powerful effect, thereby stabilizing the structure.

9.3.1.2 FT-IR Analysis

The stretching and bending motion of the molecular characteristic group bond can reflect the structure of the molecule. Observing the changes of infrared absorption peaks by FT-IR can indirectly prove whether the molecules undergo chemical reactions to generate new substances after they are combined or assembled. As the Fig. 9.3

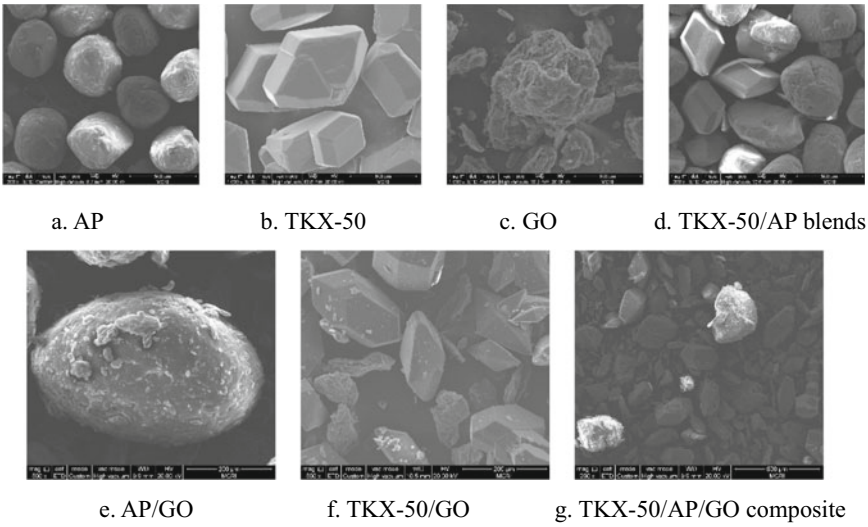

Fig. 9.2 SEM of AP, TKX-50, TKX-50/AP blends and after being loaded by GO

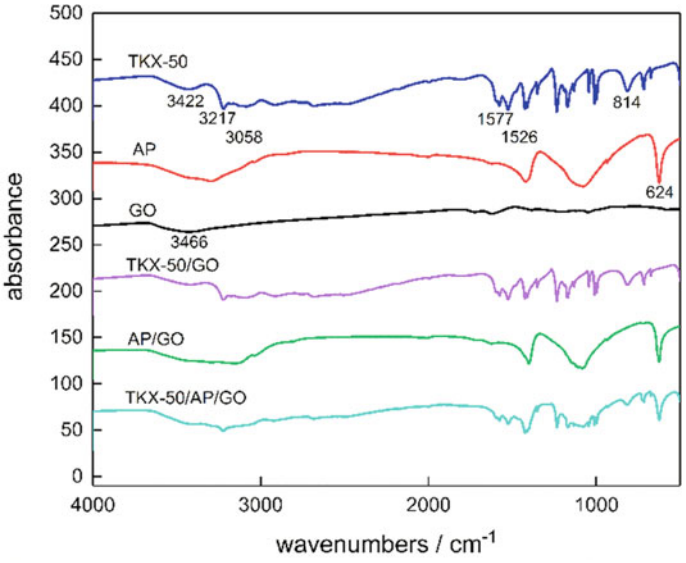

Fig. 9.3 IR of AP, TKX-50, TKX-50/AP blends and after being loaded by GO

show, the typical infrared absorption peaks of TKX-50 are: 3422 cm^{-1} represents the stretching vibration of the hydrogen–oxygen bond of the hydroxyl group on $NH3OH^+$. The absorption peaks at 3058, 1577, and 1526 cm^{-1} are the characteristic absorption of aromatic groups, namely the tetrazole ring. The 814 cm^{-1} characteristic absorption is caused by the stretching vibration of the nitrogen–oxygen bond on the tetrazole ring. The typical absorption peak of AP is 624 cm^{-1}, which is caused by the stretching vibration between the chlorine and oxygen of perchlorate. Because the main component of GO is carbon and the molecular edge is carboxyl, it is highly hydrophilic, so there is only a relatively broad absorption peak at 3466 cm^{-1}, which represents the hydroxyl vibration in the molecule. It can be seen from the infrared spectrum of GO loaded TKX-50, AP, and TKX-50/AP blends that the infrared absorption peak positions of TKX-50 and AP have not almost changed, and only some of the absorption peaks have weakened. It shows that no chemical reaction occurs during the loading process of GO, TKX-50 and AP, and the molecules are combined by physical adsorption.

9.3.1.3 PXRD Analysis

Powder X-ray can directly prove whether the crystal form of the raw material has changed, and can also indirectly reflect the combining state and coating method of the composite. Figure 9.4 is the PXRD of AP, TKX-50, TKX-50/AP blends and after being loaded by GO. It can be seen from Fig. 9.4 that the diffraction peak positions of the crystals hardly changed after loading, indicating that the GO loading adsorption of AP and TKX-50 powder has no effect on the crystal form, and the adsorption process is a physical interaction process, and it does not occur chemical reaction. In addition, the peak intensities of AP 15.24°, 19.13°, 23.70°, 27.61°, 29.98° are significantly weaker. This is because GO loads a certain crystal plane of AP and weakens the diffraction peak intensity of this crystal plane to varying degrees. The intensity of the diffraction peaks at 22.81°, 34.95°, etc. hardly changed, indicating that it is difficult for GO to adsorb and coat some crystal faces of AP. The diffraction peak intensity of almost every crystal plane of TKX-50 is reduced to different degrees, and only 33.34° is partially enhanced, indicating that the interaction between GO and TKX-50 is relatively strong, and the loading rate is high. It can be seen from Fig. 9.4c that GO has little effect on the diffraction peak intensity of the TKX-50/AP blends. It may be that the TKX-50 peak intensity is too high to cause this phenomenon.

9.3.2 Thermal Analysis

In order to study the effect of GO on the thermal decomposition performance of TKX-50, AP, TKX-50/AP blends, the thermal decomposition behavior of TKX-50/GO, AP/GO, and TKX-50/AP/GO composites is tested by DSC. As the Fig. 9.5 show, TKX-50 has two continuous exothermic decomposition peaks, which are 242.98°C

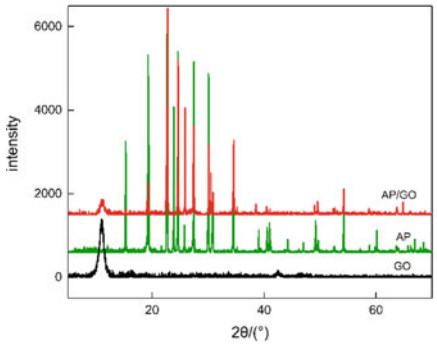

a. AP, GO, AP/GO composite

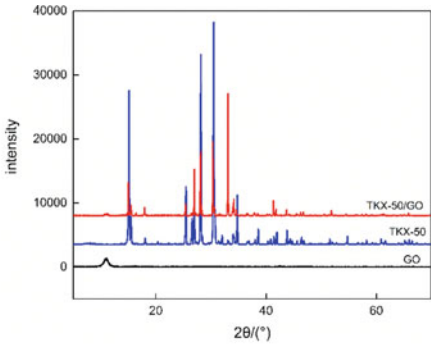

b. TKX-50, GO, TKX-50/GO composite

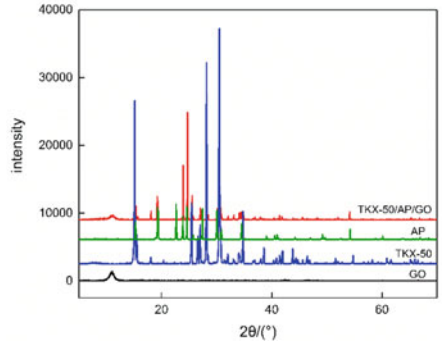

c. TKX-50, AP, GO, TKX-50/AP/GO composite

Fig. 9.4 PXRD of AP, TKX-50, TKX-50/AP blends and after being loaded by GO

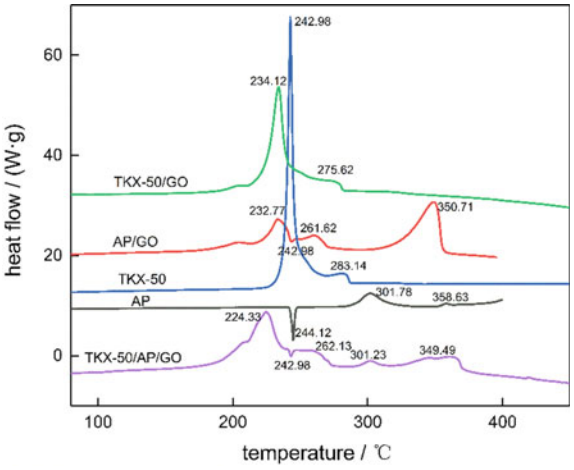

Fig. 9.5 DSC of TKX-50, AP, TKX-50/GO, AP/GO and TKX-50/AP/GO composites

and 283.14 °C respectively. The first exothermic peak has a sharp peak shape, indicating that TKX-50 exothermic violently and decomposes faster in the initial stage. After GO was loaded on the surface of TKX-50, the first decomposition peak of TKX-50 decreased by 8.86 °C, which almost coincided with the thermal decomposition peak of GO [29], and the second decomposition peak decreased by 7.52 °C. AP crystal has a melting endothermic peak at 244.14 °C. At this time, AP undergoes crystal transformation, and then there are two high-temperature exothermic decomposition peaks at 301.78 and 358.63 °C. After GO is loaded with AP, the endothermic peak of AP hardly changes, but the initial exothermic peak temperature is reduced by 40.16 °C, and the thermal decomposition is greatly advanced. After GO is loaded with the TKX-50/AP blends, the decomposition peak temperature of TKX-50 is further reduced compared with the peak temperature of TKX-50/GO complex, but the melting endothermic peak and exothermic decomposition peak of AP are almost unchanged. This may be because the carboxyl group at the edge of the GO molecule is more likely to form intermolecular hydrogen bonds with the TKX-50 molecule, and AP, as a small molecule compound, is difficult to compound with GO in the three-component system where TKX-50 exists.

9.3.3 Mechanical Sensitivity Analysis

Mechanical sensitivity is often used to characterize the safety of energetic materials, which is essential for the production, use, and transportation of energetic materials. Figure 9.6 is the mechanical sensitivity of AP, TKX-50, TKX-50/AP blends and

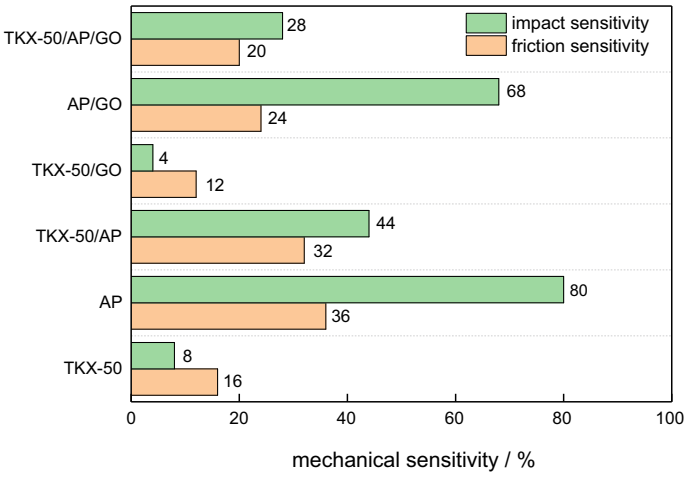

Fig. 9.6 Mechanical sensitivity of AP, TKX-50, TKX-50/AP blends and after being loaded by GO

after being loaded by GO. As the Fig. 9.6 show, the impact sensitivity of TKX-50, AP, TKX-50/AP blends, TKX-50/GO, AP/GO, TKX-50/AP/GO are 8, 80, 44, 4, 68, 28%, friction sensitivity is 16, 36, 32, 12, 24, 20%. By comparison, it is found that after GO is loaded with elementary materials, it can effectively reduce the mechanical sensitivity and improve the safety of TKX-50 and AP. This is because GO has a layered structure, which can act as a buffer when impacted or rubbed, thereby reducing the formation of local hot spots.

9.4 Conclusion

(1) TKX-50/GO, AP/GO, and TKX-50/AP/GO composites were prepared by solvent method. GO can be better loaded on the surface of TKX-50 and AP, and there is no chemical change during the loading process, only by the combination of physical adsorption force. Moreover, the interaction between TKX-50 and GO is relatively strong.

(2) In the two-component system, GO can reduce the thermal decomposition peak temperature of TKX-50 and AP by 8.86°C and 40.16°C. However, in the TKX-50/AP/GO three-component system, GO only significantly reduces the thermal decomposition peak temperature of TKX-50, and almost does not change the decomposition temperature of AP.

(3) The impact sensitivity of TKX-50 and AP are 8% and 80%, and the friction sensitivity is 16% and 36% respectively. After loading GO, the impact and friction sensitivity of TKX-50 and AP are significantly reduced, and the safety is improved.

References

1. X. Qi, X. Zhang, J. Li, et al., Influence of carbon black particle size on combustion characteristics of CMDB propellant. Chem. Propell. Polym. Mater. **10**(6), 51–53 (2012)
2. S. Li, D. He, W. Shan, et al., A study on comprehensive characteristic of RDX-CMDB propellants containing fullerene. J. Propul. Technol. **18**(6), 79–83 (1997)
3. X. Yu, The effect of carbon nanotubes on the thermal decomposition of CL-20. Chin. J. Explos. Propell. **27**(3), 78–80 (2004)
4. X. Wang, J. Li, Y. Luo, Preparation and thermal decomposition behavior of ammonium perchlorate/graphene aerogel nanocomposites. Chin. J. Explos. Propell. **35**(6), 76–80 (2012)
5. F. Kim, L.J. Cote, J. Huang Graphene oxide: surface activity and two-dimensional assembly. Adv. Mater. **22**(17), 1954–1958 (2010)
6. V.C. Tung, J.H. Huang, I. Tevis et al., Surfactant-free water-processable photoconductive all-carbon composite. J. Am. Chem. Soc. **133**(13), 4940–4947 (2015)
7. J. Kim, L.J. Cote, F. Kim, W. Yuan, K.R. Shull, J. Huang, Graphene oxide sheets at interfaces. J. Am. Chem. Soc. **132**(23), 8180–8186 (2010)
8. D. Krishnan, F. Kim, J. Luo et al., Energetic graphene oxide: Challenges and opportunities. Nano Today **7**(2), 137–152 (2012)

9. N.K. Memon, A.W. Mcbain, S.F. Son, Graphene oxide/ammonium perchlorate composite material for use in solid propellants. J. Propul. Power **32**(3), 1–5 (2016)
10. Y. Li, W.Y. Zhao, Z.H. Mi et al., Graphene-modified explosive lead styphnate composites. J. Therm. Anal. Calorim. **124**(2), 683–691 (2016)
11. Y.M. Shi, L.J. Li, Chemically modified graphene: flame retardant or fuel for combustion? J. Mater. Chem. **21**(10), 3277–3279 (2011)
12. J. Yu, J. Wang, Y. Liu, et al., Preparation and thermal properties of CL-20/GO nano-composite energetic materials. Sci. Technol. Eng. **17**(12), 93–96 (2017)
13. X. Zhang, W.M. Hikal, Y. Zhang et al., Direct laser initiation and improved thermal stability of nitrocellulose/graphene oxide nanocomposites. Appl. Phys. Lett. **102**(14), 5428 (2013)
14. R. Li, J. Wang, J.P. Shen et al., Preparation and characterization of insensitive HMX/graphene oxide composites. Propell. Explos. Pyrotech. **38**(6), 798–804 (2013)
15. L. Peng, Y. Li, Y. Yang, et al., Research progress in synthesis of energetic compounds of bicyclo- and multicyclo-tetrazoles. Chin. J. Org. Chem. **32**(4), 667–676 (2012)
16. N. Fischer, D. Fischer, T.M. Klaptke et al., Pushing the limits of energetic materials: the synthesis and characterization of dihydroxylammonium-5,5'-bistetrazole-1,1'-diolate. J. Mater. Chem. **22**(38), 20418–20422 (2012)
17. X. Huang, T. Guo, M. Liu, et al., Review on bis-azoles and its energetic ion derivatives. Chin. J. Energ. Mater. **23**(3), 291–301 (2015)
18. F. Bi, X. Fan, C. Xu, et al., Review on insensitive non-metallic energetic ionic compounds of tetrazolate anions. Chin. J. Energ. Mater. (Hanneng Cailiao) **20**(6), 805–811 (2012)
19. V.P. Sinditskii, S.A. Filatov, V.I. Kolesov et al., Combustion behavior and physico-chemical properties of dihydroxylammonium-5,5′-bistetrazole-1,1′-diolate (TKX-50). Thermochim. Acta **614**, 85–92 (2015)
20. X. Xing, S. Zhao, W. Zhang, et al., The detonation properties research on TKX-50 in high explosives. Propell. Explos. Pyrotech. **44**(4), 408–412 (2019)
21. J. Liu, G. Fan, X. Lu, et al., Detonation and Safety Performance of TKX-50 Based PBX. Chin. J. Energet. Mater. **27**(11), 902–907 (2019)
22. F. Zhao, P. Chen, S. Li, et al., Effect of ballistic modifiers on thermal decomposition characteristics of RDX/AP/HTPB propellant. Thermochimica Acta **416**(1), 75–78 (2004)
23. F. Nie, J. Zhang, Q. Guo, et al., Sol–gel synthesis of nanocomposite crystalline HMX/AP coated by resorcinol–formaldehyde. J. Phys. Chemist. Solids **71**(2), 109–113 (2010)
24. H. Zhai, Y. Zhu, Y. Lu, et al., Preparation and characteristics of CL-20/AP composite energetic materials with zero oxygen balance. Chin. J. Explos. Propell. **41**(1), 41–46 (2018)
25. Y. Lan, J. Deng, Y. Luo, Preparation and characterization of graphene aerogel/Fe_2O_3/ammonium perchlorate nanostructured energetic composite. J. Sol-Gel Sci. Technol. **74**(1), 161–167 (2015)
26. Y. Zu, Y. Zhao, K. Xu et al., Preparation and comparison of catalytic performance for nano $MgFe_2O_4$, GO-loaded $MgFe_2O_4$, and GO-coated $MgFe_2O_4$, nanocomposites. Ceram. Int. **42**, 18844–18850 (2016)
27. X. Lan, Study on Graphene Based Composites and Their Catalytic Properties (Nanjing University of Science & Technology, Nanjing, 2013)
28. L.W. Finger, R.M. Hazen, Crystal structure and compression of ruby to 46 kbar. J. Appl. Phys. **49**(12), 5823–5826 (1978)
29. H.K. Jeong, P.L. Yun, H.J. Mei et al., Thermal stability of graphite oxide. Chem. Phys. Lett. **470**(4–6), 255–258 (2009)

Chapter 10
Mechanical Response of Aramid Honeycomb Sandwich Panels Under Different Impulses

Tian Jin, Yayun Zhao, and Yuxin Sun

Abstract New materials and structures research are important for modern engineering technology. In order to study for the mechanics response of aramid fiber and honeycomb sandwich panel under impulses, honeycomb sandwich plate with aramid as sandwich layer was established, and Aluminum was used for the upper and bottom panels, the mechanical response of Aramid honeycomb sandwich panels was discussed under impulse loads of different length, size and shape. The results show that the stress extremum appears earlier and larger with the increase of impulse peak under the rectangular impulses with the same specific impulse, the maximum stress increases with the increase of specific impulse, but the growth rate decreases. Moreover, both displacement and stress are bigger under rectangular impulse compare with triangle and ladder impulses. In general, the results are able to reveal the law of Aramid honeycomb sandwich panels under short pulse load, and can be referred to future study on Aramid honeycomb panels.

10.1 Introduction

Aramid is a kind of new material, which has the advantages of light weight, low density, high specific strength, high specific stiffness, excellent impact resistance and seismic performance, good heat insulation and sound insulation performance [1–3], and has important application value [4, 5]. Its excellent material mechanics performance has been widely used in composite materials [6–8], sandwich structure panel [9, 10] and other aspects. A large number of tests and simulation studies have been

T. Jin · Y. Sun (✉)
National Key Laboratory of Transient Physics, Nanjing University of Science and Technology, Nanjing 210094, Jiangsu, China
e-mail: yxsun01@163.com; yyzh@njust.edu.cn

T. Jin
e-mail: tjin@njust.edu.cn

Y. Zhao
Hubei Aerospace Vehicle Research Institute, Wuhan 430040, Hubei, China

A. Gany and X. Fu (eds.), *2021 International Conference on Development and Application of Carbon Nanomaterials in Energetic Materials*, Springer Proceedings in Physics 276,
https://doi.org/10.1007/978-981-19-1774-5_10

conducted. Sandwich layer structure is a kind of mechanical structure with excellent mechanical properties, which is also widely developed and applied in various fields [11–13]. A large number of experimental studies have been made on the failure mode of metal honeycomb structure [14], anti-explosion performance [15–19], compression response under impact load [20–23], deformation energy absorption ability under impact/explosion load [24, 25], etc. In recent years, more and more studies have been conducted on the use of aramid fiber as honeycomb material. As a mature method of impact dynamics, numerical simulation has also been studied extensively [26, 27]. A large number of experiments [28] and simulation [30] studies have been carried out, and some applications have been obtained [30, 31]. Numerical simulation, as a mature research method of impact dynamics, has also carried out a lot of research [32]. The main geometric size of honeycomb plate has a great influence on honeycomb deformation.

In previous studies, aramid fiber was mainly used as the panel [33] and other composite materials or metals were used as the sandwich layer, and the response of materials or structures was studied, while the influence of impulses on honeycomb sandwich panels was ignored. In this paper, the mechanical response law of the honeycomb sandwich plate under impulses was studied by using different impulses with the aramid fiber as the sandwich layer and aluminum alloy as the panel.

10.2 Calculation

10.2.1 Calculation Model

The model was established in ANASYS/LS-DYNA19.0 according to the model in Fig. 10.1. The model included upper face plane, bottom face plane and honeycomb core. The core was made up of cells (Fig. 10.2), which l is 2 cm, h is 12 cm and d 0.02 cm, the total length of the core is 48 cm and width 48.5 cm. The calculation model was established by three-dimensional Lagrange element (Fig. 10.3).

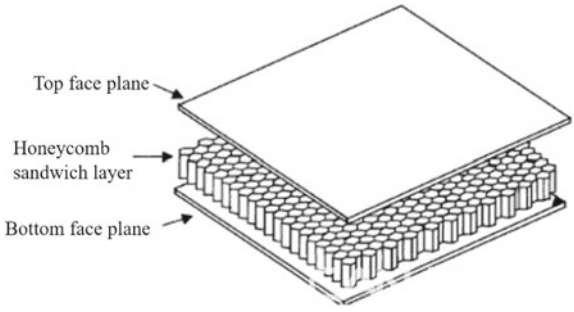

Fig. 10.1 Diagram of sandwich panel

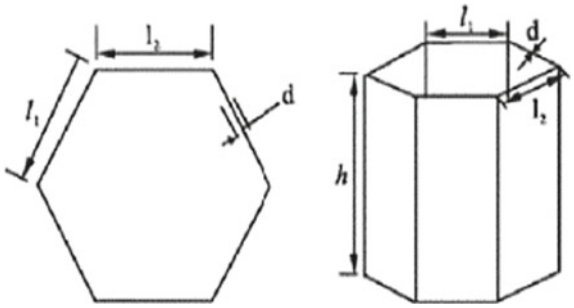

Fig. 10.2 Cell diagram

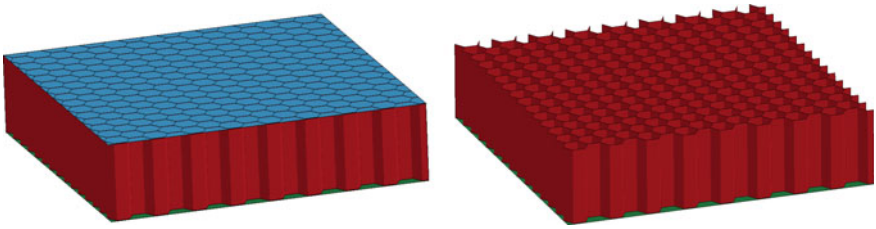

Fig. 10.3 Calculation model

10.2.2 Material Model

The linear elastic model was selected for the top and bottom face panels, the equation of the model is:

$$\varepsilon_i = \frac{\sigma_i}{E} - \frac{\mu}{E}(\sigma_j + \sigma_k)$$
$$\gamma_{ij} = \frac{\tau_{ij}}{G}$$
$$G = \frac{E}{2(1+\mu)}$$

where E is the elastic modulus, is Poisson's ratio, and G is the shear elastic modulus.

Some scholars [12, 13, 17, 18] found that accurate results could be obtained by using the isotropic ideal elastoplastic constitutive to describe the mechanical behavior of the matrix material. In this paper, the plastic follow-up hardening constitutive was used to describes the honeycomb sandwich layer, and the equation is:

$$\sigma = \mathrm{E}\varepsilon, \varepsilon \leq \varepsilon_s$$
$$\sigma = \mathrm{E}\varepsilon_s, \varepsilon > \varepsilon_s$$

The main material parameters are shown in Table 10.1.

Table 10.1 Parameter of Aramid [34]

Materials		Aramid
Density	kg/m^3	570
Elasticity modulus	GPa	0.8395
Poisson ratio		0.4
Yield stress	GPa	0.0465

10.2.3 Impulses

Three groups of different loads were used to simulate impact or explosion loads loading on the node of calculation model. The first group is three rectangular impulses with the same load concentration, different loading duration and peak value, as shown in Fig. 10.4. The second group is four rectangular impulses with the same loading time but different loading peaks, as shown in Fig. 10.5. The third group is impulses with the same load concentration, loading duration but different load shapes which including rectangles, triangles, ladders, as shown in Fig. 10.6 (Tables 10.2 and 10.3).

10.3 Numerical Results

The uniform impulses were loaded on the upper panel nodes as shown in the Fig. 10.7.

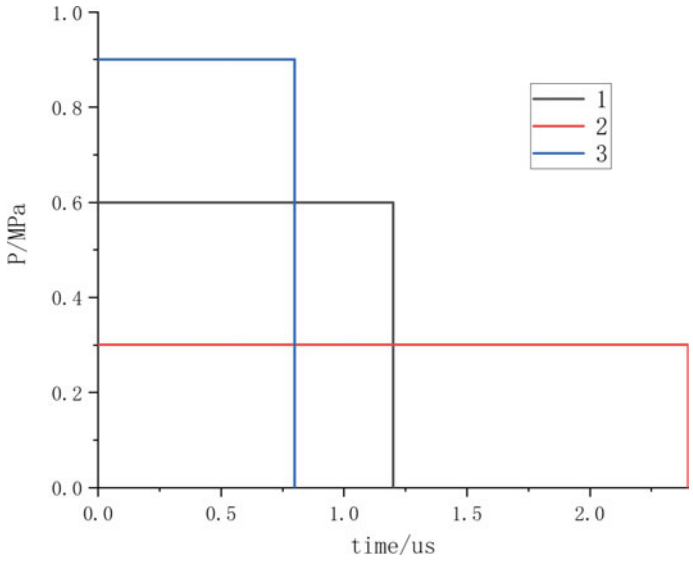

Fig. 10.4 Group 1

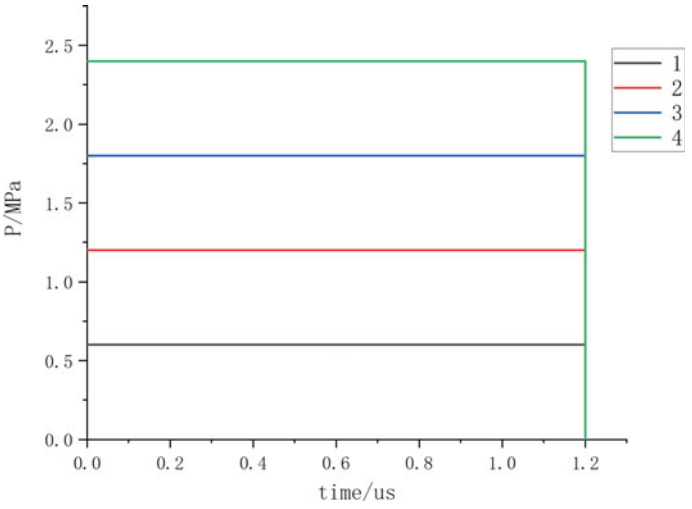

Fig. 10.5 Group 2

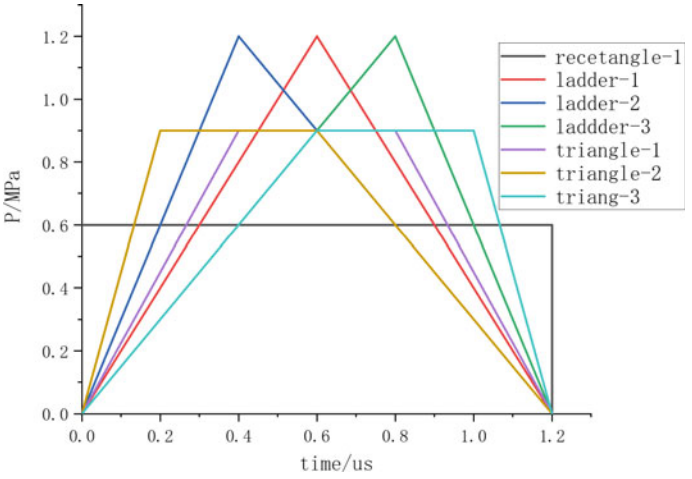

Fig. 10.6 Group 3

The location of data points was shown in the Fig. 10.7, Select reference points in the model and analyze the time history curve, two reference locations were selected, one at the panel-layer interface, and the other at about one third of the sandwich layer. The units are g-cm-us.

Table 10.2 Parameter of AL-2024 [35]

Parameter		AL-2024
Density	kg/m^3	2785
Shear modulus	GPa	27.6
Poisson ratio		0.31[36]
Yield stress	GPa	0.265
Hardening constant	GPa	0.426
Hardening exponent		0. 34
Strain rate		0. 015
Temp softening exponent	K	1. 0
Melting temp	K	775
Reference strain rate	s^{-1}	11. 0

Table 10.3 .

Group	Serial number	Shape	Duration/μs	Peak of the impulse/MPa	Specific impulse/PaS
1	1	Rectangular	1.2	0.6	0.72
	2	Rectangular	0.8	0.9	0.72
	3	Rectangular	2.4	0.3	0.72
2	1	Rectangular	1.2	0.6	0.72
	2	Rectangular	1.2	1.2	1.44
	3	Rectangular	1.2	1.8	2.16
	4	Rectangular	1.2	2.4	2.88
3	Rectangular	Rectangular	1.2	0.6	0.72
	Triangle-1	Triangle	1.2	1.2	0.72
	Triangle-2	Triangle	1.2	1.2	0.72
	Triangle-3	Triangle	1.2	1.2	0.72
	Ladder-1	Ladder	1.2	0.9	0.72
	Ladder-2	Ladder	1.2	0.9	0.72
	Ladder-3	Ladder	1.2	0.9	0.72

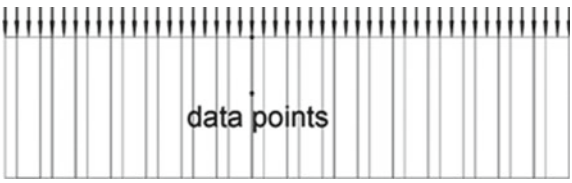

Fig. 10.7 The impulse is loaded on the top face panel and two reference data points

10.3.1 Impulses with Different Duration

To investigate the effect of impulse peak on the structure of aramid honeycomb sandwich panel under the same specific impulse, rectangular impulses were used for calculation in this section. The duration of the impulses is 0.8, 1.2 and 2.4 μs, the peak impulse is 0.9, 0.6, 0.3 MPa and the specific impulses are 0.72 PaS, as shown in Fig. 10.4.

First, the nodes displacement of the joints in the sandwich layer near the top face panel was analyzed, as shown in Fig. 10.8. In general, the maximum node displacement increases with the increase of pulse peak value. However, it can be seen that the stress fluctuates slightly in the local range, Because of the thin plate, the stress waves was transmitted and reflected several times at the panel-layer interface in extreme time.

Under the same specific impulses size, the node displacement almost the same when the peak of the impulse is smaller than 0.6 MPa, and the displacement increases significantly when the specific impulse is greater than 0.9 MPa (Fig. 10.9a) with the increase of the impulse peak, the max-z-stress appeared earlier and larger (Fig. 10.9b).

Rectangular impulse was loaded on the aramid honeycomb sandwich panel in Fig. 10.10. It can be seen that after 80 s, plastic deformation was formed in sandwich laminate attach to the top face panel. The stress wave was passed all observed positions before 50 μs. The displacement and stress were shown in Fig. 10.10.

Stress at panel-layer interface is affected by the reflection of the stress wave, it is too complicated to analysis, this location will not be discussed in the rest.

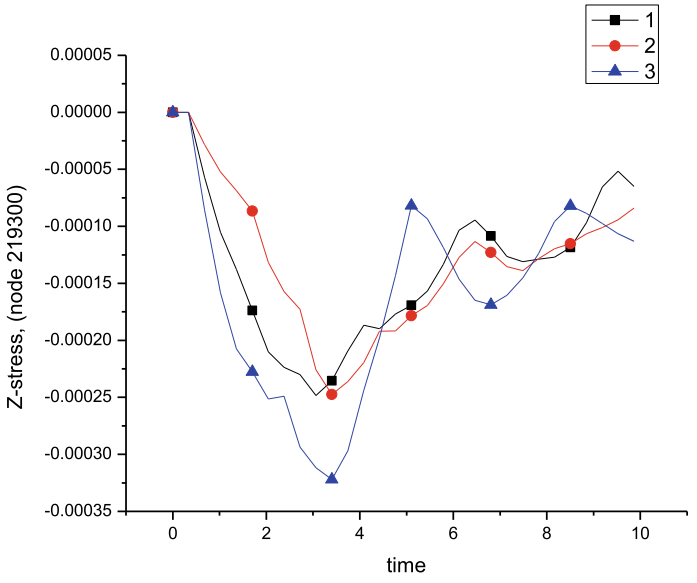

Fig. 10.8 Stress at panel-layer interface

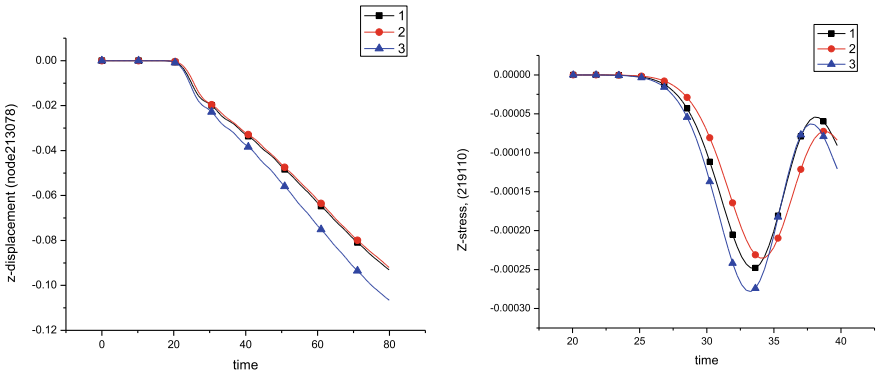

Fig. 10.9 Comparison of z-displacement–time (**a**) and stress-time (**b**) histories of the test points (group 1)

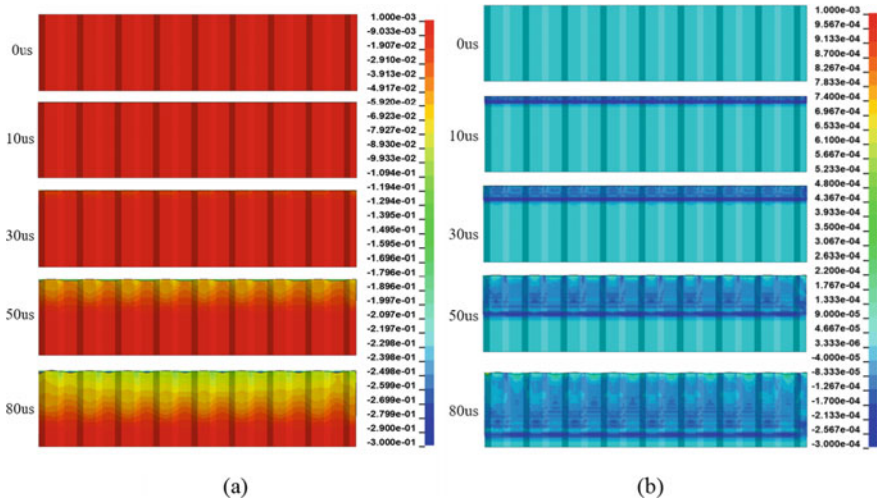

Fig. 10.10 Z-displacement (**a**) and z-stress (**b**) under rectangular impulse

10.3.2 Impulses with Different Specific Impulse

Rectangular impulses are also used for calculation, differently, the duration of the impulses is the same as 1.2 μs, the peak impulses are 0.6, 0.9, 1.2, 1.8 MPa and the specific impulses are 0.72 PaS, as shown in Fig. 10.11. Uniform loads with specific impulse of 0.72, 1.44, 2.16 and 2.88 PaS were applied on the nodes of the upper panel for a time of 1.2 μs.

According to the relationship between energy and impulse, pulse is positively correlated with energy to the quadratic power, in the known conditions, pulse peak

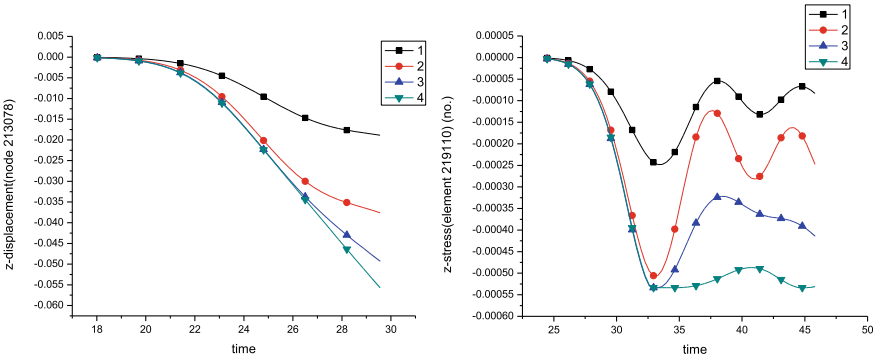

(a) (b)

Fig. 10.11 Comparison of z-displacement–time (**a**) and stress-time (**b**) histories of the test points (group 2)

for linear increase, the node z-displacement are positively correlated with the pulse amplitude was shown in Fig. 10.11a. But it also can be seen that when $t = 30$ μs, the displacement is not a linear relationship with the impulses peak, but increment decreases with the increase of impulses peak, it conforms to the impulse-energy relationship.

The law of stress is similar to displacement. Moreover, when the specific impulse increases from 0.72 to 1.44 PaS, the extreme stress doubles. However, when the specific impulse continues to increase, the extreme stress almost stops increasing, and when the specific impulse reaches 2.88 PaS, the stress at the observation point almost never decreases after reaching the extreme value (Fig. 10.11b), because when the specific impulse reaches a certain value, the observation point reaches the yield limit and enters the yield stage, and its stress–strain situation no longer satisfies Hooke's law.

As can be seen from Fig. 10.12a, among the seven pulse loads of different shape, the displacement is the largest under rectangular impulse. Other impulses have no significant difference in 20–35 μs, but with the time increase, the ladder impulses have almost no effect on the displacement in 62–80 μs, and it is the same as the triangular impulse with the same ascending and descending slope. However, under the triangular impulses, the displacement is smaller when the ascending slope is bigger (Fig. 10.12b).

Figure 10.13a shows that the overall trend of stress variation of Aramid honeycomb panels under different pulses is consistent. When the Aramid honeycomb sandwich panels are subjected to rectangular impulses, the max-stress is the largest and the first to reach the extremum. In both triangle and ladder impulses, the max-stress is larger when the ascending slope is greater than descending slope, but the max-stress of triangle appears last (Fig. 10.13b).

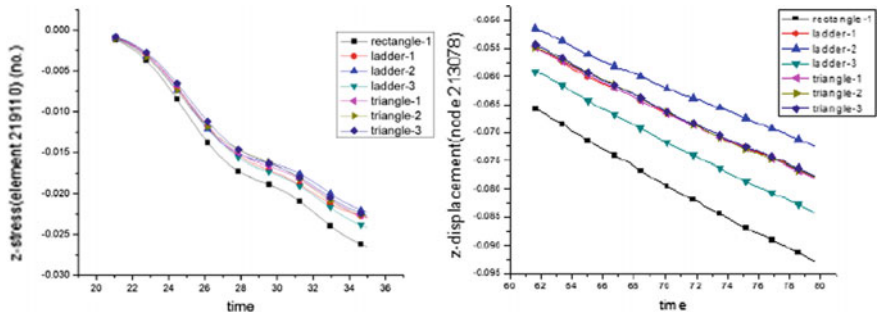

(a) 20 us-35 us (b) 62 us-80 us

Fig. 10.12 Comparison of z-displacement–time histories of the test points (group 3)

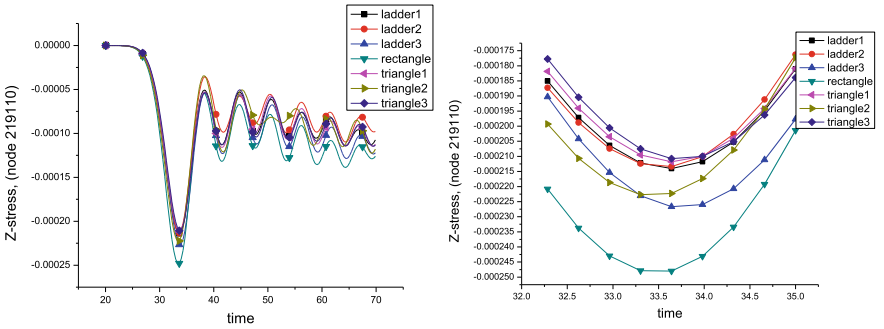

(a) 20-70 us (b) peak of stress

Fig. 10.13 Comparison of stress-time histories of the test points (group 3)

10.4 Conclusion

In this paper, the mechanical response of Aramid honeycomb sandwich panel under different conditions which include different length, size and shape is classified and discussed. It can be concluded that:

Under the condition of the same specific impulses, the displacement and stress extremum under rectangular impulse are the largest.

The displacement and stress were more affected by impulse peak compared with the specific impulse, when the rectangular pulse is applied. Even, the growth rate of displacement and stress decreases gradually with the specific impulse increases.

Under the same specific impulse, changing the initial slope of ladder impulse has almost no effect on the reference point displacement and stress, while changing the initial slope of triangular impulse has a great effect, larger initial slope causes larger stress extremum and smaller displacement, but the range of variation is smaller than rectangular impulse.

References

1. Y. Du, Development and application of Kevlar Fiber. Flying Missile **04,** 58–60 (1988)
2. B. Wang, Basic types, structure and bulletproof properties of high-performance fiber bulletproof materials. Light Text. Ind. Technol.**39**(04), 22–24 (2010)
3. L. Kang, *Study on Preparation and Impact Resistance of Kevlar Woven Fabric with 3D Composite Structure*. Zhejiang Sci-Tech University (2015)
4. Y. Chen, Development and application analysis of Kevlar Fiber. Jiangsu Text. **08**, 40–41+44 (2007)
5. Q. Zhang, S*tudy on Ballistic Impact Effect of Aluminum Honeycomb Sandwich Plate*. Beijing Institute of Technology (2014)
6. D. Zhu, Y. Ou, X. Zhang, M. Huang, Experimental study and finite element simulation of multi-scale mechanical behavior of Kevlar®29 fiber. Eng. Mech. **33**(09), 242–249+256 (2016)
7. G. Shuliang, Z. Long, H. Feng, D. Youshe, H. Junsheng, Study on mechanical properties of kevlar fiber sewing foam core composites. Mater. Sci. Technol. **21**(02), 38–44 (2013)
8. S. Xu, X. Wang, G. Zhang, J. Chen, Z. Zhang, Experimental study on dynamic compression mechanical properties of Kevlar Fiber reinforced composites. Exp. Mech. **01**, 26–33 (2001)
9. C. Ping, Z. Linghui, C. Ning, Development of electrical plate for Kevlar/Nomex honeycomb sandwich microstrip array antenna. Space Return Remote Sens. **02**, 66–70 (2008)
10. S. Shanshan, C. Bingzhi, C. Haoran, S. Zhi, Three-point bending and in-plane compression properties of KEVLAR short fiber toughened carbon fiber/aluminum honeycomb sandwich plate. J. Compos. Mater. **34**(09), 1953–1959 (2017)
11. D. Wang, W. Li, S. He, X. Li, W. Yong, Structural optimization of aluminum foam sandwich panel for bridge pier reinforcement across debris flow in mountain areas. J. Vibrat. Shock **35**(10), 108–114 (2016)
12. Z. Zhu, X. Zhu, Y. Li, Y. Chen, Research status of composite sandwich structure and its application in Marine engineering. Ship Sci. Technol. **40**(03), 1–7 (2018)
13. J. Zhang, X. Jiang, Analysis on compressive performance of typical 3D lattice sand sandwich structure and its application in automobile. Automob. Pract. Technol. **46**(09):128–129
14. Y. Zhao, Y. Sun, R. Li, Q. Sun, J. Feng, Response of aramid honeycomb sandwich panels subjected to intense impulse loading by Mylar flyer. Int. J. Impact Eng. **104**, 75–84 (2017)
15. G.N. Nurick, G.S. Langdon, Y. Chi, N. Jacob, Behavior of sandwich panels subjected to intense air blast—Part 1: Experiments. Compos. Struct. **91**(4), 433–441 (2009)
16. Z. Fan, Y. Liu, P. Xu, Blast resistance of metallic sandwich panels subjected to proximity underwater explosion. Int. J. Impact Eng. **93**, 128–135 (2016)
17. X. Li, Z. Wang, F. Zhu, G. Wu, L. Zhao, Response of aluminum corrugated sandwich panels under air blast loadings: Experiment and numerical simulation. Int. J. Impact. Eng. **65**, 79–88 (2014)
18. D.D. Radford, G.J. McShane, V.S. Deshpande, N.A. Fleck, The response of clamped sandwich plates with metallic foam cores to simulated blast loading. Int. J. Solids Struct. **43**(7–8), 2243–2259 (2006)
19. D.D. Radford, V.S. Deshpande, N.A. Fleck, The use of metal foam projectiles to simulate shock loading on a structure. Int J Impact Eng **31**(9), 1152–1171 (2005)
20. S. Avachat, M. Zhou, Compressive response of sandwich plates to water-based impulsive loading. Int. J. Impact Eng. **93**, 196–210 (2016)
21. S. Avachat, M. Zhou, Effect of face sheet thickness on dynamic response of composite sandwich plates to underwater impulsive loading. Exp. Mech. **52**(1), 83–93 (2011)
22. L. Zhang, R. Hebert, J.T. Wright, A. Shukla, J.-H. Kim, Dynamic response of corrugated sandwich steel plates with graded cores. Int. J. Impact Eng. **65**, 185–194 (2014)
23. V.S. Deshpande, N.A. Fleck, High strain rate compressive behavior of aluminum alloy foams. Int. J. Impact Eng. **24**(3), 277–298 (2000)
24. F. Zhu, L. Zhao, G. Lu, Z. Wang, Deformation and failure of blast-loaded metallic sandwich panels—experimental investigations. Int. J. Impact Eng. **35**(8), 937–951 (2008)

25. L. Jing, Z. Wang, V.P.W. Shim, L. Zhao, An experimental study of the dynamic response of cylindrical sandwich shells with metallic foam cores subjected to blast loading. Int. J. Impact Eng. **71**, 60–72 (2014)
26. S. Sun, X. Li, Mechanical properties and application prospect of high-density aramids paper honeycomb. Chem. Eng. Des. Commun. **45**(06), 132+134 (2019)
27. W. Liu, J. Yang, J. Ma, Preparation and mechanical properties of low density Aramylon paper honeycomb. Eng. Plast. Appl. **47**(08), 96–100 (2019)
28. Y. Luo, Z. Lu, M. Wang, W. Hao, Comparative study on properties of interposition aramid paper honeycomb core and aluminum honeycomb core. High-tech Fiber Appl. **44**(01), 29–33+24 (2019)
29. X. Li, X. Hu, X. Wu, B. Yu, Finite element model study on ultrasonic cutting simulation of aramid honeycomb material. J. Hangzhou Dianzi Univ. (Nat. Sci. Ed.) **39**(05), 56–61 (2019)
30. N. Zhang, Application status of aramid materials in rail transit field. Text. Rev. **07**, 30–33 (2020)
31. H. Xiao, H. Qu, G. Lan, Research on sound absorption and insulation performance of honeycomb sandwich structure filled with porous fiber. Fiber Reinforced Plast./Composites **12**, 67–71+100 (2019)
32. H. Ebrahimi, R. Ghosh, E. Mahdi, H. Nayeb-Hashemi, A. Vaziri, Honeycomb sandwich panels subjected to combined shock and projectile impact. Int. J. Impact Eng. **95**, 1–11 (2016)
33. H. Liu, C. Lu, S. Shi, Z. Sun, Interfacial properties and toughening mechanism of carbon fiber reinforced epoxy resin composites with aluminum honeycomb sandwich. J. Compos. Mater. 1–7 2021–06–13. https://doi.org/10.13801/j.cnki.fhclxb.20210526.002
34. Y. Zhao, *Dynamic Behavior of Titanium-aramid Honeycomb Sandwich Panel Subjected to Intensive Impulse Loading* (Nanjing University of Science and Technology, 2018)
35. B. Jia, J. Li, F. Zhang, Y. Deng, Numerical simulation of bird impact resistance of aeronautical aluminum alloy plate. Sci. Technol. Eng. **15**(31), 120–125 (2015)
36. W. Xinyun, S. Chan, D. Lei, J. JunSong, S. Xiaomei, The establishment of high temperature damage model for 2024 aluminum alloy and its application. J. Plasticity Eng. **26**(06), 120–127 (2019)

Chapter 11
Numerical Simulation Analysis of Dynamic Response and Damage Effect of Tunnel Under Internal Explosion

Xiang Liu, Yuxin Sun, and Rongjun Guo

Abstract An investigation on dynamic response of explosion shock wave in different tunnel structure was carried out in this paper. Straight tunnel, L-shaped tunnel and T-shaped tunnel were selected as the research objects. And simulations were conducted with 2-D fluid–structure coupled model using the AUTODYN 19.0 software. Here, the RHT model was adopted to describe the mechanical behaviour of concrete and rock, and JWL equation of state was selected for explosive. Combined with the simulation results, the propagation law of shock wave in different tunnels was analysed, and the vulnerable points in the tunnel under the action of explosion shock wave were found. The results show that the damage of tunnel caused by explosion load was mainly concentrated in a very short time after explosion. And the dynamic response has the characteristics of fast response, large load and short duration. The explosion shock wave caused great damage to the tunnel structure which was close to the burst point. At the same time, the concentrated load was generated in the corner of the tunnel, which became a vulnerable structure.

11.1 Introduction

Tunnel is an engineering building buried in the ground, which is a form of human using underground space. In wartime, it can play the functions of civil air defense evacuation, transportation reserve materials, personnel emergency shelter and so on. With the development of weapons and guidance technology in modern war, the possibility of explosion in tunnel is increasing. When the explosion occurs in the tunnel structure, the explosion load has a direct or indirect impact on the tunnel's wall and the surrounding rock outside the tunnel. Therefore, it is very important to analyze the dynamic response and damage effect of the tunnel structure under the load of explosion in the tunnel, which is the basis of the anti-explosion performance evaluation and protection design of the tunnel structure.

X. Liu · Y. Sun (✉) · R. Guo
National Key Laboratory of Transient Physics, Nanjing University of Science and Technology, Jiangsu 210094, China
e-mail: yxsun01@163.com

A. Gany and X. Fu (eds.), *2021 International Conference on Development and Application of Carbon Nanomaterials in Energetic Materials*, Springer Proceedings in Physics 276,
https://doi.org/10.1007/978-981-19-1774-5_11

There is a significant difference between the propagation of explosion shock wave in closed space and that in open three-dimensional space. Due to the tunnel structure is not easy to build and the cost is huge, the methods of model test and numerical simulation are generally used. Benselama [1] and Uystpruyst [2] pointed out that there are two modes of propagation of explosion shock wave in the roadway: one is free propagation in three-dimensional space near the burst point, and the other is quasi one-dimensional propagation far away from the burst point. The relationship between the two modes of transfer position, explosive quantity and geometry of the propagation space was proposed by numerical calculation; Alex and Michael [3] studied the propagation behavior of explosion shock waves in underground mines through a series of experiments in experimental mines. A simple proportional relationship between peak overpressure and explosive quantity and propagation space was established. Kezhi and Xiumin [4] used the three-dimensional numerical simulation program to calculate the chemical explosion flow field in the long tunnel, and compared with the experimental results. The propagation law of air shock wave along tunnel direction was concluded; Pang et al. [5] established a formula to predict the air shock wave of high explosive explosion in tunnel through experiments; Xinjian et al. [6] mapped the velocity model of shock wave propagating along a straight tunnel with equal cross section under the condition of internal explosion at the entrance of the tunnel through experiments.

For the current research of explosion in tunnel, the focus is mainly on the propagation law of explosion shock wave, which was quite complete. However, these studies generally regard the tunnel as a non-deformable structure, ignoring the dynamic response and damage of tunnel structure under the action of shock wave.

Therefore, this paper intends to carry out numerical simulation for three typical tunnel structures to analyze the dynamic response and damage effect of tunnel structure under the load of internal explosion.

11.2 Numerical Simulation Model

11.2.1 AUTODYN Software

In order to solve highly nonlinear dynamic problems, such as solid, liquid, gas and their interactions, century dynamics Inc. has developed a nonlinear dynamic analysis software AUTODYN. The company first launched a two-dimensional version of autodyn-2D in 1986 and a three-dimensional software autodyn-3D in 1991. In January 2005, AUTODYN software was acquired by ANSYS company and has been integrated into ANSYS co-simulation platform. In the past few decades, autodyn-2D/3D software has been continuously developed, with increasingly perfect functions and more convenient application. Since its development, the software has been committed to the research and development of the military industry, and has become one of the most famous numerical simulation software in the field of explosive

mechanics and high-speed collision in the world. It integrates a variety of processing technologies of finite difference, computational fluid dynamics and fluid coding, and can be widely used in various complex engineering problems, such as large strain and large deformation, Nonlinear dynamics, explosion penetration, collision and fluid solid coupling shorten the development cycle of many products. There are many material constitutive models and equations of state, which are convenient for their application in various aspects. AUTODYN version 19.0 was used in this paper.

11.2.2 Research Objects

This paper discussed three kinds of tunnel structure. Straight tunnel, L-shaped tunnel and T-shaped tunnel were selected to establish two-dimensional simulation model for numerical simulation. The concrete wall thickness of three kinds of tunnel is 0.02 m, and the thickness of surrounding rock outside the tunnel is 0.5 m. Among them, the straight tunnel's burst points are distributed in the vertical direction; the L-shaped tunnel's burst points are distributed along the diagonal of the corner; the T-shaped tunnel burst points are also distributed in the vertical direction. The tunnel structure, location of burst points and observation points are shown in Figs. 11.1 and 11.2.

A 0.5 kg spherical COMP B was used in the simulation. The concrete wall and rock use Lagrange element, the COMP B and air use Euler element. The fluid structure coupling relationship between them was established.

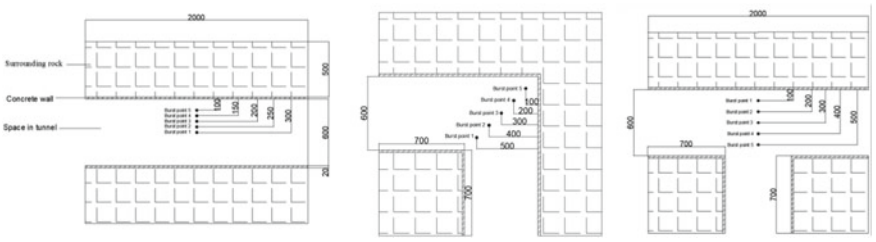

(a1) Straight tunnel (b1) L -shape tunnel (c1) T-shape tunnel

Fig. 11.1 Location of burst points in tunnels

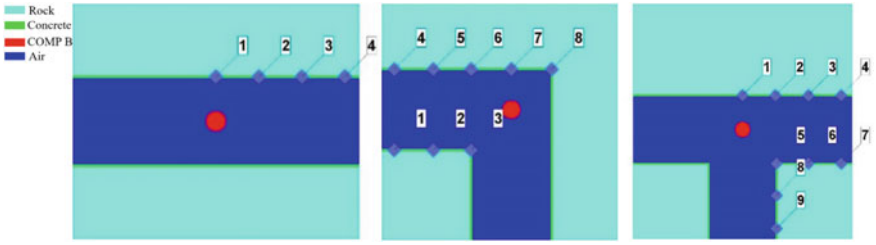

(a1) Straight tunnel (b1) L-shape tunnel (c1) T-shape tunnel

Fig. 11.2 Location of observation point in tunnels

11.2.3 Material Model

11.2.3.1 Concrete and Rock

Rock and concrete are both brittle materials, which have similar grain boundaries, holes, cracks and other defects of different sizes. Both of them have the characteristics of strain hardening, damage softening and strain rate effect, which provides the feasibility for us to use the constitutive relationship of concrete to describe the mechanical behavior of rock like brittle materials under dynamic and static loads. RHT concrete constitutive model has been widely used in the numerical simulation and analysis of explosion, impact, penetration and other problems, and achieved relatively satisfactory results.

The P-alpha EOS and RHT strength parameters of concrete and rock are mainly referred to [3, 4], and the main parameters are shown in Table 11.1.

11.2.3.2 COMP B

JWL equation of state was selected for explosive

$$p = A\left(1 - \frac{\omega}{R_1\overline{V}}\right)e^{-R_1\overline{V}} + B\left(1 - \frac{\omega}{R_2\overline{V}}\right)e^{-R_2\overline{V}} + \frac{\omega}{\overline{V}}E$$

where, A and B are the linear coefficient; R_1, R_2, ω are the non-linear coefficient; $\overline{V} = V_i / V_0$, V_i is volume of detonation product, V_0 is volume of unexploded explosive. A, B, R_1, R_2, ω are constants, which are obtained from experiments. The parameters are shown in Table 11.2.

Table 11.1 RHT model parameters of concrete and rock

Parameter	Concrete	Rock
(a) *P-alpha EOS*		
Initial density ρ_0(g/cm^3)	2.75	2.7
Pore density ρ_1(g/cm^3)	2.314	2.314
Initial pressure P_1(KPa)	2.33×10^4	2.33×10^4
Compaction pressure P_2(KPa)	6×10^6	6×10^6
Porosity index N	3	3
A_1 (KPa)	3.53×10^7	4.54×10^7
A_2 (KPa)	3.96×10^7	4.19×10^7
KPa)	9.04×10^6	4.20×10^6
B_0	1.22	0.9
B_1	1.22	0.9
T_1 (KPa)	3.53×10^7	4.54×10^7
T_2 (KPa)	0	0
(b) *RHT Strength model*		
Shear modulus G (KPa)	1.67×10^7	1.67×10^7
Compressive strength f_c (KPa)	3.5×10^4	4.8×10^4
Tension strength f_t/f_c	0.1	0.1
Shear strength f_s/f_c	0.18	0.18
Intact failure surface constant A	1.6	1.6
Intact failure surface exponent N	0.61	0.61
Tens./Comp. Meridian ratio Q	0.7	0.6805
Brittle to Ductile Transition BQ	0.0105	0.0105
Hardening slope	2.0	0.5
Elastic strength/ft	0.7	0.7
Elastic strength/fc	0.53	0.53
Fracture strength constant B_{fric}	1.6	1.6
Fracture strength exponent n_{fric}	0.61	0.61
Strain rate exponent α	0.032	0.02439
Tensile strain rate exponent β	0.036	0.02941

11.2.3.3 Air

The material model of air is assumed to be an ideal gas, and the relationship between pressure P and energy E can be determined by the following formula:

$$P = (k-1)\rho E$$

where, k is the adiabatic coefficient of gas, ρ is the density of air, E is the initial internal energy of air. The specific parameters are shown in Table 11.3.

Table 11.2 JWL model parameters of explosive materials

Parameter	Value
Density $\rho(\mathrm{g/cm^3})$	1.717
Detonation velocity D (m/s)	7980
C-J explosion pressure P (Pa)	2.95×10^{10}
Material constant A (Pa)	5.2423×10^{11}
Material constant B (Pa)	7.678×10^{9}
Material constant R_1	4.2
Material constant R_2	1.1
Material constant ω	0.34
Initial internal energy $E_0(\mathrm{J/m^3})$	8.5×10^{9}

Table 11.3 Ideal gas model parameters of air

Parameter	Value
Density $\rho(\mathrm{g/cm})^3$	1.225×10^{-3}
Internal energy $(\mathrm{mJ/mm^3})$	2.068×10^{5}
Isentropic adiabatic coefficient	1.4

11.3 Calculation Results and Analysis

11.3.1 Straight Tunnel

Figures 11.3 and 11.4 show the stress distributing graph and crack propagation process of tunnel structure under the action of explosion in straight tunnel. A strong shock wave was formed after the explosion, and the tunnel structure near the burst point was the first to be impacted and deformed. When T = 0.3 ms, stress concentration occurred, and some materials of tunnel structure enter the plastic stage. When the stress intensity was higher than the material strength, the material damage forms cracks, and the cracks were mainly concentrated near the burst point. The crack propagation at T = 5 ms was almost the same as that at T = 0.5 ms, which indicated that the material was damaged mainly in the short time at the beginning of explosion.

Figure 11.5 shows the dynamic response observed at observation points 1–4 after the explosion at burst point 1 in the straight tunnel. Observation points 1–4 are 0.3 m away from the explosion point in the Y direction, and 0, 0.3, 0.6 and 0.9 m away from the burst point in the X direction. The maximum stress of Observation points 1–4 were 80.44, 37.23, 17.51 and 14.24 MPa. The maximum strain of Observation points 1–4 were 0.029, 0.013, 0.0075 and 0.0067. In the X direction, the closer the wall structure is to the burst point, the greater the maximum stress and strain was observed. The displacement and the maximum acceleration had similar law.

Figure 11.6 is the dynamic response curve observed at observation points 1 after the explosion of different burst points. In Fig. 11.6a, the stress at burst point 5 decreased rapidly to 0 MPa after reached the maximum value of about 350 MPa.

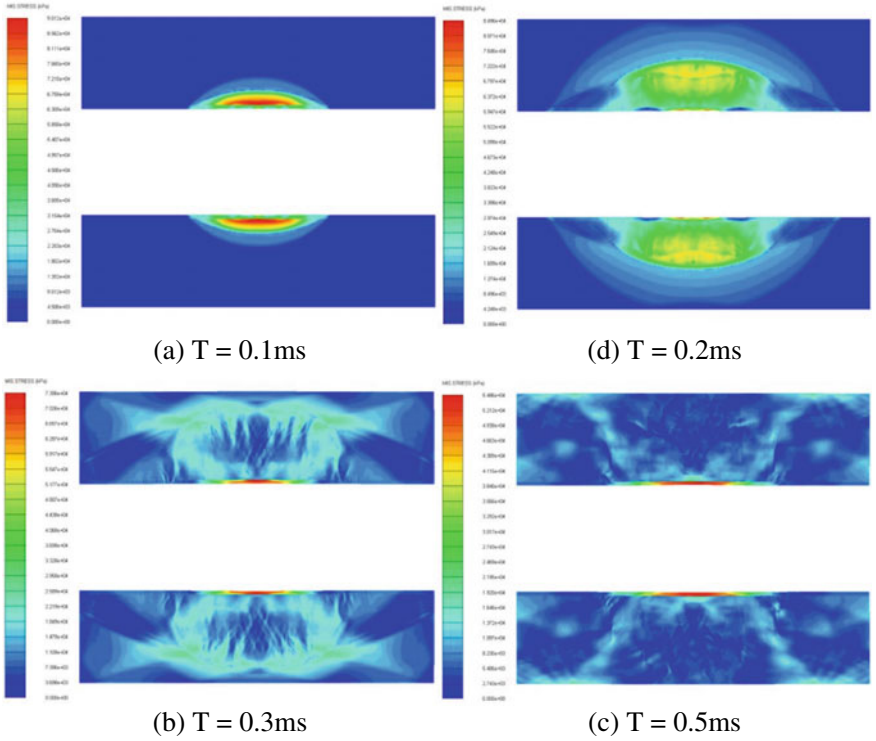

Fig. 11.3 Stress distributing graph after the explosion of burst point 3 in the straight tunnel

Which was a clear manifestation of that the structure had failed, and the failed structure couldn't bear any tensile stress anymore. In Fig. 11.6b, the maximum strains under the load of exploration which happened at burst points 1–5 were 0.028, 0.039, 0.047, 0.084 and 0.217. The closer the burst point was to the tunnel wall, the greater the maximum strain of tunnel wall structure. The stress, displacement and maximum acceleration have similar law.

In Fig. 11.6d, the response times observed at observation point 1 were 0.05, 0.03, 0.02, 0.01 and 0.003 ms. The speed increased rapidly to tens or hundreds of meters per second, and decreased to about 0 ms at 0.3 ms. The dynamic response is very fast, reaching microsecond level, and the response duration is very short, less than 0.3 ms.

The damage of explosion load to tunnel was mainly concentrated in a very short time after explosion, which has the characteristics of fast response, large load and short duration.

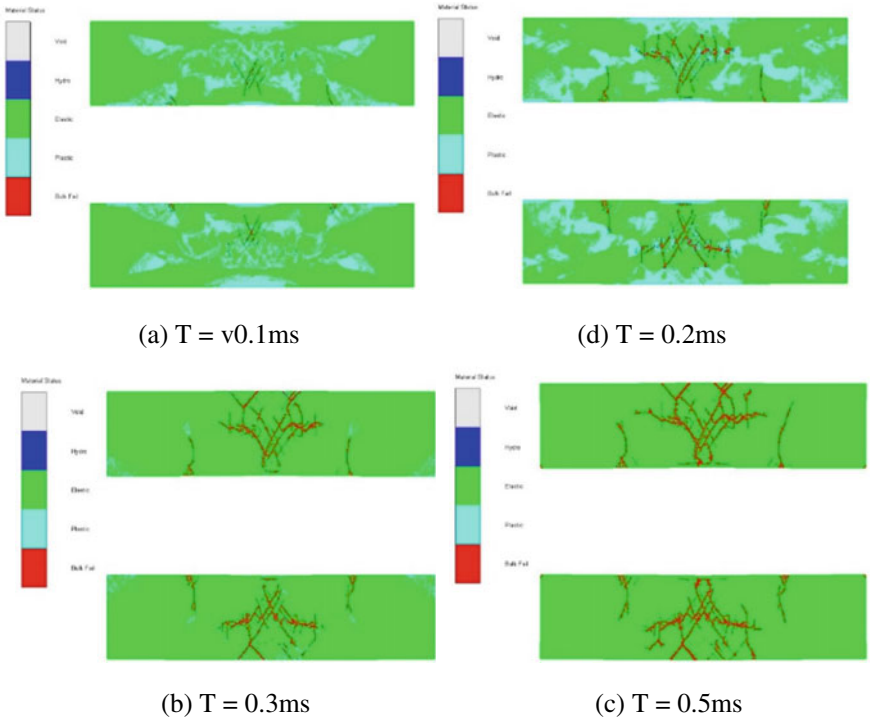

(a) T = v0.1ms (d) T = 0.2ms

(b) T = 0.3ms (c) T = 0.5ms

Fig. 11.4 Rock damage distributing graph after the explosion of burst point 3 in the straight tunnel

11.3.2 L-shaped Tunnel

Figures 11.7 and 11.8 show the stress distributing graph and crack propagation process of rock structure under the load of explosion of burst point 3 in L-shaped tunnel. The stress of the structure was mainly concentrated in the corner. The damage was mainly concentrated in the wall outside the corner, where the tunnel structure was most vulnerable to damage. When T = 0.5 ms and T = 5 ms, the damage degree of the structure was almost the same, which also shows that the damage of the structure was concentrated in 0.5 ms after the explosion, and the time was very short.

Figure 11.9 shows the dynamic response observed at observation points 1–8 after the explosion of burst point 3 in the L-shape tunnel. Observation point 3 was located at the corner of the inner wall, and the maximum stress observed at observation point 3 was 32.31 MPa. During the subsequent structural deformation, there was a residual stress of about 15 MPa. The maximum stress observed at observation points 1 and 2 were 12.77 MPa and 18.47 MPa, and there were multiple peaks gradually decreasing. When the explosive exploded at the corner of the L-shaped tunnel, the inner corner was impacted by the incident wave and the wave reflected from the outer

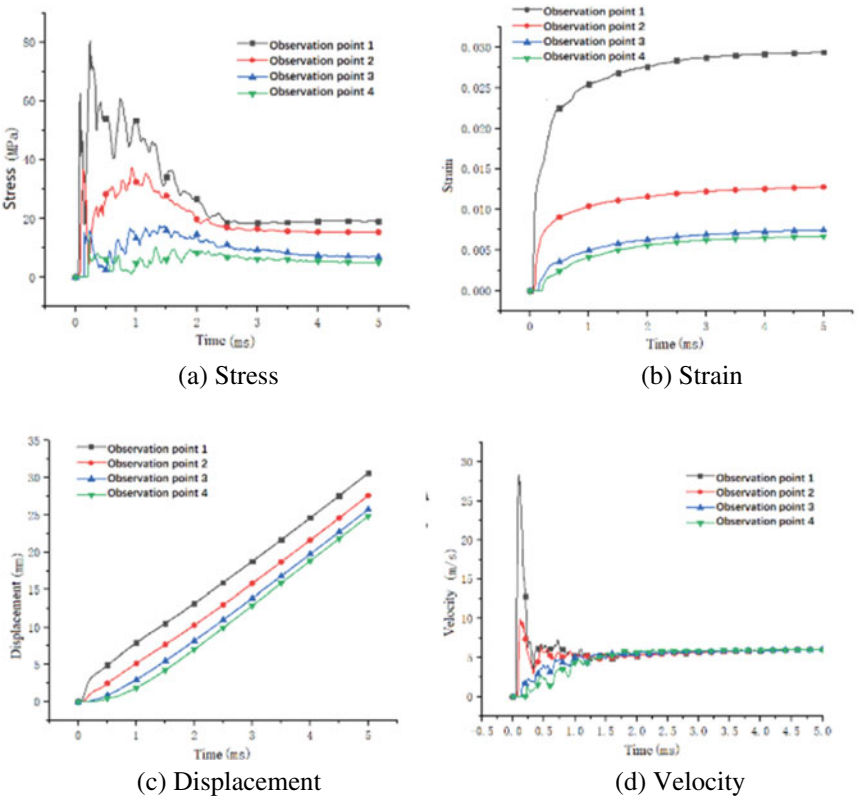

(a) Stress (b) Strain

(c) Displacement (d) Velocity

Fig. 11.5 Dynamic response observed at observation points 1–4 after the explosion of burst point 1 in the straight tunnel

corner to the inner side, and then the shock wave continued to reflect and oscillate in the tunnel.

On the outside of L-shaped tunnel, the maximum stress observed at observation points 4–8 were 17.00, 16.47, 38.57, 72.17 and 91.95 MPa. The closer to the corner, the greater the maximum stress. The maximum strain, displacement and maximum velocity have similar rules. The maximum strain observed at observation point 8 was 0.68, and that at observation point 4–7 were between 0.006 and 0.025, which was far less than that observed at observation point 8. The position of observation point 8 was the most concentrated stress and the most serious damage position.

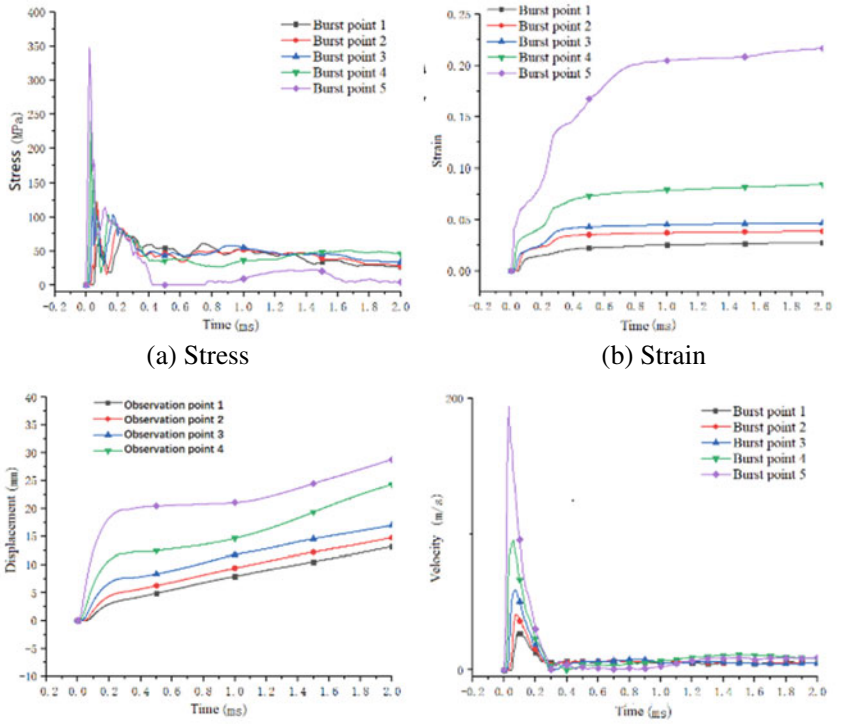

(a) Stress (b) Strain

(c) Displacement (d) Velocity

Fig. 11.6 Dynamic response observed at observation point 1 after the explosion of all burst points in the straight tunnel

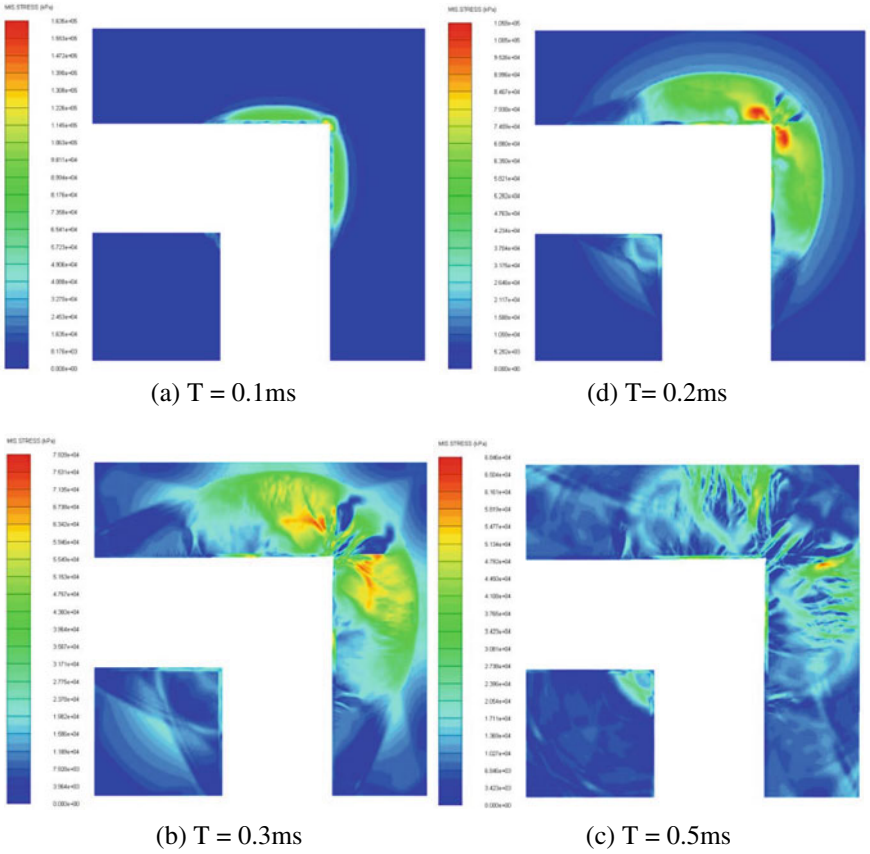

(a) T = 0.1ms (d) T= 0.2ms

(b) T = 0.3ms (c) T = 0.5ms

Fig. 11.7 Stress distributing graph after the explosion of burst point 3 in the L-shape tunnel

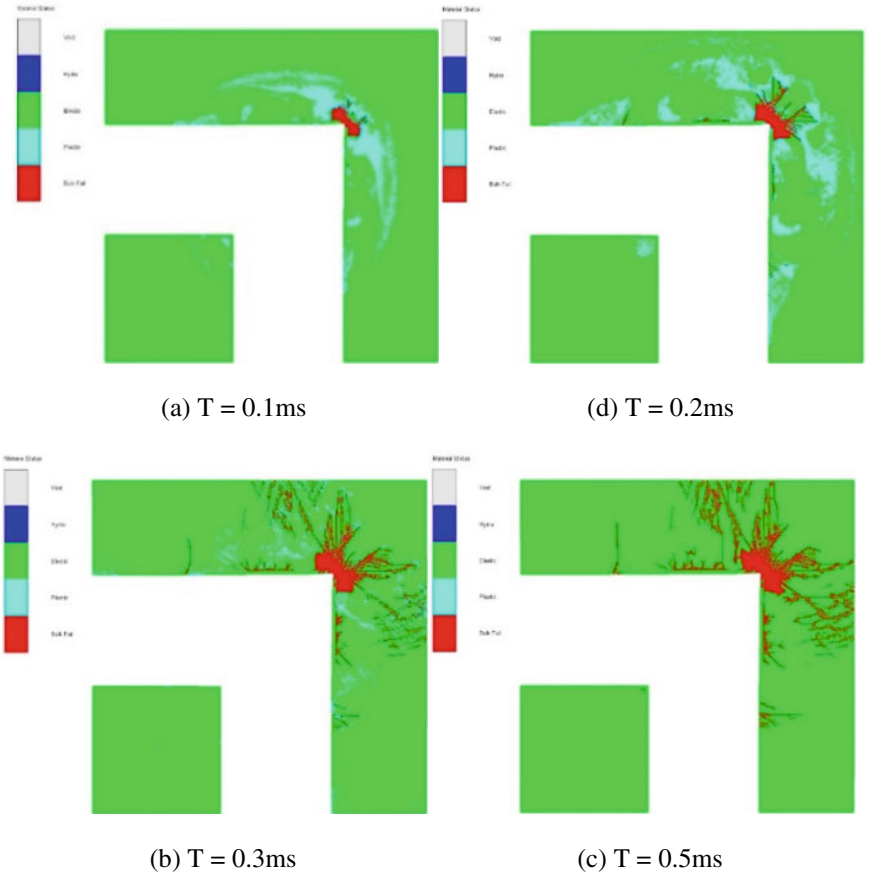

(a) T = 0.1ms (d) T = 0.2ms

(b) T = 0.3ms (c) T = 0.5ms

Fig. 11.8 Rock damage distributing graph after the explosion of burst point 3 in the L-shape tunnel

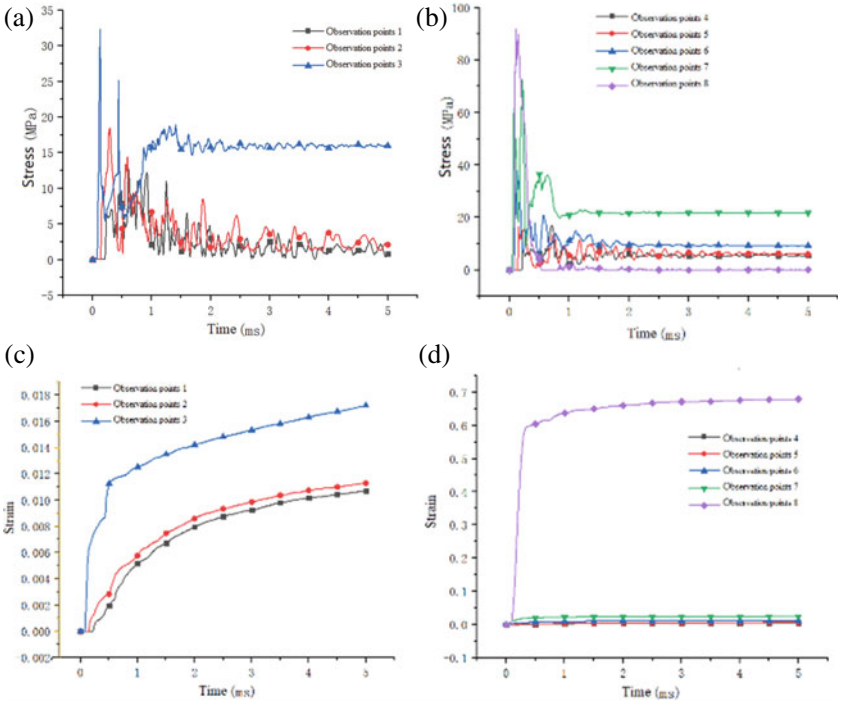

(a) The stress-time curves observed at observation points 1-3

(b) The stress-time curves observed at observation points 4-8

(c) The strain-time curves observed at observation points 1-3

(d) The strain-time curves observed at observation points 4-8

Fig. 11.9 Dynamic response observed at observation points 1–8 after the explosion of burst point 3 in the L-shape tunnel

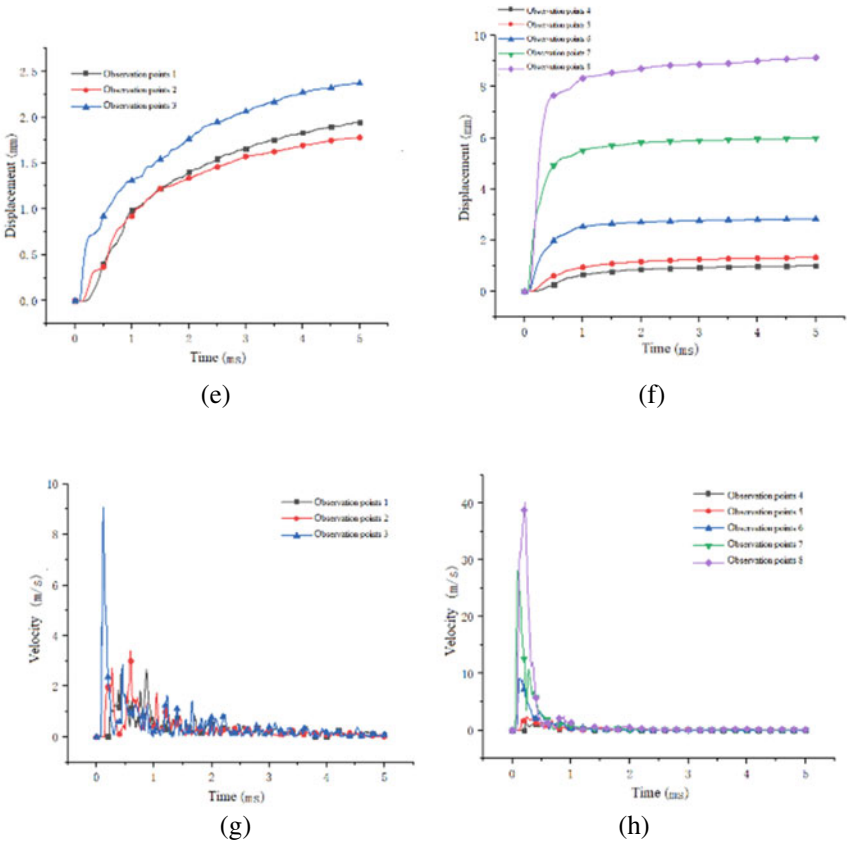

(e) (f)

(g) (h)

(e) The displacement curves observed at observation points 1-3

(f) The displacement curves observed at observation points 4-8

(g) The velocity-time curves observed at observation points 1-3

(h) The velocity-time curves observed at observation points 4-8

Fig. 11.9 (continued)

Figure 11.10 shows the dynamic response observed at observation points 3 and 8 after the explosion of all burst points in the L-shape tunnel. With the change of burst point 1 to 5, the distance of explosion center to observation point also changed. The maximum stress, strain, displacement and acceleration were negative correlated with the distance from the explosion center. In Fig. 11.10a, the stress observed at observation point 3 decreased rapidly after reaching the highest value (between 20 and 120 MPa), then fluctuated about 1 ms between 0 and 30 MPa, and finally the residual stress stabilized between 10 and 30 MPa. After the stress observed at observation

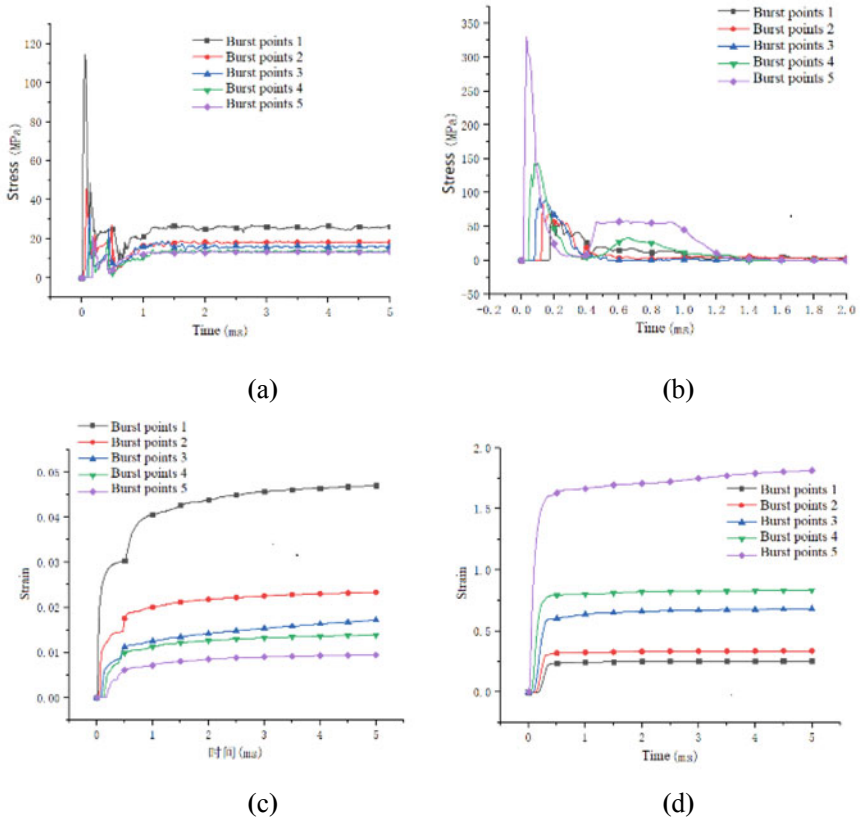

(a) The stress-time curves observed at observation point 3

(b) The stress-time curves observed at observation point 8

(c) The strain-time curves observed at observation point 3

(d) The strain-time curves observed at observation point 8

Fig. 11.10 Dynamic response observed at observation points 3 and 8 after the explosion of all burst points in the L-shape tunnel

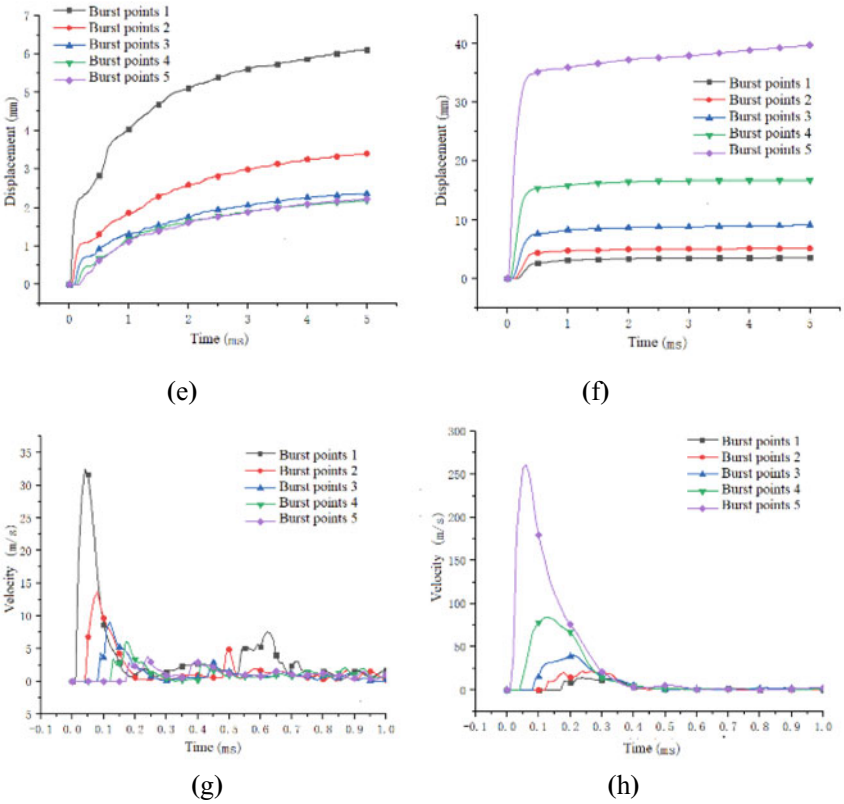

(e) The displacement curves observed at observation point 3

(f) The displacement curves observed at observation point 8

(g) The velocity-time curves observed at observation point 3

(h) The velocity-time curves observed at observation point 8

Fig. 11.10 (continued)

point 8 reached the highest value (70–330 MPa), it rapidly decreased to 0 MPa in about 0.4 ms, then fluctuated slightly in the stage of 0.4–1.2 ms, and finally returned to 0 MPa. This was because the material had failed and could not longer bear tensile stress. The duration of dynamic response was about 1.2 ms, mainly concentrated in the first 0.4 ms.

Figure 11.11 shows the variation curve of maximum stress and strain observed at observation points 3 and 8. In Fig. 11.11a, the stress change trend observed at observation points 3 was similar with observation points 8. With the increasing of the distance between the burst centers, the maximum stress decreased and the change was gradually gentle, but the maximum value observed at observation point 3 was

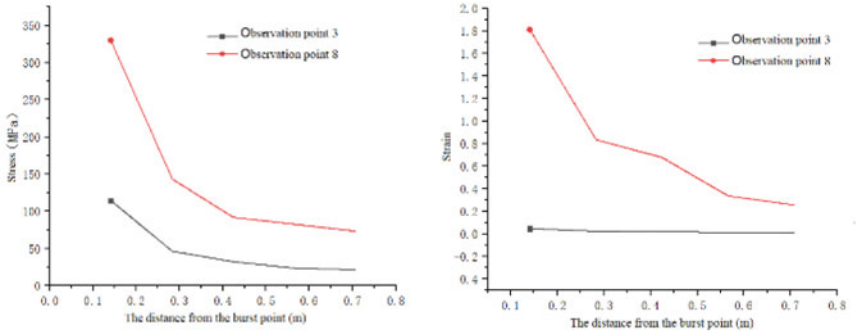

(a) Maximum stress (b) Maximum strain

Fig. 11.11 Variation curve of maximum stress and strain of observation points 3 and 8 with distance between burst points

lower than that at observation point 8. The strain value observed at observation point 8 was large (between 0.256 and 1.81), while the strain observed at observation point 3 was small (between 0.01 and 0.05), and the change was not obvious. Under the load of internal explosion in L-shaped tunnel, the corner position of the outer tunnel was the most stress concentrated position, which was more vulnerable to damage than the inner corner position.

11.3.3 T-shaped Tunnel

Figures 11.12 and 11.13 are the stress distributing graph and crack propagation process of rock structure under the explosion in T-shaped tunnel. After the explosion, the shock wave propagated to the upper wall and corners of the tunnel. The stress was concentrated on the upper wall of T-shaped tunnel. There was also stress concentration on the left and right corners, but it was relatively small. The damage of the structure was mainly in the upper wall. Compared with the straight tunnel, the damage of upper wall in T-shaped tunnel was smaller because the T-shaped tunnel has more bifurcation, which made the explosive energy spread out from the tunnel rapidly.

Figure 11.14 shows the dynamic response observed at all observation points after the explosion of burst point 3 in the L-shape tunnel. On the upper wall of the tunnel, the maximum stress observed at observation points 1–4 were 82.24, 38.88, 16.67 and 14.50 MPa, and the residual stresses were about 23, 17, 6.5 and 4.5 MPa. The maximum stress and residual stress were negatively correlated with the distance from the observation point to the burst point. The maximum strain, displacement and velocity were also the same rule. The response time was about 2 ms.

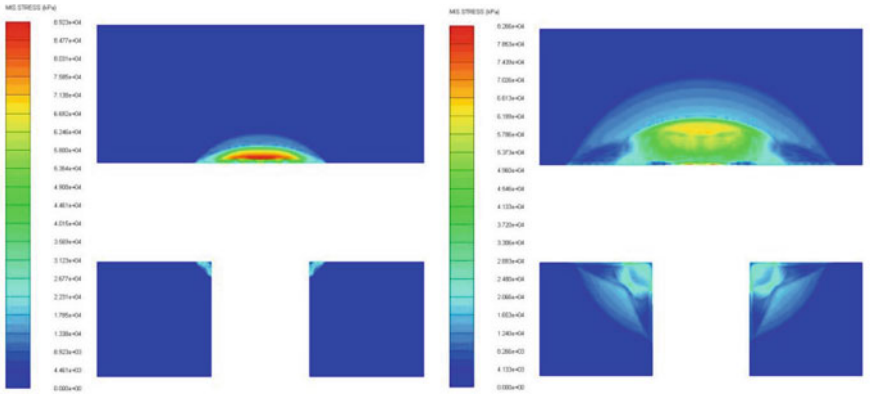

(a) T = 0.1ms (d) T = 0.2ms

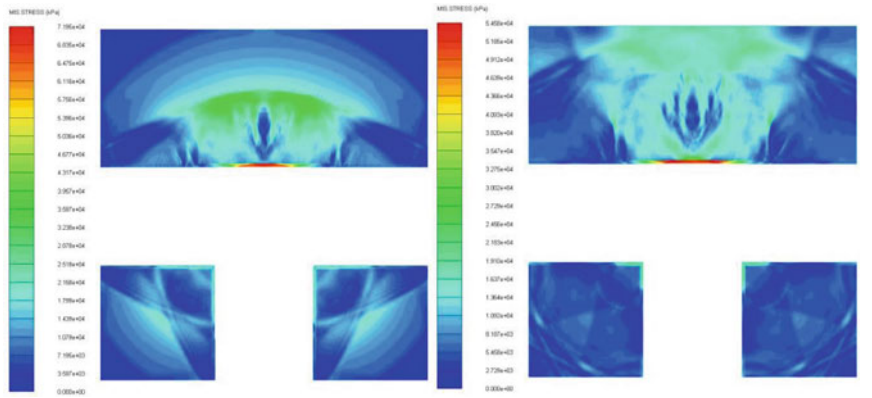

(a) T = 0.1ms (d) T = 0.2ms

Fig. 11.12 Stress distributing graph after the explosion of burst point 3 in the T-shape tunnel

At the lower side of the right corner, the stress observed at observation point 5 rised rapidly to the maximum value of 28.51 MPa after the explosion, then decreased rapidly to 0 MPa, then rised to 28.5 MPa, and then decreased slowly to the residual stress of 16.9 MPa.

The stress curves observed at observation point 6 and 8 were almost the same. After the stress reaches the maximum value of 17.81 and 19.86 MPa, it fluctuated continuously and the peak value decreased gradually. The reason was that the shock wave reflected repeatedly between the inner walls of the tunnel.

The peak value observed at observation points 7 and 9 were about 10 MPa, which decreased slowly and fluctuated continuously. In the lower right side of the tunnel wall, the farther away from the burst point, the smaller the maximum stress, strain, displacement and velocity. And the residual stress was mainly concentrated in the

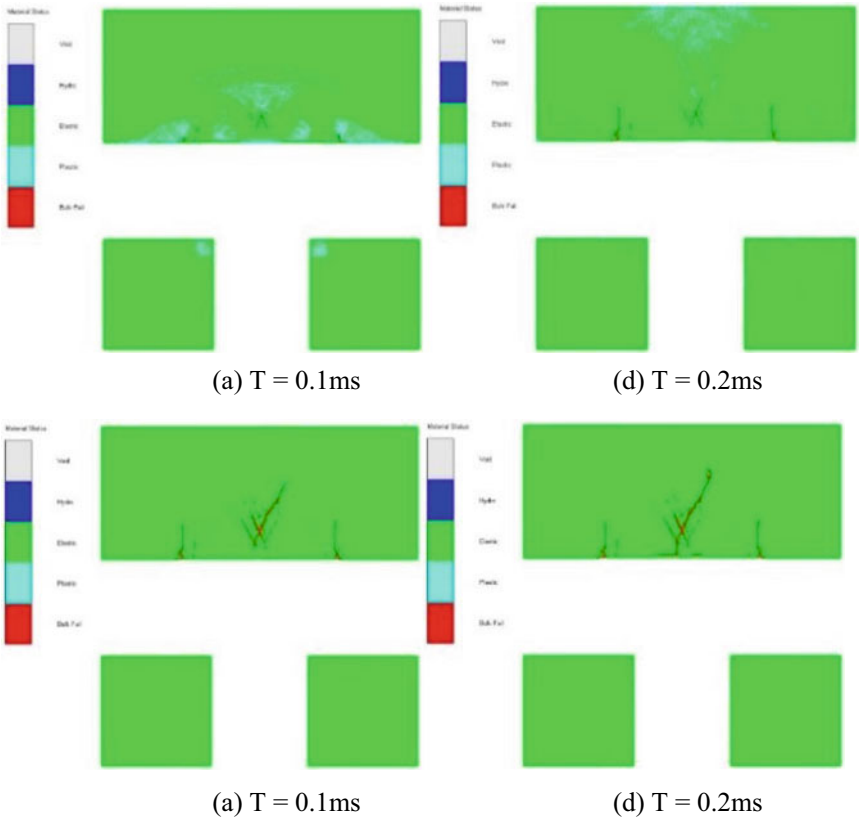

Fig. 11.13 Rock damage distributing graph after the explosion of burst point 3 in the T-shape tunnel

corner of the tunnel. Compared with the straight tunnel and L-shape tunnel, the dynamic response time was longer which reached 2–3 ms.

Figure 11.15 shows the dynamic response observed at observation points 1 and 5 at different burst points. At explosion point 1, the maximum stress reached 354.5 MPa, and then gradually decreased to 0 MPa, which indicated that the element had failed and could no longer bear tensile stress or shear stress. For other explosion points, there was residual stress observed at observation points 1, which was 20–40 MPa. The maximum stress observed at observation point 5 increased from 23.6 to 80.6 MPa, and the maximum strain, displacement and acceleration also increased gradually. The center of the upper wall and the left and right corners were vulnerable points, and the load was positively correlated with the distance between the explosion centers. Compared with the straight tunnel and L-shaped tunnel, the response time is longer, reaching 2–3 ms.

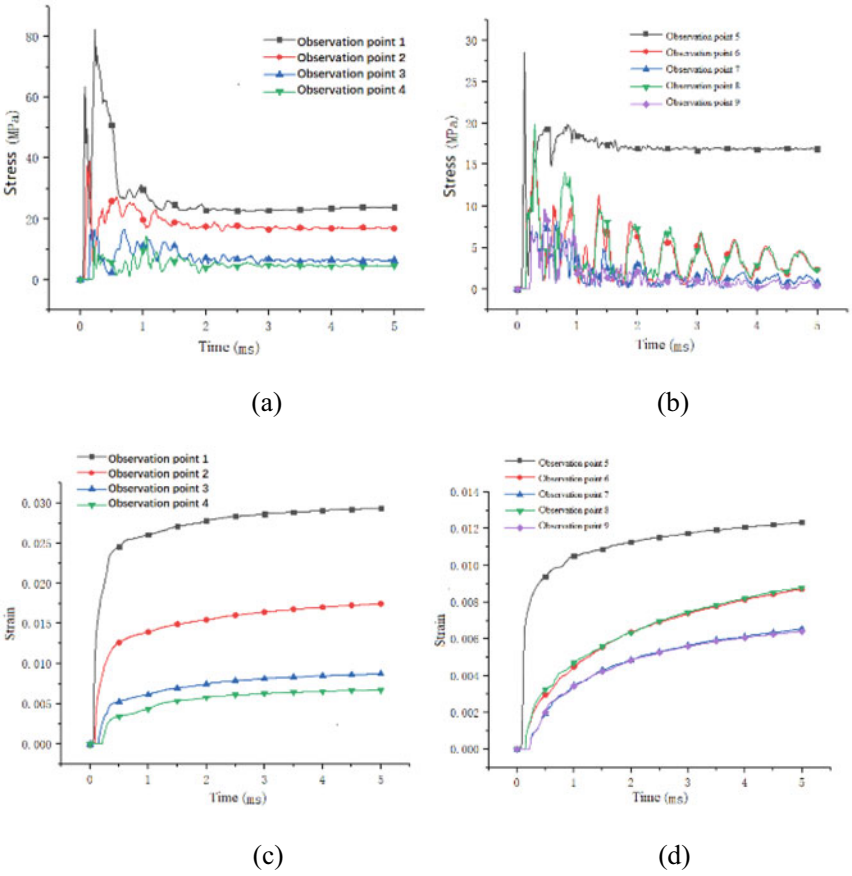

(a) The stress-time curves observed at observation points 1-4

(b) The stress-time curves observed at observation points 5-8

(c) The strain-time curves observed at observation points 1-4

(d) The strain-time curves observed at observation points 5-8

Fig. 11.14 Dynamic response observed at observation points 1–8 after the explosion of burst point 3 in the T-shape tunnel

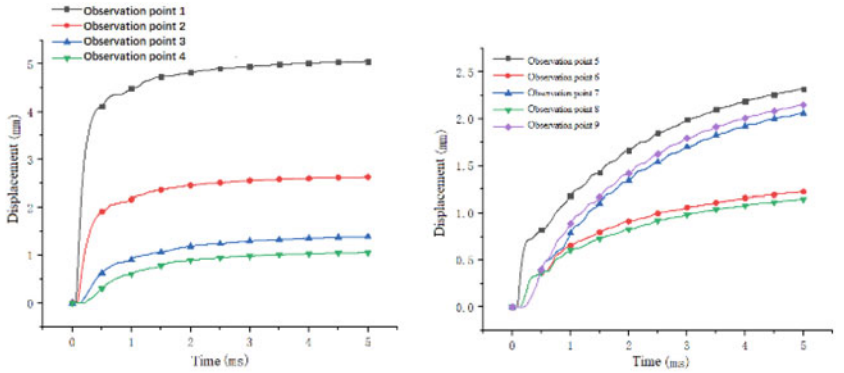

(e) (f)

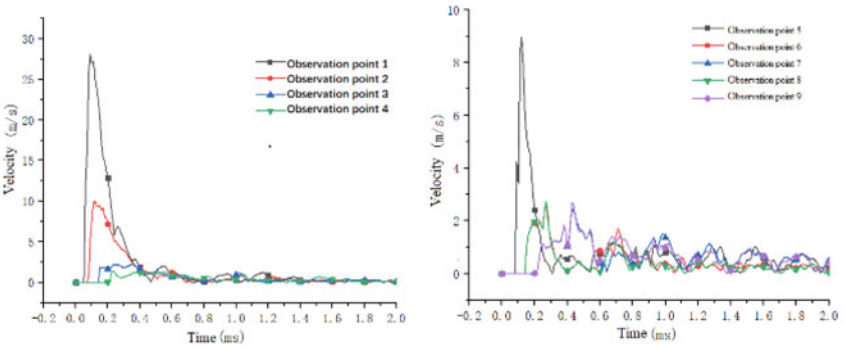

(g) (h)

(e) The displacement curves observed at observation points 1-4

(f) The displacement curves observed at observation points 5-8

(g) The velocity-time curves observed at observation points 1-4

(h) The velocity-time curves observed at observation points 5-8

Fig. 11.14 (continued)

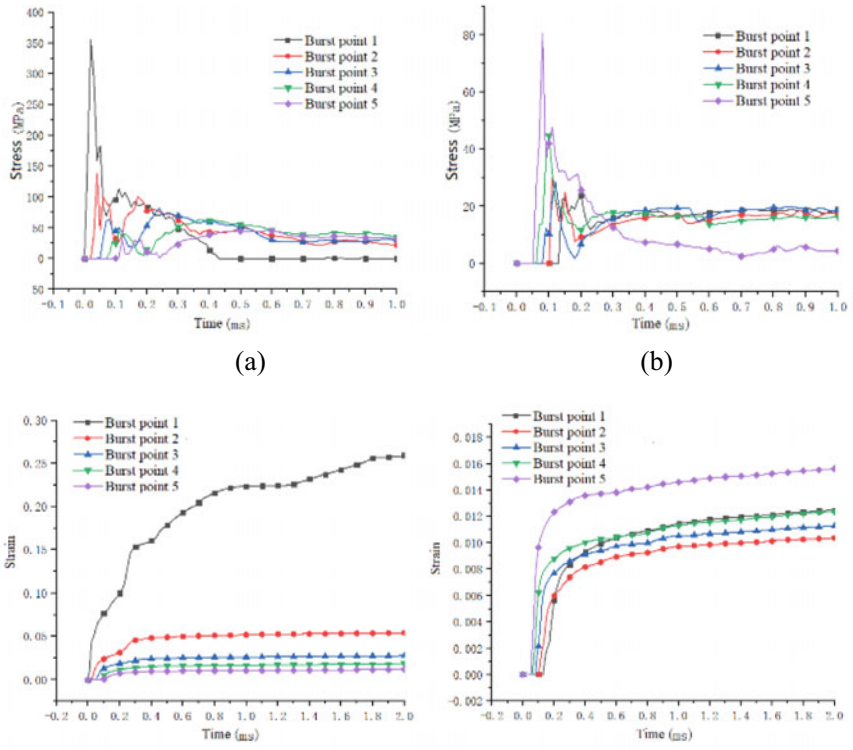

(a) The stress-time curves observed at observation point 1

(b) The stress-time curves observed at observation point 5

(c) The strain-time curves observed at observation point 1

(d) The strain-time curves observed at observation point 5

Fig. 11.15 Dynamic response observed at observation points 1 and 5 after the explosion of all burst points in the T-shape tunnel

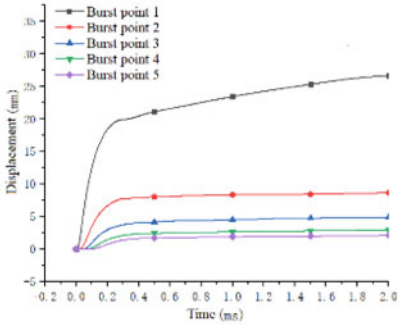

(e)

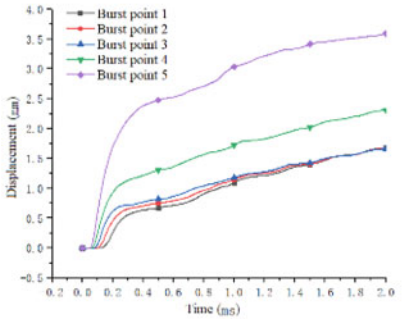

(f)

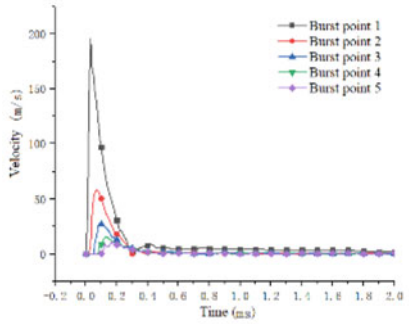

(g)

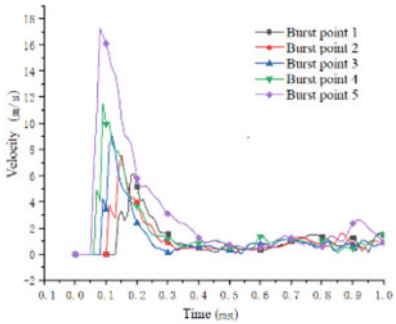

(h)

(e) The displacement curves observed at observation point 3

(f) The displacement curves observed at observation point 8

(g) The velocity-time curves observed at observation point 1

(h) The velocity-time curves observed at observation point 5

Fig. 11.15 (continued)

11.4 Conclusion

In this paper, the physical model of the explosion structure in the tunnel was established, the suitable material constitutive model and parameters were selected. The dynamic response of the tunnel structure with different shapes under the explosion load was numerically simulated, and the failure forms of tunnel and rock structure were analyzed.

The stress of concrete tunnel and rock increases rapidly under explosion load. Concrete and rock materials will have elastic strain and plastic strain. When the stress exceeds the maximum tensile stress that the material can bear, the material will fail. After failure, the material can no longer bear tensile stress or shear stress, forming cracks. With the propagation of stress, the cracks gradually expand, and the main generation and propagation time of cracks is 0–0.5 ms.

The damage of explosion load to tunnel is mainly concentrated in a very short time after explosion, which has the characteristics of fast response (0.003–0.05 ms, reaching microsecond level), large load (from tens to hundreds MPa), short duration (0.3–3 ms).

Based on the 5 kg spherical COMP B used in this paper, when the distance between the burst point and the wall is less than 0.1 m, the wall structure will fail completely; In the L-shaped tunnel, stress concentration occurs at the outer corner of the structure, and the structure with a distance of 0.3 m also fails completely; On the contrary, in the inner corner, there is no complete failure of the material. The center of the upper wall and the left and right corners of the T-shaped tunnel are the most concentrated parts to bear the explosion load, and the center of the upper wall is the most vulnerable part.

References

1. X. Ren, Q. Zhang, Y. Xue, Experimental study on propagation velocity model of blast wave of explosive B at tunnel entrance. J. Vibr. Shock **31**(7) (2012)
2. Z. Guo, C. Wang, X. Zhang, et al., Study on Multiaxial Strength Test and Failure Criterion of Concrete (Tsinghua University Press, Beijing, 2003)
3. L.I. Hongchao et al., Study on parameters determination of marble RHT model. Trans. Beijing Inst. Technol. **37**(8), 801–806 (2017)
4. B.M. Luccioni, R.D. Ambrosini, R.F. Danesi, Analysis of building collapse under blast loads. Eng. Struct. **26**(1), 63–71 (2004)
5. J. Henrych, *The Dynamics of Explosion and Its Use* (Elsevier Scientific Publishing Company, Amsterdam, 1979), pp. 178–181
6. J.R. Britt, Attenuation of short duration blast in entranceways and tunnels, in *Proceeding of the 2nd Symposium on the Interaction of Non-nuclear Munitions with Structures, Panama City Beach, Florida* (1985), pp. 466–471
7. A.M. Benselama, M.J. William-Louis, F. Monnoyer et al., A numerical study of the evolution of the blast wave shape in tunnels. J. Hazard. Mater. **181**(1–3), 609–616 (2010)
8. D. Uystepruyst, F. Monnoyer, A numerical study of the evolution of the blast wave shape in 1rectangular tunnels. J. Loss Prev. Process Ind. **34**, 225–231 (2015)

9. A.C. Smith, M.J. Sapko, Detonation wave propagation in underground mine entries. J. Mine Ventilat. Soc. South Africa, 2005 Jan/Mar, 20–25.
10. K. Yang, X. Yang, Propagation law of chemical explosion shock wave in tunnel. Explos. Shock Waves **23**(1), 1.37–1.41 (2003)
11. W. Pang, X. He, M. Li, H. Ren, Experimental study on travel time of air shock wave in tunnel. Explos. Shock Waves **23**(6), 11 (2003)
12. W.E. Baker, *Explosions in air* (University of Texas Press, Austin, 1973), pp. 7–15
13. US Army Engineer Waterways Experiment Station, Department of the Army. Fundamental of protective design for conventional weapon. Vicksburg (1986)
14. C.R. Welch, In-tunnel air blast engineering model for internal and external detonations, in *Proceeding of the 8th International Symposium on Interaction of the Effects of Munitions with Structures, Mclean, Virginia*, 195–208 (1997)
15. G. Scheklinski, Blast in tunnels and rooms from cylindrical HE-charges outside the tunnel entrance, in *Douglass H M.Proceedings of the 6th Symposium on the International of Non-nuclear Munition with Structures*, Panama City Beach, Florida (1993), pp. 68–73
16. W. Fondaw, Grant. (1993). *Mitigation of Shock Waves in a Cylindrical Tunnel by Foam*, 116
17. J.K. Yi, H. Shen, K.B. Yan, B. Bing, A review of numerical study on explosion and shock wave resistance of metal foam material. Adv. Mater. Res. **936**, 2024–2029 (2014)
18. M.D. Goel, P. Altenhofer, V.A. Matsagar, A.K. Gupta, C.Mundt, S. Marburg, Interaction of a shock wave with a closed cell aluminum metal foam. Combust. Explos. Shock Waves 51(3) (2015)
19. M. Nusser, A. Hermann, V. Senner, Corrigendum to 'artificial knee joint and ski load simulator for the evaluation of knee braces and ski bindings', in *11th conference of the International Sports Engineering Association, ISEA 2016, Procedia Engineering*, vol. 147 (2016), pp. 220–227
20. J. Lajeunesse, Implications of heterogeneity in the shock wave propagation of dynamically shocked materials. Dissert. Theses Gradw **9**, 235–238 (2015)
21. D.P.D.P. Mondal, S. Das, Effect of thickening agent and foaming agent on the micro-architecture and deformation response of closed cell aluminum foam. Einfluss des Dickungs- und Treibmittels auf die Mikrostruktur und das Deformationsverhalten von geschlossenzelligem Aluminiumschaum. Materialwissenschaft und Werkstofftechnik **41**(5) (2010)
22. T. Krauthammer, C.K. Ku, *Backfill Effects on Partially Buried Shelter Response Under Close in Conventional Explosions* (Computational Mechanics Publications LTD, Madrid, 1994), pp. 349–356
23. H.L. Brode, Blast wave from a spherical charge. Phys. Fluids **2**(2), 217–229 (1959)
24. J. Henrych, G.R. Abrahamson, *The Dynamics of Explosion and Its Use* (Academia, 1979)
25. W.E. Baker, *Explosion Hazards and Evaluation* (Elsevier Scientific Pub. Co., 1983)
26. X.H. Mao, Dynamic response of the compound structure of foam aluminum core composite sandwich material to the shock wave of gas explosion. Adv. Mater. Res. 2384 (2013)
27. P.D. Smith, P. Vismeg, L.C. Teo et al., Blast wave transmission along rough-walled tunnels. Int. J. Impact Eng. **21**(6), 419–432 (1998)
28. H. Guozhen, Y. Zan, Numerical Simulation Study on the Propagation of Shock Wave in the Corridor. Structural Engineering Committee of Chinese society of mechanics, Xi'an University of architecture and technology, editorial board of engineering mechanics, in *Proceedings of the 27th National Conference on Structural Engineering*, vol. II. Structural Engineering Committee of Chinese Society of Mechanics, Xi'an University of Architecture and Technology, editorial board of Engineering Mechanics. J. Eng. Mech. (2018)
29. Z. Yuetang, D. Xiaopeng, Y. Yijun, C. Cheng, Methods for improving the resistance of flatbed protective doorframe wall under intensive impact loading. Explos. Shock Waves **37**(03), 487–495 (2017)
30. K. Qu, Y. Yan, Y. Liu, X. Ning, Z. Li, Comparative study on propagation rules of explosive shock-wave in long straight and complex tunnel. Chin. J. Appl. Mech. **28**(04), 434–438+457 (2011)

Chapter 12
Research on the Energy Output Characteristics of Underwater Explosion of Aluminized Explosive with ETPEs as Binder

Jun Dong, Wei-li Wang, Xiaofeng Wang, Yuan-jing Wang, Teng-yue Zhang, Tian-le Yao, Mao-hua Du, Bo Tan, and Hong-tao Xu

Abstract In order to study the effect of azide energetic thermoplastic elastomers (ETPEs) on the detonation performance of aluminized explosive, two kinds of aluminized explosive formulations were design with comprise ETPEs and inert polymer (EVA) as binders. The explosive sample were prepared by chemical solvent volatilization method, and the underwater explosion energy and detonation heat value of two kinds of explosives were compared and tested. The results show that the detonation energy of aluminized explosive with ETPEs as binder is significantly higher than that with inert polymer. The total energy of underwater explosion is increased by 8.8–9.1%, and the detonation heat value is increased by 3.3–4%. It is found that

J. Dong · W. Wang · T. Yao · M. Du · B. Tan
Naval University of Engineering, Wuhan 430033, China
e-mail: welcome204dj@163.com

W. Wang
e-mail: w.l.wang@tom.com

T. Yao
e-mail: 18931970836@163.com

M. Du
e-mail: 18207157778@139.com

B. Tan
e-mail: Turbo1996@126.com

J. Dong · X. Wang (✉) · H. Xu
Xi'an Modern Chemistry Research Institute, Xi'an 710065, China
e-mail: wangxf_204@163.com

H. Xu
e-mail: baboon007@163.com

Y. Wang · T. Zhang
China Academy of Ordnance Science, Beijing 100089, China
e-mail: wyjlucky2021@163.com

T. Zhang
e-mail: zhangtengyue0201@163.com

A. Gany and X. Fu (eds.), *2021 International Conference on Development and Application of Carbon Nanomaterials in Energetic Materials*, Springer Proceedings in Physics 276,
https://doi.org/10.1007/978-981-19-1774-5_12

although the energy density of ETPEs itself is not high, and the amount of ETPEs added in the explosive formula in this study is very small, the N2 and other substances release heat in the detonation process, which improves the complete response rate of aluminum powder in the detonation process. It plays the role of similar catalyst, and improves the explosion energy of aluminum explosives.

12.1 Introduction

Energetic Thermoplastic Elastomers (ETPEs) is a kind of polymer with the characteristics of thermoplastic elastomers. It contains a large amount of energetic groups such as $–N_3$, $–NO_2$, $–ONO_2$ and has the characteristics of good mechanical properties, excellent processing performance and high energy density. Therefore, ETPEs is used to replace inert binder components in propellant and explosive formulations to increase energy [1–17]. The molecular weight and structure of ETPEs are designed according to the requirements of the explosive formulation on the mechanical properties of the binder. “A” is used to represent the energy group, which is amorphous asymmetrical substituted segments at room temperature. “B” is used to represent the energy group, which is solid symmetric substituted segments at temperatures below the melting point. Normal structures of ETPEs have (AB) n block copolymers and ABA or BAB triblock copolymers in which soft and hard segments are alternately connected. From the aspect of function, the A block imparts toughness to ETPEs, and the B block imparts strength to ETPEs, so that ETPEs contain energy and good mechanical properties. Through studying the surface and interface properties and mechanical sensitivity between ETPEs and RDX and Al powder, it is found that the ETPEs are easier to be wetted on the surface of RDX than that Al powder. Therefore, from the perspective of coating kinetics, ETPEs is easier to coat on the surface of RDX particles in the RDX-Al explosive system and reduce the mechanical sensitivity of explosives [18]. In addition, besides satisfying the preparation performance of explosives as a binder component, using a large number of energetic groups carried by ETPEs to improve the detonation energy and effect of explosives is always concerned [19–24] by many researchers. The reaction of aluminum powder needs a certain amount of energy induction, which lags behind the C-J detonation reaction in time. Therefore, it is generally believed that the secondary oxidation reaction of aluminum powder occurs after the C-J detonation reaction and releases a lot of heat. Many foreign researchers use ETPEs in the formulations of aluminized explosives such as CPX450, CPX458, CPX459 [25] to increase the detonation energy of explosives. Anderson et al. [26] found that energetic binders can improve the oxygen balance of typical aluminized explosives, greatly increase the reactivity of aluminum powder in the detonation process, and improve the completeness of the reaction of aluminum powder in the detonation process, thus improving detonation performance and mechanical power of explosives.

In view of the fact that energetic binder can improve the reaction completeness of aluminum powder in the detonation process, the thermobaric aluminized explosive

Table 12.1 Properties of ETPE based on BAMO/AMMO [28]

Name	Property	Name	Property
Solubility	Acetone, ethyl acetate	Number average relative molecular mass	About 20,000
Melting temperature/°C	90–110	Nitrogen content/%	35
Glass transition temperature/°C	−30	Density/(g/cm^{-3})	1.29
Thermal decomposition temperature/°C	259.38	H50/cm	70
Tensile strength at room temperature/MPa	5	Friction sensitivity	0
Elongation at room temperature/%	400	Shore hardness	52

with high content of aluminum powder is used as the research object in this paper. Azide energetic thermoplastic elastomers (ETPEs) with energetic materials such as RDX and HMX are used to replace the original inert binder [27]. In order to support the application of ETPEs in high explosive formulation in the future, the improvement effect of ETPEs on detonation performance of aluminized explosives is studied.

12.2 Experiment and Calculation

12.2.1 Experimental Materials

Cyclotrimethylenetrinitramine (RDX), Gan-su Yin-guang Chemical Group Co., Ltd.; ETPEs based on BAMO/AMMO, with a number average molecular mass of 2×10^4, Xi'an Modern Chemistry Research Institute; Ethylene and Vinyl acetate copolymer (EVA), number average molecular weight 3500–4500, China Petrochemical Corporation; Spherical aluminum powder, particle size range of 4.5–5.5 μm, Anshan Iron and Steel Group Co., Ltd. Except for ETPEs which is synthesized in the laboratory, the others are all industrial products (Table 12.1).

12.2.2 Explosive Formula Design

Generally, the content of aluminum powder in aluminized explosives does not exceed 20%. This is because aluminum powder reacts with explosive gas products after detonation on the C-J surface and needs to maintain a certain chemical balance with the explosive. For the thermobaric explosive, the content of aluminum powder in its formula is higher than that of ordinary aluminized explosive. The design concept is

to use excess aluminum powder to react with oxygen in the air around the target. So as to improve the effect temperature and pressure on the target. Generally, the energy release of aluminized explosive in the detonation process is divided into two stages [29]. The first stage of detonation energy release process, and the second stage of afterburning energy release process. Since the micron-Al powder used does not participate in the detonation C-J surface reaction. It reacts with the detonation product in the second stage [30], and the main reaction formula is:

$$2Al + 1.5O_2 \rightarrow Al_2O_3 \quad \Delta H_f = -414 \text{ kJ/mol} \tag{12.1}$$

$$2Al + 3CO_2 \rightarrow Al_2O_3 + 3CO \quad \Delta H_f = -826 \text{ kJ/mol} \tag{12.2}$$

$$2Al + 3CO \rightarrow Al_2O_3 + 3C \quad \Delta H_f = -1314 \text{ kJ/mol} \tag{12.3}$$

$$2Al + 3H_2O \rightarrow Al_2O_3 + 3H_2 \quad \Delta H_f = -939 \text{ kJ/mol} \tag{12.4}$$

The ETPEs selected in this study have the characteristics of high nitrogen content. The N element produces N_2 during the detonation process. Under high temperature and high pressure, aluminum powder and N_2 can react to form aluminum nitride and gives off a lot of heat.

$$2Al + N_2 \rightarrow 2AlN \quad \Delta H_f = -335 \text{ kJ/mol} \tag{12.5}$$

Therefore, in this paper, two explosive formulations with 40% aluminum powder content are designed. The ETPEs and inert polymers (EVA) are used as binders to compare detonation performance. Through underwater explosion energy and detonation heat tests, the effect of adding ETPEs on the detonation energy of aluminized explosive is studied. In order to facilitate the analysis and comparison, the ETPEs explosives means the explosive samples with ETPEs as the binder. The same to the EVA explosives (Table 12.2).

Table 12.2 Explosive formulation

Explosive sample	RDX, %	Al powder (FLQ-355A), %	Binder, %
ETPEs explosives	55	40	5 (ETPE)
EVA explosives	55	40	5 (EVA)

12.2.3 Explosive Sample Preparation

The direct granulation process is adopted. First, add the weighed explosive sample into the kneader and pour a small amount of ethyl acetate solvent to infiltrate the explosive particles. Then add the ethyl acetate-containing binder solution and stir and knead it for 10 min. At this time stop kneading and open the machine. Add aluminum powder and a small amount of ethyl acetate solvent. Continue kneading for 30 min, discharge the materials. It is sieved (8–10 mesh) and granulated by manually which the materials in a semi-dry state. The powder is dried in an oven and can be compressed for use.

12.2.4 Underwater Explosion Energy Test

The method of underwater explosion can not only measure the energy of explosives, but also analyze and research the energy distribution relationship of explosives. That is the energy output structure of the explosive. It has the characteristics of good repeatability of measurement results, rigorous theoretical basis of test methods, and advanced test design. Therefore, the underwater explosion of explosives has gradually become a test method for assessing the mechanical power of explosives. The test conditions of the underwater explosion are as follows:

Explosion pool: diameter 3.2 m, water depth 2.4 m, the pool wall and bottom are welded with steel plates to ensure the rigidity.
Sample entry water depth: 1.6 m, It is in two-thirds of the total water depth, which can offset the influence from the water surface and pool bottom.
Test sample: ϕ30 mm $\times$ 30 g compressed explosive column.
Distance measurement: 0.9 m, contrast distance is 2.90 m/$\sqrt[3]{\text{kg}}$.
Sensor: PCB138A tourmaline underwater shock wave sensor, measuring range 0–69 MPa.
Number of sensors: two, one on each side of the sample.
Sensor water penetration depth: 1.6 m, the same as the depth of the explosive sample.
Atmospheric pressure during the test: 670 mmHg.

The test layout is shown in Fig. 12.1. The ETPEs explosives and EVA explosives were suspended into the water with ropes, and detonated by a detonator. The sensors placed were used to test the shock wave overpressure and bubble period of the explosives in the water. The results are shown in Table 12.3.

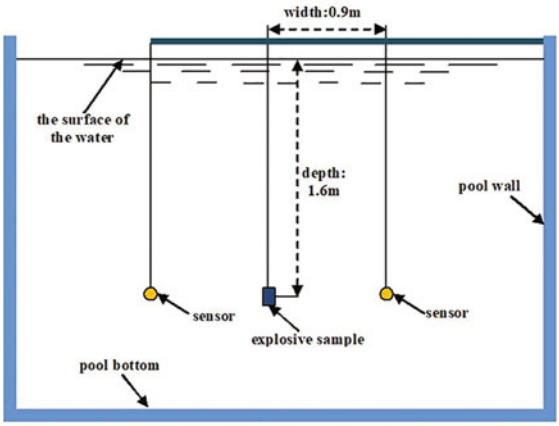

Fig. 12.1 Layout of under-water test

Table 12.3 The underwater shock wave overpressure and bubble period test of explosives ETPEs and EVA

Name	Test sample number	Quality, kg	Shock wave overpressure, MPa	Bubble cycle, ms
ETPEs explosives	1	0.03	14.35	124.5
	2	0.03	15.613	124.3
EVA explosives	1	0.03	12.915	120.4
	2	0.03	13.098	120.5

12.2.5 Explosion Energy Test

Explosion heat is tested according to GJB772A-1997 "Explosive Test Method" 701.1 adiabatic method. At a vacuum of −0.094 MPa, an experimental sample with a mass of 25 g and a diameter of 25 mm is detonated in a 5.8 L explosive heat bomb. 16.5 L of distilled water is used as the temperature measurement medium. The precision thermometer tracks and measures the water temperature in real time with 1‰ accuracy, and calculates the explosion heat value per unit mass of the measured sample according to the heat capacity value and temperature rise value of the explosion heat bomb system.

The structure of the detonation calorimeter test device is shown in Fig. 12.2. Two samples of each explosive are tested and the results are analyzed.

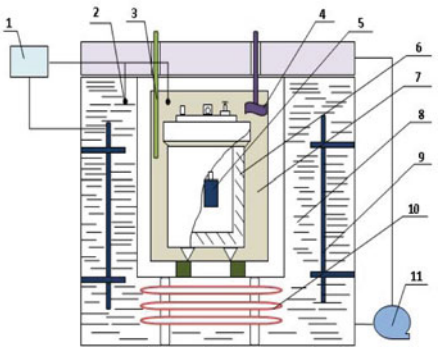

1-temperature controller, 2-platinum resistor, 3-thermometer, 4-submersible pump, 5-explosive sample, 6-device of explosive heat, 7-calorimetric barrel, 8-oauterbarrel, 9-heating plate, 10-cooling pipe, 11-pump

Fig. 12.2 Device diagram of explosive heat calorimeter

12.2.6 Calculation of Adsorption Energy of Main Components of ETPEs Explosives

In order to study the binding state of the main components in ETPEs explosives from the molecular level combined the plane wave. Basis set, VASP software is used to optimize RDX, Al_2O_3 (Al powder outer layer is Al_2O_3) and ETPEs (azidomethane was used as a simplified substitute) stable configuration. Moreover, the adsorption configuration and adsorption energy of azide methane on the surface of RDX and Al_2O_3 are calculated. The plane wave cut-off energy used in the calculation is 520 eV, and the standards for energy convergence and force convergence are 1×10^{-4} eV and 1×10^{-3} eV respectively. The exchange correlation function between electrons and electrons is calculated using the PBE functional under the generalized gradient approximation (GGA), and the van der Waals force is corrected by the DFT-D3 method. When calculating the surface, a 20 Å vacuum layer in the normal direction of the surface is added to avoid the interaction between the surfaces. The results are shown below.

12.2.6.1 Surface Construction of α-Al_2O_3 and RDX

The energies of the (111), (110), (101), (011), (100), (010), (001) crystal planes of α-Al_2O_3 (space group: R-3C) have been calculated. All surfaces contain four layers of Al_2O_3 atoms, for a total of 40 atoms. The $9 \times 9 \times 1$ Monhkorst-Pack K-point grid is used to simulate the Brillouin zone. The calculated faces are summarized in Table 12.4.

Through calculation, it can be known that the three crystal planes (110), (101) and (011) have the lowest energy, which is about—293.38 eV. Considering that Al_2O_3 is a highly symmetrical crystal, the three crystal planes don't have great different.

Table 12.4 Energy calculation of different section of Al_2O_3

Crystal plane							
Section number	(110) (ev)	(101) (ev)	(011) (ev)	(111) (ev)	(100) (ev)	(010) (ev)	(001) (ev)
1	−283.383	−293.383	−283.383	−293.1	−289.003	−286.312	−286.308
2	−278.868	−278.888	−278.887	−283.327	−289.003	−292.09	−286.308
3	−286.582	−286.582	−286.589	−283.658	−289.003	−286.097	−286.097
4	−286.651	−286.6511	−286.655	−293.09	−289.003	−289.015	−289.003
5	−278.319	−278.319	−278.319	−283.3	−289.003	−289.415	−289.003
6	−293.383	−283.383	−293.392	−293.1	−289.003	−286.308	−286.307

Therefore, the optimization result of the sixth cutting method of (110) crystal plane is selected to study the stacking adsorption behavior of azidomethane. Because RDX is a molecular crystal, it's directly add a 20 Å vacuum layer to calculate. The Brillouin zone calculation of the primitive cell adopts a 3 × 3 × 1 Monhkorst-Pack K-point grid.

12.2.6.2 Azidomethane

The azidomethane molecules are placed in a super cell of 20 Å × 20 Å × 20 Å for structural optimization, and the K-point grid is selected as 2 × 2 × 2. In the optimized structure, the bond length of the N =N double bond is 1.213 Å, and the bond length of the N–N single bond is 1.545 Å and 1.544 Å, which is the same as the standard N = N bond length of 1.25 Å and N–N bond length of 1.45 Å quite. Considering the influence of the C-H group on the other side of the azidomethane N atom, the result is reliable. The calculated total energy of the methane azido molecule is −40.975 eV.

12.2.6.3 Calculation of the Adsorption Energy of Al_2O_3+ Azidomethane

In order to choose a highly symmetrical placement position for the azidomethane molecules and avoid the interaction between the azidomethane molecules in adjacent periods, the Al_2O_3 optimization results are expanded (2 times in the X and Y directions), and then for adsorption with azidomethane, the K-point grid is set to 3 × 3 × 1. At this time, the surface system contains 167 atoms, and the distance between the azidomethane molecules in the two different periods is more than 8 Å. Place the azidomethane flat on the (110) surface of α-Al_2O_3. The distance between the atoms of the azidomethane and the α-Al_2O_3 surface atoms in the initial structure is between 1.2 and 1.8 Å, the details are shown in Fig. 12.3a.

The optimized structure is shown in Fig. 12.3b. It can be seen that the distance between the azidomethane molecule and the α-Al_2O_3 atom becomes larger, reaching more than 2.48 Å. The calculated total energy of α-Al_2O_3(110) surface after

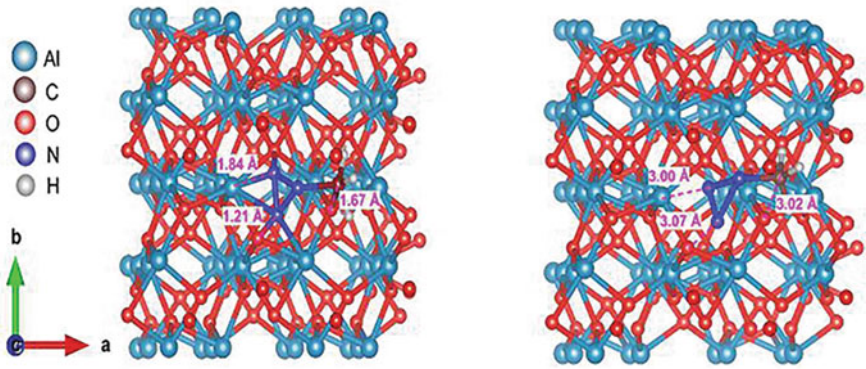

(a) Before optimization (b)After optimization

Fig. 12.3 Molecular structure of adsorption of azidomethane on Al_2O_3

adsorbing azidomethane molecule is: −1235.31 eV. The total energy of α-Al_2O_3 (110) surface and azidomethane are −1193.996 eV and −40.975 eV respectively. So the total energy of α-Al_2O_3 (110) surface adsorbing azidomethane molecules is lower than the separated two energy 0.339 eV ($\Delta E = -0.339$ eV). It's show that α-Al_2O_3 can adsorb azidomethane molecules.

12.2.6.4 Calculation of RDX + Azidomethane Adsorption Energy

Considering the position of the azidomethane molecule, the RDX crystal is expanded along the Y axis once, which means that the double cell is used for adsorption calculation. It's make the place of azidomethane molecules close to the oxygen atoms on the surface of the RDX from the side. As shown in Fig. 12.4a, the distance between azidomethane and RDX is 1.4–2.6 Å in the initial structure. In this way of placement, the surface system contains 343 atoms in total. The intermolecular distance between azidomethane in two adjacent supercells is over 9 Å, and the interaction between azidomethane molecules is negligible.

Except the K point grid is set to 2 × 1 × 1, the other calculation parameters are the same as Al_2O_3 adsorbing azidomethane molecules. The optimized structure is shown in Fig. 12.4b. It can be seen that the distance between the azidomethane and the RDX atom becomes larger, reaching more than 2.6 Å. The calculated energy after adsorption of azidomethane molecules on the RDX surface is: −2126.643. But the energy of RDX and azidomethane molecules are −2086.613 eV and −40.975 eV respectively. The calculated adsorption energy is: $\Delta E = 0.945$ eV, the adsorption energy is positive, indicating that RDX cannot adsorb azidomethane molecules.

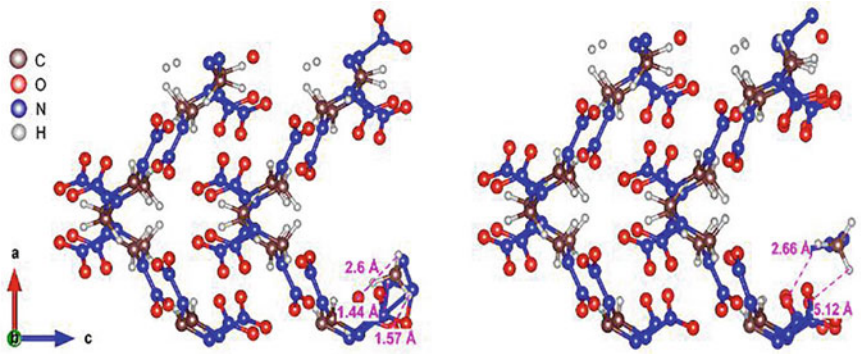

(a) Before optimization (b) After optimization

Fig. 12.4 Molecular structure of azidomethane adsorbed by RDX

12.3 Results and Discussion

12.3.1 Result and Analysis of Underwater Explosion Test of Two Explosives

The environmental media of an explosion in water or in air is different, so there is a difference between the two situation. Even if the water medium can be considered incompressible because of its special properties, the compressibility of water cannot be ignored under the high pressure of the detonation product. Underwater explosions mainly use the generated and bubble pulsation to cause damage to the target. In this study, an underwater shock wave sensor is used to measure the pressure-time curve of the ETPEs explosive sample and the comparative EVA explosive sample in water. The rising front time, peak pressure, and bubble pulsation period of the shock wave are read through the special software. Calculate the underwater specific impulse energy (shock wave energy per unit mass explosive), specific bubble energy (bubble energy per unit mass explosive) and total energy are compared and analyzed. The comparative results of underwater explosion energy are shown in Table 12.5.

Table 12.5 Underwater explosion energy of explosives ETPEs and EVA

Name	Sample No.	Specific shock wave energy, MJ kg^{-1}	Specific bubble energy MJ kg^{-1}	Total energy MJ kg^{-1}
ETPEs explosives	1	1.112	5.583	6.695
	2	1.185	5.551	6.736
EVA explosives	1	1.003	5.103	6.106
	2	1.019	5.102	6.121

Table 12.6 Comparison of underwater explosion energy of two kinds of explosives

Two explosive samples	Increase rate of specific shock wave energy, %	Increase rate of specific bubble energy, %	Increase rate of total energy, %
No. 1 sample comparison	9.8	8.6	8.8
No. 2 sample comparison	14	8.8	9.1

Through comparison, it is found that the specific shock wave energy and specific bubble energy of ETPEs explosives are significantly higher than those of EVA explosives, and the total energy increase rate of the sum of the two is significantly increased. The results of the increase rate are shown in Table 12.6.

It can be seen from the test and comparison results that after replacing the inert binder (EVA) in the typical aluminized explosive formulations with ETPEs in this study, the specific shock wave energy of the explosive under water explosion is increased by 9.8–14%, and the specific bubble energy is increased by 8.6–8.8%, the total energy increased by 8.8–9.1%. Therefor the improvement effect of energy increase is remarkable. According to the application research of ETPEs in propellants [27], the thermal decomposition of azide group on the ETPEs is independent and it is prior to that of main chain, which can not only increase the energy of the formula, but also play a role in accelerating the decomposition of propellant. In addition, Zhou et al. [31] used a single factor test to compare the underwater explosion of the 8701 explosive with the RDX/Al aluminized explosive. Through a large number of experiments, it is proved that aluminum powder reacts with RDX explosion product gas according to the reaction Eqs. (12.3) and (12.5), resulting in the increase of total explosion energy of aluminized explosive. At the same time, the slow burning reaction of aluminum powder has different effects on the overpressure and pressure decay time constant of underwater explosion shock wave. Therefore, we speculate that the addition of ETPEs to the aluminized explosive will lead to a complete detonation reaction similar to the catalytic reaction of underwater explosion. After detonation of C-J surface, ETPEs decomposes and releases a large amount of N_2. According to the Eq. (12.5), N_2 reacts exothermically with Al powder. At the same time, the reaction completion rate of aluminum powder in aluminized explosive is increased, so the energy release rate of aluminized explosive is increased. As far as the energy contribution rate of ETPEs component to explosive formula is concerned, due to its low energy density and small mass proportion in the explosive formula in this study, the energy released by pure ETPEs component will not be more obvious than EVA. In order to further confirm the above analysis results, this study has calculated and measured the detonation heat values of the two explosives.

12.3.2 Test and Analysis of Explosive Thermal Performance of Two Explosives

12.3.2.1 Theoretical Calculation

The ETPEs used in this study is formed by cross-linking polymerization of prepolymer, TDI, and BDL. The molar ratio of the three substances is 1:3:2. Therefore, according to the explosive oxygen balance and oxygen coefficient formula, the oxygen balance of ETPEs is −1.7879, and the oxygen coefficient is 0.0635. Based on this, the oxygen balance of the designed ETPEs and EVA explosive samples is calculated.

$$\begin{aligned}\text{OB (ETPEs explosive)} = &-0.216 \times 54\% - 0.89 \times 40\% \\ &- 1.7879 \times 5\% - 3.460 \times 1\% = -0.5966;\end{aligned}$$

$$\begin{aligned}\text{OB (EVA explosive)} = &-0.216 \times 54\% - 0.89 \times 40\% - 1.685 \\ &\times 3\% - 3.460 \times 3\% = -0.627:\end{aligned}$$

From the perspective of oxygen balance, improving oxygen balance is beneficial to increase the explosive heat value of explosives. On this basis, the theoretical detonation calorific value of explosives containing ETPEs and corresponding EVA explosives are calculated.

Referring to the Q(ETPEs) = 1.0097 [11] given in, the calculation results are as follows:

$$Q_o = \sum m_i Q_{oi} = 8.086;$$

Due to the lack of the density correction factor of ETPEs, the correction coefficient of polyurethane with similar molecular weight and structure to ETPEs is temporarily taken as $B = 1.680$. The molding density of ETPEs explosives is 1.924 g/cm^3, and the molding density of EVA explosives is 1.916 g/cm^3.

$$B = \sum m_i B_i = 1.429;$$

$$Q_v = Q_o - B(\rho_T - \rho)$$

$$= 8.086 - 1.429 \times (2.005 - 1.924) = 7.970\ \text{MJ kg}^{-1};$$

The theoretical explosion of EVA explosives can be shown as:

$$Q_o = \sum m_i Q_{oi} = 8.031;$$

Table 12.7 Explosion heat test results

Name	Number	Explosion heat value, kJ kg^{-1}	Name	Number	Explosion heat value, kJ kg^{-1}	increase rate of explosion heat value, %
ETPEs explosive	1	7930.9	EVA explosive	1	7621.1	4
	2	7873.8		2	7619.8	3.3

$$B = \sum m_i B_i = 1.345;$$

$$Q_v = Q_o - B(\rho_T - \rho)$$

$$= 8.031 - 1.345 \times (1.953 - 1.916) = 7.981 \text{ MJ kg}^{-1};$$

Among them, Q_o—theoretical density explosion heat; B—density correcting coefficient of the mixed explosive detonation heat; Q_v—detonation heat of mixed explosive with density ρ.

It can be seen from theoretical calculations that although the density correction coefficient of ETPEs is lacking and polyurethane is selected instead, the calculated theoretical detonation heat value of ETPEs explosives is still low, which is basically the same after comparison with the calculated detonation heat value of EVA explosives.

12.3.2.2 Experiment Results

In order to further verify the calculation results, the actual detonation heat values of the two explosives are measured by adiabatic method. The results are shown in Table 12.7.

It can be seen from the test results of the explosion heat of the two explosives that the explosion heat value of the ETPEs explosive is significantly higher than that of the EVA explosive, and it is closer to the theoretically calculated explosion heat value. This is because in the actual vacuum and oxygen-free test environment, the excessive aluminum powder reacts with the N_2 liberated by ETPEs to generate aluminum nitride and emit a lot of heat at the same time, which makes a certain contribution to improving the explosive heat value of the explosive. Although the content of ETPEs in the explosive formulation is only 5%, compared with the inert binder, the explosive heat value of the tested explosives is also increased by nearly 5%, which is consistent with the energy increase trend of ETPEs explosives in underwater explosions. Therefore, it can be inferred that if ETPEs are used in the formulation of cast PBX thermobaric explosive (the binder content of this type of explosive is generally more than 10%), as the proportion of ETPEs in the explosive formulation

Table 12.8 Calculation parameter setting and corresponding energy of each component

Structure	Van der Waals force correction method	K-point grid	Calculation accuracy	Energy (eV)
Al_2O_3	DFT-D3	9X9X1	Default precision	−298.49886
Azide methane	DFT-D3	2X2X2		−40.975415
RDX	DFT-D3	3X3X1		−1043.3066
Al_2O_3 + azide methane	DFT-D3	3X3X1		−1235.3102
RDX + azide methane	DFT-D3	2X1X1		−2126.6427

Table 12.9 Corresponding adsorption energy between components

Structure	Adsorption energy (eV)
Al_2O_3 + azide methane	−0.339345
RDX + azide methane	0.945915

increases, this will be significantly improve the energy release rate of this kind of explosive in closed environment.

12.3.3 Analysis of Adsorption Energy Among the ETPEs Explosive Components

By calculating the adsorption energy of the main components of ETPEs explosives, the individual components and the corresponding energy between the two components can be obtained, which are shown in the k.

According to the calculation results in Table 12.8, the corresponding adsorption energy between the binder with azide structure and the aluminum powder and RDX can be obtained, and the results are shown in Table 12.9.

It can be seen from the adsorption energy results that in the explosive system of RDX and aluminum powder, the azide binder is more likely to coat the surface of the aluminum powder, making the decomposition products of ETPEs easily react with the aluminum powder during the explosive detonation reaction, This improving the maximum energy output of explosives.

12.4 Conclusion

By comparing and testing the explosion energy and heat value of two explosive samples in underwater, it is found that:

1. Using ETPEs as a binder can significantly increase the explosive energy release rate of aluminized explosives in underwater and closed environments.
2. Although ETPEs have no advantages in energy density compared to RDX and other energetic materials, ETPEs as a binder component in explosives, can not only meet the requirements of explosive mechanical properties, but also improve the explosive energy output characteristics of aluminized explosives, and improve the explosion energy and heat value of aluminized explosives in underwater and confined spaces.
3. ETPEs as a new type of energetic binder, have great application prospects in aluminized explosives, especially in cast PBX aluminized explosives with higher binder content.

References

1. J.-Y. Jeong, J.K. Song, Y.-G. Kim, et al., Study on the formulation of an energetic thermoplastic propellant. J. Korean Soc. Propuls. Eng. **23**(1), 71–78
2. X. Song, C. Peng, Z. Wei, et al., Influences of relative molecular mass of BAMO-AMMO adhesive on mechanical properties of propellants. China Adhes. **26**(8), 1–3, 28 (2017)
3. H.U. Yi-wen, D.E.N.G. Min, Z.H.O.U. Wei-liang et al., Synthesis and mechanical properties of energetic thermoplastic elastomers based on glycidyl azide polymer and polycaprolactone. J. Solid Rocket Technol. **39**(4), 492–496 (2016)
4. H.U. Yi-wen, J.I.A.N. Xiao-xia, X.I.A.O. Le-qin et al., One-step preparation and mechanical properties of thermoplastic elastomer based on BAMO-THF. J. Solid Rocket Technol. **40**(3), 330–335 (2017)
5. W.A.N.G. Gang, G.E. Zhen, L.U.O. Yun-jun, Performance of P(BAMO/AMMO) based ETPE. Chin. J. Energet. Mater. **23**(10), 930–935 (2015)
6. J.S. You, S.T. Noh, Thermal and mechanical properties of poly(glycidyl azide)/polycaprolactone copolyol-based energetic thermoplastic polyurethanes. Macromol. Res. **18**(11), 1081–1087 (2010)
7. G.H. Hsiue, Y.L. Liu, Y.S. Chiu, Triblock copolymers based on cyclic ethers-preparation and properties of Tetrahydrofuran and 3,3-bis(azidomethyl) oxetane triblock copolymers. J. Polym. Sci. Part A: Polym. Chem. **32**(11), 2155–2159 (1994)
8. L.U. Xian-ming, M.O. Hong-chang, D.I.N.G. Feng et al., Synthesis and application of PBAMO/APP-based Star ETPE. Chin. J. Energet. Mater. **24**(10), 947–952 (2016)
9. Y.W. Hu, L.Q. Xiao, F.Y. Chen, et al., Preparation and performance of energetic thermoplastic elastomers based on poly(glycidyl azide), in *27th Int. Annua Conference of ICT*, Karlsruhe, Germany, 25–28 June 2015, pp. 69.1–69.5
10. L. Yong, L. Yun-jun, G. Zhen, Research development of energetic thermoplastic elastomers. New Chem. Mater. **36**(10), 31–33 (2008)
11. B. Xu, Y.G. Lin, J.C.W. Chien, Energetic ABA and (AB)n thermoplastic elastomers. J. Appl. Polymer Sci. **46**(9), 1603–1611 (1992)
12. E. Diaz, Heats of combustion and formation of new energetic thermoplastic elastomers based on GAP, PolyNIMMO and PolyGLYN. Propellants Explos. Pyrotech. **28**(3), 101–106 (2003)
13. M.A.H. Talukder, Energetic polyoxetane thermoplastic elastomer synthesis and characterization. AD-A209612 (1998)
14. G.E. Manser, D.L. Rose, Energetic Thermoplastic Elastomers. DTIC file. AD-A122909, 10 (1982)

15. K. Subramanian, Hydroxyl-terminated poly (azidomethyl ethylene oxide-b-butadiene-b-azidomethyl ethylene oxide) synthesis, characterization and its potential as a propellant binder. Eur. Polymer J. **35**(8), 1403–1411 (1999)
16. Y. Zhao, Y. Liu, L. Yang, et al., Combustion properties and thermal behavior of ETPE gun propellant and RGD7 Nitramine gun propellant. Chin. J. Energ. Mater. **20**(2), 188–192 (2012)
17. V. Vasudevan, G. Sundararajan, Synthesis of GAP-PB-GAP triblock copolymer and application as modifier in ap/htpb composite propellant. Propell. Explos. Pyrotech. **24**(5), 295–300 (1999)
18. D.O.N.G. Jun, Z.H.A.O. Sheng-xiang, H.A.N. Tao et al., RDX-Al system Coated with ETPE binder. Chin. J. Energet. Mater. **19**(3), 295–298 (2011)
19. S. Pisharath, A.H. Ghee, Synthesis and thermal decomposition fo GAP-Poly (BAMO) copolymer. Polym. Degrad. Stab. **92**(7), 1365–1377 (2007)
20. A.J. Sanderson, USP 7101955. Synthesis of energetic thermoplastic elastomers containing both polyoxirane and polyoxetane blocks. USP 7101955, 2006-09-05
21. R.S. Hamilton, V.E. Mancini, A.J. Sanderson, ETPE Man Tech Program, in *2004 Insensitive Munitions and Energetic Materials Technology Symposium*, San Francisco. CA, 2004-10-16
22. A. Provatas, Energetic polymers and plasticisers for explosive formulations—a review of recent advances. DSTO-TR-0966, 2000-04
23. A.K. Sikder, S. Reddy, Review on energetic thermoplastic elastomers (ETPEs) for military science. Propell. Explos. Pyrotechnic **38**, 14–28 (2013)
24. Y. Zhi-jian, L. Xiao-bo, H. Guan-song et al., Advances in design and research of composite explosives. Chin. J. Energet. Mater. **25**(1), 2–11 (2017)
25. A. Provatas, *Energetic polymers and plasticisers for explosive formulation—a review of recent advances* (Defence science and technology organization, Melbourne, 2000)
26. P.E. Anderson, P. Cook, A. Davis et al., The effect of binder systems on early aluminum reaction in detonation. Propellants Explos. Pyrotech. **38**(4), 486–494 (2013)
27. X. Song, F. Zhao, J. Wang, et al., Thermal behaviors of BAMO-AMMO and its compatibility with some energetic materials. Chin. J. Explos. Propellants (Huozhayao Xuebao) **31**(3), 75–78 (2008)
28. X. Gan, L. Na, X. Lu, et al., Synthesis and properties of ETPE based on BAMO/AMMO. Chin. J. Explos. Propellants (Huozhayao Xuebao) **31**(2), 81–85 (2008)
29. I. Edri, V.R. Feldgun, Y.S. Karinski, et al., On blast pressure analysis due to a partially confined explosion: III. Afterburning effect. Int. J. Protect. Struct. **3**, 311–332 (2012)
30. S. Ye-bin, H. Jun-ming, C. Mao-xin, *Military mixed explosive* (Ordnance Industry Press, Beijing, 1995)
31. J. Zhou, G. Xu, Y. Wang, Analysis of shock wave characteristics of aluminized explosive underwater explosion. Explosion **22**(1), 41–51 (2005)

Chapter 13
Effect of Nano-copper-Ultrafine Carbon Composite on Thermal Decomposition of CL-20

Wen-jing Zhou, Juan Zhao, Yan-li Ning, Min Xu, Yi-ju Zhu, and Min-chang Wang

Abstract Ultrathin carbon loaded With nano-copper (Cu-C composite) was mixed With Hexanitrohexaazazo wurtane (CL-20); Scanning electron microscopy (SEM) and transmission electron microscopy (TEM) were used to observe the dispersion of nano-copper in ultra-thin carbon and the composite on the surface of CL-20. The elemental content was analyzed by energy spectrum, and the effect of Cu-C composite on the thermal decomposition of CL-20 at different mixing ratios was analyzed by differential scanning calorimetry (DSC). The results show that the nano-copper is uniformly loaded on the ultrafine carbon and dispersed on the surface of CL-20. DSC results showed that the decomposition peak temperature of CL-20 decreased from 250.6 to 240.5 °C and the activation energy decreased from 222.4 from to 212.4 kJ/mol, indicating that the Cu-C composite had a certain catalytic effect on the thermal decomposition of CL-20.

13.1 Introduction

CL-20 is one of the high energy elemental explosives, which can meet the requirements of high energy in the military field and has broad application prospects [1, 2]. The density of ε-CL-20 reached 2.04 g/cm^3, The detonation velocity of ε-CL-20 is up to 9.5 km/s, and the detonation pressure is 42–43 GPa, both higher than HMX. Carbon materials are widely used in energetic materials, Graphite is used to improve the gloss of propellant and the dullness of mixed explosive [3], Carbon black used in propellants can improve the combustion performance. Nano-metal powder as a catalyst added to energetic materials has an obvious catalytic effect on the thermal decomposition of energetic materials [5, 6]. Nano-copper as a catalyst, has the advantages of low price and low toxicity. The application of copper for catalytic reaction is a very hot research field [7–9]. However, nano-copper is easy to agglomerate, the advantage of large specific surface area can't be effectively played.

W. Zhou · J. Zhao · Y. Ning · M. Xu (✉) · Y. Zhu · M. Wang
Xi'an Modern Chemistry Research Institute, Xi'an 710065, China
e-mail: naturemin2001@163.com

A. Gany and X. Fu (eds.), *2021 International Conference on Development and Application of Carbon Nanomaterials in Energetic Materials*, Springer Proceedings in Physics 276,
https://doi.org/10.1007/978-981-19-1774-5_13

At present, the focus of research is to deposit metal catalysts on carbon materials such as graphene, which can not only ensure that the metal catalyst does not agglomerate, but also improve the performance of energetic materials by using the addition of carbon materials. Zhang et al. [10] have reported the effect of PbSNO,@rGO nanocomposite on the thermal decomposition of CL-20, and found that the thermal decomposition of PbSnO3@rGOxCL-20 had a good catalytic effect, which reduced the thermal decomposition temperature of CL-20 by 1.32 °C. Wang et al. [11] have reported the influence of nano-PbZrO on the thermal decomposition of AP, RDX and HMX, and the results showed that the addition of PbZrO3 effectively reduced the activation energy of AP, RDX and HMX decomposition. Li et al. [12] have reported the preparation of graphene nanoparticle composites and the thermal decomposition of AP by graphene nanoparticle composites, and the results showed that Ni-graphene nanocomposites exhibited high catalytic activity, the temperature corresponding to the maximum decomposition rate of AP was reduced by 97.3 °C. Xie et al. [13] have reported the catalytic thermal decomposition of RDX-CMDB propellant was studied by TG-DSC-IR-MS. the ternary composite burning rate catalysts (lead 2,4 dihydroxybenzoate, copper p-aminobenzoate and blackening) had obvious catalytic effect on the thermal decomposition of RDX-CMDB propellant. Liu et al. [14] have reported Synthesis of a chabazite-supported copper catalyst with full mesopores for selective catalytic reduction of nitrogen oxides at low temperature. Zhang et al. [15] have reported the morphology-dependent catalytic activity of Fe2O3 and its graphene-based nanocomposites on the thermal decomposition of AP.

In this work, the nano-copper loaded on the ultrafine carbon material was used as the catalyst to avoid the agglomeration of nano-copper. After the Cu-C composite was mixed with CL-20, the dispersion of nano-copper in the ultrafine carbon and the complex on the surface of CL-20 was observed by SEM and TEM. The element content was analyzed by energy spectrum. The influence of Cu-C composite on the thermal decomposition of CL-20 was studied by DSC, and the changes of the kinetic parameters of CL-20 were calculated, which provided a reference for exploring the application of CL-20 in composite solid propellants.

13.2 Experimental

13.2.1 Materials and Instruments

Cu-C composite; Quanta600F Scanning Electron Microscope (SEM); Talos 200i Transmission Electron Microscope (TEM); XFlash 6/60 T EDS; DSC 204 HP Differential Scanning Calorimeter.

13.2.2 Cu-C Complex Mixed with CL-20

Cu-C complex and CL-20 (mass ratio 1:99, 5:95, 10:90) were respectively weighed and placed in a plastic centrifugal tube. Three mixtures of Cu-C complex/CL-20 in different proportions were obtained through vibration mixing.

13.2.3 Test Methods

13.2.3.1 Element Content of Cu-C Complex and Dispersion Characterization of Nano-copper on Ultrafine Carbon

The Cu-C complex was pasted on the sample table, and the working distance of the SEM was adjusted to 10 mm. The acceleration voltage was 20 kV, and the element content of Cu-C composite was analyzed by EDS. The particle size range of nano-copper and the dispersion of nano-copper on ultrafine carbon were observed under SEM at 20,000×.

The Cu-C complex was dispersed in ethanol and dropped on the special copper net. After drying, the dispersion of nano-copper on ultrafine carbon was observed by using TEM and energy spectrum Mapping.

13.2.3.2 Uniformity Characterization of Cu-C Complex CL-20 Mixture

The mixture of Cu-C complex/CL-20 was pasted on the sample table, the surface was spray gold and the mixing uniformity of Cu-C complex/CI-20 was observed under 2000× and 5000× by SEM.

13.2.3.3 Influence of Cu-C Complex Content on Thermal Decomposition of CL-20

DSC was used to analyze the change of thermal decomposition curve of CL-20 after adding different proportion of Cu-C complex and the thermal decomposition of Cu-C complex and CL-20 mixture at different heating rates.

13.3 Results and Discussion

13.3.1 Characterization of Cu-C Complex and CL-20

13.3.1.1 Element Content of Cu-C Complex

The element content of Cu-C complex were measured by EDS. The results are shown in Fig. 13.1 and Table 13.1.

The binding energies of K-layer electrons and L-layer electrons of copper are 8.041 keV and 0.929 keV respectively. It can be seen from Fig. 13.1 that both K-layer electrons and L-layer electrons of copper are excited. By analysis of the peak area corresponding to the binding energy, the percentage of copper was calculated to be 58.7%.

As can be seen from the results in Table 13.1. The copper content of Cu-C complex is higher than carbon content, which also contains a small amount of oxygen. The possible source of oxygen is the adsorption of carbon and the oxidation of copper surface.

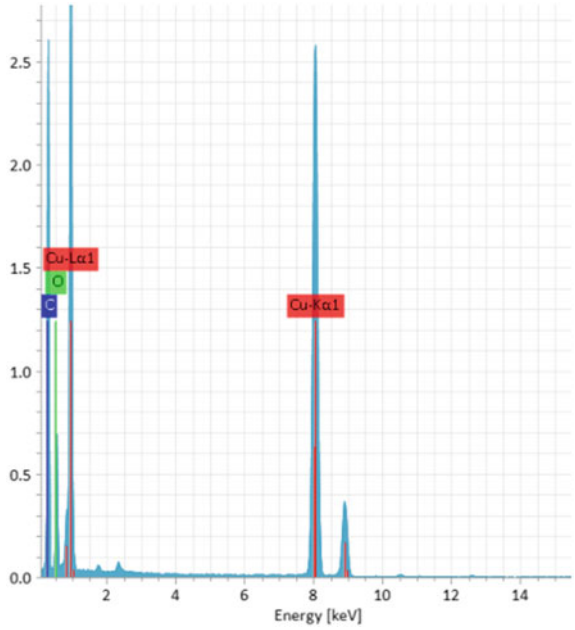

Fig. 13.1 EDS diagram of Cu-C complex

Table 13.1 Element content of Cu-C complex

Element	C	Cu	O
Mass percentage (%)	36.2	58.7	5.1

13.3.1.2 Dispersion Characterization of Nano-copper on Ultrafine Carbon

The particle size range of nano-copper and the dispersion of nano-copper on ultrafine carbon were observed by SEM and TEM. The results are shown in Figs. 13.2, 13.3 and 13.4.

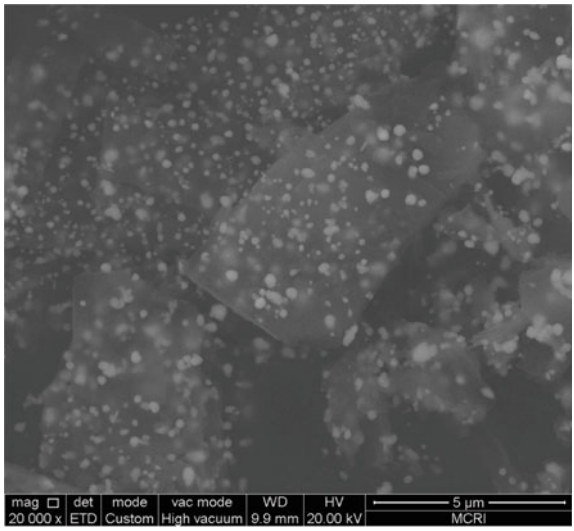

Fig. 13.2 SEM images of Cu-C complex

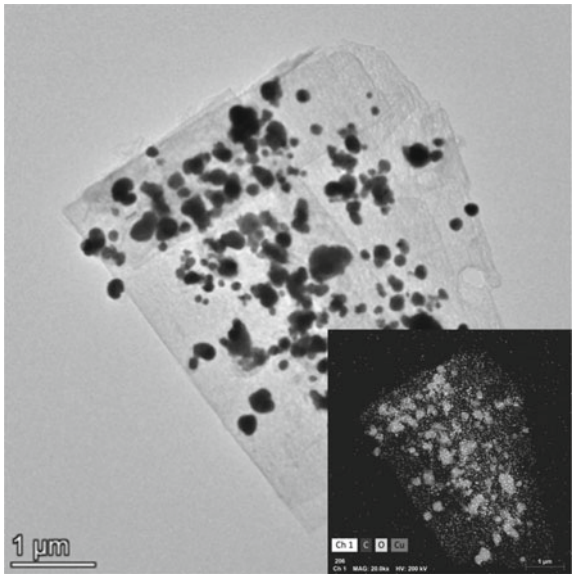

Fig. 13.3 TEM images of Cu-C complex

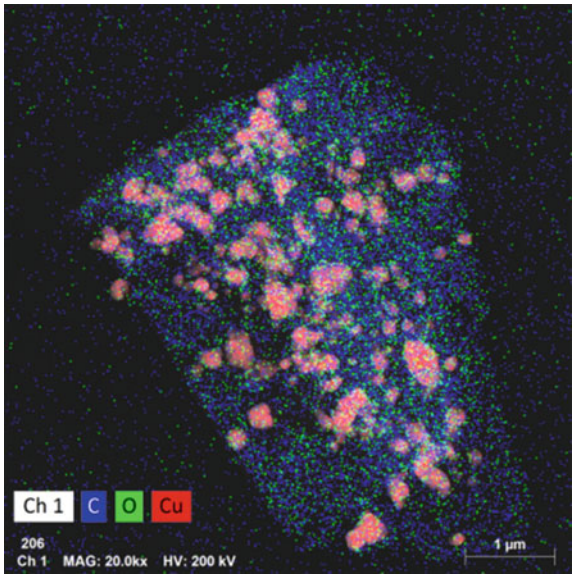

Fig. 13.4 Mapping images of Cu-C complex

The SEM images of Cu-C complex shown in Fig. 13.2. It can be seen from Fig. 13.2 that the nano-copper is spherical, and the particle size range is between 50 and 500 nm. The nano-copper was uniformly dispersed in the ultra-thin carbon. The TEM images of Cu-C complex shown in Fig. 13.3. It can be seen from Fig. 13.3 that the size of ultra-thin carbon is between 3 and 5um, and the nano-copper is mixed between the carbon film layers. The element mapping of Cu-C complex shown in Fig. 13.4, where the blue is the distribution of carbon element, the red is the distribution of copper element, and the green is the distribution of oxygen element. As can be seen from the Mapping, carbon element and oxygen element are evenly distributed in the ultra thin carbon. There on accumulation of oxygen was observed in the copper particle concentration area, indicating that oxygen in element analysis comes from carbon adsorption.

13.3.1.3 Uniformity Characterization of Cu-C Complex/CL-20

The uniformity of Cu-C composite/CL-20 mixing was observed by SEM, The results are shown in Figs. 13.5, 13.6 and 13.7.

The large particle in Fig. 13.5a is CL-20. The adsorption of Cu-C complex in the local area of CL-20 shown in Fig. 13.5b. It can be seen that Cu-C complex is adsorbed on the surface of CL-20, and the Cu-C complex is relatively uniformly dispersed on the surface of CI-20 particles. By comparing with Figs. 13.5a, 13.6a and 13.7a, it can be seen that the amount of Cu-C complex adsorbed on the surface of CL-20 also shows an increasing trend with the increase of adding proportion.

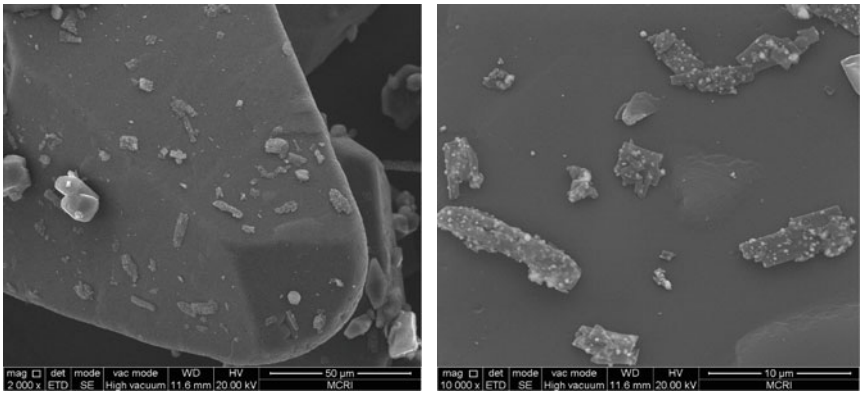

a 2000X b 10000X

Fig. 13.5 SEM images of Cu-C complex/CL-20 (mass ratio 1:99)

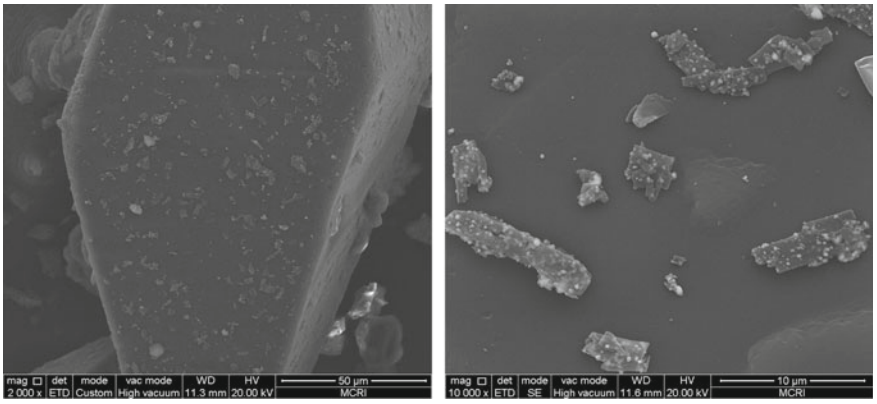

a 2000X b 10000X

Fig. 13.6 SEM images of Cu-C complex/CL-20 (mass ratio 5:95)

13.3.2 Effect of Cu-C Complex Content on Thermal Decomposition of CL-20

In order to study the influence of the content of Cu-C complex on the thermal decomposition of CL-20, the DSC curves of pure CL-20 and Cu-C complex/CL-20 mixtures with different proportions were obtained by using the heating rate of 10 °C/min, as shown in Fig. 13.8.

As can be seen from the Fig. 13.8, the thermal decomposition peak temperature of CL-20 without adding Cu-C complex is 250.6 °C. When the mass ratio of Cu-C complex to CL-20 was 1:99, the thermal decomposition peak temperature decreased 8.2 °C, and there was a shoulder peak near the thermal decomposition peak position

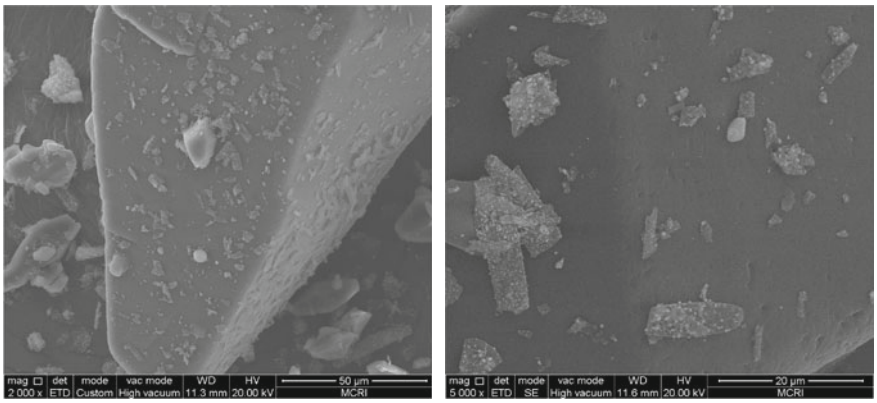

a 2000X b 5000X

Fig. 13.7 SEM images of Cu-C complex/CL-20 (mass ratio 10:90)

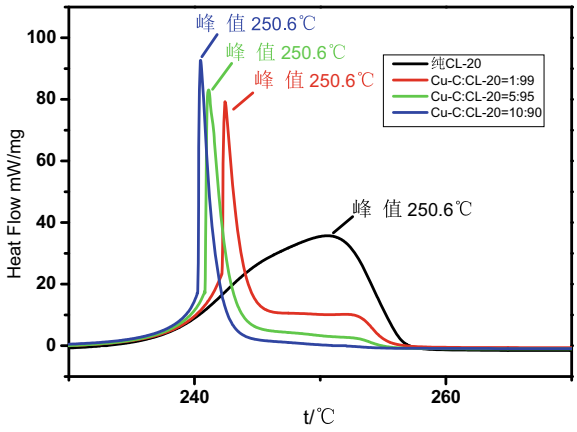

Fig. 13.8 DSC curves of different ratios of Cu-C complexes/CL-20

of pure CL-20. It may be due to the low addition amount of Cu-C complex that the catalytic sites in the Cu-C complex have been completely consumed before the complete catalytic decomposition of CL-20. When the mass ratio of Cu-C composite to CL-20 is 5:95, the thermal decomposition peak temperature is decreased by 9.5 °C. The shoulder peak near the thermal decomposition peak of pure CL-20 is significantly reduced. When the mass ratio of Cu-C complex to CL-20 was 10:90, the peak temperature of thermal decomposition decreased by 10.1 °C, and the shoulder peak disappeared completely, indicating that CL-20 was completely catalyzed by Cu-C complex.

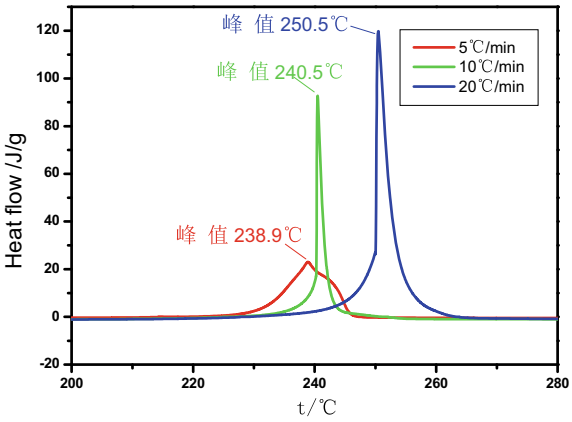

Fig. 13.9 DSC curves of different heating rates of Cu-C complexes/CL-20

Table 13.2 The activation energy of Cu-C complexes/CL-20

Heating rates (β, °C/min)	Peak temperature (T_p, K)	$10^3/T_p$	$\ln(\beta/T_p^2)$	Activation energy (E_a, KJ/mol)
5	512.1	1.95	−10.86	212.4
10	513.7	1.94	−10.18	
20	523.7	1.91	−9.53	

13.3.3 Kinetics of Thermal Decomposition of Cu-C Composite/CL-20

To study the thermal decomposition characteristics of Cu-C complex and CL-20 with a mass ratio of 10:90 at the heating rate of 5, 10 and 20 °C/min. the curve of DSC is shown in Fig. 13.9. According to the decomposition peak temperatures at different heating rates, the Kissinger equation was used to calculate the apparent activation energy of Cu-C complex/CL-20 mixture. The results are shown in Table 13.2

As can be seen from the data in Table 13.2, the apparent activation energy of Cu-C complex/CL-20 mixture is 212.4 kJ /mol, which is compared with the reported apparent activation energy of pure CL-20 of 222.4 K/mol. The addition of Cu-C complex reduced the apparent activation energy of CL-20 by 10.0 kJ/mol, indicating that the Cu-C complex played a positive catalytic role in the thermal decomposition of CL-20.

13.4 Conclusions

1. The nano-copper is spherical, and the particle size range is between 50 and 500 nm. The nano-copper is uniformly dispersed on the ultra fine carbon. After

mixing with CL-20, Cu-C complex uniformly adsorbed on the surface of CL-20 particles.

2. The thermal decomposition peak temperature of CL-20 without adding Cu-C complex is 250.6 °C. With the addition of different proportions of Cu-C complex, the thermal decomposition temperature of the composite decreased significantly. With the increase of the addition amount, the reduction range of the decomposition peak temperature increased. When the mass ratio of Cu-C complex to CL-20 was 10:90, the shoulder peak disappeared completely to the thermal decomposition peak of pure CL-20 disappeared, indicating that CL-20 was completely catalyzed by Cu-C complex.
3. The apparent activation energy of CL-20 decreased from 222.4 to 212.4 kJ/mol with the addition of Cu-C complex, which further indicated that Cu-C complex played a positive catalytic role in the thermal decomposition of CL-20.

References

1. Y. Zhu, Y. Lu, B. Gao, S. Tan, Preparation and performance of 2,4,6,8,1 0,1 2—hexanitro-2,4,6,8,1 0,1 2-hexaazaisowurtzitane/3,5—dinitrobenzoic acid (CL-20/DNBA) spherical composite. Chin. J. Energ. Mater. **25**(11), 964–968 (2017)
2. J. Liu, N. Zhao, F. Zhao, J. Song, H. Ma, Preparation of sea urchin-shaped nano-MnO_2 and its effect on thermal decomposition performance of CL-20. Chin. J. Explos. Propellants **38**(2), 19–24 (2015)
3. Y. Lan, X. Li, Y. Luo, Research progress on application of graphene in energetic materials. Chin. J. Explos. Propellants **38**(1), 1–7 (2015)
4. Xiaofei QI, Xiaohong ZHANG, Junqiang LI.Influence of carbon black particle size on combustion characteristics of CMDB propellant[J] . Chemical Pro- pellants & Polymeric Materials 2012,10(6):51–53.
5. L. Meda, G. Marra, L. Galfetti, et al., Nano—aluminum as energetic material for rocket propellants. Mater. Sci. Eng.: C **27**(5), 1393–1396 (2007)
6. H.Z. Duan, X.Y. Lin, G.P. Liu et al., Synthesis of Ni nanoparticles and their catalytic effect on the decomposition of ammonium perchlorate. J. Mater. Process. Technol. **208**(1), 494–498 (2008)
7. D. Du, X. Gao, W. Chen, Recent developments in copper-based, non-noble metal electrocatalysts for the oxygen reduction reaction. Chin. J. Catal. **37**, 1049–1061 (2016)
8. M.L. Hossain, K. Wang, F. Ye, Y. Zhang, J. Wang, Cu(I)-catalyzed cascade reaction of N-tosylhydrazones with 3-butyn-1-ol: a new synthesis of tetrahydrofurans. Chin. J. Catal. **38**, 115–122 (2017)
9. N. Nowrouzi, M. Abbasi, H. Latif, Thiol-Free route to diaryl sulfides by Cu catalyzed coupling of sodium thiosulfate with aryl halides. Chin. J. Catal. **37**, 1550–1554 (2016)
10. J. Zhang, F. Zhao, S. Xu, Y. Yang, Y. Ran, Preparation of $PbSnO_3$@rGO nanocomposite and its effect on the thermal decomposition of CL-20. Chin. J. Explos. Propellants **40**(2), 33–36 (2017)
11. W. Wang, T. Wei, H. Gao, Effects of nano $PbZrO_3$ on the decompositions of AP, RDX, HMX and the combustion of (NG/NC). Propellant Chin. J. Explos. Propellants **40**(6), 29–35 (2017)
12. N. Li, M.H. Cao, Q.Y. Wu, et al., A facile one—step method to produce Ni/graphene nanocomposites and their application to the thermal decomposition of ammonium perchlorate. Cryst. Eng. Commun. **14**(2), 428–434 (2012)

13. X.I.E. Minzao, H.E.N.G. Suyun, L.I.U. Ziru, Research on the catalytic thermal decomposition of RDX·CMDB propellants by TG-DSC·IR·MS. J. Solid Rocket Technol. **32**(5), 539–542 (2009)
14. J. Liu, J. Liu, Z. Zhao, W. Song, Synthesis of a chabazite-supported copper catalyst with full mesopores for selective catalytic reduction of nitrogen oxides at low temperature. Chin. J. Catal. **37**(5), 750–759 (2016)
15. M. Zhang, F. Zhao, H. Li, Y. Yang, Morphology-dependent catalytic activity of Fe2O3 and its graphene-based nanocomposites on the thermal decomposition of AP. FirePhysChem **1**, 46–53 (2021)

Chapter 14
Progress on the Carbon Nanotubes Applied to Energetic Materials

Xinyao Nie, Junli Kong, Zhenghong Wang, and Haijun Xi

Abstract Recent years, carbon nanotubes (CTNs) have been widely applied to energetic material (EM) fields including micro-igniter system, combustion catalyst, carrier of nitrogen-rich EMs, mechanical properties modifier, desensitization agent, Detector for waste explosives. As for micro-igniter system, the CNTs can improve the ignition performance as improvement on dispersion or electric conductivity for micro-igniter. Meanwhile, the excellent electric and thermal conductivity of CNTs also denotes that the CNTs can be used in combustion catalyst, desensitization agent, detector for waste explosives. Besides, the CNTs possess special surface properties and nanoscale effect, which means that it also can be used as a modifier to improve mechanical properties for composite EMs and a carrier of nitrogen-rich EMs after its functionalized by some groups. This paper reviews progress of CNTs applied in above applications.

14.1 Introduction

Energetic materials (EMs) are the material with stored abundant chemical energy which can be released in a fast way, such as explosives, pyrotechnics and propellants. The beginning history of EMs is the invention of gunpower in ancient China. The gunpower, widely used as firearm propellant and pyrotechnic composition, is a mixture of sulfur, charcoal, potassium nitrate. Facing to the fast development of technologies, the gunpower is no longer widely in use and replaced by advanced energetic materials and systems in both civil and military fields [1]. In past decades,

X. Nie (✉) · J. Kong · Z. Wang · H. Xi
Liaoning Qingyang Chemical Industry Corporation, Liaoyang, Liaoning, China
e-mail: xinynie@126.com

Z. Wang
e-mail: 13804190737@139.com

H. Xi
e-mail: 13634990056@139.com

A. Gany and X. Fu (eds.), *2021 International Conference on Development and Application of Carbon Nanomaterials in Energetic Materials*, Springer Proceedings in Physics 276,
https://doi.org/10.1007/978-981-19-1774-5_14

a safer energetic material with better performance, which means that high energetic, insensitive, functional nontoxic and environment friendly, is a desired material for researchers to pursue [2–4]. To satisfy requirement of EMs performance, the functional additives is always hot issue in EMs fields.

Recent years, carbon nanotubes (CNTs), a nanostructured material with hexagonal shapes connected to each other to form tube shapes, are the most prevalent novel material concerned by researchers as its unique performance including electrical thermal chemical, mechanical properties and nanoscale effects [5, 6]. CNTs were proposed as a potential additive to influence the thermal, electrical or surface properties of EMs, which could be attributed to their extraordinary importance regarding their exceptional characteristics since their emergence in 1991 [6, 7]. CNTs, possessing a high aspect ratio, can deliver electrical conductivity under relatively lower reaction kinetics, mechanisms and catalysis concentrations [8]. For that reason, the high conductivity of CNTs could be considered as the function of metallic species that apply to field emission area [9]. Besides, CNTs possess high performance on thermal conductive and unique mechanical properties including strength, elasticity, stiffness, and toughness [5, 6]. Interestingly, CNTs maintain a unique chemical network structure in the periodic table. Therefore, they are the only group which can be bonded with each other with virtuous chemical stability by the π-electron delocalization [10]. Furthermore, CNTs is their excellent lattice structure with the lack of defects that allowed CNTs to be unique materials in a wide range of applications, such electrical or thermal conductivity, energy storage, modifier, fibers, and catalyst [11]. Nowadays, CNTs have been proved that it also can be applied to the EMs field including combustion catalyst, igniter, carrier of EMs, modifier of physical properties, desensitization agent and detector of explosives.

According to the characteristics of CNTs, applications of CNTs in EMs filed are concluded in this paper, such as micro-igniter system, combustion catalyst, carrier of nitrogen-rich EMs. mechanical modifier, desensitization agent and detector for waste explosives. Furthermore, recent related progress is also reviewed.

14.2 Micro-igniter System

Recently, there has been renewed interest in nanoscale metastable intermolecular composites (nMIC) which is a type of nano-multilayer films prepared by both nano-sized fuels (e.g., Al, Si or Mg) and oxidizers (e.g. CuO or Fe_2O_3). Figure 14.1 shows a typical preparation process for nMIC. The nMIC is an novel promising nano-EM to be the micro-igniter at both numerous civilian and military applications, such as safe arm and fire device used in missiles, rockets, micropropulsion systems for microsatellites, triggering the inflation of airbags and so on, as its excellent performance on both high reaction heat and flexible size [12].

However, the application of nMIC is limited by the instability caused by the agglomeration and oxidation of nano-size metal fuels. The CNTs have been proven by many researches that is an effective addition to overcome drawbacks of nMIC.

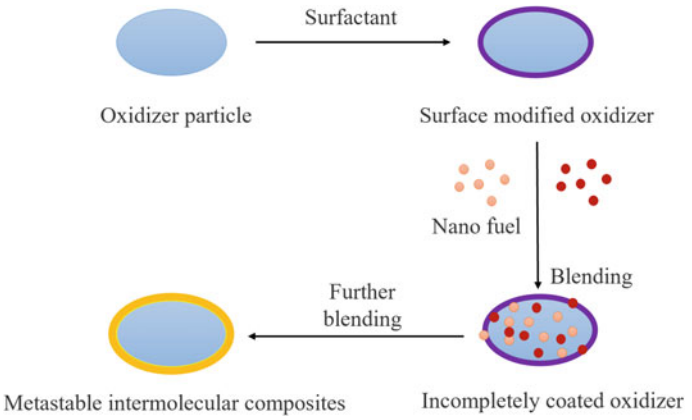

Fig. 14.1 A typical preparation process for MIC

Jeong et al. [13] report that engineering morphologies of Al/CNTs by a mechanical pulverization can enhance exothermic performance compared with pure Al as the result of improvement on thermal conductivity that is caused by a homodisperse of CNTs into Al agglomeration. The micro-interface properties can be modified to affect ignition performance by dispersion of CNTs. However, a relative poor compatibility of CNTs in EMs may result in special contribution on shorten ignition delay. Kappagantula et al. [14] investigate the effect of CNTs on the ignition performance of aluminum-teflon based energetic materials. Results show that the impact ignition delay time can be shorten by the inclusion of CNTs into Aluminum-Teflon based energetic materials as the result of the promoting hot spot formation spurred by friction and sheer interaction between CNTs (possessing high Young's modulus) and surrounding particles, as seen in Fig. 14.2. Furthermore, the excellent performance on thermal conductivity and dispersion for Aluminum-Teflon composites by addition of CNTs, provides possibilities to enhance heat transfer properties of composite nano-EMs.

Electro-ignition is a crucial method for micro-igniter. Electric conductivity of composites can be raised by assembling CNTs on nano-EMs. Guo et al. [12] prepare the KNO3@CNTs by embedding the KNO3 into CNTs and then integrating the KNO3@CNTs with a micro-igniter by electrophoretic deposition of KNO3@CNTs on a Cu thin-film microbridge. Results demonstrate that, compared micro-igniter only coated by KNO3, the explosion voltage decrease from 86.70 to 51.52 V by deposition of KNO3@CNTs on micro-igniter. In order to get a compact, flexible, and versatile micro-igniter, the multiwalled carbon nanotubes (MWCNTs)-coated paper integrating with nano-EMs is an effective method. Kim et al. [15] report a micro-igniter manufactured by coating an nano-EMs (Al/CuO nanoparticles) layer on the surface of the MWCNTs-coated paper electrode and the micro-igniter can be ignition at the applied voltages of 15 V. To improve the surface compatibility between paper electrode and nano-EMs, Kim Ho et al. [16] prepare a hybrid MWCNTs-coated

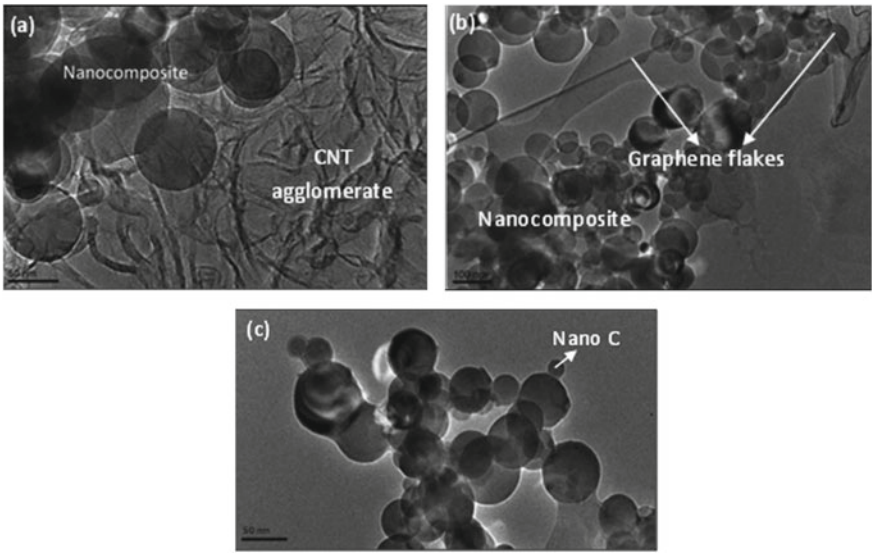

Fig. 14.2 TEM image Al/Teflon with 10% by mass CNTs (**a**), graphene (**b**), and amorphous carbon nanospheres (**c**) [14]

paper by using nitrocellulose (NC) as coating agent and then manufacturing the hybrid micro-igniter through integrating the hybrid paper with dropping an energetic that colloid consist of NC and Al/CuO nanoparticles, as seen in Fig. 14.3. Results suggest that the hybrid micro-igniter can be ignited under applied voltages below 10 V and it can successfully apply to launching a smart rocket.

Except improvement on ignition performance by increasing electric conductivity of nano-EMs igniter, utilizing photo-initiation effect of CNTs can be designed to be an

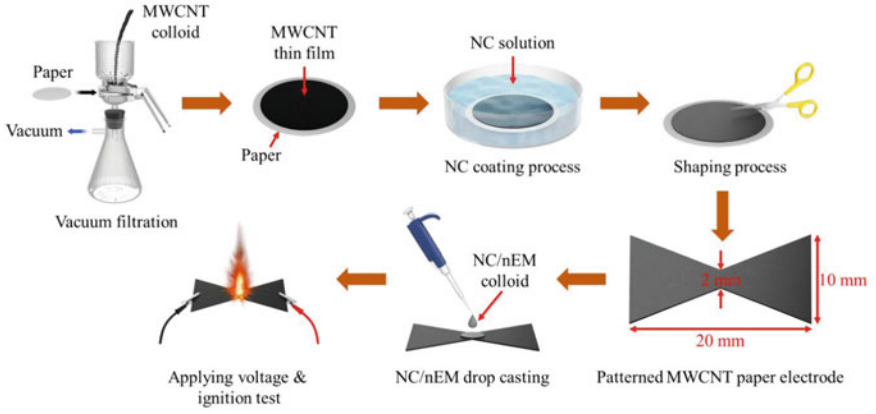

Fig. 14.3 Schematic of the fabrication process of hybrid MWCNTs-coated paper [16]

igniter. When exposed to a camera flash, the CNTs can be ignited as its photo-acoustic effects that the CNTs absorbs light emitted and transfer the energy into vibrational energy resulting in heating of the nanotube lattice [17]. Furthermore, single-walled carbon nanotubes (SWCNTs) are more easily to ignite than MWCNTs due to its lower thermal conductivity that result in a better thermal accumulation under the photo-ignition process [18]. Xu et al. [19] investigate the photo-responsive behavior of Zr/KClO4 composites in the presence or absence of CNTs. It is shown that under the same flash power density, the oxidation degree of Zr increases by increasing the addition of CNTs into Zr/KClO4 composites. Besides, sever combustion can be observed by a camera at the moment of flash. However, the light energy of a flash is not easily focused on a targeted area, which causes limiting its use for igniting nEMs under close contact [20–22]. Kim Ji et al. [22] investigate the effect of MWCNTs on the combustion and explosion characteristics of lower-power laser irradiation-ignited Al/CuO nanoparticles. Results denote that the threshold power and delay time of nano-Al/CuO ignition are reduced to ~40% and ~50% respectively by inclusion of 10 wt% MWCNTs. In addition, pressurization rate, flame propagation speed, and pressure wave speed of nEMs are significantly enhanced as the result of the heat energy from nEMs combustion transferred by MWCNTs. Yu et al. [23] prepare CL-20/MWCNTs composites by the ultrasound inhalation method. Experimental results mean that the laser ignition function of energetic composites can be achieved by the incorporation of MWCNTs into CL-20.

Overall, the application of CNTs in nEMs fields provides possibility to manufacture functional mircro-ignition system.

14.3 Combustion Catalyst

The incorporation of combustion catalyst into EMs is the most important method to improve combustion performance including increasing the burning rate, decreasing burning rate dependence on pressure and initial temperature [24]. Many researches have proven ability of forming carbon frame can enhance the catalytic activity of combustion, therefore the carbon black is always used as catalyst components [25–27]. The activity of combustion catalyst can be enhanced by changing the catalyst size from millimeter scale to nano scale [28]. In addition, incorporation of CNTs into composite combustion catalyst can improve the dispersity as the result of special surface properties of CNTs [29]. Recently, CNTs have aroused interests for many researchers working in combustion catalyst of EMs.

One of the most important evaluation of combustion catalyst performance is its effects on thermal decomposition behaviors of EMs. Liu et al. [29] investigate the influence of the composite combustion catalyst, CNTs supported Fe_2O_3 via a sol_gel method, on the AP decomposition process by thermal analysis. Compared with using nano-Fe_2O_3 as combustion catalyst, the temperature of the exothermic peak corresponding to AP decomposition is reduced from 383.4 to 329.4 °C due to the inclusion of CNTs/Fe_2O_3 composite catalyst. The higher catalytic activity

Table 14.1 Effect of CNTs on decomposition temperature for EMs

Catalyst	CNTs@Fe_2O_3 [29]	MWCNTs [30]	SWCNTs [30]	PbO·CuO/CNTs [31]
Application	AP	AP	AP	RDX
Preparation method	Sol–gel method	Solvent-antisolvent method	Solvent-antisolvent method	microemulsion method
Thermal analysis method	TG	DSC	DSC	DSC
Degradation of decomposition temperature (°C)	54.0	42.0	62.0	5.7

of CNTs/Fe_2O_3 composites than Fe_2O_3, because the aggregation of nano-Fe_2O_3 is restrained by supported of CNTs. Mahmoud et al. [30] synthesis AP/CNTs nano-composites by the solvent-antisolvent method. The needed activation energy of thermal decomposition reduces 42 °C and 62 °C respectively by incorporation of MWCNTs and SWCNTs into AP in comparison to that of pure AP particles. Ren et al. [31] prepare a nano-composites (PbO·CuO/CNTs) by microemulsion method. Compared with mixture of carbon black, copper and lead as traditional combustion catalyst for solid propellant, the nano-composites decrease thermal decomposition temperature of trinitroperhydro-1,3,5-triazine (RDX) from 232.6 to 226.9 °C, which means the nano-composites consist of PbO·CuO/CNTs significantly accelerate the decomposition of RDX. Above results are concluded in Table 14.1.

Furthermore, some works also demonstrate the improvement on combustion performance of EMs by addition of CNTs. Denisyuk et al. [32] study the effect of CNTs on combustion performance of double base propellant. The result shows that, the CNTs as a catalyst component accelerate the combustion to a higher extent than the carbon black due to a higher density of carbon frame formed during the combustion process, as shown in Fig. 14.4. Zhang et al. [33] the investigate relationship between CNTs contents and combustion performance of composite modified double base propellant. The report denotes that, the combustion performance of propellant raised by CNTs, the burning rate increases while the burning-rate pressure exponent decreases, with the increase of CNTs concentration. A recent conclusion proposed by Denisyuk [34] shows that the improvement mechanism on catalytic combustion, a carbon frame on the burning surface promoted by CNTs, can be applicable to any individual explosives and propellant compositions which depends heat of redox reactions.

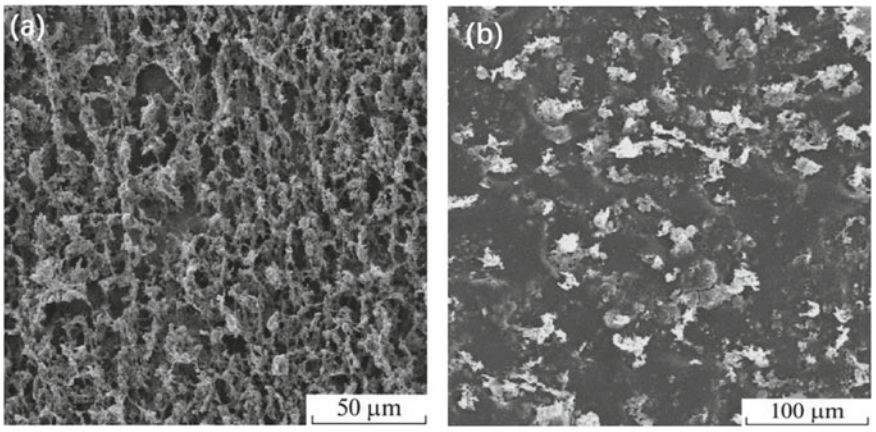

Fig. 14.4 Combustion surface of CNTs (**a**) and carbon black (**b**) as catalyst for double base propellant [32]

14.4 Carrier of Nitrogen-Rich EMs

Since the discovery of CNTs, the ability of CNTs as storage carrier is attracted much interest because the CNTs possesses unique structure and potential applications [35, 36]. The CNTs also is regarded as the carrier of loading nitrogen-rich materials with high energy density. The complex nano-materials formed by CNTs and nitrogen-rich materials is a promising nano-EMs. Yu et al. [37] perform synthesis of nitrogen-doped CNTs with chemical vapor deposition method by pyrolysizing melamine as the precursor in an atmospheric pressure. Then chemical stability of 3,3′-azo-bis(6-amino-1,2,4,5-tetrazine) (DAATO) existing inside nitrogen-doped CNTs is demonstrated by density functional theory calculation, as shown in Fig. 14.5. Hakima et al.

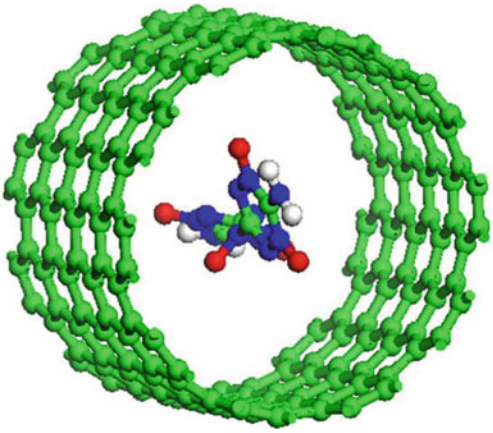

Fig. 14.5 The structure geometric of DAATO@ nitrogen-doped CNT [37]

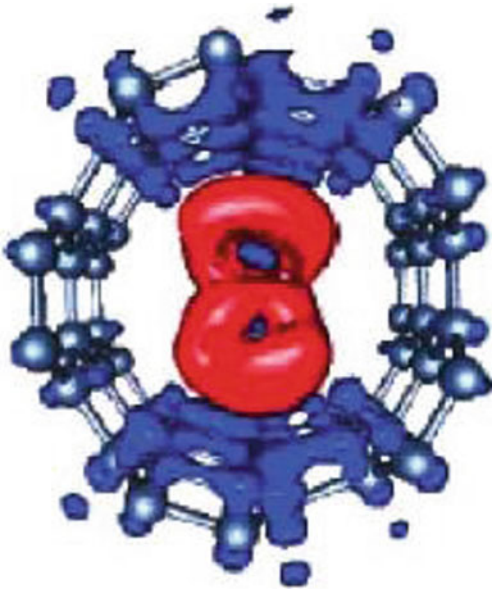

Fig. 14.6 Electronic density of the N8@CNT(5,5) system [39]

[38] demonstrate existing a type of stable structure, as seen in Fig. 14.6, polymeric nitrogen chain N8 confined inside CNTs, by molecular dynamics calculations. Wu et al. [39] report a synthesis of $MWCNT^{+}$ $N8^{-}$ by using cyclic voltammetry at ambient conditions. The temperature programmed desorption data denotes that the prepared N8- is thermal stable to 400 °C, which means its potential applicating to EM fields.

14.5 Mechanical Properties Modifier

The CNTs has been applied to mechanical properties modification of polymer composites and polymer modified asphalt for many years, because its unique characteristics such as high flexibility, extremely high tensile moduli and strengths [40, 41]. Therefore, some methods of polymer composites modification are also appropriate for composite EMs prepared with polymer as binder, including solid propellant and polymer bonded explosives (PBX). Lin et al. [42] investigate the effect of MWCNTs on high-temperature creep properties of 1,3,5-triamino-2,4,6-trinitrobenzene (TATB) based PBX. Results show that, with only 0.25% mass of MWCNTs, the creep lifetime of the PBX is extended by over 33.3% and 750% under 6 MPa and 7 MPa respectively. Wang et al. [43] use MWCNTs and carboxy-functionalized MWCNTs (COOH-MWCNTs) as filler to improve the mechanical properties of glycidyl azide polymer (GAP) and propargyl-terminated polyether (PTMP) for potential solid propellant application. Preparation process can be seen in Fig. 14.7. Results show that the

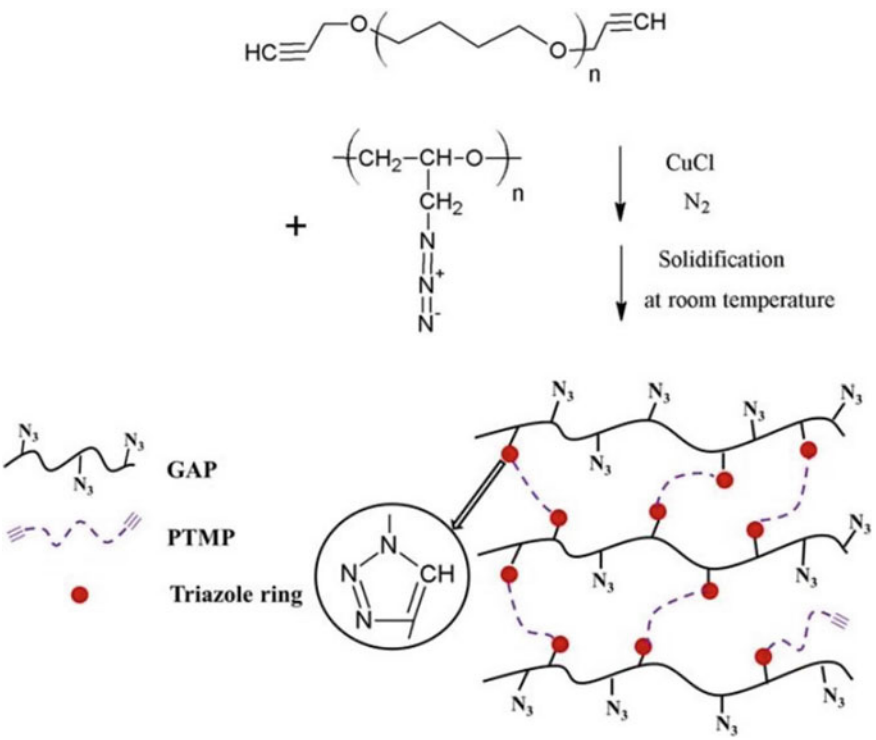

Fig. 14.7 Preparation process of GAP/PTMP composites [43]

mechanical properties of energetic polymer composites are enhanced by incorporation of MWCNTs or COOH-MWCNTs as a reason of the modification on interfacial adhesion and load transfer from polymer phase to nanofillers. Besides, the research reported by Zhang [33] demonstrates that the CNTs can be simultaneously used as both combustion catalysts and mechanical properties modifier in preparation of composite modified double base propellant.

14.6 Desensitization Agent

The excellent performance on electric and thermal conductivity of CNTs can be applied to desensitization of EMs including decreasing the electrostatic sensitivity and improving the thermal shock resistance. Rubtsov et al. [7] report that electrostatic sensitivity of explosives including trinitrotoluene (TNT), pentaerythritol tetranitrate (PETN), benzotrifuroxan (BTF), can be significantly decreased by incorporation of CNTs to improve the electric conductivity. To overcome the drawback of high electrostatic sensitivity of $Cu(N_3)_2$ as micro-initiators, Liu et al. [44] improve the

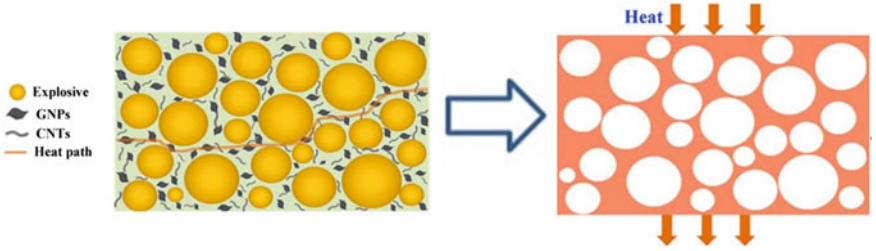

Fig. 14.8 The thermal conductive network schematic of hybrid carbon nanomaterials [45]

electric conductivity of $Cu(N_3)_2$ by supported on CNTs, through firstly depositing of nano-copper in CNTs by electrochemical deposition and then oxidization from Cu to $Cu(N_3)_2$ by gaseous hydrogen azide. He et al. [45] investigate the enhancement of thermal conductivity for highly explosive-filled polymer composites thorough hybrid carbon nanomaterials. The thermal conductive network schematic of hybrid carbon nanomaterials can be shown Fig. 14.8. Results indicate that the thermal conductivity can be effectively improved by pure CNTs or graphene nanoplatelets (GNPs). Besides, a type of hybrid carbon nanomaterial prepared by bridging interactions between CNTs or GNPs has a greater thermal conductivity than pure CNTs or GNPs, which denotes a better improvement on shock resistance of PBX.

14.7 Detector for Waste Explosives

The pollution for waste explosive, such as TNT, RDX, 1,3,5,7-tetranitro-1,3,5,7-tetrazocane (HMX) and so on, has been attracted great attention during past decades, because of their frequent uses in terrorist and war activities. The production, storage and testing of explosives pose threat to public security of the whole world [46, 47]. Based on the crisis on both ground water and soil pollution with nitroaromatic and nitramine explosive compounds around the world, a compact and low-cost detection method for explosives is needed. Compared with gas and high-performance liquid chromatography, Raman spectroscopy, immunoassay techniques, electrochemical detection has many advantages on explosive detection including portability, rapid detection, low cost, potential for real-time field test and so on [48]. Some applications of CNTs or functionalized CNTs has been demonstrate that it can be used in improving selectivity of electrode for electro-chemically detection explosive because of its fast charge transfer capability [10, 49, 50].

The method that films cover prepared by evaporation solution of suspension is the most common path using CNTs to modify electrode surface. Zhang et al. [51] report that the sensitivity and rate of glass carbon electrode (GCE) for detection of nitroaromatic compound, such 1,3,5-trinitrobenze (TNB), 2,4-dinitrotoluene (DNT) and TNT, is improved as the result of modifying electrode surface by evaporating CNTs suspension. Besides, the GCE modified by CNTs can also be applied to the

detection for nitramine explosive, such as RDX [52]. Stefanoet al. [53] decrease surface roughness of CNT modified GCE though acid functionalization CNTs by the blend of H2SO4 and HNO3. Compared with pristine CNTs, the acid functionalization CNTs shows an improvement on detectability for TNT.

To further improve detectability, composite materials containing CNTs are attracted a lot of interest in modifying electrode. Sílvia et al. [54] report a modified method for a boron-doped electrode by using a thin film consist of MWCNTs and reduce graphene oxide (rGO). The synergistic properties of both carbon nanomaterials in the thin film modified surface result in a detection limit of 0.019 μmol L^{-1} within a wide linear range for TNT, which denotes a superior performance in comparison with other electrochemical sensors produced with carbon nanomaterials. Ding et al. [55] prepare composite modified GEC, using rGO and MWCNTs as modifiers, by one-step electro-chemical deposition method. The composite modified GEC shows good electrocatalytic activity enhanced the electrocatalysis for 2,4-dinitroanisole because of the high specific surface area, porous structure, high conductivity. Zeng et al. [56] construct a complex 3D skeleton electrode printed by fabrication of nanocomposites consist of Pd nanoflowers, GO and CNTs, as seen in Fig. 14.9. Results show that the complex electrode possesses high selectivity and detection sensitivity for many nitroaromatic explosives because its unique structure that formed Pd nanoflowers are well dispersed on 3D porous carrier which is prepared by embedded CNTs to GO.

Molecularly imprinted polymer (MIP) is a kind of bionic polymer which includes recognition sites or cavities compatible with molecule in size and functionalities. The sites, holding recognition sites for explosives, are created by a printing process. Qu et al. [57] firstly synthesis MIP using arylamide as functional monomers and ethylene glycol dimethacrylate as cross-linkers and then construct MIP/MWCNTs modified electrode, as seen in Fig. 14.10. Results indicated that the MIP/MWCNT

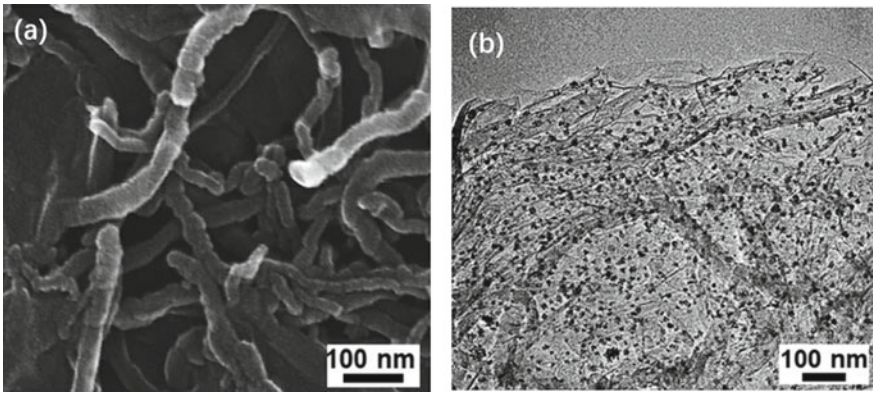

Fig. 14.9 SEM image of 3D skeleton constructed by GO and CNTs (**a**) and TEM image of 3D carbon skeleton fabricated by Pd nanoflowers (**b**)

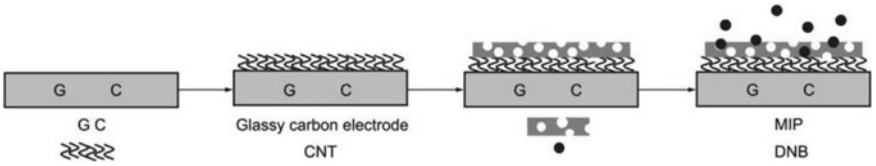

Fig. 14.10 Construction of MIP/MWCNTs modified electrode

modified electrode presented high sensitivity, good stability and improved selectivity for the electrochemical reduction of 1,3-dinitrobenzene. Besides, reports show that the MIP/CNTs modified electrode can also be used to improve selectivity and effectivity for detection of nitrocellulose, RDX and so on [58, 59].

14.8 Conclusions and Future Directions

As summarized in this paper, CNTs are widely applied to many EM fields as its unique properties. The CNTs can be used as combustion catalyst, special carrier, mechanical properties modifier, desensitization agent. Furthermore, the micro-effect of CNTs provides possibility that is used in micro-ignitor and portable detector for explosives.

However, many works only concentrate on effect of CNTs on application performance, related mechanisms and quantitative structure-function relationships are still unclear. Therefore, related mechanism should be studied to construct the quantitative structure-function relationships of CNTs applied to energetic materials in future work for supporting high performance or functional application.

Firstly, advanced quantitative characterization methods for morphology and chemical properties for nano materials should be studied to improve the precision and scientificity for supporting researches on CNTs or its nanocomposites. Furthermore, micro-interface properties are crucial to develop preparation process for composites by addition of CNTs, such as study on surface modification and interface properties CNTs, effect of CNTs on rheological properties of polymer EMs system. Finally, for construction the quantitative structure-function relationships, effect of size, shape and dispersion of CNTs on thermal and electric conductivity in the application of nEMs composites is needed to raise attention. Besides, because of the high difficulty and huge challenge on the preparation of nano-size materials and its composites, researches on advanced preparation process, such as additive manufacturing, AI assisted manufacturing and so on, should also be attracted for supporting high effective manufacture.

References

1. Q.L. Yan, M. Gozin, F.Q. Zhao et al., High energetic compositions based on functionalized carbon nanomaterials. Nanoscale **8**(9), 4799–4851 (2016)
2. M. Anniyappan, M.B. Talawar, R.K. Sinha et al., Review on advanced energetic materials for insensitive munition formulations. Combus. Explos. Shock Waves **56**(5), 495–519 (2020)
3. U.R. Nair, S.N. Asthana, A.S. Rao et al., Advances in High Energy Materials. Def. Sci. J. **60**(2), 137–151 (2010)
4. A.F. Tarchoun, D. Trache, T.M. Klaptke et al., Synthesis and characterization of new insensitive and high-energy dense cellulosic biopolymers. Fuel **292**, 120347 (2021)
5. H. Baughman Ray et al., Carbon nanotubes—the route toward applications. Science **297**, 787–792 (2002)
6. E.T. Thostenson, Z. Ren, T.W. Chou, Advances in the science and technology of carbon nanotubes and their composites: a review. Compos. Sci. Technol. **61**(13), 1899–1912 (2001)
7. I.A. Rubtsov, I.A. Rubtsov, E.R. Pruuel, et al., Electric conductivity of high explosives with carbon nanotubes. J. Phys.: Conf. Ser. **899**, 092012 (2017)
8. N. Lei, K. Kuroda, L.P. Zhou et al., Kinetic study of carbon nanotube synthesis over Mo/Co/MgO catalysts. Carbon **44**(11), 2265–2272 (2006)
9. D. Lei, Q. Menggen, H.L. Zhang et al., Field emission properties from a carbon nanotube array with parallel grid. Acta Phys. Sin. **62**(24), 357–363 (2013)
10. X. Lu, Y. Quan, Z. Xue et al., Determination of explosives based on novel type of sensor using porphyrin functionalized carbon nanotubes. Colloids Surf., B **88**(1), 396–401 (2011)
11. M. De Voider et al., Carbon nanotubes: present and future commercial applications. Science **339**, 535–539 (2013)
12. G. Rui, H. Yan, R. Shen et al., Electro-explosion performance of KNO3-filled carbon nanotubes initiator. J. Appl. Phys. **115**(17pt.1), 174901 (2014)
13. H.Y. Jeong, P.S. Kang, J.J. Bae et al., Tailoring oxidation of Al particles morphologically controlled by carbon nanotubes. Energy **55**(June 15), 1143–1151 (2013)
14. K. Kappagantula, M.L. Pantoya, E.M. Hunt, Impact ignition of aluminum-teflon based energetic materials impregnated with nano-structured carbon additives. J. Appl. Phys. **112**(2), 1–13 (2012)
15. J. Kim Kyung, et al., Nanoenergetic material-on-multiwalled carbon nanotubes paper chip as compact and flexible igniter. Carbon: Int. J. Sponsored Am. Carbon Soc. **114**, 217–223 (2017)
16. H.S. Kim, J.K. Cha, H.K. Ji et al., Highly flexible and patternable multiwalled-carbon nanotube/nitrocellulose hybrid conducting paper electrodes as heating platforms for effective ignition of nanoenergetic materials. ACS Appl. Mater. Interfaces **12**(25), 28586–28595 (2020)
17. C.D. Malec, N.H. Voelcker, J.G. Shapter et al., Carbon nanotubes initiate the explosion of porous silicon. Mater. Lett. **64**(22), 2517–2519 (2010)
18. J. Smits, B. Wincheski, N. Min et al., Response of Fe powder, purified and as-produced HiPco single-walled carbon nanotubes to flash exposure. Mater. Sci. Eng., A **358**(1–2), 384–389 (2003)
19. X. Xu, S.B. Xiang, W. Zheng et al., Photo-responsive behaviors and structural evolution of carbon-nanotube-supported energetic materials under a photoflash. Mater. Lett. **88**, 27–29 (2012)
20. M.R. Manaa, A.R. Mitchell, R.G. Garza et al., Flash ignition and initiation of explosives-nanotubes mixture. J. Am. Chem. Soc. **127**(40), 13786 (2005)
21. H. Ostmark, N. Roman, Laser ignition of pyrotechnic mixtures: ignition mechanisms. J. Appl. Phys. **73**(4), 1993–2003 (1993)
22. H.K. Ji, M.H. Cho, K.J. Kim et al., Laser ignition and controlled explosion of nanoenergetic materials: the role of multi-walled carbon nanotubes. Carbon **118**, 268–277 (2017)
23. J. Yu, J. Wang, Y. Liu et al., Preparation and properties of CL-20/split multi-walled carbon nanotubes composite energetic materials. Chin. J. Explos. Propellants **40**(3), 72–76 (2017). (in Chinses)

24. H. Tan, *The Chemistry and Technology of Solid Rocket Propellant* (Beijing Institute of Technology Press, 2015)
25. D.J. Hewkin, J.A. Hicks, J. Powling, H. Watts, Combustion of nitric ester-based propellants -ballistic modification by lead compounds. Combust. Sci. Technol. **2**, 307–327 (1971)
26. R.F. Preckel, Plateau ballistics in nitrocellulose propellants. AIAA J. **3**, 346–347 (1965)
27. A.P. Denisyuk, A.D. Margolin, N.P. Tokarev, Role of carbon black in combustion of ballistic powders with lead-containing catalysts. Combust. Explos. Shock Waves **13**, 490–496 (1977)
28. S.W. Li, F.Q. Zhao, C. Yuan, Tendency of research and development for overseas solid propellants. J. Solid Rocket Technol. **25**, 36–42 (2002). (In Chinses)
29. P. Liu, J.R. Kong, X.D. Xu et al., Preparation and catalytic activity of Fe_2O_3/CNT to thermal decomposition of ammonium perchilorate. Adv. Mater. Res. **396–398**, 837–840 (2012)
30. M. Abdelhafiz, M. Yehia, H.E. Mostafa et al., Catalytic action of carbon nanotubes on ammonium perchlorate thermal behavior. React. Kinet. Mech. Catal. **131**(1), 353–366 (2020)
31. R. Hui, Y.Y. Liu, Q.J. Jiao et al., Preparation of nanocomposite PbO·CuO/CNTs via microemulsion process and its catalysis on thermal decomposition of RDX. J. Phys. Chem. Solids **71**(2), 149–152 (2010)
32. A.P. Denisyuk, Y.M. Milekhin, L.A. Demidova et al., Effect of carbon nanotubes on the catalysis of propellant combustion. Dokl. Chem. **483**(2), 301–303 (2018)
33. Z.Z. Zhang, C.Q. Deng, J.Z. Li et al., Effects of carbon nanotubes (CNTs) on the combustion and mechanical properties of AP/CMDB propellant. Chin. J. Energ. Mater. **26**(9), 744–748 (2018). (in Chinses)
34. A.P. Denisyuk, Z.N. Aung, Y.G. Shepelev, Energetic materials combustion catalysis: necessary conditions for implementation. Propellants, Explos., Pyrotech. **46**, 90–98 (2020)
35. C.F. Liu et al., Hydrogen storage in single-walled carbon nanotubes at room temperature. Science **286**, 1127–1129 (1999)
36. J.F. Kong et al., Nanotube molecular wires as chemical sensors. Science **287**, 622–625 (2000)
37. Z. Yu, M. Jaidann, Z. Yong et al., Synthesis of high nitrogen doping of carbon nanotubes and modeling the stabilization of filled DAATO@CNTs (10,10) for nanoenergetic materials. J. Phys. Chem. Solids **71**(2), 134–139 (2010)
38. H. Abou-Rachid, A. Hu, V. Timoshevskii et al., Nanoscale high energetic materials: a polymeric nitrogen chainn8confined inside a carbon nanotube. Phys. Rev. Lett. **100**(19), 196401 (2008)
39. Z. Wu, E.M. Benc Ha Fia, Z. Iqbal, et al., N8 Polynitrogen stabilized on multi-wall carbon nanotubes for oxygen-reduction reactions at ambient conditions. Angew. Chem. **126**(46) (2014)
40. F. Muhammad, A. Naveed, M. Jamal, et al., Carbon nanotubes and their use for asphalt binder modification: a review. Emerg. Mater. Res. **9**(2), 234–247 (2020)
41. Z. Spitalsky, D. Tasis, K. Papagelis et al., Carbon nanotube–polymer composites: chemistry, processing, mechanical and electrical properties. Prog. Polym. Sci. **35**(3), 357–401 (2010)
42. C. Lin, J. Liu, F. Gong et al., High-temperature creep properties of TATB-based polymer bonded explosives filled with multi-walled carbon nanotubes. RSC Adv. **5**, 21376–21383 (2015)
43. W. Song, X.G. Changhua et al., Effects of crosslinking degree and carbon nanotubes as filler on composites based on glycidyl azide polymer and propargyl-terminated polyether for potential solid propellant application. J. Appl. Polym. Sci. **134**(39), 45359 (2017)
44. X. Liu, Y. Hu, H. Wei et al., Energetic films realized by encapsulating copper azide in silicon-based carbon nanotube arrays with higher electrostatic safety. Micromachines **11**(6), 575 (2020)
45. G. He, X. Zhou, J. Liu et al., Synergetic enhancement of thermal conductivity for highly explosive-filled polymer composites through hybrid carbon nanomaterials. Polym. Compos. **39**(suppl 3), E1452–E1462 (2017)
46. A.M. Rouhi, Chem. Eng. News **75**, 14 (1997)
47. J. Yinon, Field detection and monitoring of explosives. Trends Anal. Chem.: TRAC **21**(4), 292–301 (2002)
48. S.M. Tan, C.K. Chua, M. Pumera, Graphenes prepared from multi-walled carbon nanotubes and stacked graphene nanofibers for detection of 2,4,6-trinitrotoluene (TNT) in seawater. Analyst **138**(6), 1700–1704 (2013)

49. N. Musayeva, T. Orujov, R. Hasanov et al., Growth and functionalization of carbon nanotubes for nitroaromatic explosive detection. Mater. Today: Proc. **20**(part1), 46–49 (2020)
50. C.X. Guo, Z.S. Lu, Y. Lei et al., Ionic liquid–graphene composite for ultratrace explosive trinitrotoluene detection. Electrochem. Commun. **12**(9), 1237–1240 (2010)
51. H.X. Zhang, J.H. Zhang, Voltammetric detection of nitroaromatic compounds using carbon-nanomaterials-based electrodes. Can. J. Chem. **89**(1), 8–12 (2010)
52. B. Rezaei, S. Damiri, Using of multi-walled carbon nanotubes electrode for adsorptive stripping voltammetric determination of ultratrace levels of RDX explosive in the environmental samples. J. Hazardous Mater. **183**(1–3), 138–144 (2010)
53. J.S. Stefano, A.P. Lima, C.C. Nascentes, et al., Electrochemical detection of 2,4,6-trinitrotoluene on carbon nanotube modified electrode: effect of acid functionalization. J. Solid State Electrochem. **24**(6119) (2020)
54. F.V. Sílvia, M.N. Silva, T.F. Tormin et al., Highly-sensitive voltammetric detection of trinitrotoluene on reduced graphene oxide/carbon nanotube nanocomposite sensor. Anal. Chim. Acta **1035**, 14–21 (2018)
55. Y. Ding, S. Feng, M.A. Khan et al., Highly sensitivity electrochemical sensor based on ErGO/MWCNTs nanohybrid for 2,4-dinitroanisole electroanalysis. Microchem. J. **151**, 104226 (2019)
56. W. Zeng, D. Manoj, H. Sun et al., One-pot synthesis of high-density Pd nanoflowers decorated 3D carbon nanotube-graphene network modified on printed electrode as portable electrochemical sensing platform for sensitive detection of nitroaromatic explosives. J. Electroanal. Chem. **833**(15), 527–535 (2019)
57. Y. Qu, Y. Liu, T. Zhou et al., Electrochemical sensor prepared from molecularly imprinted polymer for recognition of 1,3-dinitrobenzene (DNB). Chin. J. Chem. **27**(10), 2043–2048 (2009)
58. X. Meng, Z. Xiao, S.K. Scott, Preparation and application of electrochemical sensor based on molecularly imprinted polymer coated multi-walled carbon nanotubes for nitrocellulose detection. Propellants, Explos., Pyrotech. **44**(10), 1337–1346 (2019)
59. A. Taher et al., Molecularly imprinted polymer nano-sphere/multi-walled carbon nanotube coated glassy carbon electrode as an ultra-sensitive voltammetric sensor for picomolar level determination of RDX. Talanta **194**, 415–421 (2019)

Chapter 15
Research Progress of Nano-combustion Catalyst Based on Graphene Loading Technology and Its Application

Dayong Li, Yuling Shao, Zhenyu Qi, Minghao Zhang, Min Xia, and Xiaozhi Zhang

Abstract Graphene has regular two-dimensional surface structure, large theoretical specific surface area (about 2630 $m^2 \cdot g^{-1}$), good electronic conductivity, excellent thermal conductivity and structural stability. It is not only a special catalyst, but also an excellent catalyst carrier. Therefore, graphene has attracted much attention in the field of catalyst since its discovery. In this paper, the application and research of graphene in the field of nano combustion catalyst and propulsion technology are briefly reviewed, so as to further explore the nano combustion catalyst based on graphene.

15.1 Introduction

In order to meet the development needs of modern "contactless" war mode, "long-range strike" whose key technologies are high-performance rocket engines and propellants in rocket and missile propulsion systems has become the main means of current war. Because the combustion performance and fuel speed of solid propellant directly affect the ballistic performance, flight speed and operating stability of rocket engines, it is very important to regulate the combustion performance of propellant. At present, the use of combustion speed catalyst has become one of the most effective methods to regulate the combustion performance of propellant. It is characterized by the fact that only a small amount of catalyst can be added to effectively

D. Li · Y. Shao · X. Zhang
China North Chemical Research Academy Group Co., Ltd., Beijing, China
e-mail: shaoyuling19870903@163.com

X. Zhang
e-mail: zhangxiaozhi475@sina.com

Z. Qi (✉) · M. Zhang · M. Xia
Beijing Institute of Technology, Beijing 100081, China
e-mail: 756895732@qq.com

M. Xia
e-mail: xminbit@bit.edu.cn

A. Gany and X. Fu (eds.), *2021 International Conference on Development and Application of Carbon Nanomaterials in Energetic Materials*, Springer Proceedings in Physics 276,
https://doi.org/10.1007/978-981-19-1774-5_15

change the fuel speed and pressure index of the propellant. After a long period of research, many kinds of fuel speed catalysts have been developed such as metal oxide catalysts, inorganic salt catalysts, organic salt catalysts, organic complex catalysts, ferrocene-based catalysts, energetic catalysts, and so on. It contains unit catalysts and multiple composite catalysts [1].

The existing solid propellant combustion catalysts are mainly metals, metal oxides, metal composite oxides, metal organic compounds, energetic compounds, nano-catalysts and new carbon materials [2]. However, with the continuous development of missile technology, the currently used combustion catalysts can no longer meet the requirements for the development of new high-performance solid propellant formulations. Therefore, it is urgent to develop a new generation of high-performance burning rate catalysts.

Graphene has a regular two-dimensional surface structure, a huge theoretical specific surface area (approximately 2630 $m^2\ g^{-1}$) and good electronic conductivity, as well as excellent thermal conductivity and structural stability. It is not only a special catalyst, but also an excellent catalyst carrier [3, 4]. The metal and its compounds can be loaded on the surface of graphene to form a supported nanocomposite catalyst. In this way, the metal and its compounds are highly dispersed on the surface of graphene in the form of nanoparticles. At this time, the catalytic performance of metals and their compounds can be significantly improved and can be "complementary" with the catalytic performance of graphene, resulting in a strong "synergistic effect". Those catalytic effects will be better than pure nano-metal oxide catalysts. Graphene-based composite catalyst is a new type of high-efficiency burning rate catalyst with broad application prospects.

15.2 Overview of Graphene

In 2004, graphene came out and became the newest carbon material in the world. Scientists from the Department of Physics and Astronomy of the University of Manchester, Professor Andre Geim and Researcher Konstantin Novoselov, used tape adhesion and peeling method to prepare graphene for the first time [5]. Graphene is another major discovery after carbon nanotubes and fullerene spheres. Professor Andre Geim and Researcher Konstantin Novoselov won the 2010 Nobel Prize in Physics for this (Fig. 15.1).

Graphene is a two-dimensional hexagonal honeycomb structure composed of a single layer of carbon atoms. Pure graphene is a crystal only one atom thick. It can be wrapped to form a zero-dimensional fullerene, rolled to form a one-dimensional carbon nanotube, and layered to form a three-dimensional graphite. So graphene is the basic unit of other graphite materials. Graphene materials also have some excellent properties of materials such as graphite and carbon nanotubes. It not only has the characteristics of ultra-thin, ultra-sturdy and ultra-strong electrical conductivity, but also has excellent electrical, thermal and mechanical properties. It is expected to be widely

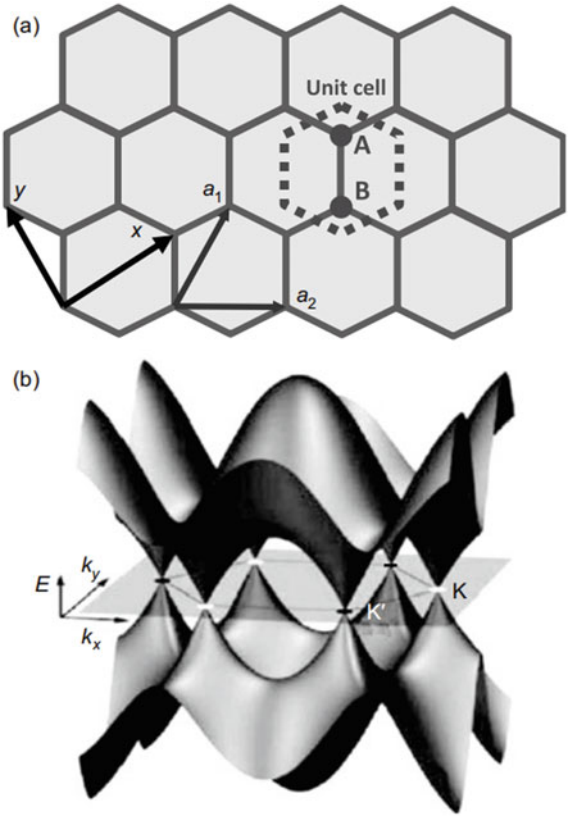

Fig. 15.1 The lattice structure (**a**) and band structure (**b**) of graphene. [6] Reprinted of **b** with permission from Ref. [7]. Copyright (2010) American Chemical Society

used in the fields of high-performance nano-electronic devices, composite materials, field emission materials, catalysis, gas sensors and energy storage. Therefore, graphene has very broad application prospects and has received extensive attention from scientists all over the world (Fig. 15.2).

There are not many preparation methods for graphene. So far, we still lack a fundamental breakthrough about the preparation of graphene. At present, in order to systematically study the physical and chemical properties and possible applications of this new type of material, people are studying the preparation methods of single-layer graphene, especially the ways to prepare a large number of graphene with stable structures. The existing preparation methods of graphene sheets are mainly as follows: mechanical exfoliation method, epitaxial growth method, chemical vapor deposition method, graphite oxide reduction method and so on [9]. At present, the effective means to characterize graphene mainly include: atomic force microscope, optical microscope, scanning tunneling microscope (STM), Raman spectroscopy, etc. [10]. Since the thickness of single-layer graphene is only 0.335 nm, it can only be clearly observed in atomic force microscopy (AFM) and scanning tunneling

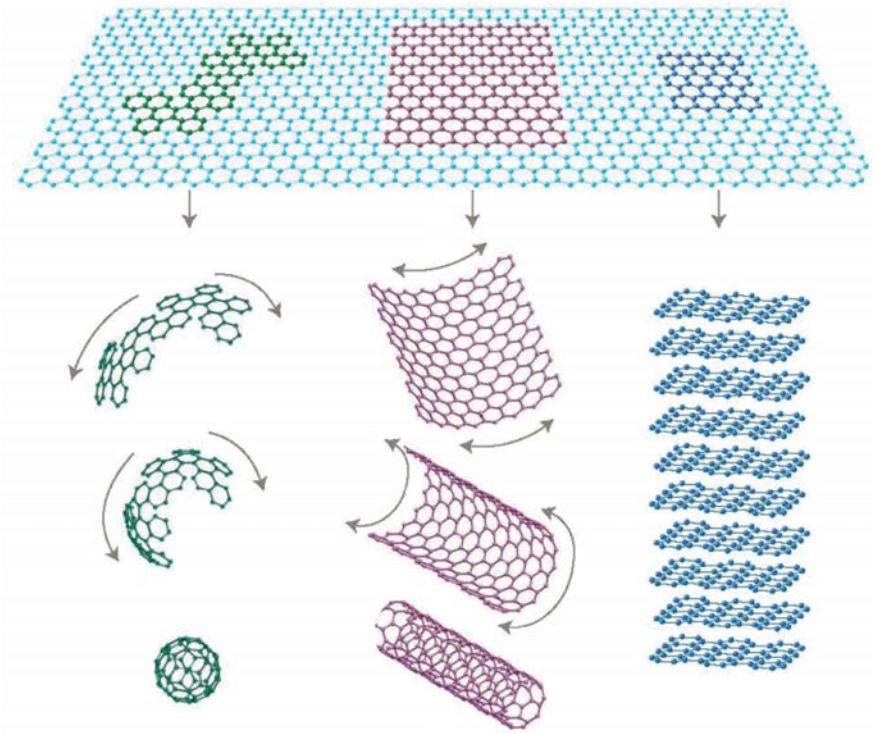

Fig. 15.2 Mother of all graphitic forms. Graphene is a 2D building material for carbon materials of all other dimensionalities. It can be wrapped up into 0D buckyballs, rolle into 1D nanotubes or stacked into 3D graphite [8]

microscopy (STM), which are the most direct and effective means to characterize graphene materials (Fig. 15.3).

15.3 Research Progress of Graphene in Nano Combustion Catalysts

15.3.1 Application of Carbon Materials in Nano Combustion Catalysts

Carbon materials are widely used in the combustion catalysts of double-base propellants, because carbon materials play a very important role in the combustion catalysis process of double-base propellants. People mixed carbon black with lead compounds and copper compounds to develop "lead-carbon" binary composite combustion catalysts and "lead-copper-carbon" ternary composite combustion catalysts, etc. The

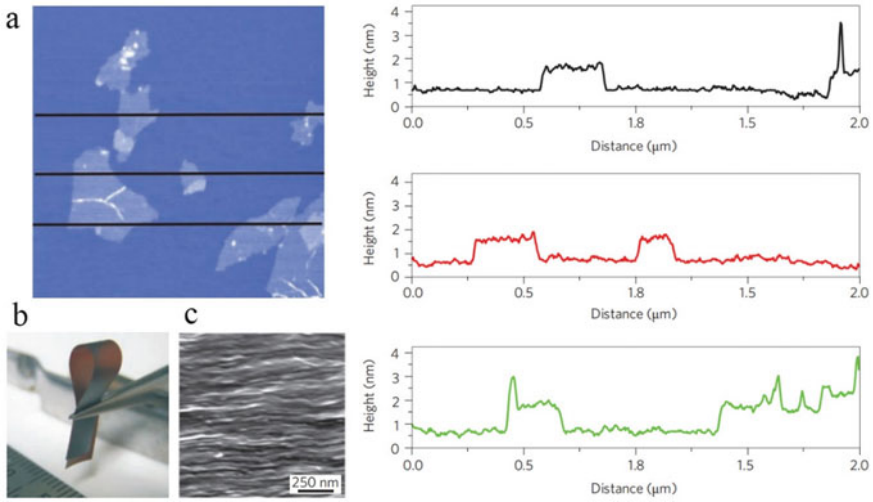

Fig. 15.3 Graphite oxide and graphene oxide. **a** An AFM (Scanning Tunneling Microscope) image of exfoliated graphene oxide sheets; the sheets are ~1 nm thick. The horizontal lines indicate the sections corresponding (in order from top to bottom) to the traces shown on the right. **b** Photograph of folded graphene oxide paper. **c** A scanning electron microscope image of the cross-section of the graphene oxide paper, showing layered structure [11]

catalytic performance of the various components of the composite catalyst can be "complementary" to produce a "synergistic effect", and its catalytic effect is significantly improved. The three-way composite catalyst composed of lead compound, copper compound and carbon black has become the most widely used catalyst in the current double-base propellant. At the same time, the "lead-carbon" catalysis theory and the "lead-copper-carbon" catalysis theory [12] of double-base propellants have also been developed (Fig. 15.4).

Carbon materials have always received extensive attention in heterogeneous catalysis. Graphite, carbon black, activated carbon, carbon nanotubes, carbon nanofibers, etc. are widely used as catalyst carriers. At the same time, it has been found that the structure of the carbon carrier has a strong influence on the performance of the supported catalyst. In the field of combustion catalysts, scientific and technological workers [13, 14] also use graphite, carbon black, activated carbon, etc. as catalyst carriers, and support catalytically active metals or metal oxides to prepare carbon-based composite combustion catalysts. The research results show that the catalytic performance of the carbon-based supported composite combustion catalyst has been significantly improved, and its catalytic performance is better than that of the composite catalyst formed by mixing metal oxides and carbon black. With the emergence and development of nanotechnology, countries all over the world attach great importance to nano-combustion catalysts, especially the advent of new nano-carbon materials-carbon nanotubes (CNTs), which has attracted more attention. There have

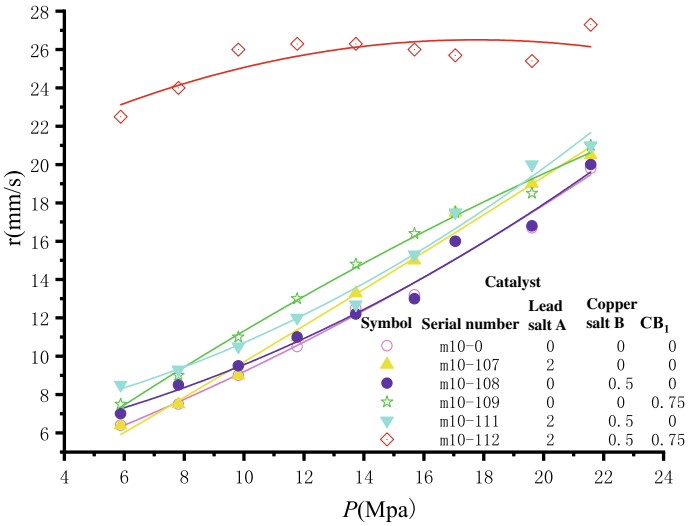

Fig. 15.4 Effect of single, double and three component catalysts on pressure exponent (n) of RDX-CMDB propellant [12]

been many new results about using carbon nanotubes as the catalyst carrier to prepare metal or metal oxide-loaded nanocomposite combustion catalysts (Fig. 15.5).

CNTs was added to Hexanitrohexaazaisowurtzitane (CL-20) by Yu et al. [16]. With the increase of CNTs addition, the initial decomposition temperature, decomposition peak temperature and heat release of CL-20 gradually decreased. The effects of CNTs, Fe_2O_3/CNTs and Fe·Cu/CNTs on the combustion performance and thermal decomposition of ammonium dinitramide (ADN) was studied by Li et al. [17] and found that these three catalysts can increase the combustion rate of ADN and reduce the pressure index, and the catalytic effect of CNTs is the most

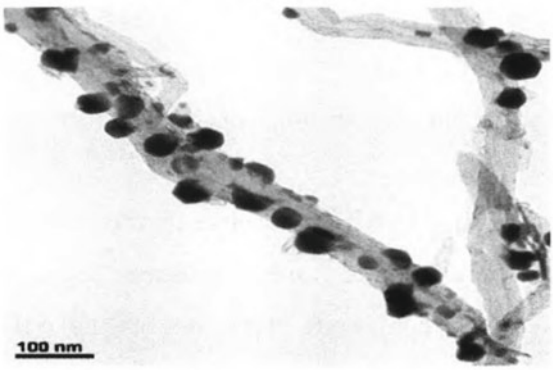

Fig. 15.5 TEM images of Bi2O3/CNTs composite [15]

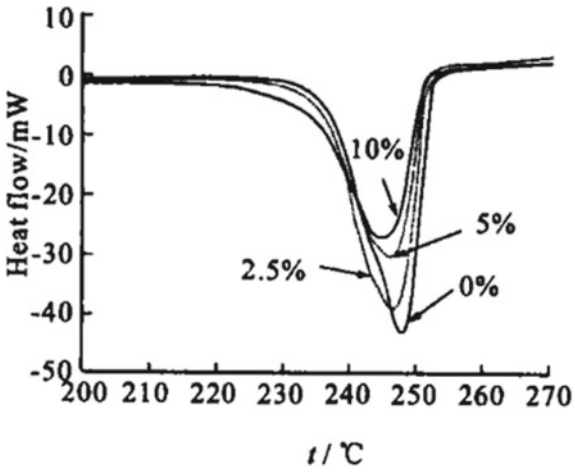

Fig. 15.6 The effect of carbon nanotubes content on DSC curve of CL-20 [16]

obvious. PbO/CuO/CNTs was synthesized by Ren et al. [18] through the microemulsion method. The new nano-catalyst can significantly accelerate the decomposition of RDX and reduce the decomposition temperature by 14.1 °C. Bi_2O_3/CNTs was prepared by Hong et al. [15] through liquid-phase chemical deposition. The composite has good combustion catalytic performance. By using this burning rate catalyst, the propellant burning rate can be increased by 74.7% at 4 MPa, and the propellant pressure index can be reduced from 0.7834 to 0.4307 at 16–22 MPa (Fig. 15.6).

Our research group [19, 20] has conducted related research and found that composite combustion catalysts prepared by using carbon nanotubes as carriers and supporting metals such as lead, copper, bismuth or metal oxides, whose catalysis is far superior to composite catalysts formed by mixing nano-metal oxides and carbon black, have a high catalytic effect on the combustion of double-base propellants.

15.3.2 Nano Combustion Catalyst Supported by Graphene and Its Application

On one hand, graphene has regular two-dimensional surface structure, and larger theoretical specific surface area (about 2630 $m^2 \cdot g^{-1}$) and better electron and hole transfer ability compared with carbon nanotubes. On the other hand, it also has some excellent properties of materials such as graphite and carbon nanotubes [8]. So it will be better than carbon nanotubes as a catalyst carrier or cocatalyst. In graphene-supported catalysts, metals or metal oxides are highly dispersed on the surface of graphene in the form of nanoparticles. Graphene is used as a template for supporting the catalyst, which can prevent the mutual agglomeration of metal or metal oxide nanoparticles on the surface of the graphene. Such properties are

conducive to giving full play to the catalytic activity of the nano-catalyst. Moreover, the good electronic conductivity of graphene can promote the electronic mobility of the supported catalyst and improve the redox reaction ability to the catalyzed substrate. Therefore, graphene will play a very good catalytic role in the propellant combustion catalysis process (Fig. 15.7).

At present, the excellent performance of catalysts supported by graphene has been confirmed in the literature: The composite photocatalytic materials of titanium dioxide (TiO_2) and graphene were prepared by Zhang et al. [21] through sol-gel method and using titanate four butyl ester and graphene as starting materials. It was found that the photocatalytic water splitting rate of TiO_2/graphene composite photocatalyst was much higher than that of commercial P25 under the same conditions, and the activity of photocatalytic water splitting increased nearly two times. Graphene oxide (go) was synthesized by Wen et al. [22] by Hummers method in liquid phase, and then graphene supported palladium (PD) catalyst was prepared by one-step chemical reduction. Compared with traditional Pd/Vulcan XC-72, the catalytic activity of Pd/graphene catalyst for ethanol electro oxidation in alkaline medium has been greatly improved. The degradation efficiency of TiO_2 / graphene oxide composite catalyst prepared by Zhang et al. [23] is obviously better than that of nano-TiO_2. The electrocatalytic performance and stability of Pt/graphene catalyst prepared by Gao et al. [13] are better than those of Pt/ultrafine graphite powder. A series of vanadium oxide/graphene (VOx/G) composite catalysts were synthesized by Dong et al. [24] by hydrazine hydrate reduction method. The structures of the catalysts were characterized by XRD, Raman and SEM. The performance of VOx/G catalysts for hydroxylation of benzene to phenol was investigated. The results showed that the vanadium active species were highly dispersed on the surface of layers of graphene support in the VOx/G catalyst prepared under suitable conditions, and the catalyst showed good catalytic activity (Fig. 15.8).

In the application of combustion catalysts, graphene is not only a special combustion catalyst, but also an excellent catalyst carrier. For example, graphene plays a dual role of catalyst and carrier in the composite combustion catalyst system of metal or metal compound and graphene. In view of the high catalytic effect of the carbon nanotube-supported metal or metal oxide composite combustion catalyst, it can be expected that the catalytic performance of the graphene-supported metal or metal oxide composite combustion catalyst will be more excellent. At present, graphene

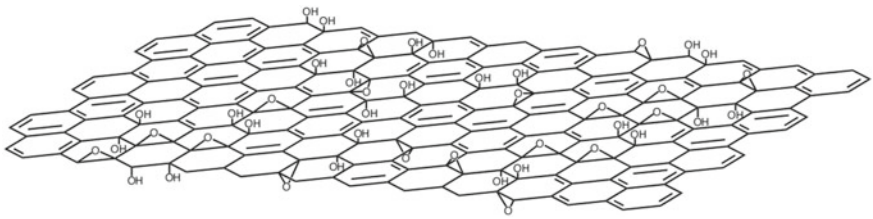

Fig. 15.7 Chemical structure of graphite oxide. For clarity, minorfunctional groups, carboxylic groups and carbonyl groups have been omitted at the edges [11]

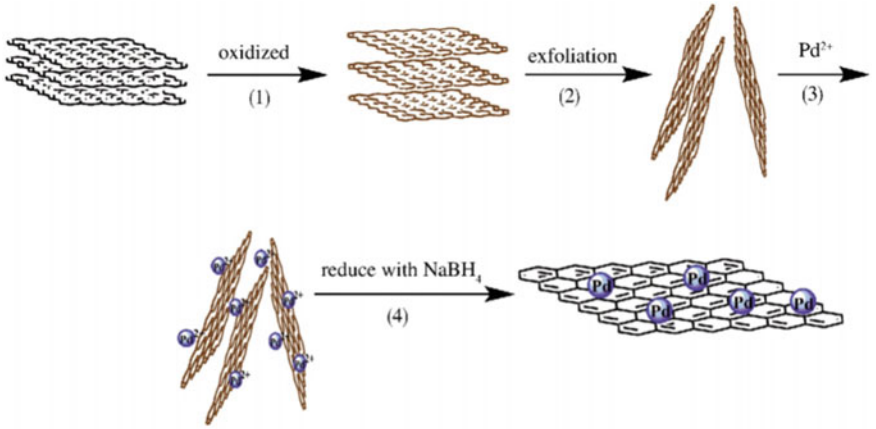

Fig. 15.8 Chemical synthesis route of Pd/graphene catalysts [22]

has been applied to solid propellants as combustion catalysts by relevant researchers: The combustion catalytic performance of Cu_2O-PbO/graphene oxide in the double-base propellant (GO1201) was studied by Li et al. [25]. The results show that GO1201 propellant has a significant overburning rate phenomenon in the low pressure range, and the "Mesa effect" appears in the high pressure range. It is an efficient double-base combustion catalyst. Bi_2O_3/graphene oxide (Bi_2O_3/GO) composite catalyst was prepared by Tan et al. [26]. They used scanning electron microscopy (SEM), transmission electron microscopy (TEM) and X-ray powder diffraction (XRD) to characterize the particle morphology, particle size and phase structure of the product, and The effect of Bi_2O_3/GO composite catalyst on the combustion performance of double-base propellant was also studied. The results showed that Bi_2O_3 in the product was uniformly supported on the surface of graphene oxide in the form of spherical particles, with an average particle size of about 40 $_{nm}$. Bi_2O_3/GO composite catalyst can significantly improve the combustion performance of the propellant, increase the burning rate of the propellant by 139% (4 MPa), and reduce the pressure index (14–20 MPa) from 0.650 to 0.253, which is a 61.0% decrease. Three graphene oxide composites including CuO/GO, Bi_2O_3/GO, and PbO/GO, whose raw materials are graphene oxide, copper nitrate, $Bi_2O_3 \cdot 5H_2O$, and lead nitrate, were prepared by An et al. [27, 28] from 204 Institute by liquid-phase chemical deposition. They studied these three graphene oxide composites excellent catalytic effect on the combustion of double-base propellant and RDX-CMDB propellant, which can all greatly increase the burning rate of the propellant and significantly reduce the pressure index. Among them, PbO/GO has the best catalytic performance. In addition, they further prepared Cu_2O-PbO/GO, Cu_2O-Bi_2O_3/GO composite catalysts, and found that this type of catalyst can make RDX-CMDB propellant exhibit significant overspeed combustion. At a pressure of 2 MPa, the burning rate of the catalyst-containing propellant increased from 3.09 to 10.20 $mm \cdot s^{-1}$, an increase of 233% (Fig. 15.9).

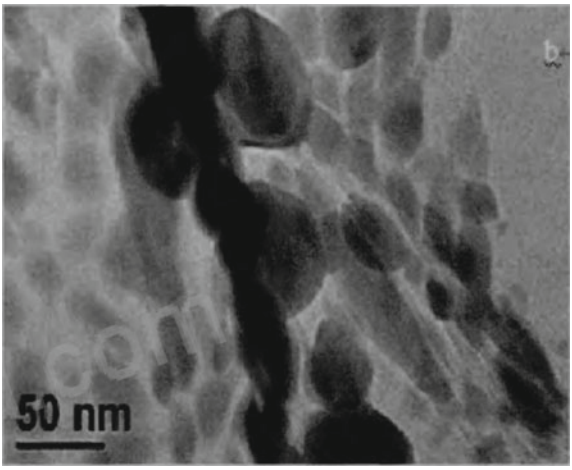

Fig. 15.9 TEM diagram of Bi_2O_3/GO composites [26]

The research on graphene-supported metal or metal oxide composite combustion catalysts is still in the initial stage. However, according to a small amount of current literature reports, the composite catalyst formed by the combination of graphene and metal or metal compound has excellent catalytic performance. It is better than a single type catalyst such as nano metal powder or metal oxide powder, and it is also better than a carbon material type combustion catalyst composed of metal or metal compound and graphite, carbon black, activated carbon, etc., which is widely used in propellants. Therefore, graphene presents a broad application prospect in solid propellant combustion catalysts (Fig. 15.10).

15.4 Outlook

Preliminary studies on graphene oxide supported composite catalysts, fullerene carboxylate lead copper salt catalysts, and metal-embedded carbon nanofiber composite catalysts have shown their excellent catalysis and good application prospects [29–31]. These carbon nanocomposite combustion catalysts are expected to have higher catalytic effects. The advantages of this type of catalyst are as follows:

1. **Reducing pollution**. Graphene oxide is composed of carbon elements which will not produce toxic and harmful gases after burning. Therefore, graphene oxide can be used not only as an environmentally friendly catalyst or catalytic promoter, but also as an environmentally friendly catalyst carrier for preparing a pollution-free, safe, and low-smoke composite burning rate catalyst.
2. **Replacing carbon black**. In order to improve the catalytic performance, it is necessary to add carbon black as a promoter when using lead compound and copper compound catalysts in the double-base propellant. Among the graphene oxide supported composite catalysts, graphene oxide can replace carbon black

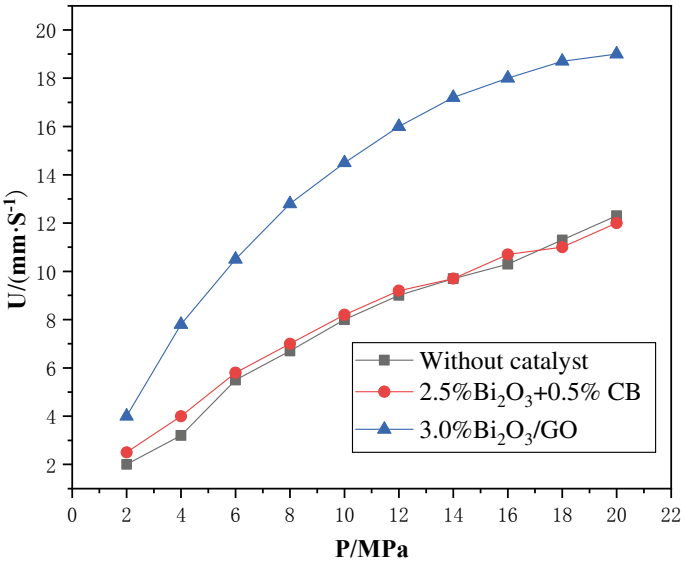

Fig. 15.10 Burning rate curve of double base propellant [26]

as a promoter. Since graphene oxide can be composited with metals or metal oxides on the nanometer scale, which has huge contact area, it can produce a stronger "synergistic effect" to strength its catalytic effect.

3. **Dispersing nanoparticles**. Graphene oxide is an ideal carrier due to its huge specific surface area. The nanoparticles formed from the introduction of the metal compound catalyst are highly dispersed on the surface of graphene oxide or in the cavity. Due to the limitation of the carrier, the nano metal particles on the surface of the graphene oxide will not agglomerate even during the combustion of the propellant. In this way, the advantages of the huge specific surface area of the nano catalyst can be exerted and a higher catalytic effect can be produced.
4. **It can be prepared as a multi-composite catalyst**. A variety of metal compounds can be used to composite the surface of graphene oxide. Because multiple catalysts have "synergies", which will be even more pronounced at the nanoscale, the catalytic effect of multi-composite catalyst is obviously better than that of unit catalyst. According to this principle, some metal compounds with good catalytic properties and low toxicity, such as radon, iron, copper, rare earth compounds and energy-containing compounds, can be used to load the surface of graphene oxide to form carbon nanocomposite combustion catalysts. During preparation, catalytic properties can be regulated by combining different metal compounds and changing the proportions of each component. Based on this, an efficient combustion catalyst can be developed.
5. **Reducing the dosage of metal compounds**. The use of graphene oxide composite catalysts can reduce the use of metal compounds, thereby reducing

environmental pollution and reducing smoke from the presence of metal oxide particles.

The further research and application of carbon nanocomposite combustion catalysts will open a new door in the field of combustion catalysts, and the closely related propulsion technology will also usher in further innovations.

References

1. Y. Wang, F. Zhao, J. Yi, New progress of study on combustion catalysts used for solid rocket propellants. Chin. J. Explos. Propellants **35**(5), 1–8 (2012)
2. Y.-L. Wang, Z.-X. Wei, L. Kang, Progress on combustion catalysts of soiid propeant. Chin. J. Energ. Mater. **23**(01), 89–98 (2015)
3. M. Liu, X. Li, Q. Yan et al., Research progress on application of new type of combustion catalysts in solid propellants. Chem. Propellants Polym. Mater. **9**(2), 29–33 (2011)
4. C. Deng, Y. Dang, Y. Zhang et al., Research situation of ammonlum perchlorate composites. Chem. Propellants Polym. Mater. **11**(3), 5–8 (2013)
5. K.S. Novoselov, A.K. Geim, S.V. Morozov et al., Science **306**, 666 (2004)
6. Z.-X. Wang, Z.-Y. Zhang, L.M. Peng, Graphene-based ambipolar electronics for radio frequency applications. Chin. Sci. Bull. **57**(23), 2956–2970 (2012)
7. P. Avouris, Graphene: Electronic and photonic properties and devices. Nano Lett **10**, 4285–4294 (2010)
8. A.K. Geim, K.S. Novoselov, The rise of graphene. Nat. Mater. **6**(3), 183–191 (2007)
9. Y.-J. Hu, J. Jin, H. Zhang et al., Graphene: synthesis, functionalization and applications in chemistry. Acta Phys. Chim. Sin. **26**(8), 2073–2086 (2010)
10. X. Li, W. Zhao, G. Chen, Research progress in preparation and characterization of graphenes. Mater. Rep. **22**(8), 48–52 (2008)
11. S. Park, R.S. Ruoff, Chemical methods for the production of graphenes. Nat. Nanotechnol. **4**(4), 217–224 (2009)
12. X.-X. Meng, X.-E. Zhang, S.-W. Li, Adjustment of combustion performance of RDX-CMDB propellant. J. Propul. Technol. **3**, 64–69 (1989)
13. H. Gao, L. He, Y. Zhang, K. Gao, H. Wang, Synthesis and methanol oxidation performance of graphene supported Pt catalyst. Power Technol. **9**, 1771–1774 (2016)
14. Y. Shen, Z. Ren, L. Zhou, J. Li, S. Yang, Research progress of nano-scale combustion catalyst for solid propellant. New Chem. Mater. **48**(08), 50–55 (2020)
15. W. Hong, Y. Xue, F. Zhao et al., Preparation of Bi2O3/CNTs composite and its combustion catalytic effect on double-base propellant. Chin. J. Explos. Propellants **35**(6), 7–11 (2012)
16. X. Yu, The effect of carbon nanotubes on the thermal decomposition of CL-20. Chin. J. Explos. Propellants **27**(3), 78–80 (2004)
17. X. Li, R. Yang, Combustion and thermal decomposition of ammonium dinitramide cataIyzed by carbon nano—tubes. New Carbon Mater. **25**(6), 444–448 (2010)
18. H. Ren, Y.Y. Liu, Q.J. Jiao et al., Preparation of nanocomposjte PbO center dot CuO/CNTs via microemulsion process and its catalysis on thermal decomposition of RDX. J. Phys. Chem. Solids **71**, 149–152 (2010)
19. Y. Zou, J. Liu, Research progress of carbon nanotubes supported metal catalysts. Petrochem. Technol. **33**, 117–119 (2004)
20. X. Li, Y. Yang, R. Yang, Preparation of carbon nanotubes supporting bismuth oxide nanometer particle and its catalysis on thermal decomposition of ammonium dinitramide. J. Synth. Cryst. **36**(5), 1127–1131 (2007)
21. X.-Y. Zhang, H.-P. Li, X.-L. Cui, Preparation and photocatalytic activity for hydrogen evolution of TiO_2/graphene sheets composite. Chin. J. Inorg. Chem. **25**(11), 1903–1907 (2009)

22. Z.-L. Wen, S.-D. Yang, Q.-J. Song, L. Hao, X.-G. Zhang, High activity of Pd/graphene catalysts for ethanol electrocatalytic oxidation. Acta Phys. Chim. Sin. **26**(6), 1570–1574 (2010)
23. Q. Zhang, Y.-Q. He, X.-G. Chen et al., Titanium oxide/graphene oxide composite structure and its photocatalytic activity. Sci. Bull. **55**(7), 620–628 (2010)
24. Y.-L. Dong, W.-N. Song, J.-C. Luo et al., Preparation of vanadium oxide/graphene catalyst and its catalytic performance. J. Eng. Heilongjiang Univ. **6**(4), 36–40 (2015)
25. W. Li, Y. Ren, H. Wang, et al., A new combustion catalyst of Cu_2O-PbO nanoparticles on graphene oxide (GO): thermal decomposition kinetics, thermal safety and burning property. Summary of the 29th Annual Conference of the Chinese Chemical Society (2014), p. 216
26. Q.-L. Tan, W.-L. Hong, X.-B. Xiao et al., Preparation of Bi_2O_3/graphene oxide composite catalyst and Study on combustion catalytic performance of Bi base propellant. Nano-process. Tech. **6**, 22–27 (2013)
27. W. Hong, X.-B. Xiao, F.-Q. Zhao, et al., A PBO/graphene oxide composite powder and its preparation method. Chinese patent: 201210404714, 2013-01-30 (2013)
28. F.-Q. Zhao, M. Zhang, Y.-J. Yang, T. An, H. Li, Z.F. Jiang, A catalyst for combustion of graphene Schiff base nickel and its preparation method. Chinese patent: 103007947A, 2013-04-03 (2013)
29. R. Dong, J. Mo, H. Zhang et al., Synthesis of the titania/graphene oxide composite photocatalyst. Chem. Ind. Eng. Prog. **33**(3), 679–684 (2014)
30. W.-X. Shi, *Preparation and Properties of Fullerene Glycine Lead/Copper Salt* (Southwest University of science and technology, SiChuan, 2012)
31. L. Gan, Y.-Z. Lin, J. Zhu, Preparation of carbon nanofibers containing transition metals and nitrogen and their application in fuel cell catalysts. Chinese patent: 102021677A, 2011-04-20 (2011)
32. X. Wang, L. Zhi, K. Müllen, Transparent, conductive graphene electrodes for dye-sensitized solar cells. Nano Lett. **8**(1), 323–327 (2008)
33. S. Paek, E. Yoo, I. Honma, Enhanced cyclic performance and lithium storage capacity of SnO_2/graphene nanoporous electrodes with three-dimensionally delaminated flexible structure. Nano Lett. **9**(1), 72–75 (2008)
34. V.C. Tung, L. Chen, M.J. Allen et al., Low-temperature solution processing of graphene-carbon nanotube hybrid materials for high-performance transparent conductors. Nano Lett. **9**(5), 1949–1955 (2009)
35. S. Guo, Preparation of Fe_2O_3/graphene oxide catalyst and its adsorption and photo-Fenton degradation of organic contaminants (Wuhan University of Technology, HuBei, 2013)
36. Y.J. Li, K.L. Wang, J.Q. Wei et al., Tensile properties of long aligned double-walled carbon nanotube strands. Carbon **43**, 31–35 (2005)
37. L. Li, Y. Xing, Pt-Ru nanoparticles supported on carbon nanotubes as methanol fuel cell catalysts. J. Phys. Chem. **111**, 2803–2808 (2007)
38. R. Yang, L. Gao, Preparation and capacitances of oriented attachment CuO nanosheets and the MWNT/CuO nanocomposites. Solid State Commun. **134**, 729–733 (2005)
39. J. Liu, W. Jiang, Z. Wang et al., Nano-NiO/straight-CNTs and Nano-NiO/branched-CNTs composites and their effects on the thermal decomposition of ammonium perchlorate. Acta Chim. Sin. **65**(23), 2725–2730 (2007)
40. C. Wang, J. Qiu, C. Liang, Synthesis of carbon nanotubes-supported Pd/SnO_2 for the hydrogenation of ortho-Chloronitrobenzene. Chin. J. Catal. **30**(3), 259–264 (2009)
41. W. Pan, X. Chen, L. Xu, Synthesis and properties of cuprous oxide/carbonnanotubes composite superfine spheresn. J. Inorg. Mater. **23**(2), 403–407 (2008)
42. J. Zhang, W. Hong, F. Zhao et al., Synthesis of SnO_2-Cu_2O/CNTs catalyst and its effect on thermal decomposition of FOX-12. Chin. J. Explos. Propellants **34**(2), 47–51 (2011)
43. F. Zhao, S. Li, B. Cai, Ecologically safe bismuth-containing catalysts for solidrocket propellants. Chin. J. Explos. Propellants **21**(1), 53–55 (1998)

Chapter 16
Mechanical, Thermal Properties and Ablation Resistance of Unsaturated Polyester Inhibitor by α-Type Zirconium Phosphate and Multi-walled Carbon Nanotubes

Lisheng Zhou, Guohui Chen, Yang Li, Aijuan Shi, Shuxin Wu, Jianxia Liu, Xiao Xiao, and Shishan Yang

Abstract Unsaturated polyesters (UP) as solid propellant inhibitor have been widely used in weapons and equipments, however, with the gradual improvement of solid propellant properties, higher and higher performance requirements are put forward for the inhibitors. In this paper, the mechanical and ablative properties of the UP inhibitor were improved by adding multi-walled carbon nanotubes (MWCNTs) and α-type zirconium phosphate (α-ZrP), the effect of the addition amount on the properties was also investigated. The results show that the addition of MWCNTs and α-ZrP can increase the tensile strength of the UP inhibitor. When the addition of MWCNTs and α-ZrP was 0.5 g and 3 g, respectively, the tensile strength of the inhibitor was 33.58 MPa, which increased by 55.7%. Meanwhile, the addition of MWCNTs and α-ZrP can significantly improve the heat and ablation resistance of the UP inhibitors. When the addition amount of MWCNTs and α-ZrP was 1 g and 3 g, the linear ablation rate is 0.41 mm/s, with a reduction of 25.5%. Therefore, MWCNTs and α-ZrP as reinforce and ablative resistant fillers show potential application prospect in solid propellant inhibitor field.

16.1 Introduction

Unsaturated polyester (UP) is a kind of thermosetting resin synthesized by polycondensation between diacid (or anhydride) and dihydric alcohol, containing unsaturated bonds and ester bonds. UP resins have advantages of strong mechanical properties,

L. Zhou · G. Chen · Y. Li · A. Shi · S. Wu · J. Liu · X. Xiao · S. Yang (✉)
Xi'an Modern Chemistry Research Institute, Xi'an 710065, China
e-mail: 1054500275@qq.com

L. Zhou
e-mail: zhoulishengandy@163.com

G. Chen
e-mail: border_chen@126.com

A. Gany and X. Fu (eds.), *2021 International Conference on Development and Application of Carbon Nanomaterials in Energetic Materials*, Springer Proceedings in Physics 276,
https://doi.org/10.1007/978-981-19-1774-5_16

good transparency, cure at room temperature and low manufacturing cost. UP resin has good adhesion performance with modified double-base propellant, so it has been widely used as solid propellant inhibitors in the field of double-base propellant and double-base propellant charges. At abroad, the Rattlesnake air-to-ground missile R400 engine, Sidewinder IIIB air-to-air missile gas generator, Hult anti-tank missile all used UP resin as propellant inhibitors [1]. UP as solid propellant inhibitor also has some defects, such as poor toughness, low elongation at low temperature, and poor ablation resistance. Yang et al. synthesized a series of polyurethane containing double bond for the modification of UP inhibitor, the results indicating that polyurethane can obviously increase the toughness of UP inhibitor [2]. In addition, with the development of weapons and equipment towards high energy and long endurance, the comprehensive performance of inhibitors faces higher technical requirements.

At present, adding flame retardant is the most common method to improve the ablative resistance of the solid propellant inhibitor. Cyclotriphosphazene derivatives have been widely studied and applied in the field of flame retardancy due to their unique P and N structures and strong molecular designability, which can endow polymers with good flame retardancy and ablative resistance [3–6]. Chen et al. studied the influences of polyphosphazene flame retardant, phexa-(4-hydroxymethyl-phenoxy)-cyclotriphosphazene to the UP inhibitor, indicating that polyphosphazene flame retardant can reduce the tensile strength and improve the ablative resistance [7]. Pereira prepared flame retardant UP nanocomposites which containing layered double hydroxides (LDH), and the fire reaction properties were evaluate by cone calorimeter, indicating that flammability of UP decreased significantly [8]. Cyclotriphosphazene derivatives have been studied as flame retardants in a variety of polymers, such as ABS resin [9], polyurethanes [10–13], epoxy resin [14–17], PET [18, 19], PC [20–22], etc., to improve their flame-retardant properties. Cao et al. [23] used aldehyde/allyl-aryloxypolyphazene-based inhibition formulas as free loading solid propellant inhibitor, the inhibitor showed excellent ablative resistance and thermal stability. In recent years, more and more attention has been paid to improving the flame retardancy of polymer matrix through the synergistic flame retardancy of functional 2D nanosheets and traditional flame retardants, zirconium phosphate (ZrP) has become a hot research topic in flame retardant industry due to its good thermal stability and catalytic carbonization effect [16, 24]. Furthermore, carbon nanotubes (CNTs) can not only be used as enhanced nanofillers [25], it also shows good effect in the research of flame retardant modification of polymer [26].

In this article, UP inhibitors containing cyclotriphosphazene flame retardant, hexa-(4-aldehyde-phenoxy)-cyclotriphosphazene (HAPCP), α-ZrP and multi-walled carbon nanotubes (MWCNTs) were prepared, and the thermal and ablation resistance properties of UPR inhibitors were also characterized and analyzed. Furthermore, we explored the effects of different content of α-ZrP and CNTs to the mechanical properties of UP inhibitors.

16.2 Experimental

16.2.1 Materials

The α-ZrP was purchased from Sunshine Technology Co. Ltd., China. The multi-walled carbon nanotubes (MWCNTs, trade mark XFQ041, with a diameter of 10–20 nm) was purchased from Nanjing XFNANO Materials Tech Co. Ltd., China. Unsaturated polyester and cobalt naphthenate were purchased from Changzhou Huake Polymer Co. Ltd., the cyclohexanone peroxide (HS-E1) was purchased from Changzhou Tianma Group Co. Ltd. HAPCP was synthesized by Xi'an Modern Chemistry Research Institute.

16.2.2 Preparation of UP Inhibitors

Different amount of UP, HAPCP, MWCNTs and α-ZrP were weighed and agitated intensely. Then the mixture was mixed by three-roller grinder for three times to obtain the pre-mixed slurry. The accelerator cobalt naphthenate and initiator HS-1 were added and mixed with the above pre-mixed slurry. The mixture was degassed under vacuum at room temperature (RT) for 10 min, then poured into mold and cured RT for 12 h. The formulations of UP inhibitors are summarized in Table 16.1.

Table 16.1 Formulations of UP inhibitors

Sample	UP (g)	HAPCP (g)	MWCNTs (g)	α-ZrP (g)
1	100	15	0	0
2	100	15	0	1
3	100	15	0	2
4	100	15	0	3
5	100	15	0.5	1
6	100	15	0.5	2
7	100	15	0.5	3
8	100	15	1	1
9	100	15	1	2
10	100	15	1	3

16.2.3 Characterization

Fourier transform infrared (FTIR) spectra were performed on a PerkinElmer Instruments Spectrum GX FTIR spectrometer in the wavenumber range of 400–4000 cm^{-1} using KBr sampling sheets. Thermogravimetric analysis (TG) measurements were performed on the TA Q50 thermogravimetric analyzer under air atmosphere at a heating rate of 20 °C·min^{-1} from room temperature to 800 °C. And all the samples were measured in open Al_2O_3 crucibles. Scanning electron microscopy (SEM) were performed on a Tescan (Vega 3 LMH) scanning electron microscope to characterize the surface morphologies of the tested samples. Tensile strength analyses were performed on a CMT 6503 tensile tester at an elongation rate of 10 mm min^{-1} according to the standard GJB 770B–2005. The linear ablation rate was measured according to the GJB 323B–2018 standard using an oxygen-acetylene ablator.

16.3 Results and Discussion

16.3.1 Mechanical Properties of UP Inhibitors

The mechanical properties of cured UP inhibitor composites were evaluated by tensile property. Figure 16.1 shows the tensile strength and elongation at break of sample **1–10**, and the relevant experimental data are summarized in Table 16.2. The tensile strength and elongation at break of UP inhibitor **1** without MWCNTs and α-ZrP are 21.56 MPa and 37.4%. According to the data in the table, the tensile strengths

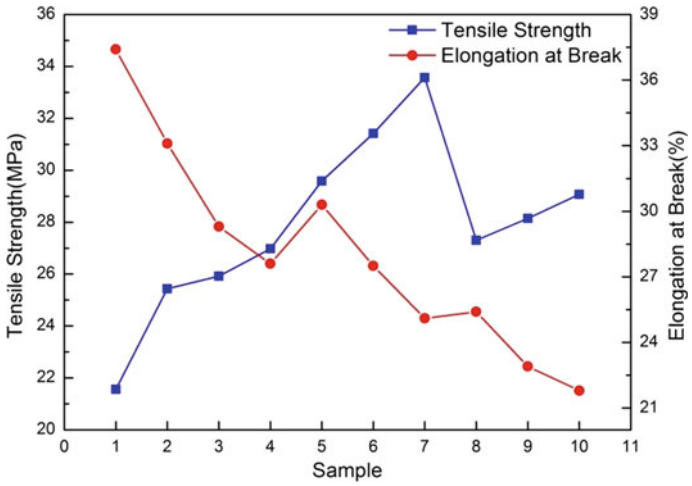

Fig. 16.1 Tensile property curves of UP inhibitors

Table 16.2 X Tensile properties of UP inhibitors

Sample	Tensile strength (MPa)	Elongation at break (%)
1	21.56	37.4
2	25.43	33.1
3	25.92	29.3
4	26.98	27.6
5	29.59	30.3
6	31.42	27.5
7	33.57	25.1
8	27.31	25.4
9	28.15	22.9
10	29.07	21.8

of UP composites were improved with the addition of α-ZrP, and the elongation decreases with the content increasing. Taking sample 2–4 as example, the tensile strengths are increased by 17.9%, 20.2% and 25.1%, respectively, compared with sample **1**. This mainly because those α-ZrP nanoplatelets have rigid two-dimensional structure, cooperated with MWCNTs can effectively strengthen the tensile strength of the composites. When the addition of α-ZrP is the same, the tensile strength of the UP composites firstly increases and then decreases with the increase of the content of MWCNTs, while the elongation decreases with the content increasing. This may due to the agglomeration phenomenon with the increase of the addition of MWCNTs, which reduces the mechanical properties of the UP composites. In this research, UP inhibitor composites have the best tensile properties when the addition of MWCNTs is 0.5 g per 100 g UP resin, especially sample 7, the tensile strength and elongation are 33.57 MPa and 25.1%, respectively, the strengths is increased by 55.7%, indicating that the UP inhibitor has excellent mechanical property.

16.3.2 Thermal Stability of UP Inhibitors

The effect of MWCNTs and α-ZrP on the thermal stabilities of UP inhibitors were evaluated by TGA, and Fig. 16.2 shows the curves of the TGA and derivative thermogravimetric analysis (DTG) of the MWCNTs, α-ZrP, sample **1**, **2**, **5** and **7**.the characteristic data of thermal degradation are summarized in Table 16.3. The data T_5, T_{10}, T_{50} mean temperatures at 5, 10 and 50% mass loss, respectively The MWCNTs is a kind of carbon material with excellent heat resistance, the char yield at 800 °C is up to 97.1%. α-ZrP shows two main decompose stage, the first stage occurs from 60–250 °C with the maximum decomposition temperature at 145 °C, which was due to the pyrolysis of crystalline water, the second stage of thermal degradation is condensation of P-OH in α-Zr $(HPO_4)_2$ to form ZrP_2O_7. The α-ZrP also has fairly high

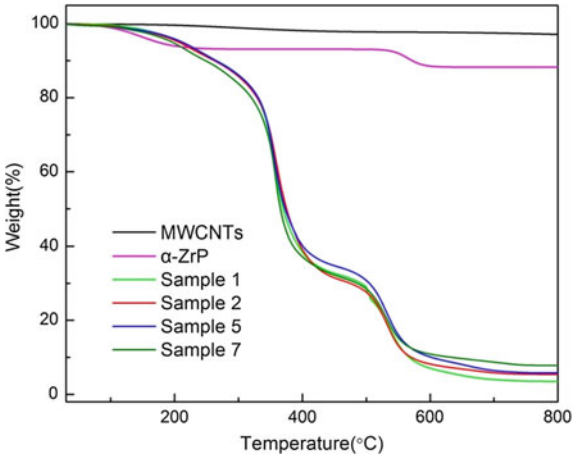

Fig. 16.2 TGA curves of MWCNTs, α-ZrP and UP inhibitors

Table 16.3 Thermal parameters of MWCNTs, α-ZrP and UP inhibitors

Sample	T_5 (°C)	T_{10} (°C)	T_{50} (°C)	Char yields at 800 °C
MWCNTs	–	–	–	97.1
α-ZrP	174	572	–	88.3
1	207	265	370	3.5
2	206	262	375	5.4
5	212	265	373	5.8
7	196	248	366	7.8

char residue at high temperature (88.3% at 800 °C) indicating excellent thermostability. The sample **1**, **2**, **5** and **7** have similar TGA curves, UP inhibitors decompose in multistep thermal degradation, the two major weight loss thermal degradation courses appear at 300–400 °C and 450–600 °C due to the decomposition of the polymer matrix networks and further thermo-oxidative decomposition of formed char, respectively. The char yields of UP inhibitors increase with the improvement of the MWCNTs and α-ZrP. The increase in residual char suggests that the addition of MWCNTs and α-ZrP improve the thermal oxidative resistance of the charred residue and char formation of UP, which can inhibit the thermal decomposition rate of UP composites. This mainly due to the synergistic effects of HAPCP, MWCNTs and α-ZrP that make the obtained UP inhibitors with retardant efficiency.

16.3.3 Ablation Resistance Properties of UP Inhibitors

Ablation resistance property is one of the key parameters of solid propellant inhibitor, the linear ablation rates of the obtained UP inhibitors were measured using an oxygen-acetylene ablator, and the results are shown in Fig. 16.3. As can be seen that the addition of MWCNTs and α-ZrP can significantly improve the ablation resistance of UP inhibitors. The linear ablation rate of sample **1** is 0.55 mm/s, indicating that this sample has poor ablation resistance. The linear ablation rates of UP inhibitor composites decrease with the additive amount of MWCNTs and α-ZrP. When the addition of MWCNTs and α-ZrP were 1 g and 3 g, respectively, per 100 g UP resin, the ablation rate is 0.41 mm/s, with a reduction of 25.5%. The HAPCP in the UP inhibitors acts as intumescent flame retardant, during the composite combustion HAPCP was decomposed to phosphazene free-radicals, these radicals can can inhibit the degradation of matrix in the condensed phase and the combustion chain reaction in the gas phase. MWCNTs and α-ZrP both have excellent thermostability and high char yield at high temperature, and not flammable during inhibitor combustion. Furthermore, the presence of MWCNTs and α-ZrP nanoplatelet can enhance the strength of the carbonization layer of UP inhibitors. So HAPCP, MWCNTs and α-ZrP have synergistic flame retardant effect to UP resin that can improve ablation resistance of UP inhibitors.

The char residues of the UP inhibitors sample **1** and **7** were collected after linear ablation test, and the surface morphologies of these samples were measured by SEM to investigate the influence of the morphology of the char layers to the ablation resistance properties, the SEM images are shown in Fig. 16.4. It can be seen that both the chars have a honeycomb structure, this may due to the intumescent flame retardant effect of cyclotriphosphazene derivative HAPCP. And the addition of MWCNTs and α-ZrP can improve the char formation during combustion process, reinforce the structural strength of the char layer, which is in accordance with TGA result. The

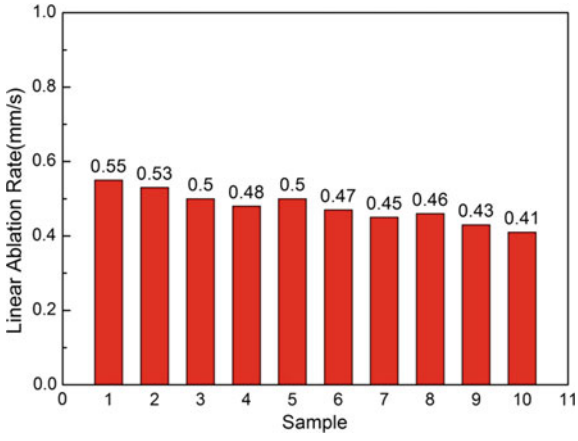

Fig. 16.3 The linear ablation rates of UP inhibitors

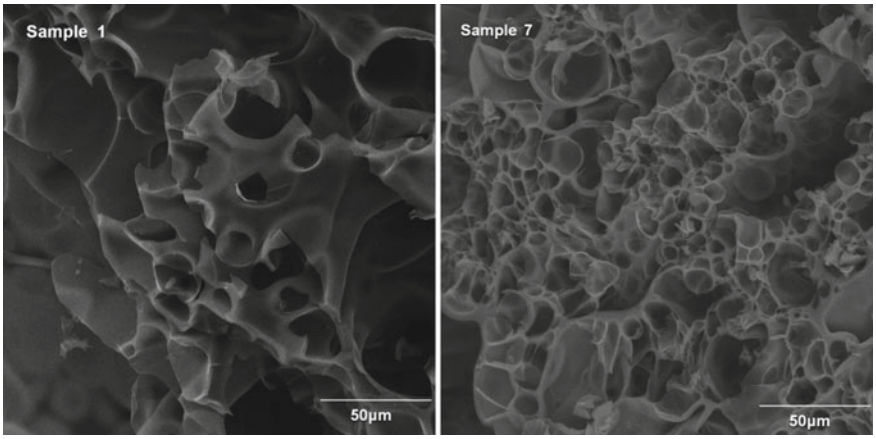

Fig. 16.4 SEM images of char morphology after linear ablation

expanded char is helpful to restrain the exchange of oxygen and heat inside and outside the char, thus improving the ablation resistance.

16.4 Conclusion

In this article, a series of UP inhibitor composites containing HAPCP, MWCNTs and α-ZrP were prepared and mechanical properties, thermal stabilities and ablation resistance properties were measured. The addition of MWCNTs and α-ZrP can improve the tensile strength of UP inhibitors as reinforce fillers but can decrease the elongation. Sample **7** has the highest tensile strength of 33.57 MPa with 0.5 g MWCNTs and 3 g α-ZrP per 100 g UP resin, which is increased by 55.7% compared with Sample **1**. According to the thermal stability results of UP inhibitors, the addition of MWCNTs and α-ZrP can improve the high temperature stability and char yield, due to the excellent heat resistance of MWCNTs and α-ZrP. Finally, the ablation resistance properties were evaluated using an oxygen-acetylene ablator. Because the combination of intumescent flame retardant HAPCP, MWCNTs and α-ZrP has synergistic flame retardant effect, the ablation resistance was improved as fillers contents increasing. In conclusion, MWCNTs and α-ZrP as reinforce and ablative resistant fillers show potential application prospect in solid propellant inhibitor field.

References

1. C. Bian, Y. Zhang, Y. Shi et al., Recent progress of coating technologies for solid propellant. Chin. J. Explos. Propellant **42**(3), 213–222 (2019)
2. S. Yang, W. Zhang, J. Wang, Research on PUUP toughened unsaturated polyester inhibitor. Modem Chem. Ind. **31**(4), 59–61 (2011)
3. B. Zhao, W. Liang, J. Wang et al., Synthesis of a novel bridged-cyclotriphosphazene flame retardant and its application in epoxy resin. Polym. Degrad. Stab. **133**, 162–173 (2016)
4. L. Zhou, G. Zhang, S. Yang et al., Synthesis and curing kinetics of cyclotriphosphazene-based multifunctional epoxy resin. Polym. Mater. Sci. Eng. **36**(5), 107–115 (2019)
5. Y. Shi, B. Yu, Y. Zheng et al., A combination of POSS and polyphosphazene for reducing fire hazards of epoxy resin. Polym. Adv. Technol. **29**(4), 1242–1254 (2018)
6. R. Schenck, G. Mer, Über die Phosphornitrilchloride und ihre Umsetzungen (I.). Berichte der deutschen chemischen Gesellschaft (A and B Series) **57**(8), 1343–1355 (1924)
7. G. Chen, L. Zhou, P. Li et al., Influences of polyphosphazene flame retardant on properties of UP coating layers. Eng. Plast. Appl. **48**(4), 129–133 (2020)
8. C.M.C. Pereira, M. Herrero, F.M. Labajos et al., Preparation and properties of new flame retardant unsaturated polyester nanocomposites based on layered double hydroxides. Polym. Degrad. Stab. **94**(6), 939–946 (2009)
9. X. Cao, Y. Yang, H. Luo et al., High efficiency intumescent flame retardancy between Hexakis (4-nitrophenoxy) cyclotriphosphazene and ammonium polyphosphate on ABS. Polym. Degrad. Stab. **143**, 259–265 (2017)
10. L. Qian, F. Feng, S. Tang, Bi-phase flame-retardant effect of hexa-phenoxy-cyclotriphosphazene on rigid polyurethane foams containing expandable graphite. Polymer **55**(1), 95–101 (2014)
11. Y. Fang, X. Du, S. Yang et al., Sustainable and tough polyurethane films with self-healability and flame retardance enabled by reversible chemistry and cyclotriphosphazene. Polym. Chem. **10**(30), 4142–4153 (2019)
12. B. Łukasz, D. Michał, J. Rafał, Thermal behaviour and flame retardancy of polyurethane high-solid coatings modified with hexakis(2,3-epoxypropyl)cyclotriphosphazene. Prog. Org. Coat. **108**, 51–58 (2017)
13. P. Zhang, D. Ma, J. Cheng et al., Effects of hexaphenoxycyclotriphosphazene and glass fiber on flame-retardant and mechanical properties of the rigid polyurethane form. Polym. Compos. **41**(9), 3521–3527 (2020)
14. L. Zhou, G. Zhang, Y. Feng et al., Design of a self-healing and flame-retardant cyclotriphosphazene-based epoxy vitrimer. J. Mater. Sci. **53**(9), 7030–7047 (2018)
15. L. Zhou, G. Zhang, J. Li, et al., The flame retardancy and thermal stability properties of flame-retarded epoxy resins based on α-hydroxyphosphonate cyclotriphosphazene. J. Thermal Anal. Calorim. (2017)
16. S. Qiu, X. Wang, B. Yu et al., Flame-retardant-wrapped polyphosphazene nanotubes: a novel strategy for enhancing the flame retardancy and smoke toxicity suppression of epoxy resins. J. Hazard. Mater. **325**, 327–339 (2017)
17. S. Yang, J. Wang, S. Huo et al., Synthesis of a phosphorus/nitrogen-containing compound based on maleimide and cyclotriphosphazene and its flame-retardant mechanism on epoxy resin. Polym. Degrad. Stab. **126**, 9–16 (2016)
18. J. Li, F. Pan, H. Xu et al., The flame-retardancy and anti-dripping properties of novel poly(ethylene terephalate)/cyclotriphosphazene/silicone composites. Polym. Degrad. Stab. **110**(000), 268–277 (2014)
19. X. Zhang, Y. Zhong, Z. Mao, The flame retardancy and thermal stability properties of poly (ethylene terephthalate)/hexakis (4-nitrophenoxy) cyclotriphosphazene systems. Polym. Degrad. Stab. **97**(8), 1504–1510 (2012)
20. Y. Yang, J. Liu, X. Cai, Antagonistic flame retardancy between hexakis(4-nitrophenoxy) cyclotriphosphazene and potassium diphenylsulfone sulfonate in the PC system. J. Therm. Anal. Calorim. **126**(2), 571–583 (2016)

21. Y. Yang, W. Kong, X. Cai, Two phosphorous-containing flame retardant form a novel intumescent flame-retardant system with polycarbonate. Polym. Degrad. Stab. **134**, 136–143 (2016)
22. H. Feng, L. Qian, L. Lu, Synergistic effect of polyimide charring agent and hexaphenoxycyclotriphosphazene on improving fire safety of polycarbonate: High graphitization to strengthen the char layer. Polym. Adv. Technol. **32**(3), 1135–1149 (2020)
23. J. Cao, X. Xiao, L. Wei et al., Study of aldehyde/allyl-aryloxypolyphosphazene-based inhibition materials for loading solid propellant (II): heat-and ablation-resistant properties and application. Chin. J. Explos. Propellants **42**(6), 577–582 (2019)
24. X. Fu, X. Wang, W. Xing et al., Two-dimensional cardanol-derived zirconium phosphate hybrid as flame retardant and smoke suppressant for epoxy resin. Polym. Degrad. Stab. **151**, 172–180 (2018)
25. D.N. Bikiaris, Nanocomposites of aliphatic polyesters: an overview of the effect of different nanofillers on enzymatic hydrolysis and biodegradation of polyesters. Polym. Degrad. Stab. **98**(9), 1908–1928 (2013)
26. G. Beyer, Short communication: carbon nanotubes as flame retardants for polymers. In: Fire and materials (2002), pp 291–293

Chapter 17
Simulation Study on Pressure Relief of Cabin Door Under Explosive Load in Cabin

Wenhui Zhao and Yuxin Sun

Abstract Anti-ship missiles can explode inside ships, so it is of great significance to study the explosion protection inside ships. In this paper, ANSYS/LS-DYNA numerical simulation software was used to simulate the explosion process of 350 kg TNT inside the cabin with and without doors based on the fluid-structure coupling algorithm. The calculation results show that by setting the door to open under a certain impulse, it is beneficial to reduce the convergence pressure at the corner of the cabin and the stress on the bulkhead, and at the same time, it can reduce the velocity and displacement of the upper bulkhead. It plays a certain role in the protection of cabin structure, and can provide ideas for improving the anti-explosion performance of typical ships.

17.1 Introduction

With the rapid development of modern anti-ship weapons, ships are facing more and more threats [1], and the protection methods tend to be diversified [2]. As a typical representative of anti-ship weapons, semi-armor-piercing anti-ship missiles usually adopt time-delay trigger fuses, which can penetrate into the hull and explode by the impact kinetic energy of warheads [3–6]. According to Demar's empirical formula [7], taking the famous Harpoon (AGM-84A) [8] in the United States as an example, when the missile warhead hits the side at a speed of 340 m/s, it needs 79.3 mm thick steel armor to resist its kinetic energy piercing, which is unbearable for modern surface ships. Therefore, it is the key to the anti-explosion structural design of ships that the missile penetrates the outboard plate and explodes in the ship cabin.

Compared with the external explosion, due to the reflection of the cabin wall, the explosion caused by internal explosion generally includes multiple pressure pulses, the pressure waveform is more complex, and the damage effect is often stronger [9–11]. Passive protection of explosive shock load is the last protection means of

W. Zhao · Y. Sun (✉)
National Key Laboratory of Transient Physics, Nanjing University of Science and Technology, Nanjing 210094, Jiangsu, China
e-mail: yxsun01@163.com

A. Gany and X. Fu (eds.), *2021 International Conference on Development and Application of Carbon Nanomaterials in Energetic Materials*, Springer Proceedings in Physics 276,
https://doi.org/10.1007/978-981-19-1774-5_17

ship defense, and scholars at home and abroad have carried out a lot of experiments and numerical simulation studies. Kong et al. [12] used Dytran software platform to simulate the explosion inside the cabin, and put forward that the opening of the bulkhead is beneficial to reduce the collection pressure at the corner of the cabin and protect the cabin structure; Du et al. [13] used Dytran to simulate the damage of ship's side protection structure under the action of internal explosion, and analyzed the propagation law of shock wave in the cabin; Hou [14] used Dytran software to simulate the dynamic response and failure of ship structure under the action of explosion load in cabin; Yan et al. [15] carried out numerical calculation research on the response of multi-layer protective structure with liquid tank under internal explosion; Zhang [16] used ANSYS/LS-DYNA software to analyze the influence of stiffeners on the peak value of overpressure at the coupling surface between plate frame and air, and the influence of the number, position and size of vent ports on the structural response of cabin with vent ports. The cabin door is an indispensable part of the ship cabin, which is in a closed state at ordinary times. When the cabin is impacted by the explosion load, if the cabin door is set, it can be opened in time by a certain impulse in a very short time after the explosion, so as to relieve the pressure. It is of great research significance to discuss this problem. In this paper, using ANSYS/LS-DYNA numerical simulation software, based on ale fluid-structure coupling algorithm, the explosion process of 350 kg TNT in cabin is simulated. By comparing the pressure distribution and structural response of cabin with and without cabin doors, the pressure relief effect of cabin doors during internal explosion is studied, and the influence of cabin doors pressure relief on reducing cabin damage is analysed. The research results can provide ideas for improving the anti-explosion performance of typical cabin.

17.2 Numerical Calculation Model

17.2.1 Structural Model

In this study, a cuboid cabin is selected, and the cabin size is set to be 20 m × 10 m × 5 m, and the bulkhead of the cabin extended outward for 1 m, simulating other connected cabins. The bulkhead thickness is 20 mm, and the cabin door is 1 m × 2 m rectangular.

The bulkhead is modelled by shell element and Lagrange algorithm, and the grid length is 0.1 m.

Considering the symmetry and reducing the calculation amount, the eighth model of the cabin without doors and the fourth model of the cabin with doors are established, as shown in Figs. 17.1 and 17.2 respectively.

TNT is located in the centre of the cabin, with a mass of 350 kg, a bottom diameter of 35 cm and a height of 220 cm. TNT modelling adopts solid element and ale

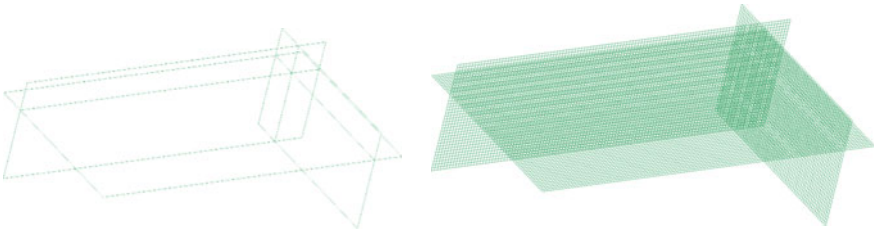

Fig. 17.1 Calculation model of cabin without cabin doors

Fig. 17.2 Calculation model of cabin with cabin doors

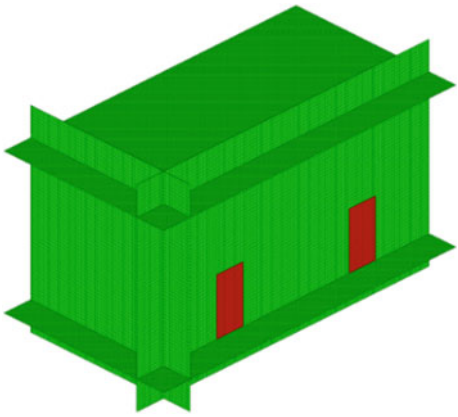

algorithm, the grid size is 2.9 cm, and the quarter calculation model is shown in Fig. 17.3.

Inside and outside the cabin, air is filled with solid element and ale algorithm, and the air grid size is 4.4 cm.

The established one-eighth model without doors and one-fourth model with doors are shown in Fig. 17.4.

The fluid–structure coupling is set between ale algorithm used in air and TNT and Lagrange algorithm used in bulkhead. Symmetric constraint is set on the symmetry plane, and non-reflective boundary is set on the boundary of air domain.

Fig. 17.3 Quarter model of TNT

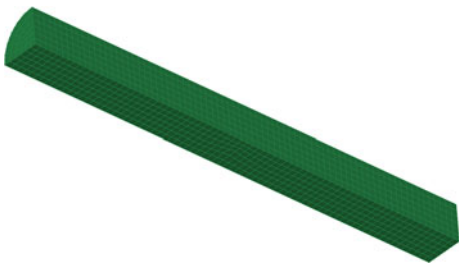

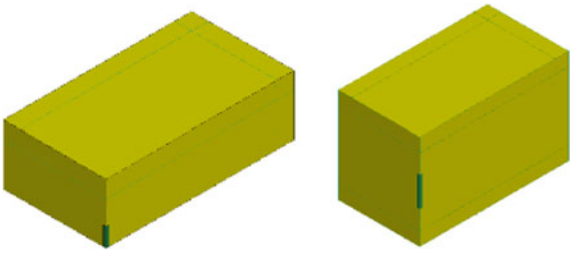

Fig. 17.4 Model without cabin doors and model with cabin doors

17.2.2 Material Model

The bulkhead material is steel, and the MAT_JOHNSON_COOK material model [17] and GRUNEISEN equation of state are adopted. The material parameters are shown in Table 17.1.

Assuming that air is an ideal gas without viscosity, the expansion process of shock wave is isentropic adiabatic process. MAT_NULL material model is adopted, and the state equation is LINEAR_POLYNOMIAL model. The linear polynomial equation of state for air is:

$$\mathrm{p} = c_0 + c_1\mu + c_2\mu^2 + c_3\mu^3 + \left(c_4 + c_5\mu + c_6u^2\right)e_0$$

Among them, $c_0 - c_6$ are constants related to gas properties; p is air pressure; μ is relative density, $\mu = \frac{\rho}{\rho_0} - 1$; Gas density ρ, initial density ρ_0, initial internal energy per unit volume e_0; V_0 is the initial relative volume. The air equation of state and material parameters are shown in Table 17.2.

MAT_HIGH_EXPLOSIVE_BURN material model and JWL equation of state [18] are selected for TNT.

The expression of state equation is:

$$\mathrm{p} = A_1\left(1 - \frac{\omega}{R_1V}\right)e^{-R_1V} + B_1\left(1 - \frac{\omega}{R_2V}\right)e^{-R_2V} + \frac{\omega E}{V}$$

Table 17.1 Material parameters of steel

ρ (g/cm^3)	Shear modulus (GPa)	Young's modulus (GPa)	A	B	N	C	M
7.8	77	20.7	0.00792	0.0051	0.26	0.014	1.03

Table 17.2 Material parameters of air

$c_0 - c_3$	c_4	c_5	c_6	V_0	ρ_0(g/cm^3)	e_0(J)
0	0.4	0.4	0	1	0.001293	0.25

Table 17.3 Material parameters of TNT explosive

ρ(g/cm^3)	v(m/s)	P_{cj}(MPa)	β
1.63	6930	18,503	0

Table 17.4 Material parameters of TNT explosive

A_1	A_2	R_1	R_2	ω	E(MPa)	V_0
3.74	0.0323	4.15	0.95	0.3	7000	1.0

In which p is pressure; V is the relative volume; E is the internal energy per unit volume of explosive; A_1, A_2, R_1, R_2 and ω are constants related to the properties of explosives; ρ is the density of explosive material; V is detonation velocity; P_{cj} is Chapman pressure; β is the combustion mark. The values of TNT explosive materials and state equation parameters are shown in Table 17.3 and Table 17.4 [19].

17.3 Research on Simulation Reliability

In order to verify the reliability of the established numerical calculation model [10, 20], the explosion model of 350 kg TNT in free air is established, and the size parameters, discrete parameters and material parameters used are consistent with those mentioned above. Set a series of Gaussian points at the horizontal position of explosion centre, output the pressure history curve of Gaussian points, as shown in Fig. 17.5, and compare the pressure extremum with the results obtained by empirical formulas in literature [21], as shown in Table 17.5.

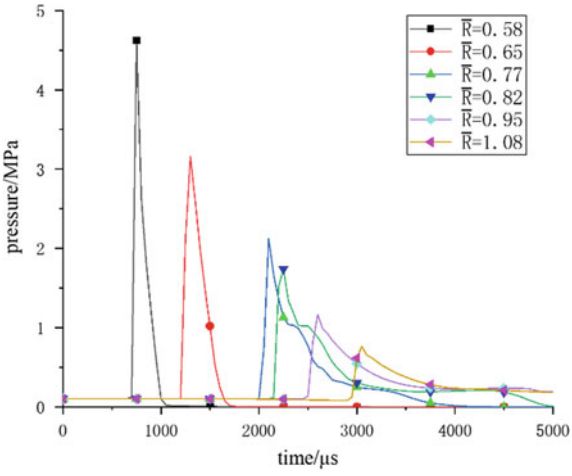

Fig. 17.5 Pressure history curve

Table 17.5 Comparison between empirical formula and simulation results

X (m)	$\overline{R}$(m·kg$^{-1/3}$)	Calculation result of empirical formula (MPa)	Simulation results (MPa)	Error (%)
4.09	0.58	4.53	4.63	2.2
4.58	0.65	3.32	3.16	4.8
5.43	0.77	2.09	2.12	1.4
5.78	0.82	1.77	1.74	1.7
6.69	0.95	1.20	1.17	2.5
7.61	1.08	0.81	0.76	6.2

It can be seen that under different $\overline{R}$, the simulation results are similar to those calculated by empirical formula, and the error is small, so the numerical simulation results are reasonable and reliable.

17.4 Numerical Calculation Results

Assume that the cabin door closer to the explosion centre is the cabin door A, and the cabin door farther from the explosion centre is the cabin door B. Output the pressure of each grid cell on the cabin door A, and carry out integral operation with respect to time. Then sum the integrals, and the total impulse curve of the cabin door A is shown in Fig. 17.6. It can be seen from Fig. 17.6 that when t = 1400 μs, cabin door A starts to be impacted by detonation wave and its impulse starts to increase. When t = 2380 μs, the total impulse of cabin door A starts to increase rapidly. When t = 3113 μs, the total impulse of cabin door A reaches 20,000 N s. It is considered that cabin door A has been opened. After removing cabin door A, restart the calculation

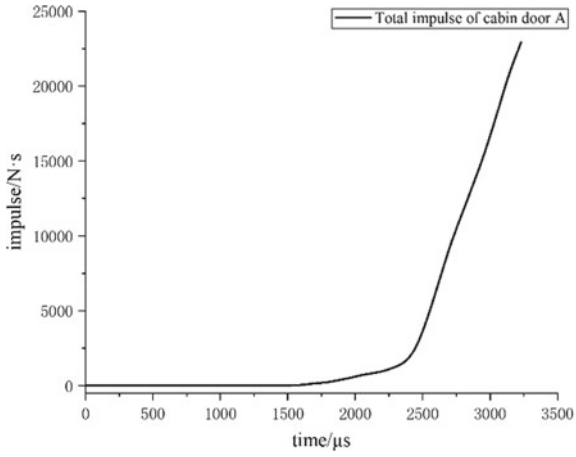

Fig. 17.6 Impulse history of cabin door A

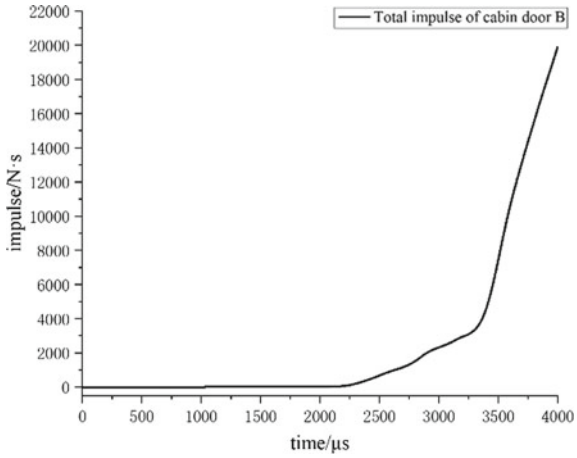

Fig. 17.7 Impulse history of cabin door B

from t = 3113 μs. In the same way, the total impulse history curve of cabin door B is output, as shown in Fig. 17.7. It can be seen from Fig. 17.7 that when t = 2085 μs, the impulse of cabin door B starts to increase; when t = 3350 μs, the impulse of cabin door B starts to increase rapidly; when t = 4004 μs, the total impulse of cabin door B reaches 20000 N·s, so it is considered that cabin door B has been opened. After removing cabin door B, restart the calculation from t = 4004 μs.

As shown in Fig. 17.8, the air pressure distribution diagram of the explosion process under the working condition of the door is output. It can be seen that the detonation wave spreads spherically. The detonation wave first reaches the upper bulkhead, which is impacted and displaced. Then, due to the restriction of the bulkhead, the propagation of detonation wave is blocked, and the pressure of the reflected detonation wave is significantly higher than that of the previous shock wave, which is about twice as high as that of the previous shock wave.

17.4.1 Stress on Cabin Bulkhead

As shown in Fig. 17.9 bulkhead element #1, #2 and #3 in the horizontal direction directly above the explosion centre are respectively taken, and the upper bulkhead centre element #4 is taken.

Output the stress of bulkhead element #1 under the working conditions with and without cabin doors, as shown in Fig. 17.10. It can be found that in the initial stage of explosion, the stress of the bulkhead under the two working conditions is consistent, because the cabin doors A and B have not been destroyed: At t = 400 μs, the shock wave begins to act on the bulkhead, and the stress on the bulkhead increases rapidly; at t = 1400 μs, the stress on the bulkhead reaches the peak value of 902 MPa, and with the shock wave bouncing away, the stress on the bulkhead decreases rapidly. Under the working condition with cabin doors, with the failure of cabin doors A

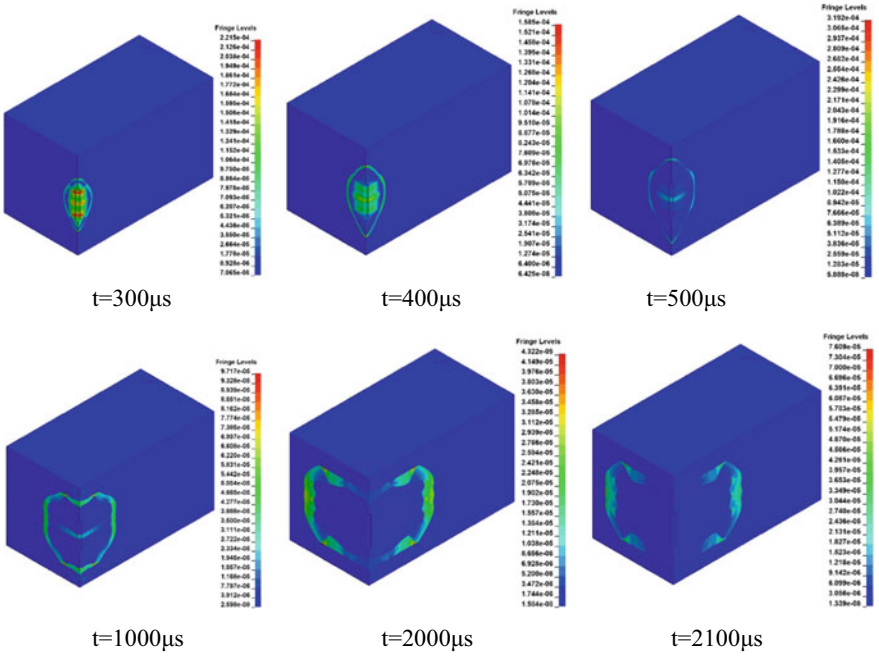

Fig. 17.8 Pressure distribution in air domain during explosion

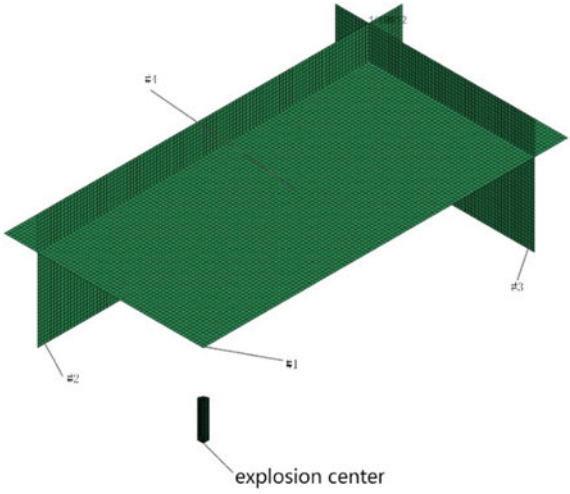

Fig. 17.9 Gauss point setting of bulkhead unit

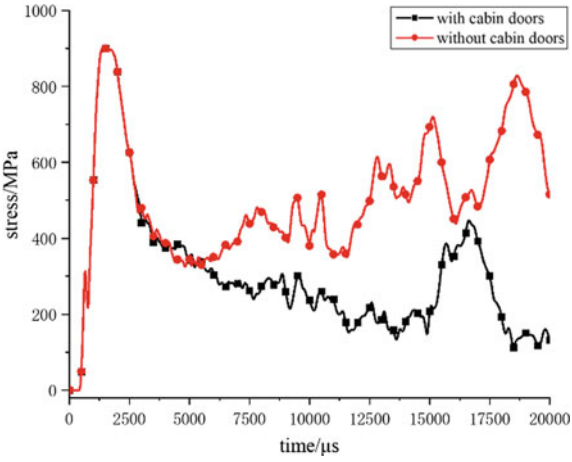

Fig. 17.10 Stress of #1

and B one after another, the pressure relief makes the stress of bulkhead show a downward trend as a whole. Due to the superposition of reflected waves, a higher stress peak occurs again at t = 15,000 μs. Under the working condition of no cabin door, because the cabin is always in a closed state, with the arrival of the shock wave again, the bulkhead stress will not continue to drop, but will remain at a higher level.

The stress of bulkhead elements #2 and #3 with the same output and explosion centre level is shown in Figs. 17.11 and 17.12 respectively. When t = 2500 μs, the shock wave reaches the bulkhead #2, and the stress of #2 starts to increase, and the stress change trend under the two working conditions is basically the same. However, the stress value of #2 under the condition with cabin doors is smaller than that without cabin doors, and the extreme stress value under the condition with cabin doors is 754 MPa, which is 19% lower than the extreme stress value of 932 MPa

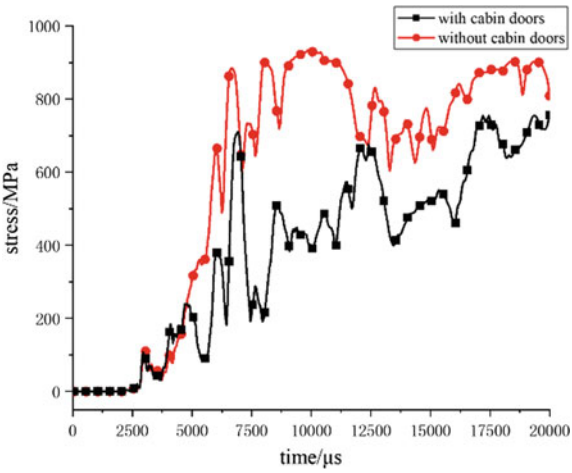

Fig. 17.11 Stress of #2

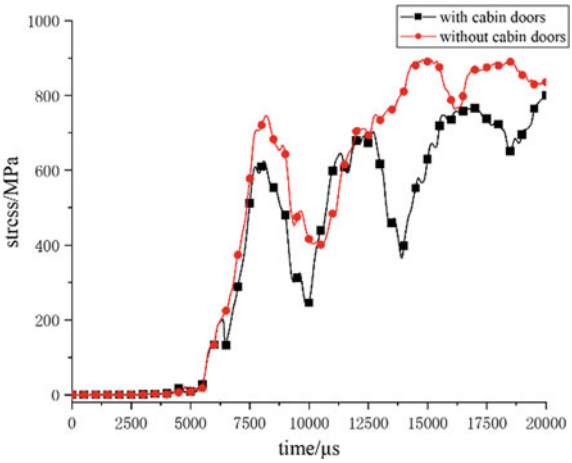

Fig. 17.12 Stress of #3

under the condition without cabin doors. At t = 5200 μs, the shock wave reaches the bulkhead #3, and the stress of #3 begins to increase. The stress extreme value under the condition with cabin doors is 765 MPa, which is 14% lower than the stress extreme value under the condition without cabin doors.

17.4.2 Bulkhead Displacement

When explosives explode in the cabin, the upper bulkhead is repeatedly acted by shock waves, which will have a great impact on the mechanical equipment in the upper cabin [11, 22]. Considering this influence, the velocity curve of the upper bulkhead #1 element is output as shown in Fig. 17.13. The displacement curve is obtained by integrating the velocity curve, as shown in Fig. 17.14. It can be found that, because element #1 is far away from the pressure relief cabin doors, the speed curves under the two working conditions are basically the same before t = 5000 μs; with the doors A and B destroyed one after another, the speed of #1 fluctuated under two working conditions, while the speed of #1 gradually increased with fluctuation under the working condition without doors, and gradually stabilized with fluctuation under the working condition with doors.

Output the velocity curve of bulkhead element #4 far from the explosion centre, as shown in Fig. 17.15, and integrate to obtain the displacement curve, as shown in Fig. 17.16. It can be found that the speed of #4 increases rapidly at t = 2800 μs and increases to 10 m/s within 2600 μs. The speed rises again after keeping this speed for a short time. After that, due to the restriction of the adjacent bulkhead, the speed decreased; with the action of the subsequent shock wave, the velocity experienced a process of rising-falling-rising sharply. For the working condition with doors, within t < 7200 μs, the speed state of #4 is basically the same as that without doors, but

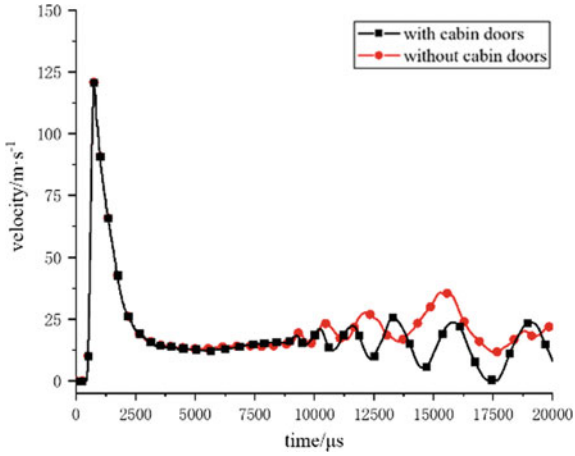

Fig. 17.13 Velocity of #1

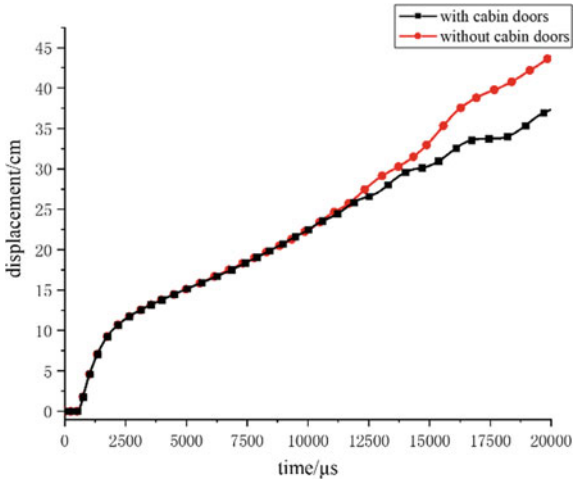

Fig. 17.14 Displacement of #1

with the opening of doors, the cabin pressure gradually decreases, and the speed of #4 starts to decrease after a slight increase, with the extreme value of 34.7 m/s, far less than that of 47.9 m/s without doors.

17.4.3 Corner Pressure

The shock wave propagates from a larger space to a smaller space, and complex interactions will occur in the propagation process, and the stroke convergence wave is much stronger than the spherical wave in the free field, thus greatly enhancing the impact load on the corner [23–25]. After the explosive charge explodes in the

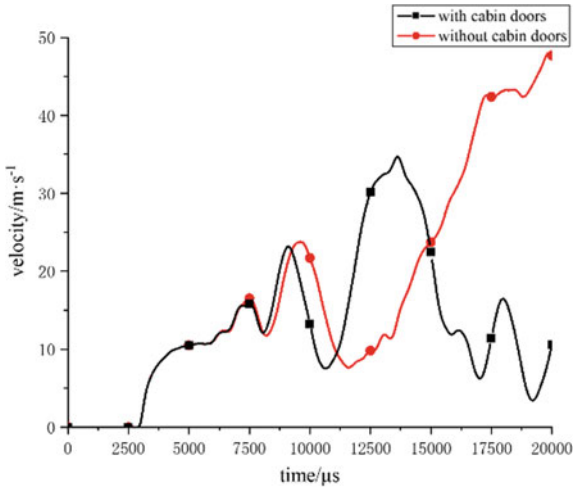

Fig. 17.15 Velocity of #4

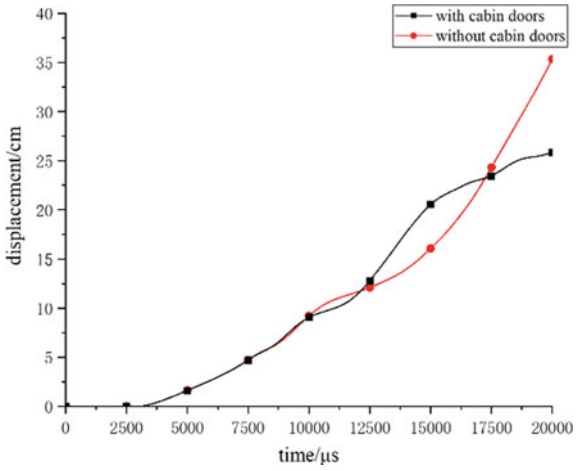

Fig. 17.16 Displacement of #4

centre of the cabin, it will form a shock wave and propagate around. When the shock wave hits the ship structure, it will form a reflection on the surface of the structure. The reflected wave interacts with the shock wave propagating in the corner, and its intensity is much greater than that of the shock wave in the free field [26, 27]. Therefore, the corner becomes the fragile part of the cabin structure, and the pressure at the corner determines the damage of the cabin structure to a certain extent [28, 29]. Output the pressure history curve of air element at the corner, as shown in Fig. 17.17. It can be found that the corner pressure with cabin doors is significantly lower than that without cabin doors, and the extreme pressure is 5.9 MPa, which is 3 MPa lower than the extreme pressure of 8.9 MPa without cabin doors. With the passage of time,

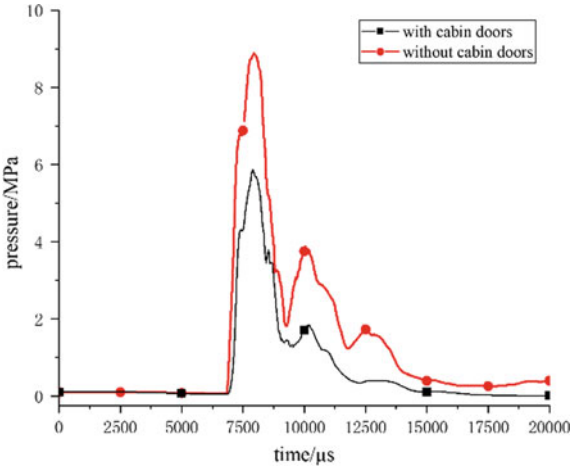

Fig. 17.17 Pressure of air element at corner

the quasi-static pressure [30, 31] can approach to the corner more quickly, and the quasi-static pressure is smaller.

17.5 Conclusion

The explosion of 350 kg TNT in the cabin was simulated by LS-DYNA. On the basis of verifying the reliability of the simulation, the pressure relief effect of the cabin door was mainly analysed, and the conclusions were as follows:

When the door is subjected to a total impulse of 20000 N s, it opens immediately, compared with the door being always closed:

1. The stress variation trend of bulkhead is basically the same, which has no obvious influence on the extreme value of bulkhead stress in height direction, but can significantly reduce the subsequent stress in height direction. It can significantly reduce the stress on the bulkhead in the horizontal direction, and the extreme value of bulkhead stress decreases by 200 MPa in the width direction and 135 MPa in the length direction.
2. The change of bulkhead velocity just above the initiation point is basically the same, but it can stabilize more quickly. The velocity extremum of the upper bulkhead far away from the explosion centre decreases significantly, and the descending speed is faster.
3. It has a significant pressure relief effect, and the extreme value of air pressure at the corner is reduced from 8.9 to 5.9 MPa, which has a certain protective effect on the corner structure.

References

1. Z. Zhang, S. Wu, Development of surface warship terminal defense system and new concept weapon system. Sci. Technol. Rev. **38**(21), 103–109 (2020)
2. M. Blade, Block II rolling airframe missile defeats incoming target in US Navy test. Naval Forces **3**, 34–35 (2016)
3. Y. Sun, et al., *Explosion Action and Charge Design* (National Defense Industry Press, 1987)
4. H. Hou, X. Zhu, Z. Mei, Study on the blast load and failure mode of ship structure subject to internal explosion. Explos. Shock Waves (02), 151–158 (2007)
5. B. Yan, X. Peng, J. Pan, Investigation of the response of broadside protection structure subjected to internal blast loading. J. Ship Mech. **13**(01), 107–114 (2009)
6. W. Yu, et al., *Ship Damage Chart* (National Defense Industry Press, 1991)
7. G. Zhao, *Engineering Mechanics of Armor Penetration* (Weapons Industry Press, 1992)
8. A.G. Piersol, J.A. Zara, J.L. Gubser et al., *Evaluation of the Harpoon Missile Captive Flight and Aircraft Gunfire Vibration Environments* (PA, USA, Inst of Environ Sci, Philadelphia, 1976)
9. Y. Yang, X. Li, X. Wang, Analysis model of explosion shock wave propagation and superposition in cuboid airtight structure. J. Milit. Technol. **37**(08), 1449–1455 (2016)
10. H. Zhai, J. Su, Z. Li et al., Measuring method for wall pressure of cabin with inner explosion. J. Vib. Meas. Diagn. **38**(5), 1069–1074 (2018)
11. J. Wang, L. Zhu, T.X. Yu, et al., *Saturation Impulse in Cabin Explosion* (International Society of Offshore and Polar Engineers, 2020)
12. X. Kong, W. Wu, X. Li, et al., Numerical simulation of explosion in ship cabin. China Ship Res. **4**(04), 7–11 (2009)
13. Z. Du, X. Li, Numerical simulation of warship broadside protective structure rupture under inner explosion. J. Ship Mech. **3**(11), 453–461 (2007)
14. H. Hou, X. Zhu, Z. Mei, Failure mode analysis of cabin explosion load and cabin plate frame structure. Explos. Impact (02), 151–158 (2007)
15. B. Yan, X. Peng, J. Pan, Study on the response of side protection structure under cabin explosion load. Ship Mech. **13**(01), 107–114 (2009)
16. M. Zhang, *Simulation Research on Anti-implosion of Ship Cabin Structure* (China Academy of Ship Research, 2018)
17. G.R.C.W.H. Johnson, A constitutive model and data for metals subjected to large strains, high strain rates and high temperatures, in *Proceedings of the 7th International Symposium on Ballistics*, 1983
18. K. Ho Choi, X. Gu, et al., Study on calibrating JWL parameters of explosives by BP neural network and cylinder energy model. J. Explos. 1–9 (2021)
19. S.N. Dang, et al., *Explicit Dynamic Analysis Based on ANSYS/LS-DYNA 8.1* (Tsinghua University Press, 2005)
20. X. Lin, *Study on Structural Damage Characteristics and Impact Response Law Under Cabin Explosion* (Harbin Engineering University, 2020)
21. Y. Xin, S. Shi, P. Cheng, et al. Comparison of empirical formulas and numerical simulation of explosion shock wave propagation in air. Sichuan Arch. **27**(5), 71–73 (2007)
22. X. Wu, J. Liu, J. Wang, et al., Experimental research on damaging characteristics of cabin model attacking from shipboard direction under close-in underwater explosion. Explos. Shock Waves **40**(11) (2020)
23. Y. Li, et al., *Explosive Mechanics* (Science Press, 1992)
24. X. Bai, X. Li, Y. Yang, Study on calculation model and distribution characteristics of explosion shock wave overpressure in enclosed space. Blasting Mater. **44**(03), 22–26 (2015)
25. C. Xing, E. Tang, D. Liang, et al., Experimental study on overpressure characteristics of explosion shock wave in confined space. J. Shenyang Univ. Sci. Technol. **36**(01), 33–37 (2017)
26. X. Jiao, *Study on Damage Effect Evaluation Method of Multi-compartment Structure Under Implosion Load* (North University of China, 2020)

27. V.R. Feldgun, Y.S. Karinski, I. Edri et al., Prediction of the quasi-static pressure in confined and partially confined explosions and its application to blast response simulation of flexible structures. Int. J. Impact Eng **90**, 46–60 (2016)
28. L. Wu, H. Hou, X. Zhu et al., Numerical simulation on inside load characteristics of broadside cabin of defensive structure subjected to underwater contact explosion. Acta Armamentarii **38**(1), 143–150 (2017)
29. V.A. Gorev, *Deformation of Beam Structures in an Internal Explosion, Moscow, Russia, 2020* (IOP Publishing Ltd., 2020)
30. X. Fan, L. Zhang, X. Wang, *Study on Theoretical Calculation of Quasi-static Pressure for Aluminized Explosive in Confined Space, Beijing, China, 2021* (IOP Publishing Ltd, 2021)
31. Q. Sun, Q. Dong, S. Yang et al., Effects of quasi-static pressure on dynamic elastic response of spherical vessels under internal blast. Chin. J. Energ. Mater. **27**(8), 698–707 (2019)

Chapter 18
Catalytic Performances of rGO-MFe_2O_4 (M = Ni, Co and Zn) for Pyrolysis of Ammonium Perchlorate

Xiaoting Hou, Ming Zhang, Fengqi Zhao, Hui Li, Yingying Zuo, and Ruiqin Li

Abstract Pyrolysis property of ammonium perchlorate (AP) are significance to the combustion properties of AP-based propellant. This study will seek to disclose the effects of the graphene-ferrite nanocomplex (rGO-MFe_2O_4, M = Ni, Co and Zn), fabricated via the facile one-pot solvothermal method, for AP pyrolysis. Among them, the rGO-$CoFe_2O_4$ own outstanding catalytic property for AP pyrolysis, and the high decomposition peak temperature (T_{HDP}) of AP + rGO-$CoFe_2O_4$ were decreased by 57.4 °C compared with pristine AP. Results of this study are helpful to understand the catalytic property and mechanism of rGO-MFe_2O_4 for AP pyrolysis.

18.1 Introduction

The properties of solid propellant is closely related to the combat effectiveness and survivability of rocket and missile engines. As the energy source of solid propellant, the oxidant used has an important impact on the combustion and energy performance of propellant [1–3]. Ammonium perchlorate (AP) is widely used as oxidant in solid

X. Hou · M. Zhang · F. Zhao (✉) · H. Li · R. Li
Science and Technology on Combustion and Explosion Laboratory, Xi'an Modern Chemistry Research Institute, Xi'an 710065, China
e-mail: zhaofqi@163.com

X. Hou
e-mail: hxt-1986@163.com

M. Zhang
e-mail: zhangm3210@163.com

H. Li
e-mail: lihui204s@163.com

R. Li
e-mail: lrq072019@163.com

X. Hou · Y. Zuo · R. Li
Shanxi North Xing'an Chemical Industry Co, Ltd., Taiyuan 030008, China
e-mail: 675898806@qq.com

A. Gany and X. Fu (eds.), *2021 International Conference on Development and Application of Carbon Nanomaterials in Energetic Materials*, Springer Proceedings in Physics 276,
https://doi.org/10.1007/978-981-19-1774-5_18

propellant because of its high oxygen content, good stability and low price [4–7]. In addition, the pyrolysis performance of AP has an important influence on the combustion property of AP-based propellant.

Nano metal oxides has excellent effect on the pyrolysis of oxidant, which can significant decrease the pyrolysis temperature and activation energy of oxidant [7–9]. Among various metal oxides, iron oxides present outstanding activity for AP pyrolysis [10–15]. The pyrolysis performance of AP, before and after mixed with Fe_2O_3 were studied using DSC. The results showed the positive effect of Fe_2O_3 on AP pyrolysis and AP based propellant combustion. Additionally, the bimetallic iron oxides own the better activity on pyrolysis of AP owing to the synergistic interactions of different metals [16]. Nevertheless, the large surface energy of nanoparticles promote their agglomeration, which has an adverse impact on their catalytic performance.

Dispersed on graphene surface can effectively inhibit the agglomeration of nanoparticles, and the excellent inherent properties of graphene are beneficial for pyrolysis of AP [7, 16–20]. The enhance catalytic properties of graphene-iron oxide nanocomplex for AP decompostion has been confirmed [19]. However, the effects of grpahene-ferrite nanocomplex on the deomposition of AP is rarely reported and needs to be revealed. Therefore, this study will try to reveal the effect of rGO-MFe_2O_4 manufactured by simple one pot solvothermal method for AP pyrolysis. Based on this, the rGO-MFe_2O_4 with best activity for AP pyrolysis is illustrated, and the mechanism is analyzed.

18.2 Experiment

18.2.1 Materials

The reagents for rGO-MFe_2O_4 preparation have analytical purity. Single layer graphene oxide (GO) was purchased from Xianfeng nano-material technology Co., Ltd of Nanjing. Ferric nitrate nonahydrate ($Fe(NO_3)_3{\cdot}9H_2O$), cobalt nitrate hexahydrate ($Co(NO_3)_2{\cdot}6H_2O$) nickelnitrate hexahydrate ($Ni(NO_3)_2{\cdot}6H_2O$), zinc nitrate hexahydrate ($Zn(NO_3)_2{\cdot}6H_2O$), and sodium hydroxide (NaOH) were provided by Aladdin Inc. AP is obtained from Xi'an Modern Chemistry Research Institute.

18.2.2 Preparation of rGO-MFe_2O_4 (M = Ni, Co and Zn)

Ultrasonic dispersion of GO in ethanol solution (1 $mg{\cdot}mL^{-1}$), and the ethanol solution of $Fe(NO_3)_3{\cdot}9H_2O$ (10 mmol) was added. Then, a certain amount of $Zn(NO_3)_2{\cdot}6H_2O$, $Co(NO_3)_2{\cdot}6H_2O$ and $Ni(NO_3)_2{\cdot}6H_2O$ were added in above solutions, respectively. After that, the pH value of the solutions was regulated to 10 by NaOH aqueous

solution. The reactants were reacted in 50 ml Teflon sealed autoclaveand at 180 °C for 24 h. After cooling to room temperature, the rGO-MFe_2O_4 nanocomplex were fabricated after washing, drying and grinding.

18.2.3 Characterization

The microstructure of the prepared rGO-MFe_2O_4 were characterized by Scanning Electron Microscope (SEM, Quanta600). The structure of rGO-MFe_2O_4 was studied using X-Ray Diffraction (XRD, EMPYREAN, PANayltical) equipment. DSC (NETZSCH STA449F3) was used to study the catalytic properties of rGO-MFe_2O_4 for AP pyrolysis with N_2 atmosphere of 50 mL min^{-1}. The mixture (1.0 ± 0.1 mg, the mass ratio of rGO-MFe_2O_4 to AP is 1:5) was placed in an Al_2O_3 crucible and tested at 5, 10, 15 and 20 °C min^{-1} in 50–500 °C. The kinetic parameter were obtained by Kissinger and Ozawa methods.

18.3 Result and Discussion

18.3.1 Composition and Morphology Analyses

The microstructure of rGO-MFe_2O_4 nanocomplex was disclosed by SEM and TEM methods, and the imagines are shown in Fig. 18.1. The maps show the uniform dispersion of MFe_2O_4 on graphene surface, indicating the formation of rGO-MFe_2O_4 nanocomplex. In addition, the HRTEM images of rGO-$CoFe_2O_4$, rGO-$NiFe_2O_4$ and rGO-$ZnFe_2O_4$ (Fig. 1g–i) show that the inter planar distances of lattice fringes are 0.248, 0.250 and 0.247 nm, respectively, which is related to the (311) plane of MFe_2O_4.

The structure of the prepared rGO-MFe_2O_4 were studied using XRD, and the results are shown in Fig. 18.2. The appearance of peaks of MFe_2O_4 in XRD curves of rGO-MFe_2O_4, which confirmed the successful fabrication of rGO-MFe_2O_4 [16, 17].

18.3.2 Catalytic Performance Analysis

The pyrolysis property of AP, catalyzed by rGO-MFe_2O_4 (M = Ni, Co and Zn) nanocomplex, were studied using DSC, and the data are shown in Fig. 18.3 and Table 18.1. The synthesized rGO-MFe_2O_4 (M = Ni, Co and Zn) have a positive effect on the pyrolysis of AP, and the effects are significantly different. The T_{HDP} of AP are 366.6, 351.5 and 310.2 °C respectively, reduced by 37.7, 52.8 and 94.1 °C

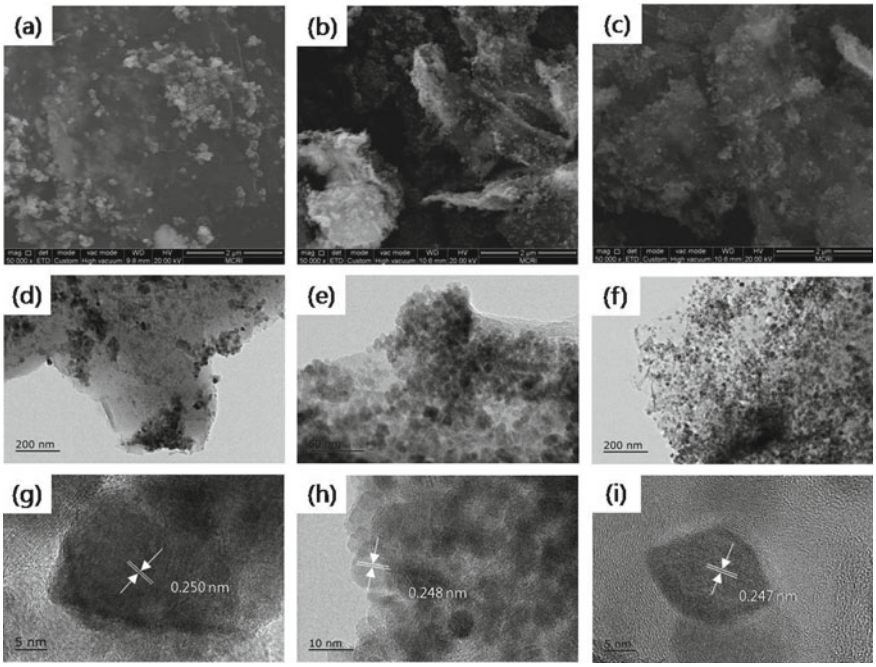

Fig. 18.1 SEM (**a**–**c**), TEM (**d**–**f**) and HRTEM (**g**–**i**) imagines of rGO-$NiFe_2O_4$ (**a**, **d** and **g**), rGO-$CoFe_2O_4$ (**b**, **e** and **h**) and rGO-$ZnFe_2O_4$ (**c**, **f** and **i**) nanocomplex

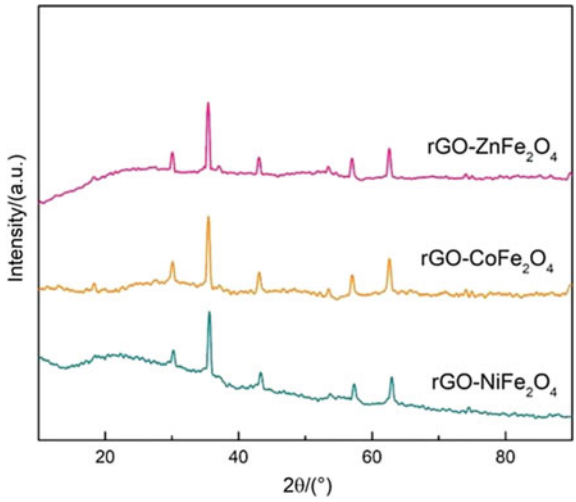

Fig. 18.2 XRD results of rGO-MFe_2O_4 nanocomplex

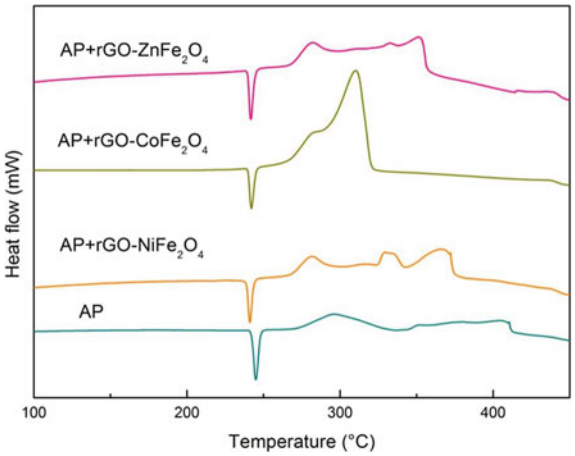

Fig. 18.3 DSC results of AP at 10 °C·min^{-1}

Table 18.1 Decomposition peak temperature of AP catalyzed by rGO-MFe_2O_4 (M = Ni, Co and Zn) nanocomplex

Oxidant	Catalysts	T_{LDP} (°C)	$T_H T_{HDP}$ (°C)
AP	/	296.3	404.3
	rGO-$CoFe_2O_4$	281.0	310.2
	rGO-$ZnFe_2O_4$	282.0	351.5
	rGO-$NiFe_2O_4$	281.5	366.6

compared with AP (404.3 °C), after the adding of rGO-$NiFe_2O_4$, rGO-$ZnFe_2O_4$ and rGO-$CoFe_2O_4$,. The outstanding property of rGO-$CoFe_2O_4$ is closely related to the synergistic interaction of Co and Fe. In addition, the outstanding property of rGO is also conductive to the pyrolysis of AP.

Additionally, the kinetic data of AP, catalyzed by preferred rGO-$CoFe_2O_4$, were calculated using Kissinger and Ozawa models (Table 18.2). The parameters show that the apparent activation energies (E_a) of AP decreases obviously after mixing with

Table 18.2 Kinetic data of AP obtained using Kissinger and Ozawa models

Catalyst	T_P (°C)	Kissinger method			Ozawa method	
		E_a (kJ mol^{-1})	LgA (s^{-1})	r	E_a (kJ mol^{-1})	r
/	T_{LTP}	113.05	8.23	0.998	116.48	0.998
	T_{FTP}	162.25	10.33	0.996	163.04	0.997
rGO-$CoFe_2O_4$	T_{LTP}	/	/	/	/	/
	T_{FTP}	146.0	11.0	0.993	148.0	0.994

rGO-$CoFe_2O_4$, which also illustrates the outstanding catalytic property of rGO-$CoFe_2O_4$. The outstanding catalytic property of rGO-$CoFe_2O_4$ for AP pyrolysis makes it a candidate catalyst for propellant containing AP.

18.3.3 Catalytic Mechanism Analysis

The pyrolysis procedure of AP includes the following steps: phase transition, low temperature decomposition (LTD) and high temperature decomposition (HTD). In the process of phase transformation, the crystal of AP changes from orthorhombic to cubic. LTD procedure is a solid-gas multi-phase reaction process. HTD procedure includes the reaction between HNO and NO, and formed N_2O, O_2, Cl_2, H_2O, NO and other products. The previous research shows that the process of electron transfer from ClO_4^- to NH_4^+ is the key step of LTD, and the step of electron transfer from O_2 to O_2^- is the control step of HTD [20]. Compared with other nanocomplex, the better property of rGO-$CoFe_2O_4$ is related to the positive effect of Fe and Co, which is conducive to the electron transfer of LTD and HTD of AP. Additionally, the outstanding thermal conductivity property of rGO help to promote the electron transfer in the decomposition procedures of AP. At the same time, the huge surface area of rGO also contributes to the adsorption and reaction of intermediate products.

18.4 Conclusions

The SEM. TEM and XRD results show the successfully fabrication of rGO-MFe_2O_4 nanocomplex, and the uniform dispersion of MFe_2O_4. In addition, the catalytic properties of rGO-MFe_2O_4 nanocomplex for the AP pyrolysis were revealed using DSC method. The rGO-$CoFe_2O_4$ owns the best performance, with the significantly reduced T_{LDP} and T_{HDP}. The T_{LDP} and T_{HDP} of AP + rGO-$CoFe_2O_4$ are decreased by 15.3 °C and 94.1 °C respectively, compared with AP. The excellent catalytic property of rGO-$CoFe_2O_4$ was also confirmed by kinetic parameters. The outstanding catalytic property of rGO-$CoFe_2O_4$ for pyrolysis of AP are not only owing to the synergistic effects of Fe and Co, but also to the excellent conductivity and surface effect of rGO, which is benefit to the reactions of intermediate products and the key steps of LTD and HTD of AP.

Acknowledgements The financial support by the National Natural Science Foundation of China (Grant number: 52027809) is gratefully acknowledged.

References

1. N.K. Dharmarathne, J.C. Mackie, E.M. Kennedy, M. Stockenhuber, Mechanism and rate of thermal decomposition of hexachlorocyclopentadiene and its importance in PCDD/F formation from the combustion of cyclodiene pesticides. J. Phys. Chem. A (2017)
2. F. Wang, L. Chen, D. Geng, J. Wu, J. Lu, C. Wang, Thermal decomposition mechanism of CL-20 at different temperatures by ReaxFF reactive molecular dynamics simulations. J. Phys. Chem. A **122**(16), 3971–3979 (2018)
3. J.M. Yang, MOF-derived hollow NiO-ZnO composite micropolyhedra and their application in catalytic thermal decomposition of ammonium perchlorate. Russ. J. Phys. Chem. A **91**(7), 1214–1220 (2017)
4. H. Cai, L. Tian, B. Huang, G. Yang, D. Guan, H. Huang, 1,1-Diamino-2,2-dintroethene (FOX-7) nanocrystals embedded in mesoporous carbon FDU-15. Microporous Mesoporous Mater. **170**, 20–25 (2013)
5. M.M. Bishop, N. Velisavljevic, R. Chellappa, Y. Vohra, High pressure-temperature phase diagram of 1,1-diamino-2,2-dinitroethylene (FOX-7). J. Phys. Chem. A **119**(37), 9739–9747 (2015)
6. M. Zhang, F. Zhao, Y. Yang, H. Li, J. Zhang, W. Ma, H. Gao, N. Li, Shape-dependent catalytic activity of nano-Fe_2O_3 on the thermal decomposition of TKX-50. Acta Phys.-Chim. Sin. 35, 0001–0009 (2019)
7. V.G. Kiselev, N.P. Gritsan, Unexpected Primary Reactions for Thermolysis of 1,1-Diamino-2,2-dinitroethylene (FOX-7) Revealed by ab Initio Calculations. J. Phys. Chem. A **118**(36), 8002–8008 (2014)
8. C. Ye, X. Ju, F. Zhao, S. Xu, Adsorption and decomposition mechanism of 1,1-diamino-2,2-dinitroethylene on Al (111) surface by periodic DFT calculations. Chin. J. Chem. **30**(10), 2539–2548 (2012)
9. X.Z. Fan, J.Z. Li, Z.R. Liu, Thermal behavior of 1,1-diamino-2,2-dinitroethylene. J. Phys. Chem. A **111**(51), 13291–13295 (2007)
10. Y. Liu, F. Li, H. Sun, Thermal decomposition of FOX-7 studied by ab initio molecular dynamics simulations. Theoret. Chem. Acc. **133**(10), 1567 (2014)
11. Z. Zheng, J. Xu, J. Zhao, First-principles studies on the thermal decomposition behavior of FOX-7. High Pressure Res. **30**(2), 301–309 (2010)
12. F. He, K.Z. Xu, H. Zhang, Q.Q. Qiu, J.R. Song, F.Q. Zhao, Two new copper-FOX-7 complexes: synthesis, crystal structure, and thermal behavior. J. Coord. Chem. **66**(5), 845–855 (2013)
13. Z.A. Dreger, Y. Tao, Y.M. Gupta, High-pressure vibrational and polymorphic response of 1,1-diamino-2,2-dinitroethene single crystals: Raman spectroscopy. J. Phys. Chem. A **118**(27), 5002–5012 (2014)
14. A. Hu, B. Larade, H. Abou-Rachid, L.S. Lussier, H. Guo, A first principles density functional study of crystalline FOX-7 chemical decomposition process under external pressure. Propellants, Explos., Pyrotech. **31**(5), 355–360 (2006)
15. V.V. Zakharov, N.V. Chukanov, N.N. Dremova, A.D. Chervonnyi, G.V. Shilov, B.L. Korsounskii, N.N. Volkova, High-temperature structural transformations of 1,1-diamino-2,2-dinitroethene (FOX-7). Propellants, Explos., Pyrotech. **41**(6), 1006–1012 (2016)
16. M. Zhang, F. Zhao, Y. Yang, T. An, W. Qu, H. Li, J. Zhang, N. Li, Catalytic activity of ferrates ($NiFe_2O_4$, $ZnFe_2O_4$ and $CoFe_2O_4$) on the thermal decomposition of ammonium perchlorate. Propellants, Explos., Pyrotech. **44**, 1–10 (2019)
17. M. Zong, Y. Huang, H. Wu, Y. Zhao, Q. Wang, X. Sun, One-pot hydrothermal synthesis of RGO/$CoFe_2O_4$ composite and its excellent microwave absorption properties. Mater. Lett. **114**, 52–55 (2014)
18. S. Huang, Y. Xu, M. Xie, H. Xu, M. He, J. Xia, H. Li, Synthesis of magnetic $CoFe_2O_4$/g-C_3N_4 composite and its enhancement of photocatalytic ability under visible-light. Colloids Surf., A **478**, 71–80 (2015)

19. L. Sun, R. Shao, L. Tang, Z. Chen, Synthesis of $ZnFe_2O_4$/ZnO nanocomposites immobilized on graphene with enhanced photocatalytic activity under solar light irradiation. J. Alloy. Compd. **564**, 55–62 (2013)
20. A. Dey, J. Athar, P. Varma, H. Prasant, A.K. Sikder, S. Chattopadhyay, Graphene-iron oxide nanocomposite (GINC): an efficient catalyst for ammonium perchlorate (AP) decomposition and burn rate enhancer for AP based composite propellant. RSC Adv. **5**(3), 1950–1960 (2015)
21. M. Zhang, F. Zhao, Y. Yang, J. Zhang, N. Li, H. Gao, Effect of rGO–Fe_2O_3 nanocomposites fabricated in different solvents on the thermal decomposition properties of ammonium perchlorate. CrystEngComm **20**, 7010–7019 (2018)
22. Y. Yuan, W. Jiang, Y. Wang, P. Shen, F. Li, P. Li, H. Gao, Hydrothermal preparation of Fe_2O_3/graphene nanocomposite and its enhanced catalytic activity on the thermal decomposition of ammonium perchlorate. Appl. Surf. Sci. **303**, 354–359 (2014)
23. Y. Fu, X. Wang, Magnetically separable $ZnFe_2O_4$–graphene catalyst and its high photocatalytic performance under visible light irradiation. Ind. Eng. Chem. Res. **50**(12), 7210–7218 (2011)
24. H. Xia, Y. Qian, Y. Fu, X. Wang, Graphene anchored with $ZnFe_2O_4$ nanoparticles as a high-capacity anode material for lithium-ion batteries. Solid State Sci. **17**, 67–71 (2013)
25. R.S. Booth, L.J. Butler, Thermal decomposition pathways for 1,1-diamino-2,2-dinitroethene (FOX-7). J. Chem. Phys. **141**(13), 134315 (2014)

Chapter 19
Numerical Study on Impact Resistance Load of Explosion Testing Pool

Jian Guan, Muhua Feng, Chuiqi Zhong, and Yuxin Sun

Abstract Because the changing process of underwater explosions is more complicated and more dangerous than explosions in the air, coupled with the rapid development of underwater weapons damage capabilities, underwater explosion research has attracted much attention. In order to study the shock wave propagation and wall stress of the underwater explosion in the pool, this paper used numerical simulation software to establish the calculation model of the explosion pool through the mapping method, and compared with the empirical formula to verified the reliability of the simulation. It was concluded that the explosion shock wave will be reflected in multiple directions and multiple times in the pool. At the junction of each pool wall, due to the stress concentration, the stress was obviously greater than the center area of the pool wall; regardless of the stress concentration area, on the same horizontal line, the closer the observation point is to the burst center, the greater the stress. On the same vertical line, because of the unloading effect of the air–water interface on the shock wave, and the shock wave propagates to the bottom of the pool and continues to propagate to the side wall after reflection, the closer to the pool center but the farther away from the bottom of the pool, the smaller the stress. This article derived the law of underwater explosion shock wave propagation and the law of stress change on the pool wall, which provided a reference for the engineering design of related explosion pools.

J. Guan · M. Feng · C. Zhong · Y. Sun (✉)
National Key Laboratory of Transient Physics, Nanjing University of Science and Technology, Nanjing 210094, Jiangsu, China
e-mail: yxsun01@163.com

J. Guan
e-mail: 15201075133@163.com

M. Feng
e-mail: arthurmu2@126.com

A. Gany and X. Fu (eds.), *2021 International Conference on Development and Application of Carbon Nanomaterials in Energetic Materials*, Springer Proceedings in Physics 276,
https://doi.org/10.1007/978-981-19-1774-5_19

19.1 Introduction

In recent years, underwater explosion has attracted much attention because the changing process of underwater explosion is more complex and more dangerous than that of air explosion, coupled with the rapid development of underwater weapon damage ability. Explosive testing pool, as a necessary platform for explosive damage assessment, is also an important place for completing warhead fragmentation test, underwater explosion damage ability parameter measurement and damage technology research [1–3]. Many scholars often conduct experimental research in explosive tank when studying underwater explosion related issues.

Heaton [4] established different ellipsoid explosive models for underwater explosion calculation, and studied the effects of non-spherical effect and energy radiation loss on the destructive ability of bubbles in the process of bubble movement. Zhang [5] obtained the empirical formula for the total longitudinal strength of hull girder under the action of bubble pulse by using the potential flow theory and combining the influence of bending moments such as wave, rock attack and bubble pulse in the ship's sailing process. Temkin [6] studied the propagation law of the pulsating pressure of the bubbles generated by a small amount of explosive in water, and then analysed the applicability of nonlinear acoustics and pointed out that many nonlinear factors could be ignored in the study of underwater explosion. Taylor [7] studied the generation and propagation process of EGWW generated by explosions in combination with his experiments in water explosion, analysed the applicable scope of linear theory and nonlinear theory, and pointed out that the nonlinear theory should be used in the analysis of shallow water explosion.

Lu et al. [8–12] studied the destruction of reinforced concrete by underwater explosions, and presented the results of a comprehensive computational study of the dynamic response of air-backed RC slabs exposed to UNDEX. Sun et al. [13] obtained the approximate regression formula of the peak pressure of the TNT near-field underwater explosion shock wave in the range of 6 times the charge radius and the aluminized explosive in a certain distance range by fitting the simulation results. Jiang et al. [16] obtained that the target bending angle sine is linear with the radial distance, and the conclusion was well validated by experimental target bending angle data. Rong et al. [20] discovered that the secondary reaction of aluminium powder significantly affected the energy structure distribution of underwater explosions.

In addition, many scholars have studied the dynamic behaviour of underwater explosion bubbles [22–35]. Gan used a simplified open floating slender structure to investigate the dynamic behaviours of the warship [22, 23], and the deformation and damage mechanisms of the simplified open floating slender structure subjected to the underwater explosion are studied using the experiment and the Coupled Eulerian–Lagrange (CEL) method. And the results indicated that the deformation and damage of the simplified open floating slender structure were mainly induced by the bubble, and the damage induced by the shock wave was not obvious. Chung et al. concluded that the whipping phenomenon by underwater explosion was confirmed through experiments and simulation. Through the experimental results and statistical analysis

Table 19.1 TNT material parameters

Density (g cm^{-3})	Detonation velocity (ms^{-1})	A	B	R_1	R_2	W
1.63	6930	3.7e8	3.7e6	4.15	0.9	0.35

of bubble radius, expansion time, pulsation period and bubble boundary motion, Wang et al. [32] clarified the dynamic process of bubble formation in near-water explosions.

This paper studies the method of anti-impact loading of the pool, and analysed the influence of different protection methods on the propagation process of explosion shock wave in the pool, the equivalent stress curve of each observation point on the pool wall, the displacement and acceleration of the pool wall, and finally obtained the most suitable anti-impact load method in the research method, which has a certain reference value for anti-impact and protection of the pool.

19.2 Numerical Calculation Model Settings

19.2.1 Material Model and Parameters

In this paper, AUTODYN (19.0) is used for numerical simulation. It is a commonly used display finite element analysis software. The materials used in the one-dimensional wedge calculation model include water and TNT. The material model is shown below.

19.2.1.1 TNT Material Model

Explosives are described by JWL equation of state, and the equation of state is:

$$P = A\left(1 - \frac{W}{R_1 v}\right)e^{-R_1 v} + B\left(1 - \frac{W\eta}{R_2 v}\right)e^{-R_2 v} + \frac{W E_0}{v} \tag{19.1}$$

Among them, A, B, R_1, R_2, and W are the algebraic parameters of the equation of state, e is the specific internal energy of the explosive, and v is the ratio of the initial density of the explosive to the density after explosion expansion. The specific parameters used are shown in Table 19.1.

19.2.1.2 Constitutive Model of Water

The polynomial equation of state of water varies according to the volume of water.

When water is compressed ($\mu > 0$), its state equation is:

Table 19.2 Material parameters of water

Density (g cm^{-3})	A_1 (kPa)	A_2 (kPa)	A_3 (kPa)	B_0	B_1	T_1 (kPa)	T_2 (kPa)
1	2.2e6	9.54e6	1.46e7	0.28	0.28	2.2e6	0

$$P = A_1\mu + A_2\mu^2 + A_3\mu^3 + (B_0 + B_1\mu)\rho_{\text{water}}e \tag{19.2}$$

When water swells ($\mu < 0$), its state equation is:

$$P = T_1\mu + T_2\mu + B_0\rho_{\text{water}}e \tag{19.3}$$

When the water is in the normal state, that is ($\mu = 0$), its state equation is:

$$P = B_0\rho_{\text{water}}e \tag{19.4}$$

Among them, μ is the ratio of the density of water after deformation (compression or expansion) to the initial density ρ_{water}, A_1 is the bulk modulus, A_2, A_3, B_0, B_1, T_1, T_2 are the constant parameters of the material, the specific parameters are shown in Table 19.2.

19.2.1.3 Riedel Hiermaier Thoma (RHT) Concrete Model

The concrete material adopts the RHT model, which includes five parts: failure surface, elastic limit surface, strain hardening, residual failure surface and damage model, which is especially suitable for studying high damage problems related to underwater explosions. And because of the completeness of the model constitutive equation in the material library, we only need to specify the density, shear modulus, and compressive strength (Table 19.3).

19.2.1.4 Steel Plate Material Model

The steel material model used in this study is 4340 steel, which uses Johnson–Cook (JC) constitutive model and Linear equation of state.

The JC model can effectively reflect the mechanical behaviour of steel under high-strength loads, and is suitable for studying the damage caused by the high-pressure explosion shock wave produced by the underwater explosion in this paper. The yield stress σ_y of the steel plate in the constitutive equation can be expressed as:

$$\sigma_y = \left[A + B(\varepsilon_P)^n\right]\left(1 + C\ln\varepsilon^*\right)\left[1 - (T_h)^m\right] \tag{19.5}$$

In the formula, ε_P is the equivalent plastic strain; ε^* is the equivalent plastic strain rate; A is the yield stress; B is the hardening constant; n is the hardening index; C

Table 19.3 Concrete material parameters

Density (g cm^{-3})	Shear modulus (kPa)	f_c (kPa)	f_t (kPa)	A_1 (kPa)	A_2 (kPa)	A_3 (kPa)	B_0	B_1	T_1 (kPa)	T_2 (kPa)
2.75	1.67e7	3.5e4	3.5e3	3.5e7	3.9e7	9.04e6	1.22	1.22	3.5e7	0

Table 19.4 Steel material parameters

Density (g cm^{-3})	Shear modulus (kPa)	A (kPa)	B (kPa)	n	C (kPa)	m (kPa)	T_m (K)	K (kPa)
7.83	8.18e7	7.9e5	5.1e5	0.26	0.014	1.03	1.793e3	1.6e8

is the strain rate constant of the steel; m is the thermal softening index. T_h is the temperature ratio, which is determined by the following Formula (19.6) through the room temperature T_t and the melting temperature T_m:

$$T_h = \frac{(T - T_t)}{(T_m - T_t)} \tag{19.6}$$

The Linear state equation is as follows:

$$\left.\begin{array}{c} P = K\mu \\ \mu = \frac{\rho}{\rho_0} - 1 \end{array}\right\} \tag{19.7}$$

Among them, K is the bulk modulus. In summary, some parameters of the steel material model are shown in Table 19.4.

19.2.1.5 Equation of State for Air

The state equation of air is the following ideal state equation:

$$P = (\gamma - 1)\rho_{air} e_0 \tag{19.8}$$

Among them, P represents pressure, γ represents adiabatic index, and e_0 is specific internal energy. The specific parameters used are shown in Table 19.5.

19.2.2 Finite Element Model

The overall calculation model of the research object in this paper is shown in Fig. 19.1, where the size of the blue water area is 8000 mm × 4400 mm × 3900 mm, the air thickness at the air–water interface is 100 mm, and the length and width dimensions are the same as the water area. The centre of the spherical explosive is 1900 mm from the water surface and 2000 mm from the bottom of the pool. The steel pool wall is

Table 19.5 Material parameters of air

γ	ρ_{air} (g/cm^3)	e_0 (μJ)
1.4	1.225	206,800

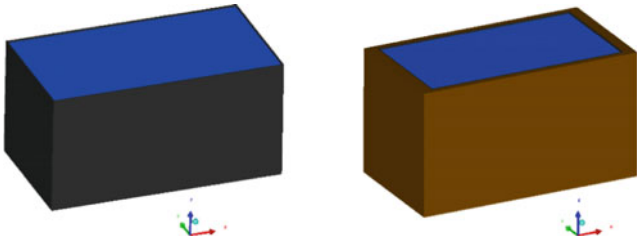

(a) explosion testing pool (b) explosion testing pool as a whole

Fig. 19.1 Calculation model of square explosion pool

close to the water area, with a uniform thickness of 40 mm, and the outer size of the concrete is 9000 mm × 5000 mm × 5000 mm. In this paper, the fluid–solid coupling method is selected. The steel wall and rubber material of the pool are meshed by Lagrange algorithm, and the rest are divided by Euler method.

This article is mainly to study the shock wave propagation in the explosion pool and the anti-explosive impact ability of the protection method, the calculation adopts a quarter model, as shown in Fig. 19.2. The grid size of the model is set to 20 mm. For explosion-related calculations, the grid size is relatively large. Therefore, the mapping method will be used to map the explosion shock wave to the explosion pool calculation model later. A Void Euler domain with a size of 4500 mm × 2500 mm × 5000 mm is established for a quarter model, and the corresponding models of water and air are filled into the Euler domain. The steel plate and concrete are divided by Lagrange grid, and the grid size is 20 mm. The explosive is spherical TNT explosive. Due to the large water area and the comparative analysis of the protective effect in this article, in order to make the protective effect obvious, the charge is set to 3 kg.

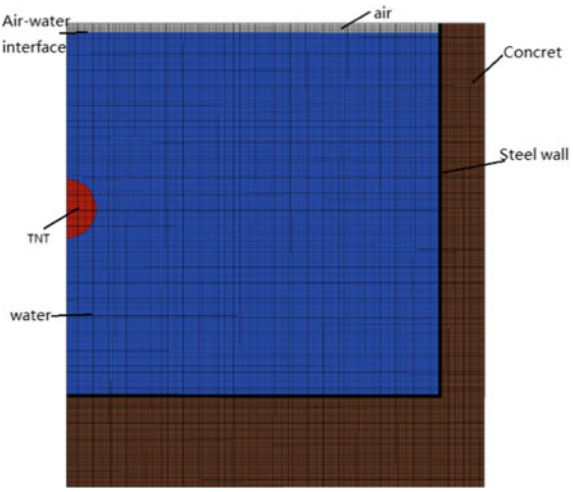

Fig. 19.2 The main view and grid division of the calculation model of the explosion pool

Because the bubble pulsation period is long, and this article mainly studies explosion pressure wave related protection, in order to save calculation time, the numerical simulation process of this article does not consider the effect of bubble pulsation in the process of underwater explosion. In addition, an outflow boundary is added to the Euler domain above the entire pool. The steel wall and the concrete share a joint node, and the automatic fluid–solid coupling processing calculation is used between the Euler domain and the LaGrange. At the same time, in order to reduce the reflection effect of the concrete boundary on the explosion shock wave, the transmission boundary is set on the three outer surfaces of the concrete (right, back and bottom of the figure).

19.3 Calculation Results and Analysis

19.3.1 Build the Mapping Model

In this paper, the one-dimensional explosion model is mapped to the three-dimensional calculation model by using the REMAP technology commonly used in Autodyn software to ensure the calculation efficiency and accuracy. Described according to Zhao, when the depth of the explosive in underwater and charging ratio of the radius of more than 10–20, and the depth of the explosive in underwater and charging the radius ratio of more than 5 ~ 10, the quantity of explosive in underwater explosion shock wave pressure peak value can be regarded as is not affected by the outside world, including the air water interface, and other media such as reflection. The ratio of charge position and charge radius discussed in this paper is greater than the above value, so it can be regarded as free field underwater explosion in a short time.

The wedge model of a 3 kg TNT underwater explosion is shown in Fig. 19.3. Because the explosive initiation position is 2000 mm away from the air–water interface, the water area in the wedge model is 2000 mm long, and the transmission boundary is also added. The explosive radius is 76.02 mm.

When we perform underwater explosion related calculations, we usually use the empirical formula of underwater explosion shock wave summarized by Cole [1], that is, for spherical TNT charges, the shock wave pressure peak value is:

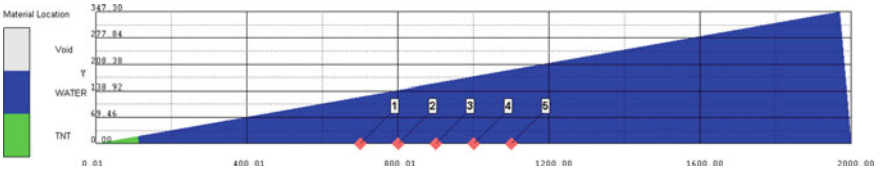

Fig. 19.3 One-dimensional model of 3 kg TNT underwater explosion

Table 19.6 3 kg TNT underwater point initiation pressure peak

The peak pressure (MPa)	Critical distance (mm)				
	700	800	900	1000	1100
Numerical simulation value	128.90	99.60	90.53	77.65	69.79
Empirical formula value	130.42	101.99	89.28	79.26	71.17
Error (%)	1.17	2.34	1.40	2.03	1.94

$$P_m = 44.1\left(\sqrt[3]{W}/R\right)^{1.5}; \quad 6 \le \frac{R}{R_0} \le 12 \tag{19.9}$$

$$P_m = 52.4\left(\sqrt[3]{W}/R\right)^{1.13}; \quad 12 \le \frac{R}{R_0} \le 240 \tag{19.10}$$

In the formula, P_m represents the peak pressure of the shock wave, and the unit is MPa. W is the mass of the explosive in kg; R is the distance from the detonation centre, unit is m; R_0 is the initial radius of the charge, also in m.

In order to verify the accuracy of the 3 kg TNT underwater explosion shock wave propagation simulation calculation, one Gauss point is set at an interval of 100 mm from 700 to 1100 mm from the explosion centre. As shown in Fig. 19.3, since the explosion distance range is 700–1100 mm, the initial radius of the charge is 76.02 mm, calculated according to Formulas (19.9) and (19.10), the simulation results and empirical formula calculation results are shown in Table 19.6. The size of the error can further illustrate the feasibility of the simulation method and parameters used. And because this article is studying the explosion in a limited area, the calculation distance of the shock wave in infinite waters cannot be too long, otherwise part of the reflected wave generated by the shock wave at the air–water interface or the steel wall will be missing. Therefore, when the wedge model is calculated to 0.5 ms, the output file. The calculation model of the explosion pool is written, and the pressure wave distribution at 0.5 ms is shown in Fig. 19.4. At this time, the shock wave is far from reaching 2000 mm, and the impact on subsequent calculations is negligible.

At the same time, because the mapping has undergone a change from a small-size grid to a large-size grid, in order to ensure the correctness of the shock wave propagation after the mapping, a three-dimensional infinite water model as shown in Fig. 19.5 is established, and the above one-dimensional data is mapped to the model, The grid size is divided as 20 mm as the explosion pool, and the infinite water size is 5000 mm × 5000 mm × 5000 mm according to the size of the explosion pool. The model adds one observation point at 2000–4000 mm in the far field, and sets an observation point every 500 mm, and compares the numerical calculation result at the observation point with the result of the empirical formula.

The 3 kg TNT underwater explosion is mapped to the three-dimensional model after 0.5 s. And the pressure curve at each observation point is shown in Fig. 19.6, which shows that the change of shock wave conforms to the empirical law.

According to the empirical Formula (19.10), the empirical formula values at each observation point under this working condition are respectively 36.21 MPa,

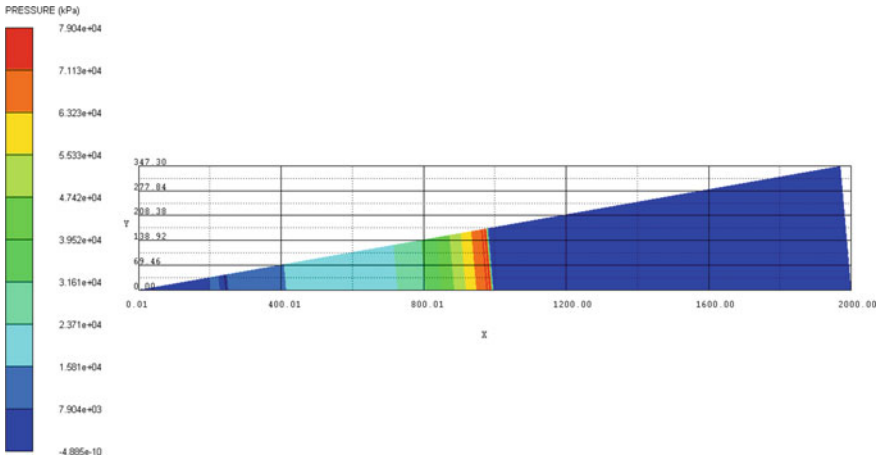

Fig. 19.4 Pressure cloud diagram of 3 kg TNT underwater explosion at 0.5 ms time

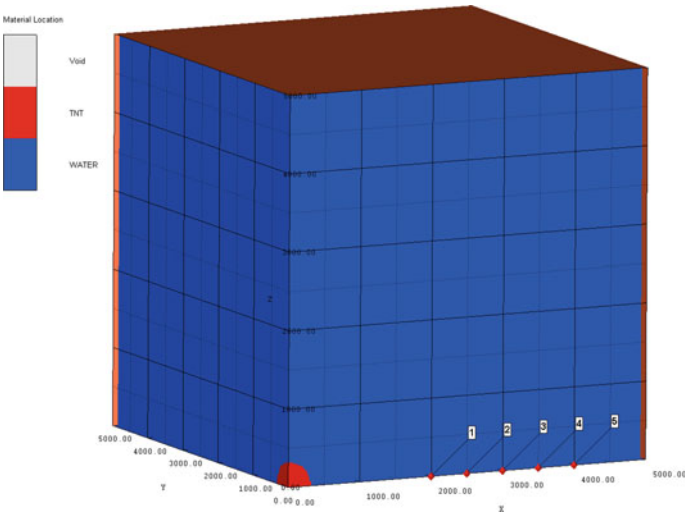

Fig. 19.5 Three-dimensional model of 3 kg TNT explosion in infinite waters

28.14 MPa, 22.90 MPa, 19.24 MPa and 16.55 MPa. By comparing the empirical calculated values with the simulation calculated values, it can be seen that the numerical calculated values are slightly less than the calculated values of the empirical formula. This may be due to the large size of the mapped grid. The error of No. 3 Gaussian point is relatively the largest, which may be caused by the fact that the time interval of data recording is not precise enough, and the moment point of the

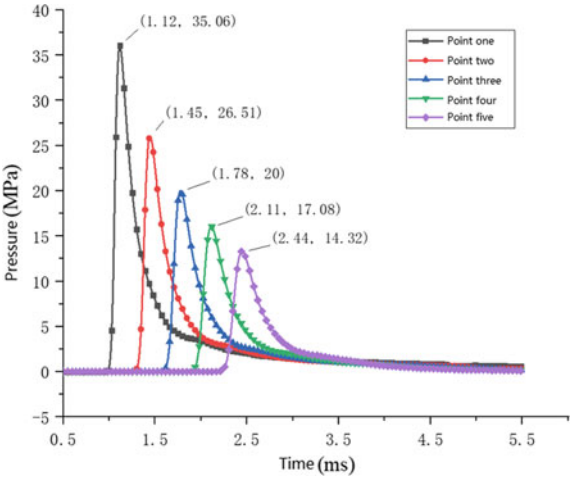

Fig. 19.6 Shock wave pressure variation curve at each observation point

highest pressure is not captured exactly. However, in general, the numerical calculated values fit well with the empirical formula values, and the error has little influence on subsequent studies.

19.3.2 Shock Wave Propagation Process and Pool Wall Stress Analysis

Since this section uses the mapping data of blast shock wave after 0.5 ms, the time mentioned below is added by default to 0.5 ms before the mapping, and the time coordinates of all relevant curves are also starting from 0.5 ms.

On the basis of the model established in Sect. 19.3.1, the 3 kg TNT charge underwater explosion trial calculation is carried out on the explosion pool model without any protective structure. The purpose is to set the Gauss point according to the analysis of the water pressure propagation cloud image and the strain cloud image of the pool wall. The water shock wave pressure cloud chart in the trial calculation simulation is shown in Fig. 19.7. For the convenience of observation, the cloud chart interval of 0.7 and 0.9 ms is 0 ~ 85 MPa, and the interval of the subsequent time is 0 ~ 50 MPa.

From the water pressure cloud diagram, it can be seen that the explosive from the detonation to 0.9 ms is basically similar to an explosion in infinite water, and the explosion shock wave propagates outward in a spherical shape. The shock wave propagated to the air–water interface and the steel plate at the bottom of the pool in about 1.1 ms. Because the density and speed of sound of the air medium are much smaller than that of the water medium, the wave impedance of the air medium is much smaller than that of the water medium. At this time, the reflected wave is mainly generated in the opposite direction to the incident wave, and the value of

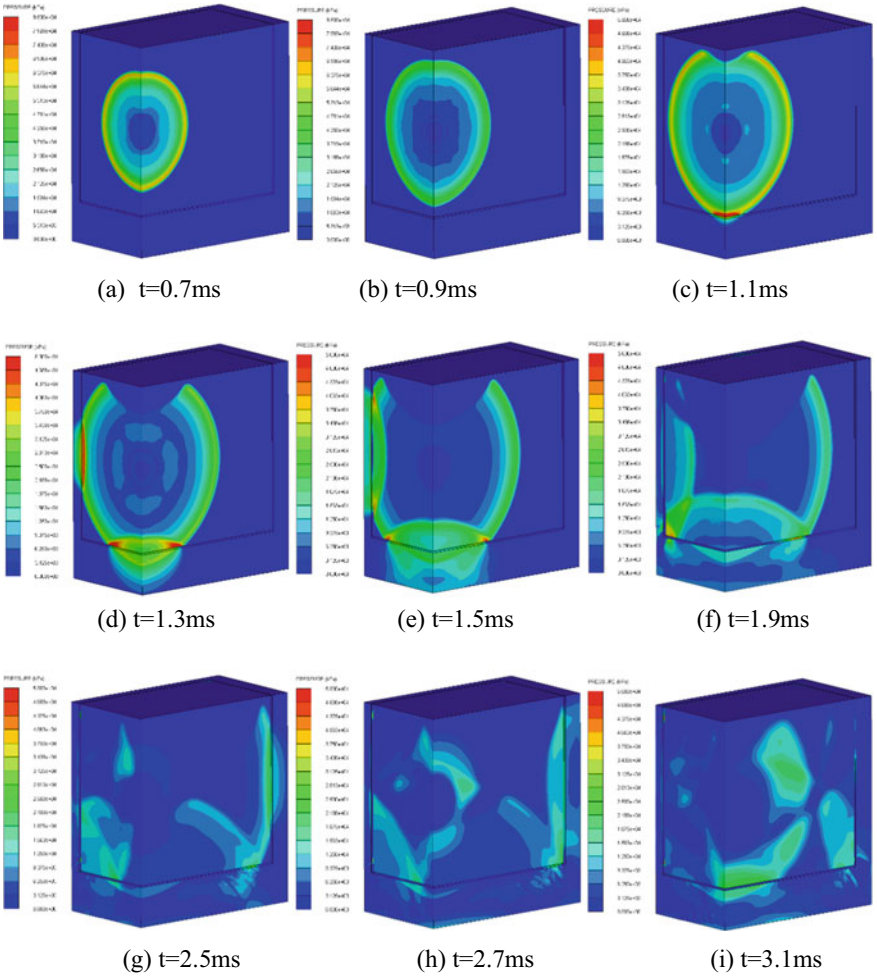

Fig. 19.7 Explosion pressure cloud diagram in a 3 kg TNT explosion pool

the transmitted wave is very small. It can be observed from the figure that when the shock wave propagates to the air–water interface, the reflection occurs and the reflected wave is in the opposite direction. However, due to the pressure display interval problem, the small transmitted wave cannot be observed from the cloud image. At the interface at the bottom of the pool, the wave impedance of the water medium is less than that of the steel medium, so the reflected wave direction is the same as the incident wave. It can be seen that a red high-pressure area does appear at the junction of the steel wall and the water, which continues to propagate downward. It is a transmitted wave. In this case, the transmitted wave is larger than the incident wave.

The three high-voltage areas in Fig. 19.7d are also formed due to the above-mentioned wave impedance difference. However, from the bottom of the pool, it can still be found that there is a reflected wave propagation trajectory that is opposite to the incident wave. This is because underwater explosions are actually the superposition of shock waves in multiple directions. Figure 19.7e–g are mainly the reflection of shock waves propagating to the closer steel wall and the bottom of the pool and the spherical propagation process to the far steel wall. And the shock waves on the left and bottom of the figure meet to form a high pressure zone, and then continue to propagate.

Figure 19.8 is the equivalent stress cloud diagram of the pool wall after the water is hidden. The purpose is to observe the stress change of the steel wall within a short time of explosive explosion. 1.1 ms after the explosive detonated, the bottom of the pool closest to the explosive centre began to produce strain. As the explosion shock wave spreads around in a spherical shape, the stress cloud image on the steel wall also spreads outward in a circular shape, as shown in Fig. 19.8b, c. Figure 19.8d, e show that the superposition of pressure waves at the corners of the two steel walls causes the stress at the corner junction to be superimposed, resulting in a stress concentration zone, as shown in the red area in Fig. 19.8e. The changes in the stress cloud diagrams in Fig. 19.8f, g show that the reflection of shock waves is also reflected in the stress change trend of the steel wall. It can be seen from the last two figures that the stress of the steel wall is reflected in the far wall in the later part of the time, and the maximum stress is at the junction of the three steel plates, because stress concentration will occur in these places. In addition, from Fig. 19.8e, h, it can be found that the closer the steel wall is to the bottom of the pool, the greater the stress, which is mainly caused by the unloading of the shock wave at the air–water interface and the reflection of the shock wave at the bottom of the pool.

According to the above two sets of cloud images, the observation points set for the research object in this paper are designed as shown in Fig. 19.9.

Among them, points 1–5 are the observation points where the water surface of the pool wall moves with the movement of the steel wall, and point 1 is the observation point at the cut-off. Points 1, 2, and 3 are on the same horizontal line as the centre of the charge, with an interval of 1000 mm between them. Points 1, 4, and 5 are on the same vertical line, and the interval is also 1000 mm. The first five Gauss points are mainly used to analyse the impact of the explosion on several locations on the steel wall of the pool within a period of time after the explosive charge, including points 3 and 5 where stress concentration will occur.

Points 6–8 are fixed observation points in the water area to analyse the difference between the shock wave pressure time history curve in the pool and the infinite water area. The three points are on the same horizontal line with the explosion centre, and the distance from the explosion centre is 2000, 3000, and 4000 mm. Observation points 9–12 also follow the steel wall, and the horizontal position and spacing are the same as points 1–3. These 4 points are used to observe the impact of the explosion on the nearby steel wall in a short time after the explosion, and the protection effect of the protection method on the slightly closer explosion.

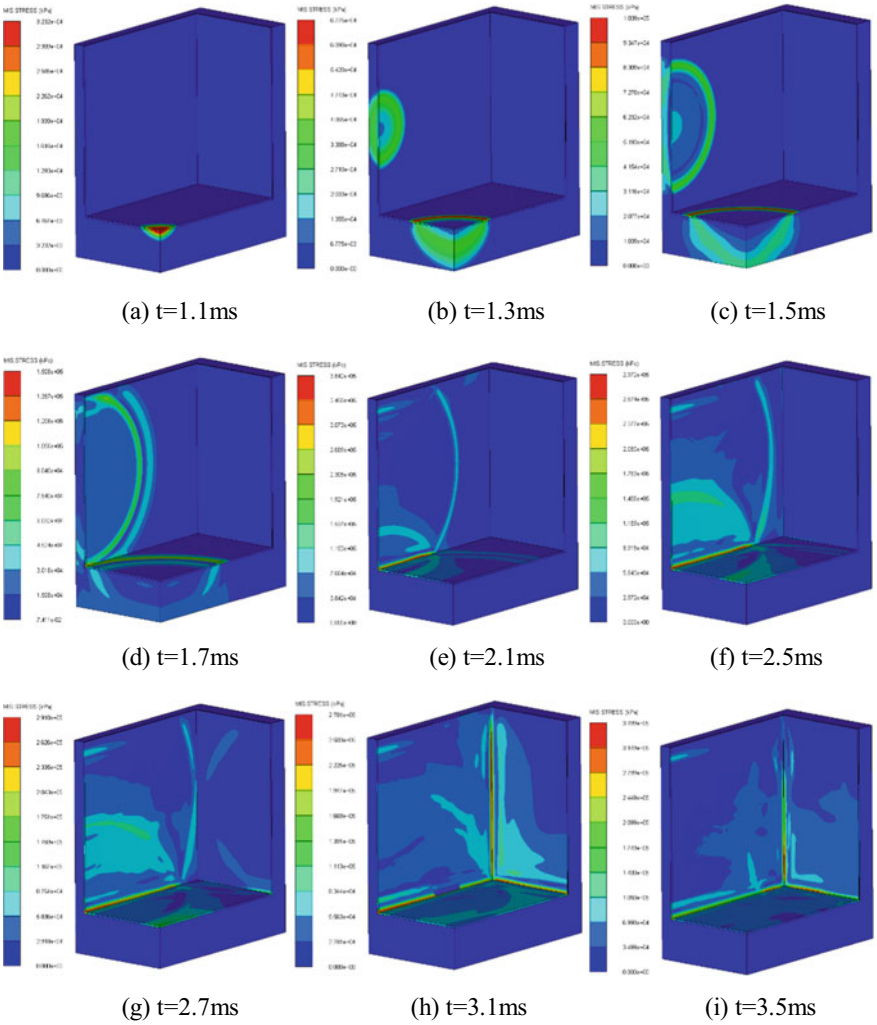

(a) t=1.1ms (b) t=1.3ms (c) t=1.5ms

(d) t=1.7ms (e) t=2.1ms (f) t=2.5ms

(g) t=2.7ms (h) t=3.1ms (i) t=3.5ms

Fig. 19.8 Equivalent stress cloud diagram of the explosion pool wall in a 3 kg TNT pool

19.3.3 Analysis of Results at Each Observation Point

19.3.3.1 Comparison of Water Pressure Time History Curves

After adding observation points according to Fig. 19.9, calculate the explosion of 3 kg TNT in the center of the pool. First, use No. 6–8 to study the general law of shock wave propagation in the pool. The time-pressure fitting curve corresponding to each point is shown in Fig. 19.10a, and the pressure at each point when exploding in infinite waters under the same conditions as in Sect. 19.3.2 compare the curves.

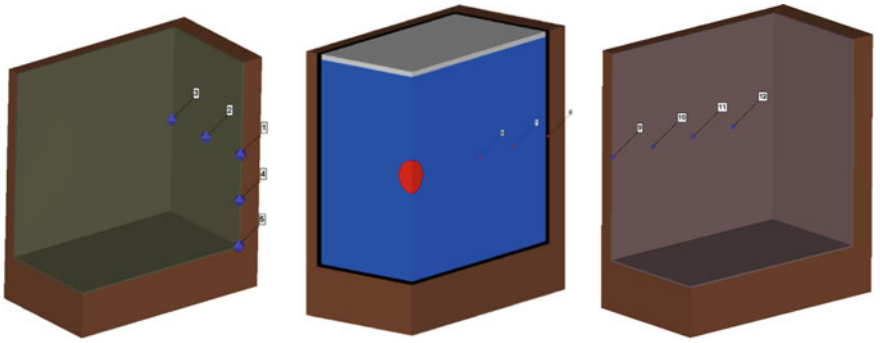

Fig. 19.9 Gauss point setting of calculation model

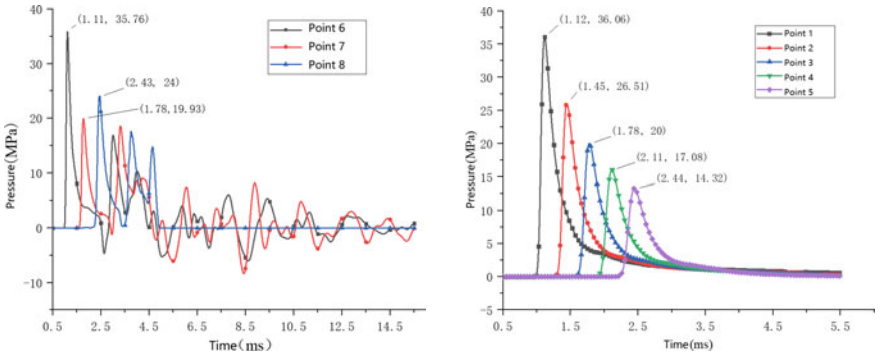

(a) The explosion in the pool (b) the explosion in the infinite water

Fig. 19.10 Pressure time history curve at the observation point

Among them, the observation points 6, 7, and 8 in Fig. 19.10a correspond to the observation points 1, 3, and 5 in Fig. 19.10b. Because the explosion shock wave will produce multi-directional and multiple reflections when it propagates to the pool wall, the pressure change curve of the shock wave in the later period of the situation in Fig. 19.10a is intricate. But the same in the two situations is that the first wave at about 3.5 Ms at 6–8 points also tends to 0, which is the same as Fig. 19.10b. In addition, the time and size of the first arrival at the peak of No. 6 and No. 1, and No. 7 and No. 3 are almost the same. However, although observation points No. 8 and No. 5 reached the peak time at the same time, the pressure of observation point No. 8 was significantly larger than that of point 5, and even exceeded the shock wave pressure at point 7 where the burst distance was closer. It can be found from Fig. 19.7g that it is because the reflected wave is generated at the No. 8 measuring point around 2.43 ms, and the shock wave is superimposed, making the peak size “abnormal”.

19.3.3.2 Analysis of Equivalent Stress Curve at Each Point of the Pool Wall

Figure 19.11 is the equivalent stress (MIS.STRESS) time history curve of each observation point on the steel wall far away from the explosion centre. Due to the stress concentration at points 3 and 5, the peak stress is larger than other observation points. In order to facilitate the observation of the individual fitting, the stress curve of the measuring points 1–5 is also separately fitted below.

The arrival times of the first wave peaks at observation points 1, 2 and 4 are similar. The stress at point 1 is the smallest because its peak arrival time is the earliest. The impact of this instantaneous shock wave on the stress of the steel wall has not been transmitted to 2 and 4, and when the shock wave propagates to points 2 and 4 over time, a superimposed peak will be generated. This leads to higher stress peaks at observation points 2 and 4 than at measuring point 1.

From the point of view of the maximum stress at each measuring point, point 4 > 1 > 2. This can be inferred that when explosives explode in a pool, the closer the blast distance, the greater the peak stress of the steel wall on the same horizontal line. In the vertical direction, because of the unloading of the shock wave by the air–water interface and the reflection of the bottom of the pool, the stress peak at point 4, which is closer to the bottom of the pool but farther from the explosion centre, is greater. The first wave crest at No. 5 observation point is slightly higher than No. 3 observation point (the highest wave crests at the two points are considered to be two, and both have been marked in the figure), and the stress peak is much larger than No. 3. This is also because the No. 3 observation point is closer to the water surface, and the shock wave propagates to the air–water interface to unload. At the same time, the shock wave propagating to the bottom of the pool has a greater impact on measuring point No. 5, which can also be seen from Figs. 19.9 and 19.10.

According to the preliminary analysis of the stress field on the side wall of the pool in Sect. 19.2.2, the stress on the pool wall closer to the burst centre has reached its peak 6 ms before. The equivalent stress time history curve at observation points

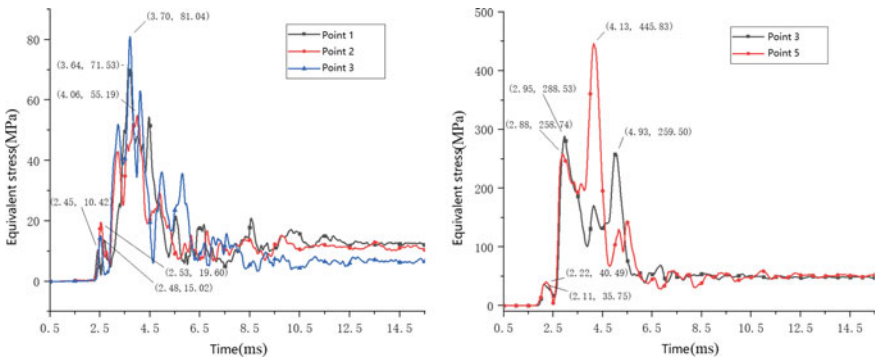

Fig. 19.11 Equivalent stress curve at observation points 1–5

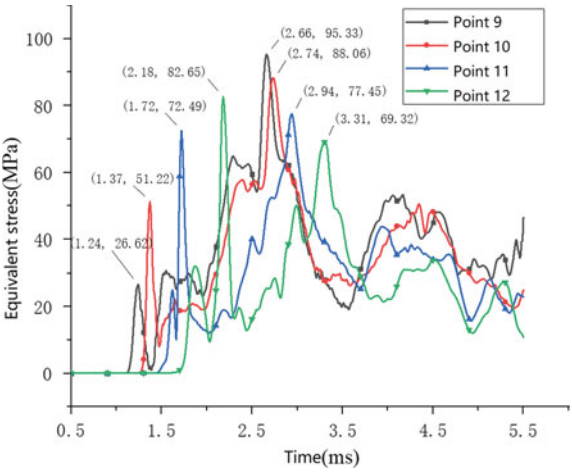

Fig. 19.12 Equivalent stress curve of observation point 9–12

9–12 on the closer pool wall is shown in Fig. 19.12. It shows that, combined with the stress cloud diagram of the steel wall at different times in Fig. 19.8, the time to reach the first wave crest at each position is matched. It can also be found that the farther the explosion distance, the greater the stress of the first wave crest (the second wave crest of observation points 11 and 12 in the figure is regarded as the first wave crest, which may be due to the large difference in the time of stress superposition. Crests). This is because during the initial propagation of the shock wave, with the increase of time, the later the arrival position is more affected by the stress superposition, which makes the stress higher. The second marked peak is generated by the superposition of the shock wave near the pool wall and the pool bottom and propagated to each observation point, as shown in the last four pictures in Fig. 19.8. The second wave crest is also the maximum stress at each point. The maximum stress at each point is as follows: the closer the observation point is to the burst centre, the larger the corresponding stress peak.

19.3.3.3 X-Direction Displacement and Acceleration Analysis of Pool Wall

A Fig. 19.13 is a time history curve of the overall displacement and acceleration of the pool wall farther from the explosion centre in the X direction. According to the analysis of the shock wave propagation process in Sect. 19.2.2, the explosion shock wave has been transmitted to the steel wall 2.5 ms before, which corresponds to the time when the steel wall starts to produce large displacements.

During the entire explosion process, the maximum displacement of the far wall in the X direction was 0.65 mm, and after 6.5 ms, it was basically maintained at about 0.53 mm. The value of the highest peak acceleration and the corresponding time are marked in the acceleration chart. The acceleration is the ratio of pressure to

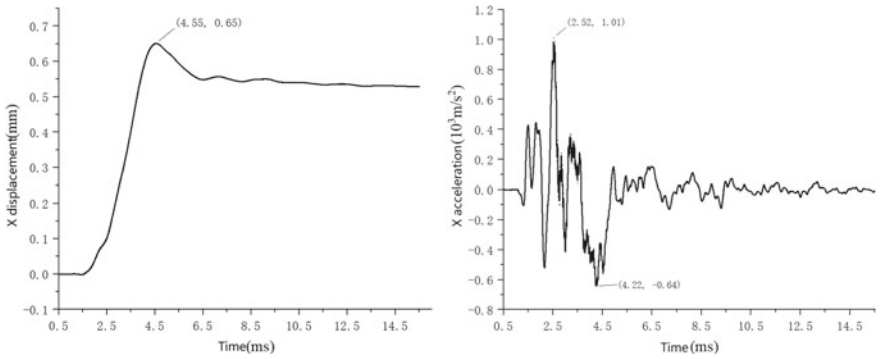

Fig. 19.13 X-direction displacement and acceleration time history curve of the farther pool wall

mass, so the larger the acceleration value, the greater the pressure on the steel wall as a whole. It can be seen from this figure that the maximum forward acceleration of the pool wall is 1.01e3 (ms^{-2}), and the maximum reverse acceleration is 0.64e3 (ms^{-2}). These parameters will be used as indicators for the impact load analysis of the protective structure below to analyse and compare the protective capabilities of each method.

19.4 Summary

In this article, a series of simulation studies of underwater explosions in a pool were carried out, and the propagation process of underwater shock waves and the stress on the pool wall were analysed. The main conclusions are as follows:

(1) The calculation model and related material parameters of the explosion pool were introduced. The explosives were filled into the model by mapping method, and the correctness of the mapping method was verified by comparing the pressure peak at each point after mapping with the empirical formula.
(2) Perform trial calculations on the pool explosion without protection, briefly analysed the explosion shock wave propagation process in the pool and the stress change process of the pool wall, and determined the key points that need to be observed. At the same time, the difference between the shock wave propagation process between the explosion in the pool and the explosion in infinite water, the stress time history curve at each point of the steel wall, the displacement and acceleration of the far steel wall in the X direction were analysed at these observation points.
(3) It was concluded that the explosion shock wave will be reflected in multiple directions and multiple times in the pool. At the junction of each pool wall, due to the stress concentration, the stress was obviously greater than the centre area of the pool wall; regardless of the stress concentration area, on the same

horizontal line, the closer the observation point is to the burst centre, the greater the stress. On the same vertical line, because of the unloading effect of the air–water interface on the shock wave, and the shock wave propagates to the bottom of the pool and continues to propagate to the side wall after reflection, the closer the burst centre but the farther away from the bottom of the pool, the greater the stress. small. The maximum displacement in the X direction of the farther pool wall was 0.65 mm, the maximum forward acceleration was 1.01e3 (ms^{-2}), and the maximum reverse acceleration was 0.64e3 (ms^{-2}).

References

1. R.H. Cole, *Underwater Explosions* (Princeton University Press, Princeton, NJ, 1948)
2. B.V. Zamyshlyayev, Dynamic loads in underwater explosion. AD-757183 (1973)
3. J.A. Deruntz et al., *The Underwater Shock Analysis (USA Version 3), A Reference Manual* (Defense Nuclear Agency, Washington, DC, 1971)
4. K.C. Heaton, Effects of non-sphericity and radiative energy loss on the migration of the gas bubble from underwater explosion. AD-A166823 (1986)
5. N. Zhang, The evaluation method of the longitudinal strength of a ship hull subjected to the bubble load in underwater explosion. Chin. J. Ship Res. **9**(6), 14–18, 25 (2014)
6. S. Temkin, Review of the propagation of pressure pulse produced by small underwater explosive charges. AD-A194642 (1988)
7. G.I. Taylor, The pressure and impulse of submarine explosion waves on plates. Ministry of Home Security Report, FC235 (1941)
8. L. Hai, X. Ren, Computational investigation on damage of reinforced concrete slab subjected to underwater explosion. Ocean Eng. **195** (2020)
9. X. Huang, J. Hu, X. Zhang et al., Bending failure of a concrete gravity dam subjected to underwater explosion. J. Zhejiang Univ. Sci. A **21**(12), 976–991 (2020)
10. S.-G. Lee, J.-S. Lee, H. Chung et al., Validation of underwater explosion response analysis for airbag inflator using a fluid-structure interaction algorithm. Int. J. Naval Archit. Ocean Eng. **12**, 988–995 (2020)
11. Z.-L. Tian, Y.-L. Liu, A.-M. Zhang et al., Jet development and impact load of underwater explosion bubble on solid wall. Appl. Ocean Res. **95** (2020)
12. Y.P. Sone Oo, H. Le Sourne, O. Dorival, *Development of Analytical Formulae to Determine the Response of Submerged Composite Plates Subjected to Underwater Explosion* (Springer Science and Business Media Deutschland GmbH, Yokohama, Japan, 2021), pp. 270–290
13. Y. Sun, J. Tian, Z. Zhang et al., Experiment and numerical simulation study on the near-field underwater explosion of aluminized explosive. Zhendong yu Chongji/J. Vib. Shock **39**(14), 171–178 (2020)
14. L. Ge, A.-M. Zhang, S.-P. Wang, Investigation of underwater explosion near composite structures using a combined RKDG-FEM approach. J. Comput. Phys. **404** (2020)
15. M. Gerdooei, M.J. Rezaei, H. Ghaforian Nosrati, Improving the performance of a multi-layer armored system subjected to shock loading of an underwater explosion (2020)
16. X. Jiang, W. Zhang, D. Li et al., Experimental analysis on dynamic response of pre-cracked aluminum plate subjected to underwater explosion shock loadings. Thin-Walled Struct. **159** (2021)
17. M. He, A. Zhang, Y. Liu, Interaction of the underwater explosion bubbles and nearby double-layer structures with circular holes. Baozha Yu Chongji/Explos. Shock Waves **40**(11) (2020)
18. T.-H. Phan, V.-T. Nguyen, W.-G. Park, Numerical study on strong nonlinear interactions between spark-generated underwater explosion bubbles and a free surface. Int. J. Heat Mass Transf. **163** (2020)

19. J. Liu, T. Tang, Z. Wei et al., Experimental research in damage effects of high-piled wharf under underwater explosion. Baozha Yu Chongji/Explos. Shock Waves **40**(11) (2020)
20. J. Rong, Z. Zhao, Z. Feng et al., Experimental study of underwater explosion performance of RDX-based aluminized explosive. Binggong Xuebao/Acta Armament. **40**(11), 2177–2183 (2019)
21. J. Zhang, S. Wang, X. Jia et al., An engineering application of Prosperetti and Lezzi equation to solve underwater explosion bubbles. Phys. Fluids **33**(1) (2021)
22. N. Gan, L.T. Liu, X.L. Yao et al., Experimental and numerical investigation on the dynamic response of a simplified open floating slender structure subjected to underwater explosion bubble. Ocean Eng. **219** (2021)
23. N. Gan, X.L. Yao, L.T. Liu et al., Research on overall damage characteristics of a hull girder under explosion bubble collapse. Ocean Eng. **188** (2019)
24. F. Gao, C. Ji, Y. Long et al., Numerical investigation of the dynamic response of CWC structures subjected to underwater explosion loading. Ocean Eng. **203** (2020)
25. J. Chung, Y. Seo, Y.S. Shin, Dynamic and whipping response of the surface ship subjected to underwater explosion: experiment and simulation. Ships Offshore Struct. **15**(10), 1129–1140 (2020)
26. N.-N. Liu, A.-M. Zhang, Y.-L. Liu et al., Numerical analysis of the interaction of two underwater explosion bubbles using the compressible Eulerian finite-element method. Phys. Fluids **32**(4) (2020)
27. Y. Chen, X. Yao, X. Cui, A numerical and experimental study of wall pressure caused by an underwater explosion bubble. Math. Probl. Eng. **2018** (2018)
28. Y. Chen, X. Yao, Dynamics of underwater explosion bubble near free surface. Ship Build. China **57**(3), 65–71 (2016)
29. X. Cui, Y. Chen, B. Su et al., Characteristics of wall pressure generated by bubble jets in an underwater explosion. Baozha Yu Chongji/Explos. Shock Waves **40**(11) (2020)
30. C.-Y. Hsu, C.-C. Liang, A.-T. Nguyen et al., A numerical study on the underwater explosion bubble pulsation and the collapse process. Ocean Eng. **81**, 29–38 (2014)
31. N. Zhang, Z. Zong, W. Zhang, Dynamic response of a surface ship structure subjected to an underwater explosion bubble. Mar. Struct. **35**, 26–44 (2014)
32. S.-S. Wang, M. Li, F. Ma, Dynamics of the interaction between explosion bubble and free surface. Wuli Xuebao/Acta Phys. Sin. **63**(19) (2014)
33. C.-C. Liang, T.-L. Teng, C.-Y. Hsu et al., *A Numerical Study of Underwater Explosion Bubble* (Trans Tech Publications Ltd, XiShuangBanNa, China, 2013), pp. 1734–1737
34. Z. Zhang, C. Wang, A.-M. Zhang et al., SPH-BEM simulation of underwater explosion and bubble dynamics near rigid wall. Sci. China Technol. Sci. **62**(7), 1082–1093 (2019)
35. H. Liang, Q. Zhang, R. Long et al., Pulsation behavior of a bubble generated by a deep underwater explosion. AIP Adv. **9**(2) (2019)

Chapter 20
Mechanical Behavior of Cast Plastic-Bonded Explosives

Hai Nan, Chunyan Chen, Yufan Bu, Yulei Niu, and Xuanjun Wang

Abstract Influential factors on the mechanical behavior of cast plastic-bonded explosives (PBXs) were investigated through compression tests in this paper. Different mechanical behaviors of PBXs were observed when PBXs were prepared with different curing temperatures, different molecular weights and different NCO/OH values of hydroxyl-terminated polybutadiene (HTPB). Based on stress–strain curves of PBXs, mechanical behavior is divided into brittle fracture and ductile fracture. The results show that PBX ranges from ductile fracture to brittle fracture when the curing temperature increases from 50 to 100 °C, molecular weights decrease from 4000 to 1500 and NCO/OH value increases from 0.8 to 1.4. Besides, the microstructure of PBXs was characterized with scanning electron microscopy (SEM), indicating that energetic particles were damaged by the brittle fracture.

20.1 Introduction

With the rapid development of energetic materials, cast plastic bonded explosives (PBXs) have attracted tremendous attention because of their good dimensional and thermal stability, and low vulnerability. But the sensitivity of PBX, in which micron-sized explosive crystals are embedded in a polymer binder matrix, is enhanced due to the cracks in the energetic crystals [1, 2], which may also generate "hot spots" in PBX loads [3]. To avoid these cracks by enhancing the mechanical properties of PBX, various methods have been developed, including introducing bonding agent to PBX and adjusting the crosslinking network of the polymer matrix [4–7].

The cracks in the energetic crystals are related to not only the mechanical property of PBX but also the mechanical behavior [8–10]. Palmer and Thompson [11, 12] demonstrated that through a quasi-static test, PBX was extensively deformed,

H. Nan · X. Wang (✉)
High-Tech Institute of Xi'an, Xi'an 710025, P.R. China
e-mail: wangxj503@sina.com

H. Nan · C. Chen · Y. Bu · Y. Niu
Xi'an Modern Chemistry Research Institute, Xi'an 710065, P.R. China

A. Gany and X. Fu (eds.), *2021 International Conference on Development and Application of Carbon Nanomaterials in Energetic Materials*, Springer Proceedings in Physics 276,
https://doi.org/10.1007/978-981-19-1774-5_20

and thus the distortion and damage of the energetic particles were avoided, and the generation of PBX "hot spots" was restrained. Thus far, the changeable mechanical behavior of thermosetting hydroxyl-terminated polybutadiene (HTPB)-based cast PBX has been investigated. The results of quasi-static and dynamic compression tests on PBX showed that the mechanical behavior of PBX is strongly influenced by strain rate and temperature [13–16]. However, the factors that influence the mechanical behavior of the thermosetting PBX have not been examined. Therefore, the effects of curing temperature, molecular weights and NCO/OH value of HTPB on the mechanical behavior of PBX were investigated in this paper. The findings are significant for the mechanical behavior control and safety of PBX.

20.2 Experiment

20.2.1 Materials

HTPB was utilized as the binder in PBX. The considered molecular weights of HTPB were 1500, 2800, 3440, and 4000, and the corresponding hydroxyl values were 1.55, 0.78, 0.61, and 0.59 mmol g^{-1}, respectively. Samples were obtained from Liming Chemical Research Institute and were pre-degassed for 4 h at 80 °C. 2,4-toluene diisocyanate (TDI) was purchased from Beijing Chemical Reagent Company and used as the curing agent. TDI was pre-redistilled before use. Dioctyl adipate (DOA) was employed as the plasticizer. Aluminum (Al) and 1,3,5-trinitroperhydro-1,3,5-triazine (research department explosive (RDX)) were utilized as energetic particles.

20.2.2 Preparation of Elastomeric Films

HTPB and TDI were stirred for 10 min at 60 °C in a vertical kneading machine (2 L) to generate a liquid–liquid mixture. Triphenyl bismuth (TPB, 0.01%) was then added to the liquid–liquid mixture and stirred for 30 min at 60 °C to produce thermosetting HTPB slurry. The slurry was then poured into a Teflon mold (12 mm × 10 mm × 2 mm) to fabricate elastomeric films. The films were cured at 60 °C until the hardness stabilized. Finally, the films were removed from the Teflon mold.

20.2.3 Preparation of Cast PBX

HTPB and DOA were stirred for 10 min at 60 °C in a vertical kneading machine (2 L) to generate a liquid–liquid mixture. Al and RDX were then added to this mixture and stirred for 1 h at 60 °C to produce a solid–liquid mixture. TPB and TDI were added

Table 20.1 Composition of HTPB-based PBX

Sample	Composition
PBX1(HTPB1500)	RDX/Al/HTPB/DOA/TDI/TPB (64.00/20.00/6.99/8.00/1.01/0.01)
PBX2(HTPB2800)	RDX/Al/HTPB/DOA/TDI/TPB (64.00/20.00/7.45/8.00/0.55/0.01)
PBX3(HTPB3440)	RDX/Al/HTPB/DOA/TDI/TPB (64.00/20.00/7.56/8.00/0.44/0.01)
PBX4(HTPB4000)	RDX/Al/HTPB/DOA/TDI/TPB (64.00/20.00/7.57/8.00/0.43/0.01)

to the solid–liquid mixture and stirred for 20 min at 60 °C to obtain the PBX slurry. The PBX slurry was then poured into the mold (Φ20 mm × 20 mm) and cured at 60 °C until the elastic modulus of PBX was constant. The PBX was then removed from the stainless steel mold. Table 20.1 shows the details of the formulation of the HTPB-based PBX.

20.2.4 Characterization

The dumbbell-shaped elastomer underwent tensile tests with an Instron Universal Testing Machine (Model 4505) at a crosshead speed of 500 mm/min. The tests followed the GJB770B-2005 test method, and the final test values were derived from an average of at least five specimens at 25 °C.

The compression tests on PBX followed the GJB 772A-97 test method under the following conditions: a temperature of 25 °C and a crosshead speed of 10 mm min^{-1}. The samples were cut in the dimensions of 20 mm × 20 mm × 3 mm.

The elastic modulus was calculated based on the compression stress–strain curves when the strain was 0.3%, and the elastic modulus was calculated using Eq. 20.1 as follows:

$$E = \sigma/\varepsilon \tag{20.1}$$

where E is the elastic modulus, and σ and ε are stress and strain, respectively.

Crosslink density was calculated based on the swelling parameters of the networks [16]. The elastomers that measured 7 mm × 7 mm × 3 mm were placed in toluene for 48 h. They were then removed from the solvent and weighed after the solvent was wiped from the elastomer surface. Subsequently, the solvent absorbed by the elastomer was released by placing the swollen elastomer in a vacuum oven at 110 °C for 3 h. The weight of the deflated elastomer was then determined. The volume fraction of the elastomer in the swollen specimen (V_1) was calculated based on the weights of the swollen and deflated specimens and the densities of the elastomers. The crosslink density of the elastomer (V_e) was obtained from using Eq. 20.2:

$$V_e = -\left[\ln(1 - V_1) + V_1 + \chi V_1^2\right] / V_s\left(V_1^{1/3} - V_1/2\right) \tag{20.2}$$

where V_s is the molar volume of the solvent and χ is the elastomer-solvent interaction parameter.

The microstructure of the compressed PBX was examined through a scanning electron microscope (SEM).

20.3 Results and Discussion

20.3.1 Mechanical Behavior of the Cast PBX

Figure 20.1 shows the results of compression tests, respectively. The failure mechanisms were characterized by brittle and ductile fractures based on stress–strain curves of PBXs. When the PBXs display a brittle fracture, stresses are often linearly related to strain in the long term. Stress has a nonlinear relationship with strain only when the load approaches maximum stress. In the event of sudden brittle fracture, stress is rapidly maximized in mechanical tests. The stress in ductile fracture is linearly related to strain in the short term and is nonlinearly associated with strain over the long term. Following crack formation, strain increases and the crack can widen gradually over a period of time. Severe deformation causes the PBX to resemble a "drum". Moreover, fractures are typically initiated at its center.

To further investigate the fracture mechanism of PBX, the RDX, post-loaded RDX and microstructure of the post-compression PBX were characterized with SEM, as indicated in Figs. 20.2a, b and 20.3, respectively. The crack can evidently be observed on the post-loaded RDX. However, no crack arises in PBXs with ductile fractures, this finding can be attributed to PBXs ductile deformation, which mainly originates from binder strain after PBXs are loaded. The severe deformation of the binder effectively protects the energetic particles from damage in the event of ductile fracture. On the contrary, the brittle fracture with small deformation generates some cracks and damages energetic particles because stress concentration appears on the hard RDX.

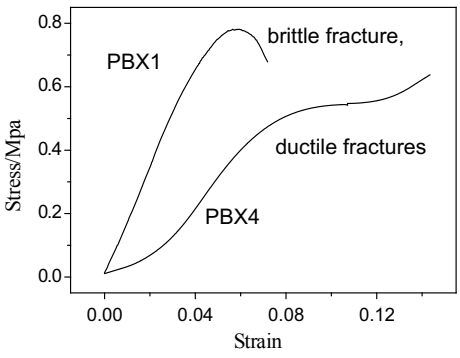

Fig. 20.1 Stress–strain curves of PBX4 in compression test

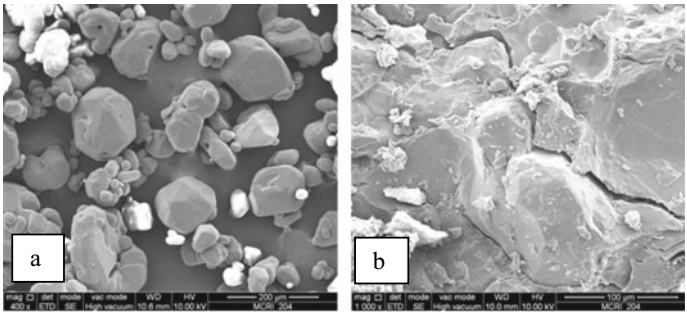

Fig. 20.2 SEM images of **a** RDX and **b** post-loaded RDX

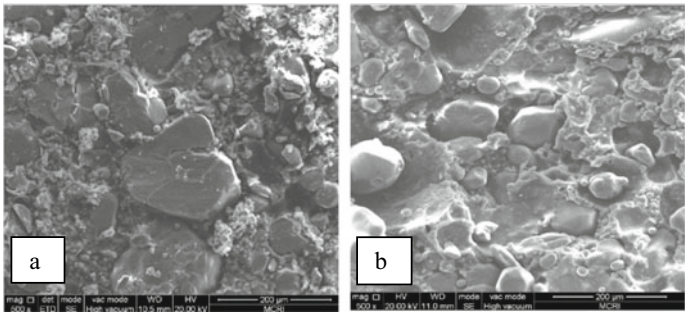

Fig. 20.3 **a** Brittle fracture and **b** ductile fracture of PBX

20.3.2 Effects of Curing Temperature on the Mechanical Behavior of Cast PBX

Curing temperature affects the mechanical behavior of PBX since a low curing temperature diminishes the elastic modulus and enhances compression strain. Figure 20.4 and Table 20.3 respectively depicts the compression curves and corresponding mechanical properties of PBX that were completely cured at different temperatures. The binder cured at 50 °C displays a large elongation at break and a low tensile strength, as shown in Table 20.2. The severe deformation in the binder absorbs the compression energy and plugs the crack in the PBX cured at 50 °C, which is in turn induced by compression stress. In the event of ductile fracture, the crack gradually widens but mends quickly, generating a platform in the stress–strain curve. The stress then increases with the strain, and the stress acting on the energetic particles is broken down by the deformation of the binder.

As indicated in Fig. 20.4, the increase in curing temperature induces an increase in the elastic modulus of PBXs and a decrease in its elongation at break. This result is attributed to the high crosslinking density of the binder and the high curing stress

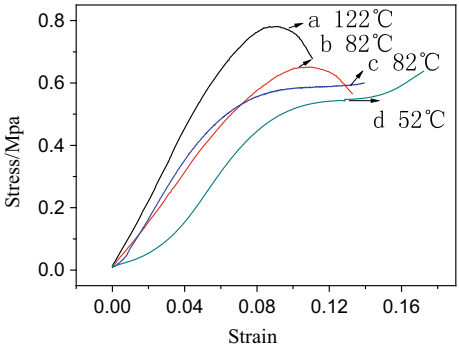

Fig. 20.4 The compression curves of PBX cured at different curing temperatures

Table 20.2 Mechanical properties of the elastomer at different curing temperature

Curing temperature (°C)	Tensile strength (MPa)	Elongation at break (%)	Crosslink density (mol/m^3)	Curing time (h)
50	1.01	181	80	144
60	1.17	128	85	123
70	1.19	112	97	90
80	1.23	101	102	75
100	1.26	95	107	50

Table 20.3 Crosslink density of the HTPB with different molecular weights

The binder	Crosslink density of the polymer (mol/m^3)
HTPB(1500)	112
HTPB(2800)	87
HTPB(3440)	81
HTPB(4000)	79

produced by increased curing velocity at high temperatures [17–19]. As a result, PBX experiences some brittle fractures.

The PBX thus displays ductile and brittle fracture behavior when the curing temperatures are 50 °C and 100 °C, respectively.

20.3.3 Effects of Molecular Weights on the Mechanical Behavior of Cast PBX

The cast PBXs that contains HTPB with different molecular weights were cured at 60 °C until the elastic modulus stabilized. The mechanical behavior of the PBXs

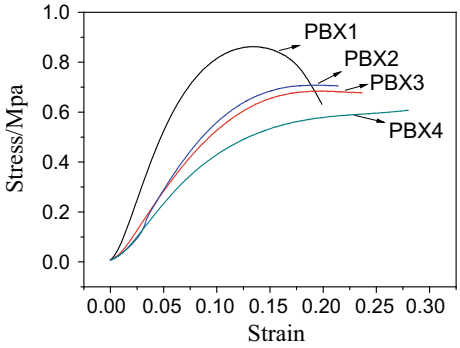

Fig. 20.5 Compression curves of PBX that contains HTPB at different molecular weights

was tested under a compression load, and the resultant test curves are presented in Fig. 20.5. When the molecular weights of the binder are low, PBX displays brittle fracture behavior and increased compression stress. The mechanical behavior of PBX transitions from brittle to ductile fracture with the increase in HTPB molecular weights, which is mainly attributed to the different crosslinking density, curing velocity and stress. Table 20.3 reveals that low molecular weight HTPB displays a high crosslinking density, moreover, excellent linear correlations are obtained between crosslink density and mechanical properties. The high crosslink density can increase stress and reduce elongation at break [7]. Meanwhile, curing velocity and stress of low molecular weight HTPB are higher than those of high molecular weight HTPB [18–20], which also renders the PBX brittle.

20.3.4 Effects of NCO/OH Value on the Mechanical Behavior of Cast PBX

With NCO/OH value ranging from 0.8 to 1.4, the mechanical behaviors of PBX change (Figs. 20.6 and 20.7). Compression strength increases and elongation at break

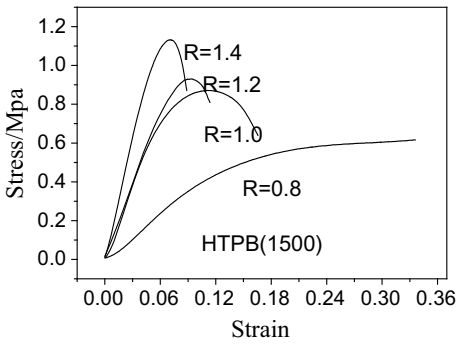

Fig. 20.6 The compression stress–strain curves of PBX including HTPB(1500) (R represents the NCO/OH value)

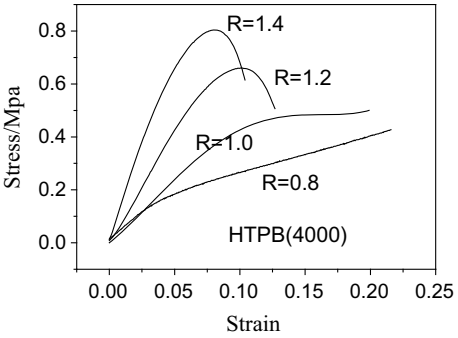

Fig. 20.7 The compression stress–strain curves of PBX including HTPB(4000) (R represents the NCO/OH value)

decreases with NCO/OH value. When NCO/OH value is 1.4 and 0.8, PBX obviously show brittle fractures and ductile fractures respectively. Effects of NCO/OH value on mechanical behavior are attributed to crosslink density of the binder, because the crosslink density of the polymer increases with NCO/OH value.

20.4 Conclusions

(1) The mechanical behavior of cast PBXs were investigated through compression tests. PBXs displayed two types of rupture behavior, namely, brittle and ductile fractures.
(2) The mechanical behavior of this cast PBX transitioned from ductile to brittle fracture, when curing temperature increased from 50 to 100 °C or NCO/OH value increased from 0.8 to 1.4. This result was attributed to the increase in crosslinking densities of HTPB.
(3) The mechanical behavior of PBX transitioned from brittle to ductile fracture as the molecular weights of HTPB increased from 1500 to 4000. This finding was attributed to the varied sizes of curing networks that led to the decrease of crosslinking densities and curing stresses.
(4) As observed in the SEM images of post-compression PBX, brittle fractures damaged energetic particles.

Acknowledgements The test support and useful discussion from Ms. Yang H. and Mr. Yang J. G. are greatly appreciated for our research.

References

1. C.B. Skidmore, D.S. Phillips, B.W. Asay, D.J. Idar, D.S. Bolme, Microstructural effects in PBX 9501 damaged by shear impact. Shock Compress. Condens. Matter 659–662 (1999)
2. V.D. Heijden, R.H.B. Bouma, Shock sensitivity of HMX/HTPB PBX's: relation with HMX crystal density, in *29th International Annual Conference of ICT*, Karsruhe, FGR, 30 June–3 July1998, pp. 65-1–65-11
3. J.E. Field, N.K. Bourne, S.J.P. Palmer, S.M. Walley, J. Sharma, B.C. Beard, Hot spot ignition mechanisms for explosives. Acc. Chem. Res. 489–496 (1992)
4. J.H. Liu, S.J. Liu, L.L. Chen, C.M. Lin, F.Y. Gong, F.D. Nie, Improving mechanical property of HMX-based PBX with neutral polymer bonding agent, in *Proceedings of the 45nd International Annual Conference of the Fraunhofer ICT*, Karlsruhe, Germany, 24–27 June 2014, pp. 56/1–56/8
5. F. Li, L. Ye, F. Nie, Y. Liu, Synthesis of boron containing coupling agents and its effect on the interfacial bonding of fluoropolymer/TATB composite. J. Appl. Polym. Sci. **105**, 777–782 (2007)
6. A. Balley, J.M. Bellerby, S.A. Kinloch, J. Shama, E.C. Baughan, M.M. Chaudhn, J.N. Sherwood, B.C. Beard, The identification of bonding agents for TATB/HTPB polymer bonded explosives. Philos. Trans. R. Soc. Lond. Ser. A **339**, 321–333 (1992)
7. J. Huang, L.N. Zhang, Effects of NCO/OH molar ratio on structure and properties of graft-interpenetrating polymer networks from polyurethane and nitrolignin. Polymer **43**, 2287–2294 (2002)
8. Z.B. Zhou, P.W. Chen, F.L. Huang, Compressional punch loading test of a polymer bonded explosive simulant using digital image correlation method. J. Beijing Inst. Technol. **19**, 390–394 (2010)
9. M. Li, J. Zhang, C.Y. Xiong, Damage and fracture prediction of plastic-bonded explosive by digital image correlation processing. Opt. Lasers Eng. **43**, 856–868 (2005)
10. P.W. Chen, H.M. Xie, F.L. Huang, T. Huang, Y.S. Ding, Deformation and failure of polymer bonded explosives under diametric compression test. Polym. Test. **25**, 333–341 (2006)
11. S.J.P. Palmer, J.E. Field, J.M. Huntley, Deformation, strengths and strains to failure of polymer bonded explosives. Proc. R. Soc. **440**, 399–419 (1993)
12. D.G. Thompson, D.J. Idar, G.T. Gray III, Quasi-static and dynamic mechanical properties of new and virtually-aged PBX 9501 composites as a function of temperature and strain rate, in *Proceedings of the 12th International Detonation Symposium* (The Office of Naval Research, Arlington, VA, 2002), pp. 363–368
13. D.J. Idar, D.G. Thompson, G.T. Gray III, W.R. Blumenthal, C.M. Cady, P.D. Peterson, W.J. Wright, B.J. Jacquez, Influence of polymer molecular weight, temperature, and strain rate on the mechanical properties of PBX 9501. Shock Compress. Condens. Matter 821–824 (2001)
14. G.T. Gray III, D.J. Idar, W.R. Blumenthal, C.M. Cady, P.D. Peterson, High and low strain rate compression properties of several energetic material composites as a function of strain rate and temperature, in *Proceedings of the 11th International Detonation Symposium*, Snowmass Village, CO (1998), pp. 76–83
15. W.R. Blumenthal, G.T. Gray III, D.J. Idar, M.D. Holmes, P.D. Scott, C.M. Cady, D.D. Cannon, Influence of temperature and strain rate on the mechanical behavior of PBX 9502 and Kel-F 800TM, in *AIP Conference Proceedings*, Woodbury (New York, 2000), pp. 671–674
16. Y.C. Xiao, Y. Sun, Z.Q. Yang, L.C. Guo, Study of the dynamic mechanical behavior of PBX by Eshelby theory. Acta Mech. **228**, 1993–2003 (2017)
17. V. Sekkar, S. Gopalakrishnan, K.D. Ambika, Studies on allophanate–urethane networks based on hydroxyl terminated polybutadiene: effect of isocyanate type on the network characteristics. Eur. Polym. J. **39**, 1281–1290 (2003)

18. C.Y. Chen, X.F. Wang, L.L. Gao, Y.F. Zheng, Effect of HTPB with different molecular weights on curing kinetics of HTPB/TDI system. Chin. J. Energetic Mater. **21**, 771–776 (2013)
19. C.Y. Chen, X.F. Wang, H.T. Xu, X.J. Feng, L.L. Gao, H. Nan, Effects of temperature on curing stresses of casting plastic bonded explosives. Chin. J. Energetic Mater. **22**, 371–375 (2014)
20. X. Jin, K. Cai, W. Liu, Y.G. Dong, S.L. Hu, J.L. Yang, Effects of monomer content on internal stresses during solidification process and properties of green bodies by gelcasting. J. Chin. Ceram. Soc. **39**, 794–798 (2011)

Chapter 21
An Optimized Preparation Study for High Efficient Fullerene Acceptor ICBA

Zhiyuan Cong, Dong Chen, Jianqun Liu, and Chao Gao

Abstract Indene-C_{60} bisadduct (ICBA) is a new fullerene electron acceptor material with high-lying lowest unoccupied molecular orbital (LUMO) level and simple one-pot preparation procedure. However, the yield and purity of the existing methods are still low, and the reaction time is relatively long, which is not conducive to reduce the cost. Here we systematically studied the preparation and purification of ICBA. The orthogonal experiment with four factors and three levels was designed. The optimized conditions were obtained as the reaction solvent, temperature, time and C_{60}-indene molar ratio were 1,2,4-trichlorobenzene, 210 °C, 1.5 h, and 1:40, respectively. Three levels of purity products can be obtained by three times column chromatography. The process stability was verified by gram scale-up reactions. The electrochemical measurements show that the prepared ICBA achieves a high LUMO level of −3.75 eV. The results indicated that the optimized preparation method would effectively reduce the cost and is expected to be widely applied in optoelectronic field.

21.1 Introduction

Currently, the demand for renewable energy resources is increasingly urgent because of the depletion of fossil energy. Solar energy has emerged as one of the most promising clean alternative green energy. The carbon-based materials, such as fullerenes, graphene, carbon nanotubes and their functionalized derivatives have attracted significant interest for solar cells due to the unique optoelectronic, thermal, mechanical properties and the abundant reserves in earth [1, 2]. Among these carbon allotropes, fullerenes show n-type-like behavior, some fullerene derivatives, such as [6,6]-phenyl-C-61-butyric acid methyl ester (PCBM) and [6,6]-phenyl-C-71-butyric acid methyl ester ($PC_{70}BM$) (Fig. 21.1), possess good solubility, high electron affinity

Z. Cong (✉) · D. Chen · J. Liu · C. Gao
State Key Laboratory of Fluorine and Nitrogen Chemicals, Xi'an Modern Chemistry Research Institute, Xi'an 710065, Shaanxi, P.R. China
e-mail: congzhy81@163.com

D. Chen
e-mail: deltace@163.com

A. Gany and X. Fu (eds.), *2021 International Conference on Development and Application of Carbon Nanomaterials in Energetic Materials*, Springer Proceedings in Physics 276,
https://doi.org/10.1007/978-981-19-1774-5_21

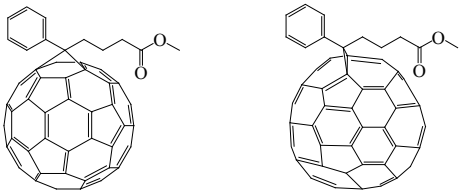

PCBM $PC_{70}BM$

Fig. 21.1 The molecular structure of PCBM and $PC_{70}BM$

and mobility, hence play important roles of electron acceptor materials in organic solar cells (OSCs) [3–6]. When blended with suitable polymer donors, the power conversion efficiency (PCE) of these fullerene-based OSCs have reached 10 ~ 11% [7, 8]. However, the weak absorption and the relative low lowest unoccupied molecular orbital (LUMO) energy level (−3.91 eV) of PCBM/$PC_{70}BM$ limit the further improvement of PCE. That is because the absorption in visible region of photovoltaic materials determines the photocurrent, while the LUMO level of the acceptor affects the open circuit voltage (V_{oc}), which is proportional to the difference between the LUMO of the acceptor and the highest occupied molecular orbital (HOMO) of the donor [9].

To enhance the absorption and increase the LUMO energy level, some new fullerene derivatives have been designed and synthesized [10–14], among which the indene-C_{60} bisadduct (ICBA) is the most successful one [15, 16]. Li et al. obtained ICBA easily through one-pot reaction from C_{60} and indene by Diels–Alder-[4+2]-cycloaddition [17, 18]. Compared to PCBM, the better solubility in organic solvents, stronger visible absorption, and higher LUMO energy level (−3.74 eV) of ICBA are achieved simultaneously. As a result, compared to PCBM-based devices, the ICBA-based devices with P3HT as donor, have showed a 45% improvement of V_{oc} and 40% improvement of PCE, respectively. After annealing treatment, the PCE was further improved of 19%. Considering the simple preparation method and high performances, ICBA has much potential in the future commercialization of fullerene-based OSCs. In addition, ICBA will also promote the development of all-carbon flexible solar cells that combining different carbon allotropes [19, 20].

According to synthesis conditions reported by Li et al. [15], when 1,2,4-trichlorobenzene was used as the solvent, and the molar ratio of C_{60} and indene is 1:20, the reaction was carried out under reflux for 12 h. After several times of purification by silica gel column chromatography with 10% toluene in hexane, ICBA was obtained with a yield of 34% and the purity is 97%. However, when *o*-dichlorobenzene was used as solvent, after 12 h reflux, ICBA only has a yield of 26%. The long reaction time and relatively low yield limit the application of this new fullerene acceptor material. To solve these problems, in this work, the synthesis and purification of ICBA were systematically studied and optimized. Firstly, ICBA was prepared according to the literature so as to identify the samples and establish an optimized purification standard. Then the effect of several important parameters such as reaction temperature, reactants molar ratio, solvent, and reaction time were

studied using an orthogonal experiment design methodology. Finally, according to the optimized process, gram scale-up reaction was carried out and pure ICBA that can be used in photovoltaic devices are obtained.

21.2 Materials and Measurements

Unless noted, all chemicals and reagents were used as received without further purification. C_{60} (99.9%) was purchased from Yongxin Co. (China). Indene (99%) was purchased from Beihe Co. (China). The *o*-dichlorobenzene, 1,2,4-trichlorobenzene, and 1,2,4,5-tetrachlorobenzene (AR) were purchased from Guangfu Co. (China). The Toluene, methanol and *n*-hexane (AR) were purchased from Kelong Co. (China). The Silica gel (200–300 mesh) was purchased from Haiyang Co. (China).

The high performance liquid chromatography were measured on a VarianPro Star, with a chromatographic column of CosmosilBuckyprep 250 × 4.6 mm. The mass spectra were measured on a Kratos PC Axima CFR plus MALDI-TOF Mass spectrometer. The electrochemical cyclic voltammetry was conducted on a CHI 660D Electrochemical Workstation with glassy carbon, Pt wire, and Ag/Ag+ electrode as working electrode, counter electrode, and reference electrode, respectively, in a 0.1 mol/L tetrabutylammonium hexafluorophosphate acetonitrile solution.

21.3 Results and Discussion

21.3.1 Sample Characterization and Analysis

In order to identify the ICBA from the reaction mixture, the literature procedures with some modifications ware first used. The synthetic route of ICBA is shown in Scheme 19.1. Under nitrogen atmosphere, C_{60} (0.14 g, 0.2 mmol) and indene (0.46 g, 4 mmol) were dissolved in 1,2,4-trichlorobenzene (10 mL). The reaction mixture was

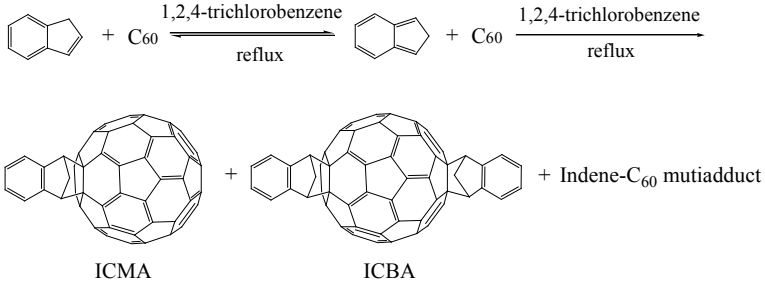

Scheme 19.1 The synthetic route of ICBA

then heated to 210 °C and refluxed for 12 h. The reaction was monitored by thin layer chromatography (TLC) with *n*-hexane as developer. At the end of the reaction, TLC showed three spots. The pale spot with the highest retention factor value (Rf) is the unreacted C_{60}, since it has the same Rf as that of the control C_{60} sample. After cooling down to room temperature, the solution was poured into 250 mL methanol. The solid was collected by filtration and washed with methanol several times. The crude product was dried and analyzed by HPLC (VarianPro Star, CosmosilBuckyprep 250 × 4.6 mm) with a flow rate of 1 mL/min. The mobile phase consisted of 70% tetrahydrofuran and 30% *n*-hexane. The crude product was divided into three main peaks with retention times (t_R) at 5.00–5.45 min (multiple peaks, 29.4%), 5.59–5.93 min (multiple peaks, 55.5%) and 7.8 min (singlet, 10.8%), respectively.

The three peaks were assigned by the time-of-flight-mass spectrometry (TOF-MS) (Fig. 21.2). The peaks at 5.00–5.45 min were indene-C_{60} mutiadduct (cald. mass: 1068, exp. mass: 1069.05 (M + H)). The peaks at 5.59–5.93 min were ICBA (cald. mass: 952, exp. mass: 953.33 (M + H)). The peak at 7.8 min was ICMA (cald. mass: 836, exp. mass: 838.13 (M + H)). Moreover, there is a peak of only 0.29% content located at 13.08 min, which is assigned as the unreacted C_{60} by compared with the t_R of control C_{60}.

The crude product was purified by three times of silica gel column chromatography to obtain ICBA with different purity levels (Table 21.1). Firstly, toluene/*n*-hexane (volume ratio = 1:200) was used as eluent. There were four stripes in the process of column chromatography. And the first outflow stripe was unreacted C_{60}. The second one is indene-C_{60} monoadduct (ICMA). The third one is ICBA, which is the main product. And the fourth one is indene-C_{60} mutiadduct. In this step, the ICBA was obtained with a yield of 40.60% and the purity is 96.66%. Secondly, the ICBA obtained from the first step was further purified and the *n*-hexane was used as eluent. It is interesting to find that the ICBA was further divided into six stripes in

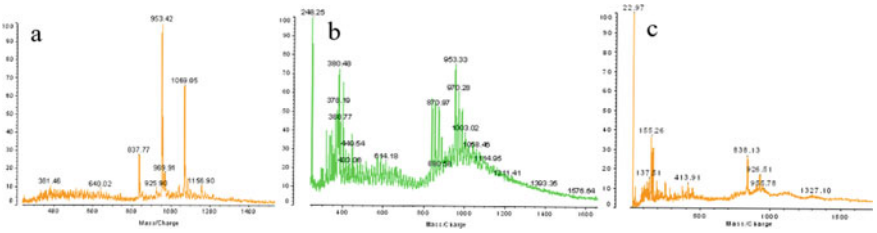

Fig. 21.2 The TOF-MS of the products: **a** indene-C_{60} mutiadduct, **b** ICBA, **c** ICMA

Table 21.1 The purification steps, yield and purity of ICBA

Purification times	Eluent	Yield (%)	Purity (%)
Step 1	toluene/*n*-hexane (1:200)	40.60	96.66
Step 2	*n*-hexane	23.40	98.71
Step 3	*n*-hexane	19.20	99.63

the process of column chromatography. And the middle four stripes are assigned to the four isomers of ICBA because of the different addition sites of indene. After the second purification, the ICBA was obtained with a yield of 23.40% and the purity is 98.71%. After repeating the elution of *n*-hexane to carry out the third purification by column chromatography, the total yield was reduced to 19.20%, however, the purity of ICBA increased as high as 99.63%.

21.3.2 Electrochemical Properties

To investigate the molecular energy levels of the ICBA prepared by us, cyclic voltammetry (CV) measurement was performed and shown in Fig. 21.3. The commercial PCBM was also tested for comparison. The oxidation (Eox) and reduction (Ered) potentials of ICBA and PCBM were obtained. For calibration, the redox potential of ferrocene/ferrocenium (Fc/Fc+) was measured. Then the HOMO and LUMO energy levels were determined according to the following equations: HOMO = −e(Eox + 4.71) (eV) and LUMO = −e(Ered + 4.71) (eV), where the unit of potential is V versus Ag/Ag+ [21]. The LUMO energy levels of ICBA and PCBM were deduced as −3.75 eV and −3.93 eV, respectively, which are basically consistent with the values reported in the literature. Importantly, the LUMO of the prepared ICBA is 0.18 eV higher than the commercial PCBM, which means our preparation and purification methods are reasonable, and the obtained ICBA can be used to improve the V_{oc} of OSCs.

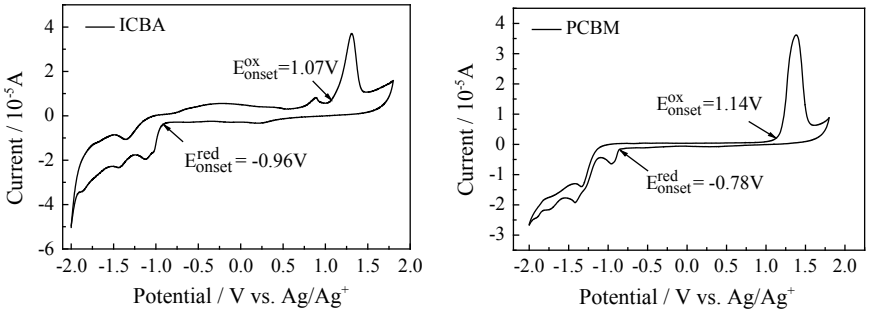

Fig. 21.3 The cyclic voltammograms of ICBA and PCBM

21.3.3 Orthogonal Experiment

The reaction conditions, including the reaction temperature, reactants molar ratio, solvent, and reaction time have important influence on the products of addition reaction. In order to further improve the yield of ICBA and reduce the cost, the orthogonal experiment was carried out. Different temperatures (180, 210, 245 °C), C_{60}-indene molar ratios (1:20, 1:30, 1:40), solvents (*o*-dichlorobenzene, 1,2,4-trichlorobenzene, 1,2,4,5-tetrachlorobenzene), and time (1.5, 3, 6 h) were used to design the orthogonal experiment with four factors and three levels. The experiment results and the conversion rate of ICBA that deduced from HPLC are showed in Table 21.2.

In order to analyze the orthogonal experimental data and obtain the optimal experimental conditions, the comprehensive average conversion rate (K) of the three levels under each factor were calculated according to the equations: K = I/N, where I is the sum of conversion rate of all levels under the same factor and N is the numbers of levels. The calculated results are showed in Table 21.3. The R value in Table 21.3 is the extreme difference of three K values under one factor, which is used to express the influence weight of a certain factor on the results. It is clear that for the temperature factor, the K value of the reaction is 54.37% at 180 °C, 60.67% at 210 °C and 32.81% at 245 °C. Therefore, the average conversion rate is the highest at 210 °C, which is the best reaction temperature. For the molar ratio factor, the K value was 43.37%, 57.98%, and 60.88% when the molar ratio of C_{60} to indene was 1:20, 1:30, and 1:40, respectively. Therefore, the average conversion rate is the highest at the ratio of 1:40. Because 1:40 is an end point in the three groups, the increased ratio of indene was further carried out. However, the results show that when the content of indene is too high, the yield is not significantly improved, but the indene-C_{60}

Table 21.2 The orthogonal experimental design of ICBA preparation

Experiment group	Temperature (°C)	Molar ratio	Solvent	Time (h)	Conversion rate (%)
1	180	1: 20	*o*-dichlorobenzene	1.5	37.04
2	180	1: 30	1,2,4-trichlorobenzene	3	49.12
3	180	1: 40	1,2,4,5-tetrachlorobenzene	6	58.11
4	210	1: 20	1,2,4-trichlorobenzene	6	60.26
5	210	1: 30	1,2,4,5-tetrachlorobenzene	1.5	60.15
6	210 (Actual: 180)[a]	1: 40	*o*-dichlorobenzene	3	62.93
7	245	1: 20	1,2,4,5-tetrachlorobenzene	3	32.81
8	245 (Actual: 180)[a]	1: 30	*o*-dichlorobenzene	6	64.67
9	245 (Actual: 210)[a]	1: 40	1,2,4-trichlorobenzene	1.5	61.60

[a]The actual temperature is because of the limit of the related solvent boiling point

Table 21.3 The K value calculation of ICBA orthogonal experiment

Number	Temperature (°C)	Molar ratio	Solvent	Time (h)
I	271.87	130.11	164.64	158.79
II	182.01	173.94	170.98	144.86
III	32.81	182.64	151.07	183.04
K1	54.37	43.37	54.88	52.93
K2	60.67	57.98	56.99	48.29
K3	32.81	60.88	50.36	61.01
R	27.86	17.51	6.63	12.72

mutiadduct is slightly increased, which also causes the waste of indene, Therefore, 1:40 is the best molar ratio of C_{60} to indene. For the solvent factor, the K values of *o*-dichlorobenzene, 1,2,4-trichlorobenzene and 1,2,4,5-tetrachlorobenzene were 54.88%, 56.99% and 50.36%, respectively. Therefore, when 1,2,4-trichlorobenzene was used as solvent, the average conversion rate was the highest, which was determined as the best solvent. For the time factor, the K value of 1.5 h reaction was 52.93%, 3 h was 48.29%, and 6 h was 61.01%.

Although the average conversion rate was the highest when the reaction time was 6 h, it reached a very high conversion rate at 1.5 h, then decreased at 3 h, and recovered at 6 h, which was slightly higher than that at 1.5 h. In order to refine the trend of conversion with time, and to minimize the influence of sampling error on the experimental data, the time condition experiment was further carried out. The reaction lasted for 16 h under the optimized temperature, solvent and molar ratio. The reaction was analyzed every 0.5 h at the beginning 2 h and then was analyzed every hour until it was finish. The results are showed in Fig. 21.4. It can be seen that the conversion rate of ICBA reaches the maximum in 1.5 h, reaching 58%. When the reaction continues, the conversion rate of ICBA does not increase, but decreases slightly at first, and then remains unchanged at about 55%. Considering the cost of reaction time, 1.5 h is supposed to be the best reaction time.

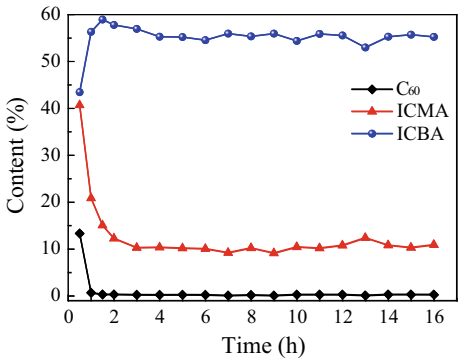

Fig. 21.4 The conversion rate of ICBA varied with time

Table 21.4 The yield and purity of ICBA at the gram scale-up reaction

Experiment	Yield (%)	Purity (%)	Purification times
1	37.0	96.71	1
2	37.0	96.65	1
3	41.9	96.21	1
4	37.3	97.20	2
5	36.0	97.76	2
6	35.0	97.85	2

21.3.4 Gram Scale-Up Reaction

According to the optimized conditions determined by the orthogonal experiment and time condition experiment, six parallel experiments were carried out with the reaction quantity enlarged to gram level. C60 (1.44 g, 2 mmol), indene (9.28 g, 80 mmol) and 100 mL of 1,2,4-trichlorobenzene were added into the reaction flask. Under the protection of nitrogen, the reaction lasted for 1.5 h under reflux at 210 °C. After cooling down, the solution was poured into 400 mL methanol to obtain the crude product. Then the crude product was purified by silica gel column chromatography. The mass ratio of silica gel to sample was 400:1. The eluent for the first purification was *n*-hexane:toluene = 200:1. The eluent for the second purification was n-hexane. The yield and purity of ICBA were summarized in Table 21.4.

21.4 Conclusions

In this paper, the preparation and purification process of high efficient fullerene acceptor material ICBA were systematically optimized. According to the optimized conditions, ICBA was prepared in gram scale with higher yield, higher purity and shorter reaction time than the previous literature methods, which means lower cost could be achieved. The stability of the process was verified by six parallel experiments. The electrochemical results show that the prepared ICBA has higher LUMO energy level than the commercialized PCBM, which is benefit to improve the V_{oc} of photovoltaic devices and is expected to be widely used in further organic and all-carbon flexible solar cells.

References

1. Y. Wang, S. Tong, X. Xu, B. Özyilmaz, K. Loh, Interface engineering of layer-by-layer stacked graphene anodes for high-performance organic solar cells. Adv. Mater. **23**, 1514 (2011)
2. J. Yang, Z. Li, X. Liu, W. Fang, G. Cui, Photoinduced electron transfer from carbon nanotubes to fullerenes: C60 versus C70. Phys. Chem. Chem. Phys. **22**, 19542 (2020)

3. G. Yu, J. Gao, J. Hummelen, F. Wudl, A. Heeger, Polymer photovoltaic cells: enhanced efficiencies via a network of internal donor-acceptor heterojunctions. Science **270**, 1789 (1995)
4. G. Li, V. Shrotriya, J. Huang, Y. Yao, T. Moriarty, K. Emery, Y. Yang, High-efficiency solution processable polymer photovoltaic cells by self-organization of polymer blends. Nat. Mater. **4**, 864 (2005)
5. Y. Kim, S. Cook, S. Tuladhar, S. Choulis, J. Nelson, J. Durrant, D. Bradley, M. Giles, I. McCulloch, C. Ha, M. Ree, A strong regioregularity effect in self-organizing conjugated polymer films and high-efficiency polythiophene:fullerene solar cells. Nat. Mater. **5**, 197 (2006)
6. J. Peet, J. Kim, N. Coates, W. Ma, D. Moses, A. Heeger, G. Bazan, Efficiency enhancement in low-bandgap polymer solar cells by processing with alkane dithiols. Nat. Mater. **6**, 497 (2007)
7. Y. Liu, J. Zhao, Z. Li, C. Mu, W. Ma, H. Hu, K. Jiang, H. Lin, H. Ade, H. Yan, Aggregation and morphology control enables multiple cases of high-efficiency polymer solar cells. Nat. Commun. **5**, 5293 (2014)
8. J. Zhao, Y. Li, G. Yang, K. Jiang, H. Lin, H. Ade, W. Ma, H. Yan, Efficient organic solar cells processed from hydrocarbon solvents. Nat. Energy **1**, 15027 (2016)
9. C. Brabec, A. Cravino, D. Meissner, N. Sariciftci, T. Fromherz, M. Rispens, L. Sanchez, J. Hummelen, Origin of the open circuit voltage of plastic solar cells. Adv. Funct. Mater. **11**, 374 (2001)
10. L. Zheng, Q. Zhou, X. Deng, M. Yuan, G. Yu, Y. Cao, Methanofullerenes used as electron acceptors in polymer photovoltaic devices. J. Phys. Chem. B **108**, 11921 (2004)
11. S. Backer, K. Sivula, D. Kavulak, J. Fréchet, High efficiency organic photovoltaics incorporating a new family of soluble fullerene derivatives. Chem. Mater. **19**, 2927 (2007)
12. F. Kooistra, J. Knol, F. Kastenberg, L. Popescu, W. Verhees, J. Kroon, J. Hummelen, Increasing the open circuit voltage of bulk-heterojunction solar cells by raising the LUMO level of the acceptor. Org. Lett. **9**, 551 (2007)
13. C. Yang, J. Kim, S. Cho, J. Lee, A. Heeger, F. Wudl, Functionalized methanofullerenes used as n-type materials in bulk-heterojunction polymer solar cells and in field-effect transistors. J. Am. Chem. Soc. **130**, 6444 (2008)
14. R. Ross, C. Cardona, D. Guldi, S. Sankaranarayanan, M. Reese, N. Kopidakis, J. Peet, B. Walker, G. Bazan, E. Van Keuren, B. Holloway, M. Drees, Endohedral fullerenes for organic photovoltaic devices. Nat. Mater. **8**, 208 (2009)
15. Y. He, H. Chen, J. Hou, Y. Li, Indene-C60 bisadduct: a new acceptor for high-performance polymer solar cells. J. Am. Chem. Soc. **132**, 1377 (2010)
16. G. Zhao, Y. He, Y. Li, 6.5% efficiency of polymer solar cells based on poly(3-hexylthiophene) and indene-C60 bisadduct by device optimization. Adv. Mater. **22**, 4355 (2010)
17. A. Puplovskis, J. Kacens, O. Neilands, New route for [60]fullerene functionalisation in [4+2] cycloaddition reaction using indene. Tetrahedron Lett. **38**, 285 (1997)
18. A. Hirsch, The chemistry of the fullerenes: an overview. Angew. Chem. Int. Ed. Engl. **32**, 1138 (1993)
19. V. Tung, J. Huang, I. Tevis, F. Kim, J. Kim, C. Chu, S. Stupp, J. Huang, Surfactant-free water-processable photoconductive all-carbon composite. J. Am. Chem. Soc. **133**, 4940 (2011)
20. J. Liu, Y. Xue, Y. Gao, D. Yu, M. Durstock, L. Dai, Hole and electron extraction layers based on graphene oxide derivatives for high-performance bulk heterojunction solar cells. Adv. Mater. **24**, 2228 (2012)
21. J. Hou, Z. Tan, Y. Yan, Y. He, C. Yang, Y. Li, Synthesis and photovoltaic properties of two-dimensional conjugated polythiophenes with bi(thienylenevinylene) side chains. J. Am. Chem. Soc. **128**, 4911 (2006)

Chapter 22
Influence of Explosion Point's Position on the Propagation Law of Shock Wave in Tunnel

Chuiqi Zhong and Yuxin Sun

Abstract In the design of tunnel structure, the damage caused by explosion should be considered. AUTODYN19.0 2D is used for numerical simulation. This paper studies the influence of explosion point's position in long straight tunnel, L-shaped tunnel and T-shaped tunnel on the formation and propagation of shock wave, and summarizes its propagation attenuation law. The results show that the farther the explosion point is from the axis, the longer the reflection and oscillation time of the shock wave in the tunnel, and the longer the time and distance to form the plane wave. In the L-shaped tunnel, when the shock wave propagates to the corner, it will be reflected and superimposed. Part of the reflected wave will return to the original tunnel, the other part will be transferred to the next tunnel, and the peak value of the reflected wave will decrease after the corner. In the T-shaped tunnel, the reflection and flow around the explosion shock wave will occur in the lower tunnel, the left tunnel and the intersection.

22.1 Introduction

In the world, many important military facilities are located in mountains or underground. With the rapid development of society, the demand for underground traffic in cities with high population density is increasing. Tunnel structure is an important structure connecting these places with the outside world. With the rapid development of modern weapons, the possibility of explosion in tunnels is increasing. The research on the formation and propagation of explosion shock wave in tunnel is becoming more and more important [1].

At present, researchers have carried out a lot of research on the propagation law of explosion shock wave in tunnels. The main research methods are theory, experiment, numerical simulation and the combination of various methods. AUTODYN 2D is suitable for the study of explosion shock wave [2]. The research focuses on the

C. Zhong · Y. Sun (✉)
National Key Laboratory of Transient Physics, Nanjing University of Science and Technology, Nanjing 210094, Jiangsu, China
e-mail: yxsun01@163.com

A. Gany and X. Fu (eds.), *2021 International Conference on Development and Application of Carbon Nanomaterials in Energetic Materials*, Springer Proceedings in Physics 276,
https://doi.org/10.1007/978-981-19-1774-5_22

propagation law of explosion shock wave [3–10], the influencing factors of explosion shock wave attenuation [11, 12], the similarity law of explosion shock wave [13] and the reflection law of explosion shock wave [14, 15]. In the case of explosion inside the tunnel, the explosion shock wave first propagates normally in the air, and then the regular or irregular reflection may occur on the solid wall, and the corresponding flow field distribution and evolution are different [16]. Before the shock wave reaches the solid wall, the fitting formula of physical quantity based on the similarity law and combined with numerical or experimental data is generally used to study the parameters of explosion field [17–20]. The accuracy of this method depends on the data size, the number of independent variables and the type of relationship. The relationship usually has a certain scope of application and scenarios. In the aspect of determining the flow field distribution of the reflected shock wave on the solid wall, besides the fitting relation method, there is also the mirror method. In this method, the solid wall is assumed to be a symmetrical plane, and a virtual explosion symmetrical to the real explosion is established on the other side of the solid wall. Then, the real and virtual explosion flow fields are determined according to the free field parameters of one-dimensional spherical explosion, and then the two are linearly or nonlinearly superimposed to obtain the flow field distribution after shock wave reflection [21–27]. The image method is easier to establish and use, can give a clearer physical image, and is not limited to the specific explosion scene. In addition, based on the image method, some researchers equivalent the reflection of explosion shock wave on the solid wall to the interaction of real and virtual explosion flow field, and established the theoretical calculation method of flow field behind the wave [16].

The experiments and numerical simulation of explosive explosion in tunnels are mainly carried out in straight wall tunnels with equal cross-section [28–32]. For specific cases, the research on the formation and propagation law of shock wave of explosion at different positions of explosion points in tunnels under different shapes is relatively scarce. Therefore, it is necessary to carry out the research on the influence of explosion point position on the propagation law of explosion shock wave in tunnels.

22.2 Simulation Model

22.2.1 Finite Element Model

In the numerical simulation, we choose AUTODYN**19.0** 2D for calculation, the tunnel model is divided into three types: rectangular long straight tunnel, L-shaped tunnel and T-shaped tunnel.

For the rectangular long straight tunnel, different explosion points are selected on the cross section, and a total of three numerical simulation calculations are set up. The specific calculation examples are shown in Table 22.1.

Table 22.1 Calculation condition

Examples	Explosive weight (kg)	Detonation
I1	0.5	(0, 0, 0)
I2	0.5	(0.1 m, 0, 0)
I3	0.5	(0.1 m, 0.1 m, 0)

The tunnel size is 0.6 m × 0.6 m × 1.3 m, two sides of the tunnel are opened, and three different explosion points are set. The explosion points are located on the same cross section, 1 m away from one end of the tunnel. The calculation model is shown in Fig. 22.1, assuming that the wall of the tunnel does not absorb the energy of the explosion shock wave through deformation, the wall of the tunnel is set as rigid boundary condition, and the exit boundary condition is set at both ends of the tunnel. The semi-infinite air field outside the opening at both ends is simulated. The grid size of the tunnel is 0.01 m × 0.01 m × 0.01 m, a total of 5,324,800 units, is used to calculate the initial state explosion of explosives by mapping. At the same time, in order to measure the pressure changes at different positions of the cross-section, different observation points are set at each cross-section due to their different symmetries. No. 1 is the center of the cross-section, and the other points are separated by 0.1 m horizontally or vertically. As shown in Figs. 22.2 and 22.3.

Both sides of the L-shaped tunnel calculation model are openings with a cross-sectional area of 0.6 m × 0.6 m. Assuming that the tunnel wall does not absorb the energy of explosion shock wave through deformation, the rigid boundary condition is set on the tunnel wall, and the outflow boundary condition is set on both ends of the tunnel to simulate the semi-infinite air field outside the openings at both ends.

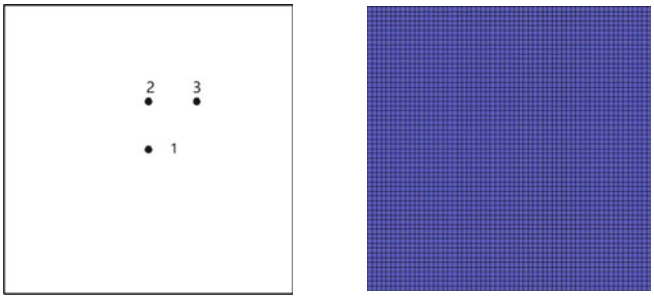

(a) Location distribution of explosion points in cross section

(b) Cross section meshing

Fig. 22.1 Computational model

Fig. 22.2 Axial observation position distribution

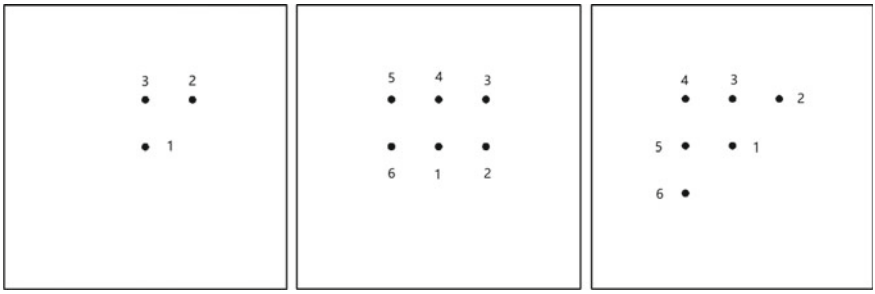

(a) Example I1 (b) Example I2 (c) Example I3

Fig. 22.3 Setting of observation points at the cross section of each example

The tunnel grid size is 0.01 m × 0.01 m × 0.01 m, and the plane diagram of the tunnel is shown in Fig. 22.4. Explosives are set at 8, 6, 4, 2 and 0 m away from the center of the tunnel corner, and the explosion points are numbered as 1–5. L1–L5 is used to distinguish the explosion points. The wall parallel to the tunnel is called the front and rear wall.

The schematic diagram of T-shaped tunnel model is shown in Fig. 22.5, 9 explosion points with an interval of 2 m are set, numbered as 1–9. Other parameters are the same as those of the previous examples, and each example is distinguished by

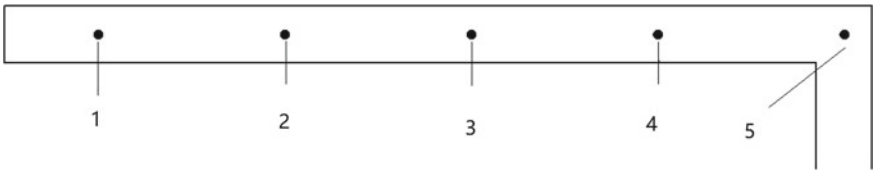

Fig. 22.4 Plan sketch of L-shaped tunnel explosion point

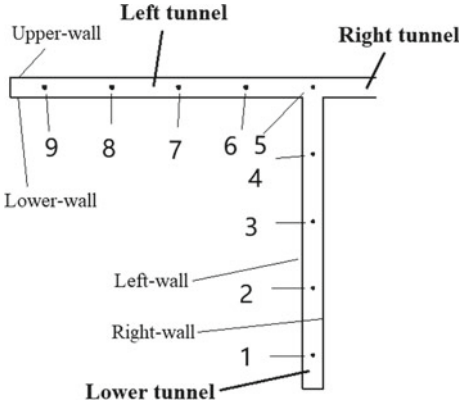

Fig. 22.5 Plane diagram of T-shaped tunnel

T1–T9. For the convenience of description, the positions of No. 1–4 are called the left tunnel, the right tunnel is called the opposite, the positions of No. 6–9 are called the lower tunnel, and the walls parallel to the paper are called the front and rear walls.

22.2.2 Material Constitutive and Equation of State

JWL equation of state is selected for explosive:

$$p = A\left(1 - \frac{\omega}{R_1\overline{V}}\right)e^{-R_1\overline{V}} + B\left(1 - \frac{\omega}{R_2\overline{V}}\right)e^{-R_2\overline{V}} + \frac{\omega}{\overline{V}}E \tag{22.1}$$

where A and B are linear coefficients, R_1, R_2, ω are the non-linear coefficients, $\overline{V} = V_i / V_0$ means the volume of detonation product divided by the volume of unexploded explosive. A, B, R_1, R_2, ω are constants, which are obtained from experiments. The parameters are shown in Table 22.2 [33].

The material model of air is assumed to be an ideal gas, the relationship between pressure P and energy E can be determined by the following formula:

$$\mathrm{P} = (k - 1)\rho E \tag{22.2}$$

where k is the adiabatic coefficient of the gas, ρ is the density of air, E is the initial internal energy of air [33]. The specific parameters are shown in Table 22.3.

Table 22.2 Materials of explosives and parameters of equation of state

Symbol	Significance	Numerical value
ρ	Density (g/cm^3)	1.717
D	Detonation velocity (m/s)	7980
P	C-J detonation pressure (Pa)	2.95×10^{10}
A	Material constant (Pa)	5.2423×10^{11}
B	Material constant (Pa)	7.678×10^{9}
R_1	Material constant	4.2
R_2	Material constant	1.1
ω	Material constant	0.34
E_0	Initial specific internal energy (J/m^3)	8.5×10^{9}

Table 22.3 Parameters of air

Symbol	Meaning	Numerical value
ρ	Density (g/cm^3)	1.225×10^{-3}
E	Initial internal energy (mJ/mm^3)	2.068×10^5
k	Isentropic adiabatic coefficient	1.4

22.3 Results Analysis

22.3.1 Propagation Law of Shock Wave at Different Explosion Points in Rectangular Straight Tunnel

Figures 22.6, 22.7 and 22.8 show the overpressure time history curves of the explosion at each observation point at each position of the cross section in the tunnel. It can be seen from the curve that in the early stage of the formation and propagation of explosion shock wave in the tunnel, the peak value of overpressure at the cross section of the same location is quite different, and the corresponding time of the peak value of overpressure is also different. The reason is that in the early stage of explosion, the shock wave reflected between the inner walls of the tunnel, and the regular plane

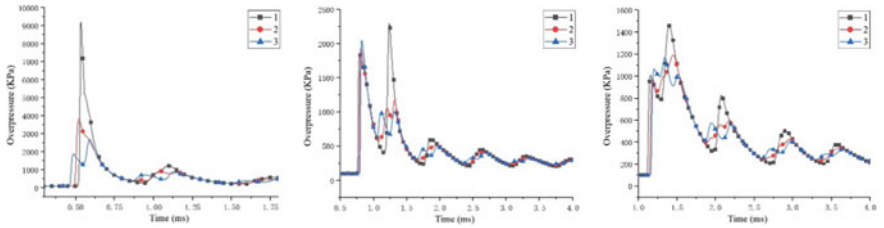

(a) L=1m (b) L=1.5m (c) L=2m

Fig. 22.6 Overpressure time history curve of each measuring point at cross section of (0, 0, 0) explosion tunnel

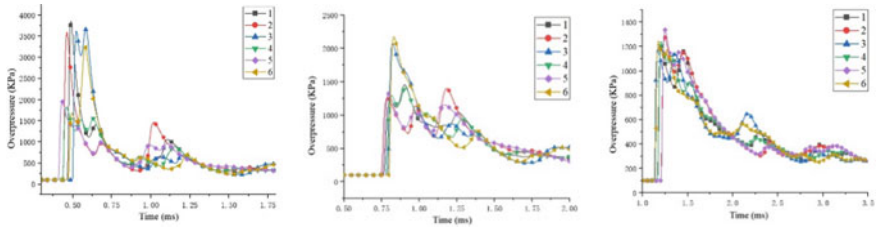

(a) L=1m (b) L=1.5m (c) L=2m

Fig. 22.7 Overpressure time history curve of each measuring point at cross section of (100 mm, 0, 0) explosion tunnel

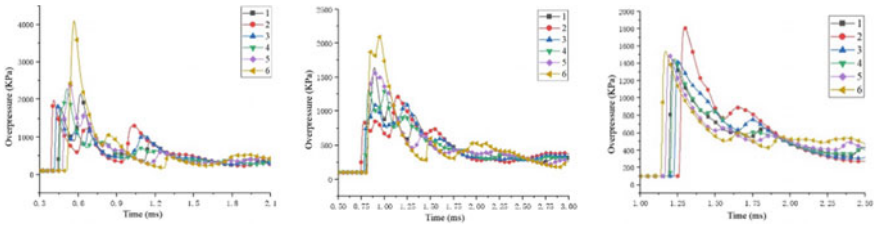

(a) L=1m (b) L=1.5m (c) L=2m

Fig. 22.8 Overpressure time history curve of each measuring point at cross section of (100 mm, 100 mm, 0) explosion tunnel

wave was not formed in the tunnel. With the increase of propagation distance, the shock wave gradually begins to transition to plane wave due to Mach reflection, so the peak value of overpressure on each cross section is closer and closer. The trend of overpressure time history curve tends to be the same, and there is a slight difference in arrival time, which is because the regular plane wave has not yet formed, as shown in Figs. 22.6c, 22.7c and 22.8c.

Therefore, in the early stage of the formation of explosion shock wave in the tunnel, the pressure in the tunnel is irregular and complex, and the pressure time history curve on the same cross section is also quite different. In practice, it is difficult to completely count the parameters at each point on the cross section, a series of observation points in the center of tunnel section are selected to study the axial propagation law of shock wave.

Figure 22.9 shows the time history curve of overpressure at different distances after explosion at different positions. It can be seen from the figure that when the shock wave reaches the observation point after explosive explosion, the pressure rises to the peak rapidly, then decreases gradually, and the rate of the drop decreases gradually. Compared with different curves, the closer the observation point is to the explosion point, the smaller the arrival time, the larger the overpressure peak value and the faster the decline rate at the beginning of the curve. There are multiple peaks in the curve, which is caused by the continuous reflection and propagation of shock wave on the tunnel wall in the process of explosion. Compared with (a), (b) and (c),

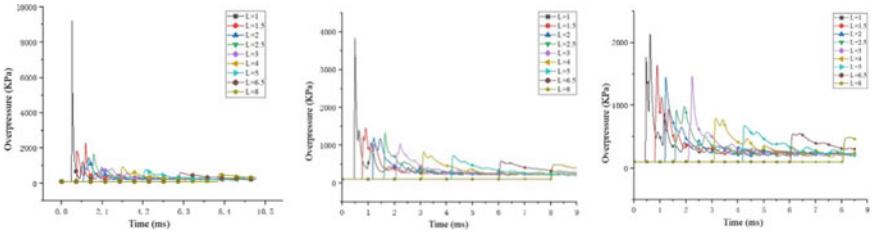

(a) (0,0,0) (b) (100mm,0,0) (c) (100mm,100mm,0)

Fig. 22.9 Time history curve of overpressure at different explosion positions

Table 22.4 Peak attenuation data of overpressure

Distance between blasting centers (m)	Peak overpressure (kPa)		
	Detonation 1	Detonation 2	Detonation 3
1	5237	3028.7	2454.8
1.5	2092.5	1639.9	1493.4
2	1273.5	1200.6	1526
2.5	1552.758	1234.318	876.734
3	822.801	932.068	1362.838
4	822.246	718.392	687.858
5	657.455	621.021	577.979
6.5	510.515	474.859	447.036
8	410.505	382.771	386.153

the overpressure time history curve of the shock wave formed by the explosion at the center is more regular, only the second wave peak of the first three observation points is higher. While the overpressure time history curve of (b) and (c) is more complex, and the higher second wave peak appears in several observation points. It indicates that the shock wave of the explosion at these two explosion points is in the process of propagation, after the wave surface of the shock wave passes through the observation point, the reflection of the subsequent shock wave on the tunnel wall is still very complex. And it takes longer time and distance to form a more regular plane wave.

The average value of overpressure peak value at each cross section of the same blasting center distance is taken to represent the shock wave overpressure of the cross section, and the attenuation data of shock wave overpressure peak value along the tunnel axis in the tunnel can be obtained. The data are shown in Table 22.4.

Figure 22.10 shows the peak attenuation curve of shock wave overpressure based on the results of different numerical calculation examples. It can be seen that in the process of propagation along the tunnel axis, the peak overpressure of shock wave gradually decreases with the increase of distance, and there is a great difference between the peak overpressure of 0 ~ 4 m, and each curve of numerical calculation fluctuates slightly. The reason is that when the shock wave propagates in this distance, the reflected waves reflected by the tunnel wall behind the shock wave surface are superimposed, resulting in the overpressure peak value of the subsequent shock wave being greater than that of the previous one. At the same time, in this distance, due to a large number of reflection and oscillation, the energy loss of shock wave is faster, and the peak value of overpressure decreases faster. With the increase of distance, the shock wave gradually forms a more regular plane wave and propagates forward, and the peak attenuation of overpressure slows down.

To sum up, the location of explosion point in cross section has a great influence on the transformation of shock wave from spherical wave to plane wave in tunnel, and the farther the explosion point deviates, the longer the distance and time to form plane

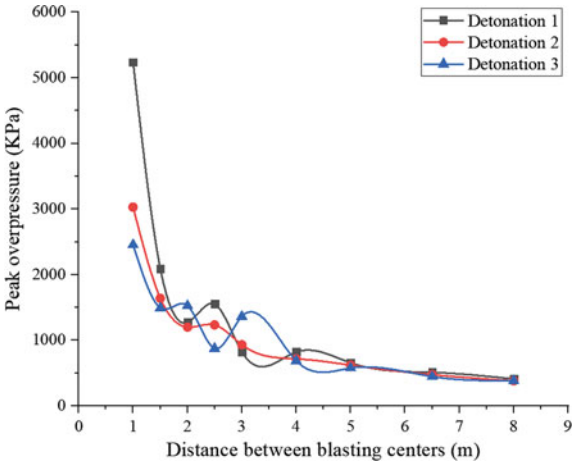

Fig. 22.10 Attenuation curve of overpressure peak with distance

wave. When the plane wave front (0 ~ 4 m) is regular, the peak value of overpressure at each observation point is different, and the distribution of overpressure is very complex. In the distance of the tunnel (more than 4 m), a more regular plane wave is formed.

22.3.2 Propagation Law of Explosion Shock Wave at Different Positions in L-Shaped Tunnel

Table 22.5 shows the overpressure peak data of explosion shock wave produced by explosion at different explosion points in L-shaped tunnel at different observation points, and Fig. 22.11 is a curve synthesized from the data in Table 22.5. Unlike the law that overpressure peak in long straight tunnel decays continuously with the increase of distance, the overpressure peak of explosion shock wave in L-shaped tunnel is not simply negatively correlated with distance, but its decay law is related to the distance between explosives and tunnel corners. In L5, the explosives are placed at the corner of the tunnel, and the overpressure peaks at 1, 1.5 and 2 m are obviously smaller than those in other cases, but they are similar to those in other cases when they spread to a long distance. In L1–L4, explosives have a certain distance from the tunnel corner. After the explosion starts, before it reaches the tunnel corner, the formation and propagation of shock wave is the same as that of a long straight tunnel. When it reaches the tunnel corner, due to complex diffraction and reflection phenomena, a high pressure zone will be formed in the tunnel mouth area, so the peak overpressure at this time will be larger than that of a long straight tunnel. For example, the overpressure at 2 m in L4 reaches 1590.8 kPa, and at 4 m in L3 reaches 1149 kPa. Then, part of the reflected wave returns along the original tunnel, and part

Table 22.5 Peak pressure of L-shaped tunnel at various observation points under various working conditions

Explosion center distance of observation point (m)	Peak pressure (kPa)					
	Rectangular straight tunnel	L1	L2	L3	L4	L5
1	9219.3	9343.9	9395.3	9362.1	9355.5	4172.2
1.5	2195.9	2217.9	2218.9	2219	2132.9	1798.5
2	1357.8	1363.6	1362.3	1362.5	1489.5	1201.7
2.5	1552.8	1586.7	1556.5	1551	775.9	1313.6
3	823.3	767.5	745.7	744.4	646.5	863.1
4	822.4	752.0	737.0	1048.5	663.6	769.2
5	657.5	640.0	632.8	525.5	481.4	668.7
6	510.5	496.2	1003.1	499.0	413.6	573.6
8	410.5	815.5	369.1	355.7	348.3	410.1

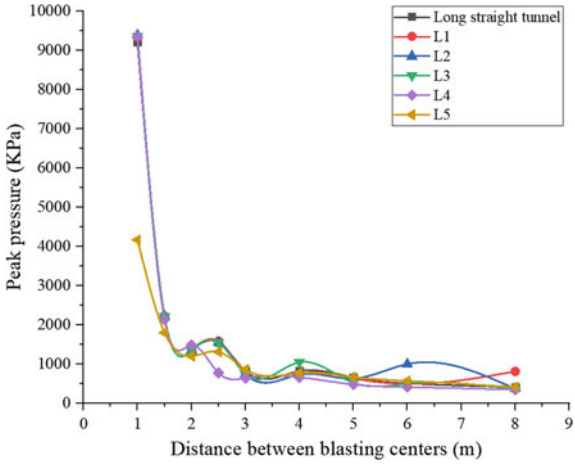

Fig. 22.11 Comparison of peak pressure attenuation curves between straight tunnel and L tunnel

of it continues to propagate forward in another tunnel. Due to the reflected energy loss, the peak value of overpressure decreases after passing through the corner. When it propagates to the other side of the tunnel and is 2 m away from the corner of the tunnel, it decreases by 17.19% in L4, 17.52% in L3 and 8.09% in L2 compared with the long straight tunnel.

Figure 22.12 shows the comparison between the overpressure time history curve measured at the corner center and the overpressure time history curve at the same distance from the straight tunnel. In the long straight tunnel, the overpressure fluctuates greatly at the observation point close to the distance, and there are several peaks, but the second and later peaks are smaller than the first wave, and show a gradual downward trend. In the L-shaped tunnel, there are obviously two larger peaks in the

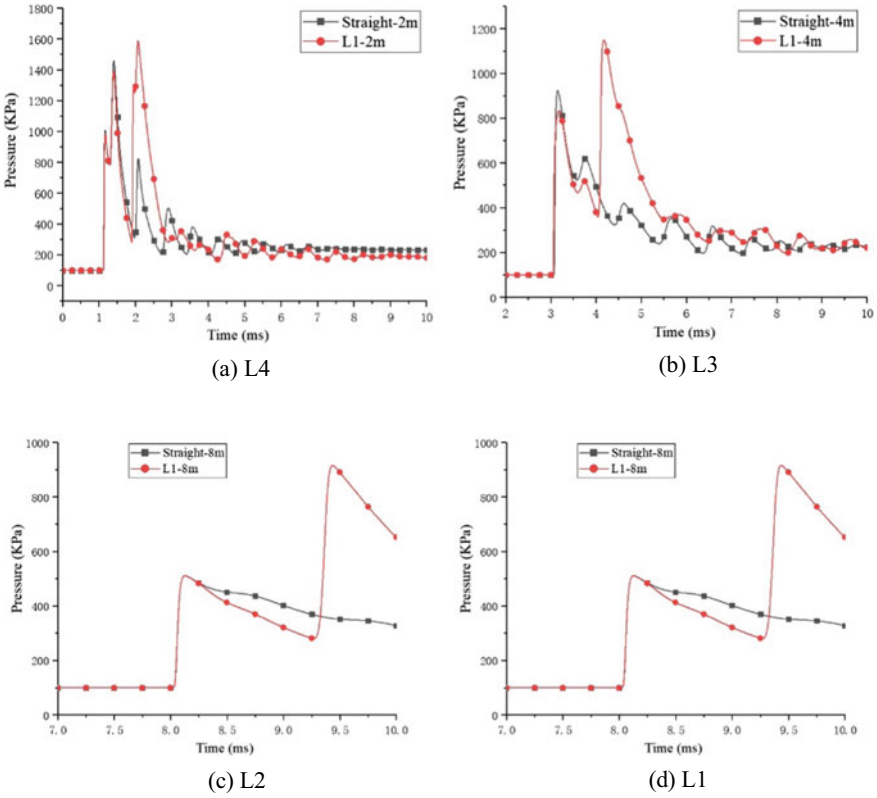

Fig. 22.12 Comparison of pressure time history curves between straight tunnel and different working conditions at the center of tunnel corner

corner overpressure curve. The arrival and peak of the first big peak in the L-shaped tunnel are almost the same as those in the straight tunnel, and the second peak is higher than the first peak. In L4, the first peak is 1389.2 kPa, the second peak is 1590.8 kPa, with an increase of 14.5%. In L4, the first peak is 834.6 kPa, the second peak is 1149.8 kPa, with an increase of 37.8%. In L2, the peak value of one wave peak is 593.4 kPa, and the second peak is 1104.4 kPa, with an increase of 86.1%. In L1, the peak value of the first peak is 511.8 kPa, and the peak value of the second peak is 916.8 kPa, with an increase of 79.1%. Due to complex propagation such as diffraction and reflection, high overpressure will occur at the corner of the tunnel, and when the first peak is small, its increase is larger.

22.3.3 Propagation Law of Explosion Shock Wave at Different Positions in T-Shaped Tunnel

It can be seen from the analysis in Sect. 22.3.2 that the propagation conditions of shock waves formed at different explosion positions in L-shaped tunnels are different. For quantitative comparative analysis, the overpressure peak values at different explosion centers under various working conditions and the overpressure peak values of straight tunnels, L-shaped tunnels and T-shaped tunnels under the same conditions are counted in Table 22.6.

By analyzing the data in the table, compared with the long straight tunnel and the L-shaped tunnel in the same situation, the peak value of the shock wave propagating

Table 22.6 Peak value of overpressure at each explosion center distance under each working condition

Explosion center distance of observation point (m)	Peak overpressure (kPa)								
	Rectangular straight tunnel	L1	T1	L2	T2	L3	T3	L4	T4
(a)									
1	9219.3	9343.9	9188.8	9395.3	9218.8	9362.1	9207.6	9355.5	9219.4
1.5	2195.9	2217.9	2189.6	2218.9	2191.9	2219.0	2191.5	2132.9	2111.6
2	1357.8	1363.6	1357.2	1362.3	1357.4	1362.5	1358.0	1489.5	1219.7
2.5	1552.8	1586.7	1551.7	1556.5	1553.0	1551.0	1554.2	775.9	702.24
3	823.3	767.5	822.8	745.7	823.0	744.4	823.0	646.5	594.3
4	822.4	752.0	822.0	737.0	822.2	1048.5	817.8	663.6	462.2
5	657.5	640.0	657.6	632.8	657.6	525.5	378.4	481.4	325.5
6	510.5	496.2	511.0	1003.1	526.7	499.0	314.6	413.6	297.3
8	410.5	815.5	435.7	369.1	268.3	355.7	251.4	348.3	248.0

Explosion center distance of observation point (m)	Peak overpressure (kPa)									
	T5		T6		T7		T8		T9	
	Right	Lower tunnel	Right	Lower tunnel	Right	Lower tunnel	Right	Lower tunnel	Right	Lower tunnel
(b)										
1	4051.1	3115.5	9429.4		9146.2		9186		9185.3	
1.5	1717.6	1369.1	2270.4		2203.1		2212.7		2205.0	
2	913	781.5	1388.7		1361.1		1360.0		1360.9	
2.5	1317.7	904.7	1226.9	613.9	1570.5		1549.8		1553.6	
3	735.7	607.4	749.2	577.6	753.2		745.3		746.6	
4	627	514.9	795.7	367.3	742.3		736.7		738.2	

(continued)

Table 22.6 (continued)

Explosion center distance of observation point (m)	Peak overpressure (kPa)									
	T5		T6		T7		T8		T9	
	Right	Lower tunnel	Right	Lower tunnel	Right	Lower tunnel	Right	Lower tunnel	Right	Lower tunnel
5	496.8	410.9	674.9	324.9	526.6	288.2	632.6		633.2	
6	395.2	351.7	518.2	323.9	427.5	221.7	491.9		494.9	
8	316.1	286.6	433.4	301.2	333.5	173.9	347.0	178.8	409.6	
9	–	–	–	–	–	–	319.9	151.4	309.7	137.6
10	–	–	–	–	–	–	282.0	234.2	283.5	156.9

to the left and right tunnels is lower when the tunnel explodes in the T-shaped lower part. The reason is that the shock wave is dispersed into two parts and there will be multiple reflections and oscillations when propagating to the intersection. In the case of explosion in the left part of T-shaped tunnel, when the shock wave propagates to the right part and the lower part of the tunnel, their overpressure peaks are lower than those in the long straight tunnel. And the overpressure in the right tunnel is higher than that in the lower part, the overpressure of lower tunnel in T5 is 76.9% of the right, T6 is 77.1%, T7 is 54.8%, T8 is 51.3% and T9 is 44.4%. Indicating that the shock wave energy in the right tunnel is greater than that in the left tunnel.

To further analyze the situation at the intersection of tunnels, the overpressure time history curve at this position under various working conditions is given, as shown in Fig. 22.13.

From Fig. 22.13, we can see that in the case of explosion at the lower part of the tunnel, there are two higher peaks in the overpressure time history curve at the intersection of the tunnel. The reason is that when the shock wave propagates to the upper wall, it will form a positive reflection wave. When the reflection wave propagates here, it will form a second higher peak. In T4, the first peak is 1219.7 kPa, and the second peak is 1113.0 kPa. The first peak is 817.7 kPa and the second peak is 521.0 kPa in T3. In T2, the first peak is 489.1 kPa and the second peak is 526.7 kPa. The first peak is 410.3 kPa and the second peak is 435.7 kPa in T1. When the distance is close, the first peak is larger than the second peak, and there are many fluctuations. The second peak is larger than the first peak, and the curve fluctuation is small when the distance is far. Compared with the lower tunnel, the curve of the left tunnel has only one obvious peak, and the peak is the same as that of the lower tunnel. The first attenuation is slightly slower than that of the lower tunnel, but since the lower tunnel has the second peak, the curve of the left tunnel decays faster after that.

At the same time, to better understand the difference of explosion shock wave propagation to the right and lower tunnel, the overpressure time history curve and impulse time history curve of 1 and 3 m blasting center distance under T5 condition and T6 condition are made, as shown in Figs. 22.14 and 22.15.

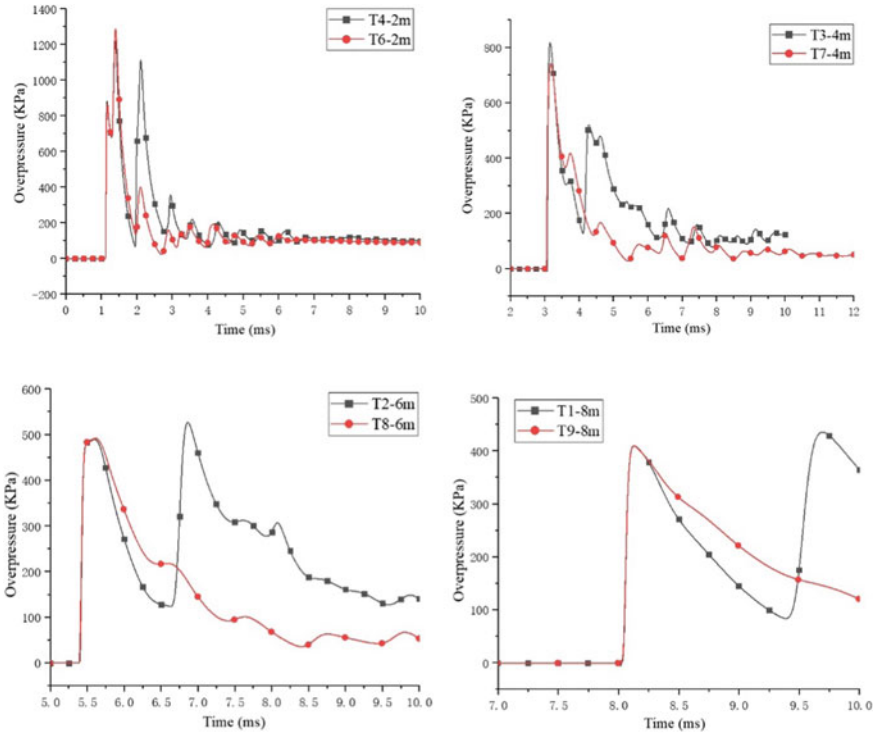

Fig. 22.13 Overpressure time history curve of tunnel corner center under various working conditions

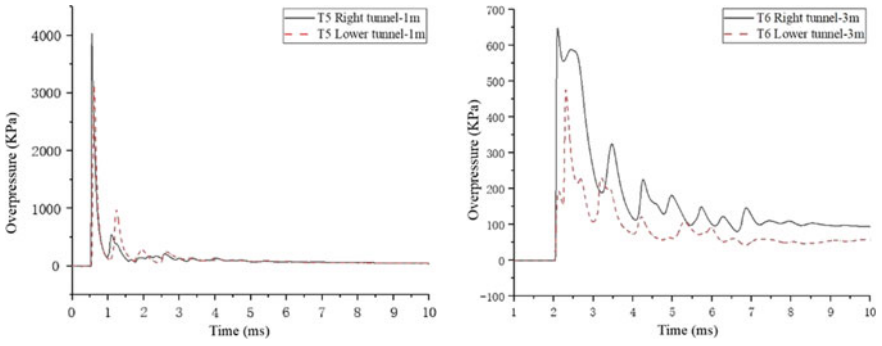

(a) At T5 condition, the distance between blasting centers is 1 m.

(b) At T6 condition, the distance between blasting centers is 3 m.

Fig. 22.14 Time history curve of shock wave overpressure

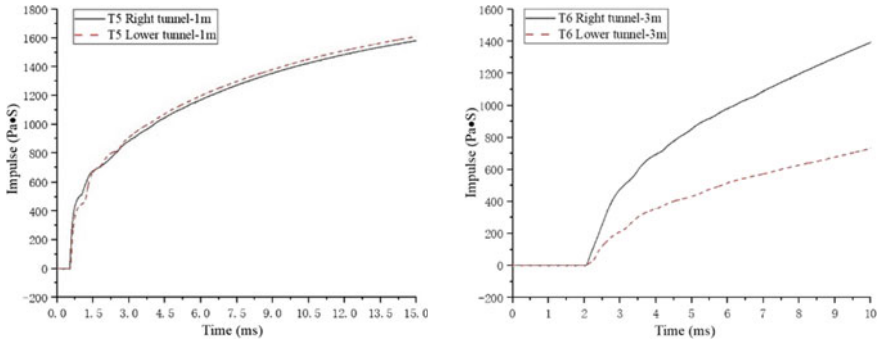

(a) At T5 condition, the distance between blasting centers is 1 m.

(b) At T6 condition, the distance between blasting centers is 3 m.

Fig. 22.15 Overpressure impulse curve

The overpressure time history curves at 1 m from the implosion center of the right and lower tunnels in T5 condition are consistent. The peak pressure in the right tunnel is higher, reaching 4051.1 kPa, and the peak pressure in the lower tunnel is 3115.5 kPa. However, the lower tunnel has a higher second wave peak, which is caused by the reflected wave of the upper wall. The impulse curves are basically overlapped and the difference is very small. In T6 condition, the peak value of overpressure and overpressure impulse in the right tunnel are significantly larger than those in the lower tunnel, which indicates that the energy of the shock wave propagating into the lower tunnel is small. By observing the overpressure curve, it is found that the oscillation of the shock wave is obvious in the new tunnel, and the attenuation rate is roughly equal.

22.4 Conclusion

In this paper, the formation, propagation and attenuation of explosion shock wave in rectangular long straight tunnel, L-shaped tunnel and T-shaped tunnel with different explosion points are studied by numerical simulation. The following conclusions are obtained:

(1) The location of explosion point in the cross section of tunnel entrance has an important influence on the formation and propagation of shock wave. The farther the explosion point is from the axis, the longer the duration of reflection and oscillation in the tunnel, the longer the distance to form a regular plane wave, and the longer the time required.

(2) In the L-shaped tunnel, the complex reflection phenomenon will occur when the shock wave propagates to the corner of the tunnel. A high-pressure area is formed at the corner of the tunnel. Part of the energy is reflected back to the

original tunnel, and part of the energy is transferred to the next tunnel. The peak pressure of the explosion shock wave formed at the L corner is lower than that of the long straight tunnel in the near field, but its attenuation speed is slower. When the distance is more than 4 m, the attenuation curve is similar to that of the long straight tunnel.

(3) In the T-shaped tunnel, when the shock wave of the lower tunnel propagates to the intersection position of the tunnel, it is mainly emitted on the upper wall. One part of the shock wave propagates to the left and right tunnels, and the other part is reflected to the original tunnel. With the increase of distance, the less energy is reflected to the original tunnel. The oblique reflection and diffraction of the shock wave in the left tunnel mainly occur at the intersection of the tunnels, and most of the energy is transferred to the right tunnel, and a small part of the energy is transferred to the lower tunnel. At the same distance, the peak pressure of the shock wave in the lower tunnel is lower than that in the left and right tunnels, but due to the reflection of the upper wall, there are double peaks, and the impulse is almost the same as that in the left and right tunnels.

References

1. S. Lei, *Attenuation Law of Blasting Shock Wave in Tunnel and Its Application* (Southwest Jiaotong University, 2018)
2. T.C. Chapman, T.A. Rose, P.D. Smith, Blast wave simulation using AUTODYN2D: a parametric study. Int. J. Impact Eng. **16**(5), 777–787 (1995)
3. S.Y. Wu, B. Zhang, F.Y. Lu, Study on propagation law of explosion wave in tunnel. J. Undergr. Space Eng. **6**(02), 396–399+435 (2010)
4. J.B. Liu, Q.S. Yan, J. Wu, Study on propagation law of explosion shock wave in tunnel. J. Vib. Shock **2009**(06) (2009)
5. X. Yang, S.Q. Shi, P.F. Cheng, Prediction and numerical simulation of overpressure peak of TNT explosion shock wave in air. Blasting **25**(1), 15–18 (2008)
6. L.N. Xu, S.N. Yong, F.D. Wang, J. Liu, Study on overpressure propagation law of explosion shock wave in tunnel. J. Test Meas. Technol. **28**(2) (2014)
7. W.B. Pang, Y.C. Li, X. He, Experimental study on arrival time law of chemical explosion shock wave in T-shaped channel. Explos. Shock Waves **2007**(01) (2007)
8. W.B. Pang, X. He, M.S. Li, H.Q. Ren, Experimental study on travel time of air shock wave in tunnel. Explos. Shock Waves **2003**(06) (2003)
9. K.Z. Yang, X.M. Yang, Propagation law of shock wave in tunnel implosion. Explos. Shock Waves **2003**(01) (2003)
10. Y.L. Zhang, S.Q. Wang, J.F. Yuan, J.F. Zhang, S.Q. Li, Propagation law of explosion shock wave in square tunnel. Energetic Mater. **28**(01), 46–51 (2020)
11. O. Pennetier, M. William-Louis, A. Langlet, Numerical and reduced-scale experimental investigation of explosion shock wave shape in underground transportation infrastructure. Process Saf. Environ. Prot. **94**, 96–104 (2015)
12. P.D. Smith, P. Vismeg, L.C. Teo, Explosion shock wave transmission along rough-walled tunnels. Int. J. Impact Eng. **21**(6), 419–432 (1998)
13. Y.Y. Miao, X.D. Li, S. Yang, Z.G. Geng, Discussion on the similarity law of explosion shock wave in tunnel. Blasting **33**(1) (2016)

14. H.Q. Lu, W.Q. Liu, The influence of the cross section shape of the tunnel on the propagation law of chemical explosion shock wave. J. Nanjing Tech Univ. **31**(06), 41–44 (2009)
15. B. Xu, H.H. Zhang, Z.J. Chen, Mach reflection of spherical shock wave on rigid wall. Explos. Shock Waves **8**(1), 25–28 (1988)
16. L.M. Jia, S.F. Wang, Z. Tian, Theoretical calculation method of reflected flow field of blast shock wave. Explos. Shock Waves **39**(06), 94–102 (2019)
17. L. Ehrhardt, J. Boutillier, P. Magnan, Evaluation of overpressure prediction models for air blast above the triple point. J. Hazard. Mater. **311**, 176–185 (2016)
18. W.Z. Xu, W.G. Wu, Y.S. Lin, Numerical method and simplified analytical model for predicting the blast load in a partially confined chamber. Comput. Math. Appl. **76**, 284–314 (2018)
19. B. Bewick, I. Flood, Z. Chen, A neural-network model-based engineering tool for blast wall protection of structures. Int. J. Prot. Struct. **2**(2), 159–176 (2011)
20. D.J. Armaghani, M. Hasanipanah, A. Mahdiyar, Air blast prediction through a hybrid genetic algorithm: ANN model. Neural Comput. Appl. **29**(9), 619–629 (2018)
21. P.C. Chan, H.H. Klein, A study of blast effects inside an enclosure. J. Fluids Eng. **116**(3), 450–455 (1994)
22. X.S. Kong, W.G. Wu, J. Li, Experimental investigation on characteristics of blast load in partially confined cabin structure. J. Shanghai Jiaotong Univ. (Sci.) **18**(5), 583–589 (2013)
23. B. Kong, K. Li, S. Li, Indoor propagation and assessment of explosion shock waves from weapons using the alternative image theory. Shock Waves **26**, 75–85 (2016)
24. Z. Wu, J. Guo, X. Yao, Analysis of explosion in enclosure based on improved method of images. Shock Waves **27**(2), 237–245 (2017)
25. M. Kandula, R. Freeman, On the interaction and coalescence of spherical explosion shock waves. Shock Waves **18**, 21–33 (2008)
26. T. Ma, *The Study for Fast Computation of Explosion Shock Wave in Air* (National University of Defense Technology, 2014), pp. 6−16
27. C.E. Needham, *Explosion Shock Waves* (Springer, New York, 2010)
28. Y.D. Zhang, L. Shuai, B. Zou, W.H. Yu, Explosion shock wave load on protective door in vertical tunnel. Explos. Shock Waves **37**(06), 1057–1064 (2017)
29. Q. Zhou, *Study on Distribution Law and Simplified Calculation of Inner Wall Overpressure Caused by Explosion in Confined Space* (Tianjin University, 2008)
30. K.K. Qu, Y.J. Yan, Y. Liu, X.Z. Ning, Z.L. Li, Comparative study on propagation law of explosion shock wave in long straight tunnel and complex tunnel. Chin. J. Appl. Mech. **28**(04), 434–438+457 (2011)
31. X.Z. Zhang, F. Jin, F.L. Kong, Q.R. Wang, F. Zhang, Study on wave dissipation effect of water under the condition of tunnel explosion. Chin. J. Appl. Mech. **29**(02), 148–153+237 (2012)
32. Q.S. Yan, *Study on Flow Field Distribution and Dynamic Response of Typical Subway Structures* (Tsinghua University, 2011)
33. C.L. Xin, Z.Q. Xue, J. Tu, X.Q. Wang, F.T. Sun, D.Y. Shi, *Manual of Common Material Parameters for Finite Element Analysis* (China Machine Press, Beijing, 2019), pp. 18–19+192–193

Chapter 23
Study on Preparation and Thermal Decomposition Performance of Copper Azide/Graphene Nanocomposite

Jianhua Chen, Lei Zhang, Feipeng Lu, Yanlan Wang, Rui Zhang, Fang Zhang, and Ruishan Han

Abstract Carbon material has been designed as substrate to improve the sensitivity characteristics of copper azide ($Cu(N_3)_2$), lots of research findings have supported this strategy. However, the thermal decomposition mechanism of $Cu(N_3)_2$ nanocomposite has not yet been revealed. In this work, graphene was used as a composite material to prepare a $Cu(N_3)_2$/graphene composite primary explosive. Differential scanning calorimeter (DSC) and thermogravimetric-infrared spectroscopy (TG-DSC-FTIR) were used to analyse its thermal decomposition performance. The results showed that the composite of graphene could delay the decomposition point of $Cu(N_3)_2$ to 215.49 °C, indicating that the heat release of composite copper azide was concentrated, and the thermal decomposition rate was accelerated. The thermal decomposition reaction kinetic results indicated that the thermal decomposition of $Cu(N_3)_2$/graphene accord with the Avrami–Erofeev equation (No. 11 Mechanism Function), and its Apparent Activation Energy (E_a) was 113.42 kJ/mol, and the exponential factor log A was 9.26 s^{-1}.

J. Chen · L. Zhang (✉) · F. Lu · Y. Wang · R. Zhang · F. Zhang · R. Han
Science and Technology on Applied Physical Chemistry Laboratory, Shaanxi Applied Physics-Chemistry Research Institute, Xi'an 710061, Shaanxi, China
e-mail: ggy628@163.com

J. Chen
e-mail: Jianhua927@163.com

F. Lu
e-mail: lufeipengv@163.com

Y. Wang
e-mail: cloudyanlan@163.com

F. Zhang
e-mail: jakey204@163.com

A. Gany and X. Fu (eds.), *2021 International Conference on Development and Application of Carbon Nanomaterials in Energetic Materials*, Springer Proceedings in Physics 276,
https://doi.org/10.1007/978-981-19-1774-5_23

23.1 Introduction

With the accelerated development of micro-ignition chips, copper azide ($Cu(N_3)_2$), a traditional green energetic material with low limit detonator charge and excellent detonation performance [1–4], has shown enormous application in primary explosives gradually [5–11]. However, $Cu(N_3)_2$ is intensely sensitive to electrostatic and mechanical stimuli, resulting the safety hazards during the synthesis and assembly, which limits the application of copper azide remarkably [12–18]. To overcome these deficiencies, utilizing the outstanding thermal and electrical conductivity of nanoscale carbon materials to fabricate novel composite structures of copper azide has become the essential research strategy to improve its sensitivity. For example, Metal–organic framework (MOF)-derive porous carbon materials are used to synthesize $Cu(N_3)_2$ [19, 20], carbon nanotubes are used to confine $Cu(N_3)_2$ [4, 17, 21–27], and three-dimensional graphene can load $Cu(N_3)$ as a skeleton [28]. All of these strategies can ameliorate the electrostatic sensitivity of $Cu(N_3)_2$ and improve its initiation ability simultaneously. However, the effect of carbon materials on the thermal decomposition mechanism of $Cu(N_3)_2$ has not been reported yet, which is particularly crucial for the safety and detonation performance of primary explosive.

Herein, a new $Cu(N_3)_2$/graphene composite primary explosive was designed, and the thermal decomposition performance and thermal decomposition mechanism of the composite initiator were tested and analyzed by DSC and TG-DSC-FTIR. It was found that graphene participates in the thermal decomposition process of $Cu(N_3)_2$. In addition, the reaction kinetic equation of $Cu(N_3)_2$/graphene was calculated by thermal decomposition kinetics, and based on the general integration method, the thermal decomposition of $Cu(N_3)_2$/graphene conformed to the Avrami–Erofeev equation and belonged to the No. 11 Mechanism Function, which could be used for in-depth study the detonation performance of $Cu(N_3)_2$.

23.2 Experiments

23.2.1 Instruments and Reagents

Instruments employed: OTF-1200X Tube Furnace (China), differential scanning calorimetry (DSC, LINSEIS Chip-DSC, Germany), infrared spectrometry (IR, Perkin Elmer Spectrum 3, USA), synchronous thermal analyzer (TG-DSC, NETZSCH STA449F3, Germany).

Reagents used: copper sulfate pentahydrate, GO dispersion, sodium azide, ascorbic acid, stearic acid, anhydrous ethanol, and, sodium hydroxide. All of the solvents and chemicals were of analytical grade and purchased commercially, and were used without further purification.

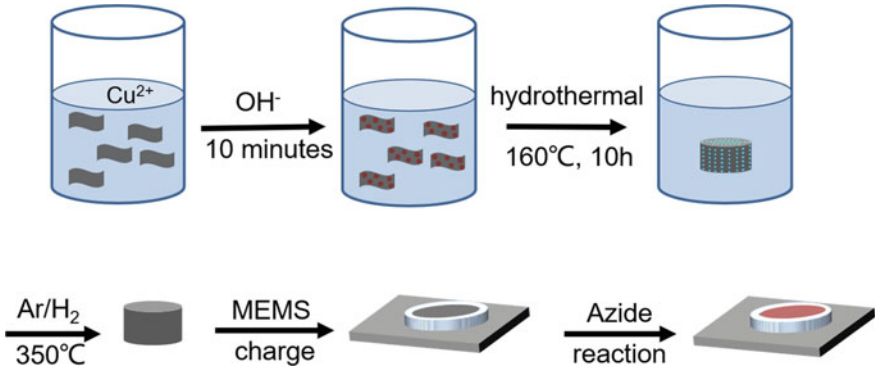

Fig. 23.1 Schematic of formation of $Cu(N_3)_2$/graphene

23.2.2 Preparation of Copper Azide/Graphene Nanocomposite

The preparation procedure of $Cu(N_3)_2$/graphene was demonstrated in Fig. 23.1. First, the 5 mL GO aqueous dispersion with a concentration of 2.5 mg/mL was added into 400 mL of deionized water, and sonicated for 20 min to ensure uniform dispersion of GO in deionized water; then the 2 mL $CuSO_4$ and NaOH solution with a concentration of 1.5 mol/L and 5 mol/L were added to the mixed solution by mechanical stirring respectively; after 10 min, 1 mL of ascorbic acid solution with a concentration of 1.2 mol/mL was added to the mixed solution with vigorous stirring, and the solid particles were precipitated. then placed them in a tube furnace, and, heat-treated at 350 °C under Ar/H_2 (95%/5%, v/v) for 3 h, the precursor of Cu/graphene for the azide reaction can be obtained. At last, under the gas–solid in-situ condition, the primary explosive of the $Cu(N_3)_2$/graphene would be prepared by azide reaction of Cu/graphene precursors with hydrazoic acid gas for 16 h. Here, it should be noted that azide acid is a highly toxic gas and should be handled carefully.

23.3 Results and Discussions

23.3.1 Thermal Analysis

The thermal decomposition performance of $Cu(N_3)_2$/graphene had been tested by differential scanning calorimeter (DSC). The sample size was 0.2 mg, the test temperature was 25 ~ 350 °C, and the nitrogen's flow rate was 50 ml/min. The measured DSC curve was shown in Fig. 23.1, where the arrow points to the exothermic direction.

It can be seen observably that the thermal decomposition peak of $Cu(N_3)_2$/graphene composites is 215.49 °C (Fig. 23.2), which is significantly delayed

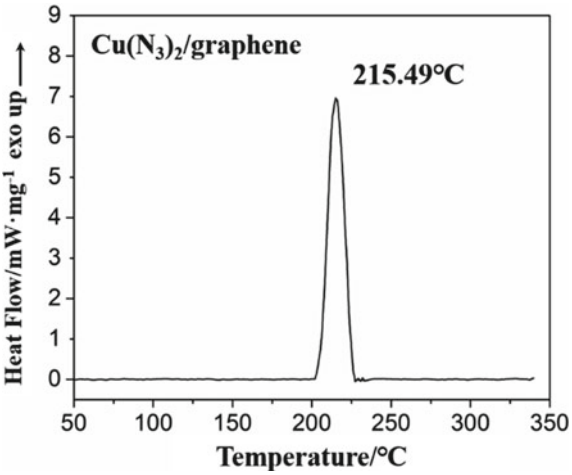

Fig. 23.2 DSC pattern of $Cu(N_3)_2$/graphene

compared to pure copper azide (207.5 °C). This may be mainly due to the close combination between copper azide and graphene. During the thermal decomposition of $Cu(N_3)_2$/graphene, the partial hot spots can be dispersed along the network-like graphene structure transiently, which is not conducive to the formation of local hot spots, resulting a delay in thermal decomposition temperature; in addition, $Cu(N_3)_2$ is very uniformly distributed on the graphene sheet, and the trigger hot spot can be transferred inside $Cu(N_3)_2$ quickly, resulting in a faster thermal decomposition rate.

23.3.2 Analysis of Thermal Decomposition Product Gas

The TG-DSC-FTIR method might have been used to identify the thermal decomposition product gas of $Cu(N_3)_2$/graphene in situ. In which, TG-DSC was simulated the thermal decomposition process of $Cu(N_3)_2$/graphene, and FTIR was used to identify the composition information of the gas released during the weight loss process. The test temperature is 25 ~ 345 °C; the heating rate is 10 K/min, and the stream rate of high-purity nitrogen is 70 mL/min. The wave amount extent is 4000 ~ 450 cm^{-1}. Those results are exhibited in Fig. 23.3.

The spectrum illustrated that more gas products released during the thermal decomposition of $Cu(N_3)_2$/graphene mainly include O–H and C–O groups. In which, the wavenumber range of 4000 ~ 3400 and 1800 ~ 1257 cm^{-1} corresponds to the O–H group, and the wavenumber range of 2406 ~ 2100 cm^{-1} corresponds to the C–O group. The analysis shows that the gas products of $Cu(N_3)_2$/graphene decomposition are mainly H_2O (g) and CO_2, except for N_2. This result indicates that graphene is involved in the thermal decomposition process of $Cu(N_3)_2$.

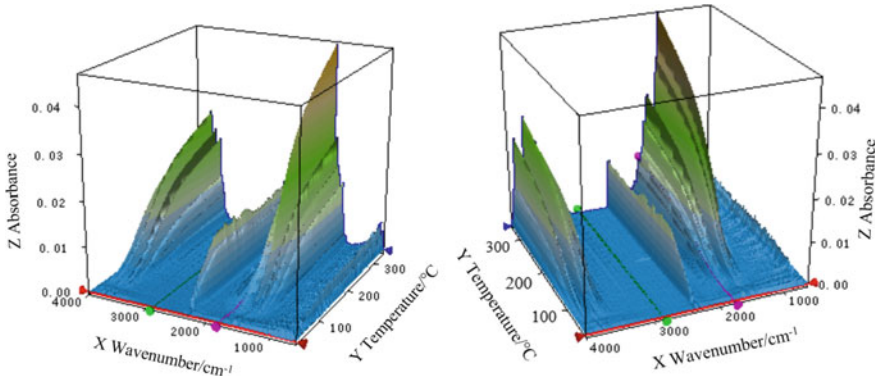

Fig. 23.3 3D TG-DSC-FTIR spectrum of gas products of $Cu(N_3)_2$/graphene

23.3.3 Thermal Decomposition Kinetic Mechanism

DSC-TG was accepted to test the thermal decomposition curve of $Cu(N_3)_2$/graphene at different heating rates (Fig. 23.4). The test temperature range was 25 ~ 350 °C, the heating rate is 5, 10, 15, 20 °C/min, the nitrogen stream rate was 50 mL/min, and the mass of each sample was 0.2 mg.

Kissinger's method as demonstrated in Eq. (23.1) [29] and Ozawa's method [30] in Eq. (23.2) were found to calculate the reaction kinetic parameters, and the KWO conversion rate method was used to determine the temperature at different reaction depths.

Kissinger's method:

$$\ln\left(\frac{\beta_i}{T_{pi}^2}\right) = \ln\frac{A_k R}{E_k} - \frac{E_k}{RT_{pi}}, \quad i = 1, 2, 3, 4 \tag{23.1}$$

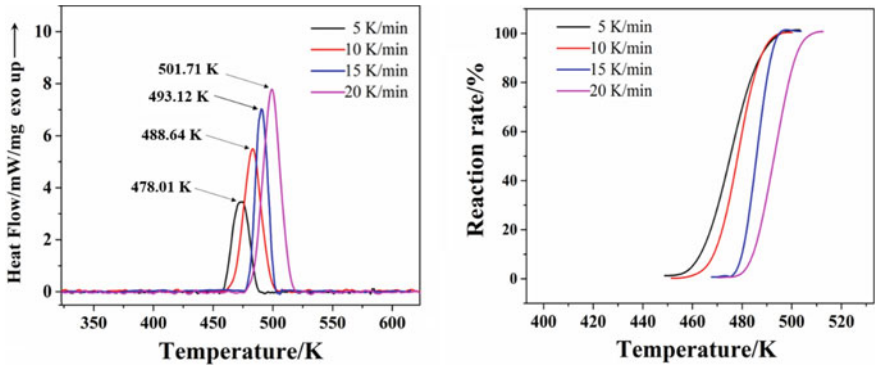

Fig. 23.4 DSC and α-T curve at different heating rates

Table 23.1 Kinetic parameters calculated by the thermal decomposition reaction of $Cu(N_3)_2$/graphene

β (K/min)	T_s (K)	T_p (K)	T_e (K)	Kissinger			Ozawa	
				E_k (kJ/mol)	A_k	R_k	E_o (kJ/mol)	R_o
5.0	458.44	478.01	488.53	111.86	8.43×10^9	0.9862	114.13	0.9886
10.0	462.66	488.64	503.17					
15.0	477.47	493.12	504.61					
20.0	481.91	501.71	521.37					

Herein, T_p was the peak temperature, β_i was heating rate, K/min; K; E_k was apparent activation energy acquired by Kissinger's method, kJ/mol; Ak was pre-exponential factor; R was optimal gas permanent, 8.314 J/K mol.

Ozawa's method:

$$\lg \beta_i = \lg\left(\frac{A_o E_o}{RF(\alpha)}\right) - 2.135 - 0.4567\frac{E_o}{RT_{pi}}, \quad i = 1, 2, 3, 4 \tag{23.2}$$

From Ozawa's method, the apparent activation energy (E_o) could be obtained, in which the $F(\alpha)$ was the integral over the mechanism function.

According to the DSC curve, the decomposition temperature T corresponding to different reaction depths is obtained, and lg β and 1/T are linearly fitted according to Eqs. (23.1) and (23.2). The apparent activation energy E_o would be acquired starting with the incline of the straight line, and the intercept can be obtained refers to pre-exponential constant A. The calculated characteristic parameters of thermal decomposition are indicated in Table 23.1.

The calculated data that the activation energy values of the thermal decomposition reaction of $Cu(N_3)_2$/graphene collected by the Kissinger and the Ozawa's method are relatively adjacent.

Based on the general integration method, linear regression analysis is performed on the corresponding lg $F(a)$ and 1/T of the thermal decomposition reaction mechanism function. The fitting results show that the thermal decomposition of $Cu(N_3)_2$/graphene belongs to the random nucleation and subsequent growth mechanism of n = 1/3, m = 3 in the reaction depth stage of 0.2 ~ 0.9, and the apparent activation energy is 113.42 kJ mol^{-1}, and the pre-exponential factor of log A is 9.26 s^{-1}. The calculated reaction kinetic equation of $Cu(N_3)_2$/graphene is shown below:

$$\frac{da}{dt} = 3 \times 10^{9.26} \exp\left(-\frac{113.42}{RT}\right) \tag{23.3}$$

The comparison shows that the thermal decomposition mechanism function of $Cu(N_3)_2$/graphene conforms to the Avrami–Erofeev equation (No. 11 Mechanism Function).

23.4 Conclusion

In summary, $Cu(N_3)_2$/graphene demonstrated in this paper is a novel primary explosive with outstanding detonation performance. We evaluated the thermal safety of $Cu(N_3)_2$/graphene by its thermal decomposition behavior, and observed the thermal decomposition reaction by DSC and TG-DSC-FTIR methods.

(1) The composite of graphene can delay the decomposition point of $Cu(N_3)_2$ to 215.49 °C, indicating that the heat release of composite copper azide was concentrated, and the thermal decomposition rate was accelerated.
(2) Graphene was involved in the thermal decomposition process of $Cu(N_3)_2$.
(3) The thermal decomposition of $Cu(N_3)_2$/graphene presents one intensive exothermic process. The apparent activation energy was 113.42 kJ/mol, and the exponential factor log A was 9.26 s^{-1}. The thermal decomposition mechanism of $Cu(N_3)_2$/graphene conforms to the Avrami–Erofeev equation (No. 11 Mechanism Function).

The analytical and kinetic analysis results of the $Cu(N_3)_2$/graphene reaction process in this study can not only provide references for in-depth study of $Cu(N_3)_2$ detonation, but also guide the design of composite primary explosives.

References

1. B.L. Evans, A.D. Yoffe, P. Gray, Physics and chemistry of the inorganic azides. Chem. Rev. **59**, 515–568 (1959)
2. F. Zhang, Y. Wang, D. Fu et al., In-situ preparation of a porous copper based nano-energetic composite and its electrical ignition properties. Propel. Explos. Pyrotech. **38**, 41–47 (2013)
3. L. Zhang, F. Zhang, Y. Wang, R. Han, J. Chen, R. Zhang, E. Chu, In-situ preparation of copper azide by direct ink writing. Mater. Lett. **238**, 130–133 (2019)
4. Y. Shen, J. Xu, N. Li et al., A micro-initiator realized by in-situ synthesis of three-dimensional porous copper azide and its ignition performance. J. Chem. Eng. J. **326**, 1116–1124 (2017)
5. H. Pezous, C. Rossi, M. Sanchez et al., Integration of a MEMS based safe arm and fire device. Sens. Actuators A Phys. **159**, 157–167 (2010)
6. C. Rossi, D. Esteve, Micropyrotechnics, a new technology for making energetic microsystems: review and prospective. Sens. Actuators A Phys. **120**, 297–310 (2005)
7. A.B. Gordienko, A.S. Poplavno, Electronic structure of CuN_3(I). Phys. Solid State **48**(10), 1844–1847 (2006)
8. T. Lindblom, H. Malmberg, Analysis of copper azide in ammunition using FTIR, in *12th Symposium on Chemical Problems Connected with the Stability of Explosives* (2001)
9. I. Kabik, S. Uman, Hazards of copper azide fuzes, in *Proceedings of Minutes of the 14th Explosive Safety Seminar* (US, 1972)
10. M. Robert, P. Jiri, *Primary Explosives* (Springer, Berlin, 2013), pp. 71–120
11. Z.M. Li, M.R. Zhou, T.L. Zhang et al., The facile synthesis of graphene nanoplatelet–lead styphnate composites and their depressed electrostatic hazards. J. Mater. Chem. A **1**(41), 12710–12714 (2013)
12. J.W. Fronabarger, M.D. Williams, W.B. Sanborn et al., DBX-1—a lead free replacement for lead azide. Propel. Explos. Pyrotech. **36**, 541–550 (2011)

13. V. Thottempudi, H. Gao, J.M. Shreeve, Trinitromethyl-substituted 5-nitro- or 3-azo-1,2,4-triazoles: synthesis, characterization, and energetic properties. J. Am. Chem. Soc. **133**, 6464–6471 (2011)
14. B.T. Fedoroff, O.E. Sheffield, S.M. Kaye, *Encyclopedia of Explosives and Related Items* (Picatinny Arsenal, Dover, NJ, 1983)
15. M. Zhou, Z. Li, Z. Zhou et al., Antistatic modification of lead styphnate and lead azide for surfactant applications. Propel. Explos. Pyrotech. **38**, 569–576 (2013)
16. M. Hu, The effect of tetrazene on the reliability of some stab detonator. Initiat. Pyrotechn. 32–34 (2016)
17. C. Yu, Z. Zheng, W. Zhang et al., Sustainable electrosynthesis of porous CuN_3 films for functional energetic chips. ACS Sustain. Chem. Eng. **8**, 3969–3975 (2020)
18. B. Li, M. Li, Q. Zeng et al., In situ fabrication of monolithic copper azide. J. Energetic Mater. **34**, 123–128 (2016)
19. Q. Wang, X. Feng, S. Wang et al., Metal-organic framework templated synthesis of copper azide as the primary explosive with low electrostatic sensitivity and excellent initiation ability. J. Adv. Mater. **28**, 5837–5843 (2016)
20. Q. Wang, L. Zhang, W. He et al., High-performance primary explosives derived from copper thiolate cluster-assembled materials for micro-initiating device. Chem. Eng. J. **389**, 124455 (2020)
21. V. Pelletier, S. Bhattacharyya, I. Knoke et al., Copper azide confined inside templated carbon nanotubes. Adv. Funct. Mater. **20**, 3168–3174 (2010)
22. X. Liu, Y. Hu, H. Wei et al., Energetic films realized by encapsulating copper azide in silicon-based carbon nanotube arrays with higher electrostatic safety. Micromachines **11**, 575 (2020)
23. C. Yu, W. Zhang, S. Guo et al., A safe and efficient liquid-solid synthesis for copper azide films with excellent electrostatic stability. Nano Energy **66**, 104135 (2019)
24. H. Pezous, C. Rossi, M. Sanchez et al., Fabrication, assembly and tests of a MEMS-based safe, arm and fire device. J. Phys. Chem. Solids **71**(2), 75–79 (2010)
25. Q. Yu, M. Li, Q. Zeng et al., Copper azide prepared by reaction of hollow CuO microspheres with moist HN_3 gas. Mater. Lett. **224**, 18–21 (2018)
26. Q. Yu, M. Li, Q. Zeng et al., Copper azide fabricated by nanoporous copper precursor with proper density. Appl. Surf. Sci. **442**, 38–44 (2018)
27. G. Zhang, J. Han, L. Yang et al., Theoretical study of the reduction in sensitivity of copper azide following encapsulation in carbon nanotubes. J. Mol. Model. **26**, 90 (2020)
28. L. Zhang, L. Yang, F. Zhang et al., In situ synthesis of three-dimensional graphene skeleton copper azide with tunable sensitivity performance. Mater. Lett. **279**, 128466 (2020)
29. H. Kissinger, Reaction kinetics in differential thermal analysis. Anal. Chem. **29**(11), 1702–1706 (1957)
30. T. Ozawa, A method of analyzing thermogravimetric data. Bull. Chem. Soc. Jpn. **38**(11), 1881–1886 (1965)

Chapter 24
A New Type of Stabilizer for Nitrocellulose: The Study of the Synthesis, the Character and the Stability of 1,2-bis(2-(2,6-dimethoxyphenoxy)ethoxy)ethane

Bei Qu, Hao Chen, and Jizhen Li

Abstract Four new stabilizers which didn't forming nitrosamine derivatives were prepared and the reaction condition were optimized. It was suggested from the electrostatic potentials that the electron-donating groups (–OCH_3, –OCH_2CH_2O–) had been observed one positive influence of the replacement of nitro group. And it was proved from the compatibility and the stablity of STAB-1 that the compatibility of STAB-1 with NC was good and the STAB-1 can stabilized NC for ten years on the HFC study.

24.1 Introduction

Nitrocellulose (NC) which is the most common energetic binder in solid rocket propellant, but it continuously slowly decomposes to release nitrous compounds gas because there are many nitric acid ester groups in the structure, and the gases increase the rate of the decomposition [1–3]. Many research groups try to search some materials to stabilized nitrate ester compound and to prevent autocatalysis of propellant. The nitrous gases are trapped by the stabilizers and form stable compounds. The common stabilizers were 4-nitro-N-phenylaniline, triphenylamine, Centralite I, Centralite II and Akardite II [6–9]. The problem with the stabilizers is that they can form nitrosamine derivatives on prolonged storage with NC and some of them are known to be carcinogenic. Therefore, there is an urge to find alternative stabilizers with the absence of an aromatic amine motif [10–13].

Substituted phenols are of wide interest in the organic chemistry [14–16]. Recently, various phenols with electron rich substituents were suggested as new stabilizers and exhibited promising effect. However, the phenols stabilizers were less stable than conventional stabilizers because of the sterically hindered with large alkyl substituents [17, 18]. Although the alkyl substituents would render the aromatic ring

B. Qu · H. Chen · J. Li (✉)
Xi'an Modern Chemistry Research Institute, Xi'an 710065, China
e-mail: jizhenli@126.com

A. Gany and X. Fu (eds.), *2021 International Conference on Development and Application of Carbon Nanomaterials in Energetic Materials*, Springer Proceedings in Physics 276,
https://doi.org/10.1007/978-981-19-1774-5_24

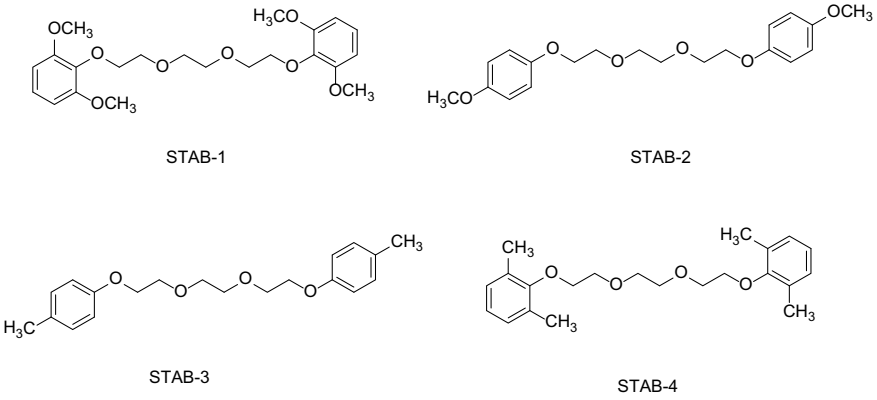

Scheme 24.1 The structure of the new stabilizers

electron rich and prone to react with the electrophilic nitrous gases, the ring would be less susceptible to substitution due to the sterically hindered of the large alkyl substituents.

The aim of this work is to synthesize four new phenol stabilizers with methoxy-substituents (the structures were listed in Scheme 24.1), which named 1,2-bis(2-(2,6-dimethoxyphenoxy)ethoxy)ethane (STAB-1), 1,2-bis(2-(4-methoxyphenoxy)ethoxy)ethane (STAB-2), 1,2-bis(2-(p-tolyloxy)ethoxy)ethane (STAB-3) and 1,2-bis(2-(2,6-dimethylphenoxy)ethoxy)ethane (STAB-4). The NC stabilizing properties of STAB-1 have been evaluated and compared with conventional stabilizers.

24.2 Experimental

24.2.1 Materials and Methods

All raw materials were purchased from commercial sources and used without further treatment. Melting points were measured in open capillaries with a Gallenkamp MPD350.BM.2.5. ^{1}H NMR spectra were recorded at 500 MHz (^{1}H) and 125 MHz (^{13}C) in $CDCl_3$ with a Varian Mercury 300. Infrared spectra were measured with FTIR. Elemental analyse was performed on a Carlo Erba 1106 full-automatic trace element analyzer. DSC measurement was carried out with a TA instrument DSC-2910. The electrostatic potentials on isosurfaces were calculated by the PBE of generalized gradient approximation (GGA) density functional with DNP basis set in Dmol3code of Materials Studio 8.0.

24.2.2 General Procedure for the Reaction

The method catalyzed by KOH [19, 20]: 2,6-dimethoxyphenol (15.42 g, 100 mol) and 1, 2-bis(2-chloroethoxy)ethane (8.42 g, 45 mmol) was dissolved in water–ethanol (1:1) 100 mL at room temperature. The potassium hydroxide (6.06 g, 108 mmol) was added over a 5 min period. The reaction was stirred at reflux for 50 h. The solids were filtered off and the solvent was evaporated. The remaining solid was dissolved in dichloromethane (100 mL), and the organic layer was washed with aqueous 1 N NaOH (50 mL) and brine (50 mL). The organic layer was dried with $MgSO_4$, filtered and evaporated to give the crude product (pale yellow viscous liquid). Recrystallization of the crude product was performed by heating the product in boiling Et_2O and then slowly cooling it to 0 °C. The product was filtered dried to afford 1,2-bis(2-(2,6-dimethoxyphenoxy)ethoxy)ethane as a white powder (17.3 g, yield 91%). M.p. 59–60 °C; ^{1}H NMR (500 MHz, $CDCl_3$-d_6): δ 6.96 (2H, t), 6.55 (4H, d), 4.14 (4H, t), 3.82 (12H, s), 3.74 (4H, t); ^{13}C NMR (500 MHz, $CDCl_3$-d_6) δ 153.7, 137.2, 123.7, 105.4, 72.2, 70.5, 56.1; IR(KBr) ν: 3448, 3027, 3097, 2940, 2890, 2865, 2839, 1607, 2190, 1803, 1567, 1499, 1478, 1444, 1373, 1294, 1255, 1135, 1105, 1047, 1021, 910, 847, 774, 733, 698, 615, 588 cm^{-1}.

1,2-bis(2-(4-methoxyphenoxy)ethoxy)ethane (17.86 g, yield 98%): M.p. 67–68 °C, ^{1}H NMR ($CDCl_3$-d_6): δ 6.85 (4H, t), 6.80 (4H, d), 4.07 (4H, t), 3.83 (4H, s), 3.75 (6H, t), 3.74 (4H, t); ^{13}C NMR ($CDCl_3$-d_6) δ 153.96, 152.98, 115.69, 114.61, 70.87, 69.94, 68.15, 55.70; IR(KBr) ν: 3444, 3057, 3014, 2959, 2931, 2902, 2871, 2838, 2786, 2700, 2590, 2545, 2474, 2345, 2125, 2050, 1986, 1905, 1866, 1740, 1626, 1509, 1453, 1385, 1332, 1287, 1250, 1229, 1189, 1132, 1116, 1072, 1055, 1031, 948, 927, 883, 821, 731, 593, 522, 449, 423 cm^{-1}.

1,2-bis(2-(p-tolyloxy)ethoxy)ethane (16.18 g, yield 98%): M.p. 66–67 °C, ^{1}H NMR ($CDCl_3$-d_6): δ 7.04 (4H, t), 6.79 (4H, d), 4.08 (4H, t), 3.83 (4H, s), 3.81 (4H, t), 2.27 (6H, t); ^{13}C NMR ($CDCl_3$-d_6) δ 156.74, 130.05, 129.87, 114.61, 69.91, 67.34, 65.85, 20.48; IR(KBr) ν: 3444, 3100, 3063, 3022, 2928, 2923, 2897, 2859, 2733, 2681, 2590, 2545, 2483, 2358, 2129, 2067, 1993, 1877, 1766, 1612, 1585, 1510, 1488, 1454, 1412, 1374, 1321, 1298, 1248, 1181, 1138, 1112, 1070, 1041, 1013, 1000, 966, 928, 875, 853, 810, 740, 585, 560, 510 cm^{-1}.

1,2-bis(2-(2,6-dimethylphenoxy)ethoxy)ethane (16.40 g, yield 95%): M.p. 67–68 °C, ^{1}H NMR ($CDCl_3$-d_6): δ 7.24 (4H, t), 6.92 (2H, d), 3.95 (4H, t), 3.86 (4H, s), 3.79 (4H, t), 2.82 (12H, t); ^{13}C NMR ($CDCl_3$-d_6) δ 155.83, 130.95, 128.80, 123.82, 71.31, 67.44, 65.87, 16.28; IR(KBr) ν: 3450, 3017, 2942, 2914, 2880, 2750, 2729, 2393, 2239, 2100, 2007, 1957, 1939, 1867, 1797, 1676, 1638, 1591, 1556, 1478, 1433, 1378, 1358, 1348, 1288, 1258, 1242, 1235, 1198, 1162, 1123, 1090, 1061, 982, 973, 953, 914, 898, 845, 811, 775, 751, 670, 573, 544, 523, 479, 463 cm^{-1}.

The method catalyzed by DCC [21]: 2,6-dimethoxyphenol (15.42 g, 100 mol) and 2,2′-(ethane-1,2-diylbis(oxy))bis(ethan-1-ol) (7.50 g, 50 mmol) was dissolved in acetonitrile 100 mL at room temperature. The dicyclohexylcarbodiimide (DCC)

(24.72 g, 120 mmol) was added over a 5 min period. The reaction was stirred at reflux for 60 h. The solids were filtered off and the solvent was evaporated. The remaining solid was dissolved in dichloromethane (100 mL), and the organic layer was washed with aqueous 1 N NaOH (50 mL) and brine (50 mL). The organic layer was dried with $MgSO_4$, filtered and evaporated to give the crude product (pale yellow viscous liquid). Recrystallization of the crude product was performed by heating the product in boiling Et_2O and then slowly cooling it to 0 °C. The product was filtered dried and the yield was 80.5%.

24.2.3 Stability Testing

24.2.3.1 The Compatibility Test

The compatibility was test by the DSC [22]. The DSC of STAB-1 with different energetic materials was undergone for the safety concern. DSC is a prevalent way in compatible test. According to *Thermal Analyses for Energetic Materials*, the compatibility of energetic materials and the other compositions are estimated by the decomposition peak temperature decrease (ΔT) of DSC curve of the energetic materials and the mixed system. The mixed system is composed by the energetic materials and the other compositions at the ratio of 1:1 by mass.

DSC measurements were carried out on a Model TA-910 USA instruments. The operation condition was as follows: heating rates 10 K min^{-1}; sample mass, 0.5 ~ 1 mg; aluminium sample cell; atmosphere, static nitrogen with 0.1 MPa.

24.2.3.2 Microcalorimetry at 85 °C

The procedure is based on the standard STANAG 4582 (2004) [23]. Several 3 ml glass vials were fully filled with NC. Heat flow measurements were conducted with a Calorimeter 2277 TAM 150 for 160 h at 85 °C. Heat flow curves, the integrated specific heat generation Q_{80h}, as well as the maximum heat flow P_{max} (after an induction period of 5 J/g) were obtained. All measurements were then evaluated according to STANAG 4582. The limit value of P_{max} is 310 μW/g for 85 °C and must not be exceeded during the first 80 h of the measurement by using the activation energies described in STANAG 4582. These time were recalculated to be an equivalent of 10 years at 25 °C.

24.3 Results and Discussion

24.3.1 Influence of Reaction Conditions on the Etherification

The etherification of 2,6-dimethoxyphenol with 2,6-dimethoxyphenol

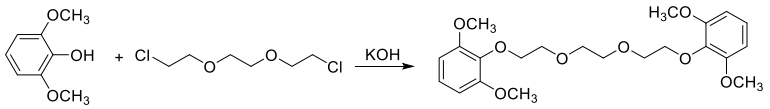

(24.1)

For the initial study, 2,6-dimethoxyphenol and 1,2-bis(2-chloroethoxy)ethane were selected as the model substrates (Scheme 24.2) to optimize the reaction conditions. It is pleasing that the etherification of 2,6-dimethoxyphenol with 1,2-bis(2-chloroethoxy)ethane catalyzed by KOH in H_2O-ethanol gave 1,2-bis(2-(2,6-dimethoxyphenoxy)ethoxy)ethane (STAB-1) in 85.0 yield (Table 24.1, Run 1). Several base were compared (Run 2–4). Substitution by NaOH led to a slightly lower yield. However, when K_2CO_3 or $NaHCO_3$ was employed, the yield was decreased and a considerable amount of side product as 2-(2-(2-(2-chloroethoxy)ethoxy)ethoxy)-1,3-dimethoxybenzene was formed.

Subsequently, several solvents were evaluated [19] (Table 24.1). In contrast to the traditional $NaCO_3$ catalyzed the etherification of a ether and halide where acetonitrile was the appropriate solvent, the employment of acetonitrile in the present reaction led to a decrease of the yield. Meanwhile, DMF or DMSO gave the product with lower yield, but the reaction temperature increased to 145 °C and the time decreased to 40 h. THF were also tested, but lower yield were observed. The reaction in toluene was not succeeded due to its lack of polarity.

The changes of yield of the etherification with time were shown in Fig. 24.1. As illustrated, the yield of STAB-1 increased with prolonging the reaction time.

Table 24.1 Etherification of 2,6-dimethoxyphenol with 2,6-dimethoxyphenol under various conditions

Run	Base	Solvent	Time (h)	Yield (%)
1	KOH	H_2O-ethanol	60	85.0
2	NaOH	H_2O-ethanol	60	81.4
3	K_2CO_3	H_2O-ethanol	60	36.5
4	$NaHCO_3$	H_2O-ethanol	60	20.8
5	KOH	CH_3CN	60	69.3
6	KOH	DMF	40	80.3
7	KOH	DMSO	40	78.1
8	KOH	THF	60	55.7
9	KOH	Toluene	60	/

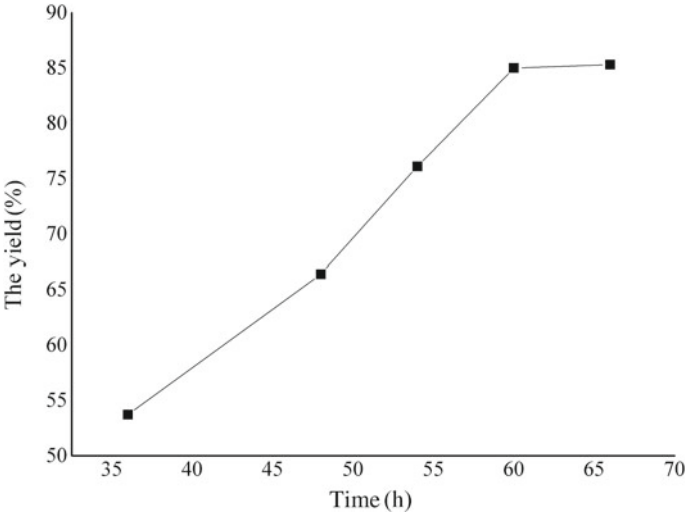

Fig. 24.1 Time-dependence curves for the etherification

However, after 60 h the yield changed slowly and became stagnated near 85%. And from the results of HPLC, it was showed that the yield of side product was 60% at 20 h while that was only 3% at 60 h. As a result, in a 60 h reaction course, the 2,6-dimethoxyphenol was condensed with 85% yield of STAB-1. The effect of temperature was summarized in Fig. 24.2. Due to the solubility of 2,6-dimethoxyphenol in

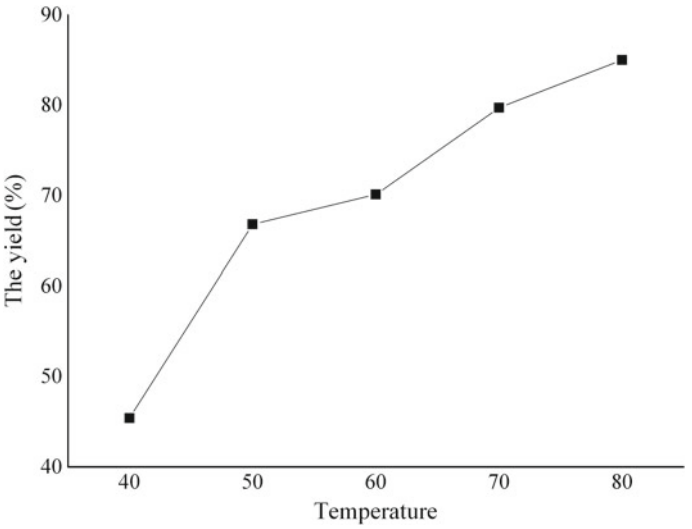

Fig. 24.2 Temperature-dependence curves for the etherification

solvent increase with the raise of the temperature, the yield first increased and then stagnated near 85% when the temperature increased to the reflux temperature.

24.3.2 Production of STAB-1 and STAB-2 with Different Methods

The preparation of STAB-1 and STAB-2 with KOH or DCC method

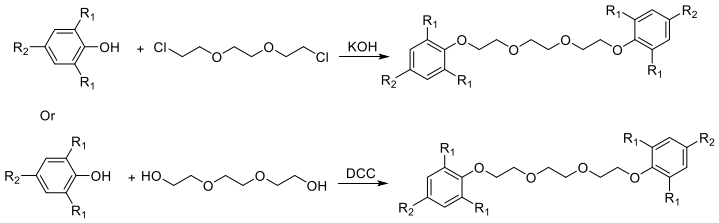

(24.2)

With optimized conditions in hand, 1,2-bis(2-(4-methoxyphenoxy)ethoxy)ethane (STAB-2), 1,2-bis(2-(4-methyphenoxy)ethoxy)ethane (STAB-3) and 1,2-bis(2-(2,6-dimethylphenoxy)ethoxy)ethane (STAB-4) were attempted to be synthesized, and the results are shown in Table 24.2. STAB-2, STAB-3 and STAB-4 were produced in 98.4% yield, 98.8% yield, and 95.0% yield respectively, while the yield of them and was higher than that of STAB-1 and the time was shorter due to the steric hindrance. The new chlorine-free approach for the condensation of hydroxybenzene and alcohol catalyzed by dicyclohexylcarbodiimide (DCC) was attempted. The yield of STAB-1 was 80.5% under the DCC method, while that of STAB-2, STAB-3 and STAB-4 were 96.0%, 96.2% and 93.7%, respectively. Although the yield was little lower than the KOH method, the advantage of the DCC method was that it did not need chlorine reagent and base which can reduce the pollution.

Table 24.2 Production of STAB with different method

Run	R_1, R_2	Method	Yield (%)
1	OCH_3, H	KOH	85.0
2	H, OCH_3	KOH	98.4
3	H, CH_3	KOH	98.8
4	CH_3, H	KOH	95.0
5	OCH_3, H	DCC	80.5
6	H, OCH_3	DCC	96.0
7	H, CH_3	DCC	96.2
4	CH_3, H	DCC	93.7

24.3.3 The Stabilizing Property of STAB-1

To understand the stability of the new stabilizers on the energetic materials, the electrostatic potentials on isosurfaces were calculated by the PBE of generalized gradient approximation (GGA) density functional with DNP basis set in Dmol3code of Materials Studio 8.0 (Fig. 24.2) [24]. For STAB-1 molecule, there are negative potentials around the electron-rich oxygen atom as expected, which made negative potentials were observed above benzene and strongly-positive potentials are located around. The distribution was propitious to the replacement of H on the benzene by the nitro group which was released from the energetic materials. And from the structure of STAB-1, it can be seen that the electron-donating group (–OCH_3, –OCH_2CH_2O–) had observed a positive influence of the replacement of nitro group. It is suggested that STAB-1 can stabilize the energetic materials from the calculation. For STAB-4 molecule, the negative potentials observed above benzene were weaker than that of STAB-1 because methoxy group was replaced by the he weaker electron-donating group methyl group (Fig. 24.3).

For STAB-2 and STAB-3 molecule, the negative potentials observed above benzene were weaker than that of STAB-1, and the reason was that only one methoxy group or methyl group was found. Although they made weaker positive potentials around the benzene, the steric hindrance were also lower than STAB-1. And there are two locations for the replacement of nitro group in STAB-2 and STAB-3, while it was only one for STAB-1.

STAB-1 was selected as the model to evaluate the stabilizing property. The compatibilities of STAB-1 and different energetic materials were examined by DSC, and the results were shown in Fig. 24.4. It was obtained from the DSC of NC that a peak located at 208.6 °C, which is the decomposition temperature. While STAB-1 was mixed with NC, a valley was appeared at 51.5 °C which was the melting point of STAB-1, and the peak temperature remained almost in invariant (206.6 °C). It was suggested from the almost unchanged decomposition temperature that STAB-1 was compatible with NC [25]. Similar with NC, STAB-1 was compatible with NC-NG.

For FOX-7, the result was interesting. The DSC curve had a valley at 115.5 °C, while two peak at 230.6 °C and 276.0 °C, respectively. As STAB-1 was mixed, the valley became small and the first peak decreased sharply, while the second peak decreased slowly. The temperature of the two peak was 233.6 °C and 273.1 °C, respectively. It was suggested that STAB-1 can be compatible with FOX-7, and the mixture can be used in short time. The compatibilities of STAB-1 and RDX was examined. To our disappointment, STAB-1 can't be compatible with these energetic materials. The reason may be that STAB-1 could not be compatible with nitramine ($N–NO_2$) compounds. From the results, it can been seen STAB-1 can be used to stabilize the kind of Nitrocellulose.

The initial stabilizing property of STAB-1 was evaluated from the heat flow calorimetry measurements [26, 27]. STAB-1 was mixed with NC for the block test. Centralite-II which was contrasted was also mixed with NC, and the results were showed in Fig. 24.5. From the figure, it can be seen that the heat flow of STAB-1 was

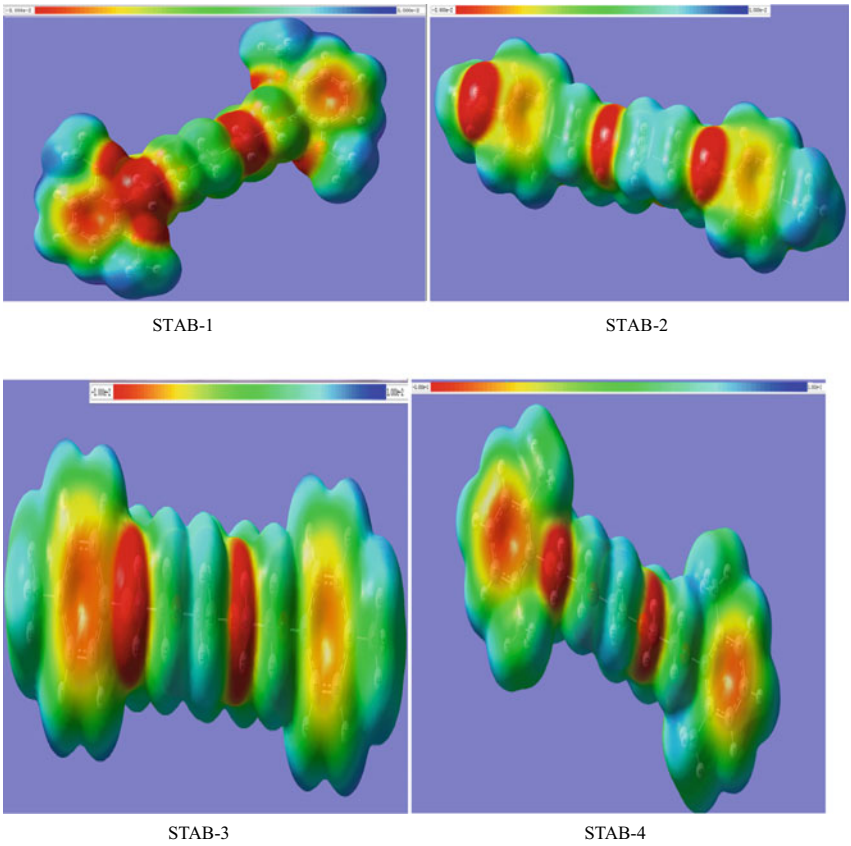

Fig. 24.3 The electrostatic potentials of STAB-1, STAB-2 and STAB-3

similar with Centralite-II. Below 30 °C, the heat flow of STAB-1 was higher than Centralite-II, and the heat flow of STAB-1 became lower than that of Centralite-II belong 40–60 °C. However, the heat flow of STAB-1 grew faster than Centralite-II when temperature was higher than 60 °C.

To evaluate the stabilizing property, samples in total of stabilized NC were prepared using STAB-1 and diphenylamine (DPA). A block test was performed by the heat flow calorimetry measurements (Fig. 24.6), and the measurements were performed at 85 °C for 181 h to ensure the stability of the NC for 10 years. And both STAB-1 and DPA passed the test. For the results from Figs. 24.5 and 24.6, it was proved that STAB-1 can stabilize NC.

Run	Energetic materials	The decomposition temperature of energetic materials(℃)	The decomposition temperature of STAB-1 and energetic materials(℃)	ΔT	The compatibility degree*
1	NC	208.6	206.6	2	good
2	NC-NG	202.4	200.4	2	good
3	FOX-7	230.6, 276.0	233.6,273.1,	3,2.9	middle
4	RDX	240.7	233.3	7.4	poor

*：0℃≤ΔT≤2℃，The system is compatible. (good)

：2℃≤ΔT≤5℃，The compatibility is slightly sensitive, and the mixture can be used in short time.(middle)

：5℃≤ΔT≤15℃，The compatibility is sensitive and not recommended in usage. (poor)

：ΔT＞15℃，the system is dangerous and forbidden to mix.

Fig. 24.4 The compatibilities of STAB-1 with different energetic materials

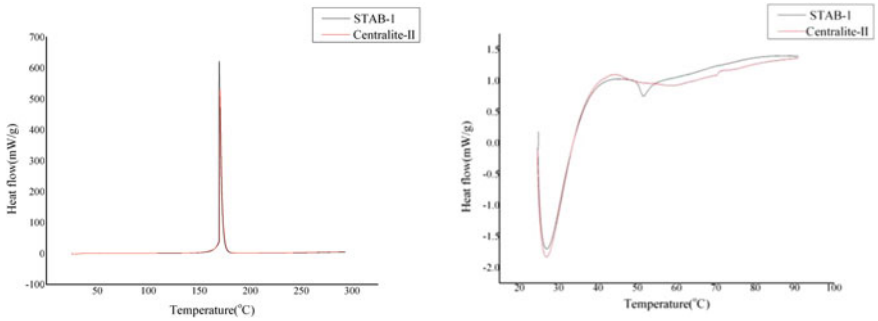

Fig. 24.5 The stabilizing propery of STAB-1

24.4 Conclusion

The new kind of stabilizers STAB-1 (1,2-bis(2-(2,6-dimethoxyphenoxy)ethoxy)ethane), STAB-2 (1,2-bis(2-(4-dimethoxyphenoxy)ethoxy)ethane), 1,2-bis(2-(p-tolyloxy)ethoxy)ethane (STAB-3) and 1,2-bis(2-(2,6-dimethylphenoxy)ethoxy)ethane (STAB-4) were prepared with the aim to obtain a nonvolatile stabilizer that cannot form N-nitroso compounds

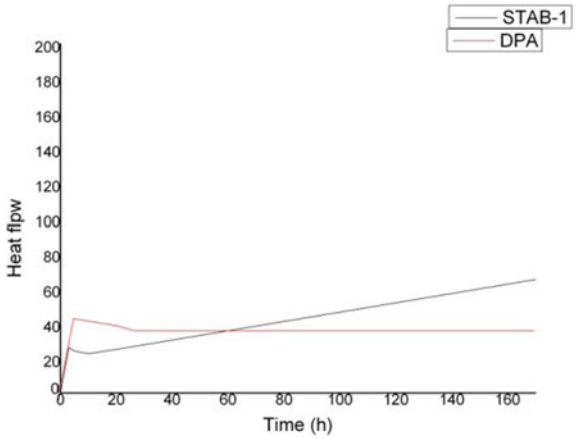

Fig. 24.6 HFC measurement of NC and STAB-1 at 85 °C

on prolonged contact with NC. The electrostatic potentials were calculated and the compatibilities of STAB-1 with energetic materials were tested. The original stablity of STAB-1 was evaluated and it can stabilized NC for ten years to the HFC study.

Acknowledgements This investigation received financial assistance from the National Science Foundation of China (Grant No. 21303133 and No. 21703167).

References

1. L. Lehky, *Technology of Propellants* (University of Pardubice, Pardubice, 2001), pp. 4–12
2. J. Petrzilek, *Relations Between Chemical Composition and Stability of Smokeless Powders* (University of Pardubice, 2000), pp. 37–38
3. F.W. Wang, X.L. Zeng, L. Xiu et al., Thermal decomposition characteristics of nitrates. Chin. J. Appl. Chem. **27**(3), 308–312 (2010)
4. T.B. Brill, P.E. Gongwer, Thermal decomposition energetic materials 69. Analysis of the kinetics of nitrocellulose at 50 °C–500 °C. Propel. Explos. Pyrotech. **22**, 38–44 (1997)
5. G. Heeb, R. Langelage, U. Schadeli, B. Vogelsanger, New stabilizers for nitrocellulose based propellants, part II, in *39th International Annual Conference of ICT*, Karlsruhe, Germany, 24–27 June 2008, pp. 90–91
6. Q. Wan, X. Sui, N.F. Wang, Quantitative method for monitoring stabilizers content of NEPE propellant by FTIR. J. Solid Rocket Technol. **36**(2), 274–277 (2013)
7. A.K. Sikder, N. Sikder, A review of advance high performance, insensitive and thermally stable energetic materials emerging for military and space applications. J. Hazard. Mater. **A112**, 1–15 (2004)
8. D.M. Badgujar, M.B. Talawar, S.N. Asthana et al., Advance in science and technology of modern energetic materials: an overview. J. Hazard. Mater. **151**, 289–305 (2008)
9. J.L. Johnson, Data collection requirements for quality evaluation (aging analysis) of energetic materials and method, in *37th International Annual Conference of ICT* (ICT, Karlsruhe, 2006), pp. 35–39
10. S. Wiker, G. Heeb, J. Petrzilek, J. Skladal, Triphenylamine—a new stabilizer for nitrollulose based propellants, part I: chemical stability studies. Propel. Explos. Pyrotech. **32**, 135–138 (2007)

11. B. Zhang, X.M. Song, Z.B. Jiang et al., A kind of method on estimating the safe storage life of propellant in depot storage. Chin. J. Explos. Propel. **28**(2), 29–31 (2005)
12. Q.M. Tang, Z. Pei, J.Y. Wu, Research on the life of solid rocket engine. Tact. Missile Technol. **2006**(2), 30–32 (2006)
13. L.L. Simon, E. Bergeron, H. Gagnon, A method to characterize gun power stabilizers, in *37th International Annual Conference of ICT* (ICT, Karlsruhe, 2006), pp. 48–49
14. M. Lamas, T. Kuokkanen, Molecular complexes in solution containing benzene-substituted crown ethers and tropylium ions. J. Phys. Org. Chem. **9**(1), 21–28 (1996)
15. L. Markku, P. Jouni, R. Kari, H. Juhani, Complexation of crown ethers and podands with tropylium cations: determination of stability constants and crystal structure of the dibenzo-24-crown-8-tropylium cation complex. Acta Chem. Scand. **52**, 563–570 (1998)
16. M. Lämsä, J. Huuskonen, K. Rissanen, J. Pursiainen, X-ray and NMR studies on host-guest inclusion complex formation between crown ethers and pyridinium compounds. Chem. Eur. J. **4**(1), 84–92 (1998)
17. O. Fryš, P. Bajerová, A. Eisner et al., Utilization of new non-toxic substances as stabilizers for nitrocellulose-based propellants. Propel. Explos. Pyrotech. **36**, 347–355 (2011)
18. S. Wilker, J. Skladal, G. Pantel, J. Petrzilek, Stability analysis of propellants containing new stabilizers, part IV: are phenols a possible alternative to aromatic amines, in *37th International Annual Conference of ICT*, Karlsruhe, Germany, 27–30 June 2006, pp. 84–85
19. M. Kimura, K. Kajita, N. Onoda et al., The development of a new nitrating agent: the unusual regioselective nitration of diphenylpolyethylene glycols and phenylpolyethylene glycols with (trimethylsilyl) nitrate-BF_3Et_2. J. Org. Chem. **55**(16), 4887–4892 (1990)
20. M. Lämsä, K. Raitamaa, J. Pursiainen, Synthesis of podands bearing aromatic end groups and complex formation with tropylium tetrafuoroborate in 1,2-dichloroethane. J. Phys. Org. Chem. **12**, 557–563 (1999)
21. R. Wen, *Organic Reactions for Drug Synthesis* (2002), pp. 132–136
22. Z.F. Yan, Y.F. Pan, Y.P. Ji et al., Synthesis and characterization of alkynyl-terminated bonding agent, in *Theory and Practice of Energetic Materials*, Qingdao, China, 16–18 Sept 2015, pp. 96–99
23. NATO Standardization Agreement STANAG 4582, *Explosives—NC Based Propellants—Stability Test Procedure and Requirements Using Heat Flow Calorimetry*, NATO AC/326 SG 1, 1st edn. (2004)
24. Y.Z. Liu, T. Yu, W.P. Lai et al., Adsorption behavior of acetone solvent at the HMX crystal faces: a molecular dynamics study. J. Mol. Graph. Model. **74**, 38–43 (2017)
25. Z.R. Liu, *Thermal Analyses for Energetic Materials* (National Defence Industry Press, Beijing, 2008), pp. 21–24
26. E.K. Stefan, P. Krumlinde, N. Latypov et al., Synthesis of stabilizers with plastizing properties for nitrocellulose propellants, in *Proceedings of the 17th Seminar on New Trends in Research of Energetic Materials (NTREM)*, Pardubice, 9–11 Apr 2014, pp. 189–194
27. P. Goede, P. krumlinde, E.K. Stefan et al., Scale-up studies of new stabilizer for nitrocellulose, in *46th International Annual Conference of ICT*, Karlsruhe, Germany, 27–30 June 2015, pp. 84–88

Chapter 25
Study on Preparation, Application and Modification of Flake Aluminium Powder

Jie Liu, Deqi Wang, and Fengsheng Li

Abstract Aluminium (Al) powder is one of fuels for solid propellants. The specific surface area of flake Al is larger than that of spherical Al powder and has higher reactivity. So, the flake Al has been prepared, applicated and further modified. Flake Al can improve thermal conductivity between components, improve mechanical sensitivity and combustion performance of propellant. Besides, by using the reaction of Al_2O_3 and TiC, the initial reaction temperature and energy release of thick flake aluminum (5 μm Flake Al)/titanium carbide (TiC) composite micro-unit have significant improvement.

25.1 Introduction

Aluminum powder (Al) is an important raw material in solid propellants [1–5]. As fuel, Al is an important component of solid propellant [6–8], which shows significant advantages, such as high combustion calorific value, low oxygen consumption and high measured specific impulse etc. [9–11]. The ignition and combustion reactivity of aluminum powder not only have a obviously impact on the combustion and energy release of solid propellant, but also have an important impact on the energy release efficiency [12–14]. In order to improve the safety of aluminum powder in the process of production, storage, transportation and use, a dense high melting point (2054 °C) alumina (Al_2O_3) film is usually formed on the surface of aluminum powder [15, 16]. However, this also makes the active aluminum inside the particle be hindered by the surface alumina film in the practical application of aluminum powder in propellant,

J. Liu (✉) · D. Wang · F. Li
National Special Superfine Powder Engineering Research Center of China, School of Chemistry and Chemical Engineering, Nanjing University of Science and Technology, Nanjing 210094, China
e-mail: jie_liu_njust@126.com

D. Wang
e-mail: deqi_wang_njust@163.com

F. Li
e-mail: lfs_njust@126.com

A. Gany and X. Fu (eds.), *2021 International Conference on Development and Application of Carbon Nanomaterials in Energetic Materials*, Springer Proceedings in Physics 276,
https://doi.org/10.1007/978-981-19-1774-5_25

which is not conducive to the contact between active aluminum and oxidation components. So, the ignition and combustion reaction activity of aluminum powder has been limited [15–18]. In addition, the combustion product Al_2O_3 will be wrapped on the surface of active Al again, which further hinders the combustion reaction, resulting in incomplete combustion of aluminum powder and reduced energy release efficiency. Therefore, how to solve the contradiction between "safety" and "efficient application", design new principles and technical approaches, and realize the purpose of effectively cracking Al_2O_3 film in the combustion process of aluminum powder to improve the reactivity and energy release efficiency of Al are urgent problems to be solved in the field of solid propellant. And it is also an important problem in the research field of aluminum-containing mixed explosives.

Compared with spherical Al powder, flake Al powder has a larger specific surface area, which means that the reactivity of flake Al will be higher than spherical Al. So, the flake Al has been prepared and applied in solid propellants [19, 20]. However, due to the low content of active aluminum in the flake aluminum, the burning rate of flake Al propellant is not significantly improved, so the flake aluminum has been further modified. Inspired by the ceramic refining process [21–28], thick flake aluminum (5 μm Flake Al)/titanium carbide (TiC) composite micro-unit has been designed and prepared by using the reaction of Al_2O_3 and TiC [29]. By embedding TiC into the surface of 5 μm Flake Al, the purpose of improving the ignition and combustion reactivity of Al has successfully achieved. The application of 5 μm Flake Al/TiC composite micro-unit in solid propellants will be further explored in future work.

25.2 Experiment Section

In order to study the application and modification of flake aluminum powder in solid propellants, flake Al, solid propellants consisting mainly of AP and Al and 5 μm Flake Al/TiC composite micro-unit were prepared, respectively.

25.2.1 The Preparation of Flake Al

Flake Al were prepared by bidirectional rotation mill. The grinding time of Al powder was 2.5 h (flake Al-1) and 7 h (flake Al-2), respectively.

25.2.2 The Preparation of Solid Propellants

Solid propellants were prepared by screw extrusion technology. Table 25.1 was the ingredient list of propellants within the tolerance range. Firstly, all the components of propellants were precisely weighed on the basis of Table 25.1. Secondly, placing

Table 25.1 Basic formulation of solid propellants

Components	NC	NG	AP	Al
Content, %	35.2 ± 2.0	25.2 ± 2.0	30.0 ± 2.0	5.0 ± 1.0

the weighed components of the propellant in a mixed solution of ethanol and acetone (volume ratio is 1:1). Then, the mixture was stirred vigorously until uniformly dispersed. Finally, the as-prepared mixture was calendered and molded, and then propellant samples were successfully prepared [20].

25.2.3 The Preparation of 5 μm Flake Al/TiC Composite Micro-Unit

5 μm Flake Al/TiC composite micro-unit was prepared by two-step ball milling. Firstly, 5 μm Flake Al was prepared by wet milling with planetary ball mill. Then the 5 μm Flake Al/TiC composite micro-unit was prepared by dry ball milling with planetary ball mill. Finally, the 5 μm Flake Al/TiC composite micro-unit was successfully prepared by two-step ball milling.

25.3 Results and Discussion

25.3.1 Morphology of Flake Al, 5 μm Flake Al and 5 μm Flake Al/TiC

The morphology of flake Al, 5 μm Flake Al and 5 μm Flake Al/TiC was characterized by scanning electron microscope [20]. As shown in Fig. 25.1a and b, most of the flake Al-1 (2.5 h) and flake Al-2 (7 h) were flake-like, and the thickness of flake Al-2 was more small than flake Al-1. With the increase in grinding time, the thickness of flake Al powder gradually became smaller. As shown in Fig. 25.1c and d, the porosity of Spherical Al propellant was larger than that of flake Al-2 propellant. As shown in Fig. 25.1e and f 5 μm Flake Al thickness was about 5 μm. And 5 μm Flake Al/TiC composite micro-unit had a structure of TiC embedded into the surface of 5 μm Flake Al.

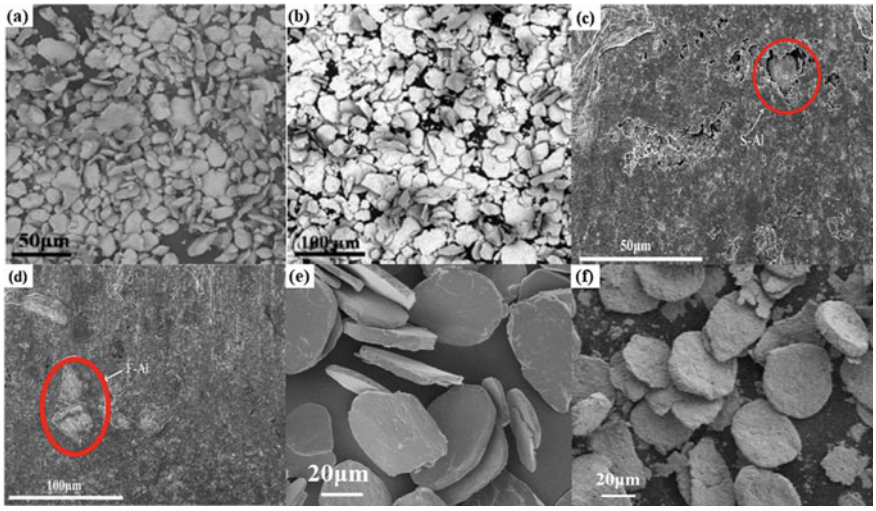

Fig. 25.1 SEM morphologies of flake Al-1 (**a**), flake Al-2 (**b**), spherical Al propellant (**c**), flake Al-2 propellant (**d**), 5 **μm** Flake Al (**e**) and 5 **μm** Flake Al/TiC composite micro-unit (**f**)

25.3.2 Application Performance of Flake Al-2 in Solid Propellants

25.3.2.1 Reactivity and Thermal Property

Figure 25.2 represented TG-DTG curves of propellant samples at the heating rate of 20 °C/min [20]. As shown in Fig. 25.2, there were two stages of thermal decomposition of the propellants. In the rapid reaction stage, the DTG peak temperature of the flake Al propellant is lowered by about 1.5 °C than that of Spherical Al propellant. This shows that flake aluminum can improve the reactivity of propellant.

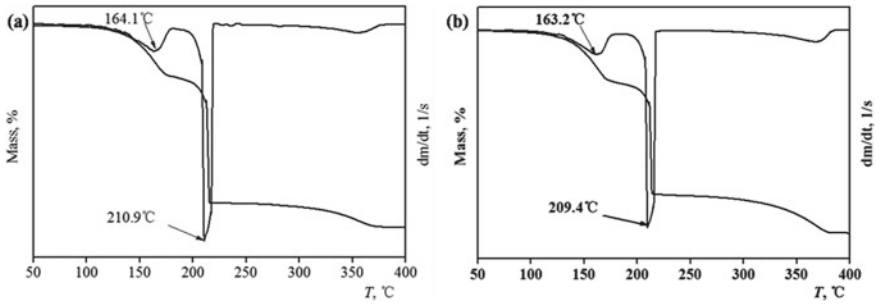

Fig. 25.2 TG-DTG curves for spherical Al propellant (**a**), flake Al propellant (**b**) at the heating rate of 20 °C/min

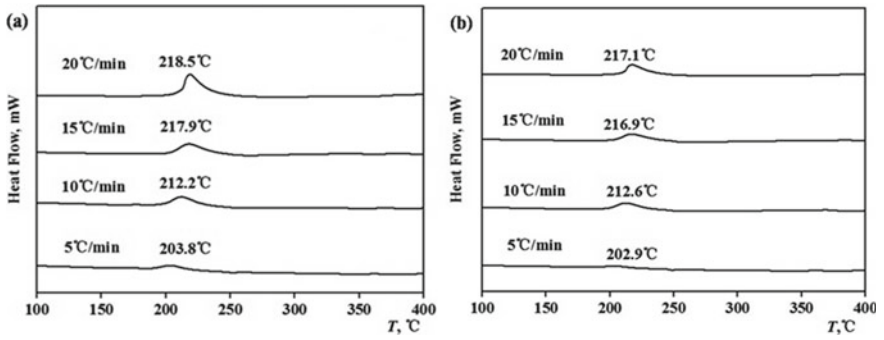

Fig. 25.3 DSC curves of spherical Al-AP-based CMDB propellant (**a**), Flake Al-2-AP-based CMDB propellant (**b**) at different heating rates

The DSC curves of the two kinds of propellant samples at different heating rates (5, 10, 15 and 20 °C/min) were shown in Fig. 25.3 [20]. The values of reaction peak temperature for the flake Al CMDB propellant are all decreased compared to that of spherical Al CMDB propellant. In general, as the specific surface area of Al powder increase, flake Al can absorb more reactive molecules onto their surface, and catalyze their reactions, which lead to a lower decomposition temperature.

The kinetic parameters for pure AP and AP/Al mixtures decomposition can be calculated according to Kissinger correlation Eq. (25.1) [30] and Arrhenius equation Eq. (25.2) [31].

$$\ln\left(\frac{\beta}{T_p^2}\right) = -\frac{E_a}{RT_p} + \ln\left(\frac{AR}{E_a}\right) \tag{25.1}$$

$$k = A\exp\left(-\frac{E_a}{RT_p}\right) \tag{25.2}$$

where β is the heating rate (K/min), T_p is the exothermic peak temperature in the DSC curve (K), R is the ideal gas constant, 8.314 J/(mol·K), E_a is the activation energy (J/mol), A is the frequency factor (/min), and k is the reaction rate constant when the T is equal to T_p (/s).

The E_a and A, 1/min of the thermal decomposition of propellants are calculated based on experimental data in Fig. 25.3 by using Eq. (25.1). The calculated results of E_a and A were shown in Table 25.2.

Table 25.2 Kinetic parameters for propellant samples

Samples	E_a, kJ/mol	A, 1/min
Spherical Al propellant	161.5	2.043×10^{17}
Flake Al propellant	162.6	2.861×10^{17}

Combined with Eq. (25.2), the E_a and A of the spherical Al propellant and Flake Al-2-AP-based CMDB propellant were brought into the equation. The reaction rate constants of spherical Al propellant and flake Al propellant can be determined as k_1 and k_2, respectively. Let $k_1 = k_2$, bring in the value of E_a and A, determine the thermal decomposition isokinetic temperature T_{is} of spherical Al propellant and flake Al propellant is 392.9 K (119.7 °C). When the temperature is less than 119.7 °C, the flake Al propellant has a small thermal decomposition reaction rate constant and good thermal stability. That means flake Al-propellant is more stable and safe during storage and transportation. When the temperature is less than 119.7 °C. The A of the flake Al propellant is higher than that of the spherical Al It means that the flake Al propellant has higher reaction rate in propellant combustion process. However, due to the active aluminum content is reduced of flake aluminum, and the thermal performance of the propellant is not greatly improved.

25.3.2.2 Sensitivity and Combustion Performances

Mechanical sensitivity results of propellant samples are given in Table 25.3. In friction sensitivity test, test pressure is 2.45 MPa. The value of P for flake Al propellant is 88%, which was lower than that of spherical Al. In impact sensitivity tests, drop hammer weight is 5 kg. The value of H_{50} for spherical Al propellant (9.3 cm) was much lower than that of flake Al propellant ($H_{50} = 26.7$ cm). It is clear that compared with spherical Al propellant, the friction and impact sensitivities for flake A propellants are decreased by 12% and 187%, respectively. These results indicated that the flake Al propellant was more insensitive to impact and friction stimuli.

The burning rates of propellant samples were shown in Table 25.3 [20]. The burning rate of flake Al propellant was increased by 5.5% from 55.0 mm/s to 58.0 mm/s, compared with that of spherical Al propellant.

Compared with spherical Al, flake Al is relatively flexible and has a larger specific surface area. Flake Al combined more closely with the components, and not easy to produce strong friction with other components of propellants. So, it is hard to form a heterogeneous bulge in the interior of the propellant. Therefore, flake A propellant may get higher heat transfer rate than that of spherical Al propellant, which is beneficial to reduce sensitivity and increase burning rate. However, the improvement of thermal and combustion properties of sheet aluminum propellant

Table 25.3 Friction and impact sensitivity of the propellant samples

Samples	Friction sensitivity	Impact sensitivity	Burning rate, mm/s
	P, %	H_{50}, cm	
Spherical Al propellant	100	9.3	55.0 ± 0.9
Flake Al propellant	88	26.7	58.0 ± 0.6

is slight. In order to give full play to the advantages of flake Al, flake Al has been further modified.

25.3.3 Modification of Flake Al

The initial reaction temperature and energy release of 5 μm Flake Al/3%TiC, 5 μm Flake Al/4%TiC, 5 μm Flake Al/5%TiC and 5 μm Flake Al/6%TiC were characterized by DSC [29]. It can be seen from Fig. 25.4 that during the reaction process of 5 μm Flake Al/TiC composite micro-unit, there were initial reaction of Al between 550 °C and 600 °C and combustion exothermic peak between 900 °C and 1100 °C.

Table 25.4 showed the initial reaction temperature of 5 μm Flake Al/TiC composite micro-unit at 20°C/min and energy release at heating rate [29]. It can be seen from Table 25.4 that initial reaction temperature of 5 μm Flake Al/5%TiC composite micro-unit is minimum. And the energy release of 5 μm Flake Al/5%TiC is the largest (21,419 J/g).

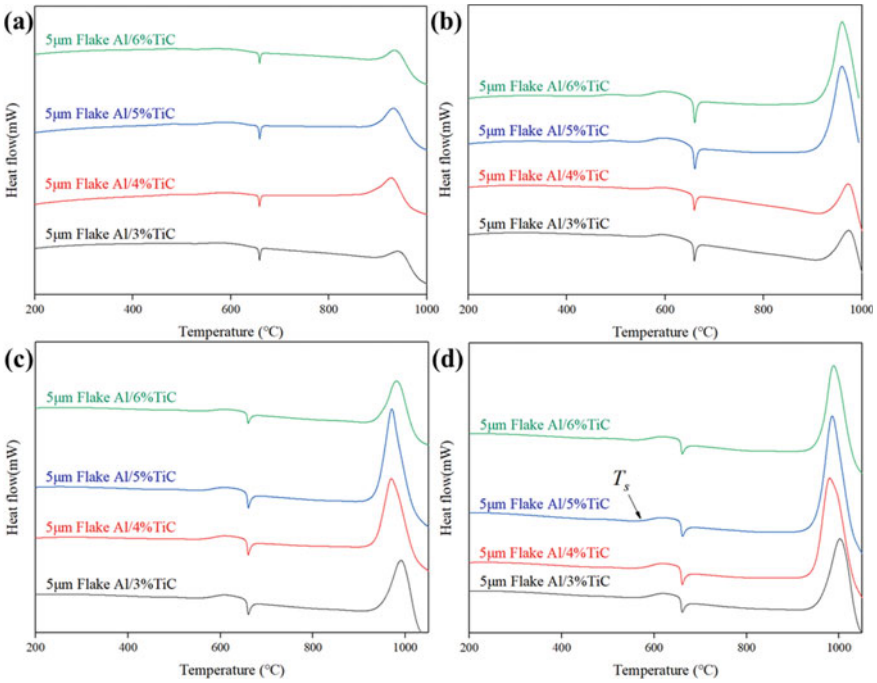

Fig. 25.4 DSC curves of samples at 5 °C/min (**a**), 10 °C/min (**b**), 15 °C/min (**c**), and 20 °C/min (**d**), respectively

Table 25.4 Initial reaction temperature at 20 °C/min and energy release at heating rate of samples

Sample	Initial reaction temperature at 20 °C/min (°C)	Energy release (J/g)			
		5 °C/min	10 °C/min	15 °C/min	20 °C/min
5 μm Flake Al/3%TiC	578.72	8142	8939	14,242	14,827
5 μm Flake Al/4%TiC	577.96	8428	9531	17,739	18,169
5 μm Flake Al/5%TiC	574.12	8763	9708	18,340	21,419
5 μm Flake Al/6%TiC	575.29	8375	9644	14,795	15,640

Compared with flake Al that there is no reaction and energy release in air under 1200 °C [29], 5 μm Flake Al/TiC composite micro-unit successfully improved the reactivity of flake Al.

25.4 Conclusions

The Flake Al has been prepared, applicated and modified. The SEM observations show that the flake Al propellant has lower porosity. That improves thermal conductivity between components, due to the increase in the specific surface area of flake Al. In addition, flake Al with a large specific surface area also improves the mechanical sensitivity and combustion performances of propellant, respectively. This provides a new path for improving security situation during the process of production, storage and application of propellants.

Because of flake Al has slightly improved propellant performance, it is necessary to modify flake Al. 5 μm Flake Al/TiC composite micro-unit was designed and successfully prepared by two-step ball milling, which had the structure of TiC embedded into 5 μm Flake Al. By using the reaction of Al_2O_3 and TiC, the initial reaction temperature, combustion reactivity and the energy release of flake Al have been improved.

References

1. K. Alexey, P. Vasiliy, M. Ksenia, K. Dmitry, Metalized solid propellant combustion under high-speed blowing flow. J. Mech. Sci. Technol. **34**, 2245–2253 (2020)
2. W. Ao, Z. Fan, L. Liu, Y. An, J. Ren, M. Zhao, P. Liu, L.K.B. Li, Agglomeration and combustion characteristics of solid composite propellants containing aluminum-based alloys. Combust. Flame **220**, 288–297 (2020)
3. P.A. Ramakrishna, N. Rathi, V. Yogeshkumar, Solid fuel rich propellant development for use in a ramjet to propel an artillery shell. Def. Sci. J. **70**, 329–335 (2020)
4. L.-Q. Xiao, X.-Z. Fan, J.-Z. Li, Z. Qin, X.-L. Fu, W.-Q. Pang, Y. Wang, Effect of Al content and particle size on the combustion of HMX-CMDB propellant. Combust. Flame **214**, 80–89 (2020)

5. K. Jayaraman, K.V. Anand, D.S. Bhatt, S.R. Chakravarthy, R. Sarathi, Production, characterization, and combustion of nanoaluminum in composite solid propellants. J. Propul. Power **25**, 471–481 (2009)
6. V.A. Babuk, V.A. Vassiliev, V.V. Sviridov, Propellant formulation factors and metal agglomeration in combustion of aluminized solid rocket propellant. Combust. Sci. Technol. **163**, 261–289 (2001)
7. K. Gnanaprakash, S.R. Chakravarthy, R. Sarathi, Combustion mechanism of composite solid propellant sandwiches containing nano-aluminium. Combust. Flame **182**, 64–75 (2017)
8. A. Dokhan, E.W. Price, J.M. Seitzman, R.K. Sigman, The effects of bimodal aluminum with ultrafine aluminum on the burning rates of solid propellants. Proc. Combust. Inst. **29**, 2939–2946 (2002)
9. F. Maggi, G. Gariani, L. Galfetti, L.T. DeLuca, Theoretical analysis of hydrides in solid and hybrid rocket propulsion. Int. J. Hydrogen Energy **37**, 1760–1769 (2012)
10. Y. Yavor, V. Rosenband, A. Gany, Reduced agglomeration in solid propellants containing porous aluminum. Proc. Inst. Mech. Eng. Part G: J. Aerosp. Eng. **228**, 1857–1862 (2014)
11. S. Sadeghipour, J. Ghaderian, MA Wahid, Advances in aluminum powder usage as an energetic material and applications for rocket propellant, pp. 100–108 (2012)
12. P. Kumar, M. Varshney, A. Manash, Combustion performance studies of aluminum and boron based composite solid propellants in sub-atmospheric pressure regimes. Propul. Power Res. **8**, 329–338 (2019)
13. J. Wang, Z. Yang, M. Wang, Effect of non-spherical particles on burning behavior during aluminum combustion. Particuology **51**, 173–183 (2020)
14. V.A. Arkhipov, A.G. Korotkikh, The influence of aluminum powder dispersity on composite solid propellants ignitability by laser radiation. Combust. Flame **159**, 409–415 (2012)
15. A. Braconnier, C. Chauveau, F. Halter, S. Gallier, Experimental investigation of the aluminum combustion in different O_2 oxidizing mixtures: effect of the diluent gases. Exp. Therm. Fluid Sci. **117**, 1–8 (2020)
16. L. Liang, X. Guo, X. Liao, Z. Chang, Improve the interfacial adhesion, corrosion resistance and combustion properties of aluminum powder by modification of nickel and dopamine. Appl. Surf. Sci. **508**, 1–10 (2020)
17. D. Liang, R. Xiao, J. Liu, Y. Wang, Ignition and heterogeneous combustion of aluminum boride and boron–aluminum blend. Aerosp. Sci. Technol. **84**, 1081–1091 (2019)
18. M. Stephens, T. Sammet, E. Petersen, R. Carro, S. Wolf, C. Smith, Performance of ammonium-perchlorate-based composite propellant containing nanoscale aluminum. J. Propul. Power **26**, 461–466 (2010)
19. S. Zheng, J. Liu, Y. Wang, F. Li, L. Xiao, X. Ke, G. Hao, W. Jiang, D. Li, Y. Li, Z. Lan, Effect of aluminum morphology on thermal decomposition of ammonium perchlorate. J. Therm. Anal. Calorim. **134**, 1823–1828 (2018)
20. D.Q. Wang, H.M. Yu, J. Liu, F.S. Li, X.X. Jin, S.J. Zheng, T.T. Zheng, Y. Li, Z.J. Zhang, D. Li, Z.G. Lan, Preparation and properties of a flake aluminum powder in an ammonium-perchlorate-based composite modified double-base propellant. Combust. Explos. Shock Waves **56**, 691–696 (2020)
21. K. Ahmad, W. Pan, Enhanced electrical and mechanical properties of alumina-based TiC composites by spark plasma sintering. Metall. Mater. Trans. A. **45**, 6271–6276 (2014)
22. D. Sun, X. Jiang, L. Su, H. Sun, C. Hu, T. Song, Z. Luo, Fabrication and mechanical properties of Al2O3–TiC ceramic composites synergistically reinforced with multi-walled carbon nanotubes and graphene nanoplates. Ceram. Int. **46**, 20068–20080 (2020)
23. A.R. Studart, U.T. Gonzenbach, E. Tervoort, L.J. Gauckler, Processing routes to macroporous ceramics: a review. J. Am. Ceram. Soc. **89**, 1771–1789 (2006)
24. X.-H. Gao, Z.-M. Guo, Q.-F. Geng, P.-J. Ma, A.-Q. Wang, G. Liu, Enhanced optical properties of TiN-based spectrally selective solar absorbers deposited at a high substrate temperature. Sol. Energy Mater. Sol. Cells **163**, 91–97 (2017)
25. X.-H. Gao, Z.-M. Guo, Q.-F. Geng, P.-J. Ma, A.-Q. Wang, G. Liu, Enhanced thermal stability and spectral selectivity of SS/TiC-Y/Al_2O_3 spectrally selective solar absorber by thermal annealing. Sol. Energy **140**, 199–205 (2016)

26. X.-H. Gao, Z.-M. Guo, Q.-F. Geng, P.-J. Ma, A.-Q. Wang, G. Liu, Microstructure, chromaticity and thermal stability of SS/TiC-WC/Al_2O_3 spectrally selective solar absorbers. Sol. Energy Mater. Sol. Cells **164**, 63–69 (2017)
27. X.-H. Gao, Z.-M. Guo, Q.-F. Geng, P.-J. Ma, G. Liu, Structure, optical properties and thermal stability of TiC-based tandem spectrally selective solar absorber coating. Sol. Energy Mater. Sol. Cells **157**, 543–549 (2016)
28. M.A. El Hakim, M.D. Abad, M.M. Abdelhameed, M.A. Shalaby, S.C. Veldhuis, Wear behavior of some cutting tool materials in hard turning of HSS. Tribol. Int. **44**, 1174–1181 (2011)
29. D. Wang, X. Cao, J. Liu, Z. Zhang, X. Jin, J. Gao, H. Yu, S. Sun, F. Li, TF-Al/TiC composite micro-unit for application potential in solid propellants. Chem. Eng. J. **425** (2021)
30. R.L. Blaine, H.E. Kissinger, Homer Kissinger and the Kissinger equation. Thermochim. Acta **540**, 1–6 (2012)
31. J.M. Rodríguez-Díaz, M.T. Santos-Martín, Study of the best designs for modifications of the Arrhenius equation. Chemom. Intell. Lab. Syst. **95**, 199–208 (2009)

Chapter 26
Fabrication of HKUST-1 Based Ink for Direct Writing of Precursors of Primary Explosives

Caimin Yang, Yan Hu, Huipeng Zeng, Xuwen Liu, Yinghua Ye, and Ruiqi Shen

Abstract As a direct-write molding technology based on the principle of layer-by-layer accumulation, inkjet printing has shown application prospects in the field of micro-sized energetic materials. Based on HKUST-1, the influence of three binders of polyvinyl alcohol, ethylcellulose, and polyvinylidene fluoride on the printing characteristics of precursor inks was explored. The binder system suitable for ink preparation was screened out, and the best printing parameters were determined. The matching rule between the printing line width and the needle aperture was studied. Moreover, the best ink formula and needle size which can achieve the target line width were selected. The optimized ink was pyrolyzed at a high temperature under an inert atmosphere to prepare a composite of nano-copper coated by porous carbon and copper azide-porous carbon composite energetic materials was in-situ prepared through a gas–solid azidation reaction. This work laid the foundation for the subsequent realization of micro-scale precision charges based on carbon-based copper azide energetic materials.

C. Yang · Y. Hu (✉) · H. Zeng · X. Liu · Y. Ye · R. Shen
School of Chemistry and Chemical Engineering, Nanjing University of Science and Technology, Nanjing 210094, China
e-mail: huyan@njust.edu.cn

C. Yang
e-mail: Ycaimin@njust.edu.cn

X. Liu
e-mail: lxw@njust.edu.cn

Y. Ye
e-mail: yyinghua@njust.edu.cn

R. Shen
e-mail: rqshen@njust.edu.cn

Micro-Nano Energetic Devices Key Laboratory, Ministry of Industry and Information Technology, Nanjing 210094, China

A. Gany and X. Fu (eds.), *2021 International Conference on Development and Application of Carbon Nanomaterials in Energetic Materials*, Springer Proceedings in Physics 276,
https://doi.org/10.1007/978-981-19-1774-5_26

26.1 Introduction

The modern battlefield environment has an increasing demand for miniaturization, intelligence, and integrated pyrotechnics. Traditional pyrotechnics cannot meet this increasing demand. Therefore, the integration of micro-electromechanical systems (MEMS) and pyrotechnics technology has become the development trend [1–3]. Obviously, traditional pyrotechnic agents are increasingly unable to meet the demand for sophisticated weapons. In order to meet the needs of the miniaturization of pyrotechnics, researchers have turned their attention to copper azide. Compared with traditional detonators such as mercury fulminate, lead azide, and lead styphnate, copper azide is less toxic, less harmful to the environment, and has better detonating properties [4, 5]. Although copper azide has a high energy density and excellent initiation ability, it is difficult to be applied in practice due to its extremely sensitive to electrostatic stimulation. Researchers have made many attempts to improve the safety during the preparation and use of copper azide, such as the use of liquid–solid azide method to synthesize copper azide film [6] and embed copper azide in the graphene framework [7–10] or carbon nanotubes [11–19]. Wang et al. [20–22] proposed a method for preparing primary explosives using carbonized metal organic framework (MOFs) as conductive porous carbon matrix and metal source. Carbonizing MOFs to produce a carbon skeleton with a porous structure and good conductivity, and evenly coating the primary explosive in such a carbon skeleton, can avoid charge accumulation in time to reduce its electrostatic sensitivity and improve its safety. Xu et al. [23] used low-cost cellulose derivatives as precursor materials to prepare copper azide porous carbon framework (CA@PC) hybrids in relatively simple steps, which reduced the sensitivity of copper azide.

In the micro-transducer, how to realize the micro-sized charge has always been a hot spot in the research field of MEMS pyrotechnics. The direct writing technique was first proposed by Hull in 1986 [24]. Combining direct writing molding technology with energetic material charge technology can realize some advanced functions and effects that cannot be achieved by traditional charge technology [25–28]. Applying inkjet printing to the charge of energetic materials can prevent researchers from directly contacting high-sensitivity explosives. Therefore, it is a very safe method of charging primary explosives. Since inkjet printing technology is compatible with MEMS technology, its application in preparing the micro-nano structure of the initial detonator of the detonation sequence can promote the rapid development of MEMS pyrotechnics.

Shen et al. [29] proposed the design of energetic ink formulations, and studied the characteristics of the ink formed by three energetic carriers (Nitrocotton (NC), polyvinyl butyral (PVB), polyglycidyl azide (GAP)) and nano-thermite. Han et al. [30] used CL-20 as the energetic component and nitrocellulose as the binder to explore the density, stability and uniformity of inks with different solvent configurations. Wang et al. [31] used PVDF and Viton as binders, mixed with nano-aluminum powder to make a thermite-like ink, and made a film by direct writing technology. Li

et al. [32, 33] prepared CL-20-based energetic ink and tested its printing performance with a pneumatic micro pen direct writing platform.

Xing [34] explored the ink formula with light-curable resin and nitrocellulose as the binder, and explored the influence of needle diameter on printing accuracy. Yao et al. [35, 36] used nano-CL-20 as the energetic component and nitrocellulose as the binder, and configured energetic ink. Ding [37] independently designed and developed a pneumatic printing nozzle suitable for melt-molded energetic materials. Liu et al. [38] used CL-20 as the energetic component to configure energetic ink, using simulation and experiment to corroborate each other, and explored the influence of needle diameter and direct writing pressure on the ink discharge rate of the needle. While researchers in the field of energetic materials are conducting detailed studies on energetic ink formulation design and printing parameters, more and more excellent ink formulations and printing methods have been unearthed [39–43].

In this work, the optimal preparation process conditions of the copper-containing MOFs material HKUST-1 were studied. Then, using copper-based MOFs as precursors, the characteristics of inks prepared under three binder systems (water-polyvinyl alcohol, isopropanol-ethyl cellulose and N,N-dimethylformamide-polyvinylidene fluoride) were explored and get a better ink formula through comparison. The matching rule between the printing line width of the ink and the needle aperture was explored, and the best ink formula and needle that can achieve the target line width were selected. The selected optimal ink was calcined at a high temperature under an inert atmosphere to prepare a porous carbon-copper composite material, and the copper azide energetic material was prepared in situ through a gas–solid phase azidation reaction. This paper proposes a new type of energy-containing charge technology suitable for high-energy, high-safety and miniaturized pyrotechnics, which is expected to meet the needs of miniaturization of weapon systems.

26.2 Materials and Methods

26.2.1 Materials

Copper acetate monohydrate ($Cu(CH_3OO)_2{\cdot}H_2O$) (J&K Scientific Co., Ltd, 98%), 1,3,5-Trimesic acid ($C_9H_6O_6$) (J&K Scientific Co., Ltd, 99.5%), N,N-Dimethylformamide (C_3H_7NO) (J&K Scientific Co., Ltd, 99%), Absolute ethanol (C_2H_6O) (Aladdin Co., Ltd, 99%), Polyvinyl alcohol (Aladdin Co., Ltd, 99%), Isopropanol (J&K Scientific Co., Ltd, 98%), Ethyl cellulose (J&K Scientific Co., Ltd, 99.5%), Polyvinylidene fluoride (–(C_2H_4O)n–) (J&K Scientific Co., Ltd, 99%), Isopropanol (C_3H_8O) (Aladdin Co., Ltd, 99%), Ethyl cellulose ($C_{23}H_{24}N_6O_4$) (Aladdin Co., Ltd, 99%), Polyvinylidene fluoride (–$(C_2H_2F_2)$n–) (Xilong Chemical Co., Ltd, 99.7%), sodium azide (AIKE Reagent Co., Ltd, 99%) were purchased commercially and used as received.

26.2.2 Preparation of HKUST-1

The metal cation (Cu^{2+}) provided by the copper acetate solution was used as the metal center and trimellitic acid was used as the organic ligand, and the coordination polymer HKUST-1 was synthesized by the ultrasonic-assisted method [44]. 0.2995 g (1.5 mmol) of copper acetate monohydrate was dissolved in 12 mL of water, and 18 mL of N,N-dimethylformamide (DMF) and 6 mL of absolute ethanol (EtOH) were mixed uniformly. 0.3152 g (1.5 mmol) of 1,3,5-trimellitic acid was added to the mixed solution of DMF and EtOH. When the copper acetate solution was mixed with the trimesic acid solution, a blue precipitate was formed. The mixed solution was sonicated at a constant temperature of 25 °C. After the sonication, it was poured into a 50 mL centrifuge tube, and centrifuged at a centrifugal speed of 9000 r/min for 10 min. After three centrifugation and washing, the blue solid precipitate was transferred to a watch glass and dried in an oven under normal pressure and 130 °C for 12 h to obtain dark blue HKUST-1 crystals.

26.2.3 Design of Ink Formula

Commonly used binders in ink formulations are: ethyl cellulose, polyvinylidene fluoride, polyvinylpyrrolidone, polyvinyl alcohol, polyglycidyl azide, fluororubber and gelatin. Taking into account the subsequent high-temperature carbonization, in-situ azide and other processes, according to the solubility and viscosity of the binder, three sets of solvent/binder systems were finally designed. The selected binders were polyvinyl alcohol, ethyl cellulose and polyvinylidene fluoride, the solvent corresponding to polyvinyl alcohol was pure water, the solvent corresponding to ethyl cellulose was isopropanol, and the solvent corresponding to polyvinylidene fluoride was N,N-dimethylformamide. The specific ink formula is shown in Table 26.1. In the ink formulation, the composition of the binder system and the quality of the binder are variables. The volume of the solvent is constant, 5 mL. The mass of the precursor HKUST-1 is also constant at 0.4 g.

26.2.4 Printing Characteristics of Selected Inks

We explored the matching rule between the printing line width of the selected ink and the aperture of the printing needle, and optimized the best ink formula and needle size that can achieve the target line width. Due to the high viscosity of the ink, even after stirring and ultrasound, there are still some tiny bubbles that cannot be removed. When the needle diameter is small, the bubbles will block the needle and cause the ink to fail to be successfully discharged.

Table 26.1 Design of ink formula

Number	Solvent/binder	Mass of the binder/g
1 (0)	Pure water/polyvinyl alcohol	0
1 (1)	Pure water/polyvinyl alcohol	0.1
1 (2)	Pure water/polyvinyl alcohol	0.2
1 (3)	Pure water/polyvinyl alcohol	0.3
1 (4)	Pure water/polyvinyl alcohol	0.4
2 (0)	Isopropanol/ethyl cellulose	0
2 (1)	Isopropanol/ethyl cellulose	0.1
2 (2)	Isopropanol/ethyl cellulose	0.2
2 (3)	Isopropanol/ethyl cellulose	0.3
2 (4)	Isopropanol/ethyl cellulose	0.4
3 (0)	DMF/polyvinylidene fluoride	0
3 (1)	DMF/polyvinylidene fluoride	0.1
3 (2)	DMF/polyvinylidene fluoride	0.2
3 (3)	DMF/polyvinylidene fluoride	0.3
3 (4)	DMF/polyvinylidene fluoride	0.4
3 (5)	DMF/polyvinylidene fluoride	0.5

In the beginning, we selected model 27G (inner diameter 0.2 mm, outer diameter 0.4 mm) as the direct writing needle with the smallest aperture. After printing many times, we found that both inks could not be smoothly discharged. After many times of printing, it is finally determined to use the three needles of model 20G (inner diameter 0.6 mm, outer diameter 0.9 mm), model 22G (inner diameter 0.4 mm, outer diameter 0.7 mm), and model 24G (inner diameter 0.27 mm, outer diameter 0.55 mm) to explore the matching rule of ink line width and needle aperture. The inks used in the experiment are inks 1 (4) and 2 (3). 1 (4) is the ink with water/polyvinyl alcohol as the binder system and the binder mass is 0.4 g, and 2 (3) is the ink with isopropanol/ethyl cellulose as the binder system and the mass of the binder is 0.3 g. The relevant printing

parameters in the direct writing process are: medicine thread length is 30 mm; needle length is 0.25 inches; needle height is 0.2 mm; X-axis movement speed is 2 mm/s, T-axis movement distance is 0.3 mm, and speed is 0.02 mm/s.

26.2.5 Pyrolytic Carbonization at High Temperature and Azide Reaction

The calcination temperature was 600 °C, the heating rate was 5 °C/min, and the temperature was kept at 600 °C for 1 h. The sample was ground into powder and placed in a porcelain ark, and the porcelain ark was pushed into the middle of the vacuum tube furnace with crucible tongs. When the heating was started, argon gas was introduced. After the temperature rose to the predetermined temperature, the temperature was kept at 600 °C for 1 h, then the instrument was turned off, the flange was unscrewed, and the porcelain ark was taken out after the temperature dropped to a suitable temperature, and the porcelain ark was naturally cooled to get samples at room temperature.

The process of azidation was to add 4 g of NaN_3 to 100 mL of water to prepare a NaN_3 solution, pour the solution into an azide container, and then remove the air in the container by blowing nitrogen. 4 g of concentrated nitric acid was weighed and poured into 100 mL of water, and it was dropped into the azidation container, and the azidation reaction proceeded for 36 h. After the experiment was over, the remaining HN_3 gas was discharged by introducing nitrogen gas and absorbed by NaOH solution.

26.3 Results and Discussion

26.3.1 Characterization and Analysis of HKUST-1

The X-ray electron diffraction (XRD) pattern of the HKUST-1 sample synthesized by the ultrasonic-assisted method is shown in Fig. 26.1. It can be seen from Fig. 26.1b, c and d that all the diffraction peaks in the XRD spectra of the samples prepared by the ultrasonic-assisted method for 60 min, 45 min and 30 min respectively are basically consistent with the diffraction peaks in the standard spectrum obtained by simulation (Fig. 26.1a), and no other obvious peaks appeared. Since the sample shown in Fig. 26.1e was sonicated for only 15 min, the reaction was not completely finished, and its diffraction peaks roughly matched the diffraction peaks of the standard spectra obtained by simulation, but there were still several impurity peaks. The XRD test results show that the sample synthesized by the ultrasonic-assisted method in this experiment is the copper-containing MOFs material HKUST-1.

Figure 26.2 shows the scanning electron microscope (SEM) images of HKUST-

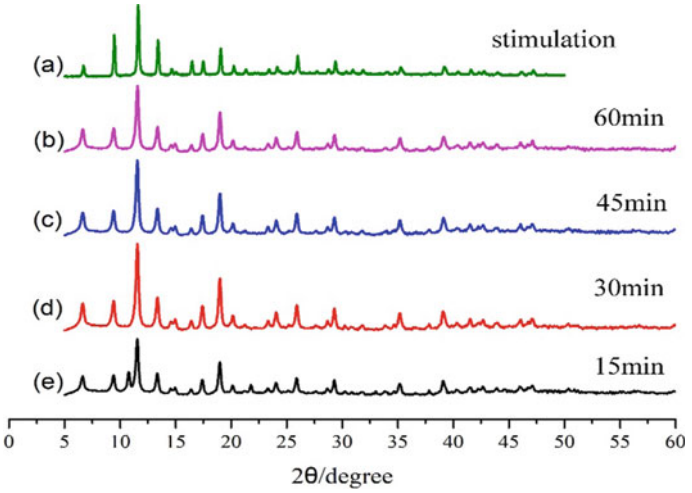

Fig. 26.1 Standard spectra of copper-containing metal organic framework material HKUST-1 (obtained by simulation) and XRD spectra of synthetic samples. **a** Standard spectrum of HKUST-1 obtained by simulation; **b** XRD spectrum of the sample obtained by ultrasound for 60 min; **c** by ultrasound for 45 min; **d** obtained by ultrasound for 30 min, **e** obtained by ultrasound for 15 min.

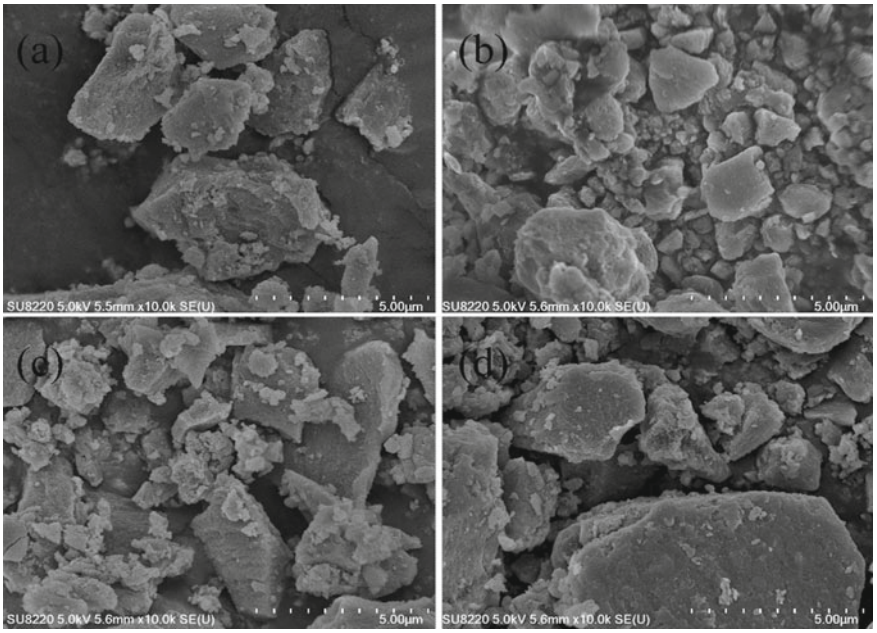

Fig. 26.2 SEM images of HKUST-1 material samples prepared under different ultrasonic time conditions: **a** Ultrasound for 60 min; **b** ultrasound for 45 min; **c** ultrasound for 30 min; **d** ultrasound for 15 min

1 material samples prepared under the conditions of 15 min, 30 min, 45 min and 60 min ultrasonic time. Different from the typical octahedral crystals prepared by the solvothermal method, the samples prepared by the ultrasonic-assisted method are in block shape with uneven particle size, most of which are between 1 and 2 μm. This may be due to the influence of ultrasound, which has changed the morphology of the crystal.

In order to further understand the crystal quality and morphology of the prepared materials, the prepared samples were characterized by high-resolution transmission electron microscopy. Figure 26.3 shows the HRTEM image of the prepared HKUST-1 sample. It can be seen from the figure that the prepared HKUST-1 has a smooth surface, no obvious defects, good crystallinity, and the entire particle is of nanometer scale. The material exhibits good homogeneity, which proves that the copper-containing metal organic framework material HKUST-1 prepared by the ultrasonic-assisted synthesis method is relatively pure and does not have impurity phases.

The material was also characterized by X-ray energy spectroscopy (EDS). This characterization measured the specified element at a certain point on the sample, and detected the three elements of C, Cu, and O in this point. Figure 26.4 shows the peaks of these three elements. The relative contents of these three elements were determined, and the mass fraction of C was 44.57%, the mass fraction of oxygen was 28.29%, and the mass fraction of Cu was 27.14%.

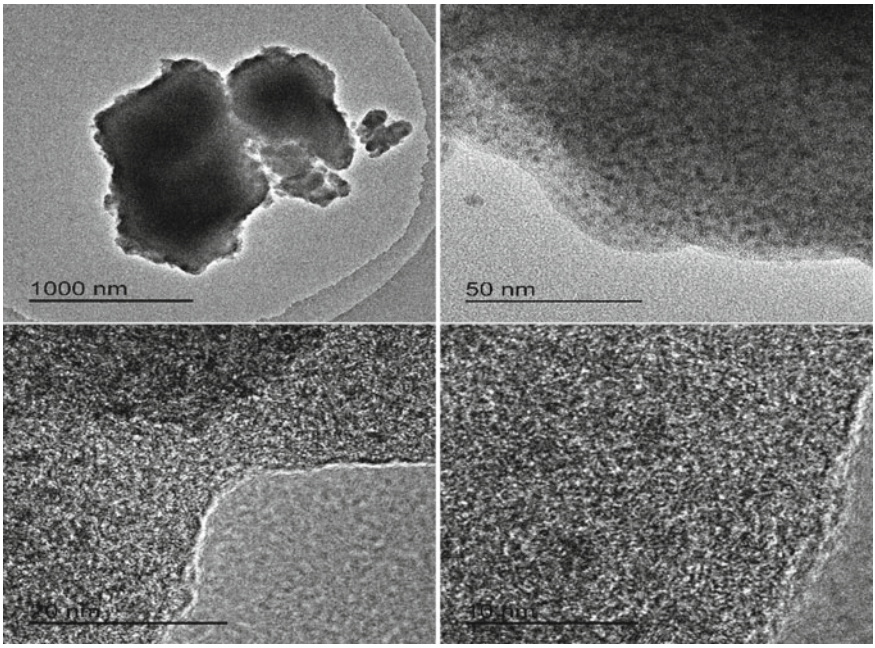

Fig. 26.3 HRTEM images of prepared HKUST-1

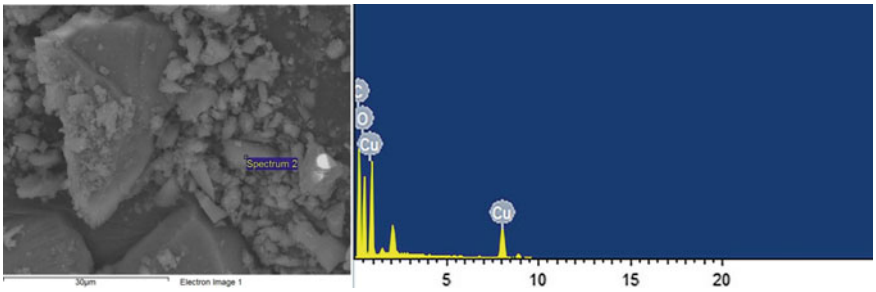

Fig. 26.4 EDS spectrum of HKUST-1 synthesized by ultrasound-assisted method

Table 26.2 The quality of products under different ultrasound time

Number	Ultrasound time/min	Mass of products/g
1	15	0.3891
2	30	0.4890
3	45	0.4892
4	60	0.4896

The weights of HKUST-1 products obtained under different ultrasound time are shown in Table 26.2. It can be seen from Table 26.2 that there is a large difference in the weight of the product when the ultrasonic time is 15 min and 30 min, while the weight of the product obtained at the ultrasonic time of 30 min and 45 min and 60 min is not much different. This shows that the reaction is basically completed when the ultrasound time is 30 min, and subsequent increases in the ultrasound time have little effect on the yield. Therefore, an optimal experimental condition for the synthesis of HKUST-1 was obtained: the same molar mass of copper acetate monohydrate and trimellitic acid were respectively prepared into solutions. Copper acetate monohydrate is dissolved in water to form a copper acetate aqueous solution; trimellitic acid is dissolved in a DMF-anhydrous ethanol composite solvent to form a trimesic acid composite solution. The volume ratio of the solvent is: DMF:EtOH:H_2O = 3:1:2. The two solutions were mixed uniformly and sonicated at a constant temperature of 25 °C for 30 min. Then the resulting solution was centrifuged, washed with water and absolute ethanol, and centrifuged. Finally, it is dried at 130 °C for 12 h to obtain HKUST-1 crystals.

26.3.2 Design of Ink Formula

The binder system of the first ink is water/polyvinyl alcohol. After the inks were allowed to stand for 24 h, they were found to have formed a layer of precipitation on the bottom of the beaker. In ink 1 (0) without the addition of a binder, delamination was the most serious. The precipitation decreases with the increase in the amount of

binder added. At 1 (3), there is only a small amount of precipitation at the bottom of the beaker. Through the direct writing of the printing equipment, it was found that the 1 (4) ink can discharge ink smoothly without clogging the needle, and the ink curing time is moderate. Therefore, the formula numbered 1 (4) is used as the best formula for water/polyvinyl alcohol binder system ink.

The binder system of the second set of inks is isopropanol/ethyl cellulose. When the ink was allowed to stand for 24 h, a layer of precipitation was formed. But compared with the ink configured with water/polyvinyl alcohol as the binder system, the blue precipitation is much less. Because the ink numbered 2 (4) is relatively viscous and extremely viscous, there are still more large bubbles in it after stirring and ultrasonic, and the curing time is short during printing, which is easy to block the needle, so we discarded it. No. 2 (3) ink has moderate viscosity and smooth ink output. Although the curing time is shorter than that of the ink configured with water-polyvinyl alcohol as the binder system, it will not block the needle. So we use the No. 2 (3) formula as the best formula for the isopropyl alcohol/ethyl cellulose binder system ink.

The binder system of the third ink is N,N-dimethylformamide/polyvinylidene fluoride. The ink has more precipitation after being left standing, and it does not decrease as the mass of the binder increases. It proves that the N,N-dimethylformamide/polyvinylidene fluoride binder system is not suitable for the ink formulation.

26.3.3 Analysis of Printing Characteristics

The XRD spectrum of the copper-containing precursor ink is shown in Fig. 26.4. It can be seen from Fig. 26.5 that the XRD spectra of the ink lines printed by the two inks roughly match the standard spectra of HKUST-1.

The SEM image of the ink line printed by the copper-containing precursor ink is shown in Fig. 26.6. It can be seen that the ink line printed by water/polyvinyl alcohol ink still maintains a loose and porous structure, while the ink line printed by isopropanol/ethyl cellulose ink is relatively dense, with many fine particles accumulated.

The water/polyvinyl alcohol ink line printed by a 20G needle is shown in Fig. 26.7a. It can be seen from the figure that the lines are uniform and smooth, and there are no bubbles. The line width is relatively uniform, and there is no obvious phenomenon of first narrowing and then widening. The line width observed under the microscope is uniform, and there is no big bend at the edge. The average line width of the line printed by the 20G needle is 2.3648 mm.

The photo of the ink line printed by the 22G needle is shown in Fig. 26.7b. It can be seen that the lines are smooth and there are no bubbles. The line width is uniform, but the line is first narrow and then wide. The line width observed under the microscope is not very uniform, and there are many bends on the edge. The average line width of the line printed by the 22G needle is 2.1168 mm.

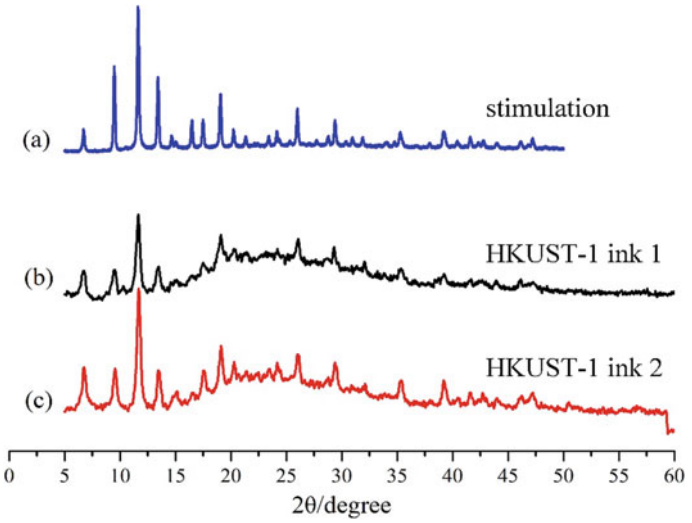

Fig. 26.5 **a** Standard XRD spectrum of HKUST-1 obtained by simulation; **b** XRD spectrum of water/polyvinyl alcohol ink (HKUST-1 ink1); **c** XRD spectrum of isopropanol/ethyl cellulose ink (HKUST-1 ink2)

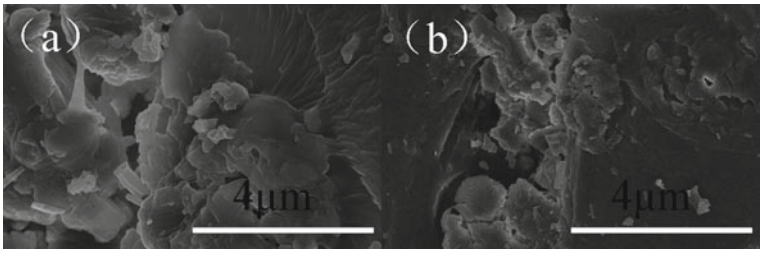

Fig. 26.6 SEM image of ink line: **a** Ink lines printed with water/polyvinyl alcohol ink; **b** ink lines printed with isopropyl alcohol/ethyl cellulose ink

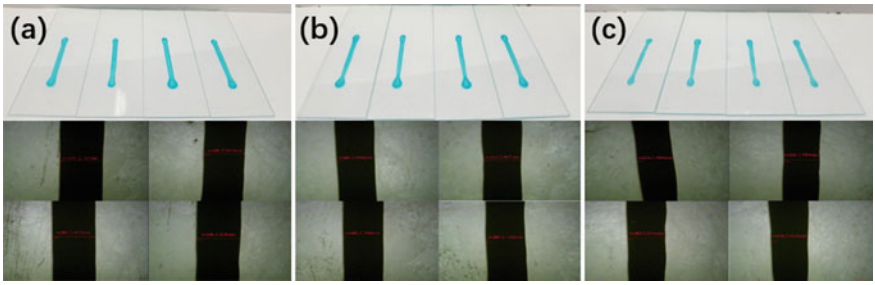

Fig. 26.7 The picture of the water/polyvinyl alcohol ink line printed with a, **a** 20G; **b** 22G; **c** 24G needle under an optical microscope

The photo of the thread printed by the 24G needle is shown in Fig. 26.7c. It can be seen from the figure that the lines are smooth and there are no bubbles. The line width is uniform, but some lines appear to be narrow and then wide. The shape of the lines observed under the microscope is not uniform, the edges are relatively irregular, meandering, and there are some tiny bubbles. The average line width of the lines printed by a 24G needle is 2.0108 mm.

The picture of the isopropanol/ethyl cellulose ink line printed by a 20G needle is shown in Fig. 26.8a. It can be seen that the lines are uniform and smooth, and there are no bubbles. The line width is relatively uniform, and there is no obvious phenomenon of first narrowing and then widening, but the two lines on the right are obviously wider than the two on the left. Under the microscope, it was observed that the lines with the smaller line width were more uniform, but the edges of the two lines with the larger line width were not neat, and the average line width of the lines was 1.8265 mm.

The photo of the ink line printed by the 22G needle is shown in Fig. 26.8b. It can be seen from the figure that the lines are smooth and there are no bubbles. Although due to the high viscosity of the ink, the ink is discharged slowly at the beginning, but the line width is relatively uniform, and there is no obvious phenomenon of first narrowing and then widening. The lines observed under the microscope are more uniform and the edges are more neat. The average line width of the lines printed by the 22G needle is 1.5600 mm.

Due to the high viscosity of the isopropanol/ethyl cellulose binder ink, there are some very tiny bubbles in it, which cannot be removed even after a long time of standing, stirring and ultrasound. When printing with a 24G needle, the tip of the needle is always blocked by small bubbles, so it is impossible to obtain the line width rule of the ink printed with the 24G needle through experiments.

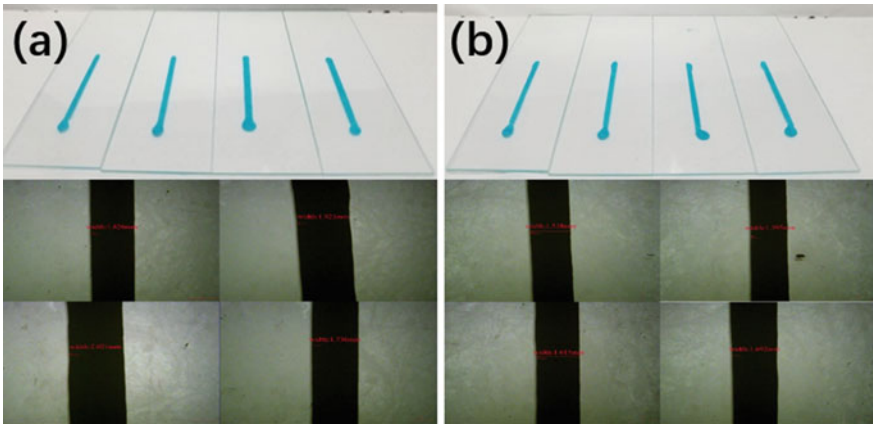

Fig. 26.8 The picture of the isopropanol/ethyl cellulose ink line printed with a, **a** 20G; **b** 22G needle under an optical microscope

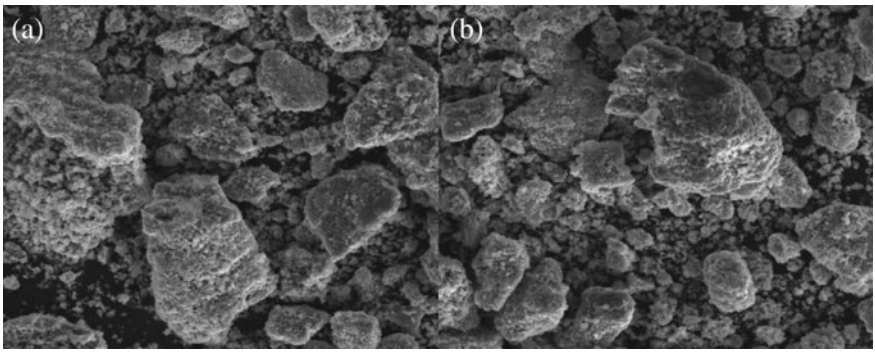

Fig. 26.9 SEM image of ink line after carbonization. **a** Water/polyvinyl alcohol; **b** isopropanol/ethyl cellulose

Based on the above, the isopropyl alcohol/ethyl cellulose binder system is better than the water/polyvinyl alcohol binder system. Its printing accuracy is high, the curing time is short, and the printed line width is uniform and the edges are neat. In addition, through experiments, it was found that the smaller the needle hole diameter, the greater the influence of bubbles when the ink is discharged. The bubble generation is not only related to ink viscosity, but also closely related to the process of adding ink to the syringe and ejecting ink during printing. After printing a sample, it is necessary to quickly print the next sample, which will help reduce bubbles in the ink.

Figure 26.9 shows the SEM image of the ink line after carbonization, which is quite different from the SEM image (Fig. 26.6) when it is not calcined. It can be seen that the microstructures of the lines printed by the two inks are basically the same after carbonization, and there are a large number of small particles accumulated and the structure is loose. The particle size obtained after the two carbonization is basically the same. In addition, the lines printed by water/polyvinyl alcohol binder inks are quite different before and after carbonization. There are no lumpy particles before carbonization. However, the lines printed by isopropanol/ethylcellulose binder ink still basically retain the morphology before carbonization, and they are all large pieces of massive particles aggregated. However, the difference in particle size before and after carbonization is obvious.

26.3.4 Preliminary Characterization of Energetic Materials

Figure 26.10 shows the XRD spectra of the energetic material prepared after carbonization and azide of ink lines printed by two inks. It can be seen from the XRD spectrum that the products of the two inks after carbonization and azide are the same, and they are all carbon-based copper azide energetic materials.

Figure 26.11 shows the infrared spectrum of the sample after azide. It can be

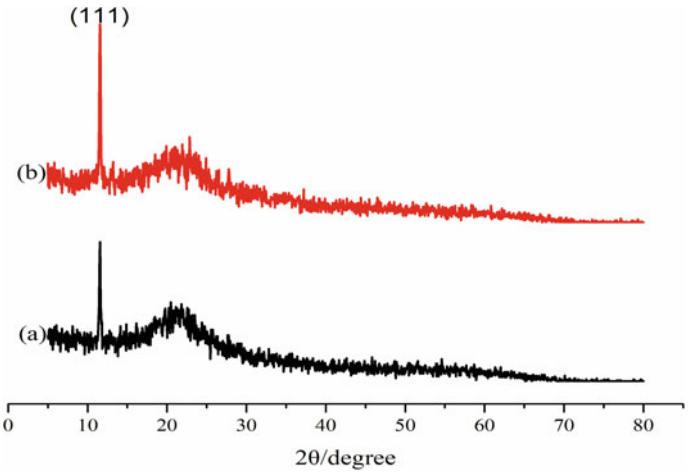

Fig. 26.10 XRD spectra of the energetic material prepared after carbonization and azide of ink lines printed by two inks: **a** Water/polyvinyl alcohol; **b** isopropanol/ethyl cellulose

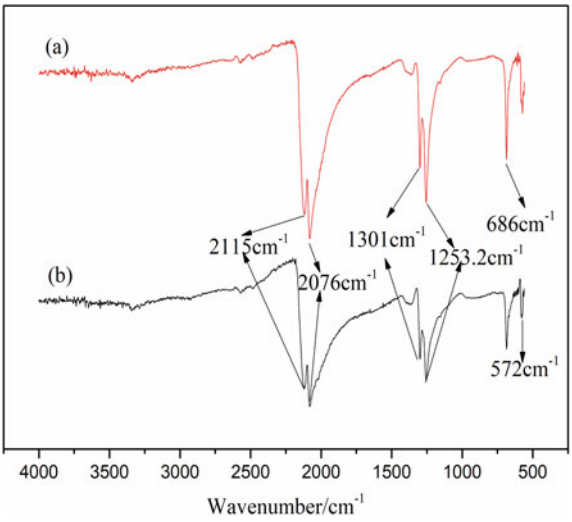

Fig. 26.11 Infrared spectra of energetic samples obtained after carbonization and azide of two inks: **a** Water/polyvinyl alcohol ink printing drug line; **b** isopropanol/ethyl cellulose

seen from the figure that the infrared spectra of the two samples after azidation are basically the same. The typical asymmetric vibration peaks of the azide-N_3 peak are shown at 2115 cm^{-1} and 2076 cm^{-1}, and the typical symmetrical vibration peaks of the azide-N_3 peak are displayed at 1301 cm^{-1} and 1253 cm^{-1}. In the Cu–N_3 system, the peaks at 572 cm^{-1} and 686 cm^{-1} can be attributed to the symmetric extension of the Cu–N bond. It can be determined from infrared spectroscopy that the ink is carbonized and azidized to produce a carbon-based energetic material with uniformly distributed copper azide.

26.4 Conclusion

HKUST-1 was synthesized by ultrasonic-assisted method, and the optimal synthesis conditions were explored. HKUST-1 was used as a copper-containing precursor, and was separately configured with three kinds of binder systems: pure water/polyvinyl alcohol, isopropanol/ethyl cellulose and N,N-dimethylformamide/polyvinylidene fluoride. Into ink, and explored the best formula. After determining the best ink formulation and printing parameters, three needles of 20G (inner diameter of 0.6 mm), 22G (inner diameter of 0.4 mm), and 24G (inner diameter of 0.27 mm) were used to explore the relationship between line width and aperture. The rule between line width and needle aperture is as follows: (a) Water/polyvinyl alcohol binder system: the average line width of the line printed by the 20G needle is 2.3648 mm, the 22G needle is 2.1168 mm, and the 24G needle is 2.0108 mm. (b) Isopropanol/ethyl cellulose binder system: for 20G needle is 1.8265 mm, for 22G needle is 1.5600 mm. Experiments show that when the aperture of the needle increases, the line width of the printed line increases significantly. The writing accuracy of isopropanol/ethyl cellulose binder ink is higher than that of water/polyvinyl alcohol binder ink. After getting the printed ink lines, they were carbonized and azidized. The infrared spectrum and XRD of the sample after the azide show that the carbon-based copper azide energetic material was prepared by the copper-containing precursor ink.

References

1. J. Kong, B. Li, A new generation of pyrotechnic technology and its application. Fundam. Defense Technol. **51**(07), 40–43 (2010)
2. E. Chu, A. He, Y. Xue et al., Development opportunities and ways of integrated pyrotechnics technology. Chin. J. Energ. Mater. **23**(03), 205–207 (2015)
3. T. Hu, Y. Zhao, Y. Zhao et al., Integration design of a MEMS based fuze. Sens. Actuators A **268**, 193–200 (2017)
4. Q. Li, Y. Pan, Y. Wang et al., Research progress of green explosives. Explos. Mater. **48**(04), 1–10 (2019)
5. L. Yang, Zhang, *Theory and Technology of New Pyrotechnic Agent*. (Beijing Institute of Technology Press, Beijing, 2019), pp. 39–54
6. C. Yu, W. Zhang, S. Guo et al., A safe and efficient liquid-solid synthesis for copper azide films with excellent electrostatic stability. Nano Energy **66**, 104135 (2019)
7. L. Zhang, L. Yang, F. Zhang et al., In situ synthesis of three-dimensional graphene skeleton copper azide with tunable sensitivity performance. Mater. Lett. **279**, 128466 (2020)
8. X. Liu, T. Li, Y. Hu et al., Copper azide nanowires@rGO energetic composite with low electrostatic sensitivity. J. Phys.: Conf. Ser. **1507**, 022004 (2020)
9. J. Chen, The functionalization of graphene oxide and the preparation and performance of its derivatives and composites. Jilin University, 2013
10. T. Li, Research on carbon-based nano-copper azide composite energetic material. Nanjing University of Science and Technology, 2018
11. V. Pelletier, S. Bhattacharyya, I. Knoke et al., Copper azide confined inside templated carbon nanotubes. Adv. Funct. Mater. **20**, 3168–3174 (2010)
12. C. Shi, Y. Hu, B. Chen et al., Preparation and characterization of composite energetic materials with embedded copper azide carbon nanotubes. Explos. Mater. **48**(05), 19–23 (2019)

13. C. Zhang, Y. Hu, R. Shen et al., Study on the preparation of carbon nanotube nanomaterials filled with copper azide. Explos. Mater. **46**(01), 1–5 (2017)
14. F. Zhang, Y. Wang, Y. Bai et al., Preparation and characterization of copper azide nanowire array. Mater. Lett. **89**, 176–179 (2012)
15. Y. Wang, F. Zhang, L. Zhang et al., Preparation of carbon nanotube array filled with copper azide by in-situ reaction method. Chin. J. Energ. Mater. **24**(04), 386–392 (2016)
16. G. Zhang, J. Han, T. Zhang et al., Theoretical study of the reduction in sensitivity of copper azide following encapsulation in carbon nanotubes. J. Mol. Model. **26**, 90 (2020)
17. B. Chen, Study on the preparation and properties of composite films with embedded copper azide carbon nanotubes. Nanjing University of Science and Technology, 2018
18. H. Wei, Research on silicon-based $Cu(N_3)_2$@CNTs composite films applied to energetic chips. Nanjing University of Science and Technology, 2019
19. X. Liu, Y. Hu, H. Wei et al., Energetic films realized by encapsulating copper azide in silicon-based carbon nanotube arrays with higher electrostatic safety. Micromachines **11**, 575 (2020)
20. Q. Wang, X. Feng, S. Wang et al., Metal-organic framework templated synthesis of copper azide as the primary explosive with low electrostatic sensitivity and excellent initiation ability. Adv. Mater. **28**, 5837–5843 (2016)
21. Q. Wang, L. Zhang, W. He et al., High-performance primary explosives derived from copper thiolate cluster-assembled materials for micro-initiating device. Chem. Eng. J. **389**, 124455 (2020)
22. Q. Wang, J. Han, Y. Zhang et al., Fabrication of copper azide film through metal−organic framework for micro-initiator applications. ACS Appl. Mater. Interfaces **11**, 8081–8088 (2019)
23. R. Xu, Z. Yan, L. Yang et al., Nanoscale homogeneous energetic copper azides@porous carbon hybrid with reduced sensitivity and high ignition ability. ACS Appl. Mater. Interfaces **10**, 22545–22551 (2018)
24. Hull, Apparatus for production of three-dimensional objects by stereolithography U.S. 4,575,330 March 1986
25. W. Yang, X. Xiao, Q. Wang et al., Research progress of additive manufacturing technology in propellant and explosive forming. Chin. J. Explos. Propellants **43**(01), 1–11 (2020)
26. X. Su, Q. Na, X. Li et al., The application of additive manufacturing technology in the field of energetic materials. New Technol. New Process **12**, 26–30 (2020)
27. G. Zeng, X. Qi, X. Liu, Several types of disruptive technological progress in the field of energetic materials. Chin. J. Energ. Mater. **28**(12), 1211–1220 (2020)
28. C. Peng, Energetic material additive manufacturing technology-emerging precision, efficient and safe preparation technology. Chin. J. Energ. Mater. **27**(06), 445–447 (2019)
29. L. Shen, Y. Ye, Y. Hu et al., Energetic ink formulation design and its application in microporous charging. Explos. Mater. **44**(05), 1–4 (2015)
30. R. Han, R. Zhang, F. Zhang et al., The influence of solvent on the performance of micro-control direct writing energetic ink. Initiators Pyrotech. **01**, 18–21 (2017)
31. H. Wang, M. Rehwoldt, R. Zachariah et al., Comparison study of the ignition and combustion characteristics of directly-written Al/PVDF, Al/Viton and Al/THV composites. Combust. Flame **201**, 181–186 (2019)
32. Q. Li, B. Ye, J. Wang et al., The design of Viton/PVA binder emulsion and its application in explosive ink. Chin. J. Energ. Mater. **27**(01), 60–67 (2019)
33. Q. Li, C. An, X. Han et al., CL-20 based explosive ink of emulsion binder system for direct ink writing. Propellants, Explos., Pyrotech. **43**(6), 533–537 (2018)
34. Z. Xing, Research on rapid prototyping technology for three-dimensional printing of energetic materials. Nanjing University of Science and Technology, 2012
35. Y. Yao, L. Wu, Y. Hu et al., Direct writing law of nano-CL-20 explosive energetic ink. Chin. J. Explos. Propellants **39**(01), 39–42 (2016)
36. Y. Yao, Nano CL-20 energetic ink formula design, direct writing law and explosive transmission performance. Chin. J. Energ. Mater. (2016)
37. X. Ding, Design and analysis of the nozzle of the 3D printing experimental system for energetic materials. Nanjing University of Science and Technology, 2017

38. Y. Liu, B. Zheng, X. Li et al., CL-20-based explosive ink direct writing deposition. Chin. J. Energ. Mater. **25**(09), 738–744 (2017)
39. Z. Zhu, J. Chen, Z. Qiao et al., Preparation and characterization of CL-20-based direct writing explosive ink. Chin. J. Energ. Mater. **21**(02), 235–238 (2013)
40. D. Wang, B. Zheng, C. Guo et al., Formulation and performance of functional sub-micro CL-20-based energetic polymer composite ink for direct-write assembly. RSC Adv. **6**, 112325–112331 (2016)
41. J. Fleck, K. Murray, F. Rhoads et al., Additive manufacturing of multifunctional reactive materials. Addit. Manuf. **17**, 176–182 (2017)
42. C. Xu, C. An, Y. Long et al., Inkjet printing of energetic composites with high density. RSC Adv. **8**, 35863–35869 (2018)
43. L. Zhang, F. Zhang, Y. Wang et al., In-situ preparation of copper azide by direct ink writing. Mater. Lett. **238**, 130–133 (2019)
44. Z. Li, L. Qiu, T. Xu et al., Ultrasonic synthesis of the microporous metal–organic framework $Cu_3(BTC)_2$ at ambient temperature and pressure: an efficient and environmentally friendly method. Mater. Lett. **63**, 78–80 (2009)

Chapter 27
Preparation and Properties of Nitrocellulose/Viton Based Nano Energetic by Direct Writing

Yuke Jiao, Shengnan Li, Shanjun Ding, Desheng Yang, Chaofei Bai, Jiaran Liu, Yunjun Luo, and Guoping Li

Abstract Direct writing technology is a promising approach for the preparation of reactive materials. The polymer binder provides a mechanically stable, processable and shapeable energetic structure for composites. Herein, Direct-writing energetic inks consisting of nitrocellulose (NC) and VitonF2311 as well as nanothermite were developed. Firstly, Fourier transform infrared spectroscopy (FT-IR) was used to analyze the intermolecular hydrogen bonds in the hybrid polymers, and the stability of the network structure was characterized by rheometer, and the mechanical properties of binders were also tested. The results show the best binder formulation is 20 wt% NC and 80 wt% F2311. The elongation at break of the binder is 600.94%, and the elastic modulus is 8.29 MPa. NC provides high tensile strength for the hybrid

Y. Jiao · S. Li · D. Yang · C. Bai · J. Liu · Y. Luo · G. Li (✉)
School of Materials Science and Engineering, Beijing Institute of Technology, Beijing 100081, China
e-mail: girlping3114@bit.edu.cn

Y. Jiao
e-mail: ykjiao97@163.com

S. Li
e-mail: lishengnan@iccas.ac.cn

D. Yang
e-mail: ydslww@163.com

C. Bai
e-mail: superbcf@163.com

J. Liu
e-mail: LJR9898@126.com

Y. Luo
e-mail: yjluo@bit.edu.cn

S. Ding
State Key Laboratory of Explosion Science and Technology, Beijing Institute of Technology, Beijing 100081, China

Y. Luo · G. Li
Key Laboratory for Ministry of Education of High Energy Density Materials, Beijing Institute of Technology, Beijing 100081, China

A. Gany and X. Fu (eds.), *2021 International Conference on Development and Application of Carbon Nanomaterials in Energetic Materials*, Springer Proceedings in Physics 276,
https://doi.org/10.1007/978-981-19-1774-5_27

binder; F2311 provides high fracture tensile rate for the hybrid binder, and as a high-energy initiator, pre-ignition reaction occurs when the temperature reaches 350 °C. Then the as-prepared inks not only has excellent rheological properties so that it can be loaded with 90 wt% nanothermite, but also possess a homodisperse for components and good combustion performance. The average flame temperature is about 2400 K at atmospheric pressure.

27.1 Introduction

As the size of energetic components tends to be more and more miniaturized and intelligent, the traditional energetic materials and charging technology cannot meet some requirements [1–3]. Nanothermites are very promising reactive energetic materials with high energy density and high ignition sensitivity [4–6]. Compared with the traditional charging methods, such as the casting and pressing of energetic materials, the direct writing technology of solvent-based ink relies on its micro-nozzle and flexible arm, which has great potential advantages for the micro-miniature applications of energetic materials [7–10]. In the additive manufacturing of suspended energetic ink for direct writing, the ink composed of particles, polymer binder and organic solvent is extruded through a 3D printing nozzle and formed [11]. Direct ink writing requires precise control of the energetic ink under flow conditions, and then solidification of the deposited material to maintain its shape. The formulation of energetic ink used in direct writing technology should meet several standards. Firstly, the ink should have good stability and the solvent should not interact with other components. Secondly, the prepared energetic ink should have suitable rheological properties and can smoothly pass through the fine print nozzle under certain pressure. Finally, the binder used in the ink should have good film-forming properties and mechanical properties to ensure that the ink can be self-supporting even if there is a span gap in the lower layer of the printed sample, and maintain its shape without cracks or cavities. In 2018, Murray et al. [12] prepared Al/CuO nanothermite by direct writing. Due to the increase of viscosity and severe particle agglomeration, the nanothermite was limited to a low mass fraction of 8 wt%. Durban et al. [13] printed micron-sized 23 wt% Al and 13 wt% CuO particles in the hydrogel matrix, but the poor stability caused by insufficient scalability or possible reactions between Al and water may limit further development. Since the binder usually does not contain energy, it is better to add the minimum amount of binder required to maintain the required mechanical properties. The integration of nanoparticles into the polymer will significantly increase the viscosity [14–18]. In order to ensure that the material can pass through the nozzle of the 3D printer, the addition amount of nanoparticles must be limited. Insufficient loading of nanothermite will make it difficult to obtain nanothermite-based energetic materials with higher energy density. This requires the development of new binders for direct writing of energetic materials to meet the requirements of ink stability, printability and appropriate mechanical properties. In 2019, Wang et al. [19] dissolved polyvinylidene fluoride (PVDF) and hydroxypropyl methyl cellulose

(HPMC) in dimethylformamide (DMF) to obtain a homogeneous polymer mixture. A printable energetic ink with a nano thermite loading particle content of up to 90% has been developed.

In this article, we report a printable formulation loaded with 10 wt% polymer and 90 wt% nanothermite. NC and vitonF2311 provide mechanical action as a binder, where NC as an energetic component to provide high tensile strength for hybrid polymer, F2311 provides high fracture tensile rate, and as high energy initiator. The influence of different binder formulations on the performance of the ink was also studied. The ink has significant shear thinning so that it can load such high solid particles and ensure it can be directly written successfully.

27.2 Materials and Methods

27.2.1 Materials and Chemicals

Nitrocellulose (NC), 11.71% nitrogen content. VitonF2311 was purchased from Chenguang Chemical Research Institute (Mianyang, China). Acetone (C_3H_6O, AR) was purchased from Beijing Tongguang Fine Chemical Company (Beijing, China). Aluminum nanoparticles (Al NPs) have an average diameter of 100 nm with a ~2–4 nm oxide shell, CuO have an average diameter of 50 nm were purchased from Shanghai Maoguo Nano Technology Co., Ltd. (Shanghai, China).

27.2.2 Ink Preparation

According to the formula in Table 27.1, NC and F2311 were added to the acetone and magnetically stirred for 3 h to obtain a clear solution. Then the Al and CuO NPs (stoichiometric ratio 2.5) were added to the above polymer solution, mixed together, and ultrasound for 1 h to form energetic ink.

Table 27.1 The formula with different polymer ratios

Sample No.	NC (g)	F2311 (g)	Al (g)	CuO (g)	Aceton (ml)
1	0	1.5	4.86	8.64	15
2	0.3	1.2			
3	0.6	0.9			
4	0.9	0.6			
5	1.2	0.3			
6	1.5	0			

27.2.3 Rheological Characterization

The rheological properties of pure polymer solutions and high-particle inks were tested using rotational RS (Thermo HAAKE, Germany) with a 20 mm diameter steel plate. The shear rate-viscosity test was carried out in the shear rate range from 0.01 to 100 s^{-1} at room temperature. The storage modulus (G') of the solution was measured by applying a frequency (1.0–100.0 Hz) in the linear viscoelastic region to evaluate the stability of the solution.

27.2.4 Printing of Inks

Printing was conducted with a Adventure 3D-printer (Adventure Technology) using a 1.0 mm inner diameter nozzle. Use G-code code to write the printing path. The printing path was 4 cm × 4 cm at a maximum write speed of 20 cm/min.

27.2.5 Polymer Samples Mechanical Properties

The AGS-J electronic universal testing machine (Shimadzu, Japan) was used to test the mechanical properties of polymer materials. The test method refers to GJB772A-1997, 417.1 tensile stress–strain curve electronic extensometer method, prepared dumbbell-shaped splines, tested at room temperature, and the tensile rate was 100 mm/s. The test was repeated three times to find the average value.

27.2.6 Characterization

The Fourier transform infrared spectroscopy (FT-IR) spectra of polymer solutions were examined on a Nicolet 8700 FTIR (American Thermo Scientific Co., Ltd.) instrument in the range of 4000–400 cm^{-1}. Printing stick was observed by a Hitachi SU8020 scanning electron microscope (SEM) coupled to an energy-dispersive spectrometer (EDS). Thermal analysis of composite materials was detected by Mettler-Toledo simultaneous thermog-ravimetry-differential scanning calorimeter (TGA/DSC) at different 10°C/min heating rate under 40 ml/min Ar flow from 30 °C to 750 °C.

27.2.7 Combustion Measurement

Weigh 25 mg sample in a closed explosive device, use MDO3000 mixed domain oscilloscope (Teck, USA) and CY-YD-205 piezoelectric sensor and YE5850 quasi-static charge amplifier (Jiangsu United Energy Electronic Technology Co., Ltd.) to obtain the pressure signal in the reaction process. The i-SPEED 726 high-speed camera (iX Cameras, UK) was used to record the combustion process in air, with a shutter speed of 5000 fps and a focal length of 50 mm. The flame temperature is measured by a 50 mm METIS H3 high-speed infrared thermometer (Germany Sancesium Company).

27.3 Results and Discussions

27.3.1 Determination of Polymer Formula for Energetic Ink

Figure 1a shows shear viscosity of F2311/NC inks with and without nano particles. Both pure polymer solutions and energetic inks exhibit significant shear thinning characteristics. Although the addition of nanothermite greatly increases the

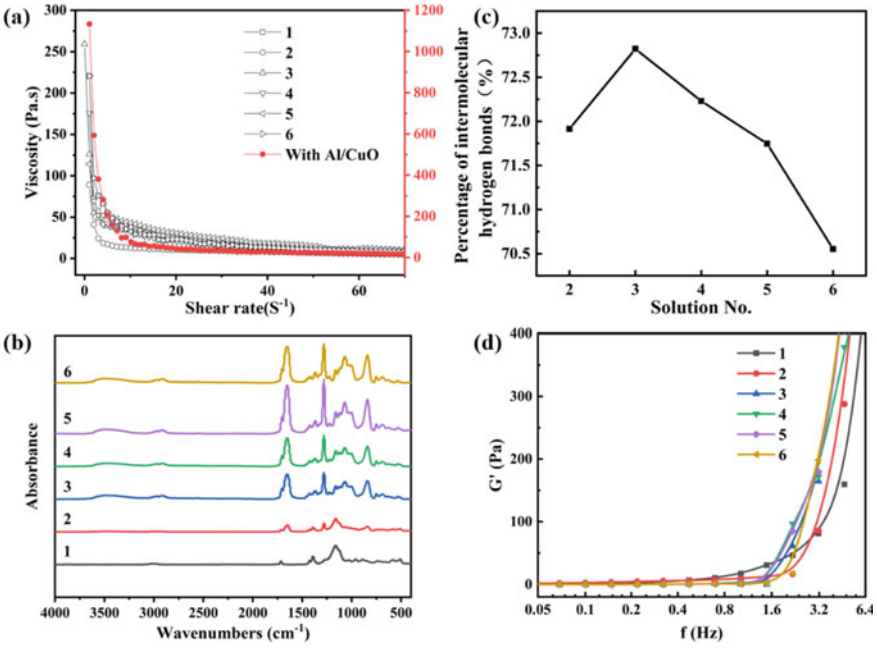

Fig. 27.1 **a** Apparent viscosity of polymer solutions and nanothermite ink as a function of shear rate. **b** FTIR spectra of F2311, NC and F2311/NC hybrid polymers. **c** The peak fitting diagram of the hydroxyl group of F2311/NC hybrid polymers. **d** G'–f rheological properties of polymer solutions

viscosity of the ink, it is similar to the viscosity of the polymer at high shear rate. This feature is very suitable for direct writing inks, allowing materials with high viscosity to pass through narrow nozzles [19]. FTIR analysis (Fig. 1b) provides an explanation for the possible interaction between F2311 and NC. There are a large number of –OH in NC molecular chains, which can form intramolecular hydrogen bonds, intermolecular hydrogen bonds (–OH…O) between NC molecular chains, and intermolecular hydrogen bonds (–OH…F) between NC and F2311 molecular chains. The –OH stretching peak of intramolecular hydrogen bonds are in the range of 3500–3300 cm^{-1}, and the intermolecular hydrogen bonds are in the range of 3570–3450 cm^{-1}. As shown in Fig. 1c, sample 2 has the largest amount of intermolecular hydrogen bonds. More intermolecular hydrogen bonds can provide a more stable solution system. In addition, the presence of hydrogen bonds can also enhance the interaction between nanoparticles [20]. The relationship between the storage modulus (G') of the F2311/NC solution and the oscillation frequency (f) is shown in Fig. 1d. When the curve shows a plateau trend that is independent of the oscillation frequency, it indicates that a stable gel network structure has been formed at this time [21]. It can be seen from the results that the curves of solutions No. 1–6 have a frequency-independent platform, and the platform height and length of sample 2 are the best, indicating that the gel network structure of the solution is more stable.

The mechanical properties of energetic materials are crucial. Polymer binders provide structural integrity and mechanical stability for energetic materials. The mechanical properties of polymer samples 1 to 6 are shown in the Fig. 27.2. The elongation at break of sample 2 is 600.94%, and the elastic modulus is 8.29 MPa,

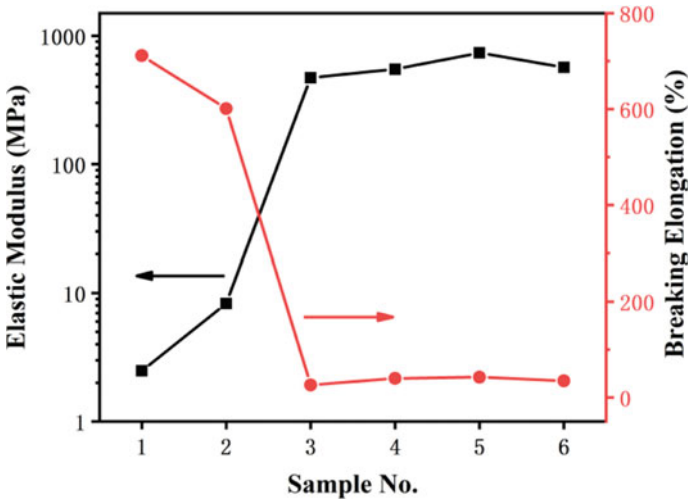

Fig. 27.2 Mechanical properties of polymers with different formulations

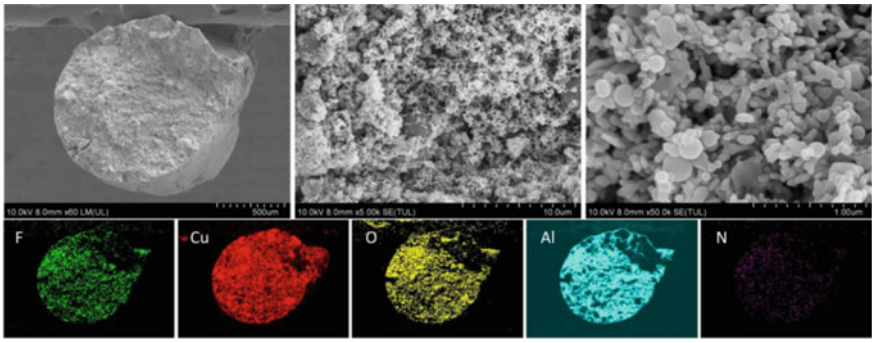

Fig. 27.3 SEM and EDS image of the cross-sectional composite rod loaded with 90 wt% Al/CuO

which is comparable to the binders commonly used in solid propellants [22, 23]. For the subsequent results, the formula was fixed to 20 wt% NC and 80 wt% F2311.

27.3.2 Characterization of Nanothermite Composite Materials

Figure 27.3 shows the SEM image of the single-layer Al/CuO nanothermites composite material. The hybrid polymer is wrapped around the nanothermite to provide a self-supporting structure for the composite material. 50 nm copper oxide particles surround the edge of 100 nm aluminum particles. The EDS results show that the components of the composite material obtained by direct writing are evenly distributed, and the Al and CuO nanoparticles are tightly assembled.

27.3.3 Thermal Properties of Nanothermite Composite Materials

In order to study the reactivity of the nanocomposite, TG-DSC thermal analysis of nanocomposites was carried out, and the results are shown in Fig. 27.4. The thermal decomposition process of nanocomposites has only a slight mass loss, which can be divided into three stages. The first stage (100–200 °C)is mainly to remove small molecules such as water and organic solvents adsorbed on the surface of the material during the preparation and storage of nanocomposites; the second stage (170–235 °C) is the thermal decomposition of 20 wt%. NC with very little heat; the third stage is 80 wt% F2311 when the temperature reaches 350 °C, a pre-ignition reaction occurs, as shown in Eq. (27.1) [24–28], and a large amount of heat is released.

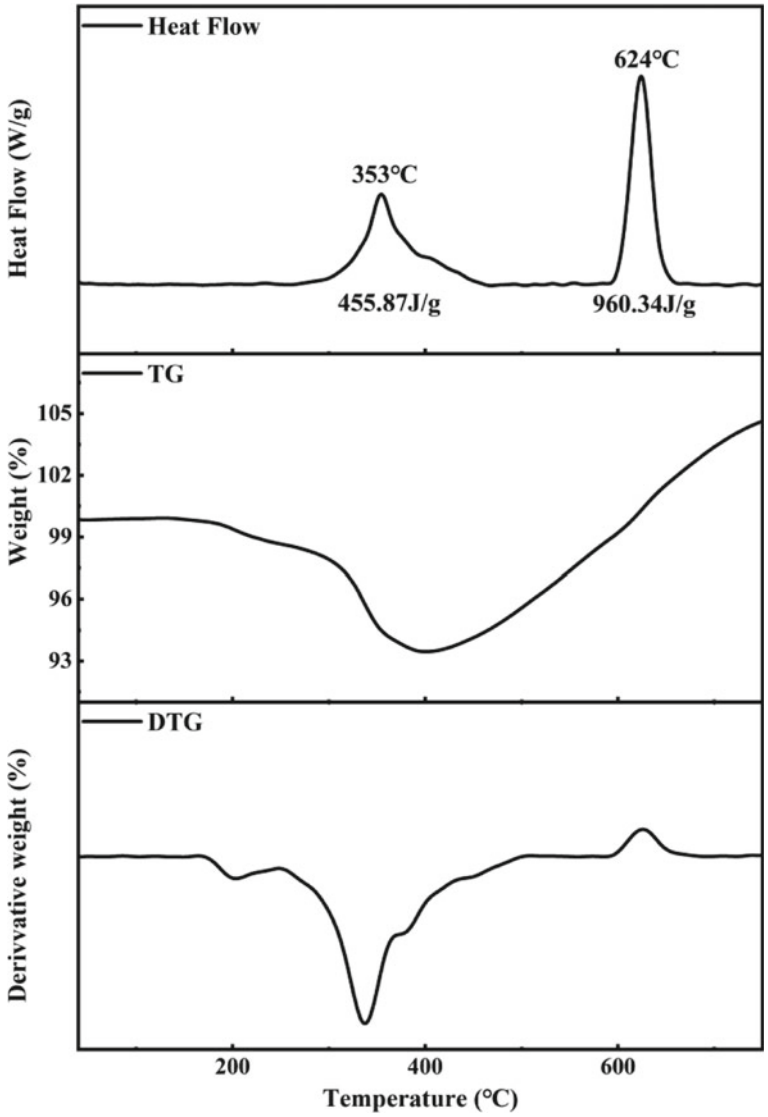

Fig. 27.4 Thermal properties of nano-thermite composite materials

$$2Al + 3C_2H_2F_2 \rightarrow 2AlF_3 + 6C + 3H_2(g) \tag{27.1}$$

The subsequent increase in quality is due to the inevitable presence of trace air in the furnace chamber, which reacts with aluminum to produce aluminum nitride or alumina at high temperatures. When the temperature is higher than 600 °C, the nanocomposite undergos aluminothermic reaction and emits a lot of heat [29, 30].

27.3.4 Combustion Performance of Nanothermite Composite Materials

The ignition of energetic materials in a constant vessel can rapidly generate high temperature and high pressure gas, which increases the internal pressure of the system. Therefore, it is of great significance to study the pressure change during combustion. The maximum pressure (Pmax) generated by combustion is used to reflect the energy output efficiency of energetic materials, and the time required to reach the maximum pressure (Rise time) is used to reflect the burning rate of materials, and the increase rate of pressure (dP/dt:Pressurization rate) is used to reflect the reaction activity of materials [31]. The results of constant volume combustion performance of nanocomposite energetic materials are shown in Fig. 27.5. It can be seen from the diagram that the pressure increases rapidly to the maximum value of 0.32 MPa within 0.00928 s after ignition, and then decreases to close to the initial position. The NC/F2311 composite nanothermite energetic materials have excellent combustion performance. The increase of system pressure is mainly due to a large amount of heat released by combustion in a closed environment, resulting in a sharp increase in air temperature and gas expansion. The decrease of pressure is mainly due to the depletion of material combustion, the reduction of energy release, the condensation of gas phase products and the intensification of heat conversion between combustion chamber gas and metal wall (Fig. 27.6).

The combustion process of nano-composite energetic materials at atmospheric pressure was recorded by high speed photography, and the combustion temperature of nano-composite energetic materials was tested. It can be seen from the figure

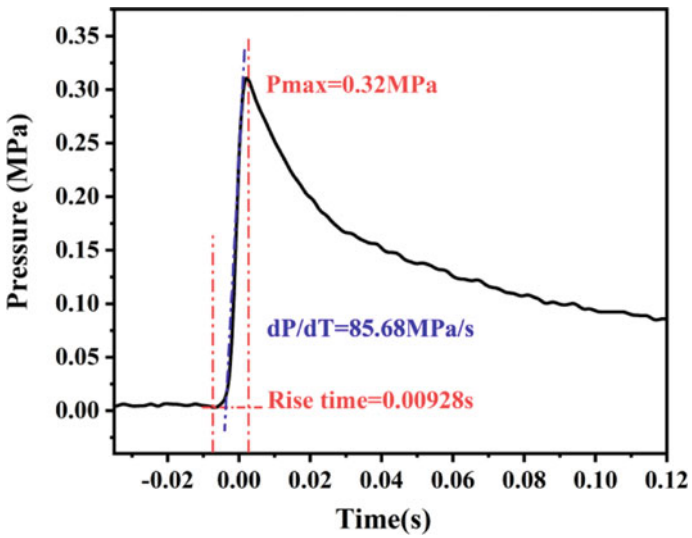

Fig. 27.5 P–t curve of of nanothermite composite materials

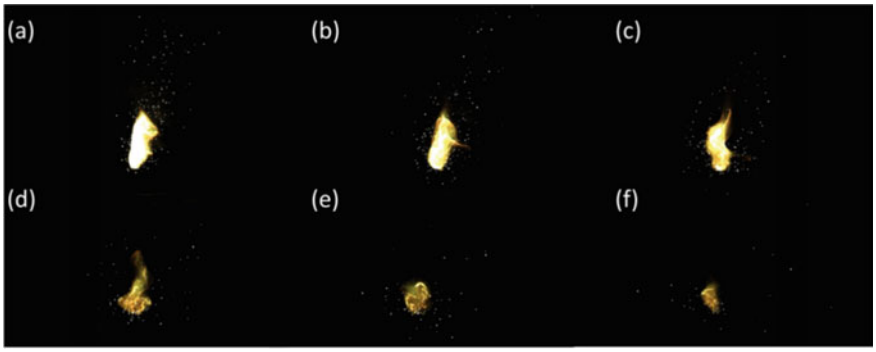

Fig. 27.6 High-speed photography photos of nanothermite composite materials

that the flame of the printing rod is close to the burning surface, and the color is yellow. The closer it is to the burning surface, the greater the flame brightness is. There are still splashing bright white particles in the gas phase, which is due to the gaseous substances generated in the combustion process of nano-composite materials will be fully burned into the gas phase, resulting in more aluminothermic reactions, fluorination reactions and a large amount of heat. The flame temperature $\approx$ 2400 K is obtained by a high-speed infrared thermometer.

27.4 Conclusion

(1) The best polymer formulation was determined based on the results of FT-IR, rheology and mechanical properties. When the NC content is 20 wt% and F2311 content is 80 wt%, the hybrid polymer has the largest number of intermolecular hydrogen bonds and the gel network structure is more stable. The elongation at break of the binder was 600.94%, and the elastic modulus is 8.29 MPa.

(2) The as-prepared energetic inks with 90 wt% nanothermite showed an excellent shear thinning at high shear rate, and self-supporting ability.

(3) EDS results showed that the components of the nanocomposites were evenly distributed, and the pre-combustion reaction occurred when the temperature reached 350 °C. When the temperature was higher than 600 °C, the nanocomposite undergos aluminothermic reaction and a large amount of heat was released.

(4) The results of constant volume combustion performance of nanocomposite energetic materials show that the pressure rapidly increases to the maximum value of 0.32 MPa within 0.00928 s after ignition. The average flame temperature was about 2400 K at atmospheric pressure.

Acknowledgements This work was financially supported by NSFC and State Administration of Science, Technology and Industry for National Defense of China (HYZ2018001).

References

1. N.V. Muravyev, K.A. Monogarov, U. Schaller et al., Progress in additive manufacturing of energetic materials: creating the reactive microstructures with high potential of applications. Propellants, Explos., Pyrotech. **44**(8), 941–969 (2019)
2. Z. Zhu, L. Lin, L. Xiangdong et al., Research on application of 3D printing technology of energetic materials. Ordnance Indus. Autom. **34**(6), 52–57 (2015)
3. S. Ding, J. Zhang, G. Zhu et al., Rationally constructed surface energy and dynamic hard domains balance mechanical strength and self-healing efficiency of energetic linear polymer materials. Langmuir **37**(30), 8997–9008 (2021)
4. W. He, P.J. Liu, G.Q. He et al., Highly reactive metastable intermixed composites (MICs): preparation and characterization. Adv. Mater. **30**(41), e1706293 (2018)
5. D. Sundaram, V. Yang, R.A. Yetter, Metal-based nanoenergetic materials: synthesis, properties, and applications. Prog. Energy Combust. Sci. **61**, 293–365 (2017)
6. C. Wu, K. Sullivan, S. Chowdhury et al., Encapsulation of perchlorate salts within metal oxides for application as nanoenergetic oxidizers. Adv. Func. Mater. **22**(1), 78–85 (2012)
7. A.C. Ihnen, A.M. Petrock, T. Chou et al., Crystal morphology variation in inkjet-printed organic materials. Appl. Surf. Sci. **258**(2), 827–833 (2011)
8. F.D. Ruz-Nuglo, L.J. Groven, 3-D printing and development of fluoropolymer based reactive inks. Adv. Eng. Mater. **20**(2) (2018)
9. C. Xu, C. An, Y. He et al., Direct ink writing of DNTF based composite with high performance. Propellants, Explos., Pyrotech. **43**(8), 754–758 (2018)
10. J. Zunino III, D. Schmidt, A. Petrock et al., Inkjet printed devices for armament applications. TechConnect Briefs **2**, 542–545 (2010)
11. H. Woods, A. Boddorff, E. Ewaldz et al., Rheological considerations for binder development in direct ink writing of energetic materials. Propellants, Explos., Pyrotech. **45**(1), 26–35 (2019)
12. A.K. Murray, W.A. Novotny, T.J. Fleck et al., Selectively-deposited energetic materials: a feasibility study of the piezoelectric inkjet printing of nanothermites. Add. Manuf. **22**, 69–74 (2018)
13. M.M. Durban, A.M. Golobic, E.V. Bukovsky et al., Development and characterization of 3D printable thermite component materials. Adv. Mater. Technol. **3**(12) (2018)
14. E.L. Dreizin, Metal-based reactive nanomaterials. Prog. Energy Combust. Sci. **35**(2), 141–167 (2009)
15. U. Teipel, U. Frter-Barth, Rheology of nano-scale aluminum suspensions. Propellants, Explos., Pyrotech. **26**, 268–272 (2001)
16. H. Wang, J.B. Delisio, G. Jian et al., Electrospray formation and combustion characteristics of iodine-containing Al/CuO nanothermite microparticles. Combust. Flame **162**(7), 2823–2829 (2015)
17. H. Wang, G. Jian, G.C. Egan et al., Assembly and reactive properties of Al/CuO based nanothermite microparticles. Combust. Flame **161**(8), 2203–2208 (2014)
18. D. Wang, B. Zheng, C. Guo et al., Formulation and performance of functional sub-micro CL-20-based energetic polymer composite ink for direct-write assembly. RSC Adv. **6**(113), 112325–112331 (2016)
19. H. Wang, J. Shen, D.J. Kline et al., Direct writing of a 90 wt% particle loading nanothermite. Adv. Mater. **31**(23), e1806575 (2019)
20. J. Shen, H. Wang, D.J. Kline et al., Combustion of 3D printed 90 wt% loading reinforced nanothermite. Combust. Flame **215**, 86–92 (2020)

21. L. Shuling, F. Hong, Z. Hong et al., Effect of ethyl cellulose on the rheological properties and oleo gel property of oil. J. Chin. Cereals Oils Assoc. **12**, 70–75 (2015)
22. W. Cun-Dong, L. Yun-Jun, X. Min, Synthesis of HTPE and properties of HTPE elastomers. Chin. J. Energ. Mater. **19**(5), 518–522 (2011)
23. W. Xupeng, L. Yunjun, W. Xiaoqing et al., Properties of GAP/PET dual-soft segments energetic polyurethane elastomer. J. Chem. Ind. Eng. (CHINA) **61**(3), 784–788 (2010)
24. Y. Mao, L. Zhong, X. Zhou et al., 3D printing of micro architected Al/CuO-based nanothermite for enhanced combustion performance. Adv. Eng. Mater. **21**(12) (2019)
25. H. Nie, L.P. Tan, S. Pisharath et al., Nanothermite composites with a novel cast curable fluoropolymer. Chem. Eng. J. **414** (2021)
26. J. Shen, Z. Qiao, K. Zhang et al., Effects of nano-Ag on the combustion process of Al–CuO metastable intermolecular composite. Appl. Therm. Eng. **62**(2), 732–737 (2014)
27. S.M. Umbrajkar, M. Schoenitz, E.L. Dreizin, Exothermic reactions in Al–CuO nanocomposites. Thermochim. Acta **451**(1–2), 34–43 (2006)
28. H. Wang, M. Rehwoldt, D.J. Kline et al., Comparison study of the ignition and combustion characteristics of directly-written Al/PVDF, Al/Viton and Al/THV composites. Combust. Flame **201**, 181–186 (2019)
29. R.-H. Fan, H.-L. Lü, K.-N. Sun et al., Kinetics of thermite reaction in Al-Fe2O3 system. Thermochim. Acta **440**(2), 129–31 (2006)
30. J. Wang, A. Hu, J. Persic et al., Thermal stability and reaction properties of passivated Al/CuO nano-thermite. J. Phys. Chem. Solids **72**(6), 620–625 (2011)
31. C. Sang, K. Chen, G. Li et al., Facile mass preparation and characterization of Al/copper ferrites metastable intermolecular energetic nanocomposites. RSC Adv. **11**(13), 7633–7643 (2021)

Chapter 28
Oxidation Mechanism of Graphene Coating on an Aluminum Slab

Xiaoya Chang and Dongping Chen

Abstract Surface engineering is a promising approach to enhance the combustion performance of energetic materials. The carbon-based coating provides several advantages in ignition temperature, processability and compatibility. This work conducted the reactive molecular dynamic simulations on aluminium slabs with graphene coating to elaborate the underlying oxidation mechanisms. The combustion evolution of coated slabs is examined under the flow impact to capture the anisotropic nature in explosion. From the analysis of stress distributions and morphological evolutions, the deformation and disruption mechanisms of bilayer graphene are discussed in detail. Successive surface collisions result in the preferable crack on the lower graphene layer close to the aluminum substrate, rather than the upper layer. Compared with alumina coating, the modified slab exhibits an enhanced heat release due to the better mass diffusion. We further identify the bond populations and oxidation products to elaborate the reaction mechanism and highlight the intense impulse of modified slab. These numerical findings are expected to provide a theoretical guidance for the design of next-generation energetic materials.

28.1 Introduction

Aluminum, with high specific energy density and earth abundance, is a promising additive in energetic-conversion applications, including space propulsion, pyrotechnics and micro-electromechanical systems [1–5]. The combustion of aluminum-based energetic materials is an exothermic process that generate heat, light and thrust rapidly [6]. The presence of the oxide shell shrinks the content of active aluminum and diminishes the energy output [7]. An aluminum particle with a diameter of 50 nm has a shell thickness of 2 nm, which corresponds to ~30% of the total

X. Chang · D. Chen (✉)
State Key Laboratory of Explosion Science and Technology, Beijing Institute of Technology, Beijing 100081, China
e-mail: dc516@bit.edu.cn

X. Chang
e-mail: xiaoya_chang@bit.edu.cn

A. Gany and X. Fu (eds.), *2021 International Conference on Development and Application of Carbon Nanomaterials in Energetic Materials*, Springer Proceedings in Physics 276,
https://doi.org/10.1007/978-981-19-1774-5_28

mass. Besides, the passivate alumina shell results in the incomplete combustion and aggregation of aluminum particles, which increase two-phase loss and decrease the specific impulse. For instance, every 10% unburned aluminum yields approximately 1% specific impulse loss [8]. To meet the demand of next-generation propellant and explosive, a feasible strategy relies on the effective passivation materials to engineering the surface functionalities. To date, two types of coating materials are often considered, that is inorganic substances (Ni, B) and organic matters (Perflouroalkyl carboxylic acids) [9]. The second type is preferred in practical considerations, which shows a lower decomposition temperature, easier processability, better compatibility [3, 9]. Many previous efforts have been dedicated to the surface engineering of aluminum particles for the rational design of next-generation energetic materials.

Graphene, a two-dimensional sheet, has the potential for nano-coating applications [10]. It has multiple benefits for the practical storage of energetic materials, including the reduced sensitivity, improved thermal stability as well as the enhanced mechanical strength [3]. Hui et al. [11] reported the synergistic oxidation of graphene on Cu by oxygen plasma. They found that the graphene coating acted as an oxygen barrier for Cu initially, but enhance the oxidation process upon a higher plasma dosage. Sabourin et al. [12] examined the combustion performance of monopropellant nitromethane with graphene sheets. The addition of graphene sheets induces a huge surge of burning rate (greater than 175%). Recently, graphene oxide (GO) and graphene fluoride (GF) attract greater attention due to the abundance of oxygenated surface functional groups [13]. The presence of surface functionalities acts as the chemical active sites and provides catalytic behavior during combustion process. Therefore, GO is considered as an effective additive to reduce the ignition energy of energetic materials and initiate the disproportionation and oxidation reactions [2, 14]. The generated heat and gaseous products are conducive to reduce aggregation and improve pressure gain. Thiruvengadathan et al. [15] measured a remarkable enhancement in the energy release from 739 to 1421 J/g for the functionalized graphene sheets (GO/Al/Bi_2O_3). Zhang and coworkers [16] found the decomposition temperature of ammonium perchlorate (AP) decreases by 106 K by adding only 10 wt% of GO. Numerous experimental studies [6, 17–19] dedicated to investigate the composite fabrication and observed a similar enhancement effect of graphene in propellants, however, the physical and chemical insights of graphene on energetic materials remain unknown at the current stage.

The computational methods in molecular modelling provide an atomistic perspective to examine the oxidation process of energetic materials containing graphene coating. Amiri et al. [20] conducted a reactive molecular dynamic simulation (RMD) of Ni substrate against hyper-thermal oxygen. They demonstrated the limited coating effect of pristine graphene in protecting Ni substrate; the graphene remained intact under lower incident energy, but failed to provide efficient protection as the incident energy increases. Besides, three oxidation stages were proposed: transformation of graphene into graphene oxide, formation of NiO nuclei, and growth of NiO clusters. Hong and his group [21] developed a reactive force field for Al/C to investigate carbon coating and its effect on the aluminum nanoparticles (ANPs). The simulation results indicated that the carbon-coated ANPs are less reactive at low temperatures. But the

particles are very susceptible to oxidation when the coating layer was removed at an elevated temperature. Jiang et al. [1] elaborated the synergistically chemical and thermal coupling between GO and GF for enhancing aluminum combustion. This study identified the generated reactive species (CF_x and CF_xO_y) but do not shed the light on the detailed reaction mechanism.

This work focus on the combustion enhancement of graphene coating on Al slabs under the flow impact. The ReaxFF force field is employed to describe the interactions between Al, C and O. The stress analysis and bond formations are considered to examine the microstructure evolution and disruption mechanism. The heat and mass transfer processes highlight the nature of combustion effect via surface engineering. The results are expected to provide a theoretical guidance for graphene-related energetic materials.

28.2 Numerical Settings

The RMD simulations are conducted to explore the effects of graphene on the oxidation at the atomic level. This method introduces a bond-order formalism and polarizable charge description to model the interatomic interactions and describe the chemical reactions. Detailed information about the reactive force field can refer to the studies by van Duin and his co-workers [22, 23]. This work employs an Al/C/H/O reactive force filed (ReaxFF) developed by Hong and van Duin [21], which has been widely used in exploiting the combustion mechanism of aluminum [24–28].

Two slab configurations are constructed to highlight the passivation effect, that is, with graphene and alpha-alumina (Fig. 28.1). The thickness of graphene coating (δ) on the aluminum particle lies in the range of 0.5–1.2 nm [2]. Here, we select the threshold value (0.5 nm), which corresponds to a bilayer graphene. The thickness of aluminum substrates is 5 nm in z-directions. The stable slabs are obtained using a canonical ensemble (NVT) in 300 K for 40 ps. The oxygen domain is relaxed independently in an isothermal isobaric ensemble (NPT) for 40 ps. The temperature and pressure are 2000 K and 10 MPa, respectively. Considering the possible flow

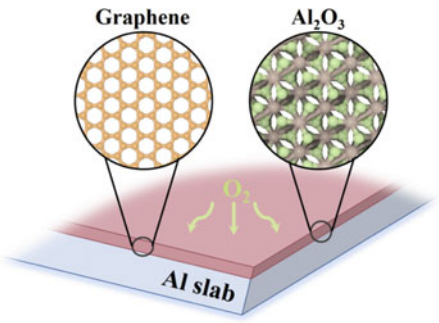

Fig. 28.1 Initial configurations of aluminum slabs with graphene and alumina coatings

effect in the propellant and explosion, 6000 oxygen molecules are added with a translational velocity ranging in 1–4 km/s along z-direction. Subsequent oxidation process is achieved in a microcanonical ensemble (NVE) for 200 ps. The atomic motion equations are integrated by the Verlet-velocity algorithm with a time step of 0.25 fs. The free boundary condition is applied along z direction to exploit the coating effect, while periodic boundary conditions are considered for both x and y directions to mimic an infinite-large slab. Note that the oxygen propagation in z-direction (that is, 266 nm) cost 60 ps for the case in 4 km/s. Therefore, the following results and discussions focus on the initial simulation stage (<60 ps). All RMD simulations and visualizations are conducted by LAMMPS [29] and OVITO [30], respectively. The species identification was conducted from the bond information.

28.3 Results and Discussions

The oxygen flow propagates toward the aluminum slab involving the intensive energy transfer between gas medium and slab surface. The mean kinetic energy of an oxygen molecule in 1 and 4 km/s correspond to 17.7 and 75.1 kcal/mol, respectively. The oxygen molecules collide on the slab successively and induce the structure perturbation. Figure 28.2 exhibits the atomic stress of bilayer graphene coatings under the flow impact in 1 km/s. The maximum stress value (130 GPa) corresponds to the intrinsic strength of graphene. Successive surface collisions at the initial stage (<3 ps) result in the local bending of upper layer and a minor crack on the second layer (Fig. 28.2b) due to the extrusion effect of Al substrate. The stress in z-direction

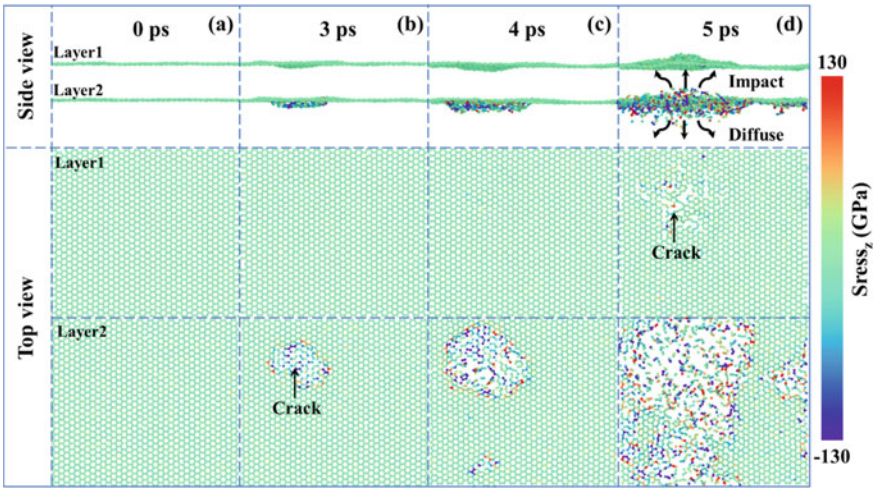

Fig. 28.2 Atomic stress of graphene coating under the impact of oxygen flow in 1 km/s from side and top views. The intrinsic strength of graphene is 130 GPa [31]

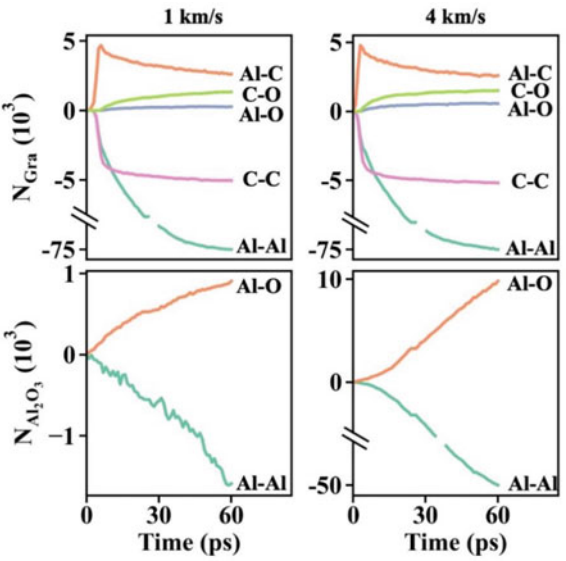

Fig. 28.3 The evolution in the bond populations for Al_2O_3/Al and graphene/Al composites. Positive and negative values indicate the increase and decrease in the number of specific bonds, respectively

(termed as $Stress_z$) of atoms reach the breakage threshold. The crack propagates in the bottom layer of graphene resulting in the breakage of a large number of C–C bonds. Carbon fragments form in the subsequent process. They either diffuse downward into the Al substrate forming the Al–C bonds, or eject upward interacting with the upper graphene layer (Fig. 28.2d). In the further evolution, the surface layer cracks and provides an access for the ejected carbon fragments to react with the gaseous oxygen. The graphene coatings disrupt completely. Similar disruption processes are observed for the case in 4 km/s, while the overall reactions are accelerated due to the higher kinetic energy in the gaseous molecules.

The exact bond populations are summarized in Fig. 28.3. The number variations of C–C, Al–Al, Al–C in 4 km/s is close to that in 1 km/s, which suggests the bilayer graphene coating make similar contribution in two flow velocity cases. However, the amount of Al–O and C–O in case of 4 km/s (555 and 1510) surpasses to that of 1 km/s (227 and 1336). It can be attributed to the superfluous oxygen flow suffice to react with ejected C radicals and diffuse into Al substrate. Thus, the entire oxidation processes are further accelerated. Above stress distribution and bond populations highlight the breakage of graphene and ejections of C radicals under the flow impact. By contrast, the diffusion mechanism governs the oxidation process of Al slabs with natural oxide layer. In case of 1 km/s, only 907 new-formed Al–O bonds are observed at 60 ps. As the flow velocity further increases, the enhanced surface collisions promote the diffusion of O atoms from oxygen shell toward Al substrate. The amount of Al–O bond reaches to 9813 at 60 ps. The completely different bond populations for case in 1 and 4 km/s suggest the crucial effect of flow impact. Figure 28.4 exhibits the O_2 adsorption number of slabs. Under the flow impact in 1 km/s, the Al slab adsorbs

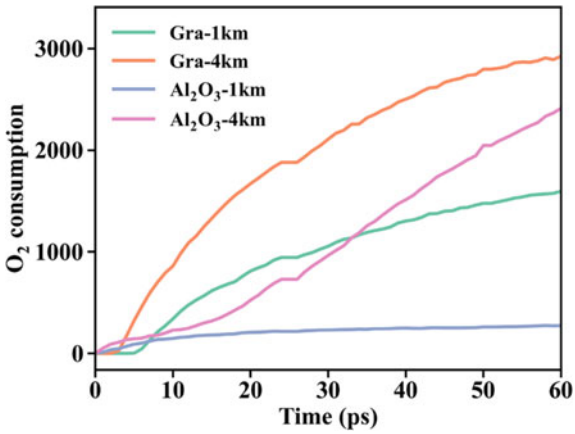

Fig. 28.4 Oxygen adsorptions on the Al slab with alumina and graphene coatings in 1 and 4 km/s

merely 200 gas molecules. While for case in 4 km/s, the O_2 adsorption undergoes a minor increase at initial stage (<15 ps) and a rapid rise in later time.

The gaseous O_2 molecules is rapidly consumed via both surface reaction of Al atoms and gas-phase reactions with carbon fragments yielding CO or CO_2 (Fig. 28.4). This explains the rapid rise of Al–O and C–O bonds in Fig. 28.3. In the graphene/Al composite, the initial molecular collisions occur on the slab surface, and no gas molecule is consumed in both two velocity cases. After the deformation and breakage of graphene coating, the ejected carbon fragments react with surrounding gas medium. Gas phase reactions dominate the entire oxidation process; more than 1595 and 2924 O_2 molecules are consumed for case in 1 and 4 $_{km}$/s, respectively. By contrast, the Al_2O_3/Al composite exhibits a much slower consumption rate of gaseous oxygen. This can be attributed to the lack of gaseous fragments as the gaseous oxygen does not have enough kinetic energy to break the Al-Al bonds even traveling at 4 km/s [25].

The flow impact also drives the motion of slab along z direction. (Fig. 28.5a). In the case of graphene/Al in a flow of 4 km/s, its displacement reaches up to ~4 nm in 20 ps, and the particle velocity corresponds to ~2 km/s. Figure 28.5b presents the temporal and spatial distributions of slab temperature. The slab region is determined by the atom number density (>30 nm^{-3}). For the slab with graphene coatings, the surface crack accompanies with C–C bond breaking, C–O bond formation and formations of Al–O bond. These three processes contribute to a higher amount of heat release in the reaction region [2] and generate an obvious temperature gradient along the direction of flow propagation. The temperature discrepancy between the surface and the bottom of slab arrives to 2722 and 2851 K at 25 ps for case in 1 km/s and 4 km/s, respectively. The thickness of slabs is reduced to 5.6 nm due to the apparent surface dissociation. The generated impulse drives the slab to travel 42 nm within the first 50 ps in a flow of 1 km/s. The displacement is enhanced up to 62 nm for the case in 4 km/s. However, the oxidation in the case of alumina coating follows a mild diffusion oxidation. Almost no temperature gradient is observed under the

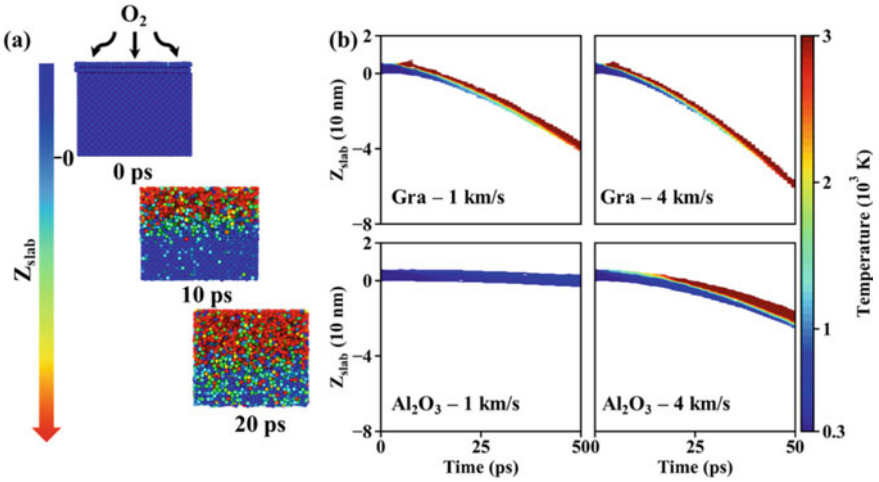

Fig. 28.5 **a** Temperature distributions of the Al slab for case with graphene coating in 4 **km**/s. **b** Temporal and spatial distributions of slab temperature. Z_{slab} refer to the displacement of slab in z direction

flow impact in 1 km/s. Further increasing the flow velocity to 4 km/s, the intense energy transfer induces an obvious temperature gradient. The slab displacement is almost 20.8 nm. It is interesting to note that the displacement in the graphene/Al case is much larger than that in the Al_2O_3/Al case. The key observation from Fig. 28.5 suggests that the surface modified Al slab yield an intense impulse and rapid heat release.

The reaction front within the slab is a key characteristic feature to describe the progress of Al oxidation, and it can be approximated via the atomic diffusion front. Figure 28.6 illustrates the diffusion front of C (in graphene) and O atom (in O_2) for the slab with graphene, and the diffusion front of Al (in Al_2O_3), O (in Al_2O_3) and O (in O_2) atom for the slab with alumina. The diffusion front is determined via the position of 30 atoms nearest to the bottom. For the slab with graphene, the disrupted graphene layer yields a large number of carbon diffusion into Al substrate and ejection toward gas medium (Fig. 28.2). In case of 1 km/s, the diffusion distance for C atoms arrives to 2.5 nm at 60 ps. The positive values of O atoms indicate that the oxygen do not participate into the oxidation process of Al slab, and the consumption of oxygen is mainly attributed to the reactions with carbon fragments from graphene (Fig. 28.4). As the flow velocity increases to 4 km/s, the intense energy transfer on slab surface promotes the heat accumulation on the upper slab (Fig. 28.5), which accelerate the diffusion of C atoms into slabs. The diffusion distance is enhanced as ~2.7 nm. Besides, the O atoms exhibit in a different manner; it diffuses into the Al slab and the diffusion front is close to that of C atoms. This suggests that the oxygen molecules participate in the oxidation of Al slab yield Al oxides. By contrast, the mild diffusion is observed for Al_2O_3/Al composite in 1 km/s. Increasing the flow velocity to 4 km/s, the diffusion process is accelerated to an extent. Therefore, the enhanced

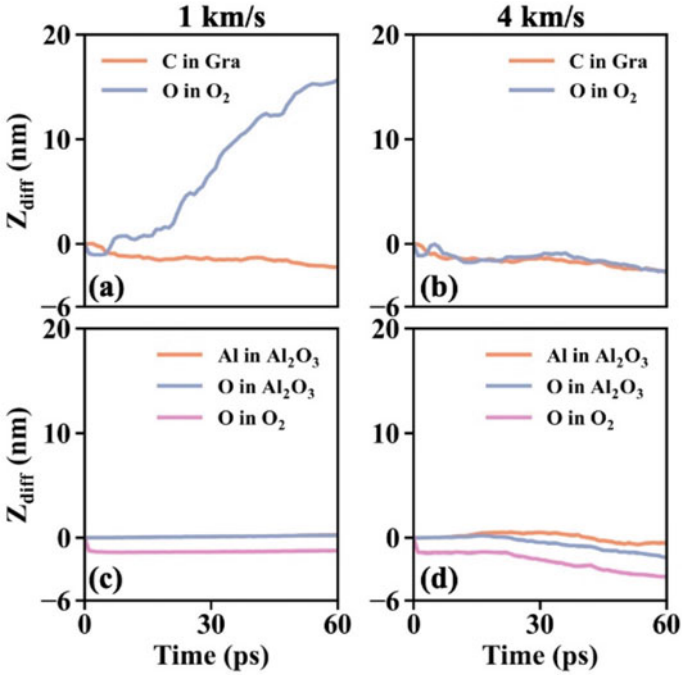

Fig. 28.6 Atomic diffusions toward Al slabs along z direction. The Z_{diff} represent the relative distance from the diffusion front to the bottom slab. Positive and negative values represent the diffusion outward gaseous medium and inward slab, respectively

mass diffusion demonstrates the remarkable contribution of graphene coating on the combustion enhancement.

The morphological evolutions, bond populations, and mass diffusion highlights the disruption and ejection of graphene coatings, which induces the numerous gas-phase reactions. Figure 28.7 presents the number of key intermediates in the oxidation of composited Al slabs, including C, CO, CO_2, O, Al, Al in case of graphene (Fig. 28.7a) and O, Al, AlO in case of Al_2O_3 (Fig. 28.7b). In case of modified slabs, the disrupted graphene yields numerous C radicals toward gaseous environment, which triggers the gas-phase reactions with O_2 via $C + O_2$ $CO + O$. The amount of CO exceeds to 1251 and 1395 the flow impact in 1 and 4 km/s. The intense flow also promotes the dissociation of Al from composited slabs to gas medium. More than 2625 Al radicals are identified, which induce the formations of Al_xO_y and Al_xC_y via $Al + O$ AlO, $AlO + O$ AlO_2, $Al + C$ AlC, $2Al + 2C$ Al_2C_2. However, for slab with Al_2O_3 coating, there is no oxidation product or only minor amount of products observed for case in 1 km/s and 4 km/s, respectively.

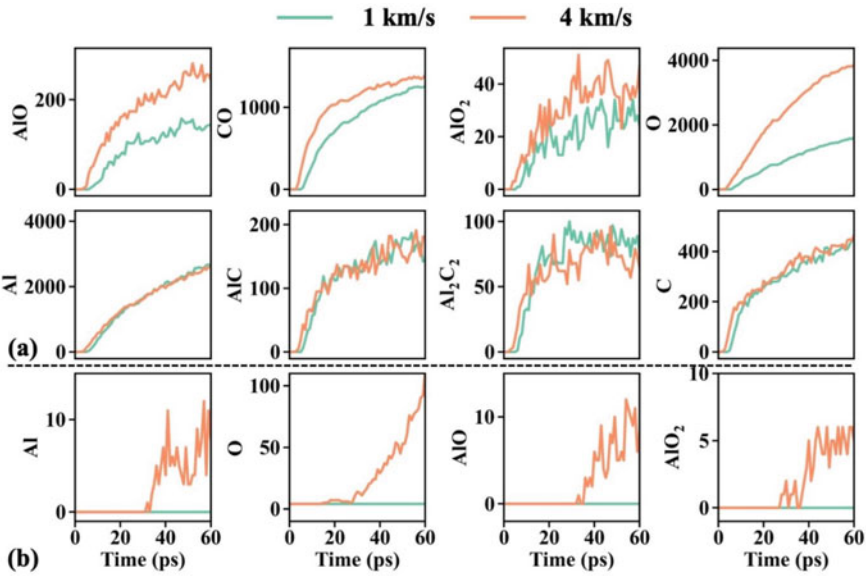

Fig. 28.7 Oxidation products of graphene-Al (**a**) and Al_2O_3-Al slabs (**b**)

28.4 Conclusions

This study sheds light on the combustion characteristics of aluminium slabs with multi-layer graphene coating. The stress distributions, bond populations, heat and mass transfer are examined to elaborate the underlying oxidation mechanism of modified slabs. Successive surface collisions result in the preferable crack on the lower graphene layer nearing the aluminum substrate, rather than the upper layer. Subsequent disruption of graphene promotes the diffusion of oxidizer inward the slabs and ejection outward the gaseous medium. Compared with alumina coating, an enhanced energy transfer process and numerous oxidation products are observed for slabs with graphene coating. These numerical findings highlight the promising effect of graphene coating on combustion enhancement, including more combustion heat, higher impulse intensity and less ignition delay. Combining the present results, we believe the strategy of using graphene and functionalized graphene to enhance ignition and combustion can be applied to other fuels and energetic materials.

Acknowledgements This paper is supported by the project of State Key Laboratory of Explosion Science and Technology (Beijing Institute of Technology). The project number is ZDKT21-0. The authors also acknowledge the support from Foundation of Science and Technology on Combustion and Explosion Laboratory.

References

1. Y. Jiang, S. Deng, S. Hong et al., Synergistically chemical and thermal coupling between graphene oxide and graphene fluoride for enhancing aluminum combustion. ACS Appl. Mater. Interfaces **12**, 7451–7458 (2020). https://doi.org/10.1021/acsami.9b20397
2. Y. Jiang, S. Deng, S. Hong et al., Energetic performance of optically activated aluminum/graphene oxide composites. ACS Nano **12**, 11366–11375 (2018). https://doi.org/10.1021/acsnano.8b06217
3. D. Sundaram, V. Yang, R.A. Yetter, Metal-based nanoenergetic materials: synthesis, properties, and applications. Prog. Energy Combust. Sci. **61**, 293–365 (2017). https://doi.org/10.1016/j.pecs.2017.02.002
4. B. Wu, F. Wu, Y. Zhu et al., Fast reaction of aluminum nanoparticles promoted by oxide shell. J. Appl. Phys. **126**, 144305 (2019).https://doi.org/10.1063/1.5115545
5. P. Chakraborty, M.R. Zachariah, Do nanoenergetic particles remain nano-sized during combustion? Combust. Flame **161**, 1408–1416 (2014). https://doi.org/10.1016/j.combustflame.2013.10.017
6. J. Wang, J. Wang, S. Wang et al., High-energy Al/graphene oxide/CuFe2O4 nanocomposite fabricated by self-assembly: evaluation of heat release, ignition behavior, and catalytic performance. Energ. Mater. Front. (2021). https://doi.org/10.1016/j.enmf.2021.01.005
7. Y.-T. Zheng, M. He, G.-X. Cheng et al., Effect of ionization on the oxidation kinetics of aluminum nanoparticles. Chem. Phys. Lett. **696**, 8–11 (2018). https://doi.org/10.1016/j.cplett.2018.02.039
8. T.-K. Liu, Experimental and model study of agglomeration of burning aluminized propellants. J. Propul. Power **21**, 797–806 (2005). https://doi.org/10.2514/1.11988
9. J. Liu, P. Liu, M. Wang, Molecular dynamics simulations of aluminum nanoparticles adsorbed by ethanol molecules using the ReaxFF reactive force field. Comput. Mater. Sci. **151**, 95–105 (2018). https://doi.org/10.1016/j.commatsci.2018.04.054
10. C.H.A. Tsang, H. Huang, J. Xuan et al., Graphene materials in green energy applications: recent development and future perspective. Renew. Sustain. Energy Rev. **120** (2020). https://doi.org/10.1016/j.rser.2019.109656
11. L.S. Hui, E. Whiteway, M. Hilke et al., Synergistic oxidation of CVD graphene on Cu by oxygen plasma etching. Carbon **125**, 500–508 (2017). https://doi.org/10.1016/j.carbon.2017.09.076
12. J.L. Sabourin, D.M. Dabbs, R.A. Yetter et al., Functionalized graphene sheet colloids for enhanced fuel/propellant combustion. ACS Nano **3**, 3945–3954 (2009). https://doi.org/10.1021/nn901006w
13. L. Tan, X. Lu, N. Liu et al., Further enhancing thermal stability of thermostable energetic derivatives of dibenzotetraazapentene by polydopamine/graphene oxide coating. Appl. Surf. Sci. **543** (2021). https://doi.org/10.1016/j.apsusc.2020.148825
14. Y. Jiang, A.R. Demko, J. Baek et al., Facilitating laser ignition and combustion of boron with a mixture of graphene oxide and graphite fluoride. Appl. Energy Combust. Sci. 1–4 (2020). https://doi.org/10.1016/j.jaecs.2020.100013
15. R. Thiruvengadathan, S.W. Chung, S. Basuray et al., A versatile self-assembly approach toward high performance nanoenergetic composite using functionalized graphene. Langmuir **30**, 6556–6564 (2014). https://doi.org/10.1021/la500573e
16. W. Zhang, Q. Luo, X. Duan et al., Nitrated graphene oxide and its catalytic activity in thermal decomposition of ammonium perchlorate. Mater. Res. Bull. **50**, 73–78 (2014). https://doi.org/10.1016/j.materresbull.2013.10.023
17. K. Kappagantula, M.L. Pantoya, Experimentally measured thermal transport properties of aluminum? polytetrafluoroethylene nanocomposites with graphene and carbon nanotube additives. Int. J. Heat Mass Transf. **55**, 817–824 (2012). https://doi.org/10.1016/j.ijheatmasstransfer.2011.10.026

18. S. Isert, L. Xin, J. Xie et al., The effect of decorated graphene addition on the burning rate of ammonium perchlorate composite propellants. Combust. Flame **183**, 322–329 (2017). https://doi.org/10.1016/j.combustflame.2017.05.024
19. J. Shen, Z. Qiao, J. Wang et al., Reaction mechanism of Al-CuO nanothermites with addition of multilayer graphene. Thermochim. Acta **666**, 60–65 (2018). https://doi.org/10.1016/j.tca.2018.06.005
20. N. Amiri, J.B. Ghasemi, H. Behnejad, Atomistic insights into the protection failure of the graphene coating under the hyperthermal impacts of reactive oxygen species: ReaxFF-based molecular dynamics simulations. Appl. Surf. Sci. **554** (2021). https://doi.org/10.1016/j.apsusc.2021.149606
21. S. Hong, A.C.T. van Duin, Atomistic-scale analysis of carbon coating and its effect on the oxidation of aluminum nanoparticles by ReaxFF-molecular dynamics simulations. J. Phys. Chem. C **120**, 9464–9474 (2016). https://doi.org/10.1021/acs.jpcc.6b00786
22. K. Chenoweth, A.C.T. van Duin, W.A. Goddard, ReaxFF reactive force field for molecular dynamics simulations of hydrocarbon oxidation. J. Phys. Chem. A **112**, 1040–1053 (2008). https://doi.org/10.1021/jp709896w
23. T.P. Senftle, S. Hong, M.M. Islam et al., The ReaxFF reactive force-field: development, applications and future directions. npj Comput. Mater. **2**, 15011 (2016). https://doi.org/10.1038/npjcompumats.2015.11
24. X. Zhang, C. Fu, Y. Xia et al., Atomistic origin of the complex morphological evolution of aluminum nanoparticles during oxidation: a chain-like oxide nucleation and growth mechanism. ACS Nano **13**, 3005–3014 (2019). https://doi.org/10.1021/acsnano.8b07633
25. X. Chang, Q. Chu, D. Chen, Shock-induced anisotropic metal combustion. J. Phys. Chem. C **124**, 13206–13214 (2020). https://doi.org/10.1021/acs.jpcc.0c02876
26. Q. Chu, B. Shi, L. Liao et al., Ignition and oxidation of core-shell Al/Al2O3 nanoparticles in an oxygen atmosphere: insights from molecular dynamics simulation. J. Phys. Chem. C **122**, 29620–29627 (2018). https://doi.org/10.1021/acs.jpcc.8b09858
27. Q. Chu, B. Shi, L. Liao et al., Size-derived reaction mechanism of core-shell aluminum nanoparticle. Appl. Phys. Lett. **117**, 133902 (2020). https://doi.org/10.1063/5.0015367
28. Q. Chu, B. Shi, L. Liao et al., Reaction mechanism of the aluminum nanoparticle: physicochemical reaction and heat/mass transfer. J. Phys. Chem. C **124**, 3886–3894 (2020). https://doi.org/10.1021/acs.jpcc.9b11410
29. S. Plimpton, Fast parallel algorithms for short-range molecular dynamics. J. Comput. Phys. **117**, 1–19 (1995). https://doi.org/10.1006/jcph.1995.1039
30. A. Stukowski, Visualization and analysis of atomistic simulation data with OVITO–the open visualization tool. Model. Simul. Mater. Sci. Eng. **18**, 015012 (2010). https://doi.org/10.1088/0965-0393/18/1/015012
31. L. Zhang, G. Hou, W. Zhai et al., Aluminum/graphene composites with enhanced heat-dissipation properties by in-situ reduction of graphene oxide on aluminum particles. J. Alloy. Compd. **748**, 854–860 (2018). https://doi.org/10.1016/j.jallcom.2018.03.237

Chapter 29
Exploring the Influence of Colloidal Graphite on Granule Casting Modified Double-Base Propellant Granules

Zhi Ren, Xiaojiang Li, Xi Zhang, Qiwen He, and Linsheng Xie

Abstract Two kinds of granules were coated and modified by colloidal graphite through mechanical method. The microstructure of colloidal graphite was observed by SEM and TEM as well as the granules and the modified granules. On the basis of the characterization of the microstructure of granules, changes of the flowability of the granules and the modified granules were tested via Carr index method and PFT power flow tester. At the same time, the mechanical sensitivity, electrostatic spark sensitivity, loading density, screen loading density of the four kinds of granules and the density of the propellants manufactured by the granules were tested. The results indicated that the microstructure of the colloidal graphite was irregular scaly which size was about 5 μm. After the granules were coated and modified by colloidal graphite, the mechanical sensitivity and electrostatic spark sensitivity was improved in some extent, while the flowability was improved greatly, therefore the loading density and screen loading density was increased, as a result, the density of the propellants were increased as well and more closely to their theoretical density respectively.

Z. Ren · L. Xie (✉)
East China University of Science and Technology, Shanghai 200037, People's Republic of China
e-mail: clxw@ecust.edu.cn

Z. Ren
e-mail: rz3258@foxmail.com

Z. Ren · X. Li · X. Zhang · Q. He
Xi'an Modern Chemistry Research Institute, Shaanxi, Xi'an 710065, People's Republic of China
e-mail: xiaojianglee@sohu.com

X. Zhang
e-mail: 3100104290@zju.edu.cn

Q. He
e-mail: hqw110520@126.com

A. Gany and X. Fu (eds.), *2021 International Conference on Development and Application of Carbon Nanomaterials in Energetic Materials*, Springer Proceedings in Physics 276,
https://doi.org/10.1007/978-981-19-1774-5_29

29.1 Introduction

Granule casting is the abbreviation for pelletized casting process [1] which also called interstitial casting [2] or ball casting process. This process is mainly consisted of two parts that is the manufacture of granules and casting-curing [3]. In the manufacture of granulation process, the solid components and part of the plasticizers in the formula were made into right circular cylinder granules which had a diameter and height of about 1 mm [4]. In casting-curing process, the granules were filled in a mould or a motor [5] and then the casting liquids mainly contained nitroglycerin were filled into the gaps of the granules [6]. The granules were infiltrated and plasticized by casting liquids in the curing process to form a macroscopic homogeneous propellant grain. The key process of the granule casting was the manufacture of the granules. The properties of the granules have a great influence on the properties of the propellants, for example, the formulation of the granules determines the intrinsic properties of the propellants. It affects the energy, combustion, mechanical properties and storage aging performance of the propellants. Besides, the flowability and sensitivity properties of the granules also influence the process safety and the manufacture of the propellant when the granules are loading into the moulds. If the flowability was poor, the loading density would also decrease, as a result, it would have a negative effect on the density of the propellant curing from the granules and casting liquids. If the sensitivity was high, the risks in storage and in use would be increased. Therefore, the increase of flowability of the granules could improve the loading density [7] so that the density and the batch stability of the propellants would be improved as well. On the other hand, decrease the sensitivity of the granules could improve the safety on the manufacture of the propellants. Dong et al. [8] added 0.1~0.2% graphite into double-base propellant, the electrostatic potential values of double-base propellant after the drying process were reduced from 2000~2700 V to 600 V. Cai [9] replaced the traditional graphite with carbon black to glaze the spherical granules and found it could also eliminate the static electricity. Bao et al. [10] found that the addition of 5% conductive graphite increases the electrical conductivity and thermal conductivity of the electrically controlled solid propellant by 13.2 and 18.9%. Nevertheless, there is no systematic report on improving the flowability, loading density and decreasing the sensitivity of the granules. The methods of modifying the granules with graphite and its effect on loading density had been reported [11] but the specific reasons and the effect on the other properties had no analysis or report.

Two kinds of different double-base propellant granules were surface coating modified by colloidal graphite in this study and then the microstructure, flowability, mechanical sensitivity, electrostatic spark sensitivity and loading density were characterized to provide references for increasing the loading density of the granules, density of the propellants, decreasing the sensitivity of the granules and developing the intrinsic safety of the manufacture and transportation process.

Table 29.1 The basic formulation of the two kinds of propellants and granules

	RDX-CMDB		AP-CMDB	
Component	Granule	Propellant	Granule	Propellant
NC/%	28~35	20~25	28~35	20~25
NG/%	1~4	25~40	1~4	25~40
RDX/%	45~50	30~36	—	—
AP/%	—	—	45~50	30~36
Al/%	8~10	4~6	8~10	4~6
Ct./%	5~8	4~7	5~8	4~7
Combustion stabilizer/%	2~4	1~3	2~4	1~3

29.2 Experiment

29.2.1 Materials

RDX-CMDB granules, Xian Modern Chemistry Research Institute; AP-CMDB granules, Xian Modern Chemistry Research Institute; Colloidal Graphite, Shanghai HuiGang Graphite Limited Corporation.

29.2.2 Manufacture of Cast Double-Base Propellant Granules

Two kinds of double-base propellant granules (RDX and AP) were manufactured via granule casting process through catalyst pre-process, absorbing, calendering, gelling, extruding and granulating procedures [12]. These two kinds of granules were multicomponent formulas which were bonded by NC and NG adhesive systems. The component of granules and propellants were given in Table 29.1.

29.2.3 Colloidal Graphite Modified the Granules

The two kinds of granules were respectively divided into two parts, one of the parts were modified in the blender while the others were not. The modify steps were taken as follow. First, 0.05% granule weights' colloidal graphite was dispersed in alcohol and then the suspension was put into the blender together with granules and some wooden balls. Secondly, the blender was turned on and rotated for 30 min in order

to uniformly distribute colloidal graphite onto the surface of the granules and then the blender was turned off and the wooden balls were removed. Thirdly, the granules were put into a water bath oven to remove the residual alcohol. Lastly, the granules were screened in a copper griddle which mesh number was 60 to remove the residual colloidal graphite. The materials on the copper griddle were kept for the subsequent experiments and tests.

29.2.4 Modified Double-Base Propellant Manufactured by Granules

The four kinds of granules prepared above were respectively filled in the same type mould and then four NG casting liquids were prepared at the same time. The NG casting liquids were cast in the moulds via vacuum casting process and then cured in a water bath oven. After a certain curing time, propellant grains were formed and then could be demoulded from the moulds. The specific components of the propellants were listed in Table 29.1.

29.2.5 Analysis and Characterization

SEM: type Quanta 600 FEG, US FEI company.

TEM: Talos F200i, US Thermo Fisher Scientific company, resolution 0.24 nm.

Laser particle size: Type 2000 Mastersizer Laser particle tester, Injector: Hydro2000MS(A) type, measuring range: 20 nm~2000 m, UK Malvern Instruments company.

Power flow test: Type PFT power flow tester, US Brookfield company, the flowability parameters of granules were tested by the ASTM D 6128–2016 [13] method.

Mechanical Sensitivity test: The impact sensitivity was tested by GJB772A-1997 [14] method 601.2, the mass of drop hammer is 2 kg, the mass of sample is 30 mg, the results is expressed as characteristic drop height H50. The friction sensitivity was tested by GJB772A-1997 method 602.1, the mass of pendulum hammer is 2 kg, the pendulum angle is 66°, the mass of sample is 20 mg, the results is expressed as explosion probability.

Electrostatic spark sensitivity test: The electrostatic spark sensitivity was tested by GJB5891.27–2006 part 27 [15], the mass of sample is 20 mg~30 mg, and the electrostatic spark sensitivity was the mean value of the 50% ignition energy or 50% ignition voltage of the sample.

Loading density test: The loading density of the granules was tested by GJB770B-2005 [16] method 402.1, every sample was tested three times to calculate the average results.

Propellant density test: Type XS204 density balance, Switzerland Mettler-Toledo group. The density of the propellants were tested by GJB770B-2005 method 401.1, the test temperature was 20 °C, every sample was tested three times to calculate the average results.

29.3 Results and Discussion

29.3.1 Analysis and Characterization of the Microstructure of Colloidal Graphite

The microstructure of colloidal graphite used in these experiments was characterized by SEM and TEM which were shown in Figs. 29.1 and 29.2. Then the EDS in SEM were used to analysis the elements in the colloidal graphite and the results were demonstrated in Fig. 29.4 and Table 29.2. In order to determine the size and size distribution of the colloidal graphite powers, laser particle size analyzer was used to test the particle size and the results was shown in Fig. 29.3.

According to the molecular orbital theory, the sp^2 hybrid orbital in the carbon atom of graphite is formed by the combination of a 2 s orbital with a $2p_x$ and a $2p_y$ orbital. The sp^2 hybrid orbitals of the adjacent carbon atoms are combined via covalent bond to form a localized σ bond and then form a regular hexagonal plane network structure. Every carbon atom has a free electron in the $2p_x$ orbital, this electron could freely move on the hybrid orbitals in the network structure similar to the metallic bonds which are called delocalized π bond or extended π bond. Therefore, the molecular structure of graphite is C–C bond which is composed of localized σ bond formed by sp^2 hybrid orbital with delocalized π bond and the length of the bond is 0.142 nm. The connection between the layers is bonded by the π electron clouds so that the binding force (Van der Waals force) is weak and the distance between the adjacent layers is 0.335~0.337 nm. Hence, the layers in graphite are easy to separate and slide [17, 18].

It could be seen from Fig. 29.1 that colloidal graphite was irregular lamellar which were accumulated together in some extent. As can be seen in Fig. 29.1c and d, the size of the single graphite sheet was about 4~6 μm and the thickness was about 50 nm. According to the adjacent layer distance of graphite, it could be speculated that the layer number of a graphite sheet was about 150. As a result, the specific surface area of colloidal graphite is large and the adsorption sites are sufficient enough to absorb on the surface of the materials that are modified by it.

It could be seen from Fig. 29.2a and b that the size of a single graphite sheet was 5 μm which was consistent with the results observed in SEM. The brightness of the graphite sheet was in consistent which demonstrated that the thickness of the graphite sheet was unequal. The thicker areas of the graphite sheet were hard to penetrate for the electrons so that these areas were dark. On the contrary, the thin

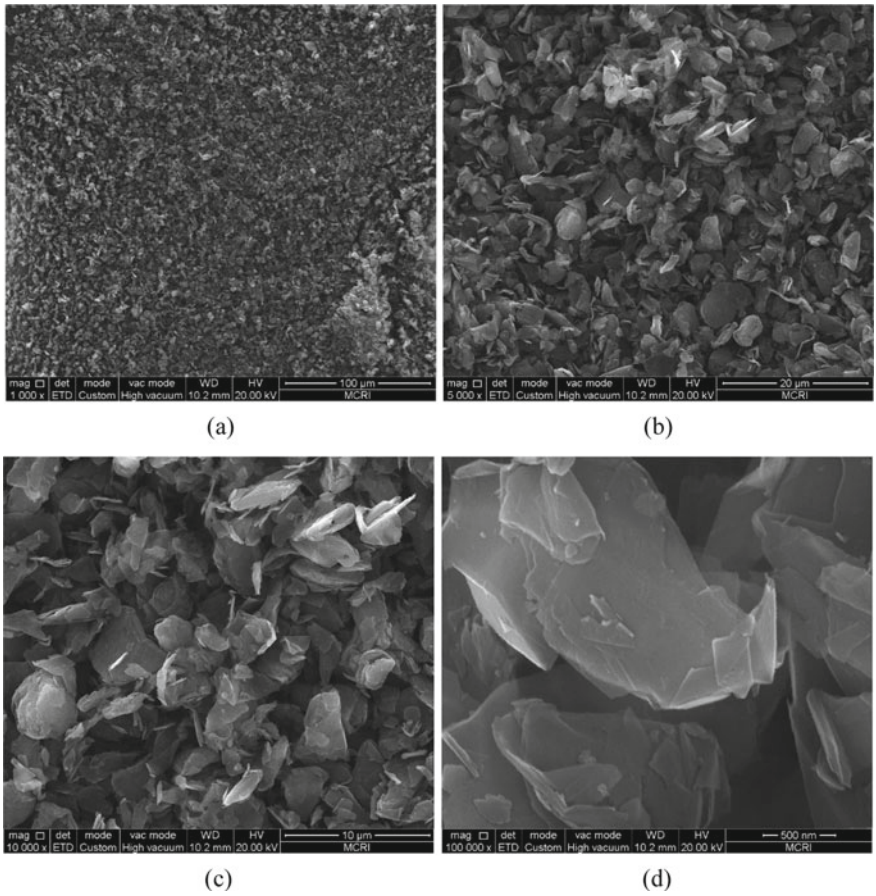

Fig. 29.1 The SEM pictures of colloidal graphite

areas of the graphite sheet were easy to penetrate for the electrons so that these areas were bright.

Figure 29.2c and d showed that the crystal cells arranged closely in a line and in order which illustrated that this colloidal graphite was hexagonal graphite in hexagonal system [19] and easy to slide between the layers.

As shown in Fig. 29.3, the D_{50} size of the colloidal graphite was 4.788 μm which was coincidence with the results in SEM and TEM. Additionally, the size distribution of the colloidal graphite powers was relatively narrow, that is 80% of the particle size were among 2.268~9.259 μm. The comparatively concentrated particle size distribution was favorable for the modification of the propellant granules.

The EDS element analyses of colloidal graphite are exhibited in Fig. 29.4 and Table 29.2. As shown, the majority component of colloidal graphite was carbon that the proportion was 94.57% by weight. Besides, there was a small amount of

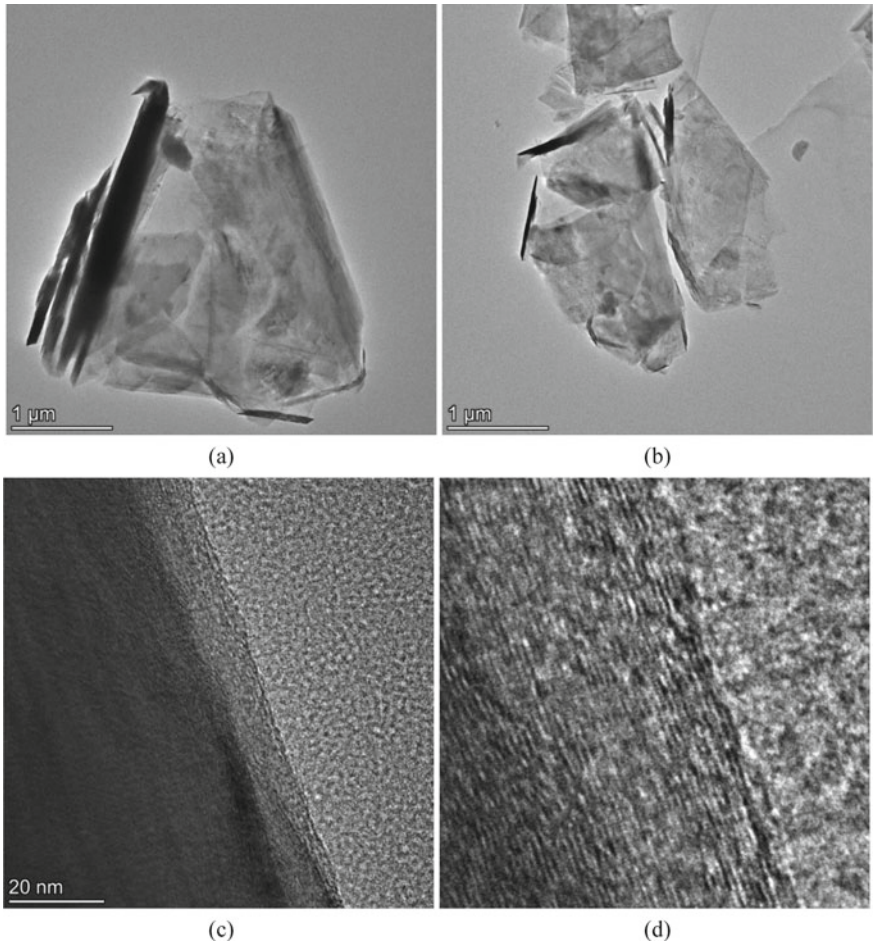

Fig. 29.2 The TEM pictures of colloidal graphite

Table 29.2 Component of two kinds of granules and propellants

Element	Weight percentage/%	Atomic percentage/%
C K	94.57	95.87
O K	5.43	4.13
total	100.00	100.00

oxygen that the content was 5.43% by weight. It can be inferred from the results that the colloidal graphite contains carbonyl group, hydroxyl group, adsorption water or other polar oxygen-containing functional groups. This is because there are two defects in the graphite lattice. One is in the edge of the regular hexagon mesh, the carbon atoms may bind with hydrogen atom, oxygen atom, hydroxyl group or

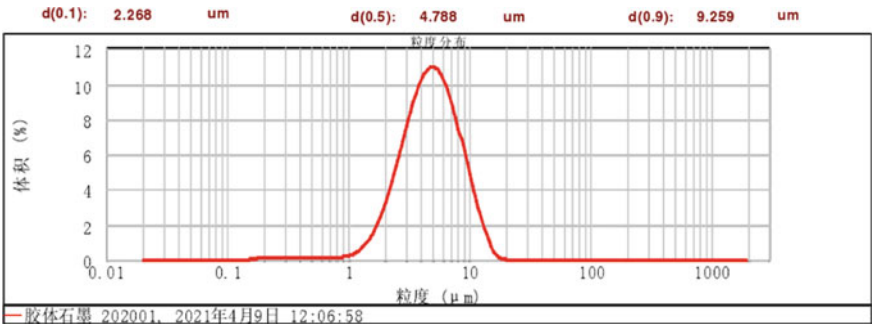

Fig. 29.3 The particle distribution of colloidal graphite

other polar functional groups. The higher graphitization degree leads to the lesser heteroatoms on the edge of the hexagon mesh. The other defect is the vacancy defect that appeared when the C–C bonds were broken. The carbon atoms in the vacancy defect areas were more active than the ones arranged in order. The polar functional groups could form intermolecular hydrogen bonds or Van der Waals force with the hydroxyl groups, nitrate groups, nitramine groups or other functional groups in nitrocellulose or hexogen or other molecules on the surface of the granules. So the defects in colloidal graphite can enhance the adsorption effect on granule surface.

29.3.2 Contrast of the Microstructure of the Granules and the Granules Coated and Modified by Colloidal Graphite

The SEM photos of RDX-CMDB and AP-CMDB granules and the granules coated modified by colloidal graphite were taken and the results were shown in Figs. 29.5, 29.6, 29.7 and 29.8.

As can be seen in Fig. 29.5a and b, the surface of the RDX-CMDB granules are rough and exist undulating folds, wrinkles and a small amount of irregular particles which may be the hexogen particles in the granules that changed its spherical appearance in the calendering, gelling and other granulation processes. While the folds and wrinkles were probably formed after the extruding process when the solvent molecules were migrated from the inside to the surface of the granules.

Figure 29.6a and b show that the scaly colloidal graphite sheets could be seen in the surface of the granules and the original undulating folds, wrinkles could hardly be seen yet. While in the low magnification photos Fig. 29.6c and d, it can also be seen that the graphite sheets accumulated on the surface of the granules and several free graphite sheets which are not connected with the other graphite sheets. From these phenomena, it can be inferred that the surfaces of the granules were almost completely coated by colloidal graphite.

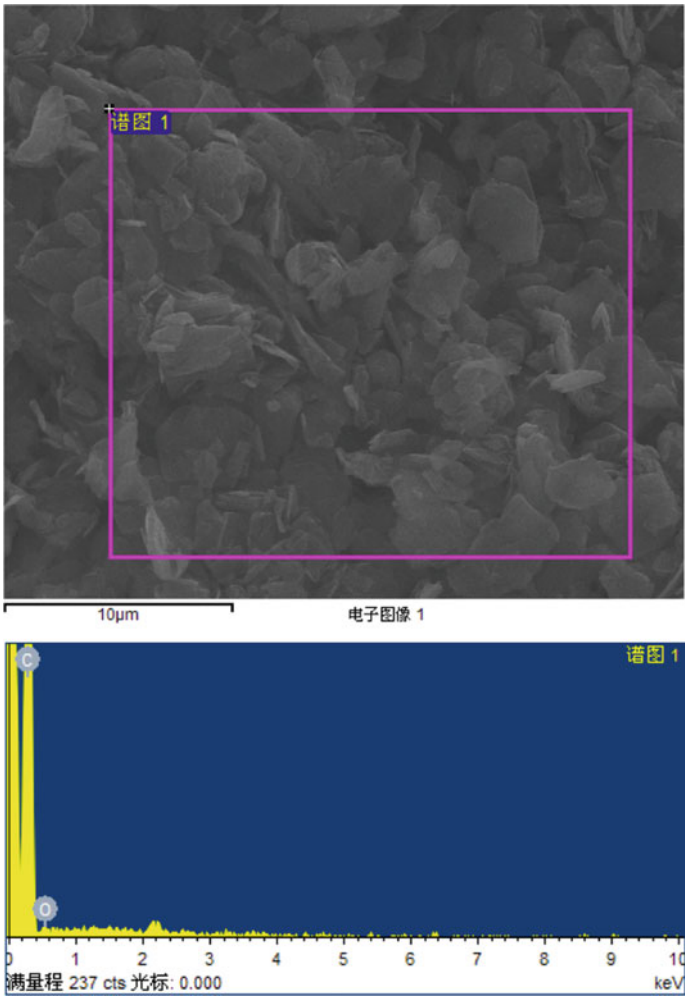

Fig. 29.4 The EDS element analysis of colloidal graphite

Figure 29.7 demonstrates the SEM pictures of the AP-CMDB granules that do not modify by colloidal graphite. As can be seen in Fig. 29.7a and b, the surfaces of the granules are relatively dense. But there are several chapped microcracks that may be formed in the process of extruding when the solvents were driven out from the inside of the granules. Besides, the nitrocellulose molecules were orientated by the mechanical force in the extruding process, therefore the granules were shrunken and the chapped microcracks emerged after the solvents were driven out of the granules. On the other hand, Fig. 29.7c and d shows the undulating folds, wrinkles on the surface of the granules were orientated in some extent and the orientation direction

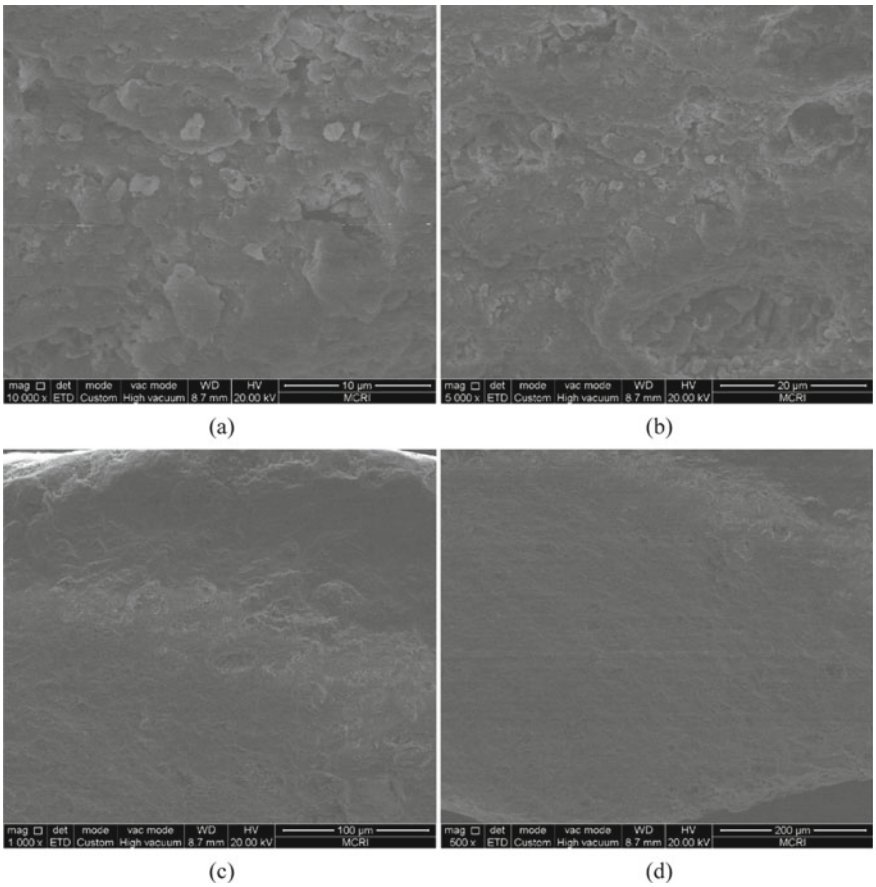

Fig. 29.5 The SEM pictures of the RDX-CMDB granules

was the axial of it, that was the direction of extruding which demonstrated the above analyses.

Figure 29.8 was the SEM photos of the AP-CMDB granules coated modified by colloidal graphite. It can be seen in Fig. 29.8a and b that the scaly colloidal graphite sheets were completely coated on the surface of the granules and the original dense with several chapped microcracks surface shown in Fig. 29.7 could hardly be seen yet. Similar to the phenomena in Fig. 29.6a and b, several free scaly graphites could be seen in Fig. 29.8a and b which demonstrated that the coating efficient is relatively high. Besides, contrast Fig. 29.7c and d with Fig. 29.8c and d it can be seen that, the oriented wrinkles were disappeared after coated modified that illustrated the colloidal graphite sheets were basically covered on the surface of the granules.

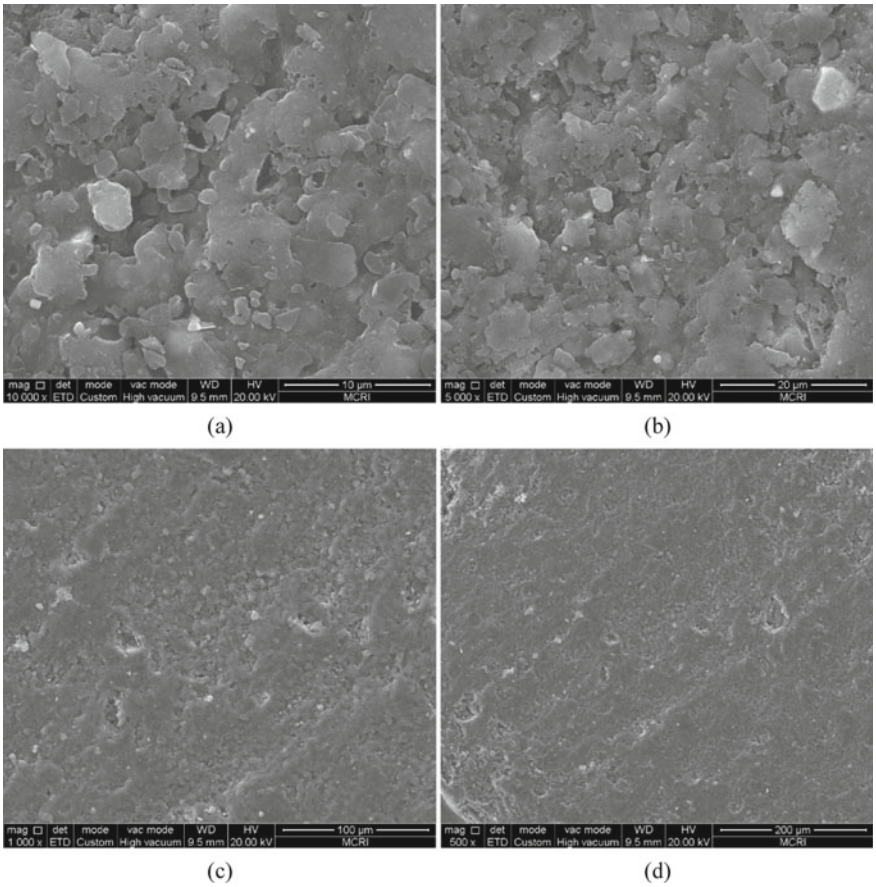

Fig. 29.6 The SEM pictures of the RDX-CMDB granules coated by colloidal graphite

29.3.3 Influence on the Sensitivity, Flowability and Loading Properties of the Granules Modified by Colloidal Graphite

The mechanical sensitivity of the two kinds of the granules before and after modifying by colloidal graphite was tested and the results were shown in Table 29.3. It can be seen in Table 29.3 that the impact sensitivity of RDX-CMDB granules was lower than AP-CMDB granules. The characteristic drop height was 1.97 times of AP-CMDB granules. On the contrary, the friction sensitivity of RDX-CMDB granules was higher than AP-CMDB granules which were 1.89 times of it. To sum up, the mechanical sensitivity of the two kinds of granules were decreased in some extent after modifying by colloidal graphite and RDX-CMDB granules decreased a lot more. The characteristic drop height of impact sensitivity of RDX-CMDB granules

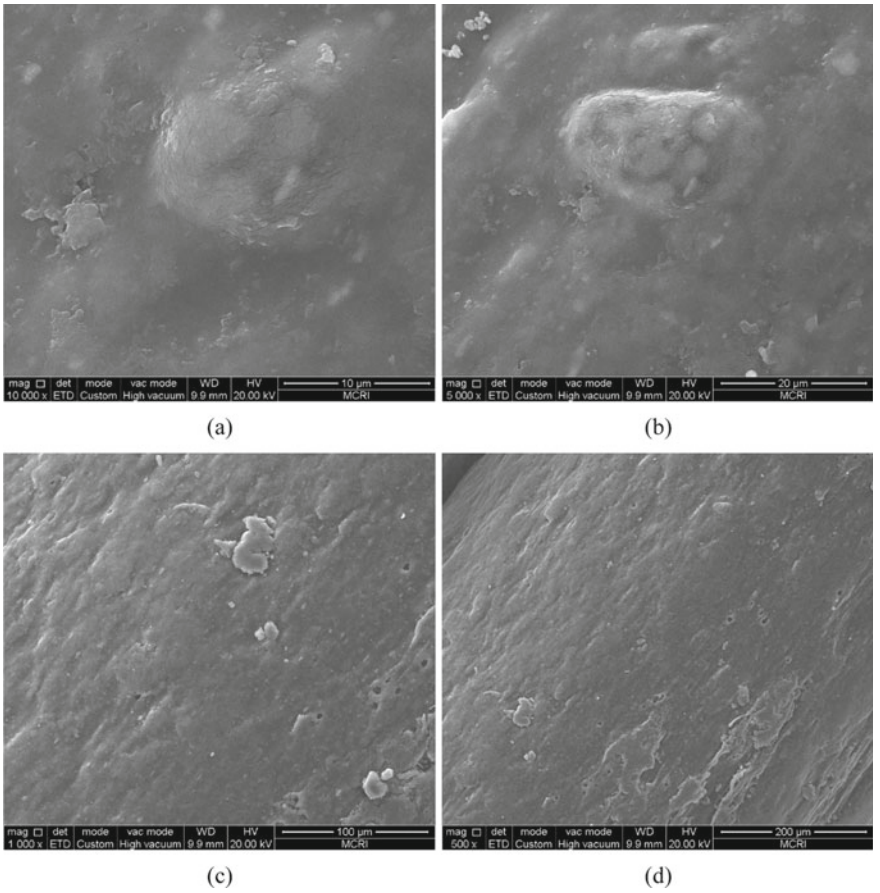

Fig. 29.7 The SEM pictures of the AP-CMDB granules

was increased from 23.2 to 28.4 cm which increased 22.4% and friction sensitivity reduced from 68 to 36% which decreased 47%. In addition, the characteristic drop height of impact sensitivity of AP-CMDB granules was increased from 11.8 cm to 14.5 cm which increased 22.9% and friction sensitivity reduced from 36 to 28% which decreased 22.2%. It can be inferred from the results that colloidal graphite could effectively decrease the external mechanical sensitivity of the two kinds of granules. One of the reasons was the RDX or AP particles exposed on the surface of the granules were covered by colloidal graphite which could be seen in Figs. 29.5 and 29.6 compared with Figs. 29.7 and 29.8 so that the external mechanical stimulations was buffered by graphite in some extent. Furthermore, part of the mechanical energy was absorbed by the sliding of graphite layers for the interaction was relatively low. As a result, the mechanical energy was attenuated partly when it act on the RDX or AP particles. So graphite coating modification could decrease the mechanical sensitivity of granules. The second reason was the edges and bulges on the surface

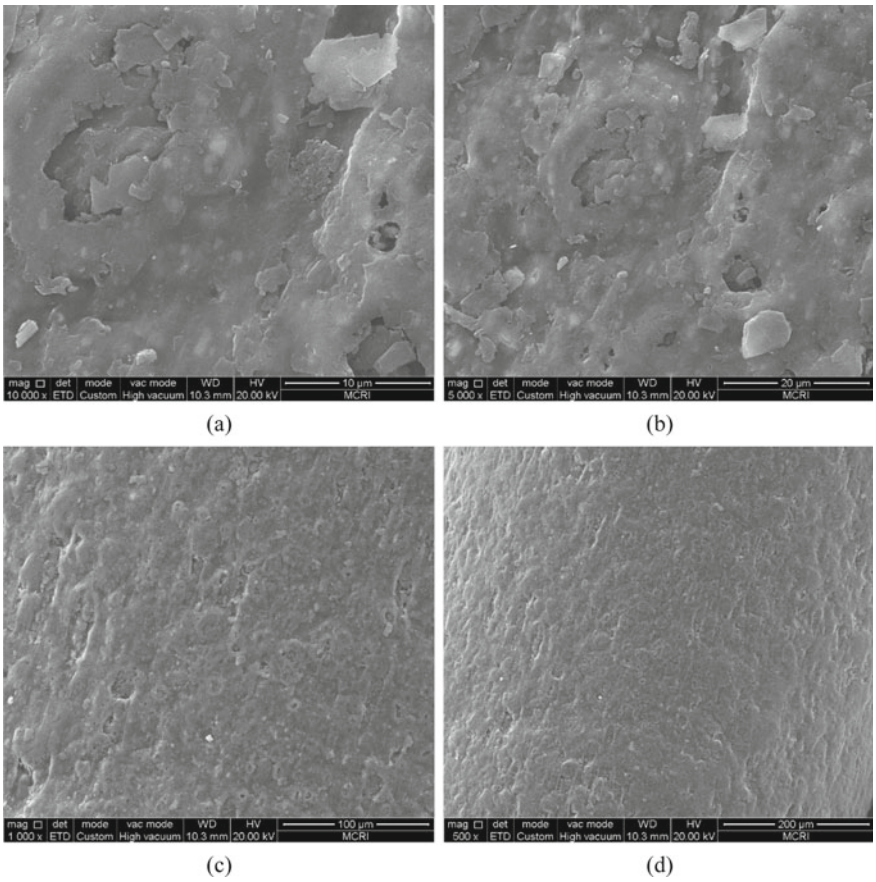

Fig. 29.8 The SEM pictures of the AP-CMDB granules coated by colloidal graphite

Table 29.3 The mechanical sensitivity of the four solid propellant granules

Samples	Impact sensitivity (characteristic drop height H_{50})/cm	Friction sensitivity/%
RDX-CMDB granules	23.2	68
RDX-CMDB granules modified by colloidal graphite	28.4	36
AP-CMDB granules	11.8	36
AP-CMDB granules modified by colloidal graphite	14.5	28

of the granules were smoothed in a certain extent. According to the hot spot theory [20], the protruding part of the solid rubbed each other when the surfaces contacted and the mechanical energy was converted to heat energy and then accumulated in these spots which led to high temperatures [21] in these contact spots that result in the combustion or detonation of the propellants. While after coating modification, the edges and bulges on the surface of the granules were smoothed or covered, so hot spots were hard to form. Moreover, the thermal conductive property of granules was increased by graphite; as a result, the heat energy was relatively quickly lost through heat conduction so it is difficult to reach the combustion or detonation temperature of the propellants.

The electrostatic spark sensitivity of the four samples were tested by GJB5891.27–2006 part 27 at 25 °C and 50% relative humidity and the results were the mean value of the 50% ignition energy or 50% ignition voltage of the sample which demonstrated in Table 29.4. The 50% ignition energy of the RDX-CMDB granules that didn't modify by colloidal graphite was 0.328 J while the AP-CMDB granules that didn't modify by colloidal graphite was 0.231 J. The electrostatic spark sensitivity of RDX-CMDB granules was 42% lower in contrast with AP-CMDB granules that demonstrated granules contained AP were more sensitive to electrostatic spark. While after coating modified by colloidal graphite the two kinds of granules were non ignition in these tests which illustrated that the coating modification could remarkably improve the electrostatic spark sensitivity. The reasons may be the electrical conductivity of the granules were increased due to the graphite on its surface which turned them into conductors or semiconductors, and part of the static electricity was easily to conduct so the electrostatic energy was difficult to accumulate. Thus, the electrostatic spark sensitivity was reduced. In addition, the lamellar materials formed by colloidal graphite on the surface of the granules played a physical isolation role and reduce the stimulation degree of external electrostatic spark, so the electrostatic spark sensitivity was greatly reduced [22].

On the basis of the above experiments, the flowability parameters of the four solid granules were tested via Carr index method [23, 24] and PFT tester. Carr index was the method that tests the angle of repose [25–27], angle of spatula, compressibility, and uniformity of particles [28]. Then find the corresponding index in the table [29] and accord to the weight of 0.25 to sum up the numbers to calculate the Carr index. The Carr index results were shown in Table 29.5 and the flow function curves tested

Table 29.4 The electrostatic spark sensitivity of the four solid propellant granules

Samples	50% ignition voltage/kV	50% ignition energy/J
RDX-CMDB granules	8.1	0.328
RDX-CMDB granules modified by colloidal graphite	Non ignition	Non-ignition
AP-CMDB granules	6.8	0.231
AP-CMDB granules modified by colloidal graphite	Non ignition	Non-ignition

Table 29.5 The flowability parameter of the four solid propellant granules

Samples	Angle of repose/°		Angle of spatula /°		Compressibility /%		Uniformity		Carr index
	Measured values	Marks	Measured values	Marks	Measured values	Marks	Measured values	Marks	
RDX-CMDB granules	33.8	21	36.4	21	10.9	22	0.50	25	89
RDX-CMDB granules modified by colloidal graphite	29.4	22.5	27.8	24	9.88	22.5	0.49	25	94
AP-CMDB granules	34.9	20	34.4	21	10.9	22	0.51	25	88
AP-CMDB granules modified by colloidal graphite	28.2	24	27.3	24	9.78	22.5	0.48	25	95.5

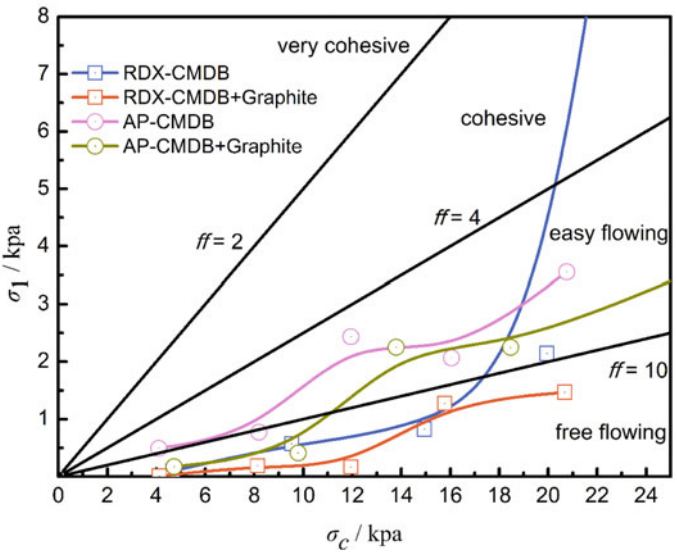

Fig. 29.9 The flow function curves of the RDX-CMDB, AP-CMDB granules and the granules coated by colloidal graphite and power flowability standard curves

by PFT tester were shown in Fig. 29.9.

It can be seen in Table 29.5 that the Carr index of RDX-CMDB granules was increase from 89 to 94 after modifying by graphite and AP-CMDB granules was increase from 88 to 95.5. The flowability of these two kinds of granules was all improved in some extent.

Flow index of particle materials is expressed as $ff = \sigma_1/\sigma_c$ = major principal consolidating stress/unconfined failure strength. The higher the flow index, the better the flowability of a particle material. Relationship between powder fluidity and flow index was shown in Table 29.6 and Fig. 29.9 [30].

It can be seen from Fig. 29.9 that the flow functions of the four kinds of granules were all below the $ff = 4$ curve when the unconfined failure strength was under about 20 kPa which demonstrate that the flowability of these granules was good. While the σ_1 of RDX-CMDB granule was sharp increased when σ_c was above 20 kPa, the flow functions of it were between $ff = 2$ and $ff = 4$ so the types of flow was

Table 29.6 Relationship between powder fluidity and flow index

Flowing index	Standard grade of flowing
$ff < 1$	None flowing
$1 \leq ff < 2$	Very cohesive
$2 \leq ff < 4$	Cohesive
$4 \leq ff < 10$	Easy flowing
$10 \leq ff$	Free flowing

cohesive. Whereas after coating modified by graphite, the flow function of RDX-CMDB granules was always under the $ff = 10$ curve which demonstrate that it was the type of free flowing. The flow function of AP-CMDB granule was always between the curve of $ff = 4$ and $ff = 10$ demonstrate that it was the type of easy flowing. While after coating modified by graphite, the flow function of it was below the $ff = 10$ curve when σ_c was less than about 11 kPa and it belonged to free flowing. While σ_c was more than about 11 kPa, the flow function was always between the curve of $ff = 4$ and $ff = 10$ demonstrate that it was the type of easy flowing. Besides, it can be seen directly from Fig. 29.9 that the flowability of RDX-CMDB and AP-CMDB granules were all improved and the former had more improvement. The results were consistent with the decrease of friction sensitivity of RDX-CMDB granules. The reason may be granules become relatively insensitive when the flowability was improved a lot.

Table 29.7 was the loading density and screen loading density of the four granules. It can be seen in Table 29.7 that the loading density of RDX-CMDB granules was increased from 1.013 to 1.095 g cm^{-3} which increased about 8.1%. And the loading density of AP-CMDB granules was increased from 1.052 to 1.107 g cm^{-3} which increased about 5.0%. Then the four granules were filled into the standard measuring cylinder through vibration sieve to test its screen loading density and the results were listed in Table 29.7. The results demonstrated that the screen loading density of RDX-CMDB granules was increased from 1.137 to 1.215 g cm^{-3} which increased about 6.9% and the screen loading density of AP-CMDB granules was increased from 1.181 to 1.227 g cm^{-3} which increased about 3.9%. To sum up, the loading density and screen loading density of the granules was increased after modifying by graphite and as a result, propellant density could also be increased as shown in Table 29.8.

Table 29.7 The loading density and screen loading density of the four solid propellant granules

Samples	Loading density/g cm^{-3}	Screen loading density/g cm^{-3}
RDX-CMDB granules	1.013	1.137
RDX-CMDB granules modified by colloidal graphite	1.095	1.215
AP-CMDB granules	1.052	1.181
AP-CMDB granules modified by colloidal graphite	1.107	1.227

Table 29.8 The theoretical density and measured density of the four solid propellants

Samples	Theoretical density /g cm^{-3}	Measured density /g cm^{-3}
RDX-CMDB propellant	1.830	1.701
Colloidal graphite coated RDX-CMDB propellant	1.830	1.738
AP-CMDB propellant	1.875	1.735
Colloidal graphite coated AP-CMDB propellant	1.875	1.761

29.3.4 The Theoretical Density and the Measured Density of the Propellants Manufactured by the Granules

According to the formulation in Table 29.1, the theoretical density of the four solid propellants was calculated via formula (29.1) [31].

$$1/\rho_p = W_1/\rho_1 + W_2/\rho_2 + \ldots + W_n/\rho_n \tag{29.1}$$

In formula (29.1), ρ_p is the theoretical density of the propellants, ρ_1 is the density of component 1, W_1 is the mass fraction of component 1, ρ_2 is the density of component 2 and W_2 is the mass fraction of component 2 and so on until ρ_n and W_n. The calculation results were shown in Table 29.8.

The four kinds of granules were manufactured into four propellants through granule casting process and the density was tested by GJB770B-2005 method. The results in Table 29.8 demonstrated that the density of RDX-CMDB propellant was increased from 1.701 to 1.738 g cm^{-3} which increased about 2.2% after coating modified by graphite and the measured density had reached 95% of its theoretical density. While the density of AP-CMDB propellant was increased from 1.735 to 1.761 g cm^{-3} which increased about 1.5% after coating modified by graphite and the measured density had reached 94% of its theoretical density.

29.4 Conclusion

(1) The microstructure of the colloidal graphite was irregular scaly which size was about 5 μm and thick was about 50 nm.
(2) After the granules were coated and modified by colloidal graphite, the impact sensitivity and friction sensitivity were improved in some extent, and the electrostatic spark sensitivity was improved greatly, the test results were all non-ignition.
(3) After the granules were coated and modified by colloidal graphite, the flowability was improved. The types of flow of RDX-CMDB granules was always free flowing. The types of flow of AP-CMDB granules changed from easy flowing to free flowing when the major principal consolidating stress was lower than about 11 kPa, on the contrary, while the major principal consolidating stress was higher than about 11 kPa, the types of flow was both easy flowing and the flowability curves were closed so the flowability was not improved significantly.
(4) After the granules were coated and modified by colloidal graphite, the loading density was increased as well as the screen loading density, hence the density of the propellants manufactured by the granules were in increased as well and more closely to their theoretical density respectively.

References

1. X.J. Li, F.Y. An, D.A. Wang, F.S. Li, Commentary on the characteristics of granule casting process. J. Winged Missiles **31**, 60–62 (2001)
2. X.J. Li, *Study on Granule Casting Process and Properties of Elastomeric Modified Cast Double Base Propellant D.* (Nanjing, Nanjing University of Science and Technology, 2007), pp. 5–7
3. A. Maraden, P. Stojan, R. Matyas, J. Zigmund, Ballistic testing and thermal behavior of cast double-base propellant containing BuNENA. J. Chin. J. Explos. Propellants **40**, 23–28 (2017)
4. D.Q. Zhang, Solid Rocket Propellant M (Beijing, Ordnance Industry Press, 1991), pp. 317–324
5. X.J. Li, Z. Ren, M. Liu, J.Q. Li, X.G. Wu, Effect of the temperature on the curing process of interstitial-casted XLDB propellant. J. Chin. J. Energ. Mater. **27**, 311–316 (2019)
6. J.H. Liu, *Physical and Chemical Properties of Gunpower* M. (Beijing University of Science and Technology Press, Beijing, 1997), pp. 9–10
7. W.Z. Ren, Z.S. Wang, *Theory and Practice of Explosives and Propellants M* (China North Chemical Industries Corporation, Beijing, 2001), pp. 561–566
8. C.Y. Dong, M.L. Guo, G.F. Li, Online detecting and elimination of electrostatic charge in propellant manufacturing process. J. Ordnance Equip. Eng. **38**, 27–30 (2017)
9. S. Cai, *Study on Preparation of Small Size Spheric Propellants and Special Industrial Explosives from Obsolete Explosives and Propellants D* (Nanjing University of Science and Technology, Nanjing, 2003), pp. 52–56
10. L.-R. Bao, H. Wang, T.-T. Zheng, S.-H. Chen, W. Zhang, X.-J. Zhang, Y.-S. Huang, R.-q Shen, Y.-H. Ye, Exploring the Influences of conductive graphite on hydroxylammonium nitrate (HAN)-based electrically controlled solid propellant. J. Propellants Explos. Pyrotech. **45**, 1790–1798 (2020)
11. R. Steinberger, P.D. Drechsel, Manufacture of cast double-base propellant. J. Propellants Manuf. Hazards Test. Adv. Chem. 1–28 (1969)
12. X.J. Li, F.S. Li, F.Y. An, Improvement of pressure exponent of smokeless EMCDB propellant by Granule-casting process. J. Nanjing Univ. Sci. Technol. **26**, 201–204 (2002)
13. American Society for Testing and Materials, ASTM D 6128–2016 standard test method for shear testing of bulk solids using the Jenike shear cell. Am. Stan. (2016)
14. Commission of Science Technology and Industry for National Defense, *GJB 772A-1997 Explosive Test Method* (National Military Standard of PRC, 1997)
15. Commission of Science Technology and Industry for National Defense, *GJB 5891.27–2006 Test Method of Loading for Initiating Explosive Device—part 27: Electrostatic Spark Sensitivity Test* (National Military Standard of PRC, 2007)
16. Commission of Science Technology and Industry for National Defense, *GJB 770B-2005 Test Method of Propellant* (National Military Standard of PRC, 2005)
17. B.L. Lv, Y. Cui, X.P. Gao, M. Wu, F. Liu, H. Su, W.L. Zhou, G.Q. Chen, Progress of tribological properties, lubrication mechanism and modification research on graphite. J. Mater. Rev. **29**, 60–66 (2015)
18. Q. Wang, J. Liu, H. Ren, Q.J. Jiao, Effect of reduced graphene oxide on the impact sensitivity and electrostatic sensitivity of B/KNO_3 ignition powder. J. Chin. J. Energetic Mater. **26**, 875–880 (2018)
19. X.Y. Chuan, Microstructure design of graphite in nanoscale. J. Inorg. Mater. **32**, 1121–1127 (2017)
20. X.X. Ren, S.X. Zhao, Advances on friction sensitivity of high energy explosives. J. Winged Missiles **48**, 91–97 (2018)
21. Q.H. Zhou, W.Z. Ren, *Physical and Chemical Properties of Gunpower* (National Defense Industry Press, Beijing, 1982), pp. 215–216
22. M.N. Qin, Y. Zhang, W. Tang, Q. Shi, W. Wang, S.J. Qiu, α-AlH_3 coated with stearic acid: preparation and its electrostatic sensitivity. J. Chin. J. Energ. Mater. **25**, 59–62 (2017)
23. W.W. Chang, C.L. Yan, L. Li, Application of Carr index method in comprehensive evaluating properties of wooden bulk materials. J. Wood Process. Mach. **26**, 42–45 (2015)

24. Y.B. Jin, S.M. Wang, Y. Lu, G. Yin, Y. Wang, T.J. Wang, Preparation and quality evaluation of mannitol-crospovidone co-processed excipient. J. Chin. J. Pharm. Anal. **37**, 724–731 (2017)
25. J. Wang, Y.F. Zhao, X.L. Qiao, X.G. Li, H. Zhao, Measurement and simulation of the angle of repose of solid filler in composite solid propellant. J. Chem. Ind. Eng. Prog. **39**, 312–318 (2020)
26. W.G. Shan, X.G. Liu, H.J. Yu, X.L. Chen, L.F. Lei, Effect of procedure parameters on the properties of cast RDX-CMDB propellant. J. Chin. J. Energ. Mater. **5**, 55–58 (1997)
27. X.Y. Zheng, L.K. Zhang, S.B. Fu, Measurement of friction coefficient between gun propellant particles and its influence on loading density. J. Ballistics **31**, 85–91 (2019)
28. J. Ashish, G. Swaroop, K. Balasubramanian, M. *Nanomaterials in rocket propulsion systems* effect of ammonium perchlorate particle size on flow, ballistic, and mechanical properties of composite propellant. chapter 8 (2019), pp. 299–362
29. L. Cui, S. Sasabe, K. Shimizu, T. Yokoyama, Development and application for measuring method of powder flowability and floodability. J. Chin. Power Sci. Technol. **18**, 72–77 (2012)
30. X.J. Ding, L.L. Liu, S.A.B. Michael, New instrument PFT for powder flow researching. J. Acad. Periodical Farm. Prod. Process. **24**, 146–150 (2012)
31. H.Q. Ding, L.Q. Xiao, X.X. Jian, Research of blends of gap-based polyurethane elastomer and NC. J. Solid Rocket Technol. **35**, 495–503 (2012)

Chapter 30
Preparation of Short Rod Shape CuO_X/GO Nanocomposites and Their Catalysis on AP

Shengnan Li, Ziteng Niu, Yuke Jiao, Shanjun Ding, Desheng Yang, Chaofei Bai, Jiaran Liu, Yunjun Luo, and Guoping Li

Abstract Nano-copper oxide (CuO) is a commonly used ammonium perchlorate (AP) catalyst, but the nano-CuO particle have obvious reunion phenomenon, which hinders the effective contact area of CuO and AP, and makes the catalytic effects is not ideal. To improve the catalytic effect of nano-CuO, CuO/GO nanocomposites were prepared under different conditions with graphene oxide (GO) as the carrier. Transmission electron mirror (TEM), scanning electron mirror (SEM), X-ray diffraction (XRD) were used to characterize the structure and TG-DSC was used to study the effect on the thermal decomposition performance of AP. The best result show that nanocomposite reduced the peak temperature of AP to 329.6 °C by 77.7 °C, while the release heat increased from 826.2 J/g of pure AP to 2019.2 J/g by 1193 J/g.

30.1 Introduction

Ammonium perchlorate (AP) is widely used in rocket propellants and is the main component of solid propellants. The thermal decomposition characteristics of AP are closely related to the combustion performance of the solid propellan. The high exothermic temperature of AP leads to unconcentrated heat release, the addition of excellent catalyst is the main method to improve the combustion efficiency of solid propellant. Therefore, it is significant to develop AP catalysts. Cu, copper oxide and its derivatives are widely used in the catalytic work of AP. Vanessa Molina et al.

S. Li (✉) · Z. Niu · Y. Jiao · D. Yang · C. Bai · J. Liu · Y. Luo · G. Li
School of Materials Science and Engineering, Beijing Institute of Technology, Beijing 100081, China
e-mail: lishengnan@iccas.ac.cn

S. Ding
State Key Laboratory of Explosion Science and Technology, Beijing Institute of Technology, Beijing 100081, China

Y. Luo · G. Li
Key Laboratory for Ministry of Education of High Energy Density Materials, Beijing Institute of Technology, Beijing 100081, China

A. Gany and X. Fu (eds.), *2021 International Conference on Development and Application of Carbon Nanomaterials in Energetic Materials*, Springer Proceedings in Physics 276,
https://doi.org/10.1007/978-981-19-1774-5_30

compound [trans-Cu(-OH)(-dmpz)]$_6$ and AP, reduced the decomposition temperature to 372.5 °C, increased the heat release by 576J/g. Graphene is a new 2D material wih high specific surface area. CuO and other nano particle can be evenly distributed on the matrix of GO, hindering the reunion of particle, increasing the contact area of CuO with AP, and exerting better catalytic performance. Wang Xuebao al studied the thermal decomposition of graphene-catalyzed AP. A thermal decomposition temperature of AP was 66.9 °C earlier after mixing graphene with AP compared with pure AP.

In this study, CuO/GO nanocomposites were prepared with graphene oxide (GO), and ethylene glycol as the solvent. Characterized by transmission electron mirror (TEM), scanning electron mirror (SEM) and X-ray diffraction (XRD), and studied the influence on the thermal decomposition properties of AP and the catalytic mechanism of nanocomposites on AP and the nanoparticle formation process.

30.2 Experimental Section

30.2.1 Materials

Graphene oxide (>95%, 5–10 μm) was purchased from Suzhou Hengqi Graphene Technology Co. Ltd. Deionized water was prepared in laboratory. Copper nitrate trihydrate, urea, ethylene glycol were obtained from Beijing Chemical Plant. AP was ourchased from Dalian North Potassium Chlorate Co. LTD.

30.2.2 Synthesis of Nanocomposites

Add 0.1125gGO to 15 ml ethylene glycol, sonicated to uniform dispersion; dissolve 6 mmol of copper nitrate trihydrate in 20 ml ethylene glycol, add 10 ml of GO dispersion to the solution and stirred until evenly mixed; 16 mmol of urea dissolved in 10 ml ethylene glycol is slowly added to the solution and stirred for 30 min; the mixture is transferred to a stainless steel autoclave and reacted at 180 °C for 4 h. The precipitates were washed three times with deionized water and ethanol (centrifuged for 10 min at 7000 r), and finally, the powder was frozen at −80 °C for 5 hours to obtain the primary product of the nanocomposite. The products were calcined in 500 °C of air and argon environment for 2 h, respectively. Take a certain amount of dried AP in the mortar, add the dried CuO/GO nanocomposite (the mass ratio of CuO/GO nanocomposite to AP is 5:95), and continue to mix it evenly, namely the CuO/AP/GO nanocomposite particles.

30.3 Results and Discussion

The XRD profile of the nanocomposites, with ethylene glycol as the solvent, is shown in the Fig. 30.1. For the nanocomposites before calcination, at 2θ = 36.7°, 42.6°, 61.9°, 74.0° the peaks correspond to (1 1 1), (2 0 0), (2 2 0), (3 1 1) crystal faces of Cu_2O, corresponding with standard card PDF#74–1230; at 2θ = 43.5°, 50.6°, 74.3°, 89.9° the peaks correspond to (1 1 1), (2 0 0), (2 2 0), (3 1 1) crystal faces of Cu, corresponding with standard card PDF#85–1326, means that the nanomaterials prepared is a mixture of Cu_2O and Cu. For nanocomposites calcined in an air environment, at 2θ = 32.6°, 38.7°, 38.9°, 46.3°, 48.8°, 51.4°, 53.6°, 58.5°, 61.6°, 66.0°, 66.3°, 68.0°, 72.5°, 75.2°, 82.4° the peaks correspond to (1 1 0), (1 1 1), (2 0 0), (1 1 -2), (2 0 -2), (1 1 2), (0 2 0), (2 0 2), (1 1 -3), (3 1 -1), (3 1 0), (1 1 3), (3 1 1), (2 2 -2), (3 1 -3) crystal faces of CuO, corresponding with standard card PDF#48–1548, without other impurities appears, indicating that the prepared products are relatively pure nanoscale CuO. For nanocomposites calcined in Ar, at 2θ = 43.5°, 50.6°, 74.3°, 89.9° the peaks correspond to (1 1 1), (2 0 0), (2 2 0), (3 1 1) crystal faces of Cu, corresponding with standard card PDF#85–1326, without other impurities appears, indicating that the prepared products are relatively pure nanoscale Cu.

Micromorphology analysis of composite nanomaterials, before calcination (a), after calcination in air (b), after calcination in argon gas (c), as shown in the Fig. 30.2. Before calcination (a), after calcination in air (b), and after calcination (c) in argon, short rod shape nanocomposites were obtained. After calcination, the dispersion of nanoparticles increases significantly. When calcination in air, the N elements contained in the product are oxidized and escape in the form of nitrogen oxide, so the product is granular on the GO surface. When calcination in argon, CuO is reduced by C to Cu and generates gas, making the nanoparticles on an uneven surface. At the same time, many folds can be observed on the GO sheet, which is because the GO surface contains large oxygen-containing functional groups, such as carboxyl and hydroxyl

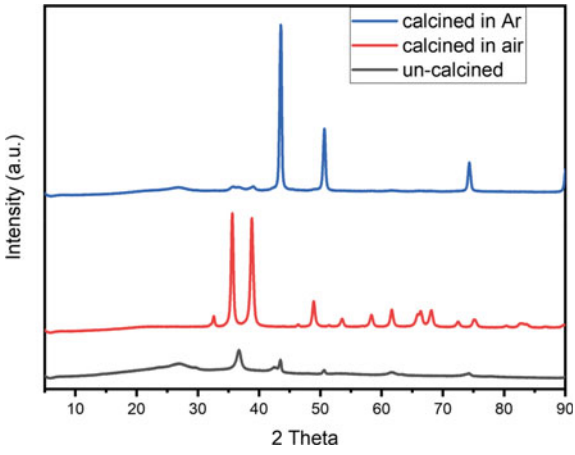

Fig. 30.1 The XRD diffraction image of the nanocomposites

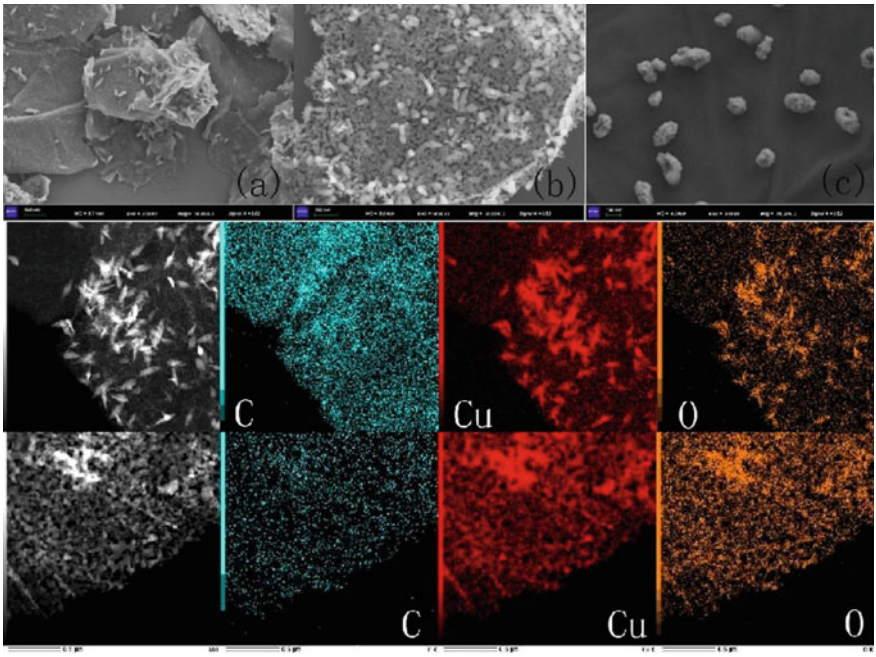

Fig. 30.2 The SEM and EDS images of the nanocomposites

groups. The presence of these folds provides more attachment sites for the nanoparticles and effectively avoids the reunion of the nanoparticles, making the CuO/GO and Cu/GO nanocomposites show better dispersion. EDS maps are of nanocomposites before calcination and in air, respectively. It can be seen that the surface elements of nanocomposites before and after calcination are mainly composed of C, Cu and O, indicating that nanoparoparticles are indeed successfully loaded on GO. But there is still reunification between CuO nanoparticles, forming leaf-like crystals. Although no obvious GO layer was observed in the TEM map of CuO/GO nanocomposite after calcination in air, C elements in the EDS map showed that the morphology of GO changed during calcination at high temperature, evenly dispersed in small particles in the sample, which increased the steric hindrace during crystal growth and reduced the particle size of nano-CuO particles (Fig. 30.2).

The DSC curve of AP shows that AP has a distinct heat absorption peak at 244.3 °C, due to the conversion of AP from oblique to cubic crystal lines for heat absorption. There is a small exothermal peak at 303.8 °C, corresponding to the first weightlessness phase present in the TG curve as well as the first downward peak in the DTG curve, in which AP has a partial decomposition as the low temperature decomposition phase of AP. A second obvious antipyretic peak appears at 408.0 °C, corresponding to the second weightlessness phase appearing in the TG curve and the second downward peak in the DTG curve, at which the AP is completely decomposed and is the main decomposition process of the AP thermal decomposition.

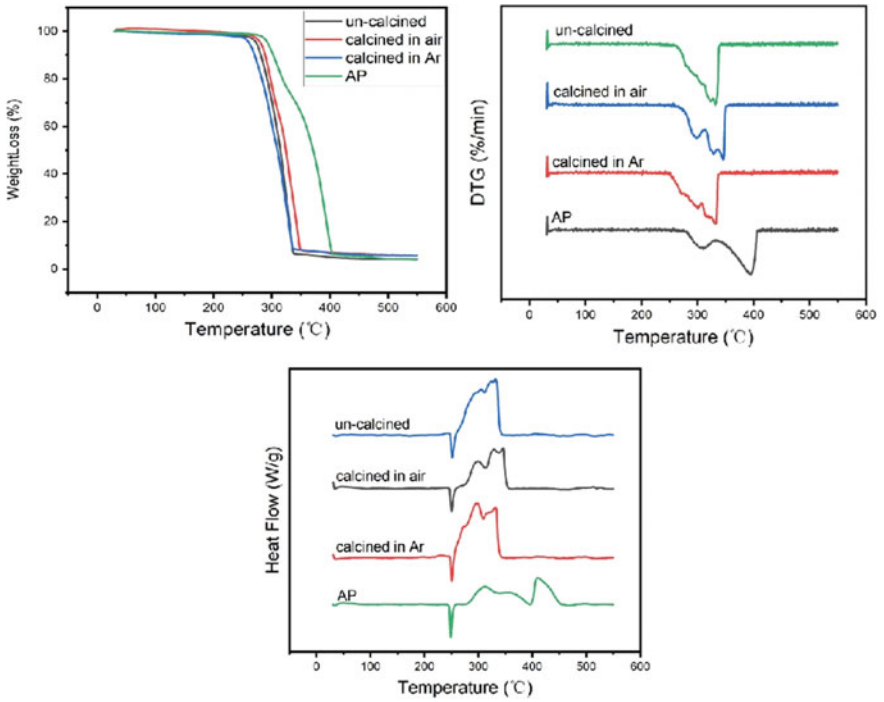

Fig. 30.3 The TG curves, DTG curves, and DSC curves of the nanocomposites and AP

A large amount of NH_3 and $HClO_4$ adsorbed on the surface of AP separate, and the de-attached $HClO_4$ decompose, producing O_2, O_2^-, ClO_4, ClO, H_2O and other substances. These decomposition products undergo drastic redox reactions with NH_3 and release a large amount of heat while generating N_2O, NO_2, and NO, which is the high-temperature decomposition stage of AP (Table 30.1).

As can be seen from the above figure, all three nanocomposites show downward heat absorption peaks around 245 °C, indicating that they have basically no effect on the crystal-type conversion process of AP. AP will undergo low temperature decomposition and high temperature decomposition reactions around 304 °C and

Table 30.1 DSC parameters of AP in the presence of different nanocomposites

Sample	Low temperature decomposition peak (°C)	High temperature decomposition peak (°C)	Total heat discharge (J/g)
AP	303.8	407.3	826.2
CuO/GO+AP(un-calcined)	298.2	340.5	1840.4
CuO/GO+AP(Air)	292.4	343.2	1224.3
Cu/GO+AP(Ar)	293.7	329.6	2019.2

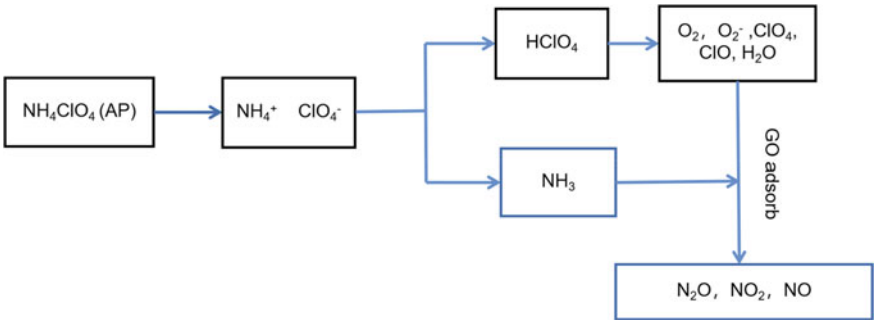

Fig. 30.4 Schematic diagram of the catalytic AP thermal decomposition in nanocomposites

408 °C, but the nanocomposite and AP compound will only have one decomposition peak, and the decomposition peak moves toward the low temperature direction, which shows that these three nanocomposites have a positive catalytic effect on the decomposition of AP, making the low temperature decomposition reaction and the high temperature decomposition reaction proceed simultaneously. Among them, the Cu/GO nanocomposite made after calcination with ethylene glycol as a solvent in the argon environment reduced the thermal decomposition peak of AP from 407.3 °C to 329.6 °C, by 77.7 °C, total heat release from 826.2 J/g to 2019.2 J/g by 1193 J/g, and the maximum increase in total heat release (Fig. 30.3).

The rate of AP decomposition depends on the rate of electron transfer and O_2 conversion to O_2^-. The transition metal oxide CuO belongs to a P-type semiconductor whose 3d orbital electrons are unfilled with positively charged holes in the valence band. When AP decomposes, large amounts of electrons and anions can be accepted by CuO, increasing the thermal decomposition rate of AP (Fig. 30.4). In summary, the elemental composition, micromorphology and specific surface area of the material were characterized using XRD, TEM and SEM, and the catalytic effect of nanocomposites on the thermal decomposition process of AP was investigated using TG/DSC. The results show that, the Cu/GO nanocomposites are able to promote the thermal decomposition process of AP, reducing the high-temperature decomposition peak of AP from 407.3 °C to 329.6 °C, decreasing by 77.7 °C, and increasing the total heat release from 826.2 J/g to 2019.2 J/g by 1193 J/g.

30.4 Conclusion

In summary, The elemental composition, micromorphology and specific surface area of the material were characterized using XRD, TEM and SEM, and the catalytic effect of nanocomposites on the thermal decomposition process of AP was investigated using TG/DSC. The results show that, the Cu/GO nanocomposites are able to promote the thermal decomposition process of AP, reducing the high-temperature

decomposition peak of AP from 407.3 °C to 329.6 °C, decreasing by 77.7 °C, and increasing the total heat release from 826.2 J/g to 2019.2 J/g by 1193 J/g.

References

1. L. Liu, F. Li, L. Tan et al., Effects of nanometer Ni, Cu, Al and NiCu powders on the thermal decomposition of ammonium perchlorate. Propellants Explos. Pyrotech. **29**(1), 34–38 (2004)
2. V.V. Boldyrev, Thermal decomposition of ammonium perchlorate. Thermochim. Acta **443**(1), 1–36 (2006)
3. C. Ping, F. Li, Z. Jian et al., Preparation of Cu/CNT composite particles and catalytic performance on thermal decomposition of ammonium perchlorate. Propellants Explos. Pyrotech. **31**(6), 452–455 (2006)
4. Y. Wang, X. Xia, J. Zhu et al., Catalytic activity of nanometer-sized CuO/Fe_2O on thermal decompositon of AP and combustion of AP-based propellant. Combust. Sci. Technol. **183**(2), 154–162 (2010)
5. X. Xu, H. Yang, Y. Liu, Self-assembled structures of CuO primary crystals synthesized from $Cu(CH_3COO)_2$–NaOH aqueous systems. CrystEngComm **14**(16) 5289 (2012)
6. J. Lee, S. Zhang, S. Sun, High-temperature solution-phase syntheses of metal-oxide nanocrystals. Chem. Mater. **25**(8), 1293–1304 (2013)
7. Q. Zhang, K. Zhang, D. Xu et al., CuO nanostructures: synthesis, characterization, growth mechanisms, fundamental properties, and applications. Prog. Mater Sci. **60**, 208–337 (2014)
8. N. Gagnon, W.B. Tolman, $CuO]^{(+)}$ and $[CuOH]^{(2+)}$ complexes: intermediates in oxidation catalysis. Acc. Chem. Res. **48**(7), 2126–2131 (2015)
9. S.G. Hosseini, R. Abazari, A facile one-step route for production of CuO, NiO, and CuO–NiO nanoparticles and comparison of their catalytic activity for ammonium perchlorate decomposition. RSC Adv. **5**(117), 96777–96784 (2015)
10. X.-L. Luo, M.-J. Wang, D.-S. Yang et al., Hydrothermal synthesis of morphology controllable Cu_2O and their catalysis in thermal decomposition of ammonium perchlorate. J. Ind. Eng. Chem. **32**, 313–318 (2015)
11. M.A. Fertassi, K.T. Alali, Q. Liu et al., Catalytic effect of CuO nanoplates, a graphene (G)/CuO nanocomposite and an Al/G/CuO composite on the thermal decomposition of ammonium perchlorate. RSC Adv. **6**(78), 74155–74161 (2016)
12. Y. Zhang, C. Meng, Facile fabrication of Fe_3O_4 and Co_3O_4 microspheres and their influence on the thermal decomposition of ammonium perchlorate. J. Alloy. Compd. **674**, 259–265 (2016)
13. B. Xue, Z. Qian, C. Liu et al., Synthesis of CuO nanoparticles via one-pot wet-chemical method and its catalytic performance on the thermal decomposition of ammonium perchlorate. Russ. J. Appl. Chem. **90**(1), 138–143 (2017)
14. Y. Ramdani, Q. Liu, G. Huiquan et al., Synthesis and thermal behavior of Cu_2O flower-like, Cu_2O-C_{60} and Al/Cu_2O-C_{60} as catalysts on the thermal decomposition of ammonium perchlorate. Vacuum **153**, 277–290 (2018)
15. Y. Hu, S. Yang, B. Tao et al., Catalytic decomposition of ammonium perchlorate on hollow mesoporous CuO microspheres. Vacuum **159,** 105–111 (2019)
16. G. Li, W. Bai, S. Ge et al., Facile preparation of Co_3O_4 microspheres and their utilization in the pyrolysis of ammonium perchlorate. Funct. Mater. Lett. **12**(02), 1950001 (2019)
17. Y. Xie, B. Liu, Y. Li et al., Cu/Cu_2O/rGO nanocomposites: solid-state self-reduction synthesis and catalytic activity for p-nitrophenol reduction. New J. Chem. **43**(30), 12118–12125 (2019)
18. P. Chandrababu, J. Thankarajan, V. Sukumaran Nair et al., Decomposition of ammonium perchlorate: exploring catalytic activity of nanocomposites based on nano Cu/Cu_2O dispersed on graphitic carbon nitride. Thermochim. Acta **691**, 178720 (2020)
19. S. Elbasuney, M. Gobara, M.G. Zaky et al., Synthesis of CuO-distributed carbon nanofiber: alternative hybrid for solid propellants. J. Mater. Sci.Mater. Electron. **31**(11), 8212–8219 (2020)

20. J. Wang, X. Lian, Q. Yan et al., Unusual Cu-Co/GO composite with special high organic content synthesized by an in situ self-assembly approach: pyrolysis and catalytic decomposition on energetic materials. ACS Appl. Mater. Interfaces **12**(25), 28496–28509 (2020)
21. Y. Zhang, K. Li, J. Liao et al., Microwave-assisted synthesis of graphitic carbon nitride/CuO nanocomposites and the enhancement of catalytic activities in the thermal decomposition of ammonium perchlorate. Appl. Surf. Sci. **499**, 143875 (2020)
22. Q. Zhou, B. Jin, J. Chen et al., Facile fabrication of Cu-doped carbon aerogels as catalysts for the thermal decomposition of ammonium perchlorate. Appl. Organomet. Chem. **34**(8) (2020)
23. H. Kechit, S. Belkhiri, A.K. Bhakta et al., The effect of iron decorated MWCNTs and iron-ionic liquid decorated MWCNTs onto thermal decomposition of ammonium perchlorate. Z. Anorg. Allg. Chem. **647**(16–17), 1607–1619 (2021)
24. V. Molina, J.L. Arroyo, D. MacLeod-Carey et al., Catalytic effect of [trans-Cu(μ-OH)(μ-dmpz)]$_6$ on the thermal decomposition of ammonium perchlorate. Polyhedron **209**, 115464 (2021)
25. J. Yan, H. Wang, B. Jin et al., Cu-MOF derived Cu/Cu_2O/C nanocomposites for the efficient thermal decomposition of ammonium perchlorate. J. Solid State Chem. **297**, 122060 (2021)
26. T. Zhang, H. Shi, Y. Zhang et al., Hollow flower-like nickel particles as the promoter of ammonium perchlorate-based solid propellant. Appl. Surf. Sci. **552**, 149506 (2021)
27. Y. Zhang, A. Song, D. Ma et al., The catalytic decomposition and kinetic analysis of ammonium perchlorate on MgO nanoflakes. J. Phys. Chem. Solids **157**, 110205 (2021)
28. S. Chen et al., Enhancing the Combustion performance of metastable Al@AP/PVDF nanocomposites by doping with graphene oxide. Engineering **6**(9), 1019–1027 (2020)
29. W. Wang et al., In-situ preparation of $MgFe_2O_4$-GO nanocomposite and its enhanced catalytic reactivity on decomposition of AP and RDX. Ceram. Int. **44**(15), 19016–19020 (2018)
30. J. Cheng et al., Functionalization graphene oxide with energetic groups as a new family of metal-free and energetic burning rate catalysts and desensitizers for ammonium perchlorate. J. Thermal Anal. Calorim. **140**(prepublish), 1–12 (2019)
31. S. Chen et al., Gaseous products evolution analyses for catalytic decomposition of AP by graphene-based additives. Nanomaterials **9**(5), 801–801 (2019)

Chapter 31
Effect of Impact Fracture of RDX-Based High-Energy Gun Propellant on the Combustion Properties

Jing Zhou, Ding Wei, and Da Li

Abstract To study the influence of impact fracture on the combustion properties of gun propellants, a series of impact tests were carried out on RDX-based high-energy gun propellants by a dropping hammer impact device. Also the combustion performance of impact damaged gun propellant samples were studied by closed bomb test on the samples before and after impact. The results indicate that the pressure index and the burning rate coefficient of each sample change regularly with the increase of crushing degree. The pressure indexes decrease from 1.044 of pristine samples to 0.865 and 0.400, respectively. The burning rate coefficients increase from 0.099 cm s^{-1} MPa^{-n} to 0.228 ^{cm} s^{-1} MPa^{-n} and 3.319 ^{cm} s^{-1} MPa^{-n}, respectively. In addition, the RDX-based high-energy gun propellants gradually change from obvious progressive surface combustion to complete degressive surface combustion. The study also reveals that the initial phase of combustion for fractured gun propellants has been boosted up, while the latter phase of combustion has been weakened reversely. With increasing the fracture degree of samples, the possibility of a sharp increase in the initial pressure and burning rate increases, which is detrimental to the stable combustion of gun propellants.

31.1 Introduction

In the development process of weapon systems with high-pressure and high-loading density charge, many countries have experienced breech blow accidents, which has aroused widespread concern. Military powerful nations like the USA and Germany have carried out a lot of researches on launch safeties, mechanical properties and

J. Zhou (✉) · D. Wei · D. Li
Xi'an Modern Chemistry Research Institute, Xi'an 710065, China
e-mail: zj3172@163.com

D. Wei
e-mail: w_ding2010@163.com

D. Li
e-mail: lida20042008@163.com

A. Gany and X. Fu (eds.), *2021 International Conference on Development and Application of Carbon Nanomaterials in Energetic Materials*, Springer Proceedings in Physics 276,
https://doi.org/10.1007/978-981-19-1774-5_31

breakage laws of gun propellants. Currently, It is generally accepted that the mechanism of breech blow caused by gun propellant charge is "impact, squeeze-crush-increase surface area-increase burning rate-increase the pressure in the chamber" [1–5]. Recently, domestic researchers have also begun to study the influence of impact fracture on the combustion properties of gun propellants. For example, Zhang and co-workers [6] used a 100 mm gas gun to study the extrusion and impact crushing of propellants over heated, measured the combustion performance of the crushed propellants, and finally obtained the increase of maximum burning vivacity and maximum burning rate coefficient of different propellants at different impact velocities. Xu et al. [7] applied the propellant bed squeeze crushing physical simulation device and closed bomb to study the combustion laws of broken propellants.

In this paper, low temperature (−40 °C) impact tests of RDX-based high-energy gun propellants [8, 9] at different impact heights were carried out by a droping hammer impact device. The influence of impact fragmentation on combustion performance of high-energy gun propellants were investigated through the closed bomb combustion tests on the gun propellants before and after impact. This study simulated the dynamic force of gun propellants in the chamber to further research their combustion performance. Above research achievements will provide guidance for the application of new generation gun propellant in high bore pressure weapons, avoiding the occurrence of bore explosion accidents [10].

31.2 Experiment

31.2.1 Experimental Sample

The gun propellant used in the experiment is a 19-hole RDX-based high-energy gun propellant. The main components of the formula are 40% NC, 30% plasticizer and 25% RDX. The high energy gun propellant has high energy characteristics, and its gunpowder power is about 1225 J/g.

31.2.2 Dropping Hammer Impact Test

Three groups of samples were prepared before the experiment. Each group consisted of 7 gun propellant grains with a weight of about 20 g. Among them, one group was used as reference sample, while the other two as test samples. The end faces of the test samples were worn down to smooth with good perpendicularity. Then the test samples were put into the impact tooling and kept at −40 °C for more than 2 h.

The impact test was carried out at the height of 17.5 cm and 55 cm with a 5 kg drop hammer. Each sample was impacted once. The samples impacted at the same height were collected as the test samples of the closed bomb.

31.2.3 Closed Bomb Experiment

The reference sample and the impacted samples were tested in closed bomb according to the GJB770A-97703 method. The chamber volume was 100 cm^3, the filling density was 0.2 $^g/cm^3$, and the ignition pressure was 10 MPa.

31.3 Results and Discussion

31.3.1 The Impact Damage and Fragmentation Degree of the Samples

The impact damage of the reference sample and the impacted samples by the drop hammer is shown in Fig. 31.1. As seen in Fig. 31.1b, the sample impacted at 17.5 cm (designated as impacted samples 1#) shows signs of whitening, indicating that there are internal microcracks. There are obvious cracks in some gun propellant grains, and one of the grains has broken angle. Figure 31.1c shows the sample impacted at 55 cm (designated as impacted samples 2#). It is seen that the damage of the sample is more serious than impacted samples 1#. The original shape of the gun propellant grain in impacted samples 2# can hardly be seen, and a lot of fragments are produced. This result demonstrates that the higher the impact height is, the more serious damage of the gun propellant is. The typical *P–t* curves are shown in Fig. 31.2. They are processed to obtain the *L-B* curves, as shown in Fig. 31.3.

The fragmentation degree [11] (PSD) of gun propellant is calculated by the change of relative initial burning surface before and after impact. It is used to characterize the impact damage of gun propellant. The formula for calculation is as follows:

（a）Reference sample （b）Impacted sample 1# （c）Impacted sample 2#

Fig. 31.1 Photographs for drop hammer impact fracture of the high-energy gun propellants

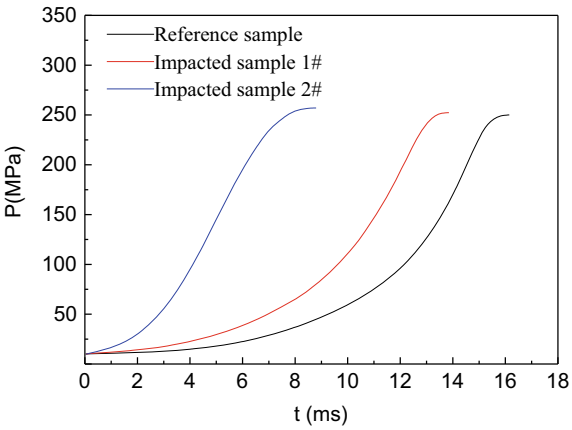

Fig. 31.2 *P–t* curves of the impacted and reference samples

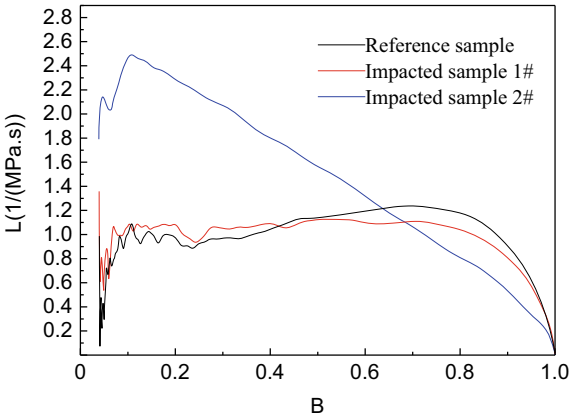

Fig. 31.3 *L-B* curves of the impacted and reference samples

$$\mathrm{PSD} = \frac{S_0}{S_0^0} \approx \frac{\omega \cdot L_0}{\omega^0 \cdot L_0^0} \approx \frac{L_0}{L_0^0} \tag{31.1}$$

In the above equation: ω and ω_0 are the charge weight of the gun propellant samples and the reference sample in the closed bomb experiment, where $\omega \approx \omega_0$; S_0 and L_0 are the initial combustion area and initial dynamic activity of the impacted sample in the closed bomb experiment, respectively; S_0^0 and L_0^0 are the initial combustion area and initial dynamic activity of the reference sample in the closed bomb experiment, respectively.

The fragmentation degrees (PSD) of gun propellants with different impact heights are obtained according to Eq. (31.1), as shown in Table 31.1.

Table 31.1 The PSD for different experimental gun propellant samples

Sample	Impacted height/cm	PSD			
		The first group	The second group	The third group	The average value
Reference sample	0	1	1	1	1
Impacted sample 1#	17.5	1.12	1.26	1.20	1.19
Impacted sample 2#	55	2.83	3.04	2.89	2.92

31.3.2 Effect of Fragmentation Degree on the Combustion Properties

The burning rate pressure index n reflects the sensitivity of gun propellant burning rate to pressure change. The burning rate of gun propellant follows the exponential burning rate law, $u = u_1 P^n$. The burning rate pressure index of gun propellant can be obtained by evaluating the logarithm of u ~ P datas collected from the combustion of gun propellants with different fragmentation degrees, that is, the slope of *lnu* ~ *lnP* curve. The *lnu* ~ *lnP* curves of burning rates for different gun propellant samples are shown in Fig. 31.4. Obviously, the pressure index of the reference samples is slightly higher than that of the impacted samples 1#, while the pressure index of the impacted samples 2# is significantly lower than the other two sample groups.

Table 31.2 shows the results of burning rate pressure index in the conventional test of closed bomb. The starting point in the table is lagging behind the neighbour point of $\Psi = 0.15$, which is about 50 MPa. The pressure corresponding to the maximum value of *dP/dt* is taken as the end pressure of combustion, which is recorded as P_{dpm}. During the combustion of propellant, the burning rate is controlled by two factors:

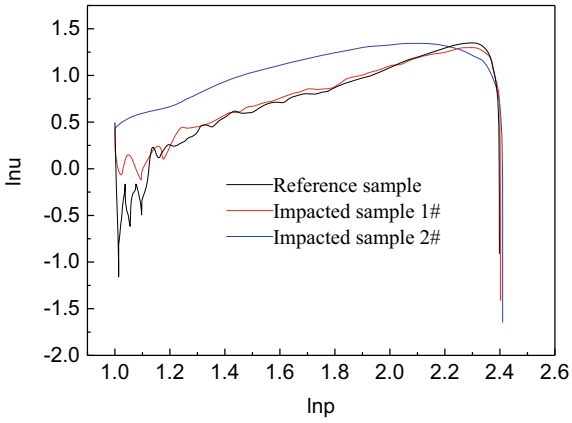

Figure 31.4. *lnu-lnP* curves of impacted and reference samples

Table 31.2 Experimental results of gun propellants by closed bomb tests

Sample	*PSD*	Characteristic quantity	*P*/MPa				P_{dpm}/MPa	P_m/MPa
			50~100	100~150	150~*P*dpm	50~*P*dpm		
Reference samples	1	Burning rate coefficient	0.108	0.121	0.542	0.099	189.44	250.05
		Pressure index	1.020	1.006	0.710	1.044		
Impacted amples 1#	1.19	Burning rate coefficient	0.173	0.264	0.494	0.228	188.21	252.32
		Pressure index	0.928	0.838	0.708	0.865		
Impacted samples 2#	2.32	Burning rate coefficient	1.910	5.093	/	3.319	134.80	253.05
		Pressure index	0.532	0.306	/	0.400		

Notes P_{dpm} is the pressure corresponding to the maximum value of *dP/dt*; The unit of the combustion rate coefficient is cm s^{-1} MPa^{-n}; P_m is the maximum pressure of combustion; The fitting degrees of pressure index of different pressure sections are greater than 0.99

chemical factor and pressure. The synergistic effect of the two factors may make the burning rate fast or slow in different pressure ranges. Consequently, different pressure sections are selected to investigate the changes of burning rate pressure index and burning rate coefficient when the test results are analyzed. In this research, three pressure sections of 50~100 MPa, 100~150 MPa and 150~*P*dpm MPa are selected for analysis [12, 13]. It can be seen from Table 31.2 that the *PSD* has significant effect on both the pressure index and the burning rate coefficient of the sample. In the range of 50~P_{dpm}MPa, with the increase of pressure, the burning rate coefficient of each sample increases, while the pressure index decreases; With the increase of fragmentation degree, both of the burning rate coefficient and pressure index change regularly. The pressure index decreased from 1.044 of pristine samples to 0.865 and 0.400, respectively. The combustion rate coefficient increased from 0.099 to 0.228 cm s^{-1} MPa^{-n} and 3.319 $^{cm}\cdot s^{-1}\cdot MPa^{-n}$, respectively. Moreover, the pressure at the end of combustion also decreases gradually, and the maximum pressure has no significant change.

The change rule of burning rate vary with pressure is the main characteristic quantity to characterize the combustion performance of gun propellants. Figure 31.5 shows the *u-p* curves of different samples. The analysis of burning rate and pressure relation shows that the initial burning rate of gun propellant increases with the increase of fragmentation degree. In the low pressure region (before about 100 MPa), the higher the impact height is, the more seriously the sample is broken and the higher the burning rate is. The burning rate of the impacted sample 1# is slightly higher than that of the reference sample, but the burning rate of the impacted sample 2# is vastly increased. This is because the structure of the reference sample is relatively compact

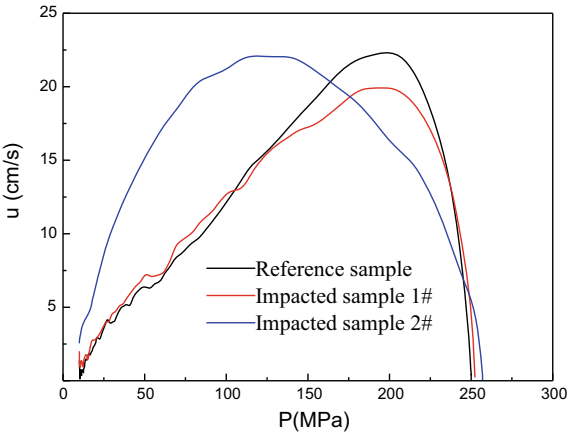

Fig. 31.5 *u-P* curves of the impacted and the reference samples

at the initial stage of combustion, which restricts the flame propagation after ignition. Then the burning area is small, so the burning rate is slow. However, due to the serious fragmentation, the structure of the impacted sample 2# is dispersive. As a result, the flame spreads very fast after ignition, the initial burning surface is large, and the burning rate is very fast.

The combustion property of the impacted sample 1# is between that of the reference sample and the impacted sample 2#. Reversely, after the pressure of about 170 MPa, the situation is opposite to that in the low-pressure section. As the fragmentation degree of the gun propellant increases, its burning rate will decrease. This is due to the burning surface of the seriously fractured sample 2# decreases during the progress of combustion, while the reference samples are intact 19 hole gun propellants, which remains progressive burning before the splitting of the gun propellant type. Therefore, the burning rate of the reference samples is higher than that of the impacted sample in the later stage of the combustion.

Figure 31.6 shows the Γ-Ψ curves of the experimental samples, where Γ is the gas generation intensity and Ψ is the percentage of gunpowder burned.

It can be seen from the figure that the initial combustion intensity of the reference sample and the impacted sample 1# is low. The value for the impacted sample 1# is slightly higher than that of the reference sample. While the combustion intensity of the starting section of the impacted sample 2# has a sudden increase. In addition, the Γ-Ψ curves show that the linear function characteristics of the reference sample curve are better than those of the impacted sample 1# and 2#. The result indicates the reference sample has obvious progressive combustion performance [14], while the impacted sample 1#

shows approximately a neutral burning and the impacted sample 2# is completely degressive burning.

The gas released in the initial stage of combustion increases as the degressive combustion performance increases, which causes the pressure in the chamber to rise rapidly. This is extremely detrimental to the safety of the launch.

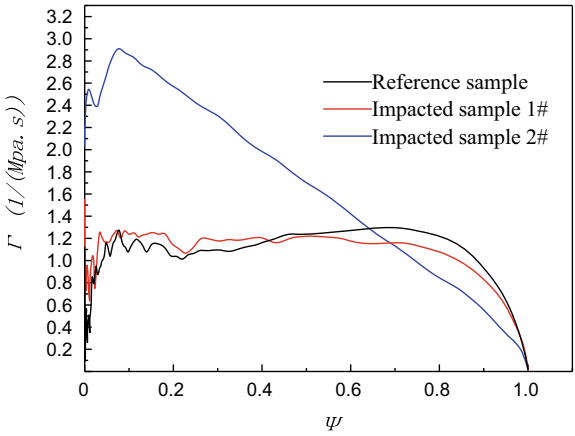

Fig. 31.6 Γ-Ψ curves of the impacted and the reference samples

Based on the above results, it is concluded that the combustion performance of the sample changes greatly after being impacted by dropping hammer at different heights. This is mainly related to the fragmentation degree of the gun propellant. With the increase of fragmentation degree, the initial combustion area of gun propellant increases, the combustion rate increases, while the final combustion rate decreases. At the same time, as the particle fragmentation will cause the geometry damage of the gun propellant, which could make the combustion characteristics of the gun propellant change from its progressive combustion to degressive combustion. However, the progressive combustion has always been the basic goal of the gun propellant in its application. Overall, the fragmentation of the gun propellant makes the initial combustion rate of gun propellant increase, the gas generation rate increase, and the possibility of a sharp increase in bore pressure increase. These can easily lead to abnormal chamber pressure and is detrimental to the safety of launching. Therefore, it is very important to improve the anti impact damage performance of the gun propellant and prevent the gun propellant from breaking in the gun bore.

31.4 Conclusion

The effect of impact damage on the combustion performance of the RDX-based high-energy gun propellant was studied by dropping hammer impact and closed bomb experiments. The results show that:

(1) As the fragmentation degree of gun propellant increases, the burning rate coefficient and pressure index change regularly. The pressure indexes decrease from 1.044 to 0.865 and 0.400, respectively. The burning rate coefficients increase from 0.099 to 0.228 cm s^{-1} MPa^{-n} and 3.319 $^{cm}\cdot s^{-1}\cdot MPa^{-n}$, respectively.

(2) With the increase of fragmentation degree, the RDX-based high-energy gun propellants gradually change from obvious progressive surface combustion to complete degressive surface combustion.
(3) After impact, the initial combustion of RDX-based high-energy gun propellants has been boosted up, while the final combustion rate decreases. In addition, the possibility of a sharp increase in the initial pressure and burning rate increases with the increase of the fragmentation degree, which is detrimental to the stable combustion of gun propellants.

References

1. W.Y. Xu,W.D. He, Z.S. Wang, Mechanical properties of JMZ gun propellants. Chin. J. Energ. Mater. **15**(3), 235–239 (2007). 1006-9941(2007)03-0235-05
2. Q. Huang, D.Q. Guo, G.R. Bian et al., Mechanical properties of single base propellant under strong dynamic load. Chin. J. Energ. Mater. **15**(5), 534–536 (2007). 1006-9941(2007)05-0534-03
3. X.T. Rui, L.F. Yun, N.S. Sha et al., Advance on launch safety for gun propellant charge. Acta Armamentarii **26**(5), 690–696 (2005). 1000-1093(2005)05-0690-07
4. B.B. Feng, X.T. Rui, H. Xu et al., Dynamic compression fracture condition of one nitroamine propellant charge during launch course. Chin. J. Explos. Propellants **35**(2), 70–73 (2012). https://doi.org/10.14077/j.issn.1007-7812.2012.02.015
5. X.T. Rui, B.B. Feng, G.P. Wang, Evaluation method of launch safety of propellant charge. Ordnance Ind. Autom. **30**(5), 56–59 (2011). https://doi.org/10.3969/j.issn.1006-1576.2011.05.017
6. M.A. Zhang, Y.H. Zhou, Q.L. Liu, Determination of buring law of fragmented grains of gun propellant. J. Ballistics (3), 63–70 (1990)
7. J.X. Xu, Effect of extrusion and fracture of gun propellant charge on combustion behavior. Chin. J. Explos. Propellants **30**(3), 69–71 (2007). https://doi.org/10.14077/j.issn.1007-7812.2007.03.019
8. J.X. Yang, W.T. Yang, F.S. Ma.et al., Effect of RDX particle size on the mechanical and combustion properties of nitramine gun propellant. Chin. J. Energ. Mater. **25**(9), 706–711 (2017). https://doi.org/10.11943/j.issn.1006-9941.2017.09.001
9. X.R. Shi, Y.J. Jia, R. Hu et al. Study on the structure feature and high pressure combustion performance of fragmented high energy gun propellants preppared by impact at low temperature. Chin. J. Explos. Propellants **40**(1):101–106 (2017). https://doi.org/10.14077/j.issn.1007-7812.2017.01.020
10. X.R. Shi, G.H. Yan, Y.J. Jia et al., Influence of RDX and NGU on the dynamic combustion stability of azidonitramine gun propellants. Explos. Mater. **49**(5), 14–19 (2020). https://doi.org/10.3969/j.issn.1001-8352.2020.05.003
11. J. Zhou, X. Yang, X.M. Chen et al., Anti-impact fracture property of RDX-based high-energy gun propellants. Chin. J. Explos. Propellants **36**(6), 86-90 (2013). https://doi.org/10.14077/j.issn.1007-7812.2013.06.017
12. G.T. Liu, S.W. Liu, H.F. Yu et al., Combustion performance of propellant containing FOX-7. Chin. J. Explos. Propellants **35**(2), 82–85 (2012). https://doi.org/10.14077/j.issn.1007-7812.2012.02.018
13. Z.Y. Huang, Z.S. Wang, W.D. He et al., Combustion property of high energy and high strength propellant. Chin. J. Explos. Propellants **28**(4), 61–63 (2005). https://doi.org/10.14077/j.issn.1007-7812.2005.04.017

14. Z.L. Ma, P. Xia, Z.D. He et al., Combustion properties of a glued consolidation gun propellant. Chin. J. Explos. Propellants **29**(5), 60–62 (2006). https://doi.org/10.14077/j.issn.1007-7812.2006.05.017

Chapter 32
Effect of Nano-LLM-105 on the Performance of Modified Double Base Propellant

Chao Zhang, Liang Ma, Cun-quan Wang, Yi-wen Hu, Jun-bo Chen, and Li-bo Yang

Abstract The effect of the particle size of LLM-105 on the combustion performance, mechanical sensitivity, mechanical properties and shock wave sensitivity of the Modified Double Base Propellant, The results showed that the LLM-105 in the formulation increased, the burning rate of the propellant under different pressures decreased significantly. When the mass fraction of LLM-105 in the formula is increased from 0 to 25%, the burning rate at 10 MPa decreases by 53.3%; The burning rate reduction effect of coarse-grained LLM-105 is better than that of fine-grained; Substituting micron LLM-105 for the nanometer, the propellant burning rate is reduced by 1.5 mm/s at 10 MPa. Nano-level LLM-105 increases the characteristic drop height H_{50} of the propellant from 21.3 to 36.4 mm, the friction sensitivity is reduced from 17 to 6%, the tensile strength of the propellant at 20 °C increased by 61%, the tensile strength of the propellant at − 40 °C increased by 33%, the tensile strength of the propellant at 50 °C increased by 37%, the shock wave sensitivity of the propellant is reduced by 35.8%.

32.1 Introduction

Modified double-base propellant (CMDB) has the characteristics of high energy and low characteristic signal, which can simultaneously improve the stealth effect and penetration capability of missiles, and is widely used in engines of various weapon systems [1–3]. Traditional CMDB propellants containing high-sensitivity

C. Zhang (✉) · L. Ma · C. Wang · Y. Hu · J. Chen · L. Yang
Xi'an Modern Chemistry Research Institute, Xi'an 710065, China
e-mail: 522746056@qq.com

Y. Hu
e-mail: huyiwenn123@163.com

J. Chen
e-mail: cjb85_@126.com

L. Yang
e-mail: yanglibo204@sohu.com

A. Gany and X. Fu (eds.), *2021 International Conference on Development and Application of Carbon Nanomaterials in Energetic Materials*, Springer Proceedings in Physics 276,
https://doi.org/10.1007/978-981-19-1774-5_32

RDX/HMX and other nitramine explosives are prone to combustion and explosion accidents under accidental collision or impact. Therefore, current airborne and ship-borne high-value weapon platforms urgently need hight-security new CMDB propellant. 2,6-diamino-3,5-dinitro pyrazine-1-oxide (2,6-diamino-3,5-dinitro pyrazine-1-oxide, ANPZO for short, code name LLM-105) is the lawrence of the United States a new elemental explosive with excellent energy and safety performance synthesized by Livermore National Laboratory. Its energy is 20% higher than TATB and 81% of HMX. It is due to the existence of π conjugate system in the molecule and the strong intra-molecular hydrogen bonding makes LLM-105 insensitive to heat, shock waves, sparks and frictional impact [4–7]. In recent years, a large numbers have done a lot of research on the performance and application of LLM-105 [6, 8–28]. After the size of the material particles is refined, because the particles are in the microscopic and macroscopic transition regions, the particles exhibit special physical and chemical properties under the action of surface effects, quantum size effects and other characteristics [29]. In addition to retaining the excellent properties of ordinary particles such as high melting point and excellent thermal stability, the fine particle LLM-105 also has the characteristics of more complete explosion energy release, faster detonation wave propagation, and more stability. The fine particle LLM-105 is added to the propulsion the formulation of the propellant will definitely affect the performance of the propellant.

In this experiment, the influence of the particle size of LLM-105 on the combustion performance and safety performance of CMDB propellant was studied, in order to provide a reference for the extensive and in-depth research, popularization and application of the new insensitive explosive.

32.2 Experiment

32.2.1 Materials

LLM-105, purity, 99%, coarse particle weight average average particle size d_{50} is 10.0 μm (Type 1), as shown in Fig. 32.1, fine particle weight average particle diameter d_{50} is 200 nm (Type 2), as shown in Fig. 32.2; 3# Nitrocellulose (NC, 12.0%N); Nitroglycerin (NG); 2 intermediate setting agent (C_2); catalysts, petrolatum (V, medical), auxiliary plasticizers and other functional additives are all industrial products.

32.2.2 Preparation of Test Samples

The formula of the smokeless CMDB propellant containing LLM-105 is shown in Table 32.1, and the catalyst adopts the internal addition method.

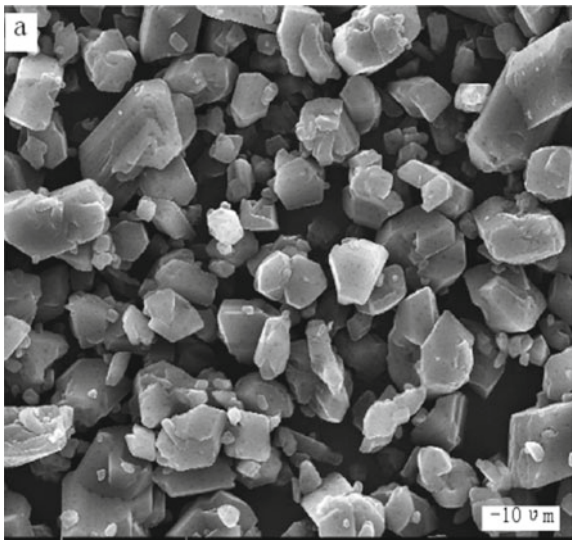

Fig. 32.1 SEM photo of Type 1

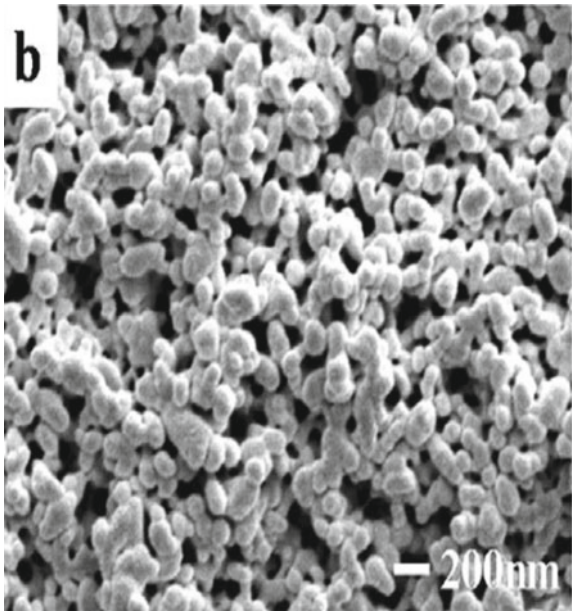

Fig. 32.2 SEM photo of Type 2

The test samples were prepared by the processes of absorption, flooding, ripening, calendering and plasticizing, and compression and stretching.

Table 32.1 Formulation of propellant

Number	NC+NG	V	C_2	LLM-105	Auxiliary plasticizers	Other
L1	78	1.0	1.5	0	6	3.5
L2	78	1.0	1.5	5(d_{50}: 200 nm)	6	3.5
L3	78	1.0	1.5	10(d_{50}: 200 nm)	6	3.5
L4	68	1.0	1.5	20(d_{50}: 200 nm)	6	3.5
L5	63	1.0	1.5	25(d_{50}: 200 nm)	6	3.5
L6	63	1.0	1.5	25(d_{50}: 10.0um)	6	3.5

32.2.3 Burning Rate Test

The burning rate pressure index n is calculated according to the Vieille relation $r = aP^n$ using the least square method, where r is the burning rate, P is the pressure, and a is a constant.

32.2.4 Friction Sensitivity Measurement

The friction sensitivity is tested by the test method specified in GJB772A-1997 Method 602.1, the temperature is 15~35 °C, the sample amount is (0.020 ± 0.001) g, the gauge pressure is (2.45 ± 0.05) MPa, swing angle 66° ± 0.5°. The friction sensitivity is expressed as the explosion percentage P.

32.2.5 Determination of Impact Sensitivity

The impact sensitivity is tested using the test method specified in GJB772A-1997 Method 601.1, the temperature is 15~35 °C, the sample amount is (0.03 ± 0.001) g, and the hammer weight is (2000 ± 2) g. The impact sensitivity is represented by the characteristic drop value H_{50} of 50% explosion rate.

32.2.6 Static Mechanical Tensile Test

Static mechanical tensile test: carried out in the INSTRON 4505 material testing machine, the test temperature is−40 °C, and the tensile speed is 100 mm/min. The test method refers to method 413.1 in GJB770B-2005.

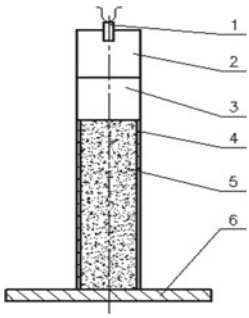

Fig. 32.3 Gap test set up

1-detonator; 2-maispring detonator, 3-the gap, 4-tube of sample, 5-sample, 6-witness plate

32.2.7 Shock Wave Sensitivity Test

In this study, the shock wave sensitivity test adopts the diaphragm test method. The partition thickness adopts the median approach method, that is, the intermediate value of the explosion and non-explosive partition thickness is taken, and the process is repeated until the difference between the explosion and the non-explosive partition is 1 mm, and the intermediate value at this time is taken as the shock wave sensitivity of the tested sample. If there is a round hole in the witness plate with the size of the sample tube in a test, the result is judged as "explosion", otherwise it is judged as "not exploding".

The schematic diagram of the separator test device is shown in Fig. 32.3. The donor drug column, separator, and sample tube are coaxial. The sample tube adopts precision drawn tube 45-φ48 mm × φ36 mm, length 140.0 mm, donor grain is cast Pentry explosive (TNT:PETN = 1:1), specification: φ50 mm × 50 mm; density is 1.58 g/mm^3, Use the 8th industrial electric detonator to detonate, the partition is made of polymethacrylic acid (plexi glass), the specification: φ50.0 mm × 0.19 mm, the verification plate is the No. 45 steel plate of 150.0 mm × 150.0 mm × 10.0 mm.

32.3 Results and Discussion

32.3.1 The Influence of LLM-105 Content and Particle Size on Propellant Combustion Performance

Figure 32.4 shows the effect of different LLM-105 content and particle size on the combustion performance of the propellant.

It can be seen from Fig. 32.4 that as the content of LLM-105 increases, the burning rate of the propellant at different pressures is significantly reduced. When the mass

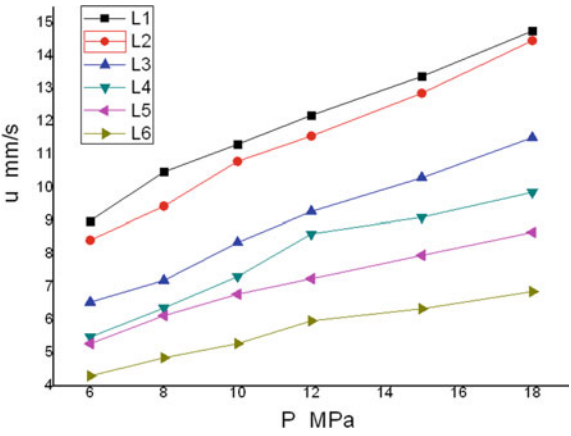

Fig. 32.4 Test results of combustion performance of propellant with different LLM-105 content and particle size

fraction of LLM-105 increases from 0 to 25%, the burning rate at 10 MPa decreases from 11.33 to 5.29 mm/s, while the pressure index increased with the increase of LLM-105 content. When the LLM-105 fraction increased from 0 to 20%, the pressure index under 6 MPa~18 MPa increased from 0.43 to 0.55.

LLM-105 can greatly reduce the burning rate of modified double-base propellant. Analysis believes that one of the reasons is that the oxygen balance coefficients of LLM-105 and NG are different. The oxygen balance coefficients of the two are − 0.37 and 0.44, respectively. After replacing NC\NG with LLM-105, its low oxygen balance inhibits the thermal decomposition of the propellant, and the composition of NO_2 in the dark area of the propellant is reduced and converted to NO When the heat is low, the propellant combustion surface temperature ts decreases, resulting in a decrease in the burning rate of the propellant.

In addition, literature [8] believes that LLM-105 is accompanied by endothermic sublimation behavior while thermally decomposing, which affects the heating of the condensed phase. In the condensed phase, LLM-105 cannot contribute heat to the rapid decomposition of the propellant. LLM-105 is in the gas phase. The heat of decomposition in the medium has a limited effect on the combustion surface temperature Ts through thermal feedback, resulting in a decrease in the burning rate of the smokeless modified double-base propellant containing LLM-105.

Comparing the experimental results of L5 and L6, it can be seen that the speed reduction effect of coarse particles of LLM-105 on the smokeless modified double-base propellant is better than that of fine particles. The burning rate of the smokeless modified double-base propellant containing coarse particles of LLM-105 in different pressure ranges is lower than that of the fine particles, and is reduced by 1.5 mm/s at 10 MPa.

The coarse particles of LLM-105 reduce the burning rate of the propellant. The analysis suggests that this may be due to the thermal conductivity of the coarse particles of LLM-105 and the difference in thermal conductivity of the finer particles [30]. The decomposition reaction rate is reduced. At the same time, due to the small

specific surface area of the coarse particles of LLM-105, the reaction rate constant and the ratio sox/so of the area of the oxidant on the combustion surface to the area of the propellant combustion surface during the thermal decomposition process are reduced, thereby making the propulsion the burning rate of the agent decreases. It can be seen that the burning rate of the modified double-base propellant can be adjusted by adjusting the particle size of LLM-105.

32.3.2 The Influence of LLM-105 Particle Size on the Mechanical Sensitivity of Propellant

The mechanical sensitivity test results of the modified double-base propellant containing the same amount of coarse and fine particle size LLM-105 are shown in Figs. 32.5 and 32.6.

Comparing the experimental results of the formulations L5 and L6 in Figs. 32.5 and 32.6, it can be seen that the fine particle LLM-105 has a better effect on the propellant sensation reduction. The characteristic drop height H_{50} is increased from 21.3 to 36.4 cm, the friction sensitivity changes even more, and the explosion probability is reduced from 17 to 6%. It can be seen that the particle size of the high energy

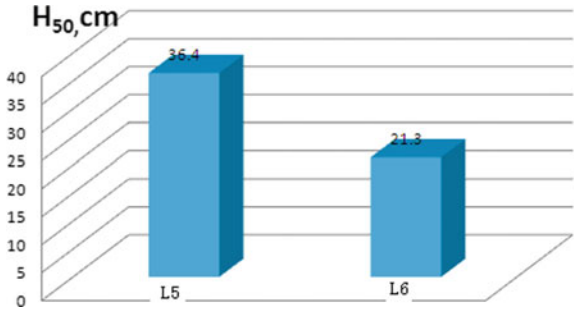

Fig. 32.5 Impact sensitivity

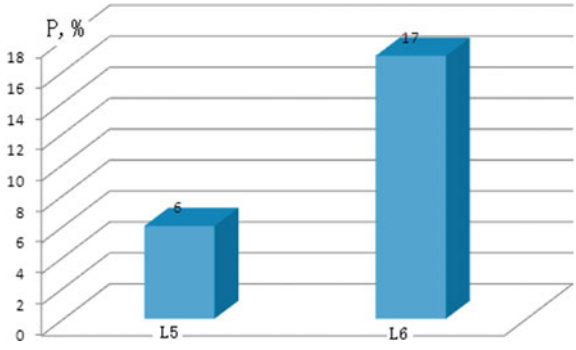

Fig. 32.6 Friction sensitivity

density material is also the main factor affecting the sensitivity of the propellant, and the sensitivity of fine particles is better than that of large particles.

The mechanical sensitivity of LLM-105 propellants containing fine particles has been reduced. This is due to the higher surface energy and better thermal conductivity and dispersibility of LLM-105 fine particles [31], and it is not easy to form hot spots. In addition, analysis believes that it may be due to the lack of edges and corners of the fine particles of LLM-105, the smaller the aspect ratio and the denser accumulation in the propellant, reducing the inter-particle void ratio, improving the normal rheology of the material, and reducing the amount of material in the sample. Air impurities reduce the probability of hot spots generated by air impurities in the process of impacting adiabatic compression, thereby playing a better role in reducing inductance.

32.3.3 The Effect of LLM-105 Particle Size on the Mechanical Properties of Propellants

The tensile strength of the modified double-base propellant containing the same amount of coarse and fine-grained LLM-105 at 20, 50 °C and −40 °C was measured. The test results are shown in Table 32.2.

From the data in Table 32.2, it can be seen that the particle size of LLM-105 is reduced, the mechanical properties are improved, the tensile strength at 20 °C is increased by 61.0%, the low temperature tensile strength is increased by 33%, and the high temperature tensile strength is increased by 37%. This is because the larger the particle size of LLM-105, the smaller the specific surface area. When the two interfaces are in contact, too large a particle size will reduce the contact surface area, which will reduce the bonding force and bond strength accordingly. Small; As the particle size of LLM-105 decreases, the specific surface area is larger, and the contact surface with the adhesive increases, so the contact is better, and the mechanical properties of pushing you are better.

Table 32.2 Influence on the mechanical properties of CMDB propellant containing LLM-105

Temperature/°C	σ_m/MPa		ε_m/%	
	L5	L6	L5	L6
50	1.92	1.37	33.1	37.2
20	9.84	6.15	13.8	20.3
−40	39.7	30.1	3.6	4.91

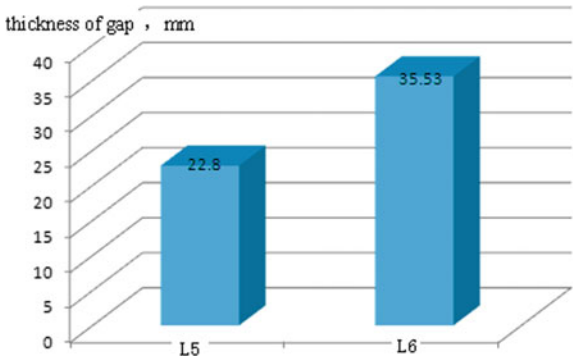

Fig. 32.7 Shock wave sensitivity

32.3.4 The Impact of LLM-105 Particle Size on Shock Wave Sensitivity

The shock wave sensitivity test results of the modified double-base propellant containing the same amount of coarse and fine-grained LLM-105 are shown in Fig. 32.7.

Comparing the thickness of the L-5 and L-6 separators in Fig. 32.7, it can be seen that the particle size of LLM-105 has a significant effect on the shock wave sensitivity. When the particle size of LLM-105 is reduced to nanometer level, the shock wave sensitivity of LLM-105 propellant containing the same amount of nanometer level is 35.8% lower than that of ordinary LLM-105 propellant.

The initiation of explosives is currently generally accepted as the "hot spot" initiation mechanism. For propellant shock wave sensitivity, the hot spot formation mechanism is cavity collapse. The accumulation of solid particles in the propellant matrix must have a large number of pores. When subjected to strong shock wave pressure from the outside, the pores in the propellant undergo strong compression and undergo plastic deformation and then collapse. The gas undergoes adiabatic compression, causing the local temperature in the propellant to rise sharply to form a hot spot. In general, as the size of solid particles and holes in the propellant matrix increase, the probability of hot-spot will also increases, leading to the high sensitivity of propellant. When the particle size of LLM-105 is as small as nanometers, the surface of LLM-105 particles becomes regular, the surface energy increases, the contact surface between the particles increases, and the thermal conductivity of the particles increases, which is not conducive to the accumulation of heat inside the propellant and the growth of hot spots. At the same time, nano-LLM-105 can also improve the compactness of the propellant, making the pores inside the propellant smaller and smaller. When subjected to shock waves, the propellant is not prone to plastic deformation, that is, it is not prone to adiabatic compression. Therefore, the sensitivity of shock wave of propellant contains nano-LLM-105 is greatly reduced.

32.4 Conclusion

(1) The particle size of LLM-105 is also the main factor affecting the burning rate of CMDB propellant. When the particle size of LLM-105 reaches the nanometer level, the burning rate of CMDB propellant under 10 MPa can be increased by 1.5 mm/s.
(2) The nano-level LLM-105 has a better effect on the propellant inductance reduction, the characteristic drop height H50 is increased from 21.3 to 36.4 cm, and the explosion probability of friction sensitivity is reduced from 17 to 6%.
(3) The particle size of LLM-105 is reduced, the mechanical properties are improved, the tensile strength at 20 °C is increased by 61.0%, the low temperature tensile strength is increased by 33%, and the high temperature tensile strength is increased by 37%.
(4) The shock wave sensitivity of LLM-105 propellant containing the same amount of nanometer grade is 35.8% lower than that of ordinary LLM-105 propellant.

References

1. C. Zhang, J.-G. Yang, J.-B. Chen et al., Study on shock wave sensitivity of modified double-base propellants containing CL-20. Chin. J. Explos. Propellants 43(5), 549–552 (2020)
2. S.-E. Liu, X.-M. Zhao, M.-L. Zhao et al., Safety performance of modified nitramine double base propellant by screw extrusion subject to mechanical stimulus. Chin. J. Energ. Mater. **18**(6), 818–820 (2013)
3. X.-H. Zhang, H.-J. Mo, Study progress on new propellants based on novel ingredients for future tactical missile. Chin. J. Exploos. Propellants **30**(1), 24–27 (2007)
4. T.D. Tran, P.F. Pagoria, D.M. Hoffman, R.L. Simpson et al., Characterization of 2,6-Diamino-3,5-Dinitropyrazine-1-Oxide (LLM-105) as an insensitive high explosive material, in *33rd International Annual Conference of ICT[C]* (Karlsruhe, Germany, 2002), June 25–28
5. A.K. Sikder, N. Sikder, A review of advanced high performance, insensitive and thermally stable energetic materials emerging for military and space applications. J. Hazard. Mater. **112**(1/2), 1–15 (2004)
6. G.U.O. Feng-bo, L.I.U. Yu-cun, L.I.U. Deng-cheng et al., Theoretical calculation of the detonation parameters of 2,6-diamino-3,5-dinitropyrazine-1-oxide. Initiators Pyrotech. **2**, 33–36 (2006)
7. U. Tarver, Tran et al., Sensitivity of LLM-105. Energ. Mater. **23**(2), 183–203 (2005)
8. F.-Y. Li, W.-P. Liu, Methods of preparation and prospect in application of Nano-powder. Chin. Powder Sci. Technol. **5**, 29–32 (2000)
9. P.F. Pagoria, G.S. Lee, A.R. Mitchell et al., Synthesis, scale-up and characterization of LLM-105. US Patent. UCRL-JC-142918 (2001)
10. T.D. Tran, P.F. Pagoria, D.M. Hoffman, J.L. Cutting, R.S. Lee, R.L. Simpson, *Characterization of 2,6-Diamino-3,5-Dinitropyrazine-1-Oxide (LLM-105) as an Insensitive High Explosive Material,33rd Int. Annual Conference of ICT [C]* (Karlsruhe, Germany, 2002), June 25–28
11. U. Tarver, Tran et al., Sensitivity of LLM-105. Energe. Mater. **23**(2), 183–203 (2005)
12. T.D. Tran, P.F. Pagoria et al., Small scale safety and performance characterization of new plastic bonded ex plosive containing LLM -105, in *12th International Detonation Symposium[C]* (San Diego, 2002)

13. X.U. Wen-xin, L.I. Bi-hong, L.I. Wan-quan et al., Application of LLM-105 based heat resistance explosive. Initiators Pyrotech. **2**, 40–43 (2012)
14. F.Q. Zhao, R.Z. Hu, H.X. Gao et al., Thermochemical proper-ties, non-isothermal decomposition reaction kinetics and quantum chemical investigation of 2,6-diamino-3,5-dinitro-pyrazine-1-oxide (LLM-105) (Chapter 4), in *New Developments in Hazardous Materials Research* ed by O.E. Bromna (Nova Science Publishers, New York, 2006)
15. Schmidt R.UCRL-WEB-145044
16. P.F. Pagoria, Synthesis of high explosive. UCID-20622–97 (1997)
17. J.L. Cutting, H.H. Cau, R.L. Hodgin et al., A small-scale screening test for HE performance: application to the new explosive LLM-105. UCRL-JC-131623,2000
18. R.K. Weese, A.K. Burnham, Exploring the physical, and thermal characteristics of a new potentially insensitive high explosive RX-55-AE-5. J. Therm. Anal. Calorim. **89**(2), 465–473 (2007)
19. R.K. Weese, A.K. Burnham, H.C. Turner et al., Exploring the physical and thermal characteristics of a new potentially insensitive high explosive RX-55-AE-5, in *North American Thermal Analysis Society 34th Annual Conference* (United States, 2006)
20. J.L. Cutting, A small-scale screening test for HE performance: application to the new explosive LLM-105, UCRL-JC-131623 (LLNL, Livermore 1998)
21. T. Tran, R. Simpson, P. Pogoria et a1., *Updates on LLM-105 Development as an Insensitive High Explosive Booster Material UCRL-PRES-145524* (LLNL, Livermore, 2001)
22. Y.-G. Liu, Z. Huang, X.-J. Yu, Progress of research of new insensitive energetic material LLM-105. Explosion Shock Waves **24**(5), 465–469 (2004)
23. P.F. Pagoria, *Synthesis Scale-up and Characterization of 2,6-diamino-3,5-dinitro pyrazine-1-oxide* (UCRL-JC-135018, 1998)
24. Y.-C. Liu, D.-C. Liu, Z.-W. Yang, Characterization of a heat-resistant explosive ANPZO. Chin. J. Energ. Mater. **20**(6), 721–725 (2012)
25. Z.-Y. Wang, J. Li, J. Yuan, Advance in energetic compounds derived from pyrazine. Chem. Intermed. **7**, 9–12 (2012)
26. P.F. Pagoria, Synthesis of LLM-105. Propellants Explos. Pyrotech. **20**(1), 38–42 (1995)
27. F. Pagoria, Synthesis, scale-up and characterization of 2,6-diamino-3,5-dinitropyrazine-1-oxide. Propellants, Explos. Protechnies **23**(3), 156–160 (1998)
28. M.-Z. Deng, J.-W. Zhou, B.-Z. Wanget al., Preparation improvement of LLM-105 explosive. Chin. J. Energe. Mater. **21**(3):294–296
29. Y.-B. Wang, M.-Z. Deng, P. Lian et al., Study on the synthesis and quantum chemistry of heat resistant explosive LLM-105. Chin. J. Explos. Propellants **36**(1), 38–41, 77 (2013)
30. F.-Q. Zhao, H.-X. Gao, S.-Y. Xu, Energy parameters and combustion characteristics of insensitive and minimum smoke propellants containing LLM-105. J. Sol. Rocket Technol. **34**(4), 497–500 (2011)
31. Y.-B. Wang, Z.-X. Ge, B.-Z. Wang, Preparation and thermal properties of fine LLM-105 with different crystal form. Chin. J. Energe. Mater. **19**(5), 523–526 (2011)
32. Z.-Y. Wang, Development on some new insensitive individual explosives abroad. Chin. J. Energe. Mater. **11**(4), 227–230 (2003)

Chapter 33
Study of Three-Dimensional Porous Graphene Oxide Aerogel for Catalyzing the Thermal Decomposition of Ammonium Perchlorate

Dongqi Liu, Hongbing Lei, Qiang Li, Haibo Ke, Fuyao Chen, Yubing Hu, Guangpu Zhang, Lei Xiao, Gazi Hao, and Wei Jiang

Abstract In this work, a three-dimensional porous graphene oxide aerogel (GA) was prepared using a hydrothermal method and vacuum freeze-drying process. The prepared GA and raw material graphene oxide (GO) were characterized by powder X-ray diffraction (XRD), scanning electron microscopy (SEM), and Fourier transform infrared spectroscopy (FT-IR). The results show that GA is fluffy and porous and can be adsorbed on the surface of ammonium perchlorate(AP) after being mixed with AP. The formation process of GA in the entire process is discussed in detail. In addition, the catalytic performance of porous GA on AP was studied. Thermogravimetry (TG)/differential scanning calorimetry (DSC) research results show that after GA and AP are mixed, the high-temperature exothermic peak is advanced from 441 to 345 °C , and the heat released $\triangle H$ is increased from 205 to 720 J/g. Three-dimensional porous GA is hoped to be a promising catalyst for AP thermal decomposition.

33.1 Introduction

Ammonium perchlorate (AP) is widely used in composite propellants as the most important oxidizer since its thermal decomposition of AP is directly related to the combustion characteristics of the composite propellants [1–5]. Therefore, reducing the pyrolysis temperature of AP and increasing the heat release of AP can effectively shorten the ignition delay time and increase the combustion rate of the propellants [6–10]. Incomplete pyrolysis of AP not only wastes AP material [11, 12], but also

The authors declare no competing financial interest.

D. Liu · H. Ke · F. Chen · Y. Hu · G. Zhang · L. Xiao · G. Hao (✉) · W. Jiang
School of Chemistry and Chemical Engineering, Nanjing University of Science and Technology, Nanjing 210094, Jiangsu, China
e-mail: hgznjust1989@163.com

H. Lei · Q. Li
Shanxi North Xing'an Chemical Industry Co., Ltd, Taiyuan 030008, China

A. Gany and X. Fu (eds.), *2021 International Conference on Development and Application of Carbon Nanomaterials in Energetic Materials*, Springer Proceedings in Physics 276,
https://doi.org/10.1007/978-981-19-1774-5_33

significantly reduces the combustion rate of the propellants [13], which has an impact on practical applications [14]. Therefore, it is very important to study the thermal decomposition of AP [15–18].

At present, there are numerous studies on AP catalysts, including metal elements, metal oxides [19, 20], composite metal oxides [21, 22], organic catalysts [23] and carbon-based materials [24, 25], etc. Among these catalysts, carbon-based materials are a kind of potential catalysts and carriers that are widely used in the field of catalyzing AP due to their good electrical conductivity and excellent surface adsorption performance [26–28]. Common carbon-based materials include graphite, carbon nanotubes, graphene oxide (GO), graphene and fullerene.

Graphite can be obtained from nature at a very low cost. Graphite is a conductive layer material and an interesting catalyst. Its conductivity is frequently used to prepare electrodes for photovoltaic cells [29]. At the same time, it has many conjugated sites and adsorption properties, allowing it to be used as a carrier in the field of chemical catalysis [30]. At present, in the field of catalytic AP, graphite is frequently doped with metals to accelerate the thermal decomposition process of AP [31]. Carbon nanotubes are one-dimensional ribbons with a variety of surface groups, such as carboxyl groups [32]. After encapsulating AP, the composite particles of AP and carbon nanotubes have more catalytic sites and accelerate the thermal decomposition of AP [33]. GO is widely used in emerging carbon-based materials [34, 35]. It has more oxygen-containing functional groups on the surface and higher activity [36]. It releases a certain amount of energy during the thermal decomposition process. It is frequently used in combining metal carriers and AP to improve catalytic efficiency [37–39].

In addition to the aforementioned carbon materials, GO aerogels (GAs) are currently emerging carbon-based materials. Due to their high elasticity, strong adsorption, porous structure and high specific surface area, they are typically used in electrochemistry and wave absorption fields [40–42]. GAs are also used to enhance the performance of energetic materials due to their porous structure and high specific surface area when combined with catalysts [43]. At present, a GA is combined with energetic materials to improve its detonation performance [44]. There are few reports on a GA catalysing AP. Therefore, in this study, three-dimensional (3D) porous GA were prepared by hydrothermal method and vacuum cold-drying technology, and their catalytic properties for AP thermal decomposition were studied by thermogravimetry/differential scanning calorimetry (TG-DSC). It was found that the obtained GA show good catalytic performance for AP thermal decomposition and have a good application prospect for further application in AP and AP-based propellants.

33.2 Experimental

All reagents used in the experiment were from commercial sources of analytical grade and used without further purification. NH_4ClO_4 were purchased from Dalian

North Potassium Chlorate Co., Ltd. GO was obtained from Suzhou Tanfeng Graphene Technology Co., Ltd. Analytical reagent-grade ethyl acetate was provided by Nanjing Chemical Reagent Co., Ltd.

33.2.1 Preparation of Three-Dimensional Porous GA

The preparation process of 3D porous GA is as follows:

In this experiment, 3D porous GA is obtained from a suspension of GO using vacuum freeze-drying technology. In the preparation process, weigh 6 mg of GO and add 30 ml of deionized water to it. The GO is dispersed in deionised water using ultrasound to a concentration of 2.0 mg/ml, and then, the mixture is poured into a Teflon-lined stainless steel autoclave vessel (standard:100 ml). In the autoclave, the mixture is heated in an oven to 180 °C and reacts for 24 h before being removed from the autoclave to cool, yielding graphene aerogel, which is then placed in a vacuum freeze-drying machine and freeze-dried for 24 h to form 3D fluffy porous GA.

33.2.2 Preparation of GA/AP Composite Materials

The preparation process of a GA/AP composite materials is as follows:

Weigh 2.5 mg of 3D GA, the final product of the previous experiment, and at the same time weigh 47.5 mg of AP and add it to a mortar to keep the GA content at 5wt%, and add a small amount of ethyl acetate to grind to make it well mixed. The mixture was placed in a 60 °C drying oven and dried for 12 h to obtain the final GA/AP composite.

33.2.3 Preparation of GO/AP Composite

The preparation process of GO/AP composite is as follows:

Weigh 2.5 mg of graphene oxide and, at the same time, weigh 47.5 mg of AP and add it to the mortar to keep the GO content at 5 wt%, which is the same as the percentage content of the above GA in AP. Add a small amount of ethyl acetate and grind it to make it evenly mixed. The mixture was placed in a 60 °C drying oven for 12 h to obtain the final GO/AP composite.

33.2.4 Measurements

Powder X-ray diffraction (XRD) was performed using Rigaku smartlab9 with Rigaku's original CBO cross optical system (rated voltage 40 kV, rated current 150 mA). The samples were analyzed using a Fourier transform spectroscopy (FT-IR) (Fourier transform infrared FT-IR ftir model Thermo Fisher IS5) in the range of 4000–500 cm^{-1}. Using high-resolution thermal field emission scanning electron microscopy (SEM) (FEI Quanta 400 FEG, USA) to observe GO, GA and their mixed state with AP. The thermal analysis experiment was conducted using METTLER TOLEDO TGA/DSC3+; the N_2 flow rate was 50 ml/min; the selected heating rate was 5, 10, 15 and 20 °C /min and the programme was heated from 35 to 535 °C.

33.3 Results and Discussion

33.3.1 Characterization of GO and GA

XRD is used to study the purity and phase structure of the prepared samples. In this experiment, the typical XRD comparison chart of GO and GA is shown in Fig. 33.1. The peak with the highest GO diffraction intensity corresponds to $2\theta = 8^{\circ}$. After being prepared into GA, the original GO sheet structure was broken, and the diffraction peak of natural graphite at $2\theta \approx 23^{\circ}$(002) was enhanced, forming a broad diffraction peak, and the interlayer spacing was about 0.399 nm (according to the Bragg equation, $2d\sin\theta = \lambda$, $\lambda = 0.154$ nm).

SEM reveals the status of GO and GA. A typical scan SEM image of the suspended flake GO and GA after cold curing in the observation result is shown in Fig. 33.2. The SEM image in Fig. 33.2a shows scattered pieces of GO raw materials, with an average lateral size of approximately 15 microns. The SEM image in Fig. 33.2b

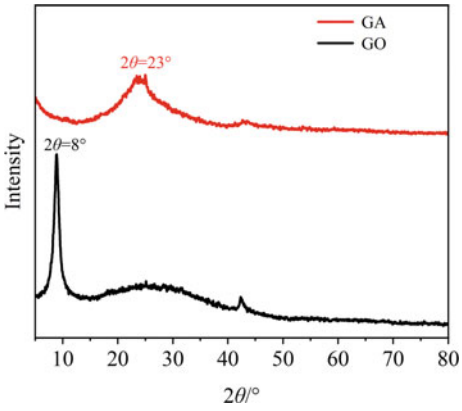

Fig. 33.1 XRD patterns of GO and GA

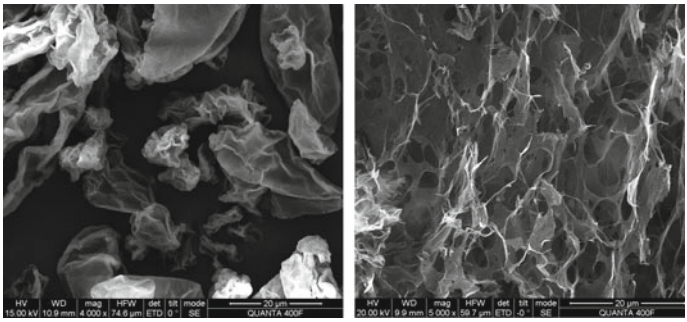

Fig. 33.2 SEM observation images of GO and GA

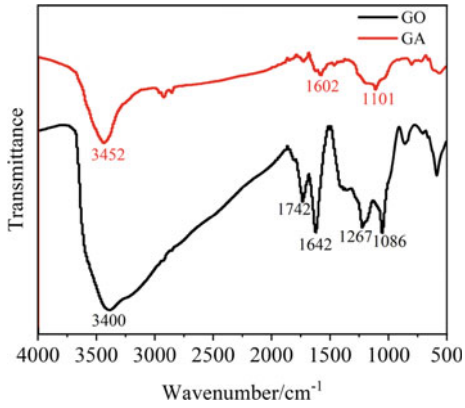

Fig. 33.3 FT-IR spectra of GO and GA

shows a network structure with 3D macropores, with pores ranging in sizes from a few hundred nanometres to a dozen micrometres, which is a fluffy porous structure.

In addition, FT-IR was used to study the structure and functional groups of the GO and GA. The results are shown in Fig. 33.3. According to Fig. 33.3, the infrared of GO shows that the C–O–C stretching vibration corresponds to 1086 cm^{-1}, the C–OH in-plane stretching vibration of the hydroxyl group corresponds to 1267 cm^{-1}, the CO–H in-plane stretching vibration corresponds to 1642 cm^{-1}, the C = O tensile vibration of the carboxyl group corresponds to 1742 cm^{-1} and the hydroxyl stretching motion of adsorbed water around 3400 cm^{-1} is not considered as a factor. The infrared of the GA shows that the tensile vibration of epoxy group C–O corresponds to 1101 cm^{-1} and the C = O tensile vibration of the carboxyl group corresponds to 1602 cm^{-1}. There is a slight change in the peak position, and the original double peaks are combined into one. The infrared spectrum of the GA is similar to that of the GO to some extent, and the in-plane stretching vibration peak of the GA has disappeared, which proves that the original layered structure of the GO has changed and the preparation was successful.

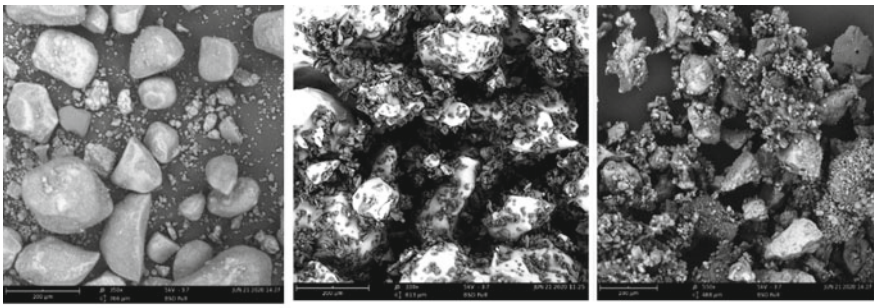

Fig. 33.4 SEM images of AP (**a**), AP + 5-wt% GO (**b**) and AP + 5-wt% GA (**c**)

33.3.2 Characterization of AP+GO, AP+GA

SEM revealed the apparent state of AP particles and the mixed state of GO/AP and GA/AP mixtures, as shown in Fig. 33.4a, b, and c. In Fig. 33.4a, the particle size of AP particles is between 50 and 200 μm. In Fig. 33.4b, GO sheets are deposited on the surface of AP to form a uniform mixture. In Fig. 33.4c, a porous cold-set GA is attached to the surface of AP particles, forming a stable and uniform compound.

33.3.3 Catalytic Activity of GA and GO

As the most important component of the composite solid propellants, the catalysis of GA on the thermal decomposition of AP was studied in this experiment as a reference for its performance in the composite propellants. In the catalyst and control experiments, the GA content in the prepared composite, i.e. AP = 5:95, GA = 5 wt%, GO and GA as a control experiment, the content in the mixture is the same, which is 5 wt%. Comparing the two prepared mixtures with pure AP through TG and DSC as shown in Fig. 33.5a and b, the heating rate is 15 °C /min. The thermal decomposition of pure AP has three peaks, one endothermic peak and two exothermic peaks, including a low-temperature exothermic peak(LTD) and a high-temperature exothermic peak(HTD). The figure shows that pure AP has an endothermic peak at 244 °C, which is caused by the crystallographic transformation of AP from an orthogonal structure to a cubic structure, commonly known as crystal orientation transformation. Pure AP has an LTD at approximately 310 °C. This is due to the existence of defects on the surface of the AP crystal, such as the unsaturation of the force field such as cracks, and these points are the potential activation sites for the decomposition of AP solids. In the first stage, the crystal itself has a large internal stress. The accumulation of reaction products aggravates the development of defects and cracks, increases the internal stress, and promotes the cracking of large

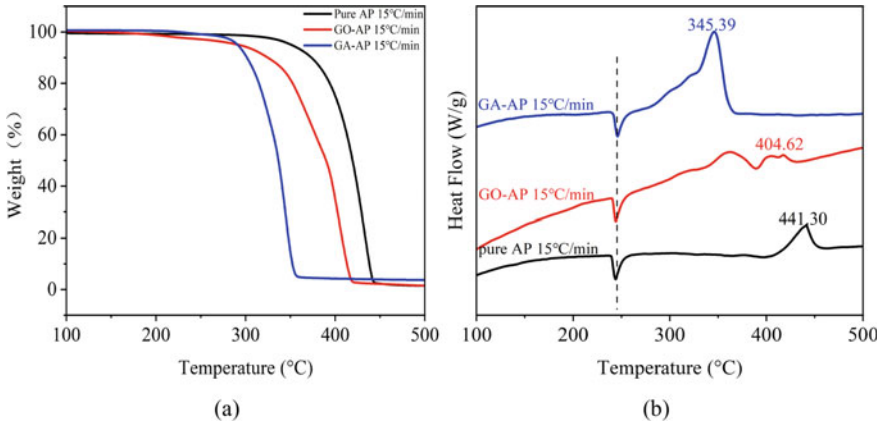

Fig. 33.5 TG (**a**) DSC (**b**) comparison chart of pure AP, GO-AP and GA-AP

crystals to generate smaller crystals, which react on the newly formed larger surface area. According to the electron transfer theory, in the ammonium and hypochlorite radicals generated by the preliminary decomposition of AP, electrons flow from the hypochlorite to ammonium to generate NH_3 and $HClO_4$. The process is as follows [22–24]:

$$NH_4ClO_4 \Leftrightarrow NH_4^+ + ClO_4^- \Leftrightarrow NH_3(a) + HClO_4(a) \Leftrightarrow NH_3(g) + HClO_4(g)$$

In this experiment, there may be low crystal surface defects when the AP low-temperature exotherm is performed locally and the crystal surface is complete, obscuring the low-temperature exotherm, so the LTD changes weakly at approximately 330 °C. When the AP heating temperature reaches 441 °C, the intermediate product is further and completely decomposed. The reaction process is that O_2 generated by the decomposition of $HClO_4$ becomes O_2^{2-} through electron transfer, O_2^{2-} and NH_3 generate nitrogen oxides and an HTD appears. The specific process is shown in Fig. 33.6.

Graphene is a conductive material. Due to the oxidation process, the conjugated structure of GO is severely damaged, so it has poor conductivity and only a catalytic effect. The catalytic effect of GO on AP is not obvious. The HTD has advanced from 441 to 405 °C, and the LTD is more obvious than in pure AP. The catalytic effect of GO on AP is not obvious, HTD has advanced from 441 to 405 °C and LTD is more obvious than in pure AP. A GA is densely porous and highly adsorbable, and its electron transfer is faster than that of the GO lamellar structure. At the same time, it can adsorb NH_3 during AP decomposition, thereby accelerating the forward progress of the reaction. The thermal decomposition rate of AP accelerates, and the low- and high-temperature decomposition peaks merge into a new HTD, which advances from 441 to 345 °C, and the heat release increases from 205 to 720 J/g, that has an obvious catalytic effect. Therefore, taking the heating rate of 15°C/min as an

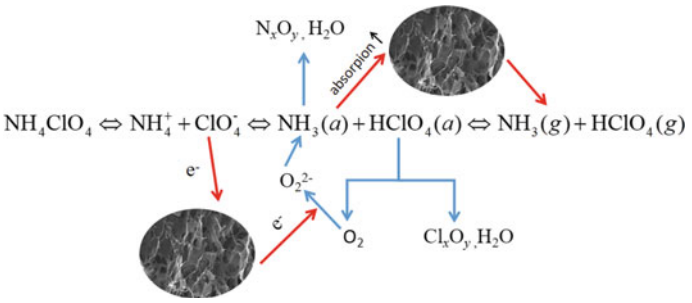

Fig. 33.6 Schematic diagram of thermal catalytic enhancement of GA for AP

example, the high-temperature decomposition peak of GO–AP was advanced from 441 to 404 °C, but the heat release was reduced from 205 to 85 J/g, and the catalytic effect of GO–AP was far less than that of the GA. Detailed data are shown in Table 33.1.

The thermodynamic parameters of the AP sample and its composite sample are further calculated, and the TG/DSC curves of the pure AP and its composite sample at different heating rates are shown in Fig. 33.7.

Using Kissinger's method, plot $1000/T_p$ and $\ln(\beta/T_p^2)$ as the abscissa and ordinate, respectively, to obtain the dynamic parameters of AP and different AP complexes. The $\ln(\beta/T_p^2)$–$1000/T_p$ graphs of AP and different AP complexes are shown in Fig. 33.8.

The linear fitting formula of $\ln(\beta/T_p^2)$–$1000/T_p$ of AP and different AP complexes is shown in Table 33.2.

Kissinger method [44]

$$\ln\left[\frac{\beta}{T_p^2}\right] = \ln\left[\frac{AR}{E_K}\right] - \frac{E_K}{RT_p}$$

The pre-referential factor A can be calculated using the intercept, or it can be directly calculated using the following formula. The difference between the two is small, and the intercept is used in this study. T_p is the temperature at the pyrolysis peak.

$$A = \beta E_a exp(-E_a/RT_p)/(RT_p^2)$$

Arrhenius equation:

$$k = A\, exp(-E_a/RT_p)$$

Substituting the obtained E_a, A and T_p into the Arrhenius equation, the reaction rate constant $k(T_p)$ corresponding to T_p can be obtained. Furthermore, the thermodynamic parameters corresponding to T_p, Gibbs free energy $\triangle G^{\neq}$, activation enthalpy $\triangle H^{\neq}$ and activation entropy $\triangle S^{\neq}$ can be calculated using the following formulas:

Table 33.1 Thermal decomposition parameters of different catalysts for AP

Heating rate	AP (HTD) (°C)	GO–AP (HTD) (°C)	GA–AP (HTD) (°C)	AP (Heat) (J/g)	GO–AP (Heat) (J/g)	GA/AP (Heat) (J/g)
5 °C/min	412.72	382.84	325.53	40.40	47.67	449.81
10 °C/min	428.51	395.14	335.31	80.65	94.58	631.92
15 °C/min	441.30	404.62	345.39	204.62	85.14	719.98
20 °C/min	449.14	520.16	352.87	226.39	104.72	922.39

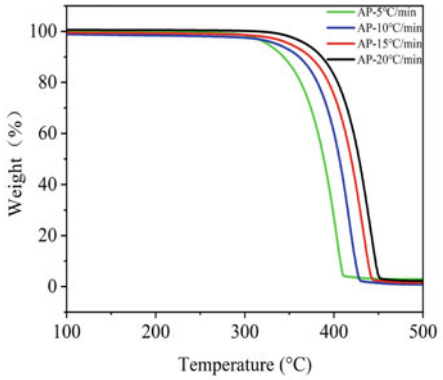

TG curve of pure AP

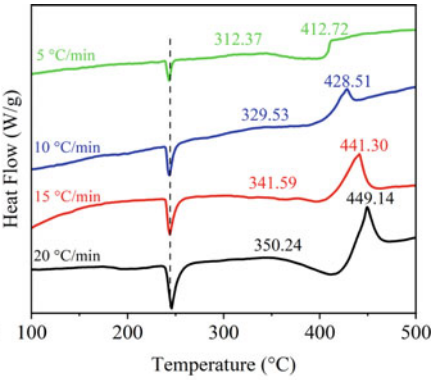

(b) DSC curve of pure AP

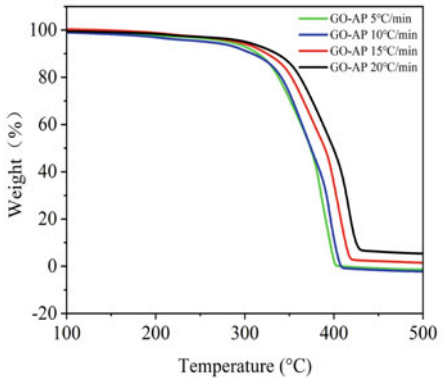

(c) TG curve of GO–AP

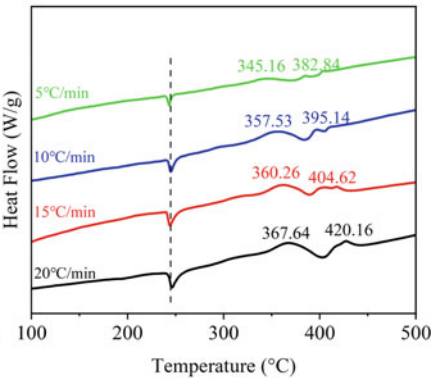

(d) DSC curve of GO–AP

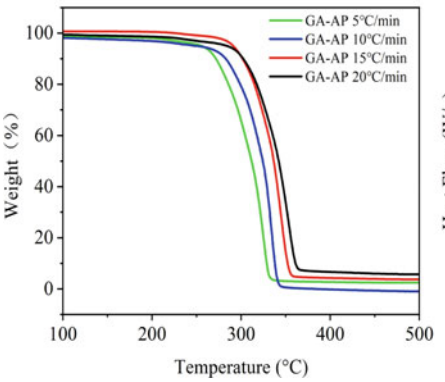

(e) TG curve of GA–AP

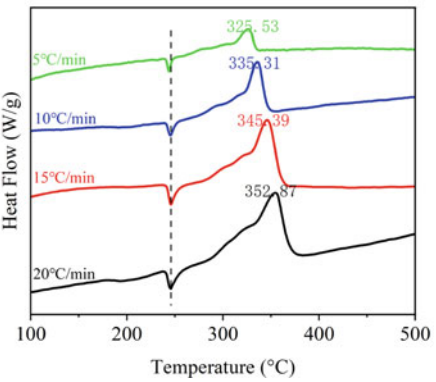

(f) DSC curve of GA–AP

Fig. 33.7 TG (**a**) and DSC (**b**) chart of pure AP and its composite sample

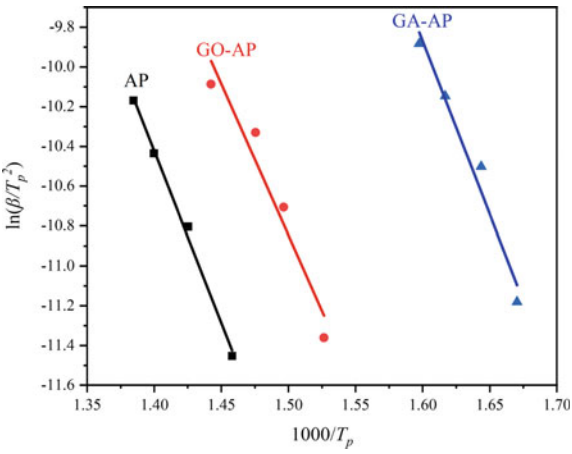

Fig. 33.8 $\ln(\beta/T_p{}^2)$–$1000/T_p$ graphs of AP and different AP complexes

Table 33.2 The linear fitting formula of $\ln(\beta/T_p{}^2)$–$1000/T_p$ of AP and different AP complexes

Sample	Linear fitting formula	R^2
AP	−17.24426x+13.71733	0.99327
GO-AP	−15.2266x+11.99242	0.91255
GA-AP	−17.42241x+18.00485	0.95833

$$k = A\exp(-\frac{\Delta E_a}{RT}) = \upsilon\exp(-\frac{\Delta G^{\neq}}{RT}) = \frac{k_B T_p}{h}\exp(-\frac{\Delta G^{\neq}}{RT}) \tag{33.1}$$

$$\Delta H^{\neq} = E_a - RT_p \tag{33.2}$$

$$\Delta G^{\neq} = \Delta H^{\neq} - T_p \Delta S^{\neq} \tag{33.3}$$

Substituting (2) and (3) into (1), the expression of $\triangle S^{\neq}$ can be obtained:

$$\Delta S^{\neq} = R\left(\ln A - \ln\left[k_B T_p/h\right]\right)$$

In (33.1)–(33.3), υ represents the vibration frequency in s^{-1}; k_B represents Boltzmann's constant, 1.3806×10^{-23} J/K, and h represents Planck's constant, 6.6262×10^{-34} J s. The unit of Gibbs free energy $\triangle G^{\neq}$ and activation enthalpy $\triangle H^{\neq}$ is kJ/mol, and the unit of activation entropy $\triangle S^{\neq}$ is J/(mol K). The results are shown in Table 33.3.

Table 33.3 shows that after AP is mixed with GA, Gibbs free energy $\triangle G^{\neq}$ shows a weakening trend. AP–GA is weaker than pure AP by >20 kJ/mol, indicating that the thermal decomposition reaction of AP and GA is simpler to perform. The reaction rate constant of AP–GA is greater than that of pure AP and GO–AP, and the rate of the thermal decomposition reaction is faster, so the catalytic effect of GA is better.

Table 33.3 Thermal decomposition thermodynamic/kinetic parameters of different samples

Sample	E_a kJ/mol	ln$A$ s^{-1}	k(T_p) s^{-1}	$\triangle S^{\neq}$ KJ/(mol K)	$\triangle H^{\neq}$ KJ/(mol K)	$\triangle G^{\neq}$ KJ/(mol K)
AP	143.4	16.6	5.67×10^{-4}	−114.1	137.5	186.3
GO–AP	126.6	14.7	4.26×10^{-4}	−167.8	121.0	178.2
GA–AP	144.8	20.9	9.11×10^{-4}	−27.6	139.7	158.7

33.4 Conclusion

In summary, 3D porous GA with excellent catalytic properties have been successfully facilely obtained from GO suspension through a fast and effective hydrothermal method and vacuum cold-drying technology. GA with porous structure ranging from hundreds of nanometers to more than ten micrometers is attached on AP that can increases the specific surface area, accelerates the electron transfer, and improves the absorption of ammonia during the thermal decomposition of the AP to reduce the Gibbs free energy in the reaction process and increase the reaction rate in order to achieve the purpose of accelerating the thermal decomposition process of AP and increasing the thermal decomposition amount of AP. This work use TG and DSC and corresponding calculations show that the prepared GA has a better catalytic effect on AP than the raw material GO, and GA will have a good application prospect in composite propellants.

Acknowledgements This work was financially supported by the National Natural Science Foundation of China (Project No. 21805139, 22005144 and 22005145), Natural Science Foundation of Jiangsu Province (BK20200471) and the Fundamental Research Funds for the Central Universities (No. 30920041106, 30921011203).

References

1. T.T. Vo, D.A. Parrish, J.M. Shreeve, Tetranitroacetimidic acid: a high oxygen oxidizer and potential replacement for ammonium perchlorate. J. Am. Chem. Soc. **136**(34), 11934–11937 (2014)
2. F. Solymosi, L. Rvsz, Thermal decomposition of ammonium perchlorate in presence of zinc oxide. Nature **192**(4797), 64–65 (1961)
3. C. Huang, Q. Liu, W. Fan et al., Boron nitride encapsulated copper nanoparticles: a facile one-step synthesis and their effect on thermal decomposition of ammonium perchlorate. Sci. Rep. **5**, 16736 (2015)
4. G. Zhang, B. Gou, Y. Yang et al., CuO/PbO nanocomposite: preparation and catalysis for ammonium perchlorate thermal decomposition. ACS Omega **5**, 32667–32676 (2020)
5. D. Zhang, Q. Li, R. Li, H. Li, H. Gao et al., Significantly enhanced thermal decomposition of mechanically activated ammonium perchlorate coupling with nano copper chromite. ACS Omega **6**, 16110–16118 (2021)

6. X. Xiao, B. Peng, L. Cai et al., The high efficient catalytic properties for thermal decomposition of ammonium perchlorate using mesoporous $ZnCo_2O_4$ rods synthesized by oxalate co-precipitation method. Sci. Rep. **8**, 7571 (2018)
7. V. Verneker, S. Deevi, S.C. Deevi, Role of alloys in the thermal decomposition and combustion of ammonium perchlorate. Combust. Flame **67**(2), 163–173 (1987)
8. P.W.M. Jacobs, H.M. Whitehead, Decomposition and combustion of ammonium perchlorate. Chem. Rev. **69**(4), 551–590 (1969)
9. S. Elbasuney, M. Yehia, Ammonium Perchlorate encapsulated with TiO_2 nanocomposite for catalyzed combustion reactions. J. Inorg. Organomet. Polym. **29**, 1349–1357 (2019)
10. P. Xu, Y. Lu, P. Ye et al., In situ synthesis of copper stearate/ammonium perchlorate shell–core composite for self-catalytic thermal decomposition. J. Therm. Anal. Calorim. (2020)
11. Kurian, Emel V. Senthur Prabu, S. Experimental investigation of waste heat recovery from the disposal of ammonium perchlorate. Mater. Today: Proc. 2021. ISSN 2214-7853
12. N.T. Manikandanath, R.S. Rimal Isaac, Superb catalytic activity of as-green synthesized copper ferrite's thermal decomposition of ammonium perchlorate. J. Mol. Struct. (130161) (2021). ISSN 0022-2860
13. Z. Zeng, E.R. Bernstein, Ammonium perchlorate and ammonium dihydrogen phosphate as energetic materials: comparison to ammonium nitrate. J. Phys. Chem. C (2019)
14. Y. Xu, Y. Wang et al., Transition metal complexes based on hypergolic anions for catalysis of ammonium perchlorate thermal decomposition. Energy Fuels **34**(11), 14667–14675 (2020)
15. J.L. Arroyo, N. Norambuena, H. Reyes, et al. Heterobimetallic catalysts for the thermal decomposition of ammonium perchlorate: efficient burning rate catalysts for solid rocket motors and missiles. Inorg. Chem. (2021)
16. Exploring the roles of ZIF-67 as an energetic additive in the thermal decomposition of ammonium perchlorate. Energy Fuels **35**(5), 4447–4456 (2021)
17. X. Sun, X. Qiu, L. Li et al., ZnO twin-cones: synthesis, photoluminescence, and catalytic decomposition of ammonium perchlorate. Inorg. Chem. **47**(10), 4146 (2008)
18. P. Ye, Y. Lu, P. Xu, Preparation of $CoFe_2O_4$@C nano-composites and their catalytic performance for the thermal decomposition of ammonium perchlorate. Chin. J. Explos. Propellants (4), 358–362 (2019)
19. G. Hao, Liu et al., Preparation of nano-sized copper β-resorcylate (β-Cu) and its excellent catalytic activity for the thermal decomposition of ammonium perchlorate. Propellants Explos. Pyrotech. (2015)
20. G. Hao, J. Liu, L. Xiao et al., Effect of drying methods on catalytic performance of nano-sized copper β-resorcylate. J. Therm. Anal. Calorim. **124**(3), 1367–1374 (2016)
21. G. Tang, S. Tian, Z. Zhou et al., ZnO Micro/nanocrystals with tunable exposed (0001) facets for enhanced catalytic activity on the thermal decomposition of ammonium perchlorate. J. Phys. Chem. C **118**(22), 11833–11841 (2014)
22. G. Hao, L. Li, B. Gou, Preparation of nano-Cu-Cr composite metal oxides via mechanical grinding method and its catalytic performance for the thermal decomposition of ammonium perchlorate. Chin. J. Explos. Propellants **042**(006), 557–565 (2019)
23. J. Zhang, B. Jin, X. Li, W. Hao, T. Huang, B. Lei, Z. Guo, J. Shen, R. Peng, Study of H2AzTO-based energetic metal-organic frameworks for catalyzing the thermal decomposition of ammonium perchlorate. Chem. Eng. J. (2020)
24. J. Chen, B. Huang, Y. Liu et al., 3D hierarchically ordered porous carbon entrapped Ni nanoparticles as a highly active catalyst for the thermal decomposition of ammonium perchlorate. Energetic Mater. Front. (2021)
25. P. Chandrababu, J. Thankarajan, Decomposition of ammonium perchlorate: exploring catalytic activity of nanocomposites based on nano Cu/Cu_2O dispersed on graphitic carbon nitride. Thermochim. Acta. 2020(178720), ISSN 0040-6031
26. J. Chen, S. He, H. Bing et al., Highly space-confined ammonium perchlorate in three-dimensional hierarchically ordered porous carbon with improved thermal decomposition properties. Appl. Surf. Sci. 457(NOV.1), 508–515 (2018)

27. P. Hou, F.S. Cannon, Effect of preparation protocol on anchoring quaternary ammonium/epoxide-forming compound into granular activated carbon for perchlorate adsorption: enhancement by response surface methodology. Chem. Eng. J. 309–317 (2013), ISSN 1385-8947
28. G. Veerappan, K. Bojan, S.W. Rhee, Sub-micrometer-sized graphite as a conducting and catalytic counter electrode for dye-sensitized solar cells. Acs Appl. Mater. Interfaces **3**(3), 857–862 (2011)
29. N. Ricke, A.T. Murray, J. Shepherd et al., Molecular-level insights into oxygen reduction catalysis by graphite-conjugated active sites. Acs Catal. (2017) acscatal.7b03086
30. A. Sz, C.A. Xiong, C. Xc et al., Metal-doped (Fe, Nd, Ce, Zr, U) graphitic carbon nitride catalysts enhance thermal decomposition of ammonium perchlorate-based molecular perovskite. Mater. Des. 199
31. Q. Fang, B. Chen, Adsorption of perchlorate onto raw and oxidized carbon nanotubes in aqueous solution. Carbon **50**(6), 2209–2219 (2012)
32. M. Abdelhafiz, M. Yehia, H.E. Mostafa et al., Catalytic action of carbon nanotubes on ammonium perchlorate thermal behavior. React. Kinet. Mech. Catal. **131**(1), 353–366 (2020)
33. J. Shen, Y. Hu, M. Shi et al., Fast and facile preparation of graphene oxide and reduced graphene oxide nanoplatelets. Chem. Mater. **21**(15), 3514–3520 (2009)
34. E. Cho, A. Ruminski, S. Aloni et al., Graphene oxide/metal nanocrystal multilaminates as the atomic limit for safe and selective hydrogen storage. Nat. Commun. **7**, 10804 (2016)
35. D. Dikin, S. Stankovich, E. Zimney et al., Preparation and characterization of graphene oxide paper. Nature **448**, 457–460 (2007)
36. W. Zhang, Q. Luo, X. Duan et al., Nitrated graphene oxide and its catalytic activity in thermal decomposition of ammonium perchlorate. Mater. Res. Bull. **50**, 73–78 (2014)
37. J. Pei, H. Zhao, Graphene oxide/Fe_2O_3 nanocomposite as an efficient catalyst for thermal decomposition of ammonium perchlorate via the vacuum-freeze-drying method. Langmuir **37**(20), 6132–6138 (2021)
38. T. An, W. He et al., Thermal behavior and thermolysis mechanisms of ammonium perchlorate under the effects of graphene oxide-doped complexes of triaminoguanidine. J. Phys. Chem. C. **122**(47), 26956–26964 (2018)
39. S. Ye, J. Feng, P. Wu, Deposition of three-dimensional graphene aerogel on nickel foam as a binder-free supercapacitor electrode. Acs Appl. Mater. Interfaces **5**(15), 7122–7129 (2013)
40. C. Wang, C. Xiong, B. Wang et al., Freeze-casting produces a graphene oxide aerogel with a radial and centrosymmetric structure. Acs Nano **12**(6) (2018)
41. E. Greco, J. Shang, J. Zhu et al., Synthesis of polyacetylene-like modified graphene oxide aerogel and its enhanced electrical properties. ACS Omega **4**(25), 20948–20954 (2019)
42. P. Li, Y. Zheng, J. Li et al., Monolithic neat graphene oxide aerogel for efficient catalysis of s → O acetyl migration. ACS Catal. **5**(6), 150422160751001 (2015)
43. C. Zhang, X. Fu, X. Zhang et al., The effects of metal complexes of nano-graphene oxide to thermal decomposition of FOX-7. Nanomaterials **10**(1), 144 (2020)
44. Y. Yu, S. Chen, T. Li et al., Study on a novel high energetic and insensitive munitions formulation: TKX-50 based melt cast high explosive. RSC Adv. **7**(50), 31485–31492 (2017)

Chapter 34
Review of Graphene-Based Energetic Compounds

Yonghu Zhu, Xiaolong Fu, Jiaxin Su, Yan Hu, and Lizhi Wu

Abstract This paper systematically introduces the latest research progress of graphene-based energetic compounds in recent years from three aspects: the preparation method of graphene-based energetic compounds, the desensitization effect and the catalytic effect of graphene-based materials on energetic materials. The preparation methods of graphene-based energetic compounds can be divided into physical combination and chemical bonding. The insensitive agent composed of graphene-based materials can reduce the mechanical sensitivity of energetic materials. Catalysts composed of graphene-based materials can significantly improve the combustion performance of energetic materials. Graphene-based composite energetic materials possess excellent combustion thermochemical properties. Finally, the key research directions and research prospects of graphene-based energetic compounds in the future are proposed.

Y. Zhu · J. Su · Y. Hu · L. Wu (✉)
School of Chemistry and Chemical Engineering, Nanjing University of Science and Technology, Nanjing 210094, China
e-mail: wulizhi@njust.edu.cn

Y. Zhu
e-mail: zhuyonghu@njust.edu.cn

J. Su
e-mail: sjx666@njust.edu.cn

Y. Hu
e-mail: huyan@njust.edu.cn

X. Fu
Xi'an Modern Chemistry Research Institute, Xi'an 710065, China
e-mail: fuxiaolong204@163.com

A. Gany and X. Fu (eds.), *2021 International Conference on Development and Application of Carbon Nanomaterials in Energetic Materials*, Springer Proceedings in Physics 276,
https://doi.org/10.1007/978-981-19-1774-5_34

34.1 Introduction

Since it was prepared by Andre and Konstantin in 2004, graphene has been favored by researchers at home and abroad [1]. Graphene is a two-dimensional carbon nanomaterial composed of a single layer of carbon atoms with sp^2 hybrid orbitals and a hexagonal honeycombed lattice structure. It is considered to be the basic unit of carbon nanotubes, fullerenes and graphite [2]. The unique structure makes graphene possess a series of excellent characteristics: the thickness of single-layer graphene is only 0.34 nm, which is considered to be the thinnest two-dimensional material in the world. At room temperature, the thermal conductivity of graphene can reach 5300 W m^{-1} k^{-1} [3]. In theory, the specific surface area of single-layer graphene can reach 2630 m^2 g^{-1} [4]. Moreover, its fracture strength can reach 12 5GPa and Young modulus can reach 1.0 TPa [5]. These excellent properties enable graphene to be used as an excellent additive or additive carrier to promote physical and chemical properties of energetic materials [6–8].

However, pure graphene is a non-energetic component, and if pure graphene is directly introduced into energetic materials, it will inevitably lead to a decrease in the energy of the entire system [9]. Therefore, researchers often perform functional treatment on graphene, and the treated graphene-based materials (such as GO, NGO, etc.) will undergo disproportionation reaction and release energy. Therefore, graphene-based materials are considered a potential energetic material which can be used to improve the whole system performance without reducing total energy output level at the same time.

This article mainly introduces the graphene-based energetic compounds preparation method, the desensitization effect of graphene-based materials on energetic materials, and the catalytic effect of graphene-based materials on energetic materials. The current problems and future development trends of graphene-based materials in the application of energetic compounds are also discussed.

34.2 Preparation Method of Graphene-Based Composite Energetic Materials

At present, there are various preparation methods of graphene-based materials, and different uses have different requirements for graphene. According to whether the graphene-based material and the energetic material form a bond, it can be divided into two types: physical combination and chemical bonding.

34.2.1 Physical Combination

The physical combination method is relatively simple. The graphene-based material and the energetic material are combined in an appropriate ratio by stirring, ultrasonic mixing, and other methods. In this paper, the physical combination methods are as follows: mechanical mixing method, ball milling method, spray drying method, self-assembly method, sol–gel method, solvent- non-solvent method and ultrasonic dispersion method.

34.2.1.1 Mechanical Mixing Method

Mechanical mixing method is the most primitive and simplest preparation method of graphene-based composites. This method directly mixes graphene-based materials with other energetic materials by simple stirring. Guan et al. [10] directly mixed the developed NGO with AP with an average particle size of 100 microns in a certain proportion to study the catalytic effect of NGO on the thermal decomposition of AP. Similarly, Zhang et al. [11] prepared n-GO/HMX and rGO/HMX composites by grinding nitrogen-mixed graphene oxide (N-GO) and rGO with HMX in a certain proportion, and studied the thermal decomposition performance of the composite energetic system. In order to study the catalytic effect of graphene on the thermal decomposition of AP, Wang et al. [12] mechanically mixed graphene and AP in a certain ratio, and analyzed its catalytic effect by means of thermal analysis.

This method does not require high equipment and is easy to operate, but the prepared product has no regular morphology, and the uniformity and controllability of the sample is relatively poor [13]. Therefore, this method can be used appropriately when the overall performance of the composite material is not high.

34.2.1.2 Ball Milling Method

In the ball milling method, hard balls in the ball mill are used to strongly impact and friction graphene-based materials and energetic materials. In this process, the two materials are crushed into nanoparticles and doped with each other to form a composite energetic system. Figure 34.1 shows the grinding and mixing process of materials and the mechanochemical effect in the ball milling process [14]. Guo et al. [15] developed LLM-105/GO composite energetic material by ball milling method, and proved that the thermal stability of the composite material was better than that of pure submicron LLM-105, and the apparent activation energy of thermal decomposition increased by 89.98 kJ /mol. Ye et al. [16] developed CL-20/GO nanocomposites by ball milling method, as shown in Fig. 34.2. And they proposed that the formation of CL-20/GO composites during ball milling could be divided into two processes: the peeling of graphite material and the refinement of CL-20, and the formation of sandwich composites.

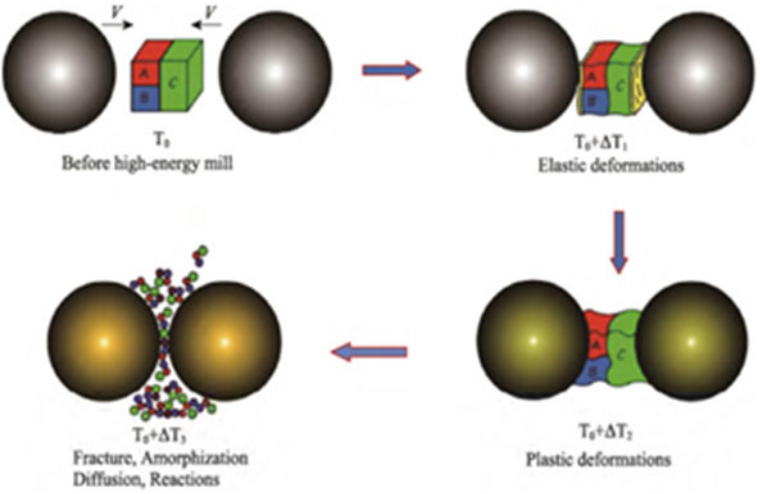

Fig. 34.1 Schematic diagram of mechanochemical effects in the ball milling process

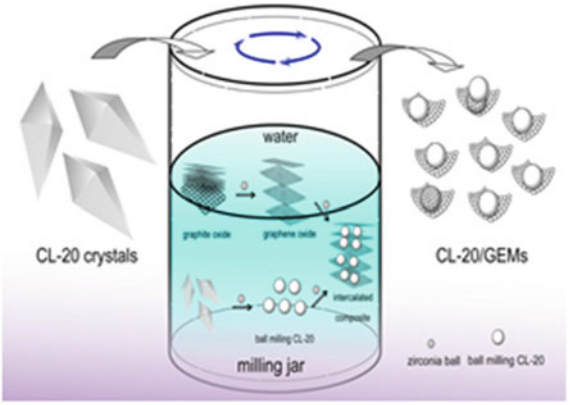

Fig. 34.2 Schematic diagram of the formation of CL-20/GO composite material

The particle size of composites prepared by this method is generally about 7–8 microns. However, the energetic material may generate local hot spots during the ball milling process, and the energetic material may also undergo crystalline changes and other reactions under the influence of high temperature and high pressure, so the safety performance needs to be improved.

34.2.1.3 Spray Drying Method

The spray drying method is to fully contact the atomized thinner composed of graphene-based material and energetic material with hot air, so that the moisture in the thinner is quickly vaporized to obtain the energetic material coated with the graphene-based materials. Wang et al. [17] prepared TKX-50/GO composite energetic materials with GO content of 1%, 3%, and 5% by liquid nitrogen freeze spray drying, and revealed the catalytic mechanism of GO on TKX-50 materials. The study found that GO was adsorbed on the surface of TKX-50, and with the increase of GO content, the three-dimensional structure of the composite material gradually became blurred, and the microstructure changed significantly. The X-ray diffraction results show that the increase of GO has no effect on the crystal form of TKX, but it can significantly promote the thermal decomposition of TKX-50.

This method can adjust the surface tension and viscosity of the liquid to adjust the morphology of the composite material. Because of its easy operation and continuous production, it has the ability of batch industrial production.

34.2.1.4 Self-Assembly Method

The self-assembly method is a way to combine different materials by using the material itself or external forces. In general, the self-assembly process is accomplished by adjusting the interaction force between particles by adjusting the surrounding environment of nanoparticles. Figure 34.3 [18] shows the GO/Fe_2O_3 nanocomposite prepared by Lan Yuanfei using self-assembly. Similarly, Li et al. [19] used electrostatic self-assembly method to uniformly load nano-scale CuO and Al particles on the GO sheet to form an Al-CuO/GO composite energetic material. Figure 34.4 shows the AP/Nal /PTFE composite developed by Yang Yulin's research group by self-assembly

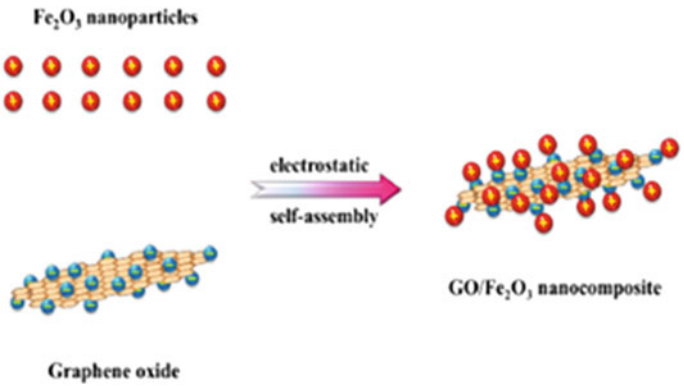

Fig. 34.3 Schematic diagram of electrostatic self-assembly of GO and Fe_2O_3 nanoparticles

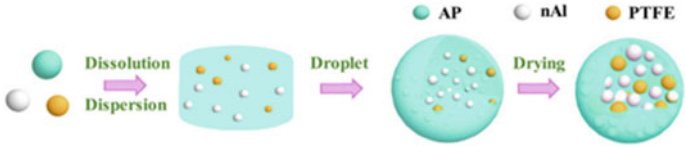

Fig. 34.4 The preparation process of Ap/nAl /PTFE composites

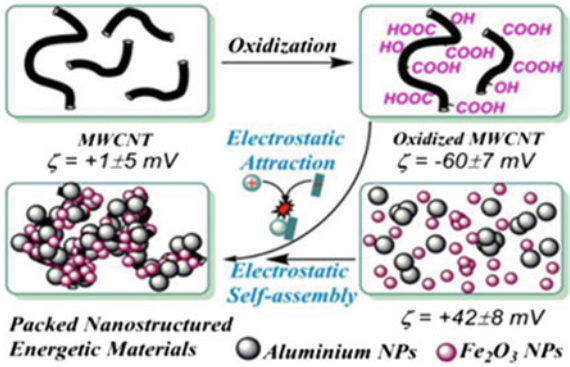

Fig. 34.5 Carbon nanotubes guide the self-assembly process of Al and Fe_2O_3

method. The composite material can significantly reduce the decomposition temperature of AP and enhance its thermal decomposition performance [20]. Zhang et al. [21] also prepared an Al/Fe_2O_3/multi-wall carbon nanotube composite energetic material through electrostatic self-assembly technology. The specific preparation process is shown in Fig. 34.5. The results show that the electrostatic self-assembly method can effectively improve the combination strength of Al and Fe_2O_3, the comprehensive performance of the composite material can be improved, and the heat release of the system can reach 2400 J/g. Similarly, Thiruvengadathan [22] also used self-assembly to prepare graphene-based composite energetic materials, as shown in Fig. 34.6.

This method can control the morphological characteristics of composite materials, and the prepared samples have high thermodynamic properties, so they also have potential application prospects, but the three-dimensional ordered metal oxide particles are required, which greatly increases costs and limits the applications.

34.2.1.5 Sol–gel Method

The sol–gel method uses inorganic substances or metal alkoxides as precursors, mixes these raw materials uniformly in the liquid phase, and then adds some energetic materials. At this time, the entire system undergoes a series of hydrolysis and condensation reactions under the combined action of the catalyst and the gelling agent to form a stable transparent sol, and then the sol is dried to form a gel with a

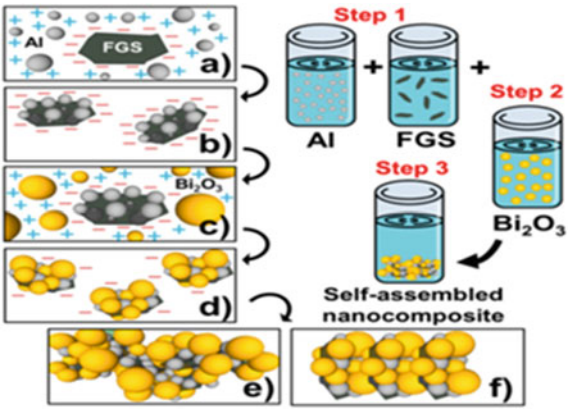

Fig. 34.6 Schematic diagram of the self-assembly of aluminum and Bi_2O_3 nanoparticles on functionalized graphene sheets (FGS)

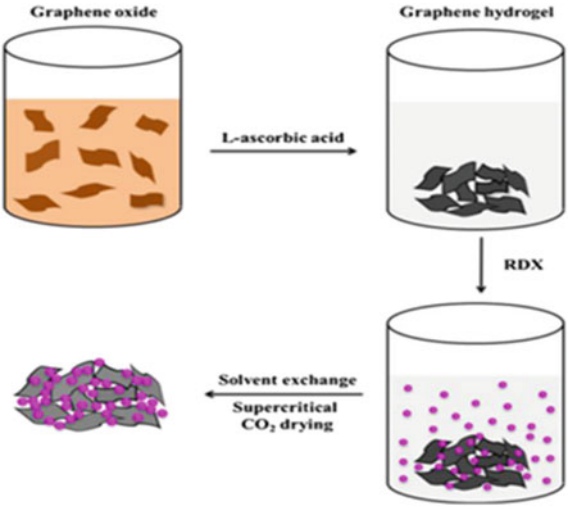

Fig. 34.7 Schematic diagram of the preparation of GA/RDX nanocomposites

certain spatial structure. The energetic material precipitates in the gel skeleton, so this method can greatly reduce the sensitivity of the energetic material. Wang et al. [12, 23] used the sol–gel method to prepare AP/GA nanocomposites to optimize the thermal decomposition properties of AP. Firstly, graphite oxide was dispersed by ultrasonic, and ascorbic acid was added to make graphene hydrogel, and then AP was added to form AP/GA nanocomposite material. SEM showed that AP particles were all condensed on the graphene skeleton.

Lan et al. [24, 25] prepared GA/RDX and Gr/Fe_2O_3 nanocomposite energetic materials by sol–gel method respectively, and their synthetic routes are shown in Figs. 34.7 and 34.8, respectively. Lan et al. [26] prepared GA/AN hydrogel by sol–gel method, and then dried it in supercritical CO_2 to obtain GA/AN nano-energetic composite material. The mass fraction of AN in the composite material can reach

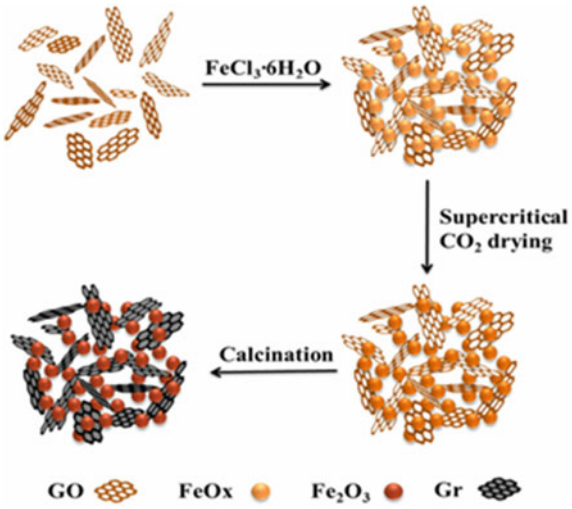

Fig. 34.8 Schematic diagram of the preparation of Gr/Fe_2O_3 nanocomposite

92.71%, the average diameter of the particles can reach 71 nm. SEM shows that AN is filled in the voids of the graphene framework, and the thermal decomposition peak of the composite material is reduced by 33.68 °C, and the heat release is increased by 532.78 J/g.

The preparation process of the sol–gel method is relatively simple, and it can obtain a composite material with high dispersibility. The particle size of the composite material can be controlled within 100 nm, and it is expected to achieve precise control of the load and the morphology of the composite material. However, the price of the precursor is relatively high, and it is difficult to realize large-scale industrial production.

34.2.1.6 Solvent-Non-Solvent Method

Solvent-non-solvent method is a method of making ultrafine powder based on the principle of crystallography. It needs to dissolve graphene-based materials and energetic materials in the same composite solvent, and then slowly drip into the non-solvent to precipitate the solute. And finally liquid–solid separation can be done. Finally, the solid is separated to obtain the composite material. Li et al. [27] used solvent-non-solvent method to prepare HMX/GO composites, they first dissolved HMX in N, N-dimethylformamide (DMF) at 40 °C, and then added 2% GO. The GO is completely dispersed in the DMF solution of HMX by ultrasound, and then the mixed solution is injected into dichloromethane. Finally, the HMX/GO composite material is obtained through suction filtration, washing and drying. The specific steps are shown in Fig. 34.9.

Yuan et al. [28] used solvent-nonsolvent method to prepare NGO/NC composite energetic materials with an NGO content of 0.5–1.5% in order to improve the thermal

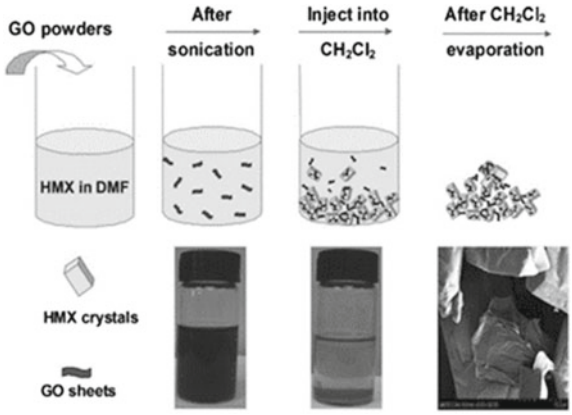

Fig. 34.9 The production scheme of HMX/GO composite material

decomposition performance of NC. The results showed that the entire system still exhibits a highly porous three-dimensional network structure. Li et al. [29] used solvent-non-solvent method, neutralization method and recrystallization methods to develop KNO_3/GO composite energetic materials. The electron microscope photo is shown in Fig. 34.10, and the results show that the solvent-non-solvent method can make GO loads more KNO_3.

Li et al. [30] expected to develop high explosive based solid propellant, so as to greatly improve the performance of solid propellant. The rGO/CL-20 fiber propellant was prepared by solvent-non-solvent method and dimension-limited hydrothermal technology, as shown in Fig. 34.11. It can be clearly seen in Fig. 34.12 that CL-20 can be stably embedded in the network structure of rGO.

In order to improve the stability of high-energy combustion agent AlH_3 in propellant, Li et al. [31] used a solvent-non-solvent method to coat the surface of α-AlH_3 with GO, and then added the coated α-AlH_3 into the propellant in a certain proportion. Through the impact sensitivity test of propellant slurry, they found that the GO coated α-AlH_3 can effectively reduce the impact sensitivity of propellant.

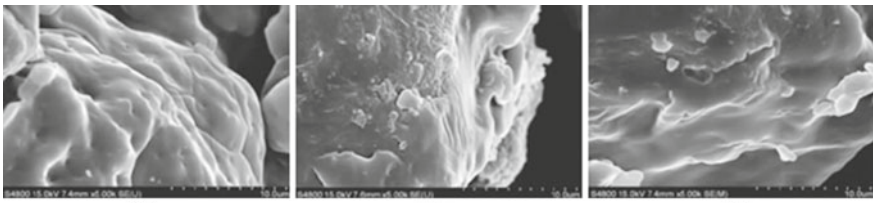

Fig. 34.10 FESEM diagram of KNO_3/GO composite prepared by **a** solvent-non-solvent method, **b** neutralization method and **c** recrystallization method

Fig. 34.11 Process of dimensional-limited hydrothermal preparation

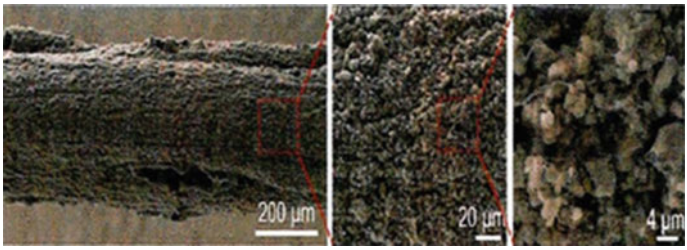

Fig. 34.12 FESEM diagram of rGO /CL-20 fiber

The solvent-nonsolvent method can control the size and shape of the particles by controlling the precipitation rate of the crystals. The disadvantage is that the solvent molecules may enter the crystal lattice and combine with the precursors of the eutectic substance, thereby affecting the purity of the final product. It is also possible to form some thermodynamically difficult to detect and separate eutectic compounds, which hinders the preparation of eutectic compounds from solution and limits the application of this method in energetic materials.

34.2.1.7 Ultrasonic Dispersion Method

The ultrasonic dispersion method uses high-power ultrasonic waves to disperse graphene-based materials and energetic materials in a solvent, and then recrystallization or drying is used to obtain a composite energetic system. He et al. [32] coated the surface of RDX crystal with graphene-based energetic coordination polymer using ultrasonic dispersion. First disperse 200 mg of graphene oxide into 200 ml of distilled water. Then, keeping the temperature of the dispersion at 70 °C, add 50 ml of a mixed aqueous solution consisting of 40 mg of 1-ethyl-3-(3-dimethylaminopropyl) carbodiimide and 30 mg of N-hydroxy-succinimide to make the entire system evenly mixed. After that, a complex precipitate is initially formed, and the specific preparation process is shown in Fig. 34.13.

Dey et al. [33] prepared the Gr-Fe_2O_3 composite energetic material (GINC) by microwave radiation ultrasonic treatment in order to evenly distribute Fe_2O_3 particles

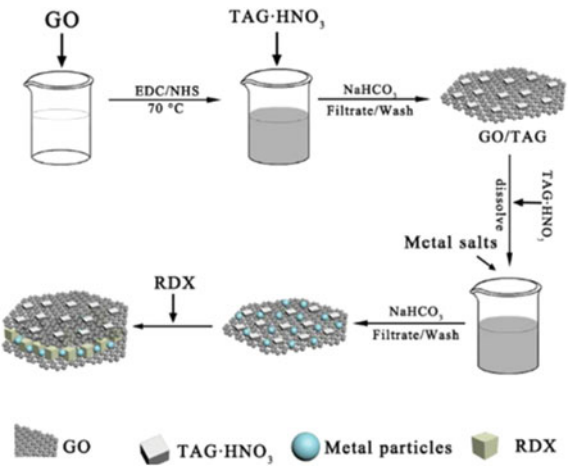

Fig. 34.13 Preparation of RDX crystal coated with GO doped tri-aminoguanidine (TAG-M) transition metal complex

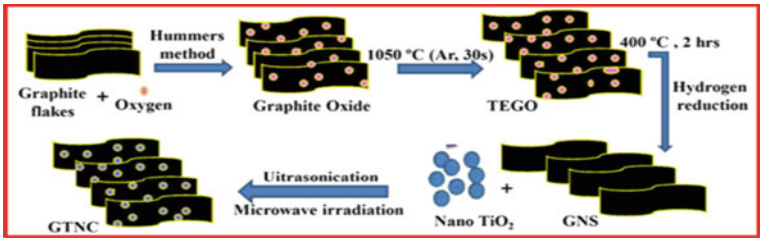

Fig. 34.14 Synthetic schematic diagram of Gr/TiO_2

on the graphene sheet. The specific process is to disperse 50 $_{mg}$ of graphene in pure ethanol under the action of ultrasound, drop into nano-Fe_2O_3 for forty minutes after dispersion and continue ultrasonic dispersion for two hours, then dry and microwave treatment to obtain the Gr/Fe_2O_3 composite material. Figure 34.14 is a schematic diagram of Dey using the same method to synthesize Gr/TiO_2 [34].

Relatively speaking, the ultrasonic dispersion method has a simple operation process, low production cost, and has the ability to transform from a laboratory to an industrialized production.

34.2.2 Chemical Bonding

The physical combination mainly relies on the electrostatic adsorption or van der Waals force between the graphene-based materials and the energetic materials. So

the stability of the combination is limited, while the chemical bonding directly forms a chemical bond between the graphene-based material and the energetic material, so the combination is relatively stronger. Many domestic universities and research institutions have done a lot of work in this field. Zhang et al. [35] from Northwestern Polytechnical University developed a graphene-based energetic 5,5'-bistetrazole coordination polymers by solvothermal method, and the preparation process is shown in Fig. 34.15. In addition, Wang Jingjing of Northwest University [36] grafted $MgWO_4$ and GO together by in-situ growth method. The specific preparation process is shown in Fig. 34.16. In order to verify that the chemically bonded composite material is

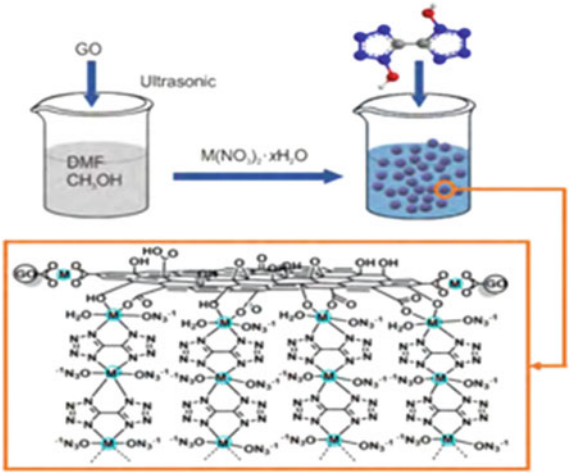

Fig. 34.15 Preparation process of graphene-based energetic 5,5'-bistetrazole coordination polymers

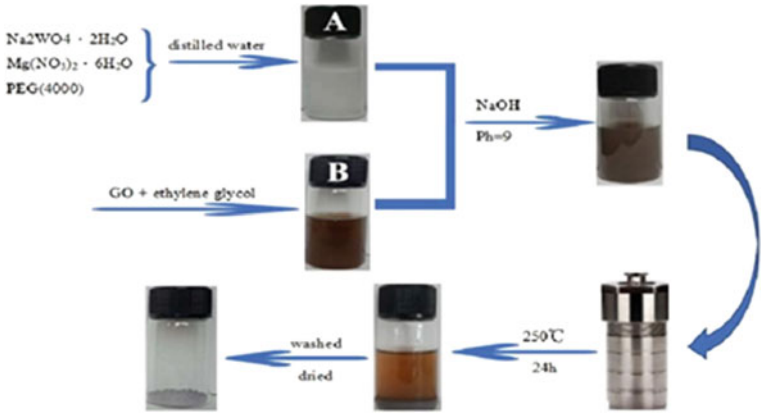

Fig. 34.16 $MgWO_4$/GO composite preparation process

more stable, they disperse the $MgWO_4$/GO composite material obtained by the self-assembly method and the in-situ growth method under ultrasonic conditions for 6 h. Finally, it is found that the composite material prepared by the self-assembly method has a delamination phenomenon, while the composite material prepared by the in-situ growth method still shows a uniform clear liquid. This indicates that the composite materials connected by chemical bonds are more stable.

In general, physical combination is the most commonly used composite method in graphene-based composite energetic materials, which can improve the catalytic decomposition performance of the system to a certain range. However, in the composite materials developed by the physical combination method, the combination strength between the graphene-based material and the energetic compound is poor, so it is easy to separate when subjected to external stimulation, which limits the catalytic performance of the entire energetic system. The chemical bonding can firmly graft the energetic material and the graphene-based material together, which can greatly improve the stability and catalytic decomposition characteristics of the composite material, but the operation is relatively more complicated and it is easy to introduce impurities (Table 34.1).

34.3 Graphene-Based Materials' Desensitization Effect on Energetic Materials

Energetic materials are widely used in military and civilian fields, mainly including propellants, explosives and pyrotechnics. However, due to poor thermal and or mechanical stability, these compounds are rarely used directly. At present, researchers have done a lot of work to reduce the sensitivity of these energetic materials. In addition to controlling the crystal morphology and particle size of the energetic materials, doping with insensitive components has become an important method [37]. Although adding some inert materials (such as stearic acid, graphite and some polymers, etc.) can reduce the mechanical sensitivity of high-energy materials, it also reduces the total energy output of high-energy materials. Modern warfare requires ammunition to have a low mechanical sensitivity on the basis of ensuring high power. Graphene-based materials (such as GO and NGO), while reducing the mechanical sensitivity of energetic materials, will also produce disproportionation reaction to release energy, which is considered as a potential energetic material. Therefore, graphene-based materials are expected to be an excellent additive for energetic materials, which can reduce the sensitivity of energetic materials while maintaining the total energy output level.

Table 34.1 Preparation methods of graphene-based materials

Author	Author unit	Composite material	Year	Ref	Preparation method	Advantages	Disadvantage
Fayang Guan	State Key Laboratory of Explosion Science and Technology, Beijing Institute of Technology	AP/NGO	2020	[10]	Mechanical mixing method	Simple equipment; easy to operate	Rough appearance; poor uniformity and controllability
Ting Zhang	Northwest University School of Chemical Engineering	N-GO/HMX, rGO/HMX	2019	[11]			
Xuebao Wang	School of Materials, Beijing Institute of Technology	Gr/AP	2012	[12]			
Kaige Guo	School of Environmental and Safety Engineering, North University of China	LLM-105/GO	2019	[15]	Ball milling	High output; simple operation	Prone to chemical reactions; poor safety
Baoyun Ye	School of Environmental and Safety Engineering, North University of China	CL-20/GO	2018	[16]			
Huayu Wang	School of Environmental and Safety Engineering, North University of China	TKX-50/GO	2020	[17]	Spray drying	Morphology controllable; industrial production	Thin coating; large heat loss
Tingting Li	School of Chemical Engineering, Nanjing University of Science and Technology	Al–CuO/GO	2018	[19]	Self-assembly method	Morphology controllable; high-quality	High cost

(continued)

Table 34.1 (continued)

Author	Author unit	Composite material	Year	Ref	Preparation method	Advantages	Disadvantage
Tianfu Zhang	School of Materials Science and Engineering, Beijing Institute of Technology	Al/Fe_2O_3/MWCNT	2016	[21]			
Xuebao Wang	School of Materials Science and Engineering, Beijing Institute of Technology	AP/GA	2012	[12]	Sol–gel method	Controllable load and appearance	High cost;
Yuanfei Lan	School of Materials Science and Engineering, Beijing Institute of Technology	GA/RDX	2016	[24]			
Yuanfei Lan	School of Materials Science and Engineering, Beijing Institute of Technology	Gr/Fe_2O_3	2014	[25]			
Yuanfei Lan	School of Materials Science and Engineering, Beijing Institute of Technology	GA/AN	2015	[26]			

(continued)

Table 34.1 (continued)

Author	Author unit	Composite material	Year	Ref	Preparation method	Advantages	Disadvantage
Rui Li	Sichuan New Materials Research Center	HMX/GO	2013	[27]	Solvent-nonsolvent method	Simple operation; low cost; controllable particle size	Uneven heat and mass transfer
Shen Yuan	Key Laboratory of Non-metallic Composite and Functional Materials of Sichuan Province, Southwest University of Science and Technology	NGO/NC	2017	[28]			
Jiakuan Li	School of Chemical Engineering, Nanjing University of Science and Technology	KNO_3/GO	2016	[29]			
Xiaodong Li	Institute of Chemical Materials, China Academy of Engineering Physics	rGO/CL-20	2018	[30]			
Lei Li	Key Laboratory of Aerospace Chemical Power Technology	GO/α-ALH_3	2019	[31]			
Wei He	Key Laboratory of Combustion, Thermal Structure and Internal Flow Field, Northwestern Polytechnical University	GO/TAG-M/RDX	2018	[32]	Ultrasonic dispersion	Simple equipment; easy to operate	Easy reunion
Abhijit Dey	High Energy Materials Laboratory, Pune, India	Gr/Fe_2O_3	2014	[33]			

(continued)

Table 34.1 (continued)

Author	Author unit	Composite material	Year	Ref	Preparation method	Advantages	Disadvantage
Abhijit Dey	High Energy Materials Laboratory, Pune, India	Gr/TiO_2	2015	[34]			
Fayang Guan	State Key Laboratory of Explosion Science and Technology, Beijing Institute of Technology	NGO	2020	[10]	Chemical bonding	Good thermal stability	Complex preparation process; easy to introduce impurities
Xuexue Zhang	Key Laboratory of Combustion, Thermal Structure and Internal Flow Field, Northwestern Polytechnical University	GO-Co-DBT, GO-Co-BT, GO-Ni-DBT, α-GO-Ni-BT and β-GO-Ni-BT	2019	[35]			
Jingjing Wang	Northwest University	$MgWO_4$/GO	2020	[36]			

34.3.1 The Desensitization Effect of Graphene-Based Materials on AP/HMX/CL-20

Based on the desensitization effect of graphene-based materials on energetic materials, a large number of scholars have been researching the work in this field. Zhou et al. [38] replaced the aluminum powder in HTPB with equal mass Al/Gr (graphene-coated aluminum powder) and found that the Al/Gr had a certain inhibitory effect on the thermal decomposition of AP, which significantly changed the decomposition peak of AP. The decomposition peak at low and high temperatures was delayed by 7 °C and 22 °C, respectively. By testing the burning rate of the propellant, it was found that replacing Al powder with Al/Gr compound could reduce the burning rate of the propellant, this is a direct sign that the decomposition of the oxidant AP is inhibited.

For HMX, different graphene-based materials also differ greatly in reducing the mechanical sensitivity of HMX. Li et al. [29] prepared HMX/GO composites and found that 2% GO can reduce the impact sensitivity of pure HMX from 100 to 10%, and the friction sensitivity from 100 to 32%. Another study found that the effect of reducing the sensitivity of NGO, graphite or rGO alone has greater limitations, but the combination of rGO and graphite can achieve the ideal effect. Coating HMX with 1% rGO and 1% graphite at the same time can reduce the collision and friction ignition probability of the entire system by 92% and 100%, respectively [39].

Similarly, graphene-based materials can also reduce the sensitivity of CL-20. GO can effectively reduce the impact sensitivity of CL-20. The characteristic drop height (H_{50}) of CL-20 is about 17.3 cm, while the characteristic drop height of composite materials containing 5% GO has increased to more than 150 cm [40]. Jin [41] used the recrystallization method to compound 2% of Gr, rGO and NGO with CL-20 respectively. After analysis, it was found that rGO had the most obvious desensitization effect on CL-20, and the critical drop height H_{50} was increased from 25.1 cm to 32.5 cm, the friction sensitivity is reduced from 100 to 72%.

In addition, graphene-based materials can be formed into a three-dimensional frame structure, and CL-20 doping into graphene foam (GF) made of graphene can effectively improve the stability of CL-20 [42], as shown in Fig. 34.17. And found that 2% of GF can increase the impact, friction and electrostatic spark critical ignition value of the composite by 2.5 J, 144 N and 0.59 J, respectively. Figure 34.18 shows the histogram of sensitivity comparison of CL-20/GF, CL-20, HMX and RDX.

34.3.2 The Desensitization Effect of Graphene-Based Materials on Materials Such as Explosives and Ignition Powders

Lead styphnate is one of the most commonly used detonating drugs. However, the sensitivity is too high, which largely limits its wider range of use. Therefore, Li

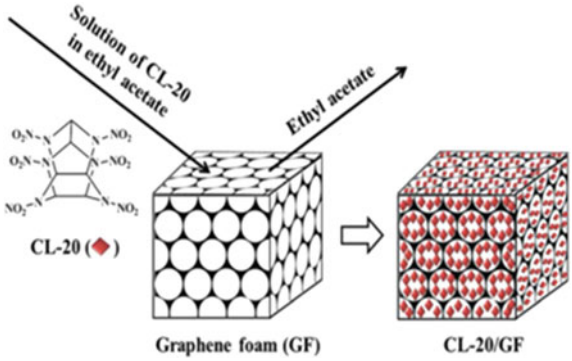

Fig. 34.17 Schematic diagram of the production of CL-20/GF

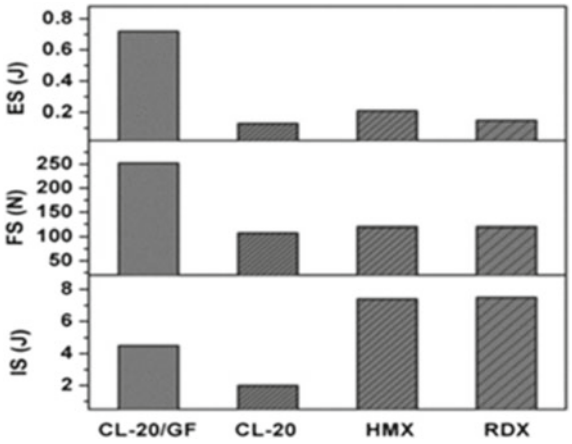

Fig. 34.18 Sensitivity comparison of CL-20/GF, CL-20, HMX and RDX

[43] introduced nano-graphene sheets into lead styphnate and developed graphene-modified lead styphnate composites (GLS). Figure 34.19 is the preparation process of composite materials. He found that graphene sheets can significantly reduce the sensitivity of lead styphnate, and as the graphene content increases within the range of 1.0%, the thermal decomposition peak also increases from 302.4 to 308.1 °C. This shows that the addition of graphene can improve the stability of lead styphnate and reduce the heat sensitivity of lead styphnate.

In addition, rGO and CNTs also have a significant desensitization effect on ignition powder, 5% rGO can increase the H_{50} value of the B/KNO_3 ignition powder system from 42.3 to 59.0 cm, its critical ignition voltage increases from 5 to 25 kV [44], 9% of CNTs can increase the characteristic drop height of the B/KNO_3 ignition powder system by 50% [45], as shown in Fig. 34.20.

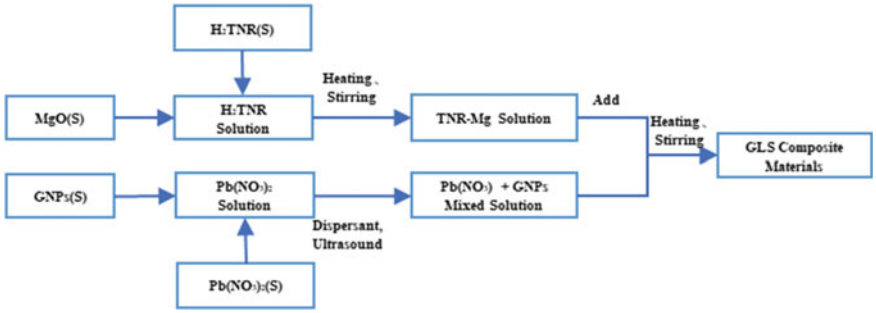

Fig. 34.19 Preparation process of GLS

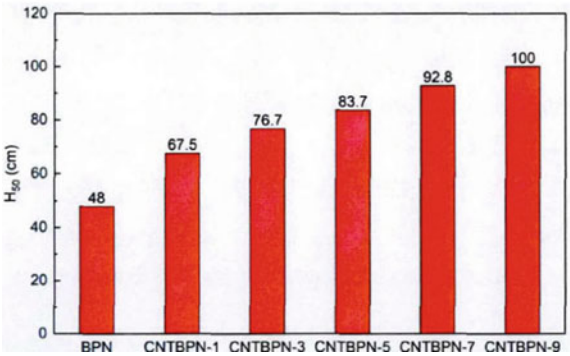

Fig. 34.20 Change of feature drop height after adding CNTs

In addition, Li [46] developed $Cu(N_3)_2$/rGO composite material, and measured by an electrostatic sensitivity tester, the 50% electrostatic ignition energy of the sample containing 15% rGO is 0.92 mJ, while the 50% electrostatic ignition energy of the sample containing 25%rGO increased to 1.43 mJ. This shows that rGO can improve the stability of the system, and as the amount of rGO increases, the electrostatic sensitivity of the system is further improved.

Graphene-based materials mainly improve the thermal stability of energetic materials in two aspects. On the one hand, their good thermal conductivity and electrical conductivity can quickly transfer energy introduced from the outside world to avoid hot spots. On the other hand, GO can induce crystallization, reduce defects in the crystal, and essentially reduce the possibility of hot spots. Besides, graphene oxide belongs to a layered structure, and the force between the layers is relatively weak. When receiving external stimuli, it is easy to slide and has a certain buffering effect, thus increasing the stability of the system (Table 34.2).

Table 34.2 The desensitization effect of graphene-based materials

Author	Author unit	Composite material	Receptor material	Added content	Desensitization effect	Year of publication	References
Chongyang Zhou	Key Laboratory of Aerospace Chemical Power Technology	AL/Gr	AP	1.34%	T_L[a] is increased by 7 °C; T_H[b] is increased by 22 °C	2020	[38]
Rui Li	Sichuan New Materials Research Center	GO	HMX	2%	H_{50}[c] is reduced by 90%; the friction sensitivity is reduced by 68%	2012	[27]
Chunhuan Niu	Southwest University of Science and Technology	rGO and graphite	HMX	1% + 1%	H_{50} is reduced by 92%, and the friction ignition probability is reduced by 100%	2018	[39]
Zhimin Li	Chinese Academy of Sciences	GF	CL-20	2%	The critical ignition values of impact, friction and electrostatic spark of the system are increased by 2.5 J, 144 N and 0.59 J respectively	2015	[42]
Zhenhua Jin	Beijing Institute of Technology	Gr, rGO and NGO	CL-20	2%	H_{50} is increased by 5.1, 7.4, 5.9 cm, respectively; friction sensitivity decreased by 12%, 28%, 20%	2016	[41]

(continued)

Table 34.2 (continued)

Author	Author unit	Composite material	Receptor material	Added content	Desensitization effect	Year of publication	References
Baoyun Ye	North University of China	GO	CL-20	5%	H_{50} increased by more than 133 cm	2018	[40]
Yin Li	Beijing Institute of Technology	rGO	B/KNO_3	1%	T_H is increased by 5.7 °C	2016	[43]
Qian Wang	State Key Laboratory of Explosion Science and Technology, Beijing Institute of Technology	rGO	B/KNO_3	5%	H_{50} is increased by 16.7 cm; critical ignition voltage increased by 20 kV	2018	[44]
Tingting Li	Nanjing University of Science and Technology	rGO	$Cu(N_3)_2$	15%, 25%	A 10% increase in rGO results in a 0.51 mJ increase in electrostatic ignition energy	2018	[46]
Zhihao Wang	China Academy of Engineering Physics	CNT	B/KNO_3	9%	H_{50} is increased by 50%	2019	[45]

[a] T_L is the low temperature decomposition peak of AP
[b] T_H is the high temperature decomposition peak of AP
[c] H_{50} is the drop height of impact sensitivity characteristic

34.4 The Catalytic Effect of Graphene-Based Materials on Energetic Materials

For graphene-based materials, it can be used as an effective catalyst or catalyst carrier [42]. Its excellent electrical and thermal conductivity can increase the reaction heat and electron transfer in the process of chemical reaction. Moreover, the large specific surface area can provide numerous adsorption sites for the catalyst to avoid agglomeration in the reaction process [47].

34.4.1 The Catalytic Effect of Graphene-Based Materials on AP

AP is currently the most commonly used component in solid propellants. It provides the oxygen required for self-sustained combustion of the propellant (the mass fraction of oxygen can reach 0.545), so it is often used as an oxidant in solid propellants [47]. The thermal decomposition of AP greatly affects the performance of the propellant. Lowering the pyrolysis temperature of AP can shorten the ignition delay time of the propellant and significantly increase its burning rate [48, 49]. According to the reference [50], for pure AP, there are three peaks on the DSC curve. The endothermic peak near 245.0 °C is the crystal form transition of AP, at this time AP transforms from orthorhombic crystal form to square crystal form. The exothermic peak near 297.0 °C is the low temperature decomposition peak of AP. The exothermic peak near 406.2 °C is the high temperature decomposition peak of AP, in which the high temperature decomposition peak is the main decomposition stage of AP, during which AP is completely decomposed. In the process of low-temperature decomposition, the decomposition product NH_3 will be adsorbed on the surface of AP in a large amount, thereby inhibiting the further decomposition of AP, as the temperature increases, NH_3 desorbs on the surface of AP and undergoes a violent oxidation_reduction reaction with the oxides decomposed by $HClO_4$, releasing a large amount of heat to form a pyrolysis peak [51].

Guan et al. [10] analyzed NGO/AP composites containing 5% NGO, and found that the low-temperature decomposition peak of the system was advanced by 21 °C, and the low-temperature decomposition activation energy was also reduced by 13.2 kJ/mol, and through the constant volume combustion test, it is found that the addition of NGO can increase the reaction heat of AP/AL system by 13%, which greatly improves the violent reaction of the system. In addition, 2% GO can reduce the decomposition temperature of AP by 32 °C. At 80 atm, replacing AP in HTPB solid propellant with GO/AP composite material containing 2%GO can increase the burning rate of propellant by 15% [52].

Graphene itself is also a kind of fuel, which can also increase the heat release to a certain extent. The high temperature decomposition peak of AP/Gr nanocomposites prepared by Wang et al. [12] is 83.7 °C lower than that of pure AP, and the total

apparent decomposition heat is increased by 1489 J/g. In addition, they also prepared AP/Gr composites by natural drying method, freeze-drying method and supercritical CO_2 drying method, respectively. The results show that the apparent heat of decomposition of the composites can be increased slightly by the three methods. The graphene-based energetic 5,5'-bistetrazole coordination polymers prepared by Zhang et al. [35] can also reduce the high temperature decomposition peak of AP by 93 °C and increase the heat release of the system by 969 J/g. The energetic catalyst can increase the heat release of the system mainly by increasing the conversion rate of NH_3 and H_2O in the AP pyrolysis stage. In addition, there are many oxygen-containing functional groups such as carboxyl and hydroxyl groups on the surface of GO. Researchers can graft energetic functional groups on the oxygen-containing functional groups to improve the performance of GO [53].

The above research shows that Gr has an obvious promotion effect on the high temperature decomposition process of AP, and functionalized graphene oxide can enhance its catalytic effect. This is because the energetic functional group grafted on the GO molecule has a certain synergistic effect with GO. On the one hand, the nitrogen dioxide produced by the cracking of the oxygen-containing functional groups on the surface of the functionalized graphene oxide sheet will promote the oxidation reaction of the decomposition product NH_3 in the initial stage of AP. On the other hand, the oxygen-containing functional groups on the surface of the functionalized graphene oxide sheet will generate rGO during thermal decomposition. NO_2 and rGO have a synergistic effect to promote the thermal decomposition of AP. Figure 34.21 [9] shows the preparation process of functionalized graphene.

34.4.2 The Catalytic Effect of Graphene Metal or Metal Oxide Composite Materials on AP

Related studies have shown that composite materials composed of graphene-based materials and metal/metal oxides can significantly improve the thermal decomposition performance of AP [54]. Figure 34.22 [55] shows that when Gr is combined with the catalyst Mn_3O_4, the thermal decomposition temperature of AP can be reduced by 141.9 °C, which obviously catalyzes the thermal decomposition of AP.

Fe_2O_3, as a commonly used metal oxide, is often used as a catalyst and added to various reactions. The composite of Fe_2O_3 and Gr can effectively catalyze the thermal decomposition of AP.

Yuan and Lan et al. [24, 56] both studied the catalytic effect of Fe_2O_3/Gr composite catalyst on AP. The experiment showed that 1% Fe_2O_3/Gr can increase the heat release of AP by 416 J/g, 2% Fe_2O_3/Gr can reduce the high temperature decomposition peak of AP by 65 °C, and the heat release will increase with the increase of the amount of Gr/Fe_2O_3. Adding 9% Gr/Fe_2O_3 can increase the heat release of the system by 1043 J/g. Figure 34.23 is a schematic diagram of the mechanism of the Fe_2O_3/Gr composite catalyzing the thermal decomposition of AP. Figure 34.24 is

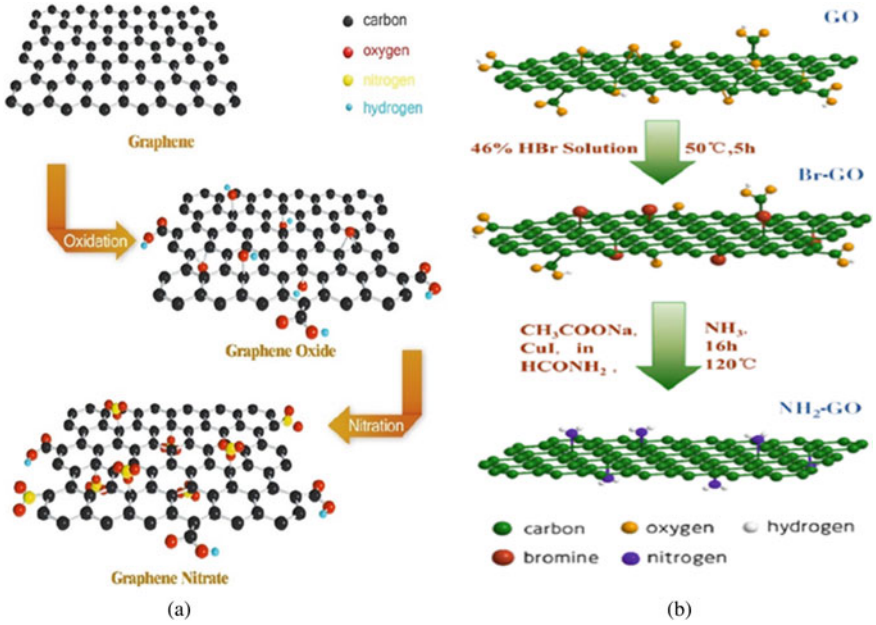

Fig. 34.21 Preparation process of NGO (**a**) and aminated graphene (**b**)

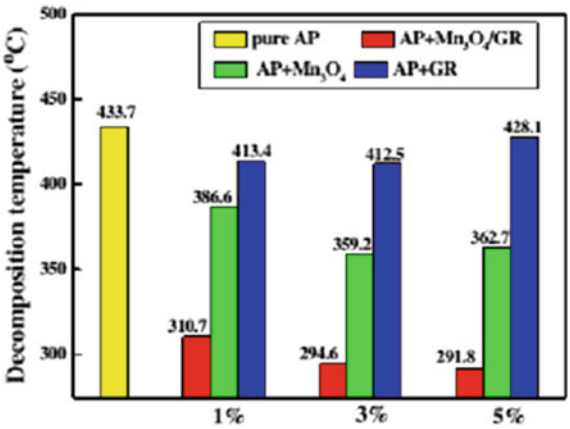

Fig. 34.22 The effect of different catalysts on the thermal decomposition temperature of AP

a schematic diagram of the second step thermal decomposition of AP catalyzed by GO/Fe_2O_3.

Dey et al. [33, 34] prepared Gr/Fe_2O_3 (GINC) and Gr/TiO_2 (GTNC) composite energetic catalysts by evenly distributing Fe_2O_3 particles and TiO_2 particles on the graphene sheet, and adding it to AP found that, 5% GINC can increase the burning

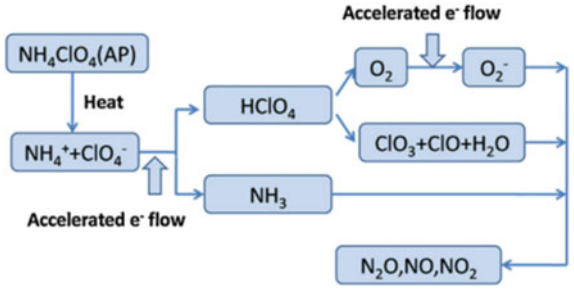

Fig. 34.23 Schematic diagram of the thermal decomposition of AP catalyzed by Fe_2O_3/Gr composite

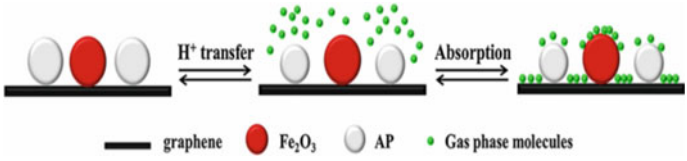

Fig. 34.24 Schematic diagram of the second step thermal decomposition mechanism of GO/Fe_2O_3/AP nano composites

rate of AP-based composites by 52%, 5% GTNC can reduce the decomposition temperature of AP from 412.9 °C to 372.5 °C, and ΔH increases from 2053 J/g to 850 J/g. Figures 34.25 and 34.26 are schematic diagrams of the decomposition mechanism of AP-based compounds after adding GINC and GTNC, respectively.

Zu et al. [57] prepared a $MgFe_2O_4$ nanocomposite coated with GO and mixed it with AP at a mass ratio of 1:4. Through thermal analysis, it is found that the high temperature exothermic peak of the system is reduced by 95.05 °C, the decomposition heat of the system is increased by 876.4 J/g, and the apparent activation energy of the system is reduced by 21.8 kJ/mol. They analyzed the catalytic mechanism and found

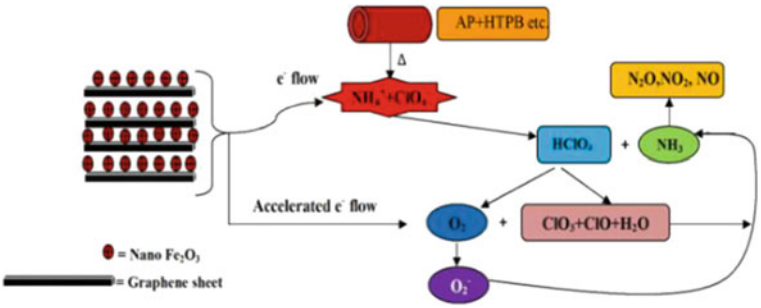

Fig. 34.25 Schematic diagram of the thermal decomposition of AP catalyzed by GINC

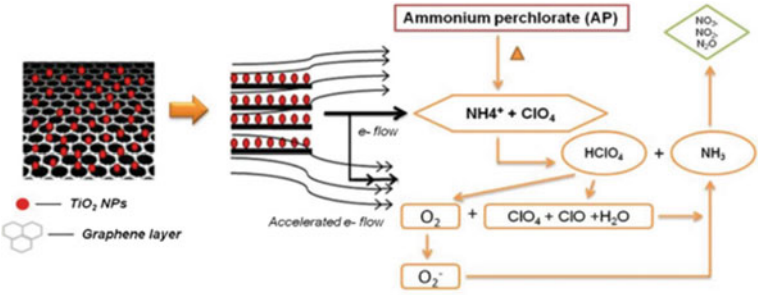

Fig. 34.26 Schematic diagram of GTNC catalyzed AP thermal decomposition

that the role of GO is to reduce the decomposition temperature of AP by increasing the rate of electron transfer in AP from ClO^{4-} to NH^{4+}. Figure 34.27 shows the catalytic mechanism of GO-coated $MgFe_2O_4$ composites.

In summary, graphene-based materials have an obvious catalytic effect on the thermal decomposition of AP. Graphene can increase the apparent heat of decomposition of AP mainly in two ways. On the one hand, graphene acts as a catalyst in the middle, on the other hand, the decomposition products of AP and graphene undergo a combustion reaction to release heat (this also causes the NH_3 adsorbed on AP during the reaction to be resolved in advance and reduces the pyrolysis peak of AP.). In addition, the catalyst composed of graphene-based materials and metal oxides can further amplify the catalytic effect of metal oxides. This is due to the huge specific surface area of graphene-based materials that can effectively disperse metal oxides, allowing them to exert the maximum catalytic effect.

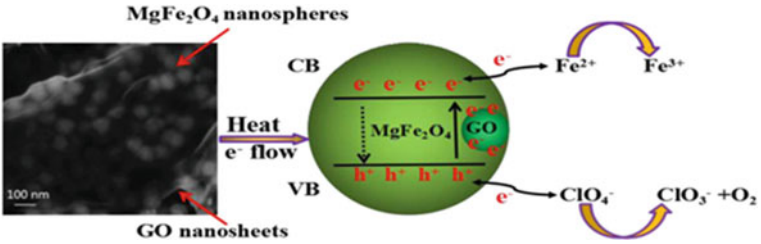

Fig. 34.27 Schematic diagram of the thermocatalytic activity mechanism of GO-coated $MgFe_2O_4$ composite

34.4.3 The Catalysis of Graphene-Based Materials on RDX, HMX and CL-20

Besides AP, researchers have also analyzed the catalytic effects of graphene-based materials on RDX, HMX and CL-20. Relevant research results show that graphene-based materials can significantly catalyze the thermal decomposition of RDX, HMX and CL-20, and greatly increase the heat release of these materials. The graphene-based energetic 5,5'-bistetrazole coordination polymers catalyst developed by Zhang et al. [35] can reduce the endothermic peak of RDX crystal form transformation by 39.54 J/g and increase the heat release by 998.0 J/g. The catalytic mechanism is mainly reflected in three aspects. First, the catalyst will decompose catalytic nano-metal oxides during the reaction. In addition, a large amount of carbon elements formed during the reaction of graphene oxide will also play a role of auxiliary catalysis. Thirdly, the catalyst contains a large number of high-nitrogen ligands, which will also release a large amount of energy during the reaction process to further catalyze the progress of the reaction. The GA/RDX nanocomposite energetic material prepared by Lan et al. [24] can reduce the decomposition peak temperature of RDX by 7.6 °C, and as the amount of GA increases, the decomposition temperature will decrease. This shows that GA can promote the RDX dissociation heat process, which is beneficial to increase the burning rate. In addition, graphene-based materials have a similar catalytic effect on HMX. The introduction of N-GO and rGO into HMX can reduce the apparent activation energy by 30.26 kJ/mol and 5.47 kJ/mol, respectively. And the exothermic decomposition peaks were advanced by 1.2 °C and 0.68 °C, respectively [11]. In addition to increasing the apparent heat release, graphene-based materials can also increase the light sensitivity of explosives. After GO is introduced into CL-20, a 50 W laser can ignite the composite energetic material and generate dazzling light [58] (As shown in Fig. 34.28). This indicates that the addition of GO can catalyze the thermal decomposition of CL-20 and increase the light absorption of the material.

In addition, in order to make up for the lack of self-sustaining combustion of CL-20, Li [30] prepared rGO/CL-20 self-supporting fibrous solid propellant, and used electric soldering iron and a camera to study the combustion performance of

(a)t=0s (b)t=1s (c)t=6s

Fig. 34.28 Laser ignition of CL-20/GO

Fig. 34.29 Self-sustained combustion of composite fiber propellant

composite fibers (As shown in Fig. 34.29). It was found that it can maintain self-sustained combustion, and the burning rate can reach 20.66 mm/s. On the one hand, this is because the addition of rGO can improve the heat transfer performance of CL-20, on the other hand, rGO will also burn and release heat. The synergy of the two is the key to achieving self-sustained combustion of composite fiber propellant.

Graphene-based materials mainly improve the catalytic effect through the following ways. Firstly, graphene-based materials have excellent thermal conductivity and can enhance heat conduction. Secondly, graphene-based materials have a high specific surface area that can absorb many reducing gas phase products and prevent the overflow of reducing gases, so as to ensure that they are fully react in the condensed phase. Thirdly, due to the presence of the graphene-based materials skeleton, the mass transfer distance between the reactants will be greatly shortened. In addition, GO also has good light sensitivity, it can quickly convert the light irradiated on the surface of the sample into heat.

34.4.4 The Catalytic Effect of Graphene-Based Materials on Materials Such as Primary Explosives

For primary explosives, graphene-based materials also have excellent performance. The composite of graphene and lead styphnate (as shown in Fig. 34.30) can increase the outgassing of the system. At 100 °C, pure lead styphnate can only release 0.4 mL/g in 24 h, while GLS containing 2.0% Gr can be decomposed 1.125 mL/g of gas [43]. This shows that graphene can catalyze the thermal decomposition reaction of lead styphnate to some extent.

Yuan et al. [28] synthesized NGO/NC composite materials containing 0.5%, 0.75%, 1.0%, 1.25%, and 1.5% NGO by the solvent-non-solvent method. When the amount is 1%, NGO has the best catalytic effect on NC, and the apparent decomposition heat can reach 2132 J/g, which is 1739 J/g more than pure NC, and with the addition of NGO from 0.5 to 1%, the apparent heat of decomposition of the composite energetic material also increases. However, when NGO exceeds 1.0%, the apparent decomposition heat of energetic materials decreases with the increase of NGO. The analysis suggests that this may be because the O-NO_2 bond energy in NC is relatively weak. When the NC initially decomposes, the O-NO_2 bond breaks

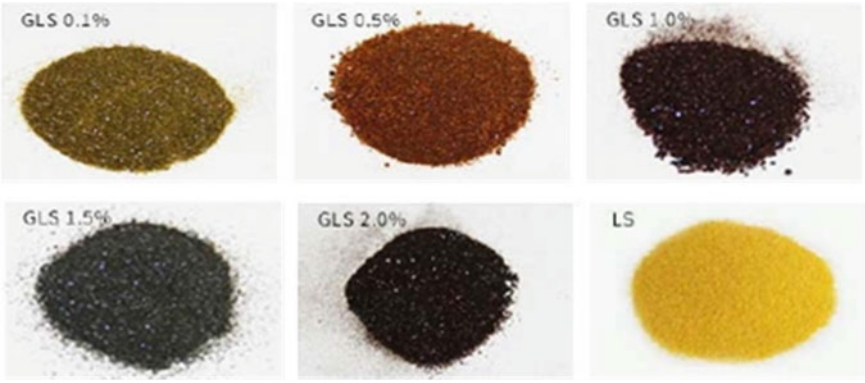

Fig. 34.30 Samples of graphene modified lead styphnate composites with different contents

to generate NO_2. The initial decomposition product further decomposes to form CH_2O, and then CH_2O reacts with NO_2 in turn. In this step of the reaction, the amount of NO_2 produced in the early stage is insufficient, and the addition of NGO can supplement NO_2. However, with the increase of NGOs, there are fewer NCs, and the NO_2 provided by thermal decomposition of NGOs is far less than that provided by NCs. Therefore, there is not enough NO_2 and CH_2O to react, so the apparent decomposition heat of the reaction is reduced.

In addition, graphene-based materials can also increase the burning rate of the unit propellant. Sabourin et al. [59] added functionalized graphene (FGS) to the nitromethane propellant. They found that adding low concentrations of FGS can more than double the linear combustion rate of nitromethane. When the concentration is as low as 0.075wt%, the linear combustion rate is increased by 47%, and the maximum combustion rate is increased by 175%. Figure 34.31 shows the combustion of nitromethane with FGS.

The above studies show that graphene-based materials have a good catalytic effect on energetic materials. On the one hand, the good thermal conductivity of graphene

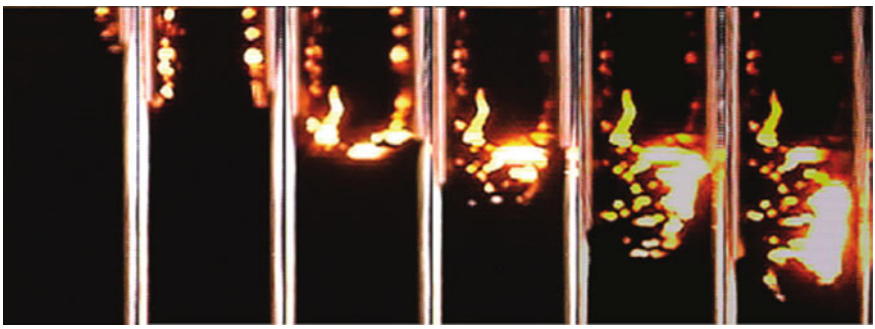

Fig. 34.31 Combustion of nitromethane containing 0.3 wt% FGS

and its derivatives can ensure the stability of combustion during the reaction of high-energy materials. On the other hand, the coating effect of graphene can prevent the leakage of reducing gases, which can ensure that the reactants can fully react in the condensed phase. And graphene and its derivatives can enhance the transfer of electrons in the reaction, thereby accelerating the reaction process (Table 34.3).

34.5 Summary and Outlook

This paper mainly summarizes the preparation methods of graphene-based energetic compounds and the desensitization and catalytic effect of graphene-based materials on energetic materials. Graphene-based materials have broken through people's cognition of conventional nanomaterials. Graphene-based materials have a dual effect on energetic materials. It can not only obtain more stable composite energetic materials, but also catalyze the thermal decomposition process of energetic materials. Therefore, graphene-based materials have huge application prospects in the field of energetic materials. However, there are still some limitations. The following aspects can be the focus of future research:

(1) The preparation method of graphene-based energetic material has a huge influence on the results. The physical combination method is relatively simple, but the stability of the system is poor, and the improvement of thermal decomposition performance is limited. For chemical bonding, although more stable energetic materials can be obtained, it also increases the probability of introducing impurities. Therefore, a simple preparation method which can not only obtain stable energetic system but also avoid the introduction of impurities is urgently needed.

(2) When graphene-based materials are combined with metal materials (such as Fe, Fe_2O_3, TiO_2, etc.), it has an excellent effect on the catalytic thermal decomposition of energetic materials. This is because the metal materials and graphene-based materials form a synergistic effect, showing the catalytic effect of multiple catalysts at the same time. Therefore, graphene/metal composite catalysts should be further studied to further improve the performance of energetic materials.

(3) Different contents of graphene-based materials have different catalytic effects on energetic materials. A trace amount of NGO can increase the decomposition heat of NC, but when the content exceeds 1%, the decomposition heat of NC gradually decreases [28]. Moreover, different graphene-based materials have different catalytic effects on the same energetic materials. Therefore, it is of great significance to find out the optimal ratio of graphene-based materials and energetic materials.

Table 34.3 The catalysis of graphene materials

Author	Author unit	Composite material	Receptor material	Added content	Desensitization effect	Year	Ref
Abhijit Dey	High Energy Materials Laboratory, Pune, India	Gr/Fe_2O_3	AP-based compounds	5%	Burning rate increased by 52%	2014	[33]
Fayang Guan	State Key Laboratory of Explosion Science and Technology, Beijing Institute of Technology	NGO	AP	5%	T_L[a] is decreased by 21 °C; the low-temperature decomposition activation energy is reduced by 13.2 kJ/mol; ΔH[b] is increased by 13%	2020	[10]
Abhijit Dey	High Energy Materials Laboratory, Pune, India	Gr/TiO_2	AP	5%	T_H[c] is decreased by 40.4 °C; ΔH increased by 850 J/g	2015	[34]
Xuebao Wang	School of Materials, Beijing Institute of Technology	GA	AP	5.6%	T_H is decreased by 83.7 °C; ΔH is increased by 1489 J/g	2012	[12]
Xuebao Wang	School of Materials, Beijing Institute of Technology	Gr	AP	10.03%, 7.59%, 5.60%	T_H is decreased by 69.7 °C, 84.2 °C and 83.7 °C; ΔH is increased by 1469 J/g, 1427 J/g and 1489 J/g	2013	[23]
Xuexue Zhang	Northwestern Polytechnical University	GO-Co-DBT	AP	25%	T_H is decreases by 93 °C; ΔH is increases by 969 J/g	2019	[35]
Yuan Yuan	Nanjing University of Science and Technology	Fe_2O_3/Gr	AP	2%	T_H is decreases by 65 °C	2014	[56]

(continued)

Table 34.3 (continued)

Author	Author unit	Composite material	Receptor material	Added content	Desensitization effect	Year	Ref
Jiang Chen	Department of Safety Science and Engineering, Zhejiang University of Technology	EFGO	AP	2.5%, 5.0%, 10%	ΔH is increased by 371 J/g, 1499 J/g and 2693 J/g	2020	[53]
Yuanfei Lan	School of Materials Science and Engineering, Beijing Institute of Technology	Gr/Fe_2O_3	AP	1%, 9%	ΔH is increased by 416 J/g and 1043 J/g	2014	[25]
Yanqing Zu	Northwestern University School of Chemical Engineering	GO/$MgFe_2O_4$	AP	25%	T_H is decreased by 95.05 °C; ΔH is increased by 876.4 J/g; and the apparent activation energy is reduced by 21.8 kJ/mol	2016	[57]
Nasir K. Memon	Purdue University, West Lafayette, Indiana	GO	AP	2%	T_H is decreased by 32 °C	2016	[52]
Xuexue Zhang	Key Laboratory of Combustion, Thermal Structure and Internal Flow Field, Northwestern Polytechnical University	GO-Ni-BT, GO-Co-DHBT	RDX	25%	GO-Ni-BT/RDX system crystal form transition endothermic peak is decreased by 39.54 J/g, GO-Co-DHBT/RDX system exothermic heat is increased by 998.0 J/g	2019	[35]

(continued)

Table 34.3 (continued)

Author	Author unit	Composite material	Receptor material	Added content	Desensitization effect	Year	Ref
Yuanfei Lan	School of Materials Science and Engineering, Beijing Institute of Technology	GA	RDX	13.58%	T_H is decreased by 7.6 °C	2016	[24]
Ting Zhang	Northwest University School of Chemical Engineering	N-GO, rGO	HMX	20%	T_H is decreased by 1.2 °C and 0.68 °C, respectively; the apparent activation energy decreased by 30.26 kJ/mol and 5.47 kJ/mol, respectively	2019	[11]
Jiaying Yu	North University of China	GO	CL-20	8.74%	The initial decomposition temperature is reduced by 23.4 °C	2017	[58]
Xiaodong Li	Institute of Chemical Materials, China Academy of Engineering Physics	rGO	CL-20		Burning rate can reach 20.66 mm/s	2018	[30]
Yin Li	Beijing Institute of Technology	Gr	Lead styphnate	2%	The outgassing volume of the system is increased by 0.725 mL/g	2016	[43]
Justin L. Sabourin	Pennsylvania State University	FGS	Nitromethane Propellant	0.075%	Combustion rate increased by 175%	2009	[59]

[a] T_L is the low temperature decomposition peak of AP
[a] T_H is the high temperature decomposition peak of AP
[c] ΔH is the apparent heat of decomposition

References

1. K.S. Novoselov, A.K. Geim, S.V. Morozov, D. Jiang, Y. Zhang, S.V. Dubonos, I.V. Grigorieva, A.A. Firsov, Electric field effect in atomically thin carbon films. Science **306**, 666–669 (2004)
2. B.Y. Nong, C.W. Lai , Z.B. Liu, B.M. Liang, X.H. Zhang, Study on microstructure and mechanical properties of graphene reinforced aluminum matrix composite. Hot Work. Technol. **46**, 144–146+150 (2017)
3. A.A. Balandin, S. Ghosh, W. Bao, I. Calizo, D. Teweldebrhan, F. Miao, C.N. Lau, Superior thermal conductivity of single-layer graphene. Nano Lett. **8**, 902–907 (2008)
4. M.D. Stoller, S. Park, Y. Zhu, J. An, R.S. Ruoff, Graphene-based ultracapacitors. Nano Lett. **8**, 3498–3502 (2008)
5. C. Lee, X. Wei, J.W. Kysar, J. Hone, Measurement of the elastic properties and intrinsic strength of monolayer graphene. Science **321**, 385–388 (2008)
6. B.Y. Ye, J.Y. Wang, C.W. An, B.S. Yu, W. Ji, H.Q. Li, Preparation and properties of CL-20 based composite energetic material. J. Solid Rocket Technol. **40**, 199–203 (2017)
7. Y.F. Lan, X.Y. Li, Y.J. Luo, Research progress on application of graphene in energetic materials. Chin. J. Explos. Propellants **46** 144–146+150 (2017)
8. C. Niu, B. Jin, R. Peng, Y. Shang, Q. Liu, Preparation and characterization of insensitive HMX/rGO/G composites via in situ reduction of graphene oxide. RSC Adv. **7**, 32275–32281
9. L. Yu, *Investigation on Graphene Functionalized with Energetic Groups Doctor* (Beijing Institute of Technology, 2015)
10. F.Y. Guan, L. Yu, H. Ren, Q.J. Jiao, J. Liu, Synthesis of nitrified graphene oxide and its catalytic activity for ammonium perchlorate decomposition. ACTA ARMAMENTARII **41**, 1323–1329
11. T. Zhang, Y. Guo, Y.Y. Li, Z.Q. Guo, H.X. Ma, Effect of nitrogen-doped graphene oxide on thermal decomposition of HMX. Chin. J. Explos. Propellants **42**, 346–351 (2019)
12. X.B. Wang, J.Q. Li, Y.J. Luo, Preparation and thermal decomposition behaviour of ammonium perchlorate/graphene aerogel nanocomposites. Chin. J. Explos. Propellants **35**, 76–80 (2012)
13. H. Wei, P.J. Liu, G.Q. He, G. Michael, Q.L. Yan, Highly reactive metastable intermixed composites (MICs): preparation and characterization. Adv. Mater. **30**, e1706293 (2018)
14. L. Zhang, J.Y. Huang, Z.H. Xiao, Y. He, K.G. Liu, Z.C. Lx, B.X. Xiang, J.P. Qu, L.B. Kong, Progress in fabrication and growth mechanisms of mullite whiskers. J. Ceram. **41**, 880–893 (2020)
15. K.G. Guo, X.L. Song, Y. Wang, C.L. Liu, Y. Kou, Preparation and characterization of submicron LLM-105 and LLM-105/GO composite energetic materials. Initiat. Pyrotech. 33–7 (2019)
16. B. Ye, C. An, Y. Zhang, C. Song, X. Geng, J. Wang, One-step ball milling preparation of nanoscale CL-20/graphene oxide for significantly reduced particle size and sensitivity. Nanoscale Res. Lett. **13**, 42 (2018)
17. H.Y. Wang, X. Cao, J.L. Wo, Y.B. Xu, Y.P. Shang, Preparetion and thermal decomposition characteristics of TKX-50/GO composit energetic materials. Chin. J. Explos. Propellants **43**, 631–635 (2020)
18. Y.F. Lan, *Investigation on Preparation and Characterization of Graphene-Based Nanocomposites and Their Catalytic Application for Ammonium Perchlorate Doctor* (Beijing Institute of Technology, 2016)
19. T.T. Li, J.K. Li, Y. Hu, Y.H. Ye, R.Q. Shen, Study on preparation and electric exploding performance of Al-CuO/graphene oxide energetic igniting bridge film. Initiat. Pyrotech. 15–9 (2018)
20. Y. Hu, B. Tao, D. Hao, R. Fan, D. Xia, K. Lin, A. Pang, Y. Yang, Fabrication and mechanistic study of AP/nAl/PTFE spherical encapsulated energetic materials with enhanced combustion performance. Chem. Eng. Sci. **222**, 115701
21. T. Zhang, Z. Ma, G. Li, Z. Wang, B. Zhao, Y. Luo, Electrostatic interactions for directed assembly of high performance nanostructured energetic materials of Al/Fe_2O_3/multi-walled carbon nanotube (MWCNT). J. Solid State Chem. **237**, 394–403 (2016)

22. R. Thiruvengadathan, S.W. Chung, S. Basuray, B. Balasubramanian, C.S. Staley, K. Gangopadhyay, S. Gangopadhyay, A versatile self-assembly approach toward high performance nanoenergetic composite using functionalized graphene. Langmuir Acs J. Surf. Colloids **30**, 6556–6564 (2014)
23. X.B. Wang, J.Q. Li, Y.J. Luo, Effect of drying methods on the structure and thermal decomposition behavior of ammonium perchlorate/graphene composites. Acta Phys. Chim. Sin **29**, 2079–2086
24. Y. Lan, X. Wang, Y. Luo, Preparation and characterization of GA/RDX nanostructured energetic composites. Bull. Mater. Sci. **39**, 1701–1707 (2016)
25. Y. Lan, G. Li, X. Li, Sol-gel method to prepare graphene/Fe_2O_3 aerogel and its catalytic application for the thermal decomposition of ammonium perchlorate. Nanotechnol. Wkly. 395 (2015)
26. Y.F. Lan, Y.J. Luo, Preparation and characterization of graphene aerogel/ammonium nitrate nano composite energetic materials. Chin. J. Explos. Propellants **38**, 15–18+38
27. R. Li, J. Wang, P.S. Jin, H. Cheng, G.C. Yang, Preparation and characterization of insensitive HMX/Graphene oxide composites. Propellants Explos. Pyrotech. **38**, 798–804 (2013)
28. S. Yuan, Z.Q. Li, X.H. Duan, Q.P. Luo, X. Liu, C.H. Pei, Preparation and thermal decomposition properties of NGO/NC composite energetic materials. Chin. J. Energ. Mater. **25**, 203–208 (2017)
29. J.K. Li, X.X. Ma, Y. Hu, Y.H. Ye, R.Q. Shen, Preparation and characterization of KNO_3/GO composite energetic materials. Explos. Mater. **45**, 1–5 (2016)
30. X.D. Li, B. Huan, Z.Q. Qiao, J. Chen, G.C. Yang, Combustion characteristic of rGO/CL-20 self-supporting fiber-shaped solid propellant. Chin. J. Energ. Mater. **26**, 1003–1008 (2018)
31. L. Li, J. Gu, D.C. Huang, B.W. Tao, H.S. Wang, Y.F. He, J.J. Hu, Desensitization of aluminum hydride(AlH3) by graphene oxide. J. Solid Rocket Technol. **42**, 66–71 (2019)
32. W. He, J.H. Guo, C.K. Cao, X.K. Liu, J.Y. Lv, S.W. Chen, P.J. Liu, Q.L. Yan, Catalytic reactivity of graphene oxide stabilized transition metal complexes of triaminoguanidine on thermolysis of RDX. J. Phys. Chem. C Nanomater. Interfaces **122**, 14714–14724 (2018)
33. A. Dey, J. Athar, P. Varma, H. Prasant, A. Sikder, S. Chattopadhyay, Graphene-iron oxide nanocomposite (GINC): an efficient catalyst for ammonium perchlorate (AP) decomposition and burn rate enhancer for AP based composite propellant. Rsc Adv. **5**, 723–724
34. A. Dey, V. Nangare, P.V. More, M.A. Shafeeuulla Khan, P.K. Khann, A.K. Sikder, S. Chattopadhyay, Graphene titanium dioxide nanocomposite (GTNC): one pot green synthesis and its application in solid rocket propellant. Rsc Adv. **5**, 63777–63785 (2015)
35. X.X. Zhang, J.Y. Lu, W. He, S.W. Chen, Z.J. Yang, Q.L. Yan, Graphene-templated energetic 5, 5′-Bistetrazole coordination polymers and their catalytic effects on thermal decomposition of RDX and AP. Chin. J. Energ. Mater. **27**, 749–758 (2019)
36. J.J. Wang, *In situ Preparation and Properties of MgWO4-GO and Cu-Co/GO Composites* Master (Northwest University, 2020)
37. X.L. Jia, C.H. Hou, J.Y. Wang, Y.X. Tan, Y.P. Zhang, C. Li, Research progress on the desensitization technology of nitramine explosives. Chin. J. Explos. Propellants **41**, 326–333 (2018)
38. C.Y. Zhou, C.J. Tang, S.X. Wu, J. Gu, Z.Y. Li, N. Yao, Combustion and agglomeration behavior of graphene-coated aluminum powder in HTPB propellant. J. Solid Rocket Technol. **43**, 38–44 (2020)
39. C.H. Niu, *The Research of Insensitive Performance forCL-20 and HMX with Carbon Nanomaterials* Master (Southwest University of Science and Technology, 2018)
40. B.Y. Ye, *Study on the Construction and Basic Application of Graphene Materials Modified Energetic Composites Doctor* (North University of China, 2018)
41. Z.H. Jin, *Comparative Research on Properties of the HNIW Modified by Nano-carbon Materials Master* (BeiJing Institute of Technology, 2016)
42. Z. Li, Y. Wang, Y. Zhang, L. Liu, S. Zhang, CL-20 hosted in graphene foam as a high energy material with low sensitivity. Rsc Adv. **5**, 98925–98928

43. Y. Li, *Studies on Lead Styphnate Modified by the New Nano-carbon Materials in Thermal Analysis Master* (Beijing Institute of Technology, 2016)
44. Q. Wang, J. Liu, H. Ren, Q.J. Jiao, Effect of reduced graphene oxide on the impact sensitivity and electrostatic sensitivity of B/KNO_3 ignition powder. Chin. J. Energ. Mater. **26**, 875–880 (2018)
45. Z.H. Wang, *Study on Nomenclature and Properties of B·KNO_3 Ignition Doped with Carbon Nanomaterials Master* (China Academy of Engineering Physics, 2019)
46. T.T. Li, *Research on Carbon based Nano CU(N3)2 Composite Energetic Materials Master* (Nanjing University of Science & Technology, 2018)
47. S. Isert, L. Xin, J. Xie, S.F. Son, The effect of decorated graphene addition on the burning rate of ammonium perchlorate composite propellants. Combust. Flame **183**, 322–329 (2017)
48. P. Ye, Y.F. Lu, P.F. Xu, X. Hu, J.X. He, Q. Wang, C.P. Guo, Preraration of $CoFe_2O_4$@C nano-composites and their catalytic performance for the thermal decomposition of ammonium perchlorate. Chin. J. Explos. Propellants **42**, 358–362 (2019)
49. J. Cheng, Y. Zheng, Z. Li, Z. Liu, L. Li, F. Zhao, S. Xu, Catalytic reaction of ammonium perchlorate with energetic cobalt complex of 2,6-diamino-3,5-dinitropyrazine-1-oxide during thermal decomposition process. J. Therm. Anal. Calorim. **129**, 1875–1885 (2017)
50. V.V. Boldyrev, Thermal decomposition of ammonium perchlorate. Thermochim. Acta **443**, 1–36 (2006)
51. L. Mallick, S. Kumar, A. Chowdhury, Thermal decomposition of ammonium perchlorate—A TGA–FTIR–MS study: Part I. Thermochim. Acta **610**, 57–68 (2015)
52. N.K. Memon, A.W. McBain, S.F. Son, Graphene oxide/ammonium perchlorate composite material for use in solid propellants. J. Propuls. Power **32**(2016)
53. J. Cheng, X.Y. Shen, R. Wang, R.X. Zhang, Z.L. Liu, Y.G. Hao, H.P. Su, Preparation and thermal decomposition behavior of energetic functionalized graphene oxide and its catalytic effect on the thermal decomposition of AP. Chin. J. Explos. Propellants **43**, 180–187 (2020)
54. M. Zhang, F.Q. Zhao, Y.J. Yang, W.G. Qu, N. Li, J.K. Zhang, Advances in the effects of graphene based materials on properties of energetic materials. Chin. J. Energ. Mater. **26**, 1074–1082 (2018)
55. N. Li, Z. Geng, M. Cao, L. Ren, X. Zhao, B. Liu, Y. Tian, C. Hu, Well-dispersed ultrafine Mn_3O_4 nanoparticles on graphene as a promising catalyst for the thermal decomposition of ammonium perchlorate. Carbon **55**, 124–32 (2013)
56. Y. Yuan, W. Jiang, Y. Wang, P. Shen, F. Li, P. Li, F. Zhao, H. Gao, Hydrothermal preparation of Fe_2O_3/graphene nanocomposite and its enhanced catalytic activity on the thermal decomposition of ammonium perchlorate. Appl. Surf. Sci. **303**, 354–359 (2014)
57. Y. Zu, Y. Zhao, K. Xu, T. Yao, F. Zhao, Preparation and comparison of catalytic performance for nano $MgFe_2O_4$, GO-loaded $MgFe_2O_4$ and GO-coated $MgFe_2O_4$ nanocomposites. Ceram. Int. **42**, 1–7 (2016)
58. J.Y. Yu, J.H. Wang, Y.C. Liu, Y.W. Yu, J.M. Yuan, S.M. Jing, Preparation and thermal properties of CL-20/GO nano-composite energetic materials. Sci. Technol. Eng. **17**, 93–96 (2017)
59. J.L. Sabourin, D.M. Dabbs, R.A. Yetter, F.L. Dryer, I.A. Aksay, Functionalized graphene sheet colloids for enhanced fuel/propellant combustion. ACS Nano **3**, 3945 (2009)

Chapter 35
A New Insight of Carbon Blacks and Burning Catalysts in Composite Modified Double Base Propellant

Xi Zhang, Xiaojiang Li, Zhi Ren, Jing Chen, Meng Liu, and Xiong-Gang Wu

Abstract The synergistic effect between carbon blacks and burning catalysts (CuO and PbO) in composite modified double base (CMDB) propellant is detailed studied in this work. It was found that CuO is much easier to adsorb on carbon blacks compared with PbO. On the contrary, PbO is prone to adsorb on nitrocellulose. The addition of carbon blacks makes CuO and PbO lie in the "right place" where they have a higher catalytic capability, leading to better combustion properties. Besides, four kinds of carbon blacks were detailed characterized from their aggregation states to chemical structures and combustion properties of CMDB propellants with these carbon blakcs were systematically studied. It was found that carbon blacks with smaller aggregations and lower disorder degrees lead to a stronger synergistic effect between carbon blacks and burning catalysts. At last, CMDB propellants with controlled combustion properties were obtained by adjusting the kinds and contents of carbon blacks used in them.

Supplementary Information The online version contains supplementary material available at (https://doi.org/10.1007/978-981-19-1774-5_35).

X. Zhang · X. Li (✉) · Z. Ren · J. Chen · M. Liu · X.-G. Wu
Xi'an Modern Chemistry Research Institute, Xi'an 710065, PR China
e-mail: xiaojianglee@sohu.com

X. Zhang
e-mail: zhangxi1992@zju.edu.cn

Z. Ren
e-mail: rz3258@foxmail.com

J. Chen
e-mail: chenjing_mcri@163.com

M. Liu
e-mail: lm30320701@126.com

X.-G. Wu
e-mail: wuxionggang6868@163.com

A. Gany and X. Fu (eds.), *2021 International Conference on Development and Application of Carbon Nanomaterials in Energetic Materials*, Springer Proceedings in Physics 276,
https://doi.org/10.1007/978-981-19-1774-5_35

35.1 Introduction

Composite modified double base (CMDB) propellants are important power sources for missiles and space vehicles [1–3]. There are several physical chemical properties for CMDB propellants to control according to the using requirements, such as mechanical properties, safety properties, energy properties and combustion properties, Pradhan, Kalal and Li et al. [2, 4–6]. Among these commanding properties, combustion properties, including burning rate and pressure exponent, are of great importance for ballistic performances of missile motors [7–9]. Generally speaking, researchers aim to obtain CMDB propellants with high burning rates and low pressure exponents [10–12].

Most CMDB propellants contain large amounts of hexahydro-1,3,5-trinitro-1,3,5-triazine (RDX) in formulations to promote their energy properties [2, 13]. However, CMDB propellants with such formulations suffer from the problem of relatively low burning rates and high pressure exponents [13–15]. Adding carbon blacks into CMDB propellants is an effective way to address this issue [16, 17]. For example, Preckel et al. have reported the addition of carbon blacks can improve the burning rate sharply and reduce the pressure exponent, leading to the plateau burning of propellants [16]. Same results were also reported by Pande and Hewkin, which further confirm the carbon black is beneficial for the combustion properties of CMDB propellants [18, 19]. Apart from that, it was found other kinds of carbon materials can also improve burning rates while reduce pressure exponents of CMDB propellants [17]. Ren and co-workers prepared carbon nanotube composite catalysts and studied their catalytic capabilities on thermal decomposition of RDX [20]. C60 and fullerene were used as additives in CMDB propellants to achieve plateau combustions by Zhao's group [17, 21]. Moreover, graphene can also enhance the catalytic activity of burning catalysts [22, 23]. Although the benefits of using carbon materials in propellants have been widely reported, there still lack of systematic studies for the influences of carbon blacks on combustion properties of CMDB propellants. For example, there are many different kinds of carbon blacks, which have different aggregation states and chemical structures [24]. But few literature reports the effects of the kinds of carbon blacks on the combustion properties of CMDB propellants.

Commonly, burning catalysts of CMDB propellants are composed of copper (Cu) and lead (Pb) complexes [20, 25, 26]. Researchers believe the addition of carbon blacks can form Cu–Pb–C composite catalysts, leading to the synergistic effect between carbon blacks and burning catalysts [20, 26]. Several theories were developed to explain the mechanisms of such synergistic effect. For example, Denisyuk et al. think that the carbon black will prevent the aggregation of CuO and PbO during the combustion process, making the burning catalysts near the combustion surface [27, 28]. Powling and co-workers consider the carbon black can accelerate the reduction of NO during the combustion process because the burning catalysts were activated by the carbon black [19]. However, these theories were based on macroscopic experimental results, such as images of combustion surface, changes of burning rates and pressure exponents, et al. A deep understanding is still needed for

the synergistic effects between carbon blacks and burning catalysts from microscopic insights.

In this work, we systematically studied the influences of carbon blacks on combustion properties of CMDB propellants. First, the synergistic effect between carbon blacks and burning catalysts was detailed analyzed. Distributions of burning catalysts (CuO and PbO) in CMDB propellants were characterized. It was found CuO is more likely to adsorb on carbon blacks compared with PbO. On the other hand, PbO is much easier to adsorb on nitrocellulose compared with CuO. Such hypothesis was confirmed by the calculation of adsorption energies between CuO, PbO and carbon blacks, nitrocellulose, respectively. We suspect such non-uniform distributions of CuO and PbO in CMDB propellants maybe the reason for the synergistic effect between carbon blacks and burning catalysts. After that, we detailed investigated the factors of carbon black which influence the combustion properties, such as the kinds, contents and grinding time of carbon blacks used in CMDB propellants and CMDB propellants with controlled combustion properties were obtained.

35.2 Experiments

35.2.1 Materials

Four different kinds of carbon blacks (CB_1, CB_2, CB_3 and CB_4) were purchased from Shanghai Jiaohua chemical industry *Co. Ltd.*, China. All the carbon blacks were chemical pure (CP). The detailed parameters of carbon blacks are listed in Table 35.1. Copper oxide (CuO, CP) and lead oxide (PbO, CP) were bought from Shanxi Boao chemical industry *CO. Ltd.*, China. Nitrocellulose (NC) and nitroglycerine (NG) were provided by Yibin North Chuan'an Chemical Industry *Co. Ltd.*, China. RDX was provided by Liaoning Qingyang Special Chemicals *Co. Ltd.*, China. Other reagents, such as acetone (Analytical Pure, AP), ethanol (AP) and additives, were all bought from Sinopharm Group *Co. Ltd.*, China. All the chemicals were used as received without further purification.

Table 35.1 The parameters of carbon blacks

Carbon black	Reflectivity (%)	Volatile matter (%)	Ash content (%)
CB_1	14	14.9	0.14
CB_2	12	13.0	0.10
CB_3	13	15.1	0.09
CB_4	15	13.3	0.16

35.2.2 Preparation of Samples

Carbon blacks and burning catalysts (CuO and PbO) were ground with desired time (0, 5, 10, 20, 30 min) with an industrial colloid mill to prepare composite burning catalysts.

35.2.3 Characterization of Carbon Blacks and Burning Catalysts

Surface morphologies of carbon blacks were characterized by a scanning electron microscopy (SEM, FEI, Quanta 600, America). Each sample was sputtering with platinum for 60 s by an ion sputtering instrument before characterized in the SEM. A transmission electron microscope (TEM, Thermo Fisher, Talos F200i, America) was used to observe the aggregation states of carbon blacks. The TEM was equipped with an energy dispersive spectrometer (EDS, Bruker, Quantax, German) and used for the elemental analysis of samples. A raman spectroscopy (Renishaw, inVia, UK) was used to characterize the chemical structures of carbon blacks. The raman spectra were excited by a laser source with the wave number of 785 nm and the power output was limited to less than 250 mW for the duration of the tests. At least 3 points were used for one sample in the raman test to make the results reliable. The intervals among each points are more than 300 μm.

35.2.4 Fabrication of the CMDB Propellants

The CMDB propellant with a desired formulation was fabricated by a granule casting method. In details, the granule casting method can be divided into two main processes: the pelletized process and casting process. Most energetic materials were added into the granules in the pelletized process and well defined small granules were prepared. After that, the granules were used for casting process to fabricate the CMDB propellant. The as prepared CMDB propellant was then treated with a certain temperature for post reaction.

35.2.5 Burning Rate Tests

The burning rates were measured by a strand burner method with the pressure ranged from 6 to 22 MPa and at room temperature. The burning rate can be calculated by Eq. 35.1, where u, b, P and n are burning rate, empirical constant, pressure and pressure exponent.

$$u = b \times P^n \tag{35.1}$$

Taking the logarithm of both sides of Eq. 35.1, we can obtain Eq. 35.2. Thus the pressure exponent can be considered as the slope of the logarithm of pressure.

$$\log u = n \times \log P + \log b \tag{35.2}$$

35.2.6 Calculation of Adsorption Energies

The adsorption energies between carbon black, nitrocellulose and burning catalysts were calculated by Materials Studio (V8.0). Models constructed for each chemicals were firstly optimized to eliminate the unreasonable conformations. Then they were used in adsorption simulations to obtain the energy changes during the adsorption processes.

35.3 Results and Discussion

35.3.1 The Synergistic Effect Between Carbon Blacks and Burning Catalysts

It has been reported that carbon blacks, combined with CuO and PbO, exhibit significant synergistic effects on the combustion properties of CMDB propellants [16–18]. Therefore, we measured the burning rates and pressure exponents of CMDB propellants with CuO, PbO and composite catalysts (CuO-CB_1, PbO-CB_1 and CuO-PbO-CB_1) as burning catalysts, respectively. The contents of these catalysts in the formulations of CMDB propellants are listed in Table 35.2.

As shown in Fig. 35.1a, $1^{\#}$ propellant shows burning rates from 7.24 to 18.66 mm/s

Table 35.2 The contents of CuO, PbO and CB_1 in CMDB propellants

Propellant number	CuO content (%)	PbO content (%)	CB_1 content (%)
$1^{\#}$	0.0	0.0	0.0
$2^{\#}$	0.9	0.0	0.0
$3^{\#}$	0.0	2.7	0.0
$4^{\#}$	0.9	0.0	0.9
$5^{\#}$	0.0	2.7	0.9
$6^{\#}$	0.9	2.7	0.9

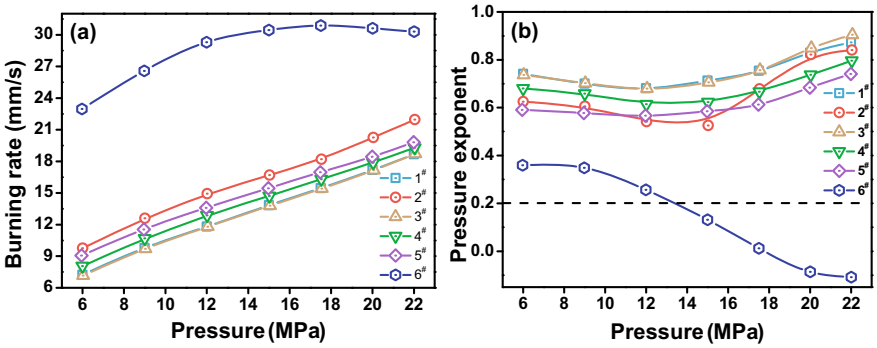

Fig. 35.1 **a** Burning rates and **b** pressure exponents of CMDB propellants with different kinds of burning catalysts

in the pressure range of 6–22 MPa. It should be noticed that there is no burning catalyst in 1# propellant. In 2# and 3# propellants, CuO and PbO were added as burning catalysts individually. However, the combustion properites, including burning rates and pressure exponents, exhibit no obvious difference between these two (2#, 3#) propellants and 1# propellant. Similar results also appeared for the 4# and 5# propellants, which used CuO-CB_1 and PbO-CB_1 as composite burning catalysts. On the contrary, 6# propellant exhibits much higher burning rates compared with 1#–5# in the pressure range of 6–22 MPa. As for pressure exponents, 6# propellant shows pressure exponents smaller than 0.2 in the pressure range of 15–22 MPa, which is to say the plateau burning phenomenon occurs in the high pressure region. For the meanwhile, other propellants (1#–5#) all show pressure exponents higher than 0.55 (Fig. 1b). All these results indicate that only the composite catalyst of CuO-PbO-CB_1 can effectively increase the burning rates and reduce the pressure exponents of CMBD propellants, leading to the plateau burning phenomenon at high pressure range.

TEM-EDS was used to characterize element compositions of the CuO-PbO-CB_1 composite catalyst. The grinding time is 20 min and the molar ratio of CuO:PbO used for grinding is 1:1.08 for CuO-PbO-CB_1 composite catalyst samples. Three individual CuO-PbO-CB_1 composite catalyst samples were used for the characterizations to make the results convinced. As shown in Fig. 2a–c, the composite catalyst exhibits a particle size ranged of 300–500 nm while CuO and PbO adsorb on CB_1 (gray region was CB_1 and light part was CuO and PbO in TEM images). Interestingly, it seems that there are much more CuO than PbO on the CB_1 substrate according to Fig. 2d–f. The elemental compositions of the composite catalyst were further calculated by the TEM-EDS results. Table 35.3 demonstrates the content of Cu ranges from 81 to 87% in the composite catalyst, while it only ranges from 13 to 19% for Pb in the composite catalyst. Such results are very different to the element compositions used for preparing samples, which have the molar ratio of 1:1.08 for Cu:Pb. This amazing phenomenon indicates there are much more CuO adsorb on carbon blacks

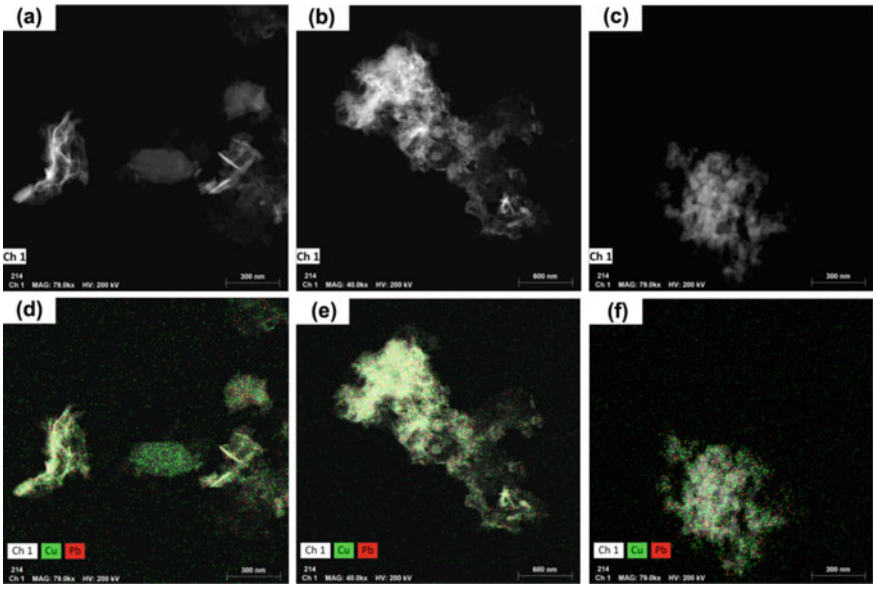

Fig. 35.2 **a–c** TEM images and **d–f** TEM-EDS analysis of CuO-PbO-CB_1 composite catalyst

Table 35.3 Pb, Cu contents (molar ratio) of CuO-PbO-CB_1 composite catalyst analyzed by TEM-EDS

Sample number	Sample-1	Sample-2	Sample-3	Average
Cu content (%)	83.91	81.61	86.50	84.01
Pb content (%)	16.09	18.39	13.50	15.99

rather than PbO, which may lead to a non-uniform distribution of burning catalysts in CMDB propellants.

We suspect the non-uniform distribution of burning catalysts in CMDB propellants may be the reason for the synergistic effect between carbon blacks and burning catalysts. Therefore, detailed studies were done for a deep understanding for the distribution of burning catalysts in CMDB propellants. First, adsorption energies between carbon black and CuO, PbO were calculated by Materials Studio (V8.0). The carbon black was considered as the combination of several micro crystals of graphite cells in the simulation. As shown in the left red region of Fig. 35.3, the adsorption energy between CuO and carbon black is −13 kcal/mol, while it is as high as 1378 kcal/mol for PbO and carbon black. In other words, CuO is prone to adsorb on carbon black since the adsorption energy is below 0. On the contrary, it is very difficult for PbO to adsorb on carbon black because the adsorption energy is much higher than 0. Such results fit well with the elemental analysis mentioned above, which indicate there are much more CuO adsorb on carbon black compared with PbO.

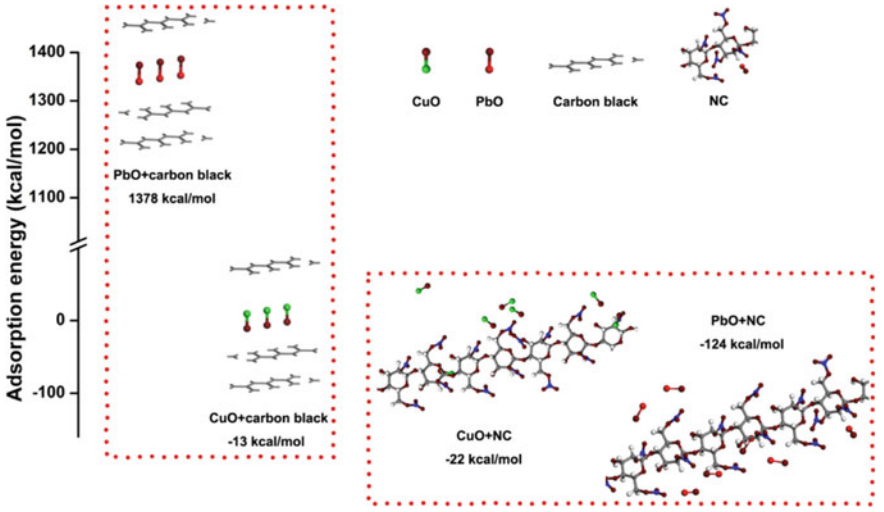

Fig. 35.3 Adsorption energies between CuO, PbO and carbon black, NC, respectively

Then there comes out another problem, where does the PbO come to? Notice that NC is acted as the bone in CMDB propellants, we suppose the burning catalysts, such as CuO and PbO, will also adsorb on NC. Thus, adsorption energies between NC and burning catalysts were calculated. In this part, 24 repeat units were used for one NC polymer chain to simplify the calculation. The right red region of Fig. 35.3 presents the adsorption energies, which are −22, −124 kcal/mol for NC and CuO, NC and PbO, respectively. It can be found PbO is easier to adsorb on NC than CuO since its adsorption energy is much lower. These calculation results imply CuO has the trend to adsorb on carbon blacks while PbO prefers to adsorb on NC in CMDB propellants. According to the elemental analysis and calculated adsorption energies, we can conclude the burning catalysts are non-uniformly distributed in CMDB propellants, for which CuO mainly adsorbs on carbon blacks and PbO mainly adsorbs on NC. Amazingly, it has been reported CuO has high catalytic activity for the decomposition of small moleculars and PbO has high catalytic activity for the decomposition of nitrogen ester [29–31]. Thus, we can conclude the addition of carbon black leads the burning catalysts (CuO and PbO) to adsorb on different places in CMDB propellants. Such a non-uniform distribution of burning catalysts makes them exhibit a better catalyst activity at correct places, resulting to the improved burning rates of CMDB propellants. Moreover, increased catalyst capability makes the burning rates reach to a maximum value at a much lower pressure compared with the CMDB propellants without the addition of carbon blacks. Therefore, the plateau burning phenomenon occurs at the high pressure region.

35.3.2 *Influences of Carbon Blacks on Combustion Properties*

We further investigated the influences of carbon blacks on combustion properties of CMDB propellants. At first, four different kinds of carbon blacks were ground with CuO and PbO to prepare composite catalysts. These carbon blacks were signed as CB_1, CB_2, CB_3 and CB_4, respectively. Figure 35.4 demonstrates different kinds of carbon blacks will lead to different combustion properties of CMDB propellants. CMDB propellant with CB_1 shows the highest burning rates compared with other carbon blacks (Fig. 4a) in the pressure region of 6–22 MPa. On the other hand, CMDB propellants with CB_2 and CB_3 have lower pressure exponents than CMDB propellants with CB_1 and CB_4 in low pressure region (6–13 MPa). Nevertheless, CMDB propellant with CB_1 exhibits the lowest exponents (less than 0.2) in the pressure region of 15–22 MPa (Fig. 4b). Thus, we can conclude CB_1 is the most suitable carbon black since CMDB propellant with CB_1 has the highest burning rate and shows a burning plateau in the high pressure region.

Although these four kinds of carbon blacks have different effects on combustion properties, their physical parameters (reflectivity, volatile and ash content) are nearly the same (Table 35.1 in experimental section). Thus, it is necessary to characterize the morphologies and chemical structures of these carbon blacks to determine the reason for their different effects on combustion properties. All these carbon blacks are aggregations of small particles with a radius of 10–50 nm (Figure S1 in supporting information). However, the aggregation states are very different. As presented in Fig. 35.5, aggregations of CB1 are around 100 nm in size, which are 400–600 nm for CB2, CB3 and CB4, respectively. Interestingly, the burning rates obey the order of CMDB propellants with CB1 > CB2 > CB3 > CB4. It seems carbon blacks with smaller aggregations can improve burning rates more effectively. As mentioned above, the addition of carbon blacks will make the CuO and PbO adsorb on different

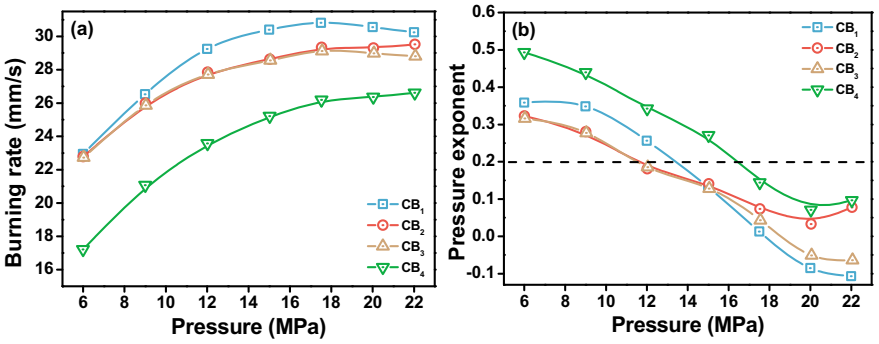

Fig. 35.4 **a** Burning rates and **b** pressure exponents of CMDB propellants with different kinds of carbon blacks in composite burning catalysts. (Contents of carbon black, CuO and PbO are 0.9, 0.9 and 2.7%, respectively.)

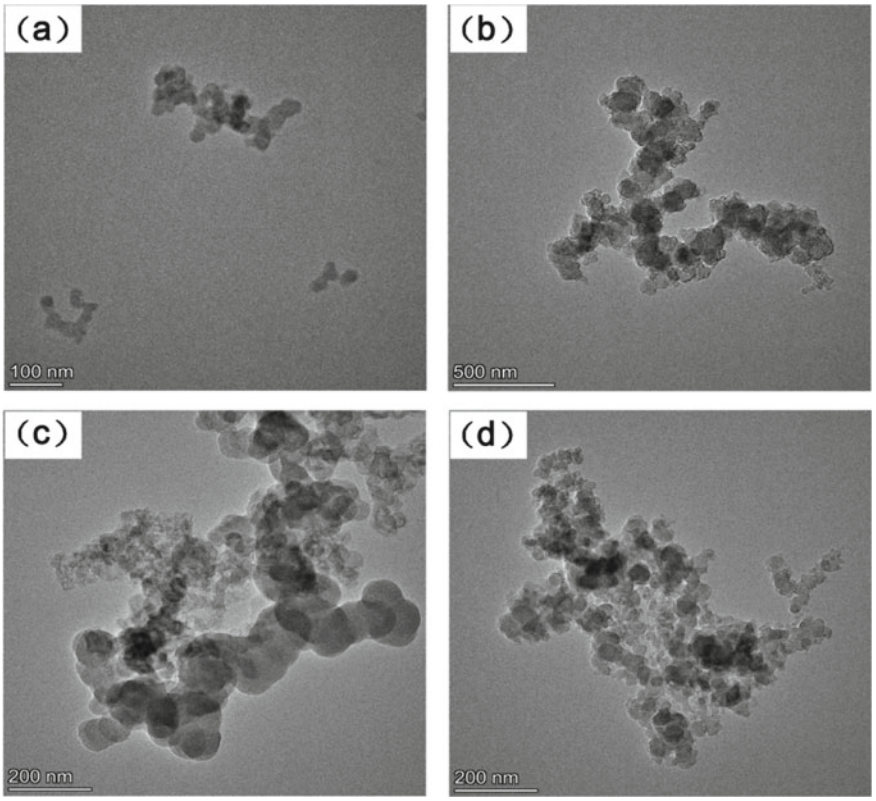

Fig. 35.5 TEM images of **a** CB_1, **b** CB_2, **c** CB_3 and **d** CB_4 after grinding for 20 min

places of CMDB propellants, leading to a non-uniform distribution of burning catalysts. Smaller aggregations of carbon blacks have higher specific surface areas, which are beneficial to the non-uniform distribution of burning catalysts. Thus they exhibit a stronger synergistic effect.

It should be noted the aggregations of CB_2, CB_3 and CB_4 have similar sizes as shown in Fig. 35.5, but their influences on combustion properties are quite different either. Therefore, chemical structures of carbon blacks were also characterized by a raman spectroscopy to further illustrate the differences among these carbon blacks. Figure 35.6 presents the raman spectra of these carbon blacks. D-band and G-band appeared at 1340 and 1580 cm^{-1} in these spectra, which represented for the defects and regularities of graphite cells. As widely known, carbon black are composed of micro crystals of graphite cells [24], thus ratios of D-band to G-band can reflect disorder degrees of carbon blacks. The ratios are 0.93, 0.94, 1.05 and 1.25 for CB_1, CB_2, CB_3 and CB_4, respectively (table S1 in supporting information). Compared CB_2, CB_3 and CB_4, the sizes of their aggregations are nearly the same but their disorder degrees are very different. According to Figs. 35.4 and 35.6, it is obvious

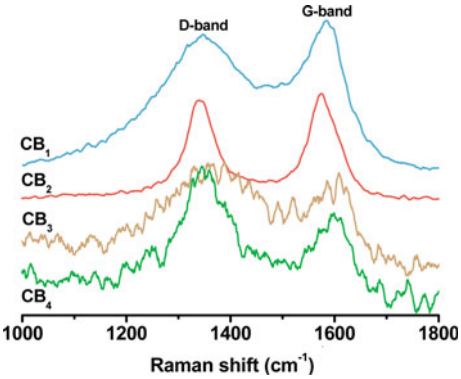

Fig. 35.6 Raman spectra for CB_1, CB_2, CB_3 and CB_4, respectively

higher disorder degrees of carbon blacks will cause lower burning rates and higher pressure exponents. Van der Waals force is the main interaction for the adsorption process of burning catalysts on carbon blacks and nitrocellulose. Increased regularity of carbon blacks leads to increased Van de Waals force for the adsorption process. Therefore, carbon blacks with higher regularities have stronger adsorption capabilities, benefiting to the non-uniform distribution of burning catalysts and resulting in better combustion properties of CMDB propellants.

Moreover, both the optimum contents and grinding time of carbon blacks were determined to obtain CMDB propellants with desired combustion properties. In this part, CB_1 was used as the model since CMDB propellants with CB_1 exhibit the best combustion properties. Figure 7a demonstrates the burning rates increase with the increasing of CB_1 content used in CMDB propellants. The burning rates are up to 30 mm/s at the pressure region of 16–22 MPa when the CB_1 content is higher than 0.9%. On the other hand, pressure exponents decrease when the CB_1 content increases at the pressure region of 15–22 MPa, and the plateau burning phenomenon occurs

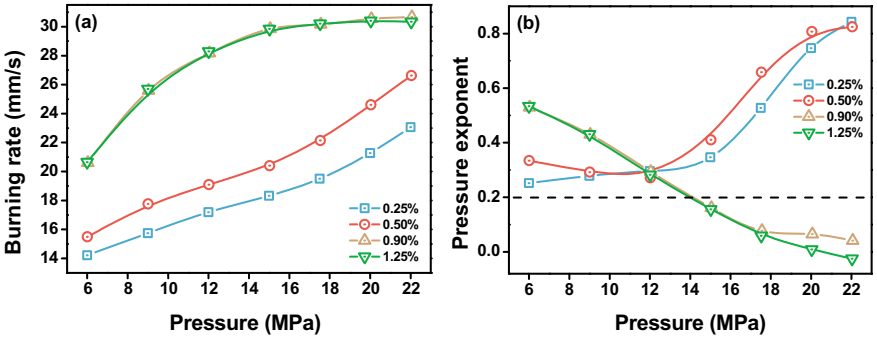

Fig. 35.7 **a** Burning rates and **b** pressure exponents of CMDB propellants with different contents of CB_1 (Contents of CuO and PbO are 0.9 and 2.7%, respectively)

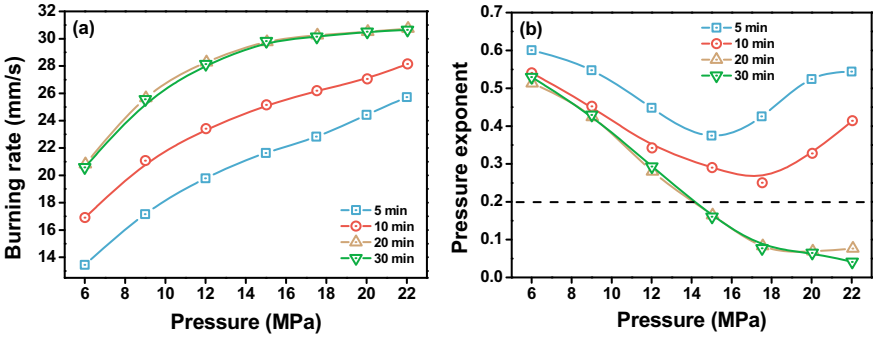

Fig. 35.8 **a** Burning rates and **b** pressure exponents of CMDB propellants with CB_1 in composite burning catalysts for different grinding times (Contents of CB_1, CuO and PbO are 0.9, 0.9 and 2.7%, respectively)

when CB_1 content is above 0.9% (Fig. 7b). However, the combustion properties show slight changes when the CB_1 content is higher than 0.9%.

Grinding time of carbon blacks is another key parameter which influences combustion properties of CMDB propellants. The aggregations of carbon blacks exhibit a very big size without grinding before use (Figure S1 in supporting information), while the sizes of aggregations become 100–600 nm after grinding for 20 min (Fig. 35.5). As a consequence, the burning rates of CMDB propellants increase along with the grinding time (Fig. 8a). At the same time, pressure exponents decrease with the increasing of grinding time (Fig. 8b). As mentioned above, a smaller size of carbon black aggregations is beneficial for the non-uniform distribution of CuO and PbO in CMDB propellants, leading to better combustion properties. However, the burning rates and pressure exponents are nearly the same when grinding time is higher than 20 min, which can be ascribed to the size of carbon black aggregations cannot be further reduced by longing the grinding time.

35.4 Conclusion

The synergistic effect between carbon blacks and burning catalysts is detailed studied in this work. The burning rates can be greatly improved and a burning plateau occurs at the high pressure region (15–22 MPa) by adding carbon blacks into CMDB propellants. Then mechanisms of such synergistic effect were studied by both elemental analysis and molecular simulations. We found the addition of carbon blacks will make CuO and PbO adsorb on different places of CMDB propellants, making them exhibit better catalyst capabilities at correct places. Furthermore, the factors of carbon blacks were investigated to obtain CMDB propellants with desired combustion properties. In detail, we analyzed the aggregation state, regularity, content and grinding time

of carbon blacks used in CMDB propellants to find their influences on combustion properties.

References

1. Q. Tang, X. Fan, J. Li, F. Bi, X. Fu, L. Zhai, Experimental and theoretical studies on stability of new stabilizers for N-methyl-P-nitroaniline derivative in CMDB propellants 2017. J. Hazard. Materi. **327**, 187–196
2. S.K. Pradhan, V. Kedia, P. Kour, Review on different materials and their characterization as rocket propellant 2020. Mater. Today: Proc. **33**, 5269–5572
3. Z. Wu, N. Liu, W. Zheng, J. Chen, X. Song, J. Wang, C. Cui, D. Zhang, F. Zhao, Application and properties of CL-20/HMX cocrystal in composite modified double base propellants. Propellants Explos Pyrotech. **45**, 92–100 (2020)
4. R.K. Kalal, S.K. Jangid, H. Shekhar, P.S. Alegaonkar, A. Kumar, Thermo-physical properties and combustion wave aspects of RDX contain low aluminium composite propellant. Combust. Flame **218**, 12–17 (2020)
5. F. Zhang, D. Zhu, Q. Liu, Z. Liu, P. Du, Study on the effect of RDX content on the properties of nitramine propellant. Def. Technol. **13**, 246–248 (2017)
6. J. Li, Q. Jiao, H. Ren, Safety analysis on truing process of solid propellant. Def. Technol. **14**, 612–615 (2018)
7. R.W. Armstrong, B. Baschung, D.W. Booth, M. Samirant, Enhanced propellant combustion with nanoparticles. Nano Lett. **3**, 253–255 (2003)
8. L. Xiao, X. Fan, J. Li, Z. Qin, X. Fu, W. Pang, Y. Wang, Effect of Al content and particle size on the combustion of HMX-CMDB propellant. Combust. Flame **214**, 80–89 (2020)
9. S. Liu, J. Li, G. Zhu, W. Wang, Y. Liu, Mixing and combustion enhancement of turbocharged solid propellant ramjet. ACTA Astronaut. **143**, 193–202 (2018)
10. X. Guo, F. Li, H. Song, G. Liu, L. Kong, M. Li, Combustion characteristics of a novel grain-binding high burning rate propellant. Propellants Explos. Pyrotech. **33**, 255–260 (2008)
11. X. Guo, F. Li, J. Liang, W. Jiang, L. Zhao, The influence of spherical granular propellants on the combustion properties of high-burning-rate propellant. Int. J. Energ. Mater. Ch. **9**, 467–476 (2010)
12. A.E.D.M. Heijden, A.B. Leeuwenburgh, HNF/HTPB propellants: influence of HNF particle size on ballistic properties. Combust. Flame **156**, 1359–1364 (2009)
13. H. Singh, J. Upadhyay, D. Chimurkar, V. Ghorpade, A. Kotbagi, A. Kumar, M. Gupta, Comparative studies of pressure sensitization of zirconium carbide and zirconium silicate on burning rates in a RDX-AP based composite propellant. Propellants Explos. Pyrotech. **39**, 180–184 (2014)
14. B. Wang, X. Liao, Z. Wang, L.T. DeLuca, Z. Liu, Y. Fu, Preparation and properties of a nRDX-based propellant. Propellants Explos. Pyrotech. **42**, 649–658 (2017)
15. L. De Luca, F. Cozzi, G. Germiniasi, I. Ley, A.A. Zenin, Combustion mechanism of an RDX-based composite propellant. Combust. Flame **118**, 248–261 (1999)
16. R.F. Preckel, Pleateau ballistics in nitrocellulode propellants. AIAA J. **3**, 346–347 (1965)
17. F. Zhao, S. Li, W. Shan, S. Li, Influence of C_{60}, fullerene,-soot, and carbon black on combustion properties of catalyzed RDX-CMDB propellants. J. Propul. Technol. **21**, 72–76 (2000)
18. S.M. Pande, V.S. Sadavarte, D. Bhowmik, D.D. Gaikwad, H. Singh, Ballistic modification of nitramine propellants with special reference to NG-PE-PCP-based high energy propellants. Propellants Explos. Pyrotech. **37**, 707–712 (2012)
19. D.J. Hewkin, J.A. Hicks, J. Powling, H. Watts, The combustion of nitric ester-based propellants: ballistic modification by lead compounds. Combust. Sci. Technol. **2**, 307–327 (1971)
20. H. Ren, Y. Liu, Q. Jiao, X. Fu, T. Yang, Preparation of nanocomposite PbO CuO/CNTs via microemulsion process and its catalysis on thermal decomposition of RDX. J. Phys. Chem. Solids **71**, 149–152 (2010)

21. S. Li, F. Gao, F. Zhao, S. Li, Catalytic mechanism of fullerene in RDX-CMDB propellants. J. Propul. Technol. **21**, 76–78 (2000)
22. S. Isert, L. Xin, J. Xie, S.F. Son, The effect of decorated graphene addition on the burning rate of ammonium perchlorate composite propellants. Combust. Flame **183**, 322–329 (2017)
23. J.L. Sabourin, D.M. Dabbs, R.A. Yetter, F.L. Dryer, I.A. Aksay, Functionalized graphene sheet colloids for enhanced fuel/propellant combustion. ACS Nano **3**, 3945–3954 (2009)
24. M. Inagaki, F. Kang, M. Toyoda, *Advanced Materials Science and Engineering of Carbon* (Tsinghua University Press, Beijing, 2013)
25. U. Teipel, *Energetic Materials, Particle Processing and Characterization* (WILEY-VCH Verlag GmbH & Co. KGaA, Weinheim, 2005)
26. J. Li, P. Niu, X. Fan, G. Zhang, H. Yu, X. Fu, Q. Tang, Preparation and application of nano carbon-supported PbO CuO composite catalysts. Chin. J. Explos. Propellants **39**, 59–63 (2016)
27. A.P. Denisyuk, A.D. Margolin, N.P. Tokarev, V.G. Khubaev, L.A. Demidova, Role of carbon black in combustion of ballistic powders with lead-containing catalysts. Combust. Explo. Shock. **13**, 490–496 (1977)
28. A.P. Denisyuk, L.A. Denidobal, V.I. Galkin, The primary zone in the combustion of solid propellants containing catalysts. Combust. Explo. Shock. **31**, 161–167 (1995)
29. N. Kubota, *Propellants and Explosives: Thermochemical Aspects of Combustion* (WILEY-VCH Verlag GmbH & Co. KGaA, Weinheim, 2002)
30. Y. Wang, X. Xia, J. Zhu, Y. Li, X. Wang, X. Hu, Catalytic activity of nanometer-sized CuO, Fe_2O_3 on thermal decomposition of AP and combustion of AP-based propellant. Combust. Sci. Technol. **183**, 154–162 (2011)
31. T. An, F. Zhao, Q. Yan, Y. Yang, Y. Luo, J. Yi, W. Hong, Preparation and evaluation of effective combustion catalysts based on Cu(I), Pb(II) or Cu(II), Bi(II) nanocomposites carried by graphene oxide (GO). Propellants Explos. Pyrotech. **43**, 1087–1095 (2018)

Chapter 36
Novel Pyrazol-Functional Covalent Organic Framework for Noble-Metal Nanoparticles Immobilization

Feipeng Lu, Shenghua Li, Jianhua Chen, Aifeng He, and Yin Wang

Abstract The immobilization and uniform dispersion of Noble Metal Nanoparticles (NMNPs) show great significance in many fields (e.g. catalysis, photoelectric etc.) to enhance its performance and reusability. Covalent organic frameworks (COFs), which are born with many advantages (stability, in built functional ligands, regular channels, etc.), are potential substrates for the synthesis of fine and high dispersed NMNPs. In this work, we propose the pyrazol-functional COFs strategy for the immobilization and uniform dispersion of NMNPs. Various M@COF-DAI (M = Pd, Ir, Pt) complexes are obtained with fine (1.74, 1.99 and 2.25 nm), uniform dispersed, and high metal content (20.47, 17.18, 29.46%) NMNPs. These NMNPs show high catalytic activity, excellent stability, and reusability in the *p*-nitrophenol reduction reaction. This results are superior to those NMNPs immobilized by other materials (e.g. graphene, MOFs, un-functionalized COFs), provide a high efficient immobilization strategy of NMNPs.

F. Lu (✉) · J. Chen · A. He · Y. Wang
Science and Technology On Applied Physical Chemistry Laboratory, Shaanxi Applied Physics-Chemistry Research Institute, Shaanxi, China
e-mail: lufeipengv@163.com

J. Chen
e-mail: jianhua927@163.com

A. He
e-mail: haf780724@163.com

Y. Wang
e-mail: francis1251@126.com

S. Li
School of Materials Science and Engineering, Beijing Institute of Technology, Beijing, China
e-mail: lishenghua@bit.edu.cn

A. Gany and X. Fu (eds.), *2021 International Conference on Development and Application of Carbon Nanomaterials in Energetic Materials*, Springer Proceedings in Physics 276,
https://doi.org/10.1007/978-981-19-1774-5_36

36.1 Introduction

Noble Metal Nanoparticles (NMNPs) (Pd, Pt, Au, etc.) show excellent catalytic activity own to its excellent specific surface area and atom utilization, Tsunoyama et al. [1] NMNPs have been widely used in many reactions (e.g. reduction, C-H activation, hydrogenation, coupling, and dehalogenation reactions) [2, 3]. During the storage and use process of NMNPs, the NMNPs' aggregation or shape change can easily occur due to its high surface energy, yet its activity can be seriously weakened. Maintain the activity of NMNPs remains a significant challenge in the synthesis, storage, and use process of NMNPs.

Porous materials [4], such as porous organic cage [5], carbon nitride [6], covalent organic frameworks (COFs) [7], porous organic polymers (POPs) [8], covalent triazine frameworks (CTFs) [9], metal organic framework (MOFs) [10], and so on [11, 12], have been employed as substrates in pursuing for stable and fine NMNPs. Among them, COFs, one class of crystalline carbon based porous materials, have gained rapid progress ever since the first report by Yaghi's group in 2005 [13, 14]. Its features of framework structure, covalent linkage, and functional ligands make it various specialities materials and promising applications in various scenarios (e.g. gas storage and separation, energy conversion and storage, optoelectronic, and catalysis materials) have been ingeniously reported [15]. In this regard, COFs could be promising substrates for the growth and immobilization of NMNPs, for reasons that: (1) the in-built covalent bond within COFs give it inherent stability as substrate, (2) the functional ligands within COFs provide nucleus for the growth of NMNPs, (3) the regular channels within COFs can provide restriction for the growth of NMNPs. So far, many COFs have been investigated for the application of NMNPs immobilization. Among these reported COFs-support NMNPs, large and low metal content NMNPs (Pd nanoparticles size distribution around 10 nm, Pd content range from 6.4 to 10.2%, Wang's and Banerjee's groups have reported Au nanoparticles size distribution around 5 nm, Pd content range from 2.2%) in 2011 and 2014 respectively [7a–c], with COFs synthesized with un-functional benzene and 1,3,5-triformylbenzene (TFB)/1,3,5-triformylphloroglucinol (TFP). Meanwhile, with thioether functional COF as substrate, fine Pd nanoparticles (size distribution around 1.8 nm, Pd content 26.3%) is obtained by Zhang's group [7e]. This indicate that the effective functional group can be vital factors for the immobilization of NMNPs.

Basing on the target-oriented strategy, suitable selection of COF ligands can get double achievements with half works. Inspired by the growth mechanism of MOFs, coordination bonds between the N/O atoms in COFs and transition metal atoms could be an effective method for the immobilization of metal atoms, [10] and thus boost the growth of NMNPs with the immobilized metal atoms as nucleus. Thus, we present a pyrazol-functional COFs (COF-DAI) strategy for the immobilization and uniform dispersion of NMNPs. 4,7-Diamino-1H-indazole (DAI) can be ideal ligand for the construction of COF-DAI, for its pyrazol-function can provide effective N coordination atoms for the nucleation of NMNPs; 1,3,5-triformylbenzene (TFB), 1,3,5-triformylphloroglucinol (TFP), and 1,3,5-tris(*p*-formylphenyl)-benzene (TFBB) are

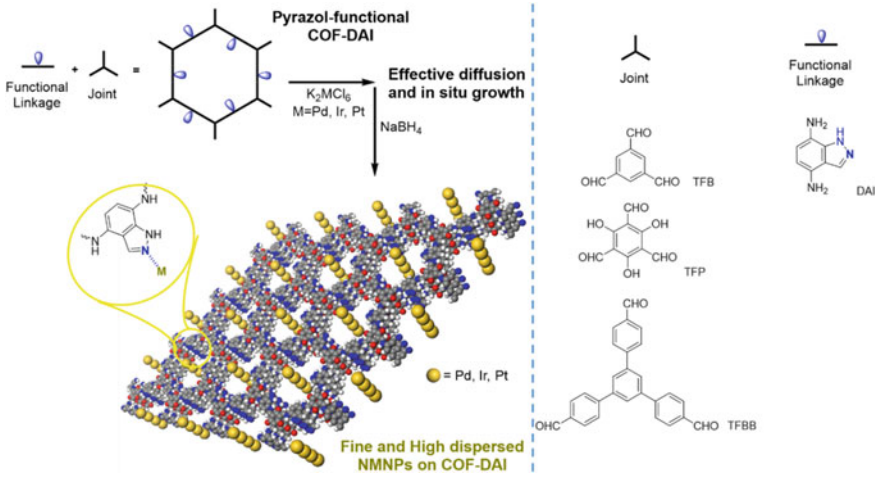

Scheme 1 The synthesis strategy of COF-DAI immobilized NMNPs

employed as joints to construct COF-DAI with various channel width. Ideally, only three stages are needed for the assembly of fine and uniform dispersed NMNPs on COF-DAI (M@COF-DAI), as shown in Scheme 1.

36.2 Results and Discussion

Initially, various COF-DAI (named as COF-DAI-TFB, COF-DAI-TFP, and COF-DAI-TFBB) were synthesized with solvent thermal method, details shown in experimental section. The chemical composition of the COF-DAI was characterized via ^{13}C cross-polarization/magic-angle spinning (CP/MAS) solid-state NMR and Fourier transform infrared (FT-IR) method. In the ^{13}C CP/MAS NMR spectra, the ^{13}C chemical shifts range from 183.5 to 107 ppm (COF-DAI-TFP) and 158.5 to 116.3 ppm (COF-DAI-TFB and COF-DAI-TFBB), the detailed assignments were depicted in Fig. 1a–c. As shown in the FT-IR spectra (Fig. 1d–f), peaks in 1582 and 1258 cm^{-1} stand for the C=C and C–N bonds, which indicated the formation of sole ketone form linkage in COF-DAI-TFP, the ketone form C=O peak was merged within the C=C stretching peak as a shoulder (1635 cm^{-1}), due to the peak broadening in the extended structure [16]; 1658 cm^{-1} (C=C) in COF-DAI-TFB and COF-DAI-TFBB indicated the completed condensation reaction. These observations can be strong evidence for the covalently linkage between these building units, and ultimately built up the polymeric macromolecules via imine bonds.

The crystalline character of the COF-DAI was revealed by powder X-ray diffraction (PXRD) and deduced via Theoretical simulation method (Fig. 2a–c). The PXRD spectra reveal main peaks at 4.55° and 27.2° for COF-DAI-TFP, 5° and 9°

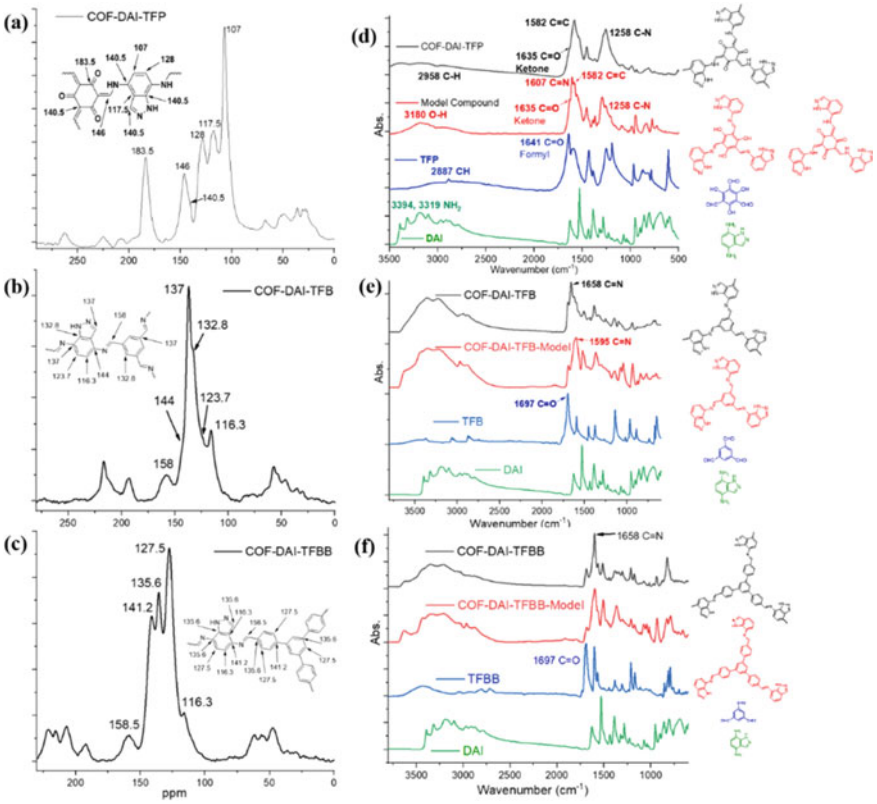

Fig. 36.1 The ^{13}C CP/MAS NMR and FT-IR spectra of COF-DAI

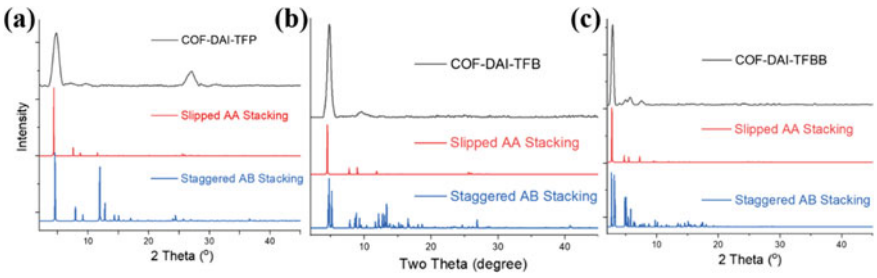

Fig. 36.2 The PXRD and optimize spectra of COF-DAI

for COF-DAI-TFB, 2.75° and 5.5° for COF-DAI-TFBB, respectively. Meanwhile, the stacking of two-dimensional (2D) hexagonal layers into slipped AA and staggered AB stacking COFs models were anticipated with Materials Studio v6.0.0 [17], force-field calculation was employed to optimize the bond length and angels in the

constructed structure. Thus, these COFs' slipped AA stacking models were proved with R_{WP} value 24, 22.9, and 5.9%, further confirmed the formation of slipped AA stacking of COF-DAI (Fig. 36.2).

COF-DAI's Morphology were investigated by high-resolution transmission electron microscopy (HR-TEM) and scanning electron microscope (SEM). Thin transparent sheets stacked into rod-like structure, small crystalline grains stacked into spheroidal structure, and small highly crystalline grains stacked into nanotube structure were observed in these SEM and HR-TEM. The porous character of COF-DAI was identified by Brunauer–Emmett–Teller (BET) surface area analysis (on the basics of nitrogen sorption isotherms at 77 K). The BET surface area of COF-DAI-TFB, COF-DAI-TFP, and COF-DAI-TFBB were evaluated to be 417.4, 136, and 214.1 m^2/g, respectively. Their thermogravimetry analysis were employed to investigate COF-DAI-TFP's thermostability, the obtained results reveal the good thermos stability up to 275, 200, and 300 °C with less than 13.8% weight loss.

Basing on these novel COFs, Pd NMNPs was obtained. The parameters such as morphology, size, metal content, and their interactions with substrates, may affect their catalytic properties significantly [2, 18]. XRD, FT-IR, XPS, SEM, EDS Mapping Scan, HR-TEM, selected area electron diffraction (SAED), and inductively coupled plasma-mass spectrometry (ICP-MS) characterization of Pd@COF-DAI-TFP were conducted. The SEM images and FT-IR spectra of Pd@COF-DAI-TFP reveal that the rod-like morphology and the chemical environment of COF-DAI-TFP were kept after the introduction of Pd NMNPs [7c]. Meanwhile, Pd NMNPs on COF-DAI-TFP were confirmed by HR-TEM. HR-TEM images shown that the average size of Pd nanoparticles were 1.74 nm with narrow size distribution and high metal content 20.47% observed in Pd@COF-DAI-TFP sample (Fig. 3a–c). Any unsupported Pd NMNPs couldn't be observed in the HR-TEM image, which indicated that the Pd NMNPs were fully cladded by the COF-DAI-TFP cavities, that caused their lattice fringes couldn't be clearly measured. Pd NMNPs on the surface of COF-DAI-TFP shown interplanar spacing of 0.23 nm, this could be corresponded to the (111) facet of face-centred cubic (fcc) Pd NMNPs [7e]. The EDS mapping images of C, N, O, and Pd, as well as the HAADF-STEM further conformed the excellent disparity of Pd NMNPs on COF-DAI-TFP without any agglomeration (Fig. 3d–h). The SAED and XRD patterns of Pd@COF-DAI-TFP shown the crystalline character of Pd NMNPs on COF-DAI-TFP. Meanwhile, Pd NMNPs on COF-DAI-TFB and COF-DAI-TFBB were also conducted, fine and high dispersed Pd NMNPs were obtained on COF-DAI (Fig. 36.4). These results demonstrated the NMNPs immobilization general applicability of pyrazol-functional COFs (COF-DAI series).

To evaluate the importance of the pyrazol-functional group, the comparison of Pd@COF-DAI-TFP with Pd@COF-DAB-TFB (DAB: 1,4-diaminobenzene, TFB: 1,3,5-triformylbenzene) and Pd@COF-DAB-TFP were conducted (Table 36.1). As the Pd@COF-DAB-TFB and Pd@COF-DAB-TFP had been reported by Wang's and Banerjee's group with similar method [7a–c]. The TEM images shown the Pd NMNPs size of Pd@COF-DAB-TFB and Pd@COF-DAB-TFP ranged around 10 nm, their Pd content were 7.1% and 10.2% (Table 36.1), more importantly, most of these Pd NMNPs can be observed on the surface of COFs. The Pd NMNPs characters

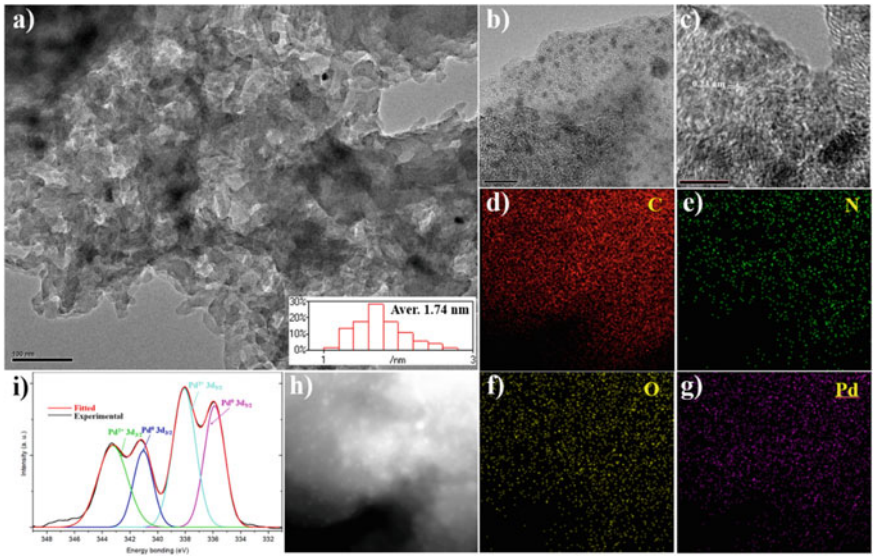

Fig. 36.3 Characterization of Pd@COF-DAI-TFP: **a** low and **b–c** high magnification TEM image of Pd@COF-DAI-TFP, inset is the size distribution of Pd NMNPs; **d–g** energy dispersive spectroscope (EDS) Mapping Scan of composition element, C, N, O and Pd; **h** high-angle annular dark-field scanning transmission electron microscopy (HAADF-STEM) image; **i** Pd 3d region in the X-ray photoelectron spectroscopy (XPS) spectra of Pd@COF-DAI-TFP

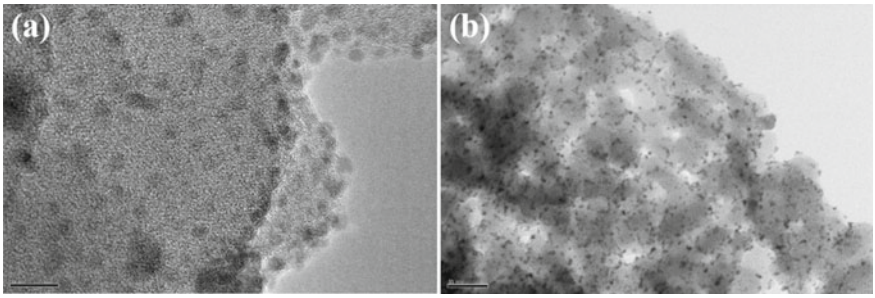

Fig. 36.4 TEM images of Pd NMNPs on COF-DAI-TFB and COF-DAI-TFBB

of Pd@COF-DAI-TFP shown better performance than that of Pd@COF-DAB-TFB and Pd@COF-DAB-TFP (1.57 VS 10 nm, Pd-ICP data VS 7.1 and 10.2%).

The interactions between NMNPs and COF-DAI-TFP were fully characterized by XPS measurement. From the XPS spectra of Pd 3d region (Fig. 3i), two sets of doublets of Pd were observed, which corresponded to its high energy band ($3d_{5/2}$) and low energy band ($3d_{3/2}$). The binding energy peaks 341.0 eV ($3d_{3/2}$) and 335.9 eV ($3d_{5/2}$) of Pd were assigned to Pd^0 species, while the binding energy peaks 343.2 ($3d_{3/2}$) and 338.1 eV ($3d_{5/2}$) of Pd corresponded to Pd^{2+} species. The Pd^{2+} species

Table 36.1 Summary of the typical performances of NMNPs immobilized by various COFs

Materials	Metal	Size (nm)	Metal content (%)
COF-DAB-TFB	Pd	10	7.1
COF-102	Pd	2.4 ± 0.5	30
COF-DAB-TFP	Pd	10	6.4–10.2
COF-DAB-TFP	Au	5	2.2
COF-DETH-TFPT	Pt	10	
COF-Thio-TFP	Pd, Pt	Pd: 1.8, Pt: 1.7	Pd: 26.3 Pt: 34.3
COF-DAI-TFP	Pd, Ir, Pt	Pd: 1.57, Ir: 1.7, Pt: 2.18	Pd: 20.47 Ir: 17.18 Pt: 29.46

might be caused by the re-oxidation process of Pd^0 in air [7e, 20], The XPS results of Pd^0 3d region in Pd@COF-DAI-TFP shown higher value than that of the standard XPS values of Pd^0 3d region ($3d_{3/2}$: 340.36 eV, $3d_{5/2}$: 335.1 eV), that might be caused by the interactions between Pd NMNPs and the COF-DAI-TFP. Meanwhile, the bonding energy of N 1 s in Pd@COF-DAI-TFP shown the higher value than that of COF-DAI-TFP. These changes could be caused by the interactions between Pd NMNPs and COF-DAI-TFP. These results demonstrated that the pyrazol-functional group played key role for the high efficient immobilization and uniform dispersion of NMNPs.

Devoting to the synthesis of ultrafine and highly dispersed NMNPs, its catalytic activity was fatal parameter for its further application, its catalytic activity was tested with the metal-catalysed hydrogenation reduction reaction. *p*-Nitrophenol was selected as the reactant for the reduction reaction, for reasons that: (1) *p*-nitrophenol was pollutant, and its reduction product was key raw material for chemical industry; (2) the metal-catalysed reduction reaction of *p*-nitrophenol had been verified as a model reaction to evaluate the catalytic activity of NMNPs; (3) the reduction reaction of *p*-nitrophenol could be easily monitored by UV–Vis spectroscopy (the absorption peak at 400 nm was the characteristic peak of *p*-nitrophenol and $NaBH_4$ mixed aqueous solution); (4) the Pd@COF-DAI-TFP could be dispersed into aqueous and organic solutions via slight ultrasonic treatment, which indicated its feasibility as heterogeneous catalyst [20]. The reduction reaction of *p*-nitrophenol with the catalysis of Pd@COF-DAI-TFP was conducted with the following process: Aqueous suspension of Pd@COF-DAI-TFP (0.5 mg/mL, 30 μL) was poured into the aqueous solution (water, 1 mL; *p*-nitrophenol, 1 mM, 0.3 mL; $NaBH_4$, 0.5 M, 1 mL). The reduction reaction accelerated upon the addition of Pd@COF-DAI-TFP aqueous suspension. As shown in Fig. 5a, the 400 nm peak decline and the 300 nm new peak appearance indicated the reduction of *p*-nitrophenol and the produce of *p*-aminophenol, respectively [7c, 21]. The reduction reaction was almost finished within 0.7 min, and it was completely finished within 3 min (Fig. 5a). Two control experiments (reduction without additives and with COF-DAI-TFP) were performed (Fig. 5b). Without any additives, only 20% *p*-aminophenol was reduced in 20 *min*;

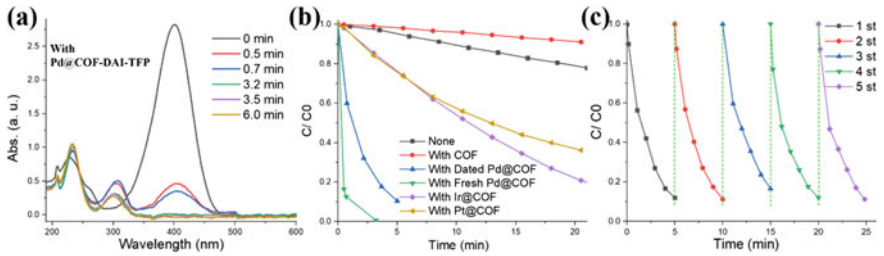

Fig. 36.5 **a** Time-depend UV–Vis spectroscopy of the reduction of *p*-nitrophenol with the catalyse of Pd@COF-DAI-TFP; **b** reduction of *p*-nitrophenol in various conditions; **c** recycling test of the reduction of *p*-nitrophenol with the catalyse of dated Pd@COF-DAI-TFP

with the additive of COF-DAI-TFP, only 10% *p*-aminophenol was reduced in 20 *min*. That might be caused by the adsorption of *p*-aminophenol by COF-DAI-TFP, the reduction rate was reduced by the separation of *p*-aminophenol and the reductive agent. Once the addition of Pd@COF-DAI-TFP, the hydrogen adsorption by Pd NMNPs on COF-DAI-TFP [21], as well as the *p*-aminophenol adsorption by COF-DAI-TFP enhanced the reduction rate greatly. Stability and reusability were important parameters for heterogeneous catalyst. Dated Pd@COF-DAI-TFP (after exposed to air for 50 *days*) catalytic *p*-nitrophenol reduction and its HR-TEM measurement were conducted. The HR-TEM images shown the highly dispersed Pd NMNPs on COF-DAI-TFP, only a few of large NMNPs observed. With the catalysis of dated Pd@COF-DAI-TFP, 90% of the reduction reaction complete within 5 min (Fig. 5c), demonstrated the high catalytic activity of dated Pd@COF-DAI-TFP and the excellent stability of Pd@COF-DAI-TFP. The catalytic activity of dated Pd@COF-DAI-TFP shown a little lower than that of fresh Pd@COF-DAI-TFP, that could be caused by the aggregation of small amount Pd NMNPs after exposed to air for 50 days. Dated Pd@COF-DAI-TFP's cyclic catalysis experiment were conducted, the reduction rate remained nearly unchanged after 5 reduction cycles, the conversion rate of *p*-aminophenol remains 90% at the 5st reduction cycle (Fig. 5c). These results illustrated the excellent catalytic activity and stability of Pd@COF-DAI-TFP, which further demonstrated COF-DAI series were promising substrate for NMNPs.

36.3 Conclusion

In conclusion, a series of novel pyrazol-functional COFs (COF-DAI-TFB, COF-DAI-TFP, and COF-DAI-TFBB) were designed and employed as substrate for NMNPs. The fine (average size 1.74 nm), highly dispersed, and high metal content (20.47%) Pd NMNPs on COF-DAI-TFP was reached and fully characterized. Meanwhile, Pd NMNPs on COF-DAI-TFB and COF-DAI-TFBB shown fine and highly dispersed characteristics. Fine Ir and Pt NMNPs (average size, Ir: 1.99, Pt: 2.25 nm) were also obtained on COF-DAI-TFP. Moreover, the catalytic activity of Pd@COF-DAI-TFP

was tested with the reduction reaction of *p*-nitrophenol, which identified the excellent activity, stability, and reusability of NMNPs on COF-DAI-TFP. Compared with un-functional COFs, COF-DAI series shown superior performance in the field of NMNPs immobilization. These results not only demonstrated the key role of pyrazol-function in COFs for the immobilization and uniform dispersion of NMNPs, but also proved its general applicability. This work emphasized the availability of the pyrazol-functional COFs in the field of NMNPs immobilization, further investigations on these COF materials can be conducted for various potential applications.

36.4 Experimental Section

Synthesis of COF-DAI-TFB:

TFB (13.2 mg, 0.08 mmol), 4,7-diamine-1H-indazole (DAI) (18.1 mg, 0.12 mmol), *o*-dichlorobenzene (1.3 mL), and methanol (0.7 mL) were added into pyrex tube (5 mL). Ultrasonic treatment (10 min) was used to obtain a homogeneous mixture. Acetic acid aqueous solution (0.2 mL, 3 M) was added to the reaction. The tube was experienced 3 freeze–pump–thaw cycles to emptied the inner air and sealed off. The sealed tube was heated to 100 °C and kept undisturbed for 72 h. Brown powder was collected by centrifuge, washed with DMF (10 mL) and ethanol (10 mL) for 4 times, respectively. COF-DAI-TFP (yield 87%) was obtained after dried for 24 h (90 °C under vacuum).

Synthesis of COF-DAI-TFP:

TFP (17.4 mg, 0.08 mmol), 4,7-diamine-1H-indazole (DAI) (18.1 mg, 0.12 mmol), *o*-dichlorobenzene (1.3 mL), and methanol (0.7 mL) were added into pyrex tube (5 mL). Ultrasonic treatment (10 min) was used to obtain a homogeneous mixture. Acetic acid aqueous solution (0.2 mL, 6 M) was added to the reaction. The tube was experienced 3 freeze–pump–thaw cycles to emptied the inner air and sealed off. The sealed tube was heated to 100 °C and kept undisturbed for 72 h. Dark-red powder was collected by centrifuge, washed with DMF (10 mL) and ethanol (10 mL) for 4 times, respectively. COF-DAI-TFP (yield 89%) was obtained after dried for 24 h (90 °C under vacuum).

Synthesis of COF-DAI-TFBB:

TFBB (22.3 mg, 0.07 mmol), 4,7-diamine-1H-indazole (DAI) (15.5 mg, 0.105 mmol), *o*-dichlorobenzene (0.5 mL), and methanol (1.5 mL) were added into pyrex tube (5 mL). Ultrasonic treatment (10 min) was used to obtain a homogeneous mixture. Acetic acid aqueous solution (0.2 mL, 12 M) was added to the reaction. The tube was experienced 3 freeze–pump–thaw cycles to emptied the inner air and sealed off. The sealed tube was heated to 100 °C and kept for 96 h. Light-brown powder was collected by centrifuge, washed with DMF (10 mL) and ethanol (10 mL) for 4

times, respectively. COF-DAI-TFBB (yield 76%) was obtained after dried for 24 h (90 °C under vacuum).

Synthesis of M@COF:

K_2PdCl_6 was dissolved in water (3 mL), COF-DAI (10 mg) was dispersed into ethanol (5 mL), mixing K_2PdCl_6 aqueous solution with COF-DAI in methanol suspension, all solvent was evaporated (under vacuum and stirring) to deposited the metal precursor onto COF-DAI. K_2PdCl_6@COF-DAI was re-dispersed in ethanol (10 mL), $NaBH_4$ (2 mmol) was added to the ethanol suspension and reduction for 15 h. NMNPs@COF-DAI was obtain by centrifugation, washed with ethanol/water mixed solution (V: V 1: 1, 10 mL) and ethanol (6 mL) for 8 times, respectively. NMNPs@COF-DAI were dried for 12 h (under vacuum at room temperature).

Reduction of *p*-aminophenol with the catalysis of M@COF-DAI:

M@COF-DAI-TFP was dispersed into aqueous solution easily via slightly ultrasonic treatment. The M@COF-DAI-TFP aqueous suspension (0.5 mg mL-1, 30 μL) was added to the mixture of water (1 mL), *p*-nitrophenol (1 mM, 0.3 mL), and $NaBH_4$ (0.5 M, 1 mL) aqueous solution for catalysis.

Cyclic catalysis experiment was conducted with the following method. Kept the amount of Pd@COF-DAI (0.5 mg mL^{-1}, 30 μL), $NaBH_4$ (0.5 M, 1 mL), and water (1 mL). Additional *p*-nitrophenol (1 mM; 0.3 mL for 1st, 0.345 mL for 2st, 0.397 mL for 3st, 0.456 mL for 4st, 0.525 mL for 5st) was added to the cuvette upon the previous reduction completed. Meanwhile, the reduction process was monitored by UV–Vis spectroscopy to evaluate the catalysis performance of M@COF-DAI-TFP.

References

1. (a) H. Tsunoyama, H. Sakurai, Y. Negishi, T. Tsukuda, J. Am. Chem. Soc. **127**, 9374–9375 (2005); (b) Z. Yuan, J. Wang, L. Wang, W. Xie, P. Chen, Z. Hou, X. Zheng, Bioresour. Technol. **101**, 7088–7092 (2010); (c) X. Zhou, W. Xu, G. Liu, D. Panda, P. Chen, J. Am. Chem. Soc. **132**, 138–146 (2010); (d) Y. Lei, F. Mehmood, S. Lee, J. Greeley, B. Lee, S. Seifert, R.E. Winans, J.W. Elam, R.J. Meyer, P.C. Redfern, D. Teschner, R. Schlögl, M.J. Pellin, L.A. Curtiss, S. Vajda, Science **328**, 224–228 (2010); (e) Z. Yuan, L. Wang, J. Wang, S. Xia, P. Chen, Z. Hou, X. Zheng, Appl. Catal., B **101**, 431–440 (2011); (f) M. Haruta, Angew. Chem., Int. Ed. **53**, 52–56 (2014)
2. (a) A. Corma, P. Serna, Science **313**, 332–334 (2006); (b) L.M. Liz-Marzán, Langmuir 22, 32–41 (2006); (c) S. Eustis, M.A. El-Sayed, Chem. Soc. Rev. **35**, 209–217 (2006); (d) A. Corma, H. Garcia, Chem. Soc. Rev. **37**, 2096–2126 (2008); (e) Y. Xia, Y. Xiong, B. Lim, S.E. Skrabalak, Angew. Chem. Int. Ed. **48**, 60–103 (2009); Angew. Chem. **121**, 62–108 (2009); **f** T.K. Sau, A.L. Rogach, F. Jäckel, T.A. Klar, J. Feldmann, Adv. Mater. **22**, 1805–1825 (2010); (j) X. Liu, D. Gregurec, J. Irigoyen, A. Martinez, S. Moya, R. Ciganda, P. Hermange, J. Ruiz, D. Astruc, Nat. Commun. **7**, 13152 (2016); **h** S.M. Ansar, C.L. Kitchens, ACS Catal. 6, 5553–5560 (2016); (i) J. Liu, K. He, W. Wu, T. Song, M.G. Kanatzidis, J. Am. Chem. Soc. **139**, 2900–2903 (2017)
3. (a) R.M. Navarro, B. Pawelec, J.M. Trejo, R. Mariscal, J.L. Fierro, J. Catal. **189**, 184–194 (2000); (b) Y. Wan, H. Wang, Q. Zhao, M. Klingstedt, O. Terasaki, D. Zhao, J. Am. Chem.

Soc. **131**, 4541–4550 (2009); (c) T. Park, A.J. Hickman, K. Koh, S. Martin, A.G. Wong-Foy, M.S. Sanford, A.J. Matzger, J. Am. Chem. Soc. **133**, 20138–20141 (2011); (d) Y. Shiraishi, Y. Takeda, Y. Sugano, S. Ichikawa, S. Tanakac, T. Hiraia, Chem. Commun. **47**, 7863–7865 (2011)

4. (a) R.J. White, R. Luque, V.L. Budarin, J.H. Clark, D.J. Macquarrie, Chem. Soc. Rev. **38**, 481–494 (2009); (b) Q. Zhu, Q. Xu, Chem **1**, 220–245 (2016); c W. Tu, Y. Xu, S. Yin, R. Xu, Adv. Mater. **30**, 1–29 (2018)
5. (a) R. McCaffrey, H. Long, Y. Jin, A. Sanders, W. Park, W. Zhang, J. Am. Chem. Soc. **136**, 1782–1785 (2014); (b) J. Sun, W. Zhan, T. Akita, Q. Xu, J. Am. Chem. Soc. **137**, 7063–7066 (2015); (c) L. Qiu, R. McCaffrey, Y. Jin, Yu Gong, Y. Hu, H. Sun, W. Park, W. Zhang, Chem. Sci. **9**, 676–680 (2018); (d) N. Sun, C. Wang, H. Wang, L. Yang, P. Jin, W. Zhang, J. Jiang, Angew. Chem. Int. Ed. **58**, 2–8 (2019); Angew. Chem. **131**, 2–8 (2019)
6. (a) X. Li, X. Wang, M. Antonietti, Chem. Sci. **3**, 2170–2174 (2012); (b) R. Nazir, P. Fageria, M. Basu, S. Pande, J. Phys. Chem. C **121**, 19548–19558 (2017)
7. (a) S. Ding, J. Gao, Q. Wang, Y. Zhang, W. Song, C. Su, W. Wang, J. Am. Chem. Soc. **133**, 19816–19822 (2011); (b) P. Pachfule, S. Kandambeth, D.D. Díazbc, R. Banerjee, Chem. Commun. **50**, 3169–3172 (2014); (c) D.D. Díazbc, R. Banerjee, J. Mater. Chem. A **2**, 7944–7952 (2014); (d) L. Stegbauer, K. Schwinghammer, B.V. Lotsch, Chem. Sci. **5**, 2789–2793 (2014); (e) S. Lu, Y. Hu, S. Wan, R. McCaffrey, Y. Jin, H. Gu, W. Zhang, J. Am. Chem. Soc. **139**, 17082–17088 (2017)
8. (a) J. Sun, L. Jing, Y. Tian, F. Sun, P. Chen, G. Zhu, Chem. Commun. **54**, 1603–1606 (2018); (b) L. Jing, J. Sun, F. Sun, P. Chen, G. Zhu, Chem. Commun. **9**, 3523–3530 (2018); **c** Y. Huang, Q. Wang, J. Liang, X. Wang, R. Cao, J. Am. Chem. Soc. **138**, 10104–10107 (2016); (d) F. Liu, X. Liu, D. Astruc, H. Gu, J. Colloid Interface Sci. **533**,161–170 (2019); (e) X. Shao, X. Yang, J. Xu, H. Duan, Y. Huang, T. Zhang, Chem **5**, 1–13 (2019); (f) H. Fu, Z. Zhang, W. Fan, S. Wang, Y. Liu, M. Huang, J. Mater. Chem. A **7**, 15048–15053 (2019)
9. (a) C.E. Chan-Thaw, A. Villa, P. Katekomol, D. Su, A. Thomas, L. Prati, Nano Lett. **10**, 537–54 (2010); (b) K. Kamiya, R. Kamai, K. Hashimoto, S. Nakanishi, Nat. Commun. **5**, 5040 (2014); (c) R. Kamai, K. Kamiya, K. Hashimoto, S. Nakanishi, Angew. Chem., Int. Ed. **55**, 13184–13188 (2016); Angew. Chem. **128**, 13378–13382 (2016)
10. (a) H. Jiang, T. Akita, T. Ishida, M. Haruta, Q. Xu, J. Am. Chem. Soc. **133**, 1304–1306 (2011); (b) L. Chen, R. Luque, Y. Li, Chem. Soc. Rev. **46**, 4614–4630 (2017); (c) L. Jiao, H. Jiang, Chem **5**, 1–19 (2019)
11. (a) S.H. Joo, S.J. Choi, I. Oh, J. Kwak, Z. Liu, O. Terasaki, R. Ryoo, Nature **412**, 169–172 (2001); (b) C. Nethravathi, E.A. Anumol, M. Rajamathi, N. Ravishankar, Nanoscale **3**, 569–571 (2011); (c) H. Yin, H. Tang, D. Wang, Y. Gao, Z. Tang, ACS Nano **6**, 8288–8297 (2012); (d) L. Shang, T. Bian, B. Zhang, D. Zhang, L. Wu, C. Tung, Y. Yin, T. Zhang, Angew. Chem., Int. Ed. **53**, 250–254 (2014); Angew. Chem. **126**, 254–258 (2014); (e) A. Han, W. Chen, S. Zhang, M. Zhang, Y. Han, J. Zhang, S. Ji, L. Zheng, Y. Wang, L. Gu, C. Chen, Q. Peng, D. Wang, Y. Li, Adv. Mater. **30**, 1–7 (2018)
12. (a) W. Wang, W. An, B. Ramalingam, S. Mukherjee, D.M. Niedzwiedzki, S. Gangopadhyay, P. Biswas, J. Am. Chem. Soc. **134**, 11276–11281 (2012); (b) Q. Wang, W. Jia, B. Liu, A. Dong, X. Gong, C. Li, P. Jing, Y. Li, G. Xu, J. Zhang, Hierarchical structure based on Pd(Au) nanoparticles grafted onto magnetite cores and double layered shells: enhanced activity for catalytic applications, J. Mater. Chem. A **1**, 12732–12741 (2013)
13. (a) A.P. CÔté, A.I. Benin, N.W. Ockwig, M. O'Keeffe, A.J. Matzger, O.M. Yaghi, Science **310**, 1166–1170 (2005); (b) S. Kandambeth, A. Mallick, B. Lukose, M.V. Mane, T. Heine, R. Banerjee, J. Am. Chem. Soc. **134**, 19524–19527 (2012); (c) T. Zhou, S. Xu, Q. Wen, Z. Pang, X. Zhao, J. Am. Chem. Soc. **136**, 15885–15888 (2014); (d) G. Lin, H. Ding, D. Yuan, B. Wang, C. Wang, J. Am. Chem. Soc. **138**, 3302–3305 (2016); (e) X. Zhuang, W. Zhao, F. Zhang, Y. Cao, F. Liu, S. Bia, X. Feng, Polym. Chem. **7**, 4176–4181 (2016); (f) H. Ding, J. Li, G. Xie, G. Lin, R. Chen, Z. Peng, C. Yang, B. Wang, J. Sun, C. Wang, Nat. Commun. **9**, 5234 (2018); (g) Q. Gao, X. Li, G. Ning, H. Xu, C. Liu, B. Tian, W. Tang, K.P. Loh, Chem. Mater. **30**, 1762–1768 (2018)

14. (a) X. Feng, X. Dinga, D. Jiang, Chem. Soc. Rev. **41**, 6010–6022 (2012); (b) J.W. Colson, W.R. Dichtel, Nat. Chem. **5**, 453–465 (2013); (c) S. Ding, W. Wang, Chem. Soc. Rev. **42**, 548–568 (2013); (d) U. Díaz, A. Corma, Coord. Chem. Rev. **311**, 85–124 (2016); (e) J.L. Segura, M.J. Mancheño, F. Zamora, Chem. Soc. Rev. **45**, 5635–5671 (2016); (f) C.S. Diercks, O.M. Yaghi, Science **355**, 1–8 (2017); (g) S. Das, P. Heasman, T. Ben, S. Qiu, Chem. Rev. **117**, 1515–1563 (2017); (h) F. Beuerle, B. Gole, Angew. Chem., Int. Ed. **57**, 4850–4878 (2018); Angew. Chem. **130**, 4942–4972 (2018); (i) M.S. Lohse, T. Bein, Adv. Funct. Mater. **28**, 1–71 (2018); (j) S. Kandambeth, K. Dey, R. Banerjee, J. Am. Chem. Soc. **141**, 1807–1822 (2019); (k) X. Chen, K. Geng, R. Liu, K. Tan, Y. Gong, Z. Li, S. Tao, Q. Jiang, D. Jiang, Angew. Chem., Int. Ed. https://doi.org/10.1002/anie.201904291; Angew. Chem. https://doi.org/10.1002/ange.201904291; (l) Y. Song, Q. Sun, B. Aguila, S. Ma, Adv. Sci. **6**, 1–34 (2019)
15. (a) D.N. Bunck, W.R. Dichtel, Angew. Chem. Int. Ed. **124**, 1921–1925 (2012); Angew. Chem. **124**, 1921–1925 (2012); (b) L. Stegbauer, K. Schwinghammer, B.V. Lotsch, Chem. Sci. **5**, 2789–2793 (2014); (c) Y. Peng, Z. Hu, Y. Gao, D. Yuan, Z. Kang, Y. Qian, N. Yan, D. Zhao, ChemSusChem **8**, 3208–3212 (2015); (d) H. Xu, S. Ding, W. An, H. Wu, W. Wang, J. Am. Chem. Soc. **138**, 11489–11492 (2016); (e) H. Xu, S. Tao, D. Jiang, Nat. Mater. **15**, 722–727 (2016); (f) L. Li, X. Feng, X. Cui, Y. Ma, S. Ding, W. Wang, J. Am. Chem. Soc. **139**, 6042–6045 (2017); (g) Q. Sun, B. Aguila, L.D. Earl, C.W. Abney, L. Wojtas, P.K. Thallapally, S. Ma, Adv. Mater. **30**, 1–9 (2018); (h) C.S. Diercks, S. Lin, N. Kornienko, E.A. Kapustin, E.M. Nichols, C. Zhu, Y. Zhao, C.J. Chang, O.M. Yaghi, J. Am. Chem. Soc. **140**, 1116–1122 (2018); (i) P. Pachfule, A. Acharjya, J. Roeser, T. Langenhahn, Mi. Schwarze, R. Schomäcker, A. Thomas, J. Schmidt, J. Am. Chem. Soc. **140**, 1423–1427 (2018); (j) P. Shao, J. Li, F. Chen, L. Ma, Q. Li, M. Zhang, J. Zhou, A. Yin, X. Feng, B. Wang, Angew. Chem. Int. Ed. **57**, 16501–16505 (2018); Angew. Chem. **130**, 16739–16743 (2018); (k) A. Mal, R.K. Mishra, V.K. Praveen, M.A. Khayum, R. Banerjee, A. Ajayaghosh, Angew. Chem. Int. Ed. **57**, 8443–8447 (2018); Angew. Chem. **130**, 8579–8583 (2018); (l) P. Wang, Q. Xu, Z. Li, W. Jiang, Q. Jiang, D. Jiang, Adv. Mater. **30**, 1–7 (2018); (m) Q. Lu, Y. Ma, H. Li, X. Guan, Y. Yusran, M. Xue, Q. Fang, Y. Yan, S. Qiu, V. Valtchev, Angew. Chem. Int. Ed. **57**, 6042–6048 (2018); Angew. Chem. **130**, 6150–6156 (2018); (n) W. Cao, W. Wang, H. Xu, I.V. Sergeyev, J. Struppe, X. Wang, F. Mentink-Vigier, Z. Gan, M. Xiao, L. Wang, G. Chen, S. Ding, S. Bai, W. Wang, J. Am. Chem. Soc. **140**, 6969–6977 (2018); (o) X. Wang, L. Chen, S.Y. Chong, M.A. Little, Y. Wu, W. Zhu, R. Clowes, Y. Yan, M.A. Zwijnenburg, R.S. Sprick, A.I. Cooper, Nat. Chem. **10**, 1180–1189 (2018); (p) Q. Sun, Y. Tang, B. Aguila, S. Wang, F. Xiao, P.K. Thallapally, A.M. Al-Enizi, A. Nafady, S. Ma, Angew. Chem. Int. Ed. **58**, 8670–8675 (2019); Angew. Chem. 131, 8762–8767 (2019); (q) L. Wang, J. Zhou, Y. Lan, S. Ding, W. Yu, W. Wang, Angew. Chem. Int. Ed. **58**, 9443–9447 (2019); Angew. Chem. **131**, 9543–9547 (2019)
16. S. Kandambeth, A. Mallick, B. Lukose, M.V. Mane, T. Heine, R. Banerjee, J. Am. Chem. Soc. **134**, 19524–19527 (2012)
17. Materials Studio Release Notes v.6.0.0 (Accelrys Software, San Diego, 2011)
18. (a) H. Tsunoyama, H. Sakurai, Y. Negishi, T. Tsukuda, J. Am. Chem. Soc. **127**, 9374–9375 2005; (b) Z. Yuan, J. Wang, L. Wang, W. Xie, P. Chen, Z. Hou, X. Zheng, Bioresour. Technol. **101**, 7088–7092 (2010); (c) X. Zhou, W. Xu, G. Liu, D. Panda, P. Chen, J. Am. Chem. Soc. **132**, 138–146 (2010); (d) Y. Lei, F. Mehmood, S. Lee, J. Greeley, B. Lee, S. Seifert, R.E. Winans, J.W. Elam, R.J. Meyer, P.C. Redfern, D. Teschner, R. Schlögl, M.J. Pellin, L.A. Curtiss, S. Vajda, Science **328**, 224–228 (2010); (e) Z. Yuan, L. Wang, J. Wang, S. Xia, P. Chen, Z. Hou, X. Zheng, Appl. Catal., B **101**, 431–440 (2011); (f) M. Haruta, Angew. Chem., Int. Ed. **53**, 52–56 (2014)
19. (a) A.F. Lee, S.F. Hackett, J.S. Hargreaves, K. Wilson, Green Chemistry **8**, 549–555 (2006); (b) A. Wang, H. Xu, J. Feng, L. Ding, Y. Tong, G. Li, J. Am. Chem. Soc. **135**, 10703–10709 (2013); (c) L. Li, H. Zhao, J. Wang, R. Wang, ACS Nano **8**, 5352–5364 (2014); (d) L. Li, C. Zhou, H. Zhao, R. Wang, Nano Research **8**, 709–721 (2015); (e) H. Zhong, C. Liu, Y. Wang, R. Wang, M. Hong, Chem. Sci. **7**, 2188–2194 (2016)
20. (a) W. Xu, J.S. Kong, Y.E. Yeh, P. Chen, nat. mater. **7**, 992–996 (2008); (b) P. Zhang, C. Shao, Z. Zhang, M. Zhang, J. Mu, Z. Guo, Y. Liu, Nanoscale **3**, 3357–3363 (2011); (c) S. Wunder, Y.

Lu, M. Albrecht, M. Ballauff, ACS Catal. **1**, 908–916 (2011); (d) P. Hervés, M. Pérez-Lorenzo, L. M. Liz-Marzén, J. Dzubiella, Y. Lu, M. Ballauff, Chem. Soc. Rev. **41**, 5577–5587 (2012); (e) T. Aditya, A. Pal, T. Pal, Chem. Commun. **51**, 9410–9431 (2015); (f) P. Zhao, X. Feng, D. Huang, G. Yang, D. Astruc, Coord. Chem. Rev. **287**, 114–136 (2015)

21. (a) M. Yamauchi, H. Kobayashi, H. Kitagawa, Chem. Phys. Chem. **10**, 2566–2576 (2009); (b) S.B. Kalidindi, H. Oh, M. Hirscher, D. Esken, C. Wiktor, S. Turner, G.V. Tendeloo, R.A. Fischer, Chem. Eur. J. **18**, 10848–10856 (2012)

Chapter 37
Density Functional Theory Study on Mechanism of Enhanced Catalytic Decomposition of Nitromethane on Hydroxylated Graphdiyne

Chi Zhang, Xiurong Yang, Jianyou Zeng, Yinghui Ren, Zhaoqi Guo, and Haixia Ma

Abstract As a new carbon material, graphdiyne (GDY) has special sp, sp^2 hybridized orbitals, which may be a good candidate of combustion catalyst for energetic materials (EMs). The catalytic effect of GDY and hydroxyl group pre-absorbed GDY (OH-GDY) on the decomposition of nitromethane (NM) was investigated using Density functional theory (DFT). The transition states of the initial decomposition reactions of NM on these two surfaces and the corresponding activation energy as well as the heats of reaction were studied. The results show that NM mostly adsorbs on pristine GDY surface via weak dispersion forces. While, NM and the intermediate products can react with O-GDY or OH-GDY by the exchange of protons or oxygen atoms. Different pathways of NM reacting with GDY, O-GDY and OH-GDY to form CH_2OH were investigated and the rate determining step was found with the energy barrier of 16.127 kcal/mol. The reaction mechanism of this step is elucidated to be that the proton of OH-GDY transfers from hydroxyl to the oxygen atom of NM to form an intermediate of CH_3NOOH^+. The theoretical calculation provides the mechanism of NM reacting with GDY and OH-GDY and proves that the functionalized GDY can enhance the performance of NM-based propulsion systems.

C. Zhang · X. Yang · J. Zeng · Y. Ren · Z. Guo · H. Ma (✉)
School of Chemical Engineering/Xi'an Key, Laboratory of Special Energy Materials, Northwest University, Xi'an 710069, China
e-mail: mahx@nwu.edu.cn

C. Zhang
e-mail: 243250303@qq.com

X. Yang
e-mail: 1667312161@qq.com

J. Zeng
e-mail: 2534081107@qq.com

Y. Ren
e-mail: yiren@nwu.edu.cn

Z. Guo
e-mail: zqguo@nwu.edu.cn

A. Gany and X. Fu (eds.), *2021 International Conference on Development and Application of Carbon Nanomaterials in Energetic Materials*, Springer Proceedings in Physics 276,
https://doi.org/10.1007/978-981-19-1774-5_37

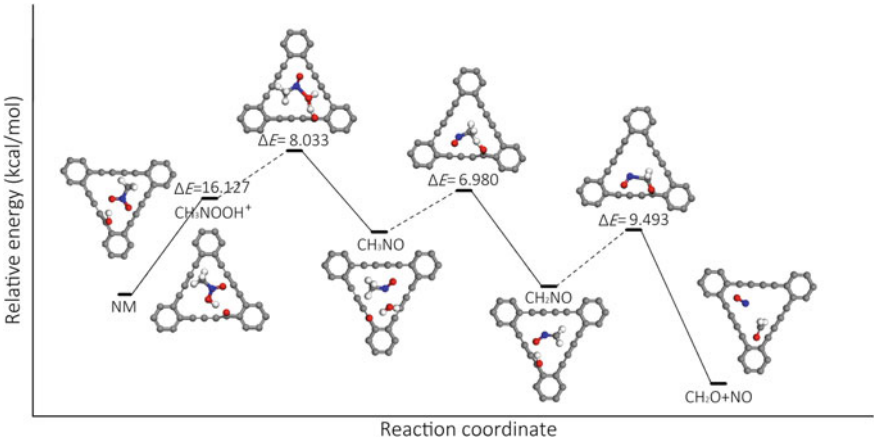

37.1 Introduction

Nitromethane (NM) is considered as a promising candidate of environmentally friendly fuels for future high-speed propulsion systems because of its high energy density, short ignition times, low toxicity and low costs [1–5]. However, the pure NM usually cannot satisfy the requirement for propulsion with high energy release, high detonation velocity and high detonation velocity. So that additive is a possibly effective way to improve the performance of NM. The additives such as Ni, Al powder, amorphous silicon oxide and functionalized graphene sheets were proved to be an effective catalyst for the burning of neat NM by previous research [6–8], especially the functionalized graphene sheets can greatly enhance the burning rate even with low concentrations. However, the mechanism of the EMs catalyzed by additives usually cannot be studied using existing experimental techniques, because the intermediates always exist shortly, which cannot be easily to be captured or detected by equipment. Furthermore, the ignition and combustion processes of NM are complex although the structure of it is simple. Thus, theoretical calculation provides us a good method to study the decomposition paths of NM on additives. Asatryan and co-worker [9] found that the decomposition reaction of NM begins with unimolecular dissociation, the scission of C–N bond which generate methyl and nitrogen dioxide is an event with large activation barrier of 60 kcal/mol. The pristine graphene was fond to have little catalytic effect on NM molecule [10]. While Liu et al. [11] concluded that the decomposition of NM on functionalized graphene sheets begins with proton transfer and the intermediates such as $CH_2NO_2^-$, CH_3NO, or $CH_3NO_2H^+$ quickly undergo additional reactions.

Carbon has many different types of allotropes including fullerenes [12, 13], nitrocellulose [14], carbon nanotubes [15, 16] and graphene [17–19] because it possesses

different hybridized states such as sp, sp_2, sp_3 and different bonding states. Moreover, the element carbon is able to bond with other species to make every allotrope generate many derivatives. Although there are many allotropes, scientists are still interested in novel carbon allotropes with new bonding characteristics and unique properties Such as 2D graphdiyne (GDY). GDY has attracted extensive attention by its unique structure and properties since Li et al. [20] successfully synthesized the large-area GDY film. The large triangular ring with 18 C atoms, which is composed of benzene ring and C≡C bonds, makes GDY possess rich carbon chemical bonds, high conjugation, uniform dispersion of channel configuration and controllable electronic structure. Now, GDY shows good application prospect in photocatalysis [21], spintronics [22], transistors [23], metal-free catalysis [24–26] and lithium ion battey [27]. Our previous work proved that GDY can promote the cleavage of C–N bond, thus the thermal decomposition of RDX was enhanced [28]. Zhang et al. [29] confirmed that the formation of hydroxylated graphdiyne (OH-GDY) is energetically more favorable than that of pristine GDY. Therefore, we take the density functional theory (DFT) investigation on the decomposition behavior of NM on functionalized GDY and pristine GDY to find out the potential application of GDY on energetic materials. Similar with graphene, NM interacts weakly with pristine GDY, mostly physisorption on GDY surface via dispersion forces. Thus, we focus on the initial portions of the reaction graph describing NM decomposition mechanism on OH-GDY, to seek out the potential application of GDY.

37.2 Computational Method and Models

The DFT calculations were performed using the nonlocal generalized gradient approximation (GGA) function by employing the Perdew-Burke-Ernzerhof (PBE) [30] correlation function in $Dmol^3$ package [31] of Materials Studio program (Version 8.0). Van der Waals correction was proposed by Grimme (i.e., DFT-D2 method). Brillouin zone sampling was calculated using a Monkhorst–Pack grid with respect to the symmetry of system and the electronic occupancies were determined according to a Methfessel–Paxton scheme with an energy smearing of 0.005 Ha (1 Ha = 627.51 kcal/mol), the meshes were set to *k*-points 3 × 3 × 1 for GDY. The convergence criteria for geometry optimization was set to the tolerance for the energy, maximum force, maximum displacement and SCF on all atoms of 1.0×10^{-1} Ha, 0.002 Ha/Å, 0.005 Å and 1.0×10^{-6} Ha, respectively. The double numerical plus polarization (DNP) was used to get more accurate results.

The complete LST/QST approach (liner/quadratic synchronous transit) was employed to search transition state (TS) structure and to calculate the activation energy (E_a) of the redox reaction of NM and its decomposition products. The value of E_a was calculated as follows:

$$E_a = E_{TS} - E_{IS}$$

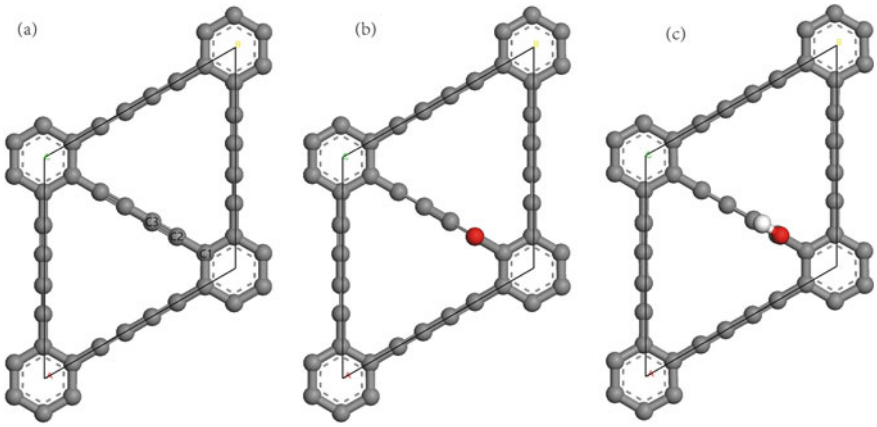

Fig. 37.1 Geometric structures of **a** pristine GDY, **b** O-GDY, **c** OH-GDY, the gray, red, and white balls represent C, O and H atoms, respectively

where E_{TS} and E_{IS} are the "total energy" of the TS and the initial states (IS), respectively. The frequency calculation and nudged elastic band (NEB) tools were used to confirm the minimum energy pathway (MEP).

The pristine and functionalized GDY structures used in this work were show in Fig. 37.1, the primitive cell of pristine GDY containing 18 carbon atoms. The optimized cell parameter of graphdiyne is 9.463 Å, the mean C–C bond length in hexagon is 1.428 Å, the C_{sp2}–C_{sp}, C_{sp}–C_{sp} and $C_{sp}\equiv C_{sp}$ bond lengths in the diacetylenic links are 1.400, 1.342 and 1.232 Å, respectively. These values are in good agreement with the research previously [32, 33], which implies that the constructed model is reasonable and the computational approach is appropriate. The pre-adsorbed O atoms are expected to emerge with the proton transfer reaction on OH-GDY. In order to simplify the calculation, the reactions between NM and O atom adsorbed on the OH-GDY surface were calculated on the isolated O-GDY surface.

37.3 Results and Discussion

37.3.1 The First Step of Decomposition Reaction of NM

On the basis of the structures of NM molecule, the pristine and functionalized GDY, five possible reaction pathways of CH_3NO_2 were studied. The structures of the IS, TS and FS which along the minimum energy path (MEP) of the five reactions were shown in Fig. 37.2, and energy barriers (E_a) and reaction heats (E_r) of elementary steps are detailed listed in Table 37.1. It can be seen from the energy profile that all possible reactions in the first step were endothermal. In four pathways, the reaction had no transition state that the total energy of all structures in the path coordinate of

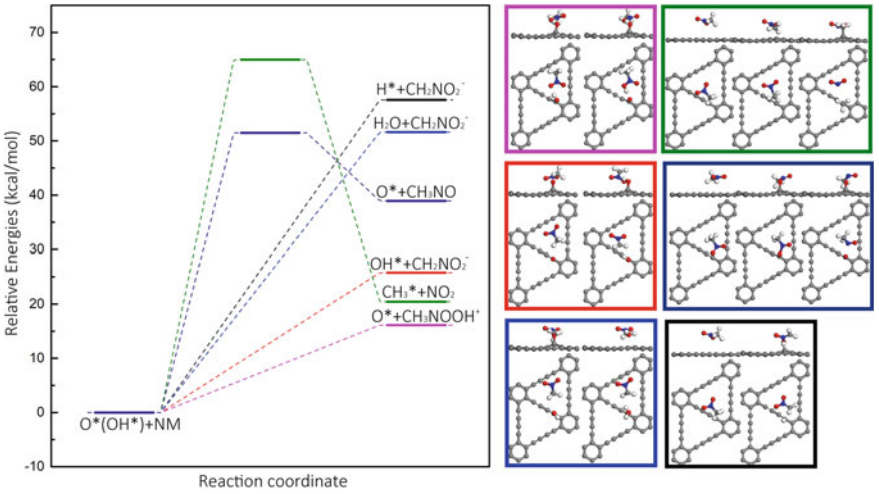

Fig. 37.2 The energy profile of the first step of decomposition reaction path of NM on GDY. The structure of the IS, TS and FS which along minimum energy path (MEP) are shown in the same color with the corresponding reaction of NM. The grey, blue, red, and white balls indicate C, N, O and H atoms. The symbol * indicate the species bonding to C1 site of GDY

Table 37.1 The activation energy (E_a) and heat of reaction (E_r) of the first step of decomposition reaction path of NM on GDY

Reactions	E_a	E_r
$OH^* + CH_3NO_2 \rightarrow O^* + CH_3NOOH^+$	–	16.127
$^* + CH_3NO_2 \rightarrow CH_3{}^* + NO_2$	64.994	20.436
$O^* + CH_3NO_2 \rightarrow OH^* + CH_2NO_2{}^-$	–	25.796
$^* + CH_3NO_2 \rightarrow O^* + CH_3NO$	51.477	38.904
$OH^* + CH_3NO_2 \rightarrow H_2O + CH_2NO_2{}^-$	–	51.616
$^* + CH_3NO_2 \rightarrow H^* + CH_2NO_2{}^-$	–	57.578

The symbol * indicate the species bonding to C1 site of GDY (Unit in kcal/mol)

TS search were higher than that of IS while lower than that of FS, which indicated that the reverse reaction may be a spontaneous process. Thus, no barriers were reported for these pathways in Table 37.1. The most feasible reaction pathway in the first step was NM molecule interacting with OH-GDY and the H atom transferred from hydroxyl group to oxygen atom of NM, which was an endothermal reaction without activation energy barrier. The initial state and final state configurations of the proton transfer are shown in Fig. 37.2 (pink box). When NM is adsorbed on OH-GDY surface, the NM molecule adsorbed on the 18C-ring and formed hydrogen bond with H atom of OH group, the distance between H of hydroxyl and O of NM is 1.702 Å and the O–H bond length is 1.011 Å, longer than 0.977 Å when no adsorbate on the surface. In the final state of this reaction, the CH_3NOOH^+ species still adsorbed on the 18C-hexagon, the O–H bond length in CH_3NOOH^+ is 0.998 Å and the hydrogen

bond length is 1.548 Å, the corresponding C–O bond length decreases from 1.362 to 1.293 Å with the proton gradually transferring from OH-GDY to O atom of NM, and N–O bond extends from 1.268 to 1.362 Å. In consideration of the relatively lower energy barrier of this pathway, the product CH_3NOOH^+ was selected to be the reactant in the next step.

The other three non-barrier pathways as shown in Fig. 37.2 (black, red and blue boxes) were proton transferring processes, too, with the proton transferring from the methyl group of NM to the catalyst substrates. On the surfaces of GDY or O-GDY, the protons bond with carbon atom or oxygen atom, respectively. While on OH-GDY surface, the proton interacted with hydroxyl group to form H_2O molecule. It can be seen that the functionalized GDY exhibited higher activity than pristine GDY in the reaction pathways. The hydroxyl group exhibited more significant catalysis than pre-adsorbed oxygen atom, when it acted as proton donor. The product $CH_2NO_2^-$ of these pathways could easily capture H atom from hydroxyl group and spontaneously form the intermediate product CH_2NOOH.

The energy barrier of C–N bond broken (green box in Fig. 37.2) was as high as 64.994 kcal/mol which is slightly higher than that in gas phase without catalyst, indicates that the pristine GDY has no catalysis, but with negative catalytic effect for this pathway. The reaction of the N–O bond broken of NM was shown in Fig. 37.2 (navy box) and has a high energy barrier of 51.477 kcal/mol. In the FS structure of this pathway, the dissociated oxygen atom interacted with C atom to form a C–O bond with the GDY.

37.3.2 The Second Step of Decomposition Reaction of NM

Since the reaction to produce CH_3NOOH^+ species has the lowest energy barrier, seven possible reaction pathways starting with CH_3NOOH^+ were studied in this step, the corresponding reaction equations, energy barriers and reaction heats were list in Table 37.2. The IS, TS, and FS structures of these seven reactions were shown

Table 37.2 The activation energy (E_a) and heat of reaction (E_r) of the second step of decomposition reaction path of NM on GDY

Reactions	E_a	E_r
$OH^* + CH_3NOOH^+ \rightarrow H_2O + CH_2NOOH$	31.395	−14.075
$O^* + CH_3NOOH^+ \rightarrow OH^* + CH_2NOOH$	7.732	−7.104
$OH^* + CH_3NOOH^+ \rightarrow O^* + CH_4 + HNO_2$	34.719	−6.162
$OH^* + CH_3NOOH^+ \rightarrow O^* + H_2O + CH_3NO$	8.033	−5.634
$* + CH_3NOOH^+ \rightarrow CH_3* + HNO_2$	41.147	−1.683
$* + CH_3NOOH^+ \rightarrow OH^* + CH_3NO$	23.381	6.897
$* + CH_3NOOH^+ \rightarrow H^* + CH_2NOOH$	22.039	14.644

The symbol * indicate the species bonding to C1 site of GDY (Unit in kcal/mol)

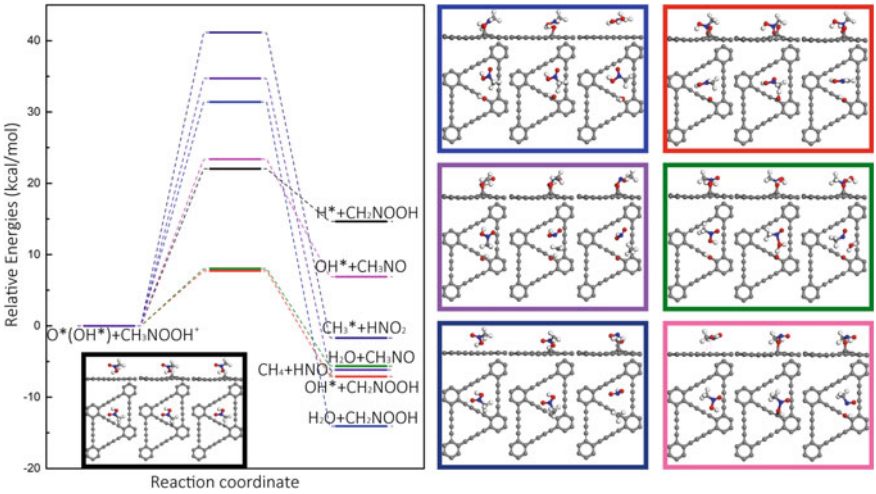

Fig. 37.3 The energy profile of the second step of decomposition reaction path of NM on GDY. The structure of the IS, TS and FS which along minimum energy path (MEP) are shown in the same color with the corresponding reaction of NM. The grey, blue, red, and white balls indicate C, N, O and H atoms. The symbol * indicate the species bonding to C1 site of GDY

in Fig. 37.3. The minimum energy barrier pathway in this step was shown in red box of Fig. 37.3, which formed CH_2NOOH species and the activation energy barrier and reaction heat were 7.732 and −7.104 kcal/mol, respectively. When CH_3NOOH^+ adsorbed on the O-GDY, the whole species was perpendicular to the surface. The O atom adsorbed on the central site of the 18C-ring and the distance was 1.030 Å. The three H atoms of methyl were not in the plane defined by C–N–O atoms. In the transition state of this pathway, a H atom transferred toward the pre-adsorbed oxygen atom and bond with it, which made the methyl also move toward the O atom and caused the whole CH_3NOOH^+ slightly tilted to the surface. The C–H bond length elongated from 1.100 to 1.308 Å, and the forming O–H bond length was 1.294 Å. In the final state, the H atom continued to move toward O atom, which leads to the completely breaking of C–H bond, then, the hydroxyl group adsorbing on GDY surface with O–H bond length 0.979 Å formed. As the methylene moved back, the CH_2NOOH intermediate adsorbed on the central site of the 18C-ring via vertical orientation. The bond length of C–N changes from 1.457 to 1.306 Å, indicating that the C–N bond may change from single bond to double bond. And all atoms of the CH_2NOOH species move into a same plane except H atom of hydroxyl group. Because of the lowest activation energy barrier in this pathway, the CH_2NOOH intermediate was selected as one initial structure of the next step.

There were two other pathways also generated the intermediate CH_2NOOH as shown in Fig. 37.3 (blue and black boxes), which the reactant CH_3NOOH^+ interacted with OH-GDY and pristine GDY, respectively. The energy barriers of the methyl dehydrogenation reaction of CH_3NOOH^+ species were significantly lower than NM,

indicating that CH_3NOOH^+ has a higher reactivity. The energy barrier of the methyl dehydrogenation reaction on OH-GDY was higher the that on pristine GDY, but the reaction on OH-GDY was exothermic which is contrary to the endothermic reaction on pristine GDY.

Another intermediate product CH_3NO was also selected as one initial structure of the next step, because the energy barrier of the pathway was 8.033 kcal/mol which is slightly higher than the lowest activation energy barrier. The structure of initial state of this reaction pathway was shown in Fig. 37.3 (green box). The CH_3NOOH^+ species adsorbed on the OH-GDY via parallel orientation. The O–H bonds of CH_3NOOH^+ species and hydroxyl group which adsorbed on GDY were parallel to each other. In the transition state of this pathway, the distance between the two hydroxyl groups decreases and the N–OH bond length increases from 1.409 to 1.896 Å. The C–O bond of the OH group adsorbed on GDY rotated and the H atom moves toward the O atom of CH_3NOOH^+ species and formed O–H bond with a bond length of 1.336 Å. In the final state, the N–O bond and O–H bond completely broke and generated H_2O molecule and CH_3NO species. The C–N bond length increased from 1.455 to 1.492 Å. The reaction heat of this pathway was -5.634 kcal/mol. When the CH_3NOOH^+ species interacted with pristine GDY, it also could generate CH_3NO via N–OH bond broken directly then the dissociated OH group adsorbed on GDY, but the process changed into an endothermic reaction and the energy barrier increased remarkably.

The pathways involved C–N bond broken also have been studied, as shown in Fig. 37.3 (violet and navy boxes). The energy barriers of these pathways were higher than all other pathways in this step. However, comparing with the process of C–N bond broken of NM molecule in the first step, the barrier decreased evidently, indicating that the hydrogenation of nitro group activated all bonds of NM molecule. In the TS of the two processes, the four atoms of methyl moved into a same plane. For the reaction on OH-GDY, the C atom of methyl was attacked from the back of N–C bond to form methane and nitrite acid. While on pristine GDY, the products were nitrite acid and methyl group because of the absence of hydroxyl group.

37.3.3 The Third Step of Decomposition Reaction of NM

Because two intermediate products generated in the second step were selected as the reactants of the third step, this step can be divided into two main pathways that denoted by third step A (started with CH_2NOOH species) and third step B (started with CH_3NO species). The structures of IS, TS and FS along the pathways were shown in Figs. 37.4 and 37.5, and the corresponding activation energies and reaction heats of those reactions were listed in Tables 37.3 and 37.4, respectively.

For the third step A, the minimum energy barrier pathway (red box in Fig. 37.4) was the dehydroxylation reaction of the CH_2NOOH on OH-GDY, the energy barrier and reaction heat of this pathway were 11.937 and 7.409 kcal/mol, respectively. The process was same as the reaction pathway of $OH^* + CH_3NOOH^+ \rightarrow O^* +$

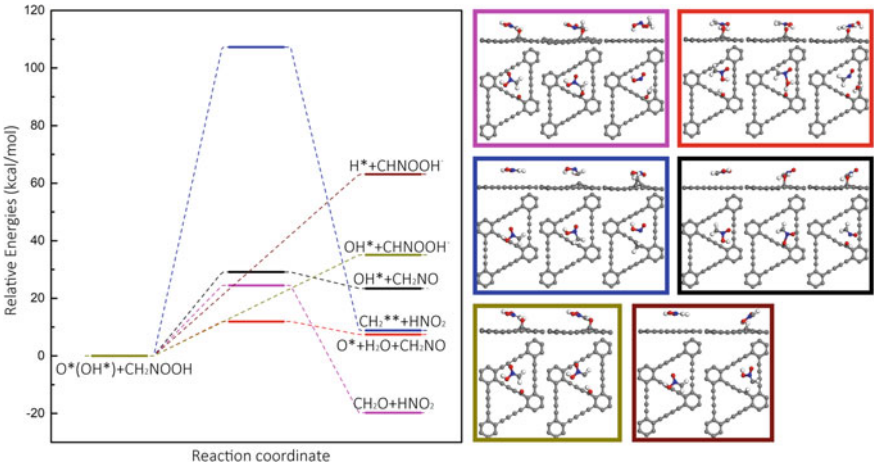

Fig. 37.4 The energy profile of the third step A of decomposition reaction path of NM on GDY. The structure of the IS, TS and FS which along minimum energy path (MEP) are shown in the same color with the corresponding reaction of NM. The grey, blue, red, and white balls indicate C, N, O and H atoms. The symbol * indicate the species bonding to C1 site of GDY

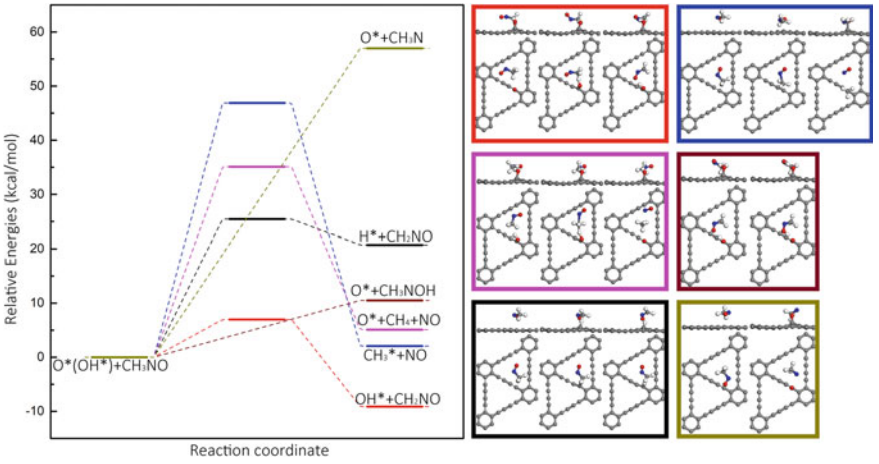

Fig. 37.5 The energy profile of the third step B of decomposition reaction path of NM on GDY. The structure of the IS, TS and FS which along minimum energy path (MEP) are shown in the same color with the corresponding reaction of NM. The grey, blue, red, and white balls indicate C, N, O and H atoms. The symbol * indicate the species bonding to C1 site of GDY

$H_2O + CH_3NO$. There was another pathway generated the CH_2NO species as shown in black box of Fig. 37.4. The N–O bond of CH_2NOOH cleaved, followed by the dissociated OH group which will later interact with C atom to adsorbed on pristine GDY. The energy barrier of this pathway increased to 29.116 kcal/mol and the

Table 37.3 The activation energy (E_a) and heat of reaction (E_r) of the third step A of decomposition reaction path of NM on GDY

Reactions	E_a	E_r
$O^* + CH_2NOOH \rightarrow CH_2O + HNO_2$	24.501	−19.728
$OH^* + CH_2NOOH \rightarrow O^* + H_2O + CH_2NO$	11.937	7.409
$^* + CH_2NOOH \rightarrow CH_2^* + HNO_2$	107.254	8.853
$^* + CH_2NOOH \rightarrow OH^* + CH_2NO$	29.116	23.441
$O^* + CH_2NOOH \rightarrow OH^* + CHNOOH^-$	–	35.110
$^* + CH_2NOOH \rightarrow H^* + CHNOOH^-$	–	63.130

The symbol * indicate the species bonding to C1 site of GDY (Unit in kcal/mol)

Table 37.4 The activation energy (E_a) and heat of reaction (E_r) of the third step B of decomposition reaction path of NM on GDY

Reactions	E_a	E_r
$O^* + CH_3NO \rightarrow OH^* + CH_2NO$	6.980	−9.135
$^* + CH_3NO \rightarrow CH_3^* + NO$	46.878	2.059
$OH^* + CH_3NO \rightarrow O^* + CH_4 + NO$	35.108	5.103
$OH^* + CH_3NO \rightarrow O^* + CH_3NOH$	–	10.510
$^* + CH_3NO \rightarrow H^* + CH_2NO$	25.446	20.736
$^* + CH_3NO \rightarrow O^* + CH_3N$	–	57.002

The symbol * indicate the species bonding to C1 site of GDY (Unit in kcal/mol)

reaction has a heat requirement of 23.441 kcal/mol. We also studied the methylene dehydrogenation of CH_2NOOH as shown in dark yellow box of Fig. 37.4, but the process was difficult to proceed since it needs to overcome an energy barrier of 35.110 kcal/mol. Two pathways involving the break of C–N bond were shown in Fig. 37.4 (blue and pink boxes). One is directly break on pristine GDY and the other is break by the attacking of the oxygen atom on O-GDY. The directly break of C–N bond has a very high energy barrier of 107.254 kcal/mol with the heat requirement of 8.853 kcal/mol. And the dissociated methylene adsorbed on the bridge site between the C1-C2 of diacetylenic link, and the generated nitrous acid adsorbed on the center of the 18C-ring via Van der Waals force. On O-GDY, the C atom of CH_2NOOH interacted with the pre-adsorbed oxygen atom to form a formaldehyde molecule and nitrous acid with the physisorption interaction with GDY.

For the third step B, the pathway that the methyl of CH_3NO dehydrogenated on O-GDY, as shown in red box of Fig. 37.5, has the lowest activation energy barrier of 6.980 kcal/mol, and a heat release of 19.728 kcal/mol. In the transition state of this pathway, as the whole CH_3NO species moved from the center site of 18C-ring to the pre-adsorbed oxygen atom, a C–H bond of methyl elongated from 1.098 to 1.375 Å and the H atom bonded with the pre-adsorbed oxygen atom with a bond length of 1.214 Å. In the final states, with the twirl of CH_2NO species, the C–H bond broke completely, thus a hydrogen bond formed between O atom of CH_2NO species

and the new formed OH group. The similar reaction process also happened in the pathway that the methyl of CH_3NO dehydrogenated on pristine GDY (black box of Fig. 37.5), but it was an endothermic reaction and the energy barrier increased to 25.446 kcal/mol.

The pathway that N–O bond was broke followed by the dissociated oxygen atom which was adsorbed on GDY (dark yellow box of Fig. 37.5) was an endothermic reaction without energy barrier. And the heat requirement was 57.002 kcal/mol. There was another pathway also an endothermic reaction without energy barrier, which the proton transferred from OH-GDY to the O atom of CH_3NO species with a heat requirement of 10.510 kcal/mol. There were two pathways involved C–N bond broken in third step B as the second step, just the product HNO_2 change to NO. The reaction processes in the pathways were also same as that of the corresponding pathways in the second step, but the energy barrier increased.

It is reported that the most probable product CH_2NO generated both from the third step A and B was considered to be a very reactive intermediate product [11]. The CH_2NO species can easily interact with O to form an unstable species CH_2ONO which would decompose into CH_2O and NO. So that the process that CH_2NO interact with O and generated CH_2O was studied and shown in Fig. 37.6. The energy barrier and reaction heat were 9.493 and −16.355 kcal/mol, respectively. In the transition state, the C–N bond of CH_2NO rotated and the C atom bonded with the O atom of O-GDY. In the final state, the C–N bond and C–O bond broke to generate CH_2O and NO molecules which were adsorbed on GDY surface via Van der Waals force. The relatively low energy barrier of this reaction on functionalized GDY agreed with the literature that CH_2NO was a very reactive intermediate product.

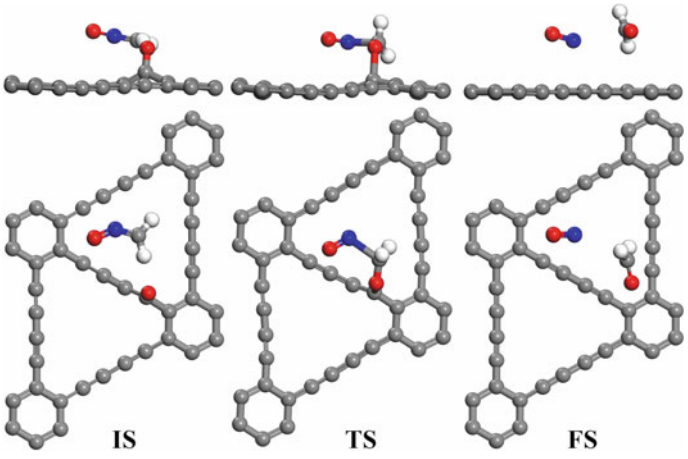

Fig. 37.6 The structure of the IS, TS and FS which along minimum energy path (MEP) in the process that CH_2NO interact with O and generated CH_2O. The grey, blue, red, and white balls indicate C, N, O and H atoms

37.3.4 Mechanism Analysis

The formation of intermediates and products, the depletion of reactant during the reaction routes can be utilized to illustrate by analysis the reaction pathways. Because the intermediate CH_3NOOH was further decomposed to CH_2NOOH or CH_3NO along two different reaction routes, the two reaction routes were summarized. NM $\rightarrow$ CH_3NOOH $\rightarrow$ CH_2NOOH $\rightarrow$ CH_2NO $\rightarrow$ CH_2O and NM $\rightarrow$ CH_3NOOH $\rightarrow$ CH_3NO $\rightarrow$ CH_2NO $\rightarrow$ CH_2O were denoted by route A and route B, respectively. And the corresponding energy barriers were 16.127 $\rightarrow$ 7.732 $\rightarrow$ 11.937 $\rightarrow$ 9.493 kcal/mol and 16.127 $\rightarrow$ 8.033 $\rightarrow$ 6.980 $\rightarrow$ 9.493 kcal/mol, respectively. In both routes, the rate-determining step was the first step that the proton transferred from OH-GDY to NM. Because the relatively higher energy barrier of the third step in route A, route B is considered the more preferable pathway. The spread of the intermediate products on the functionalized GDY which was not discussed in this work may also affect the reaction routes.

37.4 Conclusions

In this work, the reaction mechanism of NM on the GDY were identified in detailed through DFT calculation. Comparing with pure GDY, the O- and OH-GDY usually tend to promote the reactions of NM to the paths with low activation energy and large heat release. It was found that the reactions on pristine GDY had higher energy barriers than that on functionalized GDY in each step. The minimum energy pathway of the decomposition of NM to forming CH_2O was found and determined by studying the possible intermediates step by step, which was started with NM molecule through the path NM $\rightarrow$ CH_3NOOH^+ $\rightarrow$ CH_3NO $\rightarrow$ CH_2NO $\rightarrow$ CH_2O. The first process which the proton transferred from OH-GDY to NM to generate the activation species CH_3NOOH^+ was the rate-determining step. Thus, the functionalized GDY can be a good catalysis for improving the reaction rate and efficiency of NM.

Acknowledgements This work was supported by the Foundation of State Key Laboratory of Coal Conversion (Grant. No. J20-21-904) and Natural Science Basic Research Program of Shaanxi (No. 2021JM-322)

References

1. T. Edwards, Liquid fuels and propellants for aerospace propulsion: 1903–2003. J. Propuls. Power **19**(6), 1089–1107 (2003)
2. L.Q. Maurice, H. Lander, T. Edwards et al., Advanced aviation fuels: a look ahead via a historical perspective. Fuel **80**(5), 747–756 (2001)

3. H. Qi, M. Zhong, S.H. Zh, F.S. Liu, Q.J. Liu, Inversely deducing the initiation mechanism of energetic materials under pressure from possible defect states in nitromethane. Chem. Phys. Lett. **749**, 137470 (2020)
4. J. Xu, Y. Bian, Y. Liu, D. Zhai, Reactive molecular dynamics study of thermal decomposition of nanocarbon energetic composite materials. Comput. Mater. Sci. **131**, 126–131 (2017)
5. G.H. Dong, H.S. Ge, D.H. Li, Density functional theory study on the temperature of nitromethane molecule under pressure. Chin. J. At. Mol. Phys. **32**(2), 181–189 (2015)
6. J.L. Sabourin, D.M. Dabbs, R.A. Yetter et al., Functionalized graphene sheet colloids for enhanced fuel/propellant combustion. ACS Nano **3**(12), 3945 (2009)
7. N. He, C. Xiang, W. Li, Q. Zhang, Experimental study on deflagrating characteristics of nitromethane-aluminum powder. Acta Armamentarii **39**(1), 111–117 (2018)
8. J.A. Benziger, Mechanistic study of nitromethane decomposition on Ni catalysts. Mechan. Stud. Nitromethane Decompos. Ni Catal. **1982**, 1–20 (1982)
9. R. Asatryan, J.W. Bozzelli, J.M. Simmie, Thermochemistry of methyl and ethyl nitro, RNO_2, and nitrite, RONO, organic compounds. J. Phys. Chem. A **112**(14), 3172–3185 (2008)
10. Y.Z. Liu, Y. Kang, W.P. Lai, T. Yu, Z.X. Ge, Reaction mechanism of nitromethane on the graphene surface: a theoretical study. Chin. J. Energ. Mater. **23**(9), 871–876 (2015)
11. L.M. Liu, R. Car, A. Selloni, D.M. Dabbs, I.A. Aksay, Enhanced thermal decomposition of nitromethane on functionalized graphene sheets: ab initio molecular dynamics simulations. J. Am. Chem. Soc. **134**(46), 19011–19016 (2012)
12. H.W. Kroto, J.R. Heath, S.C. O'Brien, R.F. Curl, R.E. Smalley, C60: Buckminsterfullerene. Nature **318**, 162–163 (1985)
13. K. Hirata, K. Yamada, A. Chiba, Y. Hirano, K. Narumi, Y. Saitoh, Experimental characterization of ultrafast phenomena of secondary-ion emission induced by nanoscale energy deposition processes of energetic C-60 impacts. J. Appl. Phys. **127**(21), 214302 (2020)
14. B.X. Han, Compatibility and thermal decomposition mechanism research of nitrocellulose/Cr_2O_3 nanoparticles. Acta Physica-Chimica Sinica **36**(6), 1907020 (2020)
15. A. Hirsch, The era of carbon allotropes. Nat. Mater **9**, 868–871 (2010)
16. J.E. Um, T. Yeo, W. Choi, J.S. Chae, H.S. Kim, W.J. Kim, Enhanced energy release from homogeneous carbon nanotube-energetic material composites. Sci. Adv. Mater. **8**(1), 167–170 (2016)
17. K. Novoselov, V. Fal′ko, L. Colombo et al., A roadmap for graphene. Nature **490**, 192–200 (2012)
18. F.Y. Guan, H. Ren, L. Yu, Q.Z. Cui, W.J. Zhao, J. Liu, Nitrated graphene oxide derived from graphite oxide: a promising energetic two-dimensional material. Nanomaterials **11**(1), 58 (2021)
19. T. Zhang, C.C. Li, W. Wang, Z.Q. Guo, A.M. Pang, H.X. Ma, Construction of three-dimensional hematite/graphene with effective catalytic activity for the thermal decomposition of CL-20. Acta Physica-Chimica Sinica **36**(6), 1905048 (2020)
20. G.X. Li, Y.L. Li, H.B. Liu, Y.B. Guo, Y.J. Li, D.B. Zhu, Architecture of graphdiyne nanoscale films. Chem. Commun. **46**, 3256–3258 (2010)
21. P. Wu, P. Du, H. Zhang, C.X. Cai, Graphdiyne as a metal-free catalyst for low-temperature CO oxidation. Phys. Chem. Chem. Phys. **16**, 5640–5648 (2014)
22. J.J. He, S.Y. Ma, P. Zhou, C.X. Zhang, C.Y. He, L.Z. Sun, Magnetic properties of single transition-metal atom absorbed graphdiyne and graphyne sheet from DFT+U calculations. J. Phys. Chem. C **116**, 26313−26321 (2012)
23. S. Wang, L.X. Yi, J.E. Halpert, X.Y. Lai, Y.Y. Liu, H.B. Cao, R.B. Yu, D. Wang, Y.L. Li, A novel and highly efficient photocatalyst based on P25-graphdiyne nanocomposite. Small **8**, 265–271 (2012)
24. Y.Y. Pan, Y.Y. Wang, L. Wang, H. Zhong, R. Quhe, Z. Ni, M. Ye, W.N. Mei, J.J. Shi, W. Guo, J. Yang, J. Lu, Graphdiyne-metal contacts and graphdiyne transistors. Nanoscale **7**, 2116–2127 (2015)
25. H. Shen, Y.J. Li, Z. Shi, A novel graphdiyne-based catalyst for effective hydrogenation reaction. ACS Appl. Mater. Interf. **11**(3), 2563–2570 (2019)

26. R.J. Liu, H.B. Liu, Y.L. Li, Y.P. Yi, X.K. Shang et al., Nitrogen-doped graphdiyne as a metal-free catalyst for high-performance oxygen reduction reactions. Nanoscale **6**(19), 11336–11343 (2014)
27. B. Jang, J. Koo, M. Park, H. Lee, J. Nam, Y. Kwon, H. Lee, Graphdiyne as a high-capacity lithium ion battery anode material. Appl. Phys. Lett., **103**, 263904 (2013)
28. J.Y. Zeng, N.N. Zhang, T. Zhang, E.G. Yao, F.Q. Zhao, H.X. Ma, Thermal decomposition of graphdiyne/RDX composites. Chin. J. Explos. Propellants **4**, 474–483 (2021)
29. P. Zhang, S.Y. Ma, L.Z. Sun, Hydroxylated graphyne and graphdiyne: first-principles study. Appl. Surf. Sci. **361**(15), 206–212 (2016)
30. B. Delley, From molecules to solids with the $DMol^3$ approach. J. Chem. Phys. **113**, 7756–7764 (2000)
31. J.P. Perdew, K. Burke, M. Ernzerhof, Generalized gradient approximation made simple. Phys. Rev. Lett. **78**(7), 1396–1396 (1997)
32. L.D. Pan, L.Z. Zhang, B.Q. Song et al., Graphyne- and graphdiyne-based nanoribbons: density functional theory calculations of electronic structures. Appl. Phys. Lett. **98**(17), 666 (2011)
33. B.G. Kim, H.J. Choi, Graphyne: hexagonal network of carbon with versatile Dirac cones. Phys. Rev. B Condens. Matter **86**(11), 2904–2912 (2012)

Chapter 38
Determination of Chlorobenzene in Graphene by Gas Chromatography Mass Spectrometry

Yi Lu, Guojian Guo, Xinran You, Lijun Wu, Qining Xun, and Xia Liu

Abstract The content of chlorobenzene in graphene was determined by gas chromatography mass spectrometry. The four methods of solvent soaking method, Soxhlet extraction method, ultrasonic method, ultrasonic solvent soaking method and the extraction effect of the extraction parameters on the content of chlorobenzene in graphene were investigated respectively. The results show that the ratio of solvent to graphene is 30:1. The method of immersing in solvent for 1 h after ultrasonic for 8 min can achieve the maximum extraction of graphene chlorobenzene by repeating twice. The influence of the type of chromatographic column, the temperature of the column oven and the split ratio on the test results were investigated. The results showed that the best effect is when the column oven temperature is 100 °C and the split ratio is 10:1. The spiked recovery rate of the method is between 93.4 and 107.3%, the repeatability is 5.6%, the stability is 9.3%, the method detection limit is 0.00048%, and the sample detection limit is 0.015%. It can be used for trace chlorine in graphene. Accurate determination of benzene.

Y. Lu (✉) · G. Guo · X. You · L. Wu · Q. Xun · X. Liu
Shandong Non-Metallic Materials Institute, Jinan 250031, Shandong, China
e-mail: titi_ly@sina.com

G. Guo
e-mail: ggj_2009@126.com

X. You
e-mail: yxr2012@163.com

L. Wu
e-mail: marely1236@126.com

Q. Xun
e-mail: xunqining1977@sohu.com

X. Liu
e-mail: liuxia@163.com

A. Gany and X. Fu (eds.), *2021 International Conference on Development and Application of Carbon Nanomaterials in Energetic Materials*, Springer Proceedings in Physics 276,
https://doi.org/10.1007/978-981-19-1774-5_38

38.1 Introduction

Graphene is a nanomaterial composed of a single atomic layer of carbon. It has excellent thermal, electrical, and mechanical properties. It has been successfully applied to energetic materials such as propellants, explosives, and energetic ionic liquids, realizing energetic materials. The combustion performance, mechanical performance, and mechanical sensitivity performance of the gas are improved [1–4].

The liquid phase separation method is one of the important methods that can prepare graphene in batches. The basic principle is to soak the graphene in chlorobenzene and use the method of ultrasonic vibration to use the intermolecular force of chlorobenzene to be close to the intermolecular force of graphene. The characteristics of the intermolecular intercalation under the action of ultrasonic external force, so as to achieve the preparation of graphene. The advantage of this method is that the quality of graphene is significantly higher than that of the mechanical exfoliation method. The disadvantage is that chlorobenzene will remain in the graphene to a certain extent, which will significantly affect the performance of graphene energetic materials, such as reducing the combustion performance and deterioration of energetic materials. Mechanical sensitivity of energetic materials, etc. Therefore, it is of great significance to accurately determine the content of chlorobenzene in graphene [5–8].

Gas chromatography mass spectrometry has the advantages of low detection limit, high accuracy, and good repeatability. It has been successfully applied to the determination of chlorobenzene content in plastic [9], leather [10], surface water [11], and air [12]. In this paper, this technique is applied to the determination of chlorobenzene content in graphene. The digestion method, ICP test conditions, detection limit, repeatability and recovery rate of standard addition were investigated respectively.

38.2 Experiment

38.2.1 Materials

(1) Acetone: chromatographically pure, with a purity of not less than 99.9%.
(2) Chlorobenzene: The purity is not less than 99%.
(3) Standard stock solution (1%): Weigh 1 g (accurate to 0.1 mg) of chlorobenzene, add it to 99 g of acetone (accurate to 0.1 mg), shake and mix well, and store at 4 °C.
(4) Standard working solution: Dilute the standard stock solution with acetone to obtain a series of standard working solutions with concentrations of 0.01, 0.02, 0.03, 0.05 and 0.1%.
(5) Water: Three times distilled water.

38.2.2 Instruments and Consumables

(1) Gas chromatography mass spectrometer: with EI source.
(2) Electronic balance: Sensitivity 0.1 mg.
(3) Ultrasonic machine: The volume is greater than 100 ml.
(4) Disposable filter membrane: 0.45 μm.
(5) Disposable needle tube: the volume is greater than 5 ml.
(6) Conical flask with stopper: 50 ml, glass material.
(7) Pipette gun: qualified after verification.
(8) Chromatography sample bottle: 2 ml, glass material.

38.2.3 Instrument Working Conditions

(a) Chromatographic column: Polar column DB-WAX, 30 m × 0.320 mm × 0.25 μm.
(b) Column temperature: the initial temperature is 50 °C, keep for 10 min, and increase the temperature to 100 °C at 10 °C/min, keep 10 mim.
(c) Temperature of the injection port: 280 °C.
(d) Chromatography-mass spectrometry interface temperature: 280 °C.
(e) Ion source temperature: 230 °C.
(f) MS quadrupole temperature: 150 °C.
(g) Solvent delay: 4 min.
(h) Carrier gas: high-purity helium gas with a flow rate of 1.0 mL/min.
(i) Ionization method: EI.
(j) Injection volume: 1.0 μL.
(k) Split ratio: 10:1.

38.2.4 Principle of the Method

The graphene sample is immersed in acetone, and the chlorobenzene in the graphene is fully transferred to the acetone by ultrasonic at a specific temperature and a specific time. The graphene in the extract is filtered out with a filter membrane, and then the external standard method is used. The gas chromatography-mass spectrometer is used for the determination.

Table 38.1 Extraction effect of chlorobenzene with different soaking time

Extraction time (h)	6	12	24	36	48	60
Measured value of chlorobenzene (%)	0.094	0.128	0.155	0.173	0.206	0.208

38.3 Results and Discussion

38.3.1 Sample Preparation Method

The extraction effect of chlorobenzene in graphene by four methods: solvent immersion method, Soxhlet extraction method, ultrasonic method, and ultrasonic solvent immersion method were investigated respectively.

38.3.1.1 Solvent Immersion Method

The solvent soaking method is the simplest method to extract organic impurities. It is to directly soak graphene in a solvent in an Erlenmeyer flask with a stopper to achieve the extraction of chlorobenzene from the graphene. The main parameter to be investigated is the extraction time.

Therefore, we have investigated the extraction effect of different soaking times. It needs to be explained that the graphene soaked in acetone will gradually deposit after standing for a period of time, and the extraction efficiency will decrease. Therefore, we manually shake the plug cone once every 4 h. Bottle to re-disperse the graphene into the acetone solvent to improve the extraction efficiency. Another issue that needs attention is the temperature. The higher the temperature, the higher the extraction efficiency. However, because acetone is a volatile solvent, the temperature should not be too high. Also, because the solvent immersion method usually takes a long time, higher temperature will bring about volatilization. The loss will be very obvious. We have determined through experiments that the temperature cannot be higher than 35 °C, and the volatilization will be very obvious if it is higher than 35 °C for a long time, so the extraction temperature is set at 35 °C.

After determining the extraction temperature, we specifically investigated the extraction effect of 6, 12, 18, 24, 48, and 60 h soaking time. See Table 38.1. It can be seen that as the soaking time increases, the extraction effect gradually improves. It remained basically unchanged around 48 h. It can be seen that the extraction of chlorobenzene in graphene can be achieved by the soaking method, but the efficiency is very low, requiring 48 h.

38.3.1.2 Soxhlet Extraction Method

Because the extraction time of the solvent soaking method is too long, we consider trying to adopt the accelerated extraction method, the first thing that comes to mind is

the Soxhlet extraction method. Soxhlet extraction, also known as sand extraction, is a method of extracting compounds from solid materials. The Soxhlet extraction method uses the principle of solvent reflux and siphon to achieve continuous extraction of the required components in the solid mixture. When the liquid level of the solvent under reflux in the extraction cylinder exceeds the siphon of the Soxhlet extractor, the solvent in the extraction cylinder flows back into the round-bottomed flask, that is, siphon occurs. When the temperature rises and the reflux starts again, the solid matter can be extracted by the pure hot solvent before each siphon. The repeated use of the solvent shortens the extraction time, so the extraction efficiency is significantly improved.

For this study, we found through experiments that due to the low density of graphene, graphene cannot stay in the extractor during Soxhlet extraction, but will flow or siphon along with the solvent, and even partially agglomerate to block the siphon. The result is that the effect of solvent concentration and purification is not much better than that of solvent direct immersion method, which does not achieve the expected effect.

38.3.1.3 Ultrasound Method

Through further research, we found that the solvent itself has a good dissolving effect on the target organic impurities, and the main thing that affects the purification effect is the agglomeration of graphene, so we tried to use ultrasound for extraction.

For the ultrasonic extraction method, the ultrasonic time is a key parameter. Generally, the longer the ultrasonic time, the better the extraction effect, but the ultrasonic time is not as long as possible. For this project, the extraction efficiency and safety should also be considered. In terms of safety, the main consideration is that acetone is a volatile solvent. The temperature of acetone will rise rapidly during the ultrasonic process, which will significantly accelerate the volatilization of acetone. Although the target chlorobenzene is not as volatile as acetone, it has been dissolved in acetone. Among them, the volatilization of acetone causes the loss of chlorobenzene to a certain extent, resulting in low test results, so a reasonable ultrasonic time needs to be determined.

This project investigated the extraction effects of 4, 6, 8, 10, 12, and 14 min respectively. The results are shown in Table 38.2, which can be seen:

(1) The effect of ultrasonic extraction is significantly better than that of direct solvent soaking. The content of chlorobenzene reached 0.122% in only 10 min

Table 38.2 Extraction effect of different extraction time

Extraction time (min)	4	6	8	10	12	14
Measured value of chlorobenzene (%)	0.036	0.073	0.098	0.122	0.134	0.145
Quality loss (%)	0.2	0.6	1.2	3.6	8.3	15.8

of ultrasonic, which is close to the effect of direct solvent soaking for 12 h of 0.128%.

(2) As the ultrasound time increases, the content of chlorobenzene gradually increases, but at the same time the overall mass loss also shows an accelerated upward trend, reaching 3.6% at 10 min and 15.8% at 14 min. The results show that although the effect of extracting chlorobenzene only by ultrasonic method is very efficient, it is difficult to solve the problem of volatilization loss, and the effect is not ideal.

38.3.1.4 Ultrasonic Solvent Immersion

Since ultrasound can speed up the extraction effect, and it is difficult to solve the problem of volatilization loss, the ultrasound method can be combined with the solvent immersion method. From the above research, it is found that the mass loss at 8 min of ultrasound is 1.2%, which is still within an acceptable range., Then we consider first sonicating for 8 min, then solvent soaking, and then sonicating for 8 min then solvent soaking, how to repeatedly determine an optimal time.

According to the above conditions, we conducted experiments. The results are shown in Table 38.3. It can be seen that the extraction efficiency of solvent soaking after ultrasonic is significantly improved than that of direct soaking, indicating that ultrasonic can accelerate the precipitation of chlorobenzene. On the other hand, the chlorobenzene concentration reached the maximum value of 0.261% after sonicating for 8 min and then immersing in the solvent for 1 h. Repeating this process did not further increase the concentration of chlorobenzene. The best extraction effect has been achieved.

On the other hand, because graphene samples are usually expensive, the amount of graphene is usually not too much, and the amount of corresponding solvent must be appropriate. On the one hand, the amount of solvent should not be too low. If it is too low, there may be the problem of saturation of the above-mentioned organic impurities, so that all the organic impurities in the graphene cannot be extracted. On the other hand, the amount of solvent should not be too large. If it is too large, it will greatly dilute the concentration of organic impurities, which is not conducive to subsequent instrument measurement. Even if the solvent can be concentrated by heating and volatilization, it will inevitably cause the loss of organic impurities by

Table 38.3 Extraction effect after different extraction treatments in sequence

Extraction time	Ultrasound for 8 min	Soak for 1 h	Ultrasound for 8 min	Soak for 1 h	Ultrasound for 8 min	Soak for 1 h
Measured value of chlorobenzene (%)	0.096	0.114	0.246	0.261	0.262	0.262

Table 38.4 The extraction effect of different solvent/graphene dosage ratios

Solvent/graphene	10:1	20:1	30:1	40:1
Extraction	Very viscous, unable to filter out the extract	Viscous, difficult to filter out the extract	0.258%	0.264%

volatilization. Wait for a series of questions. Therefore, it is necessary to determine a reasonable solvent/graphene dosage ratio through experimental research.

The extraction effects of solvent/graphene dosage ratios of 10:1, 20:1, 30:1, and 40:1 were investigated respectively, as shown in Table 38.4. It can be seen from the table that when the solvent/graphene dosage ratio is 10:1 and 20:1, the system is viscous and it is impossible or difficult to filter out the extract. From the ratio of 30:1, an ideal extract can be obtained. 30:1 and 40:1 extracts have little difference in specific test results. Taking into account the convenience of operation and the detection limit of samples with lower chlorobenzene content, the optimal solvent/graphene dosage is set at It's 30:1.

In summary, the solvent/graphene dosage ratio is 30:1. The method of using ultrasonic for 8 min and then solvent soaking for 1 h, repeated twice can achieve the maximum extraction of graphene chlorobenzene, while taking into account the detection limit of subsequent tests. The method only needs 2 h and 16 min to complete, the effect is better than the 48 h of the direct solvent soaking method, and the extraction effect is significant.

38.3.2 Determination of Chlorobenzene

In this study, a gas chromatograph was used to determine the organic impurities in graphene, and a mass spectrometer and library were used to achieve qualitative analysis of organic impurities in graphene, and then an external standard method was used to achieve accurate quantification of impurities. The key parameters that need to be optimized include column type, oven temperature, and split ratio.

38.3.2.1 Column

To obtain a good spectrum for a gas chromatograph, the choice of a chromatographic column is the first problem that needs to be solved. The choice of chromatographic column can generally be selected according to the principle of "similar compatibility". That is, it is selected according to the principle that the polarity of the separated components is similar to that of the stationary liquid. Since the types of organic impurities in graphene are unknown in this project, three columns of non-polar column, weakly polar column, and polar column were investigated respectively. The test results are shown in Table 38.5, from which the test results of the three chromatographic columns can be seen The difference is not large, but because the peak shape

Table 38.5 Test results of chromatographic columns with different polarities

Column polarity	Non-polar column	Weak polarity column	Polar column
Measured value of chlorobenzene (%)	0.259	0.258	0.261

of the non-polar column is not sharp (Fig. 38.1), it is not as sharp as the peaks of the weakly polar column (Fig. 38.2) and the polar column (Fig. 38.3), resulting in less

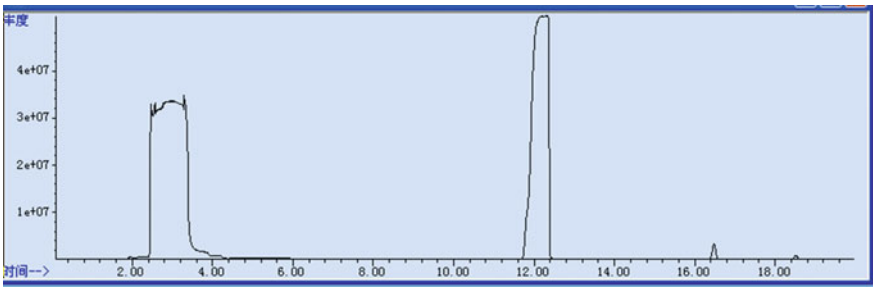

Fig. 38.1 Non-polar gas chromatography-mass spectrogram

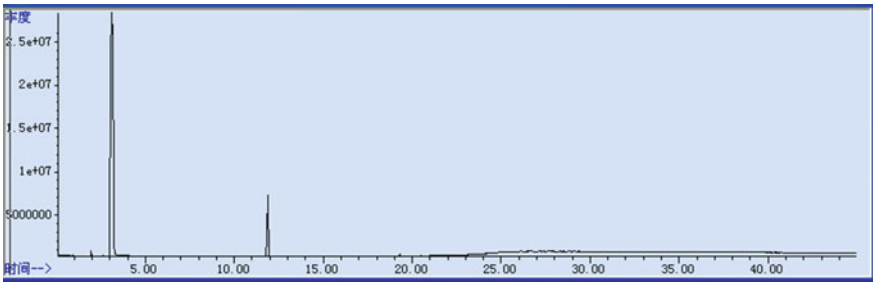

Fig. 38.2 Gas chromatography-mass spectrogram of weak polarity column

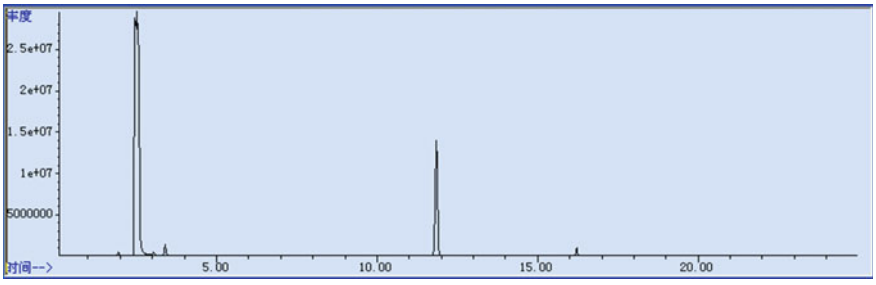

Fig. 38.3 Polar column gas chromatography-mass spectrogram

Table 38.6 The influence of different oven temperature on the test effect

Oven temperature (°C)	50	75	100	125
Test effect	No peak	No peak	Sharp peak	Sharp peak

repeatable results. Sexual column and weakly polar column. Therefore, this project does not use a non-polar column, and can choose a polar column or a weakly polar column.

38.3.2.2 Oven Temperature

Oven temperature is an important operating parameter, which directly affects separation efficiency and analysis speed. The selection of column temperature needs to consider the boiling point range of the mixture, the ratio of the stationary liquid and the sensitivity of the identifier. Increasing the column temperature can shorten the analysis time, and lowering the column temperature can increase the selectivity of the chromatographic column, which is beneficial to the separation of components and the improvement of the stability of the chromatographic column. Generally, a column temperature equal to or higher than the average boiling point of the sample is more appropriate. Even if the most difficult to separate components have the best possible degree of separation, the lower temperature should be used as much as possible, but the retention time is suitable and not Smearing is in degrees.

In this project, the test results of the oven temperature of 50, 75, 100 and 125 °C were investigated respectively. See Table 38.6. It can be seen from the table that there is no peak of chlorobenzene at 75 °C, and at 100 °C and above. The peaks can appear at times and are sharp, so the oven temperature is set at 100 °C.

38.3.2.3 Split Ratio

The split ratio is one of the important reasons for chromatographic separation. Generally speaking, the larger the split ratio, the sharper the peak shape and the better the quantitative repeatability. However, the larger the split ratio, the lower the signal intensity, so a reasonable split ratio needs to be determined.

In this study, the test results of split ratios of 1:1, 5:1, 10:1, 20:1, and 30:1 were investigated respectively, as shown in Table 38.7. It can be seen that the peak of the spectrum is sharp when the split ratio reaches 10:1. Therefore, the split ratio is determined to be 10:1.

Table 38.7 The impact of different split ratios on the test results

Split ratio	1:1	5:1	10:1	20:1	50:1
Test effect	Not sharp	Not sharp	Sharp	Sharp	Sharp

Table 38.8 Standard addition recovery rate of gas chromatography mass spectrometry

Standard addition rate	50% plus standard	100% plus standard	50% plus standard
Measured value of chlorobenzene (%)	93.4	107.3	95.8

Table 38.9 Repeatability results of chlorobenzene content in graphene determined by gas chromatography

Measured value of chlorobenzene				RSD
0.253%	0.274%	0.259%	0.235%	5.6%
0.269%	0.271%	0.246%	–	

Table 38.10 Stability results of chlorobenzene content in graphene determined by gas chromatography

Measured value of chlorobenzene				RSD
0.258%	0.253%	0.295%	0.315%	9.3%
0.286%	0.325%	0.286%	–	

38.3.2.4 Standard Recovery Rate

The recovery rate of standard addition by gas chromatography is shown in Table 38.8. It can be seen that the recovery rate of standard addition is 93.4–107.3%.

38.3.2.5 Repeatability Experiment

The same experimenter continuously measured the same sample 7 times in the same day. The calculated repeatability is shown in Table 38.9. From the table, it can be seen that the repeatability is 5.6%.

38.3.2.6 Stability Experiment

Test 7 times at different time (interval of 1 day). The calculated stability is shown in Table 38.10. From the table, it can be seen that the stability is 9.3%.

38.3.2.7 Detection Limit

Prepare 0.01% chlorobenzene in acetone, measure 11 times, calculate the detection limit with 3 times the standard deviation, see Table 38.11.

Table 38.11 Determination results of detection limit of gas chromatography mass spectrometry

Measured value						SD	Detection Limit (3SD)
0.0104%	0.0102%	0.0100%	0.0102%	0.0099%	0.0100%	0.00016%	0.00048%
0.0100%	0.0100%	0.0103%	0.0100%	0.0102%	–		

Because the extraction ratio of the graphene sample with acetone is 30:1, the detection limit of the chlorobenzene content in graphene is $0.00048\% \times 30 = 0.015\%$.

38.4 Conclusion

The determination of chlorobenzene content in graphene samples was achieved by using gas chromatography mass spectrometry. It is determined that the ultrasonic solvent soaking method is used to achieve sufficient extraction of chlorobenzene in graphene. The detection limit of the method was determined, and the reliability of the method was verified by adding standard recovery experiment and repeatability experiment. The repeatability RSD of the content of chlorobenzene in the measured graphene sample is 5.6%, and the recovery rate of standard addition is between 93.4 and 107.3%. This method is convenient and fast, with low detection limit and high data reliability.

References

1. H. Ze, On the application of graphene in energetic materials. China High-tech Zone **23**, 39 (2017)
2. Y. Lan, X. Li, Y. Luo, Research progress in the application of graphene in energetic materials. J. Propellants Explos. **38**(01), 1–7 (2015)
3. H. Zhang, X. Jia, L. Xu, Research progress of graphene in micro-smoke propellants. Shandong Chem. Indus. **50**(05), 79–80 (2021)
4. H. Jiang, X. Li, E. Yao, F. Zhao, S. Xu, H. Hao, Y. Luo, Research progress of highly active nano (non-)metal powders for solid propellants. Chem. Propellants Polym. Mater. **12**(06), 58–65 (2014)
5. S. Wang, J. Wang, J. Zhang, X. Guo, P. Liu, Q. Yan, Graphene oxide-based energetic coordination polymer on the thermal decomposition and combustion catalysis of four-component composite propellant. J. Propellants Explos. **44**(03), 308–315 (2021)
6. H. Wang, J. Wu, Y. Xu, Y. Shang, X. Cao, The effect of graphene oxide on the thermal properties of TKX-50 energetic material. J. North Univ. China (Nat. Sci. Edn) **41**(03), 255–260 (2020)
7. H. Wang, X. Cao, J. Wu, Y. Xu, Y. Shang, Preparation and thermal decomposition characteristics of TKX-50/GO composite energetic material. Chin. J. Explos. **43**(06), 631–635 (2020)
8. M. Zhang, F. Zhao, Y. Yang, W. Qu, N. Li, J. Zhang, Research progress on the influence of graphene-based materials on the properties of energetic materials. Energ. Mater. **26**(12), 1074–1082 (2018)

9. X. Zhu, J. Tong, H. Zhan, Q. Ye, J. Liu, Determination of the migration of chlorobenzene and p-dichlorobenzene in food contact high temperature materials by gas chromatography-mass spectrometry. Packag. Eng. **41**(05), 91–96 (2020)
10. H. Shen, H. Cheng, Y. Lin, Z. Zhou, F. Huang, Z. Zhu, C. Han, Simultaneous determination of 11 chlorobenzene compounds in leather products by gas chromatography-mass spectrometry. Qual. Tech. Supervis. Res. **01**, 7–10 (2017)
11. Y. Chen, Determination of 1,3,5-trichlorobenzene in surface water by liquid-liquid extraction-gas chromatography-mass spectrometry. Sci. Technol. Innov. Appl. **10**, 139–140 (2020)
12. J. He, Y. She, G. Chen, W. Rong, R. Meng, J. Hu, B. Wu, Simultaneous determination of three chlorobenzene compounds in the air of workplace by portable gas chromatography-mass spectrometry. Chin. Occup. Med. **47**(3), 339–342 (2020)

Chapter 39
Simulation of Impact Initiation of Explosives Based on a Meshless Method

Zhiming Guo, Xianzhen Jia, and Zesheng Liu

Abstract In this paper, the conservative reproducing kernel smoothed particle hydrodynamic (CRKSPH) method is used to simulate the impact initiation process of ANFO and predict the propagation of shock waves arising from the detonation inside the shell and the resultant shell deformation. In calculations, the use of CRKSPH is found to effectively improve calculation accuracy. The explosive reaction and product expansion process are characterized by the JWL++ equation of state (EOS). The calculation results reproduce the impact ignition process by fragments, explosive detonation process, shell deformation response, and explosive reaction distribution. This study quantitatively analyzes the physical value of three measure points and finds the evolution rule, which is of certain guiding significance for the research on ammunition safety. In addition, this study shows that CRKSPH is practically valuable in calculating the impact initiation of explosives.

39.1 Introduction

In recent years, the impact resistance of ammunition and explosives has attracted increasing attention. The research on impact initiation by fragments is of guiding significance for the studies on ammunition safety in the combat environment on the one hand; on the other hand, it also provides engineering guidance and technical standards for the safe transportation and storage of ammunition. At present, one relatively mature view on the mechanism of impact initiation of explosives is the hotspot initiation theory. The theory states that when an explosive is subjected to

Z. Guo
School of Mechatronics Engineering, North University of China, Taiyuan 030051, Shanxi, China
e-mail: sedisim@nuc.edu.cn

X. Jia (✉)
Xi'an Modern Chemistry Research Institute, Xi'an 710065, Shaanxi, China
e-mail: jiaxz1027@163.com

Z. Liu
PLA, 63850 troops, Baicheng 137000, Jilin, China
e-mail: 13596806288@139.com

A. Gany and X. Fu (eds.), *2021 International Conference on Development and Application of Carbon Nanomaterials in Energetic Materials*, Springer Proceedings in Physics 276,
https://doi.org/10.1007/978-981-19-1774-5_39

impact, the impact wave reflects and undergoes adiabatic compression in the cavities, gaps, and locations of impurities or density discontinuities inside the explosive, leading to the rise of local temperature and thus producing hotspots that ignite the surface of the explosive particles surrounding them, resulting in a stable detonation.

Up to date, extensive research has been made on impact initiation of shelled charges by fragments. Dai et al. [1] calculated the theoretical and simulation speed thresholds of five types of fragments impacting TNT charges with the LS-DYNA software and fitted the theoretical head shape coefficient of fragment simulating projectiles (FSP). Zhang et al. [2] simulated the penetration process of impinged cylindrical shell by EFP with the LS-DYNA software and identified the change rule of its impact initiation capacity with different strike angles.

Zhao et al. [3] studied the protection of explosives by composite shells against the impact of fragments and explored their pressure peak and energy change. Chen et al. [4] studied the damage effect of near-field strong impact waves on covered TNT and investigated its impact initiation process through experiments and the LS-DYNA3D software. They worked out the critical thickness of the covered plate for detonating TNT during contact explosion, and the gap distance of covered TNT's sympathetic detonation during non-contact explosion. Many scholars at home and abroad have conducted research on the impact initiation of explosives, and a series of semi-empirical denotation initiation criteria based on approximate calculation have been drawn. Walke and Wasley [5] proposed the critical energy criterion for impact initiation, namely, the one-dimensional short pulse initiation criterion of heterogeneous explosives.

Smoothed particle hydrodynamics (SPH) is a completely meshfree Lagrangian numerical method that discretizes the integral or partial differential equations governing medium movements based on particle approximation and expresses the values of continuous field variables by convolving the nature of discrete particles (e.g., mass, momentum and energy) and the interpolation kernel (usually denoted by W). SPH is characterized by evident material interfaces. In addition to the ability to accurately describe material interfaces in Laplace calculations, SPH retains the advantages of meshless methods, suitable for addressing various issues concerning large deformation and moving boundaries of fluids, such as material damage and fracture, explosive detonation, and impact penetration [6–9]. SPH was first proposed by Lucy [10] and Gingold [11] in 1977 and applied to astrophysics at the beginning. Afterwards, Swegle et al. [12] applied it to simulate explosions, and Liu used it to simulate the detonation process of shaped charges for the first time.

Although SPH has been successfully applied in many fields, it has some prominent drawbacks. The most serious is the lack of zeroth-order consistency, also known as "E0 errors" [13, 14]. Another common drawback lies in the artificial viscosity formula required to accurately capture the shock front. The standard viscosity calculation formula proposed by Monaghan and Gingold [15] has excessive damping, leading to that the results obtained are seriously distorted. Despite various revision methods having been developed, viscosity calculation is still a problem to be addressed.

A meaningful attempt to solve the zeroth-order accuracy problem is the reproducing kernel (RK) method [9, 16]. The RK method improves the interpolation

kernel of SPH by adding degrees of freedom, realizing the accurate reproduction of any order polynomials. In this way, SPH's E0 errors can be completely eliminated. Nonetheless, the method results in the asymmetry of kernels in the particles. This paper utilizes conservative reproducing kernel smoothed particle hydrodynamics (CRKSPH) [16] with an RK, and re-derives the momentum conservation equation based on RK interpolation. CRKSPH can accurately maintain linear conservation of momentum to achieve a certain accuracy, effectively eliminating E0 errors and avoiding the excessive use of artificial viscosity.

Hence, this paper numerically simulates the impact initiation process of explosives using meshless CRKSPH and the JWL++ EOS [17] and explores the interaction mechanism in the denotation process.

39.2 Theory of Computation

While retaining many advantages of traditional SPH, CRKSPH improves its disadvantages, especially unduly high artificial viscosity and E0 errors. To be specific, compared to traditional SPH, CRKSPH has three major changes: (a) the use of a linear RK function, (b) the use of a conservative governing equation, and (c) complete constitutive model.

39.2.1 Linear RK Function

In order to address the problem that SPH cannot reconstruct the polynomial of the required order, some correction terms are added to the kernel function for the interpolation of traditional SPH, in an effort to accurately reproduce constants and linear or higher order terms. This interpolation method is called reproducing kernel method (RPKM), and the reproducing kernel formula can be extended to any order. The RK interpolation formula and the gradient of the variable field are expressed as Eqs. (39.1) and (39.2), respectively:

$$\left\langle F\left(x_i^{\alpha}\right)\right\rangle = \sum_j V_j F_j W_{ij}^R \tag{39.1}$$

$$\left\langle \partial_\gamma F\left(x_i^{\alpha}\right)\right\rangle = \sum V_j F_j \partial_\gamma W_{ij}^R \tag{39.2}$$

CRKSPH replaces the classic SPH kernel ($W_{ij} \rightarrow W_{ij}^R$) with the enhanced RK kernel, enabling it to accurately reproduce any linear field and avoiding the E0 errors in the interpolation of classic SPH.

39.2.2 Conservative Governing Equations

Regarding RK interpolation and gradient, CRKSPH employs some derivative methods in the MLSPH structure to establish governing equations in conservation form. Suppose that the interpolation uses the universal kernel function $\psi(x)$, where the conserved density U and flux F are defined as:

$$U = \begin{bmatrix} 1/\rho \\ V^{\partial} \\ u + v^{2/2} \end{bmatrix}, F(U) = \begin{bmatrix} V^{\alpha} \\ \sigma^{\alpha\beta} \\ \sigma^{\alpha\beta} V^{\beta} \end{bmatrix}, \sigma^{\alpha\beta} = -P\delta^{\alpha\beta} = \tau^{\alpha\beta} \tag{39.3}$$

By interpolation function and volume integral:

$$\int_v \psi\rho \frac{DU}{Dt} = \int_v \psi\, \partial_\alpha F(U) \tag{39.4}$$

the kinetic momentum and energy equation can be obtained:

$$\begin{aligned} m_i \frac{Dv_i^{\alpha}}{Dt} &= \frac{1}{2}\sum_j \sigma_i^{\alpha\beta} + \sigma_j^{\alpha\beta}\left(V_i \partial_\beta \psi_j - V_j \partial_\beta \psi_i\right) \\ m_i \frac{Du_i}{Dt} + m_i v_i^{\partial} \frac{Dv_i^{\alpha}}{Dt} &= \frac{1}{2}\sum_j \left(\sigma_i^{\alpha\beta} v_i^{\beta} + \sigma_i^{\alpha\beta} v_j^{\beta}\right)\left(V_i \partial_\alpha \Psi_j - V_j \partial_\alpha \psi_i\right) \\ \Rightarrow m_i \frac{Du_i}{Dt} &= \frac{1}{2}\sum_j \sigma_j^{\alpha\beta}\left[v_j^{\beta} - v_i^{\beta}\right]\left(V_i \partial_\alpha \psi_j - V_j \partial_\alpha \psi_i\right) \end{aligned} \tag{39.5}$$

where the force pairs are anti-symmetric. Therefore, the momentum equation derived in this way, coupled with the form of RK, can ensure the precise linear conservation of momentum.

39.2.3 Complete Constitutive Model

39.2.3.1 Metal Constitutive Model

For metal materials, the most commonly used constitutive relationship to simulate high-strain-rate flow under transient load is the Johnson–Cook constitutive model:

$$\sigma_y = \left(A + B\varepsilon^{p^n}\right)\left(1 + Cln\dot{\varepsilon}^*\right)\left(1 - T^{*m}\right)$$

Table 39.1 Johnson–Cook model parameters for aluminum

A(MPa)	B(MPa)	C	n	m	T_{room}(K)	T_{melt}(K)
175	380	0.0015	0.34	1.0	273	775

Table 39.2 Parameter values of the Tillotson EOS for aluminum

A(GPa)	B(GPa)	a	b	α	β	$\frac{e_0}{\mathrm{KJ}} \cdot \mathrm{g}^{-1}$	$\frac{e_s}{\mathrm{KJ}} \cdot \mathrm{g}^{-1}$	$e^{'}/\mathrm{KJ} \cdot \mathrm{g}^{-1}$
75.20	65.00	0.50	1.63	5.00	5.00	5.00	3.00	15.00

$$T^* = \frac{T - T_{room}}{T_{melt} - T_{room}}$$

where ε^{p^n} is the effective plastic strain, $\dot{\varepsilon}^*$ is the strain rate, T is the temperature, and A, B, C, n and m are experimental parameters. The metal material used in this paper is aluminum, and the specific parameter values are shown in Table 39.1.

With regard to the EOS for metals, Tillotson's EOS is utilized, by which the dynamic behavior of metal materials including phase transition under high-temperature, high-pressure, and high-strain-rate conditions can be accurately described. The pressure expressions of the four phase regions are as below:

$$p_1 = \left(a + \frac{b}{\omega_0}\right)\eta\rho_0 e + A\mu + B\mu^2$$

$$p_2 = \left(a + \frac{b}{\omega_0}\right)\eta\rho_0 e + A\mu$$

$$p_3 = p_2 + \frac{(p_4 - p_2)(e - e_s)}{\left(e_s^{'} - e_s\right)}$$

$$p_4 = a\eta\rho_0 e + \left(\frac{b\eta\rho_0 e}{\omega_0} + A\mu e^{\beta x}\right)e^{-ax^2}$$

$$\eta = \frac{\rho}{\rho_0}, \mu = \eta - 1, \omega_0 = 1 + \frac{e}{e_0\eta^2}$$

where $a, b, A, B, \alpha, \beta, e_0, e_s,$ and $e_s^{'}$ are material parameters (to be obtained from experiments), and $p_1 \sim p_4$ correspond to the pressures of the four phase regions. The specific parameter values are shown in Table 39.2.

39.2.3.2 Explosive EOS

JWL++ , an ANFO EOS developed by Souers et al. [17], is associated with the ignition and growth model, but it has a simpler form and fewer fitted constants. The

Table 39.3 Parameter values of ANFO EOS

Material	G	b	$\rho_0/(\mathrm{Kg\ m^{-1}})$	E_0 (J)	Ultimate pressure (MPa)	Volume-fraction limit
ANFO	3.5083e−7	1.3	1160	5.558e6	200	0.01

rate equation is as follows:

$$\frac{\mathrm{d}f}{\mathrm{d}t} = G(1-F)P^b \tag{39.6}$$

where F is the degree of reaction in the unit, P is the pressure, and G and b are fitted constants. In addition, there are other forms of JWL++ models. The parameter values are shown in Table 39.3.

39.3 Calculation Model and Simulation Results

39.3.1 Calculation Model

Considering symmetry and calculation efficiency, the 3D model is simplified as a 2D plane, and the particle model established is shown in Fig. 39.1. The fragment on the left side has a 3 mm diameter; the shell on the right side has an inner diameter of 12 mm and a thickness of 2 mm.; and the diameter of the charge is 12 mm. The model consists of 25,400 particles, and the velocity of the fragment is 500 m/s.

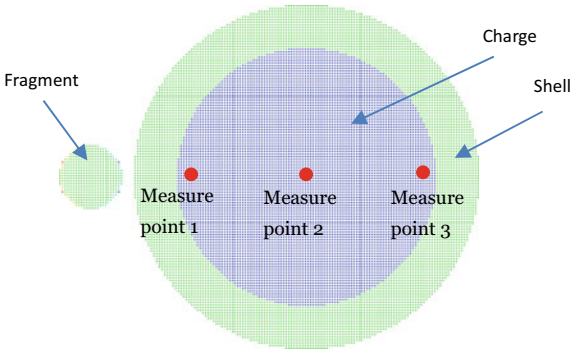

Fig. 39.1 Particle computational model

39.3.2 Simulation Results

Simulation calculation is carried out based on working conditions using the simplified model, and the pressure nephograms at different times during the impact detonation process can be obtained, as shown in Table 39.4. The nephogram at each time point shown in the figure is the effect of the particle dispersion result interpolated on the grid.

As illustrated by the pressure nephograms at each time point in Table 39.3, the explosive is ignited under the impact of about 3 us (ANFO ignition pressure is 200 MPa), after which the pressure surges and rapidly propagates to the inside and boundary of the explosive. The pressure wave is reflected to form a tensile wave after reaching the inner edge of the shell for the first time, and then the formed tensile wave re-propagates to the inside of the explosive. As a result, the incident waves and reflected waves in all directions are superimposed inside the explosive to form Mach waves with higher pressure, for example, the pressure distributions at 10 us and 14 us in Table 39.4. After that, after multiple reflections and superpositions inside the shell, the shock wave, coupled with detonation products, causes the shell to expand and undergo plastic deformation. Meanwhile, the reaction degree of the explosive also rapidly advances from left to right over time, and the reaction is basically completed at about 14 us, with the reaction degree at each point close to 1 (Table 39.5).

Figure 39.2 presents the pressure change curves at the three measure points in the model with time. From the curve in Fig. 2a (measure point 1), it can be seen that the explosive is detonated by impact at about 2 us, and thereafter, the pressure increases

Table 39.4 Pressure evolution process of the explosive

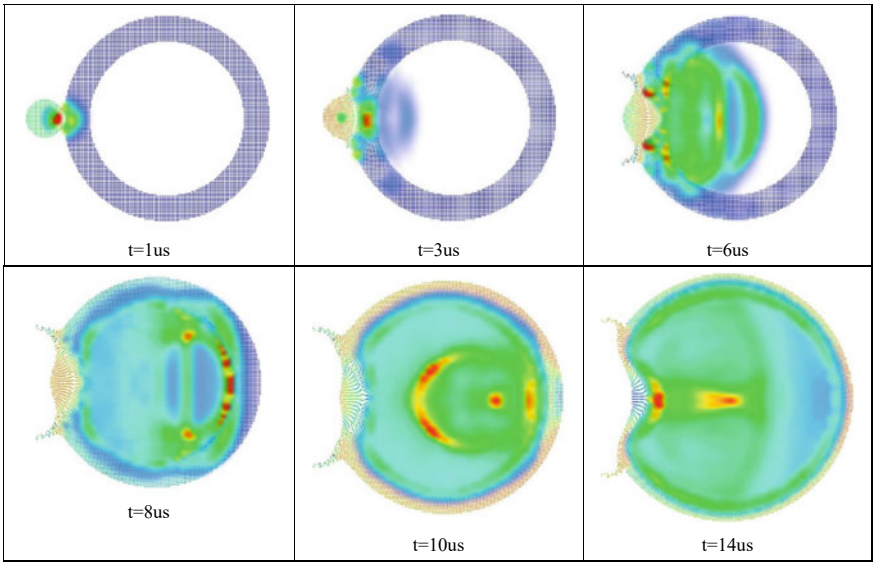

Table 39.5 Reaction fraction evolution process of the explosive

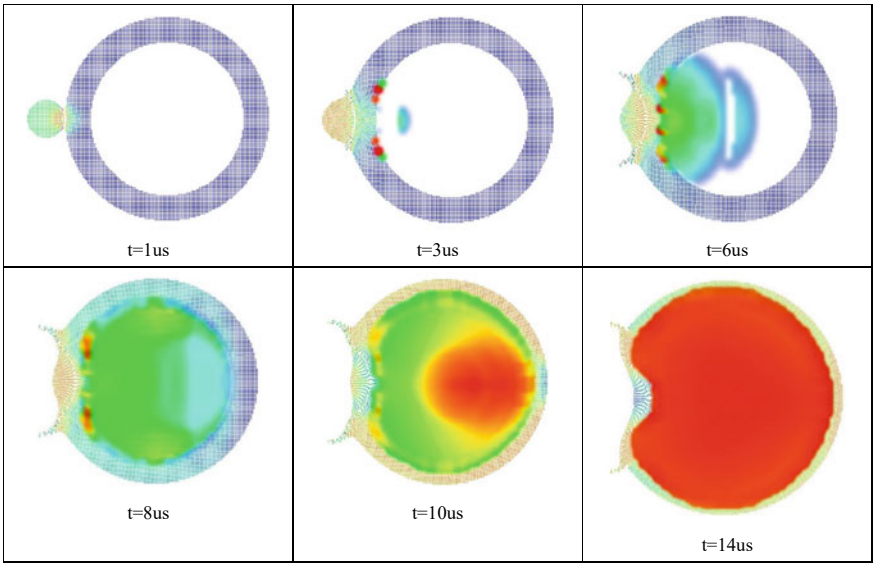

to a certain extent with time until 10 us. When the shock wave propagates to the rightmost end of the explosive for the first time, the pressure value is the first peak in the curve shown in Fig. 2c (measure point 3). Then, the pressure is reflected by the shell to form a transmitted wave, which is the second peak in the curve shown in Fig. 2c (measure point 3). After that, the transmitted wave continues to propagate towards the left, and the peak of the curve shown in Fig. 2b corresponds to the pressure value when the transmitted wave passes. When the wave reaches the leftmost end, it transforms into a larger pressure wave at measure point 1, corresponding to the peak of the curve in Fig. 2a.

The time history curve of the reaction degree at the explosive center (measure point 2) is shown in Fig. 39.3. As illustrated, the ignition reaction starts at the center of the explosive at about 5 us, followed by the rapid increase of the reaction degree. The degree of reaction reaches the maximum at about 14 us, and the reaction is completed at about 17 us.

39.4 Conclusion

By simulating the impact initiation process of ANFO, this paper draws the following conclusions:

(1) Regardless of the specific chemical constituents of ANFO, CRKSPH combined with JWL++ EOS allows us to reproduce the impact initiation process of the explosive and obtain quantitative calculation results.

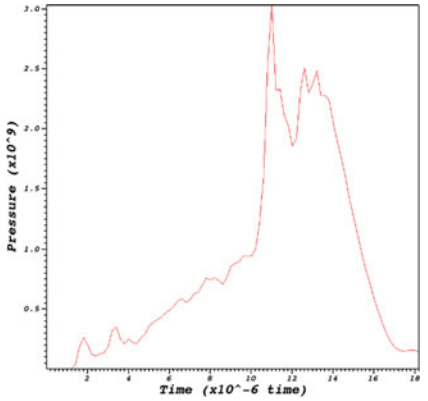

(a) Measure point 1 Pressure-time curve

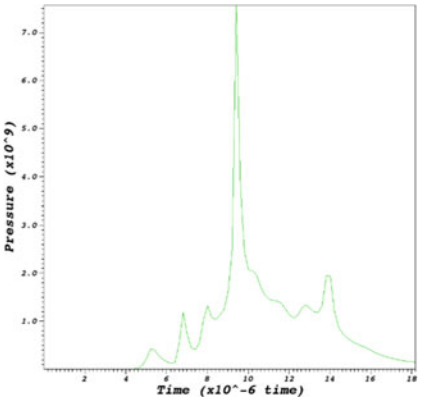

(b) Measure point 2 Pressure-time curve

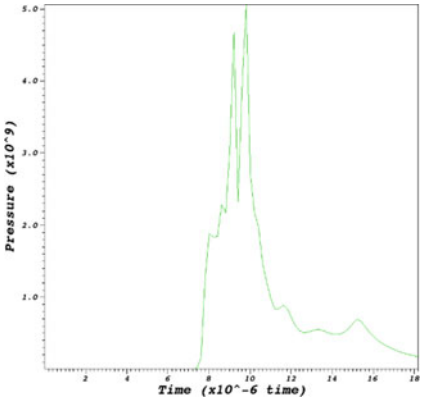

(c) Measure point 3 Pressure-time curve

Fig. 39.2 Pressure–time curves of the three measure points

(2) Meshless CRKSPH can effectively simulate explosive denotation, product flow, and large plastic deformation of metal shells.

(3) CRKSPH combined with an appropriate explosive EOS and particle-to-grid interpolation can accurately capture the propagation process of pressure waves in an explosive after it is initiated by impact. The exploration of the propagation process can guide the structural and safety design of explosives and ammunition and thus improve their safety.

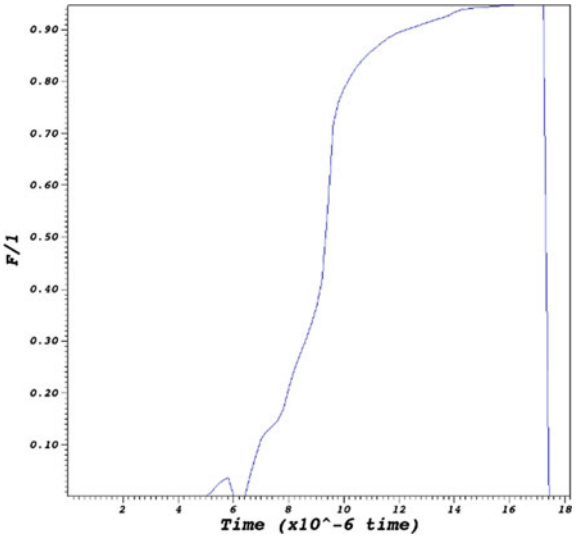

Fig. 39.3 Time history curve of reaction degree at the center of the explosive (measure point 2)

References

1. G.C. Dai, X. Jia, Z.X. Huang, M. Xia, D.R. Tang, S.M. Chen, Y.P. Tan, Influence of fragment head coefficient on the critical velocity of shock initiation of TNT. Explos. Mater. **49**(02), 34–39 (2020)
2. K. Zhang, Y.S. Sui, C. Ji, C.X. Zhao, S.G. Zhang, X. Wang, Numerical analysis of impact initiation of cylindrical covered charge with EFP at different strike angles. Initiators Pyrotech. **03**, 49–52 (2020)
3. Y.F. Zhao, Z.C. Lu, Y.X. Dong, E.F. An, S.S. Feng, Influence on shock initiation of composite shell charges under the impact of fragments. J. Vibrat. Shock **38**(20), 126–130+147 (2019)
4. X.W. Chen, J.X. Wang, K. Tang, R.M. Chen, L. Zhou, C.J. Hao, Experimental and numerical study of shock initiation of covered TNT by near-field shock wave. Chin. J. High Press. Phys. **33**(01), 127–134 (2019)
5. F.E. Walker, R.J. Wasley, Critical energy for shock initiation of fuze train explosive. Explosivstoffe **17**(1), 9–13 (1969)
6. M.B. Liu, G.R. Liu, K.Y. Lam A one-dimensional meshfree particle formulation for simulating shockwaves. Shock Waves **13**(3), 201–211 (2003)
7. M.B. Liu, G.R. Liu, K.Y. Lam et al., Meshfree particle simulation of the detonation process for high explosives in shaped charge unlined cavity configurations. Shock Waves **12**(6), 509–520 (2003)
8. M.B. Liu, G.R. Liu, Z. Zong et al., Computer simulation of high explosive explosion using smoothed particle hydrodynamics methodology. Comput. Fluids **32**(3), 305–322 (2003)
9. M.B. Liu, G.R. Liu, K.Y. Lam et al., Computer simulation of shaped charge detonation using meshless particle method. Fragblast **7**(3), 181–202 (2003)
10. L.B. Lucy, A numerical approach to the testing of the fission hypothesis. Astron. J. **82**, 1013–1024 (1977)
11. R.A. Gingold, J.J. Monaghan Smoothed particle hydrodynamics: theory and application to no-spherical stars. Monthly Not. R. Astron. Soc. **181**, 375–398 (1977)
12. J.W. Swegle, S.W. Attaway, On the feasibility of using Smoothed Particle Hydrodynamics for underwater explosion calculations. Comput. Mech. **17**(3), 151–168 (1995)

13. J.P. Morris, A study of the stability properties of smooth particle hydrodynamics. Publ. Astron. Soc. Austr. **13**, 97–102 (1996)
14. O. Agertz, B. Moore, J. Stadel, D. Potter, F. Miniati, J. Read, L. Mayer, A. Gawryszczak, A. Kravtsov, A. Nordlund, F. Pearce, V. Quilis, D. Rudd, V. Springel, J. Stone, E. Tasker, R. Teyssier, J. Wadsley, R. Walder, Fundamental diferences between SPH and grid methods. Mon. Not. R. Astron. Soc. **380**(3), 963–978 (2007)
15. J.J. Monaghan, R.A. Gingold, Shock simulation by the particle method SPH. J. Comput. Phys. **52**(2), 374–389 (1983)
16. N. Frontiere, C. Raskin, J. Owen, CRKSPH—a conservative reproducing kernel smoothed particle hydrodynamics scheme. J. Computat. Phys. **332**, 160–209 (2016). https://doi.org/10.1016/j.jcp.2016.12.4
17. P.C. Souers, S. Anderson, J. Mercer, E. McGuire, P. Vitello, JWL++: a simple reactive flow code package for detonation. Propellants Explos. Pyrotech. **25**, 54–58 (2000) (cited on pages 130, 152, 164–166)

Chapter 40
Study on Low Vulnerability of RDX-Al Based Cast Explosives

Jun Zhang, Sihua Zhu, Ying Shi, Jinpin Wang, Qingpo Wu, Wei-li Wang, and Yucun Liu

Abstract In order to assess the low vulnerability of RDX-based aluminum-containing cast explosives, relevant test methods based on Compilation of Applicable Test Methods for Formula Evaluation of Military Mixed Explosives. Four standard tests of 7.62 mm bullet impact, 12.7 mm bullet impact, slow cook-off tests and fast cook-off tests were carried out. According to the test standard, the vulnerability of the agent is comprehensively evaluated from the aspects of sample residual state, projectile damage state, witness plate damage state, shock wave over pressure and response grade. Findings demonstrate that RDX-based aluminum-containing cast explosives are insensitive to bullet impact and burning stimuli, and there is no response to the impact of the 7.62 mm bullet. Furthermore, the other three tests manifest an insensitive explosive with high safety, combustion reaction and good low vulnerability.

J. Zhang · S. Zhu (✉) · J. Wang · Q. Wu · W. Wang
School of Ordance Engineering, Naval Engineering University, Hubei 430033, Wuhan, China
e-mail: cinly_zhu@163.com

J. Zhang
e-mail: zhangjun_pbx@163.com

J. Wang
e-mail: glttok@sohu.com

Q. Wu
e-mail: qingpo@yeah.net

W. Wang
e-mail: 858769430@qq.com

Y. Liu
School of Safety and Environmental Engineering, Central North University, Shanxi 030051, Taiyuan, China
e-mail: lyc2ct@sina.com

Y. Shi
Junior Middle School of Henglin, Hubei 431700, Tianmen, China
e-mail: 694850430@qq.com

A. Gany and X. Fu (eds.), *2021 International Conference on Development and Application of Carbon Nanomaterials in Energetic Materials*, Springer Proceedings in Physics 276,
https://doi.org/10.1007/978-981-19-1774-5_40

40.1 Introduction

With the advancement of modern warfare to be high, refined and sophisticated, the comprehensive performance of weapons and ammunition is more and more demanding. The war environment is deteriorating day by day, and the ammunition may be attacked by the enemy before it is put into use, resulting in casualties and equipment damage, thus putting us in a passive state [1–3]. Therefore, it is particularly significant to improve the survivability of weapons and ammunition in the battlefield environment, and the application of low vulnerability can greatly improve its security. In order to improve the survivability of weapons and ammunition and reduce the explosion accidents caused by accidental stimulation (shooting, burning, fragment impact, martyrdom explosion, jet impact), countries throughout the world assess the safety of their weapons and ammunition, low vulnerability explosives committed to meet the requirements of the use of weapons and ammunition [4, 5]. In 2011, the United States revised the standard MIL-STD-2015C on the basis of the original military standard MIL-STD-2015D for insensitive ammunition, and defined the evaluation test items, test methods and corresponding qualification criteria. At the same time, NATO has also developed evaluation criteria for insensitive munitions (SYANAG4107) [6, 7]. Relevant domestic research institutions and universities have also carried out research work on low vulnerable explosives. Guan et al. [8] replaced part of RDX with nitroguanidine or NTO. The impact sensitivity decreased obviously, and the reaction level of shooting and Susan experiment grade was low; Yun et al. [9] studied the effect of FOX-7 on the safety performance of the formula. The results examined that the friction sensitivity decreased, and the electrostatic spark sensitivity decreased obviously, while the slow cook-off tests and fast cook-off tests response times were increased by 58 and 18.5%, respectively. Cao et al. [10] prepared the pouring explosive GOL-42 with solid content (90%HMX/Al = 75/15), fast burning, slow burning, bullet impact test, and the corresponding degree is low reaction grade combustion reaction; Referring to American MIL-STD-2015C, Gao et al. [11] studied the vulnerability characteristics of PMX-1 explosive under the conditions of 12.7 mm bullet impact, slow cook-off tests and fast cook-off tests. The test results showed that the explosive has combustion reaction in the three tests.

This research refers to the relevant test standards and requirements of GJB772A-1997 *Explosive Test methods 603.1 7.62 mm Rifle Method* and *Compilation of Applicable Test Methods for Military Mixed Explosive Formula Evaluation.* Low vulnerability tests such as 7.62 mm bullet impact, 12.7 mm armor-piercing incendiary impact, slow cook-off tests and fast cook-off tests are carried out on RDX-based cast aluminum-containing explosives, so as to lay a solid foundation for the formulation design and vulnerability study of cast PBX explosives.

40.2 Test

40.2.1 Sample Preparation

The formula and preparation technology of pouring PBX explosive proceeds with RDX as the main explosive, Al powder as high energy additive and HTPB/IPDI as binder system. The sample was prepared according to the procedures of raw material pretreatment, slurry premixing, slurry kneading, slurry pouring, sample curing and demolding.

(a) 7.62 mm bullet impact test sample:

Use special tooling to prepare test sample, bare grain size Φ60 mm × 60 mm;

(b) 12.7 mm armor-piercing incendiary bullet impact test sample:

The slurry was poured into the simulated shell, and the end cover was closed after solidification. The inner diameter of the shell was Φ50 mm × 75 mm, the thickness of the shell was 2 mm, and the shell and end cover were made of 45# steel;

(c) Slow/fast cook-off tests sample:

The slurry was poured into the simulated shell, and the end cover was closed after solidification. The inner diameter of the shell was Φ60 mm × 240 mm, the shell thickness was 2 mm, and the shell and end cover materials were made of 45# steel.

40.2.2 Test Conditions

40.2.2.1 7.62 mm Bullet Impact Test

The 7.62 mm bullet impact test was carried out according to the *603.1 7.62 mm Rifle Method of* GJB772A-1997 *Explosive Test Method.* The grain was placed on a fixed frame at the 25 mm from the muzzle of the gun, and the bullet was shot radially along the column. The test number was 10, and the number of the test was numbered with a marker. The response degree was comprehensively judged by observing the test phenomenon and recovering the wreckage. The state of the test grain is shown in Fig. 40.1.

40.2.2.2 12.7 mm Bullet Impact Test

According to *Compilation of Applicable Test Methods for Military Mixed Explosive Formulation Evaluation Method 704.1* "Explosive 12.7 mm Bullet Impact Test", the 12.7 mm bullet impact test was carried out on the grain. The grain was placed away

Fig. 40.1 Diagram of sample

(a) Diagram of sample

(b) Diagram of bullet speed test

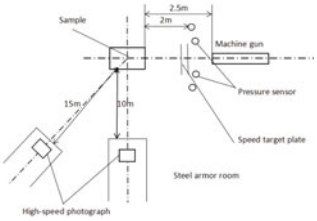

(c) Diagram of test site layout

Fig. 40.2 **a** Diagram of sample. **b** Diagram of bullet speed test. **c** Diagram of test site layout

from the muzzle 25 mm, the bullet velocity was 850 ± 40 m/s, and the bullet was fired along the column radially. The test number was 5 rounds. The response degree was comprehensively judged by observing the test phenomenon, recovering sample wreckage and shock wave over pressure.

The sample placement state, bullet velocity test and test site layout diagram are shown in Fig. 2a–c

40.2.2.3 Slow Cook-Off Tests

"Slow cook-off tests of Explosives", that is, the slow cook-off tests of the shelled grain was carried out according to *Compilation of Test Methods for Formula Evaluation of Military Mixed Explosives, Method 701.1*.

The test conditions are as follows, the test condition is that the E-type thermocouple fixed on the outer wall of the shell body is heated by the thermal control system; the heating rate is 1 °C/min; the burning body is heated until the response or the temperature reaches 400 °C; four A3 steel witness plates are erected around; the size is 500 mm × 500 mm; the thickness is 6 mm. The slow burning characteristics are evaluated according to the response temperature and the deformation of the grilled shell. The on-site layout diagram is shown in Fig. 3a.

Fig. 40.3 Diagram of slow burning sample

40.2.2.4 Fast Cook-Off Tests

"Fast cook-off tests of Explosives", that is, the rapid burning test of the shelled grain was carried out according to the *Compilation of Test Methods for Formula Evaluation of Military Mixed Explosives, Method 702.1*.

The test projectile is installed in the rapid cook-off tests device, and four thermocouple sensors are installed around the test projectile. The flame temperature is more than 800 °C and continue more than 6 min. The cook-off tests characteristics are evaluated according to the severity of the reaction of the test projectile. The schematic diagram of the on-site layout is shown in Fig. 40.4.

Fig. 40.4 Diagram of fast cook-off sample

Fig. 40.5 Response status of 7.62 mm bullet impact test

40.3 Test Results and Analysis

40.3.1 Bullet Impact Test

40.3.1.1 7.62 mm Bullet Impact Test

Ten effective radial bullet impact tests were carried out on the sample grain with 7.62 mm bullets. The test results are shown in Fig. 40.5. The bullet passes through the grain radially, and the grain is intact without any reaction. According to the test standard, the response level of 7.62 mm bullet impact test is "unreacted".

40.3.1.2 12.7 mm Bullet Impact Test

The impact test of five effective radial bullets was carried out with 12.7 mm armor-piercing incendiary. The test results are shown in Table 40.1. It can be seen from Table 40.1 that the bullet velocity meets the requirement of 850 ± 20 m/s. The overpressure sensor of shock wave does not measure the overpressure value. The response grade

Table 40.1 The results of 12.7 mm bullet impact test

Number	Firing speed m/s	Overpressure ΔP_i (MPa)	Reaction rate				Test results
			1	2	3	4	
1	836	Without overpressure		√			Unburned
2	834	Without overpressure	√				Unburned and Unexploded
3	838	Without overpressure		√			Unburned
4	836	Without overpressure		√			Unburned
5	839	Without overpressure	√				Unburned and Unexploded

Fig. 40.6 Response status of 12.7 mm bullet impact test

of 3 rounds of 5 rounds test is grade 2, that is, combustion reaction. Additionally, the reaction grade of 2 rounds is grade 1, that is, unburned and unexploded.

The test and the debris after combustion are shown in Fig. 40.6. The bullet passes through the test along the radial direction, and the sample shell is broken through. Meanwhile, the test grain burns, and the combustion flame can be seen obviously. The front cover of the shell maintains the overall condition, and the rear cover is shot off by the bullet. The side wall of the shell is intact, and there is no rupture or fragmentation. After the residual combustion in the shell, the appearance and shape of the grain remains the same as that of the charge. According to the test standard, the response level of 12.7 mm bullet impact test is "combustion" response. 7.62 mm bullet impact test did not produce any reaction. Compared with 12.7 mm bullet impact test, 3 rounds were burning and 2 rounds were unexploded. The main reason was that 12.7 mm bullet was armor-piercing incendiary. The kinetic energy produced by bullet impact caused the combustion reaction of grain. In fact, the main reason was that the incendiary effect of combustion bomb caused the possibility of combustion of test grain.

40.3.2 Slow Burning Test

Figure 40.7 shows the state of the sample after the slow baking test, it can be seen that the heating sleeve remains intact, the front and rear two witness plates are washed

Fig. 40.7 Response status of slow cook-off

down by the end cover, the left and right two remain upright, and there are no obvious fragment impact marks and deformation on the witness board. The two end covers of the roasted bomb body are washed away by the burning gas products of the grain, which is darker than the debris after the 12.7 mm bullet hits and burns. The slow heating process shows that the grain decomposes first, and with the gradual increase of temperature, the heat released by the decomposition cannot be released, and it is isolated from the external air, and the combustion is not sufficient.

According to the test standard, it is judged that the result of slow roasting test is "combustion".

40.3.3 Fast Cook-Off Tests

Figure 40.8 shows the state after rapid cook-off tests. Figure 8a shows four temperature sensors to measure the combustion temperature and duration. It can be seen that the temperature rises to more than 800 °C in 120 s, and the highest temperature is 891 °C. Meanwhile, the duration is more than 120 s (6 min). The burning temperature meets the test standard, and the temperature decreases with fuel consumption.

As can be seen in Fig. 8b, the whole test projectile is completely wrapped in flame. The temperature around the test projectile tested by four sensors is higher than 800 °C and the duration is longer than 6 min.

Figure 8c shows the state of the test projectile after the completion of the test. It can be seen from the figure that one end cover of the projectile is washed away. If there is deformation, there are no explosion marks and deformation on the witness plate, and the reaction of the grain is mild and intact, which is basically consistent with the color of the 12.7 mm bullet impact test grain reaction.

The analysis examines that after the fast cook-off tests fuel is ignited, the temperature rises rapidly to more than 500 °C within 60 s, and the combustion reaction occurs, and the gas products produced make the pressure in the projectile body rise rapidly to the restraint strength of the projectile body and make one end cover flush

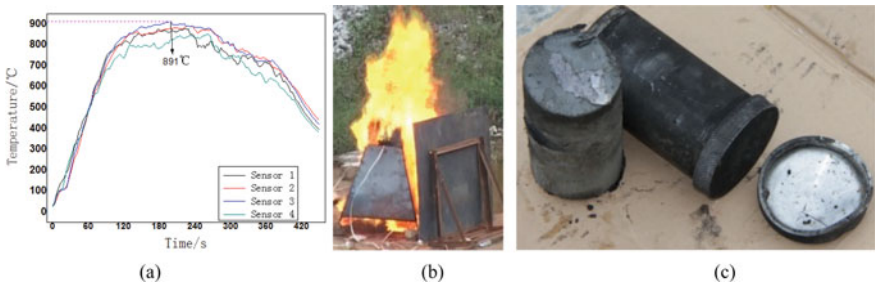

Fig. 40.8 Response status of fast cook-off

away. It reacts with oxygen in the air, resulting in the full combustion of the grain, so the color of the grain is lighter and lighter after combustion. The witness board is kept intact and there is no fragment impact trace. According to the test standard, the result of rapid burning test is "combustion".

40.3.4 Analysis of Low Vulnerability Test

The vulnerability of ammunition is related to the safety of its whole life cycle, especially in the harsh battlefield environment, and its charge, that is, explosive sensitivity is an important index to measure the performance of explosives. The initiation mechanism of the explosive can be explained by the "hot spot" theory. There are two mechanical actions of impact and friction when the 7.62 mm bullet passes through the bare charge at a certain speed, and the test results show that there is no reaction. Combined with the composition of the grain formula (13%HTPB/TDI binder system) and scanning electron microscope photos, it can be seen from Fig. 9a before slurry curing that the HTPB/TDI bonding system has good adhesion. The explosive particles and Al powder particles are uniformly coated on the surface of the binder system because of its strong wetting ability. When the bullet hits the grain, the particles are wrapped by binder, which can cause overall plastic deformation, disperse the local stress concentration in time, reduce the mechanical force between the bullet and explosive particles, and it is not easy to form hot spots.

The initiation mechanism of 12.7 mm armor-piercing incendiary and slow/fast cook-off tests can be explained by the thermal initiation mechanism of explosive. The essence of the process of armor-piercing incendiary and cook-off tests is that the explosive decomposes and burns under the action of heat, releasing a large amount of heat. When the heat dissipation is less than the reaction heat, the reaction is accelerated gradually, which leads to deflagration or explosion of the explosive. The existence of binder has a direct influence on various sensitivities of explosives. When heated externally, HTPB/TDI binder system decomposes before explosives to produce gas to crack the end cover of the test shell, and the gas released from the

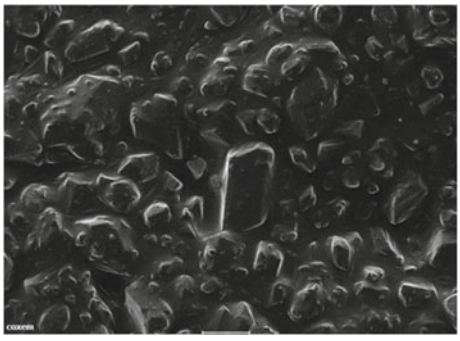

Fig. 40.9 The SEM of slurry solidification before

reaction of explosives is released to the surrounding environment, thus taking away a large amount of heat, and the binder decomposes and absorbs heat, which slows down the reaction grade of explosives, so the grain only has combustion reaction.

40.4 Conclusion

The main results are as follows:

(1) The results of 7.62 mm bullet impact test show that the cast mixed explosive of HTPB/TDI bonding system does not react under the action of impact and friction. 12.7 mm armor-piercing combustion bomb penetrates 5 test samples, of which 3 have combustion reaction and 2 are unburned and unexploded. The main reason is that the combustion bomb produces heat source to make it react, and the reaction grades of the two bullet impact tests meet the standard requirements of low vulnerability.
(2) The results of slow burning test and fast burning test show that the aluminum-containing cast explosive based on RDX can burn slowly under the action of external heat accumulation, and can maintain the complete shape of the grain.
(3) Based on the test results of bullet impact and baking test, the low vulnerability analysis of 7.62 mm bullet impact is carried out. The main effect of grain response is "hot spot" initiation mechanism, while that of 12.7 mm armor-piercing incendiary bomb and roasting test grain is thermal initiation mechanism.

Based on the above test results, the typical aluminum-containing explosive is insensitive to external stimuli and meets the requirements of low vulnerability.

References

1. MIL-STD-2015D, *Hazard Assessment Tests for Non-nuclear Munition* (2011)
2. U.R. Nair, S.N. Asthana, A.S. Rao et al., Advance in high energy materials. Def. Sci. J. **60**(2), 137–151 (2010)
3. D.M. Badgujar, M.B. Talawar, S.N. Asthana et al., Advance in science and technology of modern energy materials: an overview. J. Hazard. Mater. **151**(2–3), 289–305 (2008)
4. W. Xin, Current situation of study on insensitive composite explosives in USA. Chin. J. Explos. Propellants **30**(2), 78–80 (2007)
5. Ofnavy HFPMS, Department of the Navy, Marine Corps Institute **169**(4), 301–306 (2007)
6. P.J. Davies, A. Provatas, *Characterisation of 2,4-dinitroanisole: An Ingredient for Use in Low Sensitivity Melt Cast Formulations* (2006)
7. E.W. Sheridan, G.D. Hugus, G.W. Brooks, Enhanced blast explosive. US, US7972453 (2011)
8. L. Guan et al., Study on low vulnerability of cast-cured PBX aluminized explosive. Energetic Mater. **12**(1), 20–22 (2004)
9. X. Xiao et al., Safety performance of FOX-7 based casting PBX. Energetic Mater. **27**(11), 942–948 (2019)

10. S. Cao et al., Design and performance of a low vulnerability PBX with HMX and Al. Energetic Mater. **4**(1), 1–9 (2021)
11. L. Gao et al., Experimental study on vulnerability of the explosive PMX-1. Energetic Mater. **18**(006), 699–701 (2010)

Chapter 41
Study on the Construction and Basic Application of Fluorinated Graphene Modified Magnesium Borohydride

Fang DU, Yanwei Wang, Huisi Wang, Danchun Huang, Yanqing Ding, Hong Chen, Lei Li, Bowen Tao, and Jian Gu

Abstract Chemical rocket propulsion can be benefited by using hydrogen-storage materials that are able to store high volumes of hydrogen at ambient conditions which can be released during combustion. $Mg(BH_4)_2$ draws great attention from researchers all over the world due to its high hydrogen content of 14.9 wt.% and the high calorific value element of Mg and B in nature. $Mg(BH_4)_2$ has good compatibility with HMX, Cl-20, HTPB, but it has poor compatibility with GAP and AP. Fluorinated graphene@-$Mg(BH_4)_2$ nanocomposite has been designed and prepared with graphite oxide (GO). The compatibility, safety and technological properties of the coating materials and the main components of the GAP-based propellant were studied. The

F. DU · Y. Wang · H. Wang · D. Huang · Y. Ding · H. Chen · L. Li · B. Tao · J. Gu (✉)
Science and Technology on Aerospace Chemical Power Laboratory, Xiangyang 441003, PR China
e-mail: gujian9804@163.com

F. DU
e-mail: dufang0123@163.com

Y. Wang
e-mail: 907171313@qq.com

H. Wang
e-mail: 631343533@qq.com

D. Huang
e-mail: huangdc199208@163.com

Y. Ding
e-mail: 546271623@qq.com

H. Chen
e-mail: 1297179758@qq.com

L. Li
e-mail: lilei2009e@163.com

B. Tao
e-mail: taobowen@163.com

Hubei Institute of Aerospace Chemotechnology, Xiangyang 441003, PR China

J. Gu
Laboratory of Emergency Safety and Rescue Technology, Xiangyang 441003, PR China

A. Gany and X. Fu (eds.), *2021 International Conference on Development and Application of Carbon Nanomaterials in Energetic Materials*, Springer Proceedings in Physics 276,
https://doi.org/10.1007/978-981-19-1774-5_41

results show that the performance of the NEPE propellant is stable after adding the coated $Mg(BH_4)_2$.

41.1 Introduction

Chemical rocket propulsion can be benefited by using hydrogen-storage materials that are able to store high volumes of hydrogen at ambient conditions which can be released during combustion. Particularly, metal hydrides, metal complex hydrides, metal amides/imides and ammonia borane can promote the decomposition of components of propellants, improve combustion properties and enhance energy performances.

The application of hydrogen-storage materials as additives to improving energy performance is a research topic of current interest because they provide higher burning rates and greater impulse, as well as lower average molecular weight. In recent years, a series of important research has been taken. For example, as a combustion agent, AlH_3 has been applied in high-energy propellant. MgH_2 and hydrogen-storage alloys are also expected to improve specific impulse when they are used in propellants because of their high combustion heat and low molecular weight gaseous product H_2O generated from combustion of the released H_2. Compared with AlH_3, materials, which have a higher number of hydrogen content per molecule, like MgH_2 and hydrogen-storage alloys, metal hydrides, metal complex hydrides are promising candidates as additives in high-energy solid propellant. Magnesium boron, $Mg(BH_4)_2$ is a potential hydrogen storage material with high hydrogen capacity of 14.9 wt% which is twice that of MgH_2(7.6 wt%) and 1.5 times that of AlH_3(10.1 wt%). It may a good candidates for space propulsion [1].

Actual application of hydrides in chemical rocket propulsion represents a challenge since safety performance and stability concerns are not completely resolved and shelf-life of final energetic products is still unsolved. Although thermal decomposition temperature of several hydrides is more than 100 °C, most of them have a very limited compatibility with space propulsion component (oxidizer and binder ingredients) [2]. Also, the phenomenon of dehydrogenation can occurs during storage [3, 4].The density of $Mg(BH_4)_2$ is 0.78 g/cm^3. $Mg(BH_4)_2$ and has a hexagonal structure with lattice parameters a = 10.047 Å, c = 36.34 Å and V = 3176 Å [9] and is a single phase. Its decomposition temperature is more than 300 °C [5]. There are a lot of reports on synthesis and theoretical performance of $Mg(BH_4)_2$ [7–11]. It is expected to increase the burning rate, decrease the agglomerates using $Mg(BH_4)_2$ as solid propellants component. Using $Mg(BH_4)_2$ to substitute of metal fuel, gravimetric specific impulsewill be increased because of the heat of combustion of $Mg(BH_4)_2$ [12].

Graphene is regarded as a very promising material for various applications in a vast range of nanotechnologies [13–15]. Graphene oxide, which has similar advantages of graphene, such as large specific surface area, good conductivity, excellent chemical stability etc. The surface of graphene oxide has a lot of active group (–OH, –COOH,

epoxy etc.). Functionalized graphene can be synthesised from graphene oxide based on demand. The fluorinated graphene (FGS) is a derivative of graphene oxide, which is with excellent properties of high thermal stability, good lubricating performance and stable chemistry. Meanwhile, it is a two-dimensional material, which inherits the advantages of ultralight density and superlarge specific surface of graphene, so it has a broad application prospect.

In this paper, the $Mg(BH_4)_2$ was coated with FGS by means of liquid self-assembly process. $Mg(BH_4)_2$ samples before and after treated were characterized through hydrogen content (H%) analysis, FTIR, DSC-TG and SEM, etc. At the same time, the effects of $Mg(BH_4)_2$ and FGS@ $Mg(BH_4)_2$ on the mechanical sensitivity of a novel high-energy solid propellant were also investigated. The results demonstrate that there is only a little FGS on the surface of $Mg(BH_4)_2$, which won't affect the effective H% and release efficiency of hydrogen. FGS@ $Mg(BH_4)_2$ also reduces the mechanical sensitivity of solid propellant containing $Mg(BH_4)_2$, which will remarkably promote the application of $Mg(BH_4)_2$ in the novel high-energy solid propellant.

41.2 Experimental

41.2.1 Materials and Methods

The fluorinated graphene (Fig. 41.1) was first prepared by direct hydrothermal method with the available and inexpensive raw materials. The $Mg(BH_4)_2$ was coated with FGS by means of liquid self-assembly process (Fig. 41.2). The total process was divided into three parts. Firstly, FGS was dispersed in polar solvent. Secondly, $Mg(BH_4)_2$ was stirred and suspended by the solvent in the boiling flask-3-neck. Finally, FGS dispersion was dropped into the boiling flask-3-neck.

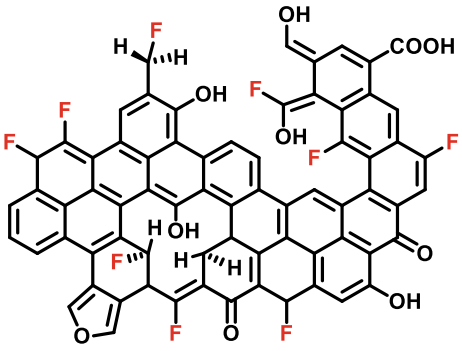

Fig. 41.1 Structure of fluorinated graphene

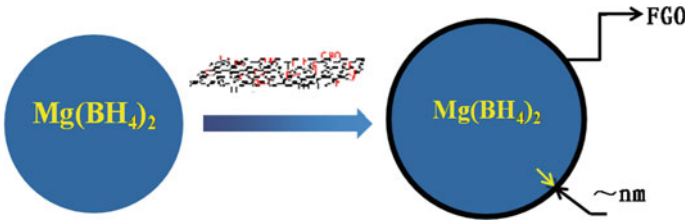

Fig. 41.2 Schematic phase of liquid self-assembly process

41.2.2 Characterizations

Fourier transform infrared absorption spectroscopy (FTIR, Bruker Tensor 27) was used to carrie out phase structure identification of $Mg(BH_4)_2$ and FGS @ $Mg(BH_4)_2$.The thermal analysis experiments were conducted using a High-temperature Thermogravimetry Differential Scanning Calorimeter. We applied a heating rate of 10 °C/min and flow rate of 50 mL/min of N_2. Apex II X-ray diffractometer (XRD) was used to performe the crystallographic structure of $Mg(BH_4)_2$ and FGS @ $Mg(BH_4)_2$. The morphology was observed by Scanning electron microscopy (SEM). Tecnai G20S-Twin system operating was used to record transmission electron microscope (TEM) images.

41.3 Results and Discussions

41.3.1 Infrared Spectroscopy

FTIR spectra were taken from the products. Figure 41.3 shows the FTIR spectra of $Mg(BH_4)_2$ and FGS@ $Mg(BH_4)_2$ prepared by the way mentioned above. In the spectra, typical features of the $[BH_4]$ group can be observed, i.e. in the regions between 2150 and 2400 cm^{-1} and 1100 and 1300 cm^{-1} was the stretching and deformation of B–H bonds, respectively. At 2383, 2293, and 2226 cm^{-1} are the B–H1 absorption band. Aplit into two contributions at 1126 and 1263 cm^{-1} are bending vibration of B–H2. H bridge or H interaction between the complex anion and the metal was observed around 2380 cm^{-1}.

41.3.2 XRD Patterns

The XRD pattern of $Mg(BH_4)_2$ and FGS@ $Mg(BH_4)_2$ was showed in Fig. 41.4.

One diffraction peak at $2\theta = 15°$ corresponding demonstrates that the fluorinated graphene has been successfully coated $Mg(BH_4)_2$.

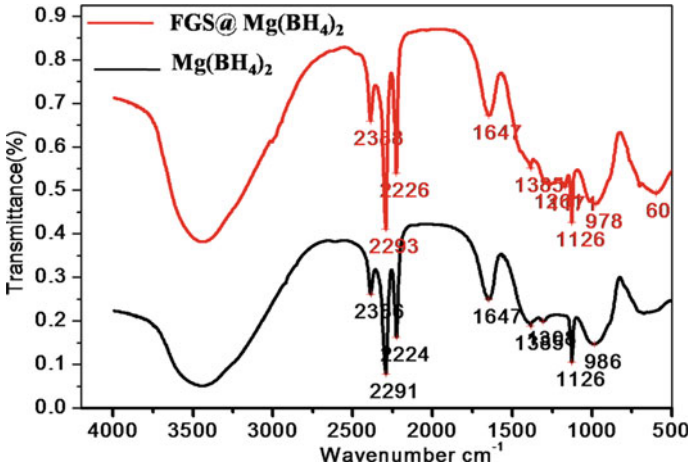

Fig. 41.3 FTIR spectra of $Mg(BH_4)_2$and FGS@ $Mg(BH_4)_2$

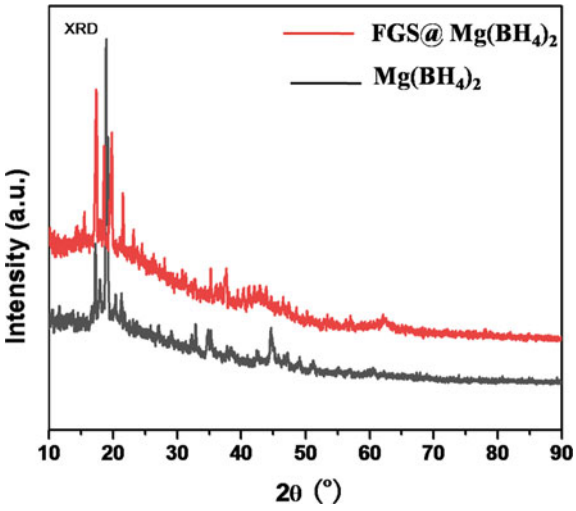

Fig. 41.4 XRD spectrum of $Mg(BH_4)_2$ and FGS@ $Mg(BH_4)_2$

41.3.3 Elemental Analysis

In order to compare hydrogen before with after coating, the elemental analysis was taken. Figure 41.5 shows the H% of $Mg(BH_4)_2$ and FGS@ $Mg(BH_4)_2$.

The results demonstrate that there is only a little FGS in the complex of FGS@$Mg(BH_4)_2$, which won't affect the effective H% and release efficiency of hydrogen.

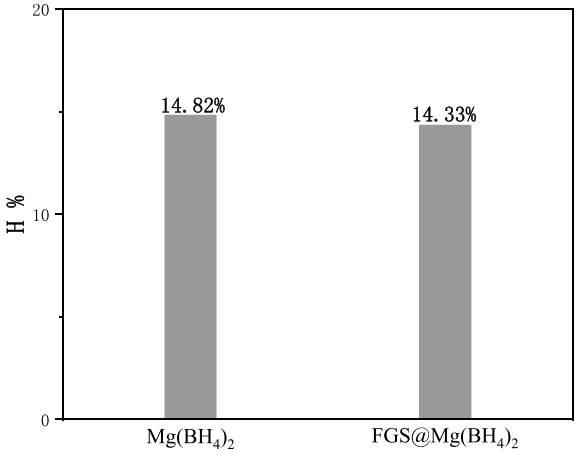

Fig. 41.5 H% of $Mg(BH_4)_2$ and FGS@ $Mg(BH_4)_2$

41.3.4 SEM and TEM Images

Figure 6a, b are respectively the SEM image of $Mg(BH_4)_2$ FGS@$Mg(BH_4)_2$.There is no obvious difference in the SEM image of $Mg(BH_4)_2$ and FGS@$Mg(BH_4)_2$. Meanwhile, as illustrated in Fig. 6c, d, FGS layers were showed in the TEM image, and the FGS layers are at nano-scale.

41.3.5 Compatibility of FGS@ $Mg(BH_4)_2$ with the Main Components of Solid Propellant

In order to apply new energetic material to composite solid propellant, physical mixture and DSC method were used to estimate the compatibility with components of propellant formula. The pure substance and the mixture all be tested by DSC. Comparing the values of $\triangle T_P$ as described in Eq. (41.1) can evaluate the compatibility. In Table 41.1, the evaluated standard of compatibility for explosive and contracted materials are outlined. The DSC curves of GAP/NG/BTTN, AP and $Mg(BH_4)_2$, FGS@ $Mg(BH_4)_2$ mixture systems in respective traces are displayed in Figs. 41.3–41.5.

$$\Delta T_p = T_{P1} - T_{P2} \tag{41.1}$$

where T_{p1} is the peak temperatures of pure substance (in °C),T_{p2} is the peak temperatures of mixtures (in °C).

As shown in Table 41.1, $Mg(BH_4)_2$ is compatible with both HMX and Cl-20. $Mg(BH_4)_2$ is absolutely hazardous to AP. These composition cannot be used in the

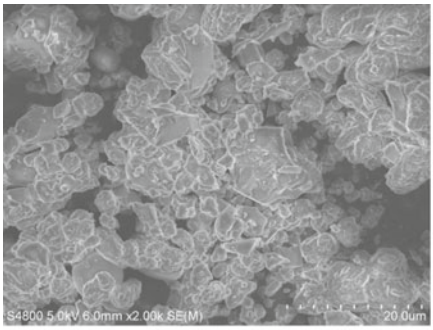

(a) SEM of $Mg(BH_4)_2$

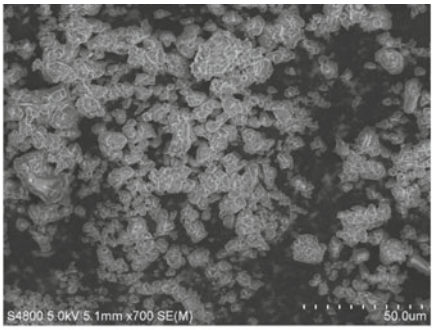

(b) SEM oF FGS@$Mg(BH_4)_2$

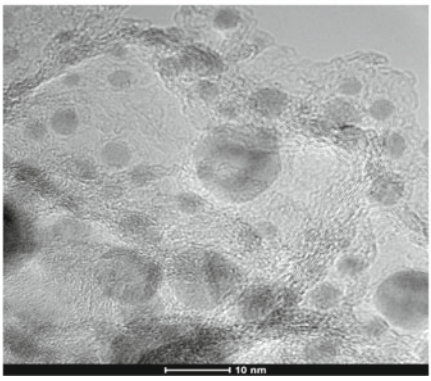

(c) TEM of FGS@$Mg(BH_4)_2$

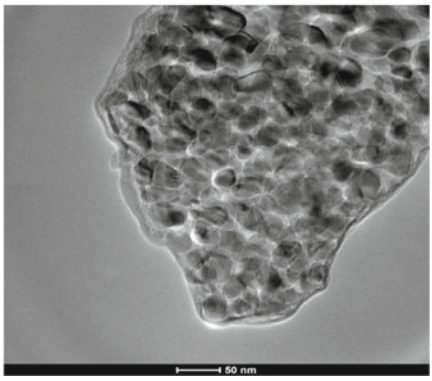

(b) TEM of FGS@$Mg(BH_4)_2$

Fig. 41.6 SEM and TEM images of $Mg(BH_4)_2$ and FGS@$Mg(BH_4)_2$

Table 41.1 Compatibility of samples

System		Peak temperature		ΔT_p (°C)	Rating
Single system	Mixture system	T_{p1} (°C)	T_{p2} (°C)		
HMX	$Mg(BH_4)_2$/HMX	282.2	282.6	−0.4	Yes
Cl-20	$Mg(BH_4)_2$/Cl-20	242.9	245.6	−2.7	Yes
AP	$Mg(BH_4)_2$/AP	307.7,440.2	287.5,422.5	20.2,17.7	No
HTPB	$Mg(BH_4)_2$/HTPB	370.7	368.4	2.3	Yes
GAP/NG/BTTN	$Mg(BH_4)_2$/GAP/NE	195.2,245.4	195.0	0.2	Yes

same system solid propellant and the decomposition of AP will be accelerated via the catalysis of $Mg(BH_4)_2$.

As displayed in Fig. 41.7, AP melted at approximate 242.7 °C and then decomposed at low temperature of 307.7 °C and high temperature of 440.2 °C. For the mixture of $Mg(BH_4)_2$ and AP, the decomposition temperature of the mixture system

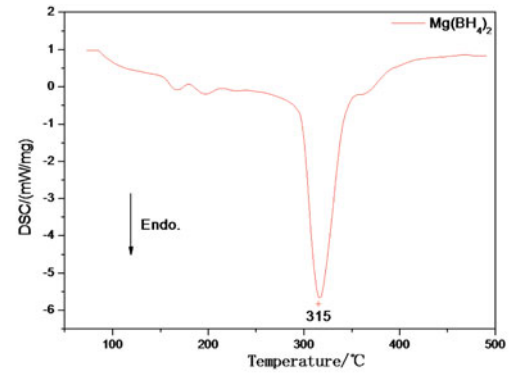

(a) $Mg(BH_4)_2$.

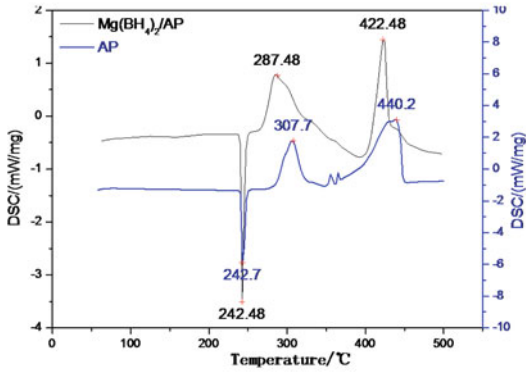

(b) $Mg(BH_4)_2$/AP and AP

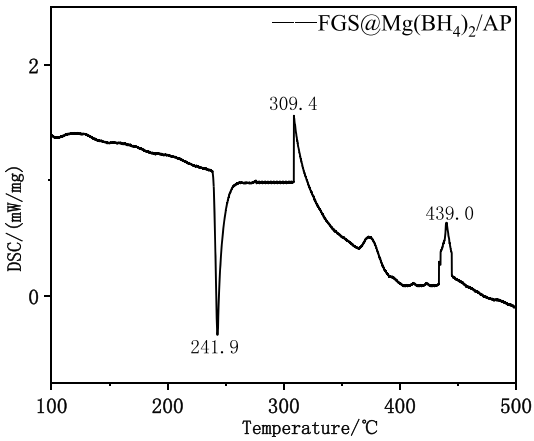

(c) FGS@$Mg(BH_4)_2$/AP

Fig. 41.7 DSC curves of $Mg(BH_4)_2$, $Mg(BH_4)_2$/AP and FGS@ $Mg(BH_4)_2$/AP

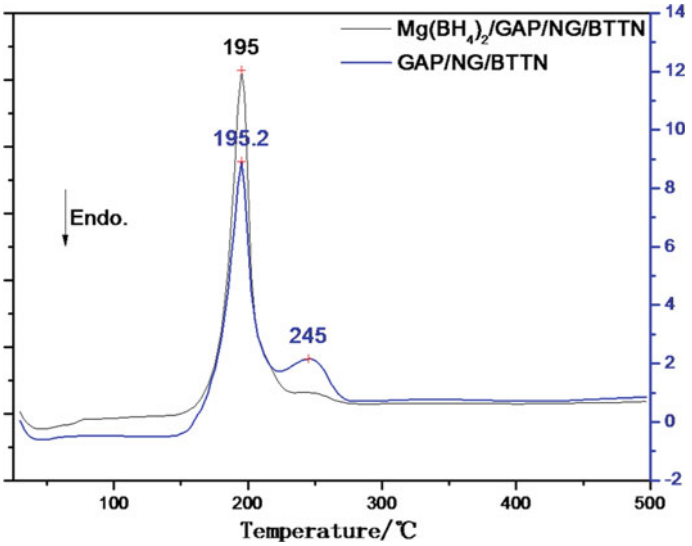

Fig. 41.8 DSC curves of $Mg(BH_4)_2$ with bonding agent

is lower than AP. The difference between maximum decomposition temperature of AP and $Mg(BH_4)_2$/AP is more than 3 °C, the mixture $Mg(BH_4)_2$/AP system is therefore considered incompatibility. For the mixture of FGS@$Mg(BH_4)_2$/AP, the decomposition temperature is higher than pure AP system. However the difference between maximum decomposition temperature of FGS@$Mg(BH_4)_2$/AP and AP is just 1.7 and 1.2 °C. It can be inferred that the FGS@$Mg(BH_4)_2$/AP system is of good thermal stability.

Figure 41.8 shows that the maximum decomposition of GAP/NG/BTTN is observed at 195.2 °C, respectively. The decomposition peak of $Mg(BH_4)_2$/GAP/NG/BTTN shift to lower temperature obviously, which is 195.0 °C. The difference between maximum decomposition temperature of $Mg(BH_4)_2$/GAP/NG/BTTN and GAP/NG/BTTN is less than 3 °C. The $Mg(BH_4)_2$/GAP/NG/BTTN systems are therefore considered compatible. However, Fig. 41.9 shows that the mixture of $Mg(BH_4)_2$/GAP/NG/BTTN is placed at air atmosphere, after a period of time, a lot of bubbles are generated. The mixture of $Mg(BH_4)_2$/GAP/NG/BTTN and FGS@$Mg(BH_4)_2$/GAP/NG/BTTN are contrasted at the same time. As shown in the Fig. 41.10, when stored 0 day at air atmosphere, there is no gas both in the mixture of $Mg(BH_4)_2$/GAP/NG/BTTN and FGS@$Mg(BH_4)_2$/GAP/NG/BTTN. But when stored 7 $_{days}$ at air atmosphere, the mixture of $Mg(BH_4)_2$/GAP/NG/BTTN has a lot of bubbles, while the mixture of FGS@$Mg(BH_4)_2$/GAP/NG/BTTN almost has none bubble. It can be inferred that the FGS@$Mg(BH_4)_2$/GAP/NG/BTTN system is of good thermal stability.

Fig. 41.9 Mixture $Mg(BH_4)_2$ and GAP/NG/BTTN

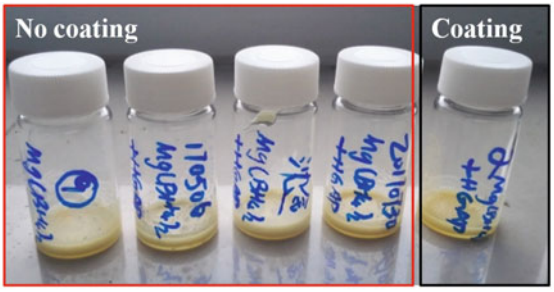

(a) 0 day

(b) 7 day

Fig. 41.10 Mixture $Mg(BH_4)_2$, FGS@ $Mg(BH_4)_2$ and GAP/NG/BTTN

41.3.6 Safety Performance Evaluation

The safety of GAP-based solid propellant is performed on both $Mg(BH_4)_2$ and FGS@$Mg(BH_4)_2$. Friction sensitivity, impact sensitivity and electrostatic spark with different composition were tested (Table 41.2).

The mechanical sensitivities (impact (IS) and friction (FS) and electrostatic spark) of these energetic polymers were determined by the traditional BAM method. As seen from Table 41.2, The friction sensitivity, impact sensitivity and electrostatic spark

Table 41.2 The friction sensitivity, impact sensitivity and electrostatic spark of $Mg(BH_4)_2$ and GAP-based solid propellant before and after coating

Samples	Friction sensitivity (%)	Impact sensitivity I_{50} J)	Electrostatic spark E_{50} (mJ)	Rating
$Mg(BH_4)_2$	0	> 49	327.5	Yes
FGS@$Mg(BH_4)_2$	0	> 49	347.5	Yes
GAP/NG/BTTN/$Mg(BH_4)_2$	0	3.33	101.6	No
GAP/NG/BTTN/$Mg(BH_4)_2$/AP	100	2.20	128.2	No
GAP/NG/BTTN/$Mg(BH_4)_2$/AP/HMX	100	4.79	49.78	No
GAP/NG/BTTN/$Mg(BH_4)_2$/CL-20/HMX	100	2.03	43.22	No
GAP/ NG/BTTN/FGS@ $Mg(BH_4)_2$	0	35.6	48.59	Yes
GAP/ NG/BTTN/Al(Q1)/FGS@ $Mg(BH_4)_2$	16	25.8	70.32	Yes
GAP/NG/BTTN/Al(Q1)/FGS@ $Mg(BH_4)_2$/AP	20	20.2	103.2	Yes
GAP/NG/BTTN/Al(Q1)/FGS@ $Mg(BH_4)_2$/HMX/AP	28	18.6	41.08	Yes
GAP/NG/BTTN/Al(Q1)/FGS@ $Mg(BH_4)_2$/CL-20/AP	32	16.6	39.82	Yes

of $Mg(BH_4)_2$ and FGS@$Mg(BH_4)_2$ both performed good. However, the mixture of $Mg(BH_4)_2$ and GAP-based solid composition propellant showed relatively low impact sensitivity and high friction sensitivity. Especially the impact sensitivity of GAP/NG/BTTN/$Mg(BH_4)_2$ fell within the range of 2.03–4.79 J. The friction sensitivity of GAP/NG/BTTN/$Mg(BH_4)_2$/AP showed high to 100%. After $Mg(BH_4)_2$ replaced by FGS@$Mg(BH_4)_2$, the impact sensitivity of the mixture all showed higher than 16 J. And the friction sensitivity of the mixture all showed lower than 32%.

41.4 Conclusions

- $Mg(BH_4)_2$ was coated with FGS by means of liquid self-assembly process. $Mg(BH_4)_2$ samples before and after treated were characterized through hydrogen content (H%) analysis, FTIR, DSC-TG and SEM, etc.
- $Mg(BH_4)_2$ is compatible with HMX, Cl-20 and HTPB. $Mg(BH_4)_2$ is absolutely hazardous to AP and GAP/NG/BTTN. After coating with FGS, FGS@$Mg(BH_4)_2$ can be compatible with AP and GAP/NG/BTTN.
- The effects of $Mg(BH_4)_2$ and FGS@ $Mg(BH_4)_2$ on the mechanical sensitivity of a novel high-energy solid propellant were also investigated. The results demonstrate that there is only a little FGS on the surface of $Mg(BH_4)_2$, which won't affect the effective H% and release efficiency of hydrogen. FGS@ $Mg(BH_4)_2$

also reduces the mechanical sensitivity of solid propellant containing $Mg(BH_4)_2$, which will remarkably promote the application of AlH_3 in the novel high-energy solid propellant.

References

1. B. Sakintuna, F. Lamari Darkrim, M. Hirsher, Metal hydride materials for solid hydrogen storage: a review. Int. J. Hydrogen Energy **32**, 1121–1140 (2007)
2. L.T. DeLuca, L. Rossettini, C. Kappenstein, V. Weiser, Ballistic characterization of AlH_3-based propellants for solid and hybrid rocket propulsion. AIAA Paper 2009–4874 (2009)
3. M. Chan, C.E. Johnson, Evaluation of AlH3 for propellant applications, in *Proceedings of 8-IWCP, International Workshop on Rocket Propulsion: Present and Future*, ed. by L.T. DeLuca. Paper No. 33 (2002)
4. L. George, S.K. Saxena, Structural stability of metal hydrides, alanates and borohydrides of alkali and alkali-earth elements: a review. Int. J. Hydrogen Energy **3**(5), 5454–5470 (2010)
5. L.T. De Luca, L. Galfetti, F. Severini, L. Rossettini, L. Meda, G. Marra et al., Physical and ballistic characterization of AlH_3-based space propellants. Aerosp. Sci. Technol. **1**(1), 18–25 (2007)
6. F.A. Cotton, G. Wilkinson, C.A. Murillo, M. Bochmann, *Advanced Inorganic Chemistry*, 6th ed. (Wiley, 1999)
7. F. Maggi, G. Garian, L. Galfetti, L.T. DeLuca, Theoretical analysis of hydrides in solid and hybrid rocket propulsion. Int. J. Hydrogen Energy **37**, 1760–1769 (2012)
8. G.L. Soloveichik, Y. Gao, J. Rijssenbeek et al., Magnesium borohydride as a hydrogen storage material: Properties and dehydrogenation pathway of unsolvated $Mg(BH_4)_2$. Int. J. Hydrogen Energy **34**, 916–928 (2009)
9. R.A. Varin, Ch. Chiu, Z.S. Wronski, Mechano-chemical activation synthesis (MCAS) of disordered Mg(BH4)2 using NaBH4. J. Alloys Compd. **462**, 201–208 (2008)
10. G.L. Soloveichik, J.-C. Zhao. Method for manufacturing magnesium borohydride. United States Patent, 2008; US 7,381,390 B2
11. A.K. Geim, Graphene: status and prospects. Science **324**, 1530–1534 (2009)
12. G. Kalita, M.E. Ayhan, S. Sharma, S.M. Shinde, D. Ghimire, K. Wakita, M. Umeno, M. Tanemura, Low temperature deposited graphene by surface waveplasma CVD as effective oxidation resistive barrier. Corros. Sci. **78**, 183–187 (2014)
13. K.S. Novoselov, V.I. Falko, L. Colombo, P.R. Gellert, M.G. Schwab, K. Kim, A road map for graphene. Nature **490**, 192–200 (2012)
14. J. Ning, L. Hao, X.F. Zhang, M.H. Liang, L.J. Zhi, High-quality graphene grown directly on stainless steel meshes through CVD process for enhanced current collectors of supercapacitors. Sci. China **57**, 259–263 (2014)
15. J. Gu, X.P. Zhang, A.M. Pang, J. Yang. Facile synthesis and photoluminescence characteristics of blue-emitting nitrogen-doped graphene quantum dots. Nanotechnology **27**, 165704 (2016)

Chapter 42
Synthesis of Co-ordination Energetic Graphene Oxide and Thermal Decomposition for the Combustion of Ammonium Perchlorate

Haibo Ke, Zhe Zhang, Wang Wang, Yu Cheng, Qiangqiang Lu, Dongqi Liu, Lei Xiao, Fengqi Zhao, Wei Jiang, and Gazi Hao

Abstract In this study, a new co-ordination energetic graphene oxide (CEGO) based on Cu^{2+} as the co-ordination centre was synthesised using 4-amino-1,2,4-triazole as the energetic ligand. X-ray diffractometry, scanning electron microscopy, Fourier transform infrared spectroscopy and X-ray photoelectron spectroscopy results showed that CEGO was successfully synthesised. Then, the catalytic effect of CEGO on the thermal decomposition of ammonium perchlorate (AP) was investigated using differential scanning calorimetric techniques and thermogravimetric analysis. The results revealed that the decomposition peak temperature and Gibbs free energy of the CEGO/AP composite decreased by 88.4 °C and 13.7 kJ/mol compared with pure AP, respectively. At this time, compared with pure AP (132.9 J/g) and other AP composites, the heat release of the CEGO/AP composite increased to 1580.6 J/g, which was the highest. Overall, as an energetic combustion catalyst, CEGO has a significant catalytic effect on AP and can be incorporated into AP-based propellants.

H. Ke · W. Wang · Q. Lu · D. Liu · L. Xiao · W. Jiang · G. Hao (✉)
National Special Superfine Powder Engineering Research Center of China, School of Chemistry and Chemical Engineering, Nanjing University of Science and Technology, Nanjing 210094, China
e-mail: hgznjust1989@163.com

D. Liu
e-mail: ldqnjust1997@163.com

L. Xiao
e-mail: 15005161138@163.com

W. Jiang
e-mail: superfine_jw@126.com

Z. Zhang · Y. Cheng
Shanghai Space Propulsion Technology Research Institute, Huzhou 313000, China
e-mail: zzfarfromok@163.com

F. Zhao
Xi'an Modern Chemistry Research Institute, Xi'an 710065, China
e-mail: zhaofqi@163.com

A. Gany and X. Fu (eds.), *2021 International Conference on Development and Application of Carbon Nanomaterials in Energetic Materials*, Springer Proceedings in Physics 276,
https://doi.org/10.1007/978-981-19-1774-5_42

42.1 Introduction

Ammonium perchlorate (AP), a widely used oxidant, plays a crucial role in solid propellant systems. To some extent, the combustion performance of AP affects the energy output of the overall propellant system; thus, considerable efforts have been made to improve the combustion performance of AP [1–3]. Moreover, it was reported that adding a combustion catalyst to an AP system can significantly accelerate the thermal decomposition process of the AP, thereby improving the overall performance of the AP-based propellant such as ballistic performance, combustion performance and energy level [4]. Therefore, it is pertinent to incorporate combustion catalysts into AP.

Initially, common materials used for combustion catalysts include nano-metals and their oxides (such as Fe_2O_3), composite metal complexes (such as $CuCr_2O_4$) and composite combustion catalysts [such as CuO/graphene oxide (GO)] [5–9]. Metal oxides are traditional combustion catalysts and have good performance. For example, Zhang et al. [10] controlled the compounding time to study the best catalytic effect of nano-$CuCr_2O_4$ on an ultrafine AP. When the milling time was in the range of 6–12 h, nano-$CuCr_2O_4$ was most evenly dispersed on the ultrafine AP. At this time, the decomposition temperature and Gibbs free energy of the nano-$CuCr_2O_4$/ultrafine AP composite were the lowest, which decreased by 78.1 °C and 25.16 kJ/mol, respectively. In addition, Alizadeh-Gheshlaghi et al. [11] synthesised $CuCo_2O_4$ via the sol–gel method, which could advance the peak temperature of AP decomposition from 443.6 to 340.8 °C and had good catalytic activity for AP. However, the catalytic performance of these inert combustion catalysts encounters bottlenecks in the catalytic process, which cannot meet the future development requirements of high-energy AP-based propellants.

With the development of science and technology, GO, as a two-dimensional carbon material, has attracted extensive research attention due to its large specific surface area, excellent electrical and thermal conductivity as well as unique band structure [12–15]. It was found that when nano-metal oxides were loaded on GO sheets because GO could accelerate electron transfer during the decomposition of AP, synergistic catalysis with nano-metal oxides could significantly improve the catalytic thermal decomposition rate of AP. For example, Li et al. [16] successfully loaded Mn_3O_4 onto graphene (GR) sheets via the solvothermal method to form a Mn_3O_4/GR nano-composite. The results showed that the nano-composite had a good catalytic effect on AP; it could reduce the high-temperature decomposition peak temperature of AP by 141.9 °C. Zhu et al. [17] used the in situ deposition method to load CuO nano-particles onto GO sheets to form a CuO/GO nano-composite. It was found that the high-temperature decomposition peak temperature of AP advanced from 414 to 315 °C with the addition of 2-wt% CuO/GO nano-composites, and the catalytic effect was better than that of a single-component CuO (334 °C). Although the GO composite catalyst significantly increases the thermal decomposition rate of AP, the catalyst itself is not an energetic component; therefore, energy is wasted in the process of catalysing AP and propellants.

Recently, the energisation of GO has become a hot topic because there are numerous oxygen-containing groups on the surface of GO sheets, such as –COOH, –OH and C–O–C, which broadens the idea of functional modification of GO, such as modifying energetic components on the surface of GO through acylation or esterification reactions [18–20]. Thus, the energy level and catalytic activity can be improved. For example, Zhang et al. [21] prepared a monolayer nanoscale GO (NGO) with the nitro group via the nitrification of GO with mixed sulphur and nitrate acid. It was found that when 10-wt% NGO was added, the high-temperature decomposition peak temperature advanced by 106 °C and the apparent decomposition heat of AP increased from 875 to 3236 J/g, indicating that NGO had a significant catalytic effect on AP and considerably improved the apparent decomposition heat of AP. Therefore, GO can be energised and used as an energetic combustion catalyst for an AP-based propellant system, which solves the problem of energy reduction due to the introduction of an inert combustion catalyst to a certain extent.

However, the covalent modification of GO still has some drawbacks. Because the activity of oxygen-containing groups on the surface of GO is not high, organic reagents are often added to activate the functional modification of GO, which makes the experimental process and subsequent separation and purification more complicated [22–24]. By contrast, the co-ordination modification on the GO matrix has become a popular idea [25]. For example, Cohen et al. [26] synthesised two energetic complexes based on GO using 5,5′-azo-1,2,3,4-tetrazole and 4,4′-azo-1,2,4-triazole as ligands and Cu^{2+} as the co-ordination centre. The energetic complexes had low sensitivity, high thermal stability and the same detonation performance as hexahydro-1,3,5-trinitro-1,3,5-triazine (RDX). Moreover, Zhang et al. [27] prepared several novel GO-based bis-tetrazole energetic co-ordination polymers (ECPs) via the solvothermal method. These ECPs as energetic catalysts had a significant catalytic effect on the thermal decomposition of AP and RDX. The heat releases of AP and RDX catalysed by GR-templated bis-tetrazoles were 2757.0 and 2898.0 J/g, respectively, which improved more than 50% compared with pure AP and RDX. The endothermic peak of AP corresponding to the crystal transformation also reduced to 23.2 kJ/mol. The successful preparation of such energetic co-ordination compounds confirmed the feasibility of the idea of co-ordination modification of GO.

In this study, a novel Cu^{2+} co-ordination energetic GO (CEGO), which comprised GO, 4-amino-1,2,4-triazole (ATA) and Cu^{2+}, was synthesised through co-ordination bonds of which ATA is the energetic ligand. As a high azole compound, ATA has excellent energy performance and high enthalpy of formation and is eco-friendly with low impact sensitivity [28–30]. Moreover, nitrogen atoms in its ring have lone pair electrons and abundant co-ordination sites, which are easy to co-ordinate with transition metals. In addition, GO has excellent electron transport performance. Cu^{2+} with good catalytic activity is used as the co-ordination centre to bond the former two substances through co-ordination bonds to achieve a synergistic catalytic effect. Further, the structure of CEGO is characterised in detail, and its catalytic performance for AP is studied as a combustion catalyst.

42.2 Experimental

All reagents were of analytical grade, except AP, and they were directly used without further purification. AP was of industrial grade and was purchased from Dalian Perchloric Acid Ammonium Factory. GO was purchased from Suzhou Tanfeng Graphene Technology Co., Ltd. 4-amino-1,2,4-triazol, CuO and $Cu(NO_3)_2$ were purchased from Shanghai Macklin Biochemical Co., Ltd. Ethyl acetate was purchased from Nanjing Chemical Reagent Co., Ltd.

42.2.1 Synthesis of CEGO

In this subsection, we present the details of the synthesis of CEGO. First, GO was added to deionised water and ultrasonically dispersed at 20 °C for 30 min to obtain a dispersed GO solution (50 mL, 1.0 mg/mL). Then, 282 mg (1.5 mmol) $Cu(NO_3)_2$ was weighed and dissolved in 20 mL deionised water. After ultrasonic dispersion for 30 min, it was slowly added to GO dispersion, heated and stirred at 60 °C for 12 h to obtain a black–green mixed solution. Afterwards, it was ultrasonically separated into the ATA solution (10 mL, 16.8 mg/mL), added to the mixed system, stirred and heated at 60 °C for 12 h. Finally, it was centrifuged for washing and vacuum freeze-dried for 24 h to obtain CEGO.

42.2.2 Synthesis of CEGO/AP and Other AP Composites

The CEGO/AP composite was synthesised by simple mechanical grinding methods. The details are as follows. First, CEGO and pure AP were mixed at a mass ratio of 5:95 to obtain a mixture of 40 mg and placed in a mortar, and ethyl acetate (1 mL) was added. To avoid changing the particle size of the mixture as much as possible, the grinding strength was controlled, which meant gently grinding for 30 min until everything was properly mixed. Finally, the mixture was dried for 20 min in a 60 °C oven. A CEGO/AP composite with 5-wt% CEGO was obtained after complete drying.

Further, other AP composites were synthesised with the same mass ratio; the synthesised composites include ATA/AP, CuO/AP and GO/AP.

42.2.3 Measurements

Powder X-ray diffractometry (XRD) was performed with a Rigaku smartlab9 instrument at voltage and current of 40 kV and 150 mA, respectively. Fourier transform

infrared (FT-IR) spectroscopy of the samples was performed (Nicolet iS5) in the range of 400–4000 cm^{-1}. The morphology of ATA was examined using a stereoscopic microscope (Leica M165), and those of GO and CEGO were examined using a high-resolution thermal field scanning electron microscope (Quanta 400 FEG) equipped with an energy dispersion X-ray spectrometer (EDS); corresponding chemical compositions were determined using the EDS. X-ray photoelectron spectroscopy (XPS) measurements were performed using an ESCALAB 250Xi spectrometer equipped with a pass energy of 30 eV with a power of 100 W (10 kV and 10 mA) and a monochromatised Al·Kα X-ray source. In addition, scanning electron microscopy (SEM) was performed.

The thermal analysis experiment was performed using METTLER TOLEDO TGA/DSC3+; the N_2 flow rate was 50 ml/min, the selected heating rate was 5, 10, 15 and 20 °C/min, and the system was heated from 35 to 520 °C. The kinetic parameters for the exothermic decomposition of pure AP and AP composites were obtained using the Kissinger method [31].

42.3 Results and Discussion

In this study, CEGO was synthesised in two steps. First, Cu^{2+} was connected by co-ordination bonds to oxygen atoms in the GO sheets, which were mainly provided by oxygen-containing groups (–COOH, –OH). Further, nitrogen atoms in ATA co-ordinated with Cu^{2+} to yield CEGO. The corresponding synthesis process of CEGO is illustrated in Fig. 42.1.

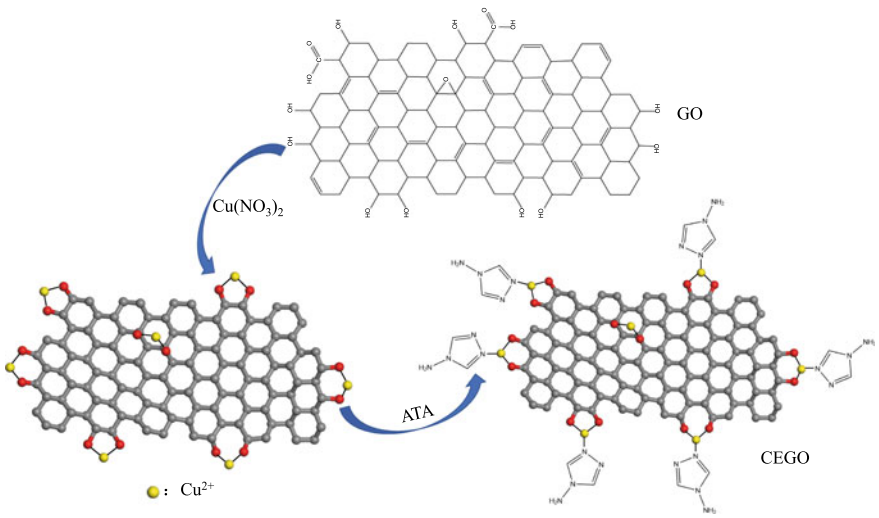

Fig. 42.1 Synthesis process of co-ordination energetic graphene oxide (CEGO)

42.3.1 XRD and FT-IR Analyses

The structural information of ATA, GO and CEGO was analysed using XRD and FT-IR.

Figure 42.2 depicts the XRD patterns of ATA, GO and CEGO. The peak with the highest GO diffraction intensity corresponds to $2\theta = 8.9°$, which is quite similar to CEGO ($2\theta = 10.0°$), indicating that the co-ordination modification process slightly affected the structure of GO. Moreover, the XRD pattern of CEGO displays a broad diffraction peak near $2\theta = 24.6°$, possibly attributed to the co-ordination of ATA on CEGO sheets, which is consistent with the regional concentration of ATA diffraction peaks. However, the characteristic peaks of Cu^{2+} were not found in the XRD spectrum of CEGO, which was probably because the content of Cu^{2+} was too small to reach the detection range.

To verify the successful functionalisation of GO, FT-IR spectroscopy of GO and CEGO were performed (Fig. 42.3). Compared with GO, the characteristic peaks of

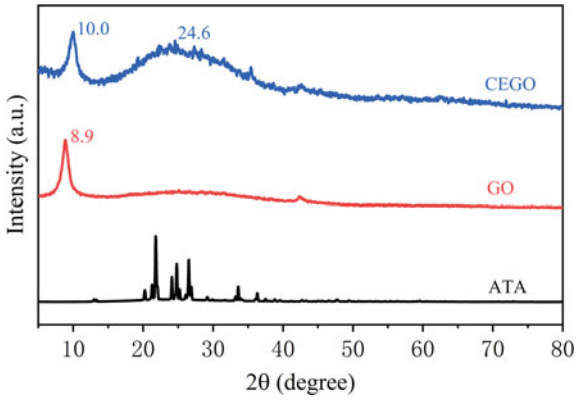

Fig. 42.2 XRD patterns of 4-amino-1,2,4-triazole (ATA), graphene oxide (GO) and CEGO

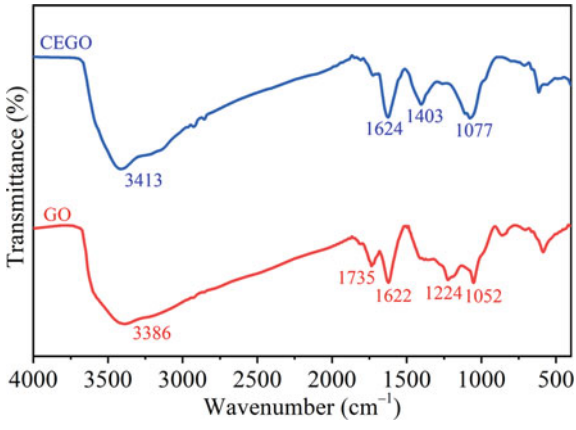

Fig. 42.3 FT-IR spectra of GO and CEGO

CEGO at 1735 and 1224 cm^{-1}, corresponding to the characteristic peaks of C=O and C–OH, respectively, disappeared. The carbonyl group (C=O) belongs to the carboxyl group in the GO surface functional group, and C–OH belongs to the hydroxyl group. Cu^{2+} formed co-ordination bonds with hydroxyl and carboxyl groups, which led to the disappearance of the two characteristic peaks. The characteristic peak of CEGO at 1624 and 1077 cm^{-1} are attributed to the stretching vibration peak of the C=C and C–O bonds, respectively. In addition, CEGO had a new characteristic peak at 1403 cm^{-1}, corresponding to the –NH bond, which came from ATA. Finally, the FT-IR results showed that Cu^{2+} and ATA were connected to GO through co-ordination bonds, and CEGO was successfully synthesised.

42.3.2 SEM and EDS Analyses

The morphology of ATA measured using a stereoscopic microscope is depicted in Fig. 4a. As shown in Fig. 4a, ATA was white transparent crystal particles. Owing to its high hygroscopicity, the crystal particles quickly bonded into clusters in the air. Figure 4b–h shows SEM images and EDS surface elemental analyses of GO and CEGO. The stacked GO sheets had several wrinkles (Fig. 4b), which was mainly due to the varying degrees of oxidation on the surface of the sheets. The CEGO sheets (Fig. 4c) exhibited a rough bulky surface, probably due to the complexation with Cu^{2+} and co-ordination with the ligands. CEGO was tested using EDS to obtain the distribution of the C, N, O and Cu elements (Fig. 4d–h). Among them, the O element belonged to the GO surface oxidation functional group. Further, the EDS surface elemental analyses confirmed the presence of Cu and N atoms, indicating that the GO bonded with Cu, which in turn co-ordinated with the ATA ligands.

42.3.3 XPS Analysis

To further verify the chemical-binding relationship between GO and Cu^{2+} and the energetic ligand (ATA), XPS was employed. In the survey spectra (Fig. 5a), compared with GO, there is an obvious N 1 s peak, and new peaks of Cu $2p_{1/2}$ and Cu $2p_{3/2}$ appeared in the CEGO spectrum. In Fig. 5b, the peak-fitting spectra of C 1 s of GO clearly indicate a considerable degree of oxidation, showing different oxygen-containing functional groups. CEGO showed new peaks in C 1 s curves (Fig. 5c), attributable to the formation of co-ordination bonds between Cu^{2+} and oxygen-containing groups on the GO sheets; C–O–Cu bonds (287.5 eV) were obtained, and the C 1 s peak at 285.8 eV (C–N) originated from further co-ordination of ATA with Cu^{2+}. The corresponding co-ordination effect was more obvious in the peak-fitting spectra of N 1 s of CEGO (Fig. 5d), including the N 1 s peaks at 399.9 eV (=N–) and 400.7 eV (NH, –N–N–). In addition, the positively charged N^+ at 402.1 eV was formed due to the successful co-ordination with the Cu^{2+}, and a trace amount

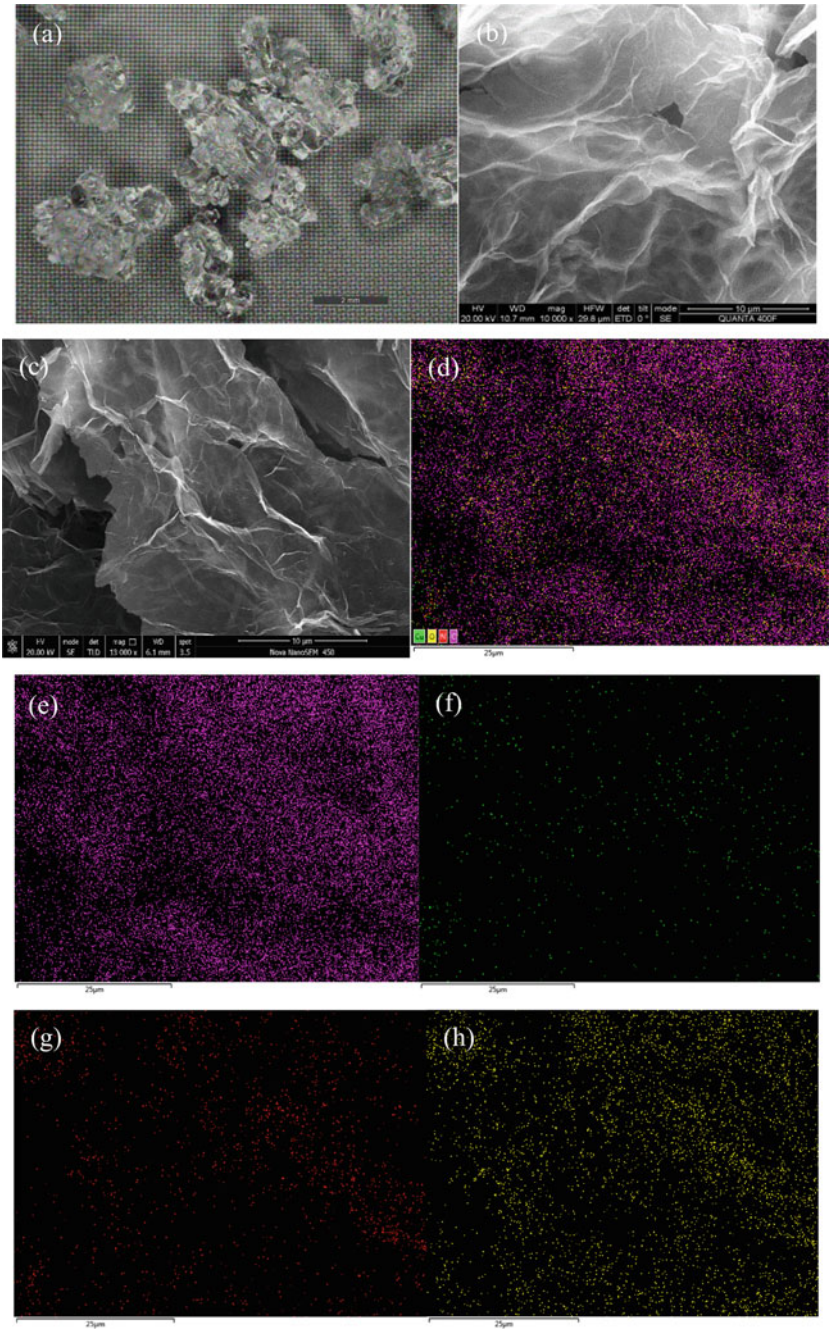

Fig. 42.4 The morphology of **a** ATA; SEM of **b** GO and **c** CEGO; **d–h** EDS of CEGO

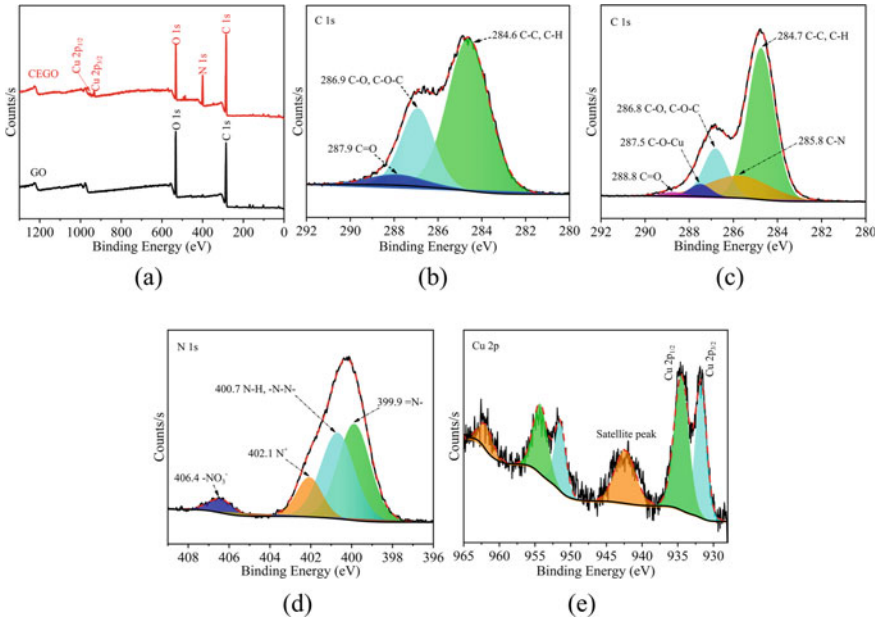

Fig. 42.5 XPS spectra of **a** the survey spectra of GO and CEGO; **b** the peak-fitting spectra of C 1 **s** of GO; **c**–**e** the peak-fitting spectra of C 1 s, N 1 s and Cu 2p of CEGO

of NO_3^- was observed (406.4 eV). The XPS of Cu 2p (Fig. 5e) was divided into two peaks of 731.7 and 734.5 eV, belonging to the Cu $2p_{1/2}$ and Cu $2p_{3/2}$ spin–orbit peaks of Cu^{2+}, respectively, which could be assigned to the corresponding Cu–O and Cu–N bonds, respectively.

42.3.4 Catalytic Performance of CEGO/AP and Other AP Composites

Figure 42.6 shows the DSC curves of ATA, GO and CEGO at a heating rate of 10 °C/min. The CEGO was reported to mainly decompose with a peak temperature of 402.3 °C, accompanied by a small amount of decomposition at 198.1 °C, which was close to the temperature decomposition peak of GO (204.2 °C), corresponding to the decomposition and shedding of oxygen-containing groups on the GO sheets. In addition, there was an endothermic peak of the energetic complex (ATA) at 86.7 °C, which was inferred to the crystal transformation takes place at this stage. With the increase of temperature, the ATA decomposed and exothermed, and the corresponding peak temperature was 295.4 °C at this time, which was 106.9 °C lower than the temperature decomposition peak of CEGO, indicating that the thermal stability of CEGO was significantly increased after the formation of ATA and GO

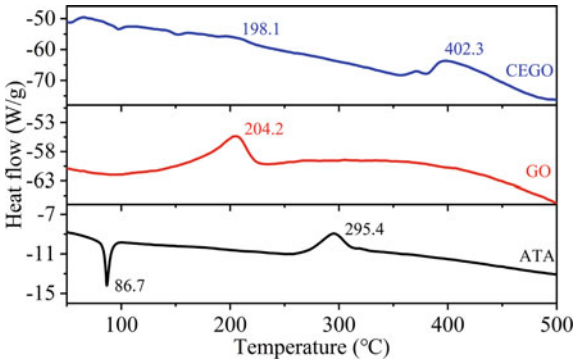

Fig. 42.6 DSC curves of ATA, GO and CEGO at a heating rate of 10 °C/min

complex. Moreover, compared with GO (988.6 J/g), CEGO had a fairly high heat release (3167.2 J/g).

Table 42.1 shows the thermal decomposition performance data of pure AP and AP composites. The differential scanning calorimetric (DSC) and thermogravimetric (TG) curves of pure AP and AP composites at a heating rate of 10 °C/min are depicted in Fig. 42.7. From Fig. 7a, compared with pure AP's two distinct periods of weightlessness, AP composites tended to fuse during the two weightlessness stages; the CEGO/AP showed only one weightlessness stage. The corresponding effect could also be seen in the DSC curve (Fig. 7b), the low-temperature decomposition peak of CEGO/AP disappeared, the high-temperature decomposition peak temperature, T_H, advanced from 419.2 to 330.8 °C and the heat release was the highest (1580.6 J/g), whereas the heat release for pure AP was only 132.9 J/g. Moreover, from the TG curves and Table 42.1, the initial decomposition temperature of CuO/AP was significantly earlier than that of other AP composites, the low- and high-temperature decomposition peak temperature, T_L and T_H, respectively, of the corresponding DSC curve advanced by 31.1 °C and 83.9 °C respectively, but the heat release (1101.8 J/g) was lower than that of CEGO/AP. By contrast, the catalytic effect of GO on AP was not obvious, the T_H moved forward by only 21.7 °C (Fig. 7b), which might be because the oxygen-containing groups on GO reduced the conductivity between the lamellar and

Table 42.1 Thermal decomposition performance data of pure AP and AP composites

Sample	T_e (°C)	T_c (°C)	T_m (°C)	T_L (°C)	T_H (°C)	Q (J/g)
AP	276.8	417.6	406.6	297.9	419.2	132.9
CuO/AP	255.9	343.4	333.4	266.8	335.3	1101.8
ATA/AP	272.4	380.8	319.7	–	320.9	1042.0
GO/AP	264.5	396.8	389.1	289.6	397.5	352.1
CEGO/AP	258.1	339.8	330.8	–	330.8	1580.6

Note T_e is the initial decomposition temperature; T_c is the terminal decomposition temperature; T_m is the maximum weight loss temperature; T_L is the low-temperature decomposition peak temperature; T_H is the high-temperature decomposition peak temperature; Q is the heat release

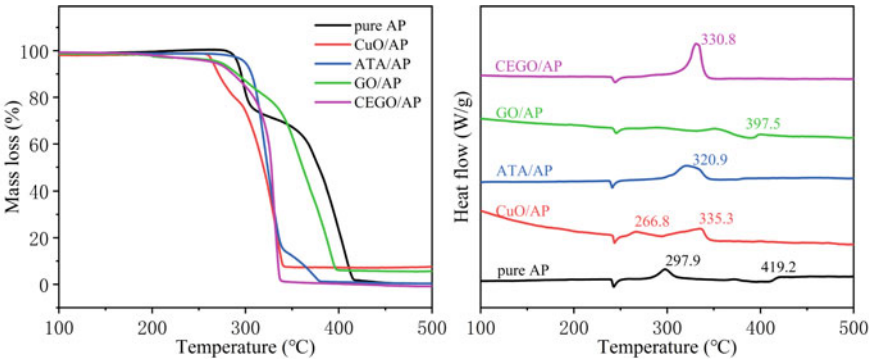

Fig. 42.7 TG (**a**) and DSC (**b**) curves of pure AP and AP composites at a heating rate of 10 °C/min

then affected the electron transport, thereby adversely affecting the catalytic effect of AP. In addition, the temperature decomposition peak of ATA/AP was 320.9 °C, which was slightly earlier than that of CEGO/AP, but the heat release (1042.0 J/g) was significantly lower than that of CEGO/AP, meant that the catalytic effect of ATA on AP was mainly due to energy content and preferential thermal decomposition, while CEGO was an excellent candidate combustion catalyst that could actually accelerate the thermal decomposition of AP.

To further study the pyrolysis of pure AP and AP composites, the thermal decomposition kinetic parameters were calculated. The DSC curves of pure AP and AP composites at different heating rates are shown in Fig. 42.8.

According to the T_H at different heating rates (Fig. 42.9), the figures were plotted with $1000/T_p$ and $\ln(\beta/T2\ P)$ as the abscissa and ordinate, respectively, by linear fitting, and the corresponding $\ln(\beta/T2\ P) \sim 1000/T_p$ diagram of pure AP and AP composites are shown in Fig. 42.9.

The Kissinger method was employed to calculate the thermal decomposition kinetic parameters of the pure AP and AP composites; the corresponding equation of this method can be expressed as follows:

$$\ln\left(\frac{\beta}{T_p^2}\right) = -\frac{E_a}{RT_p} + \ln\left(\frac{AR}{E_a}\right) \tag{42.1}$$

where β denotes the heating rate (K/min), E_a denotes the activation energy (kJ/mol), A denotes the pre-exponential factor (min^{-1}), and R represents the molar gas constant (8.314 J mol^{-1} K^{-1}). Further, E_a and A of pure AP and AP composites can be obtained according to the linear fitting equations in Fig. 42.9; the results are summarised in Table 42.2.

$$T_{p0} = T_{pi} - a\beta_i - b\beta_i^2 - c\beta_i^3 \tag{42.2}$$

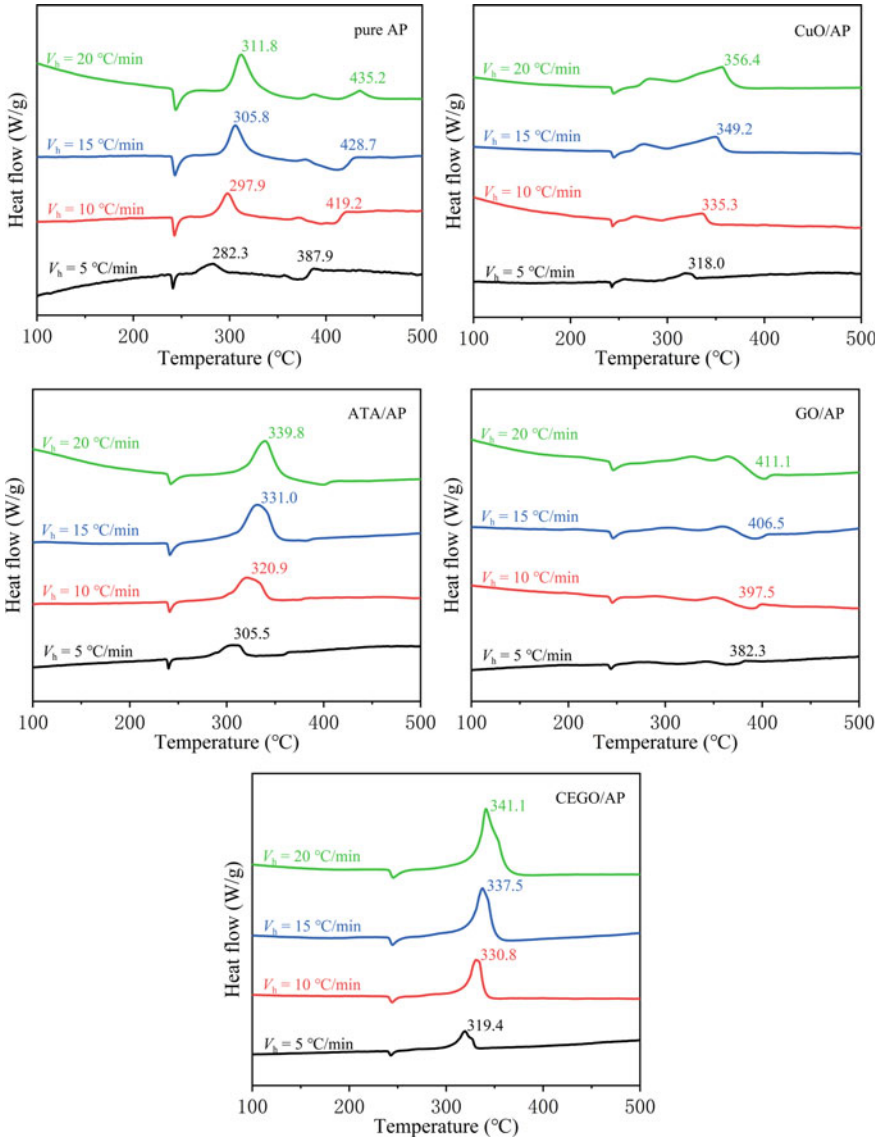

Fig. 42.8 DSC curves of pure AP and AP composites at different heating rates

$$\Delta S^{\neq} = R\left[\ln A - \ln \frac{k_B T_{p0}}{h}\right] \tag{42.3}$$

$$\Delta H^{\neq} = E_a - RT_{p0} \tag{42.4}$$

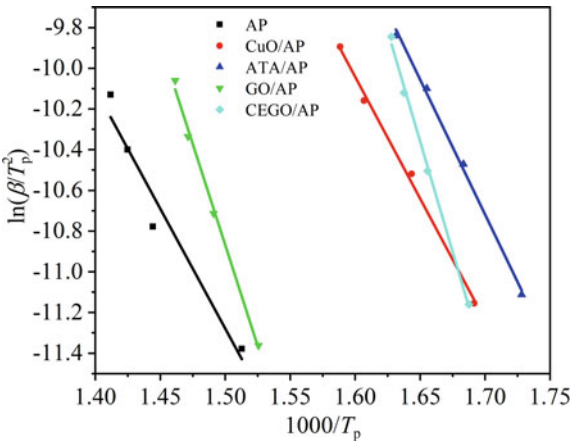

Fig. 42.9 The ln(β/T2 P)~1000/T_p diagram of pure AP and AP composites

Table 42.2 Kinetics, thermodynamics and thermal stability parameters of pure AP and AP composites

Sample	T_{p0} (°C)	ln$A$	E_a (kJ/mol)	$\Delta S^{\neq}$ (J mol^{-1} K^{-1})	$\Delta H^{\neq}$ (kJ/mol)	$\Delta G^{\neq}$ (kJ/mol)
AP	316.0	15.8	97.9	−153.6	93.0	183.5
CuO/AP	300.6	18.5	99.5	−130.7	94.7	169.7
ATA/AP	280.8	21.3	110.2	−106.9	105.6	164.8
GO/AP	359.1	28.8	164.9	−45.9	159.7	188.7
CEGO/AP	301.7	35.4	180.2	9.7	175.4	169.8

$$\Delta G^{\neq} = \Delta H^{\neq} - T_{p0}\Delta S^{\neq} \tag{42.5}$$

where T_{pi} represents the decomposition peak temperature at a specific heating rate β_i, T_{p0} (K) is the corresponding decomposition peak temperature is when β approaches 0, k_B represents the Boltzmann constant (1.381×10^{-23} J/K), and h denotes the Planck constant (6.626×10^{-34} J s); $\Delta S^{\neq}$, $\Delta H^{\neq}$ and $\Delta G^{\neq}$ are the activation entropy, enthalpy and Gibbs free energy, respectively.

To obtain $\Delta S^{\neq}$, $\Delta H^{\neq}$ and $\Delta G^{\neq}$ of the decomposition reaction of pure AP and AP composites, the peak temperature (T_{p0}) should be calculated using Eq. (42.2). Then, Eqs. (42.3)–(42.5) can be used to calculate the relevant parameters in Table 42.2.

The $\Delta G^{\neq}$ of CEGO/AP was 169.8 kJ/mol, which was 13.7 kJ/mol lower than that of pure AP, and the corresponding T_{p0} significantly advanced. It is indicated that CEGO has a significant catalytic effect on pure AP. Moreover, compared with pure AP and other AP composites, the $\Delta S^{\neq}$ of CEGO/AP was the largest and positive, indicating that the confusion degree of CEGO/AP was high, which meant that CEGO could facilitate the thermal decomposition reaction of AP.

42.4 Conclusion

In summary, using the co-ordination modification method, a new energetic combustion catalyst CEGO was successfully synthesised. Then, DSC and TG were used to study the catalytic performance of CEGO/AP and other AP composites, and the corresponding kinetic and thermodynamic parameters were analysed. The results showed that CEGO had a significant catalytic effect on the thermal decomposition of AP, and the heat release of AP considerably increased after adding 5-wt% CEGO. Overall, these results show that the synthesis of CEGO by co-ordination modification paves a pathway for developing energetic combustion catalysts.

Acknowledgements This work was financially supported by the National Natural Science Foundation of China (Project No. 21805139, 22005144 and 22005145), Natural Science Foundation of Jiangsu Province (BK20200471) and the Fundamental Research Funds for the Central Universities (No. 30920041106, 30921011203).

Notes The authors declare no competing financial interest.

References

1. S. Chaturvedi, P.N. Dave, A review on the use of nanometals as catalysts for the thermal decomposition of ammonium perchlorate. J. Saudi Chem. Soc. **17**(2), 135–149 (2013)
2. S.G. Hosseini, M.A. Alavi, A. Ghavi et al., Modeling of burning rate equation of ammonium perchlorate particles over Cu-Cr-O nanocomposites. J. Therm. Anal. Calorim. **119**(1), 99–109 (2015)
3. J. Yang, W. Zhang, Q. Liu et al., Porous ZnO and ZnO-NiO composite nano/microspheres: synthesis, catalytic and biosensor properties. RSC Adv. **4**(93), 51098–51104 (2014)
4. Q. Yan, F. Zhao, K.K. Kuo et al., Catalytic effects of nano additives on decomposition and combustion of RDX-, HMX-, and AP-based energetic compositions. Prog. Energy Combust. Sci. **57**, 75–136 (2016)
5. N. Yan, L. Qin, J. Li et al., Atomic layer deposition of iron oxide on reduced graphene oxide and its catalytic activity in the thermal decomposition of ammonium perchlorate. Appl. Surf. Sci. **451**, 155–161 (2018)
6. G. Hao, H. Li, C. Mao et al., Preparation of nano-Cu-Fe composite metal oxides via a mechanical grinding method and its catalytic performance for the thermal decomposition of ammonium perchlorate. Combust. Sci. Technol. **193**(6), 1–18 (2019)
7. G. Singh, I. Kapoor, R. Dubey et al., Preparation, characterization and catalytic behavior of $CdFe_2O_4$ and Cd nanocrystals on AP, HTPB and composite solid propellants, Part: 79. Thermochim. Acta **511**(1–2), 112–118 (2010)
8. M.A. Fertassi, K.T. Alali, Q. Liu et al., Catalytic effect of CuO nanoplates, a graphene (G)/CuO nanocomposite and an Al/G/CuO composite on the thermal decomposition of ammonium perchlorate. RSC Adv. **6**(78), 74155–74161 (2016)
9. Y. Yuan, W. Jiang, Y. Wang et al., Hydrothermal preparation of Fe_2O_3/graphene nanocomposite and its enhanced catalytic activity on the thermal decomposition of ammonium perchlorate. Appl. Surf. Sci. **303**, 354–359 (2014)
10. D. Zhang, Q. Li, R. Li et al., Significantly enhanced thermal decomposition of mechanically activated ammonium perchlorate coupling with nano copper chromite. ACS Omega **6**(24), 16110–16118 (2021)

11. E. Alizadeh-Gheshlaghi, B. Shaabani, A. Khodayari et al., Investigation of the catalytic activity of nano-sized CuO, Co_3O_4 and $CuCo_2O_4$ powders on thermal decomposition of ammonium perchlorate. Powder Technol. **217**, 330–339 (2012)
12. A.C. Neto, F. Guinea, N. Peres et al., The electronic properties of graphene. Rev. Mod. Phys. **81**(1), 109–162 (2009)
13. S. Stankovich, D.A. Dikin, G. Dommett et al., Graphene-based composite materials. Nature **442**(7100), 282–286 (2006)
14. Y. Zhu, S. Murali, W. Cai et al., Graphene and graphene oxide: synthesis, properties, and applications. ChemInform **22**(35), 3906–3924 (2010)
15. A.A. Balandin, S. Ghosh, W. Bao et al., Superior thermal conductivity of single-layer graphene. Nano Lett. **8**(3), 902–907 (2008)
16. N. Li, Z. Geng, M. Cao et al., Well-dispersed ultrafine Mn_3O_4 nanoparticles on graphene as a promising catalyst for the thermal decomposition of ammonium perchlorate. Carbon **54**, 124–132 (2013)
17. J. Zhu, G. Zeng, F. Nie et al., Decorating graphene oxide with CuO nanoparticles in a water-isopropanol system. Nanoscale **2**(6), 988–994 (2010)
18. T. Kuila, S. Bose, A.K. Mishra et al., Chemical functionalization of graphene and its applications. Prog. Mater Sci. **57**(7), 1061–1105 (2012)
19. S. Niyogi, E. Bekyarova, M.E. Itkis et al., Solution properties of graphite and graphene. J. Am. Chem. Soc. **128**(24), 7720–7721 (2006)
20. J. Azevedo, L. Fillaud, C. Bourdillon et al., Localized reduction of graphene oxide by electrogenerated naphthalene radical anions and subsequent diazonium electrografting. J. Am. Chem. Soc. **136**(13), 4833–4836 (2014)
21. W. Zhang, Q. Luo, X. Duan et al., Nitrated graphene oxide and its catalytic activity in thermal decomposition of ammonium perchlorate. Mater. Res. Bull. **50**, 73–78 (2014)
22. K. Pytlakowska, M. Pilch, B. Hachula et al., Energy dispersive X-ray fluorescence spectrometric determination of copper, zinc, lead and chromium species after preconcentration on graphene oxide chemically modified with mercapto-groups. J. Anal. At. Spectrom. **34**(7), 1416–1425 (2019)
23. L. Hostert, S.F. Blaskievicz, J.E. Fonsaca et al., Imidazole-derived graphene nanocatalysts for organophosphate destruction: powder and thin film heterogeneous reactions. J. Catal. **356**, 75–84 (2017)
24. N.A. Kumar, H. Choi, Y.R. Shin et al., Polyaniline-grafted reduced graphene oxide for efficient electrochemical supercapacitors. ACS Nano **6**(2), 1715–1723 (2012)
25. Q. Yan, A. Cohen, N. Petrutik et al., Highly insensitive and thermostable energetic coordination nanomaterials based on functionalized graphene oxides. J. Mater. Chem. A **4**, 9941–9948 (2016)
26. A. Cohen, Y. Yang, Q. Yan et al., Highly thermostable and insensitive energetic hybrid coordination polymers based on graphene oxide-Cu(II) complex. Chem. Mater. **28**(17), 6118–6126 (2016)
27. Y. Liu, C. He, Y. Tang et al., Tetrazolyl and dinitromethyl groups with 1,2,3-triazole lead to polyazole energetic materials. Dalton Trans. **48**(10), 3237–3242 (2019)
28. C. Zheng, Q. Qian, Y. Liu et al., Synthesis, crystal structure and characterizations of new 3,4,7,8-tetrachloro-1,10-phenanthroline Zn(II) complex. J. Chem. Crystallogr. **40**(1), 19–24 (2010)
29. Z. Guo, X. Liu, X. Chen et al., Design and synthesis of two energetic coordination polymers based on copper ion and 1H,1′H-[5,5′-bitetrazole]-1,1′-diol: a comparative study of the structure-property relationships. J. Solid State Chem. **268**, 55–61 (2018)
30. Y. Wang, L. Yi, X. Yang et al., Synthesis, crystal structure, and characterization of new tetranuclear Ag(I) complexes with triazole bridges. Inorg. Chem. **45**(15), 5822–5829 (2006)
31. R.L. Blaine, H.E. Kissinger, Homer Kissinger and the Kissinger equation. Thermochim. Acta **540**, 1–6 (2012)

Chapter 43
Research Progress on the Application of Fluorinated Graphene in Energetic Materials

Saiqin Meng, Xiaolong Fu, Liping Jiang, La Shi, and Jiangning Wang

Abstract Fluorinated graphene has many special properties as a derivative of graphene containing fluorine atom. In recent years, it has attracted the extensive attention of energetic materials researchers. In this paper, the preparation of fluorinated graphene, the application of fluorinated graphene in energetic materials, the theoretical calculation of fluorinated graphene-based energetic composite and the influence of fluorinated graphene on the performance of energetic materials are reviewed. In addition, the problems and future development of graphene fluoride in energetic materials are discussed.

43.1 Introduction

High-tech weapons and equipment systems require propellants to have higher energy levels in modern warfare. Aluminum (Al) has low toxicity and high specific energy density [1]. Boron (B) has high volumetric and gravimetric energy densities [2]. Therefore, nano-Al powders and nano-B powders are usually used as additives to improve the energy level of solid propellants [3, 4]. However, Al-powders are prone to agglomerate and the surface oxide layer of B-powders will reduces the combustion efficiency during their combustion process [5–9]. The additives, such as fluoropolymers [10–17], metals [18, 19], can enhance their combustion performance.

S. Meng · X. Fu · L. Jiang · L. Shi · J. Wang (✉)
Xi'an Modern Chemistry Research Institute, Xi'an 710065, China
e-mail: wangjiangning001@sohu.com

S. Meng
e-mail: msq204@163.com

X. Fu
e-mail: fuxiaolong204@163.com

L. Jiang
e-mail: jiangliping204@163.com

L. Shi
e-mail: shla_204@163.com

A. Gany and X. Fu (eds.), *2021 International Conference on Development and Application of Carbon Nanomaterials in Energetic Materials*, Springer Proceedings in Physics 276,
https://doi.org/10.1007/978-981-19-1774-5_43

Graphene oxide (GO) and fluorinated graphene (GF or FG) are two typical derivatives of graphene. Graphene oxide and its derivatives have made great progress in reducing the sensitivity of energetic materials [20, 21] and promoting the thermal decomposition of energetic materials [22, 23]. Fluorinated graphene exhibits many exceptional properties, such as adjustable magnetic properties [24], tunable bandgap [25], peculiar surface properties [26]. In recent years, as a fluorine-containing substance, the strong thermal stability of fluorinated graphene [27] and the highly active fluorine-containing groups produced by thermal decomposition have attracted the interest of scholars in the field of energetic materials (EM). They have conducted some studies on the applications about the fluorinated graphene in energetic materials and have achieved some progress.

In this paper, we summarized the recent research progress of fluorinated graphene in energetic materials. The preparation of fluorinated graphene, the application of fluorinated graphene in energetic materials, the theoretical calculation of fluorinated graphene-based energetic composites and the characteristics of fluorinated graphene in energetic materials were reviewed.

43.2 Preparation of Fluorinated Graphene for Energetic Materials

Since FG was first prepared in 2010 [28, 29], currently, there are many methods for preparing FG with the development of science and technology, such as, solvent-assisted sonochemical exfoliation of fluorinated graphite [30, 31], mechanochemical fluorination [32, 33], direct gas fluorination [34, 35], solvent fluorination [36, 37] and plasma fluorination [38, 39]. Among them, the FG which was prepared by direct gas fluorination, solvent fluorination and plasma fluorination had the advantages of good uniformity and controllable fluorine content. These determined that it could be used in the research of energetic materials.

43.2.1 Direct Gas Fluorination

Wang et al. [40] used F_2/N_2 mixed gas to fluorinate honeycombed graphene oxide (GO) which was dispersed in ethanol, through controlling the content of F_2, they obtained some FG samples with different fluorination degrees at 180 °C. Figure 43.1 shows the fluorination process. GO has significant advantages as raw material for preparing fluorinated graphene, the oxygen-containing groups separated from GO advanced the distribution and proliferation of F_2 during the preparation process, which led to better uniformity of fluoridation. After the characterizations of XPS, AFM and TEM, the uniformity of fluorination was proved better.

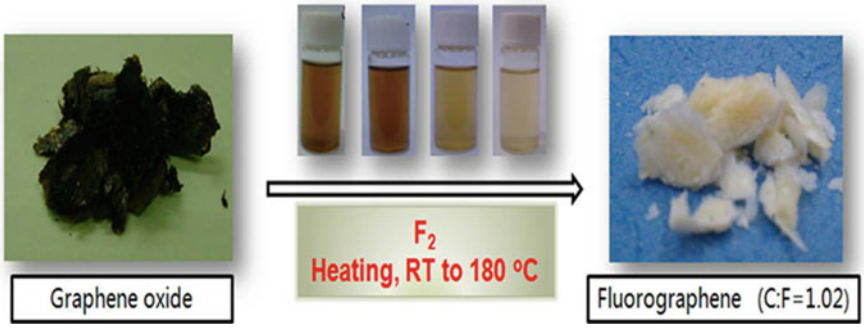

Fig. 43.1 Photographs of the fluorinated (right) and nonfluorinated GO (left), the inset was the ethanol dispersion of FGO with different fluorine content. Reprinted with permission from Ref. [40]. Copyright 2013 American Chemical Society

Robinson et al. [41] used xenon difluoride (XeF_2) gas to fluorinate graphene, graphene sheets were fixed on the copper or SiO_2/Si substrates for preparing FG films. When the copper substrate was used, they found the product with a fluorine content of 25% (C_4F) can only be fluorinated on the side that touches F_2. When the SiO_2/Si substrate was used, they found the product with a fluorine content of 100% (C_1F_1) can be completely fluorinated. The reason for those phenomena is that the etching effect of XeF_2 gas on copper substrate is poor but on SiO_2/Si substrate is effective. Figure 43.2 is the XPS analysis of fluorine functionalization during XeF_2 exposure. According to Fig. 43.2, the graphene on the SiO_2/Si substrate has a higher fluorination rate, which is caused by the difference in the substrates.

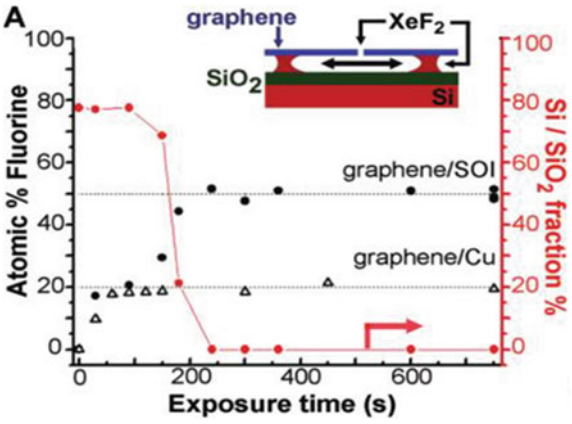

Fig. 43.2 The fluorine fraction and silicon fraction for different samples. (inset) Cartoon showing the etching process on the SiO_2/Si substrates. Reprinted with permission from Ref. [41]. Copyright 2010 American Chemical Society

43.2.2 Solvent Fluorination

Wang et al. [42] synthesized fluorinate graphene sheets (FGS) used based the hydrothermal reaction between GO and HF, the degree of fluoridation can be readily controlled by changing the reaction temperature, reaction times and the dosage of HF, which is an simple and effective synthesis method. Figure 43.3 is the HRTEM and AFM images of the FGS. From Fig. 43.3b, c, FGS shows irregular atomic arrangement, which is led by the change in thickness, density or composition. According to Fig. 43.3e, f FGS shows a typical two-dimensional structure.

Zhao et al. [43] used diethylaminosulfur trifluoride (DAST) to preparate FG with GO as starting material at room temperature, difference organic solvents, such as dichloromethane, THF, pyridine, 1,2-dichloroethane and o-dichlorobenzene, were used to control the structure and fluorination rate of fluorinated graphene. Figure 43.4 is the image for the synthesis of FG by the reaction between GO and DAST. From Fig. 43.4, most oxidizing group were replaced by fluorine atom after DAST fluorination. Through the elemental analysis, FG_{DCB} shown the highest fluorination rate (23.1%) and FG_{None} shown the lowest fluorination rate (3.6%). The process was a cost-effective, large-scale preparation route, which avoided the hazardous issues caused by high temperature and F_2 gas.

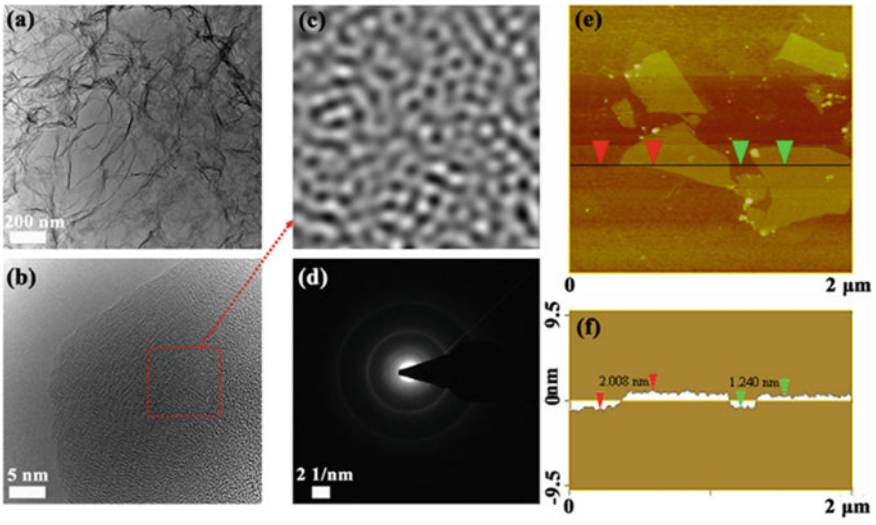

Fig. 43.3 **a** TEM and **b** HRTEM images of the synthesized FGS. **c** Magnified image of the red section in Fig. 43.3b. **d** Selected area electron diffraction pattern of FGS sample. **e–f** The AFM image and thickness of FGS. Reprinted from Ref. [42]. Copyright 2012 with permission from Elsevier

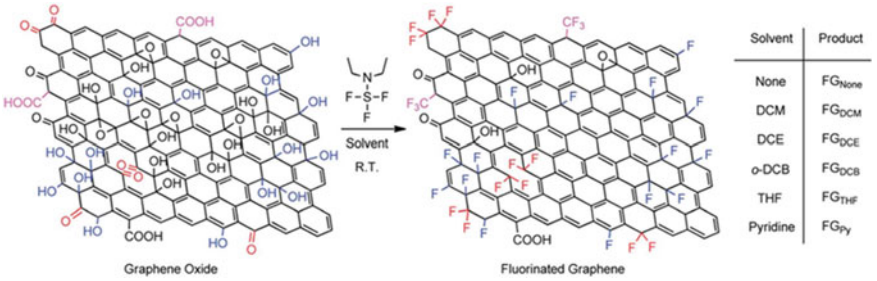

Fig. 43.4 The synthesis process of fluorinated graphene through the reaction of GO and DAST at room temperature. Reprinted from Ref. [43]. Copyright 2013 with permission from Royal Society of Chemistry

43.2.3 Plasma Fluorination

Jan et al. [44] presented a secure, clean and simple method for widely fluorinating by laser-ablation-assisted decomposition of gaseous SF_6 molecules. Figure 43.5 shows the image of fluorination route by laser ablation in the SF_6 atmosphere. Through the XPS and Raman spectroscopy analysis, they found that the fluorination content was positively correlated with the laser pulse numbers, the fluorination content increased with the increase of laser pulse numbers before the laser pulses reached the saturation value.

Tahara et al. [45] developed a highly controllable fluorination route by the fluorine radicals in Ar/F_2 plasma. The degree of fluorination was controlled by changing the reaction time. Spatially homogeneous fluorination was showed through the Raman mapping. Figure 43.6 is the image of reactive ion etching (RIE) system for fluorinating.

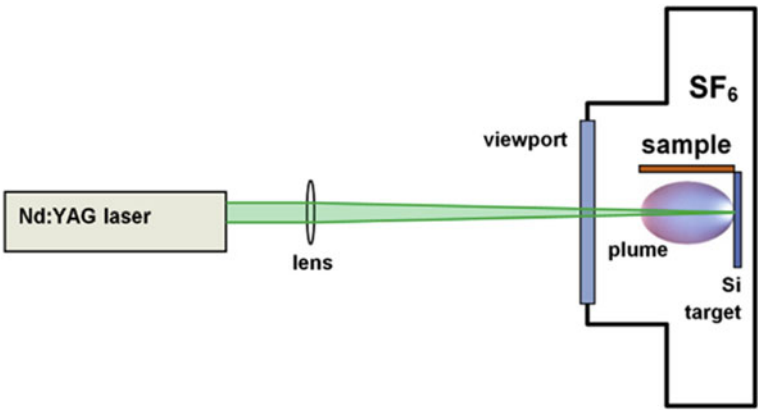

Fig. 43.5 Image of fluorination route by laser ablation in the SF_6 atmosphere. Reprinted from Ref. [44]. Copyright 2019 with permission from Elsevier

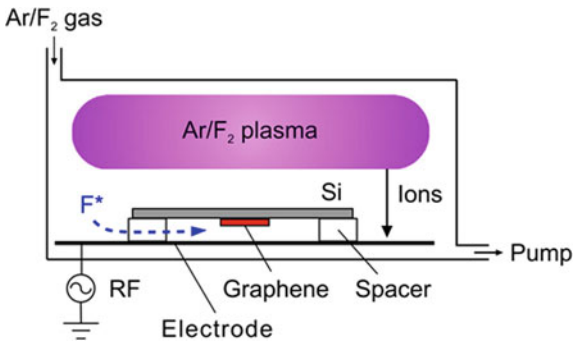

Fig. 43.6 The image of reactive ion etching (RIE) system for fluorinating. Reprinted from Ref. [45], with the permission of AIP Publishing

43.3 Application of Fluorinated-Graphene in Energetic Materials

43.3.1 Preparation of Aluminum/Fluorinated-Graphene Based Energetic Materials

Aluminum (Al) powder tended to form relatively large agglomerations during the combustion process, the introduction of fluoropolymers (polytetrafluoroethylene, perfluoropolyether and polyvinylidene fluoride) can inhibit the agglomeration. In recent years, as a fluorine-containing oxidizer, fluorinated graphene and graphite fluoride were used to prepare of Al/fluorinated-graphene composites for studying the effect on the combustion of aluminum powder.

Wang et al. [46] prepared nano-Al/CF (graphite fluoride) composites from nano aluminum and graphite fluoride in ethyl acetate with magnetic stirring, the composites sample were obtained after drying in the vacuum. Figure 43.7 is the FE-SEM surface appearance of the sample. Figure 43.7b shows the rough surface appearance about the composites, which is caused by the adhesion of nano-Al particles to the surface of CF. The layered structure of nano-Al/CF particles can be clearly observed from Fig. 43.7c, d. These indicate that the adhesion of nano-Al to the surface of CF can improve promote interfacial contact and mass transmission. EDS mapping (Fig. 43.7e, f) further illustrate the uniformity of and nano-Al/CF. The uniformity may give rise to high combustion performance.

Jiang et al. [47] prepared Al/GO (graphene oxide)/GF (fluorinated graphene) composite by a mechanical mixing method. Figure 43.8 shows the preparation process of Al/GO/GF composite. In this process, sonication plays an important role. Wang et al. [48] also used the sonication process to prepare a series of nano-thermite composites (FGO/Al, FGO/Al/Bi_2O_3 et al.).

Figure 43.9 shows the SEM image of Al/GO/GF composite, according to Fig. 43.9, the composite is mainly composed by Al particles with the adhesion of GO and GF on its surface. Figure 43.9 illustrated that the uniformity of the composite.

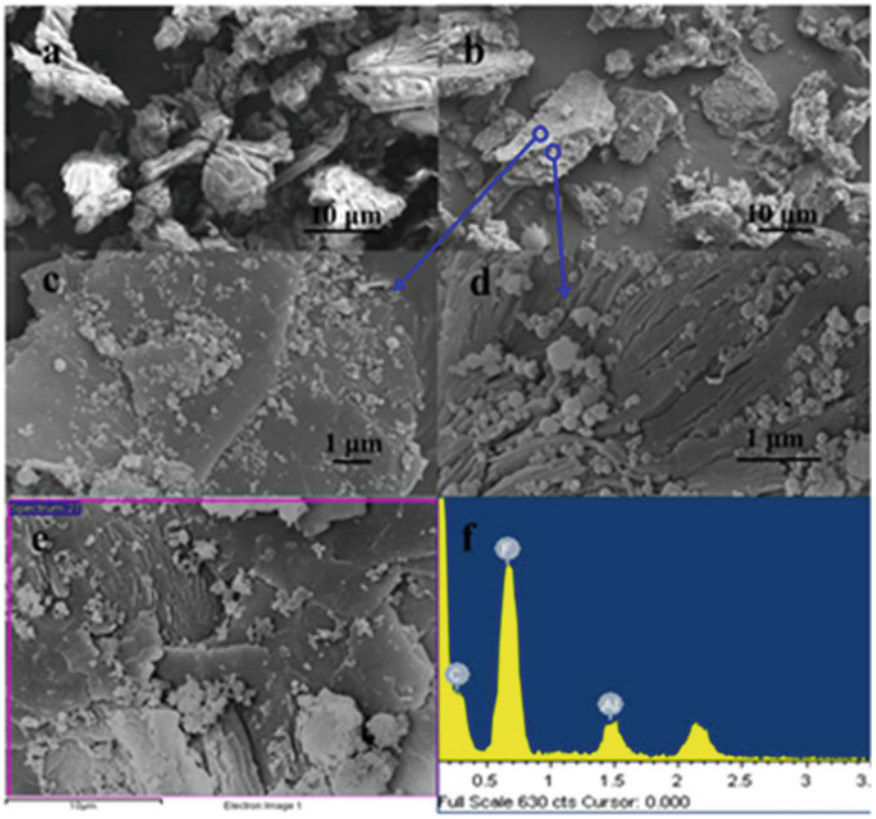

Fig. 43.7 **a** SEM image of graphite fluoride. **b** SEM image of nano-Al/CF. **c**, **d** High-magnification FE-SEM images of nano-Al/CF. **e**, **f** EDS mapping of Al, F and C elements of nano-Al/CF. Reprinted from Ref. [46]. Copyright 2021 with permission from Elsevier

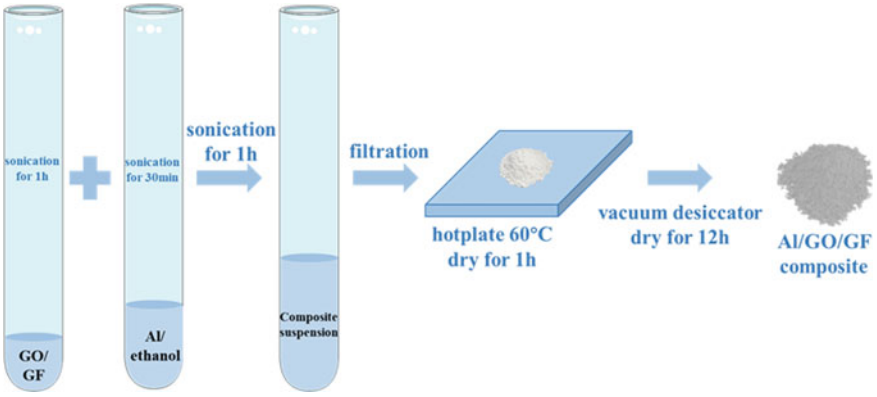

Fig. 43.8 The preparation process of Al/GO/GF composite

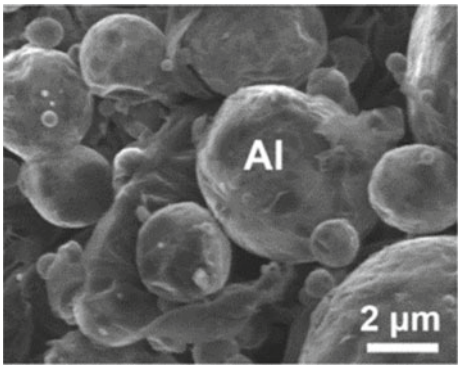

Fig. 43.9 SEM images of Al/GO/GF composite. Reprinted with permission from Ref. [47]. Copyright 2020 American Chemical Society

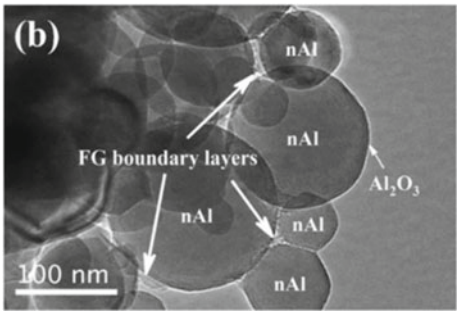

Fig. 43.10 TEM micrographs of nano-Al/FG. Reprinted from Ref. [49]. Copyright 2021 with permission from Elsevier

Zhu et al. [49] used nano-Al powders, FG (fluorinated graphene) powders, AP powders and cyclohexane solvent to prepare the composites with different FG content by a magnetic stirrer, an ultrasonic disperser and a vacuum dryer. Figure 43.10 is the TEM image of nano-Al/FG. Figure 43.10 shows the interfacial contact between FG boundary layer and nano-Al. Considering the structure, there is no agglomeration in this composite. At the same time, the decomposition products of FG will make the Al_2O_3 shell on the surface of nano-Al disappear during the combustion of the composite, which will enhance the combustion efficiency.

43.3.2 Preparation of Boron/FG Based Energetic Materials

The oxide shell on the surface of boron limited the aerospace applications of boron (B) [50]. The additives (metals, fluorine-containing oxidizers) can enhance the ignition and combustion properties of boron. Moreover, in 1996, an increase in the pressure exponent and burning rate was observed for boron-based fuel-rich propellants containing fluorinated graphite [51].

Wang et al. [52] used acoustic resonance and solvent evaporation methods to prepare fluorinated graphene coated boron composites, boron powder was added

into GF/ethyl-acetate uniform dispersion liquid for ultrasonic treatment and acoustic resonance, when the solvent was removing from the solid precipitate, GF will form a coating layer on the surface of B due to the physical interaction. Figure 43.11 and Fig. 43.12 are the SEM image and EDS image of GF coated B composites, in Fig. 43.11, the B surface of coated with GF has rougher appearance, which indicated that GF is perfectly attached to the surface of B. Figure 43.12 further illustrates B has been completely and homogeneously coated by GF.

Jiang et al. [53] used a LabRAM II mixer and polypropylene containers to mix the B particles with the GO (graphene oxide) and GtF (fluorinated graphite). Figure 43.13 is the SEM and EDS images of samples. They show the uniform structure of these

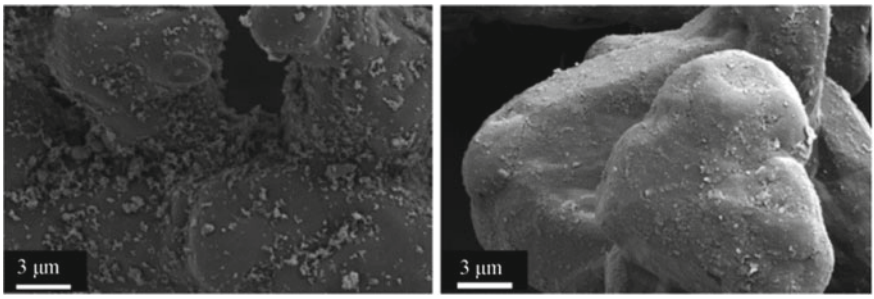

Fig. 43.11 SEM photographs of B coated with GF. Reprinted from Ref. [52]

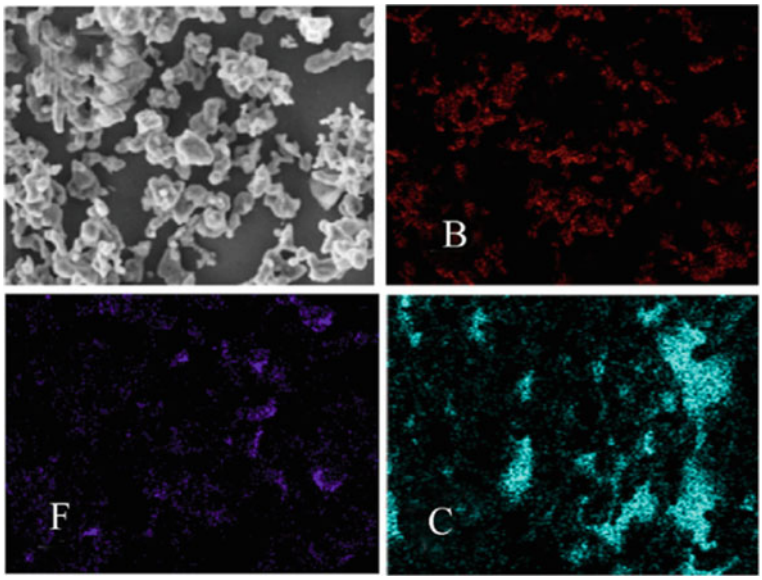

Fig. 43.12 EDS images of GF coated B composites. Reprinted from Ref. [52]

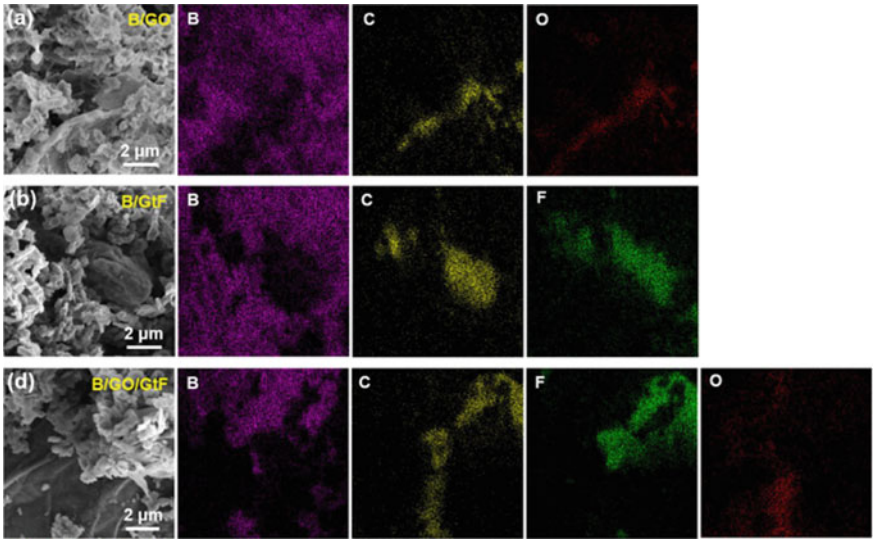

Fig. 43.13 SEM and EDS images of composites. **a** B/GO. **b** B/GtF. **c** B/GO/GtF. Reprinted from Ref. [53]. Copyright 2021 with permission from Elsevier

composites. Specially, according to Fig. 43.13d, the F element is near the O element, it indicates a good compatibility between graphene oxide and fluorinated graphite.

43.4 Theoretical Calculation About the Fluorinated-Graphene-Based Energetic Materials

Theoretical calculations, such as quantitative calculations and molecular force fields, have great significance for the application of energetic materials. At present, some theoretical calculation results on fluorinated-graphene-based energetic materials have guiding value for practical applications.

Jiang et al. [47] conducted reactive molecular dynamics (RMD) simulations for these composites: Al/GO, Al/GF, and Al/GO/GF. Figure 43.14 shows the RMD simulation results. Firstly, from Fig. 43.14a–c, the Al/GF/GO appeared greater uniformity than Al/GO and Al/GF at 150 ps, which indicated that Al/GO/GF will decompose more completely than others. Secondly, the number of C-C bond breaks can reveal the rate of decomposition, from Fig. 43.14d, the number of in Al/GO/GF (1818 at 150 ps) is higher than the average value in Al/GO and Al/GF (1426 at 150 ps), which implied that more GO and GF will decompose in Al/GO/GF. Thirdly, according to Fig. 43.14e, the Al/GF shown a higher degree of diffusion and Al oxidation than the Al/GO, it implied that the decomposition species from GF facilitated Al oxidation/fluorination. Finally, it can be seen from Fig. 43.14f that the relative potential

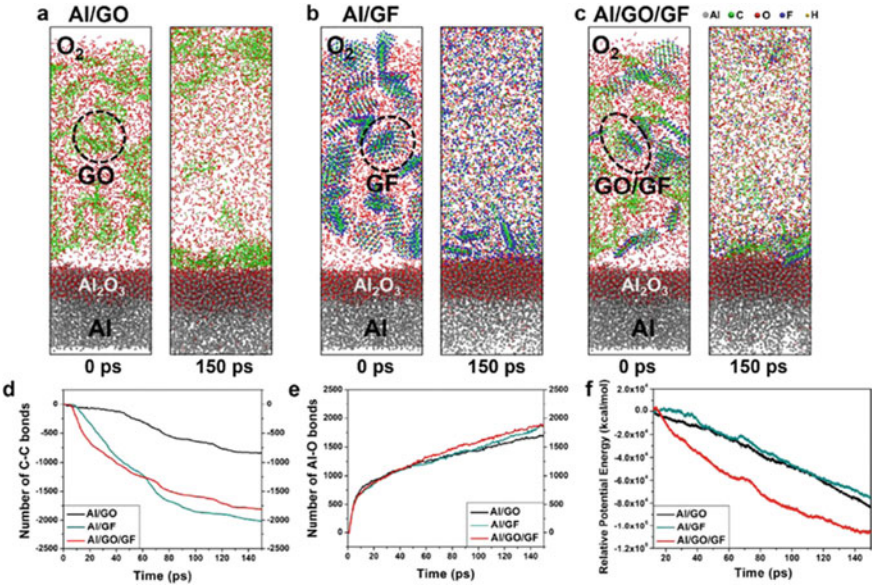

Fig. 43.14 RMD simulation results about Al/GO, Al/GF, and Al/GO/GF composites with O_2 at 2500 K at t = 0 and 150 ps (gray, Al atoms; green, C atoms; red, O atoms; blue, F atoms; yellow, H atoms). **a** Al/GO composites with GO:O_2 = 1:1. **b** Al/GF composites with GF:O_2 = 1:1. **c** Al/GO/GF composites with GO/GF:O_2 = 1:1. **d** The number of the C-C bonds versus time. **e** The number of the Al-O bonds versus time. **f** The relative potential energy versus time (lower relative potential energy means more heat release). Reprinted with permission from Ref. [47]. Copyright 2020 American Chemical Society

energy of Al/GO/GF decreased the fastest and the energy release was the largest, it indicated that Al/GO/GF reacts more quickly and exudes more heat. The RMD simulations results shown that the GO and GF can effectively improve the combustion properties of Al particles, Al/GO/GF composites exhibited higher energetic performance.

Tang et al. [54] used quantitative calculation to explore the adsorption mechanism of CL-20 on fluorinated graphene with different C/F ratio, Fig. 43.15 is the photos about the electron density difference between CL-20 and fluorinated graphene. According to Fig. 43.15a, four oxygen atoms in CL-20 receive electrons from graphene, while the nitrogen-containing region lose electrons. According to Fig. 43.15b–g, the lower the degree of fluorination, the smaller influence on the electron transfer between CL-20 and fluorinated graphene. On the contrary, the larger the degree of fluorination, the greater influence on the electron transfer between CL-20 and fluorinated graphene. Therefore, a larger degree of fluorination will lead to lower binding energy between CL-20 and fluorinated graphene.

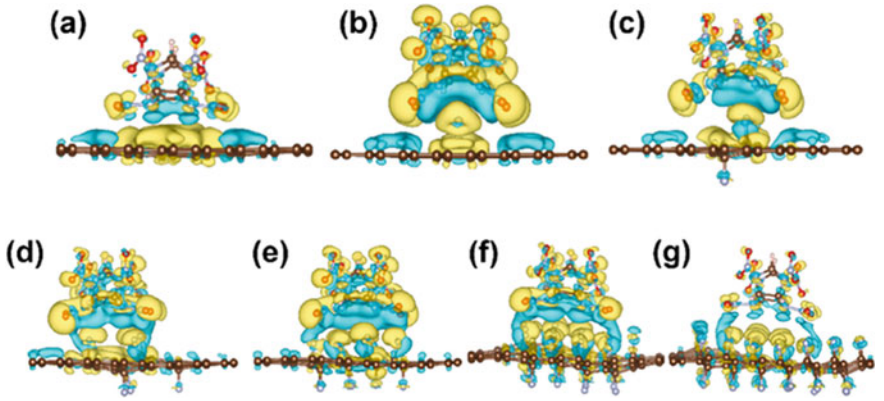

Fig. 43.15 Isosurface images of the electron density difference for CL-20 adsorbed on graphene with different degrees of fluorination of **a** 0%, **b** 0.9%, **c** 3.6%, **d** 7.1%, **e** 14.3%, **f** 28.6% and **g** 57.1%. Yellow: Electrons accumulation. Blue: electrons depletion. Reprinted from Ref. [54]. Copyright 2021 with permission from Elsevier

43.5 Characteristics of Fluorinated Graphene in Energetic Materials

43.5.1 Influence of Fluorinated-Graphene on the Decomposition of Energetic Materials

Zhu et al. [49] presented the TG-DTG and DSC results for different Al/AP-FG samples with different FG content. From the results of TG-DTG, FG will reduce the two heat release peak temperatures, which indicates that the existence of FG can influence the decomposition of AP and even change the decomposition process of AP [55, 56] into one stage. In addition, higher fluoridation degree can enhance the reactivity of AP. Figure 43.16 is the DSC images, according to Fig. 43.16, higher fluorination degree leads to the increase of melting peak temperature about AP, the exothermic peak and exothermic heat of the composites will also decrease when the fluorinated graphene is introduced. It indicates that he existence of FG may promote the decomposition of AP. Through TG-DTG and DSC analysis, it is proved that the fluorinated graphene significantly promoted the thermal decomposition of AP.

Wang et al. [52] study the thermal reaction of boron coated with fluorinated graphene, the TG-DSC curves are used to studied the decomposition. Fluorinated graphene can reduce the temperature of exothermic peak comparing with KNO_3/B. In addition, the reaction heat decreases at first and then increases with the fluorinated graphene content, it shows an overall increasing trend. These results reveal that fluorinated graphene can promote combustion of boron.

Wang et al. [48] studied the influence of FGO on the thermal decomposition about Al-contained composites. Figure 43.17 is the DSC results. Compared to the

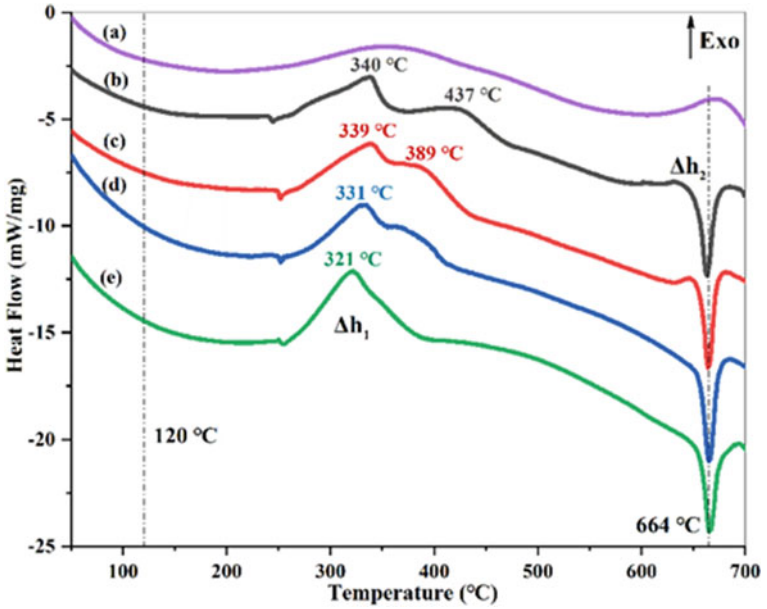

Fig. 43.16 DSC curves of the composites at the heating rate of 20 °C min^{-1}. **a** FG sample. **b** Al/AP sample. **c** Al/AP-FG_{10} sample. **d** Al/AP-FG_{15} sample. **e** Al/AP-FG_{20} sample. Reprinted from Ref. [49]. Copyright 2021 with permission from Elsevier

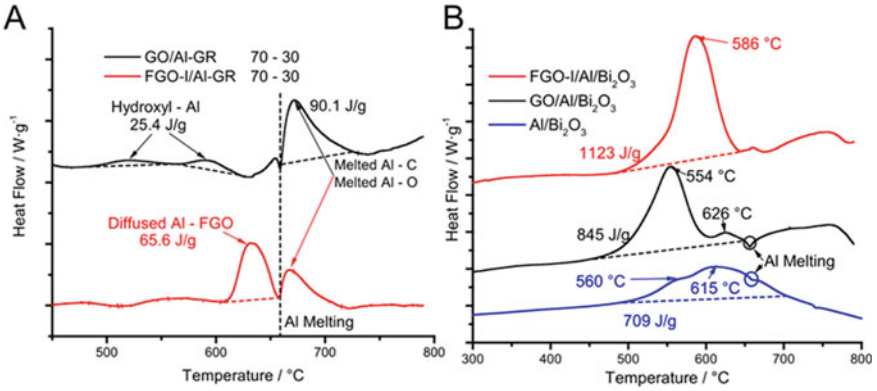

Fig. 43.17 DSC images of different composites. **a** GO/Al-GR and FGO-I/Al-GR. **b** FGO-I/Al/Bi_2O_3, GO/Al/Bi_2O_3 and Al/BiO_3. Reprinted from Ref. [48]. Copyright 2021 with permission from Elsevier

GO/Al-GR (GR stands for graphene-rich) in Fig. 43.17a, the exothermic peak of FGO-I/Al-GR is located between 610 and 660 °C, which indicates that Al_2O_3 film is weakened by the fluorine-containing groups, it will cause a better Al diffusion before the melting of Al. From Fig. 43.17b, in terms of FGO-I/Al/Bi_2O_3, the melting of Al was not observed, because Al was consumed completely before the melting of Al. The reason is the reaction of the fluorine-containing groups and Al_2O_3 film, then Al particles react earliest with Bi_2O_3 nanoparticles. Moreover, FGO-I/Al/Bi_2O_3 shows the highest energy release, which is 60% higher than Al/Bi_2O_3 and 33% higher than GO/Al/Bi_2O_3. This study shows that the presence of FG can not only promote the reaction of Al through etching the Al_2O_3 shell, but also further increase the energy level of the composite.

43.5.2 Influence of Fluorinated-Graphene on the Ignition of Energetic Materials

Wang et al. [52] studied the influence of nano-Al or GF on the ignition properties of boron powder, the ignition delay time of different composites are shown in Fig. 43.18. In terms of nano-Al coated KNO_3/B, the higher the nano-Al content is, the shorter the ignition delay time is. It is caused by the higher reactivity and better flammability of nano-Al. However, in terms of KNO_3/B coated with GF, the higher the fluorinated graphene content is, the longer the ignition delay time is, which is related to the endothermic effect during decomposition of fluorinated graphene. This research shows that the existence of fluorinated graphene will increase the ignition delay time of boron-based composites.

Tang et al. [54] researched the laser-induced ignition of CL-20 covered by fluorinated graphene with different fluorination degrees. The images of combustion process about different fluorinated graphene are shown in Fig. 43.19, it shows that the lower the degree of fluorination, the shorter the ignition delay time (the shortest is 60 ms), which is mainly due to the high heat release of fluorinated graphene under laser

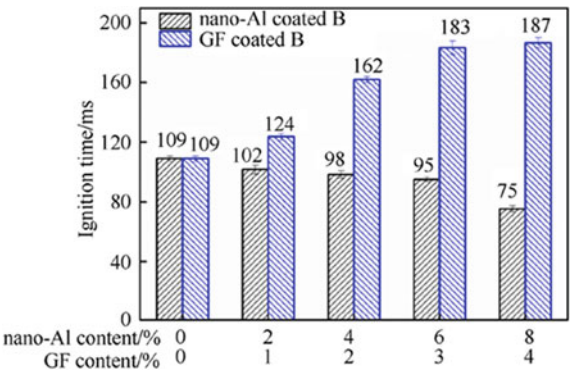

Fig. 43.18 Ignition delay time of different composites. Reprinted from Ref. [52]

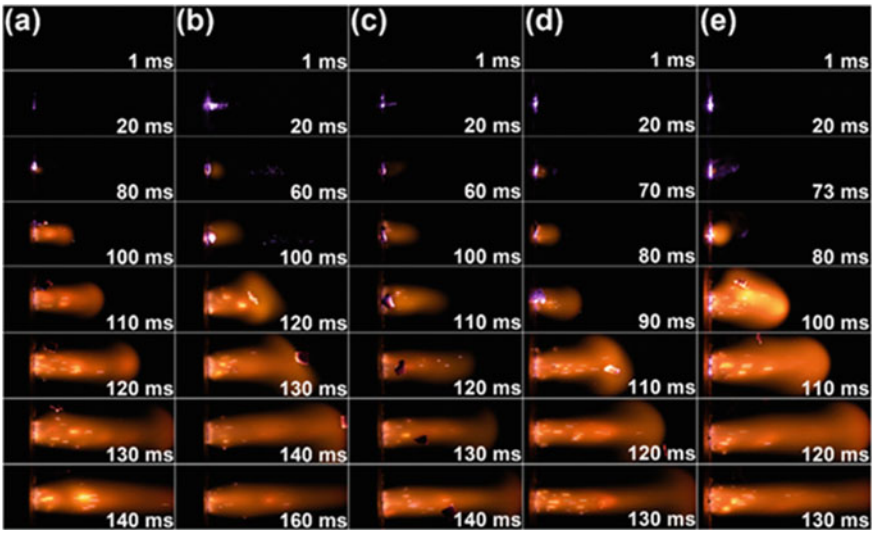

Fig. 43.19 Laser induced ignition images for CL-20 under series fluorinated graphene with different fluorination degrees. **a** Graphene, **b** FG-1, **c** FG-2, **d** FG-3 and **e** FG-4. Reprinted from Ref. [54]. Copyright 2021 with permission from Elsevier

irradiation. In addition, the calculation and simulation results also show that fluorinated graphene with a lower fluorination degree will have a better laser-induced ignition performance. This study demonstrates the potential of fluorinated graphene for laser-induced ignition.

43.5.3 Influence of Fluorinated-Graphene on the Combustion of Energetic Materials

Jiang et al. [47] studied the burning process of Al-based composites by the Xe flash lamp ignition. Figure 43.20 shows the high-speed video snapshots. First, Al/GF composite was not ignited but others all were ignited, it reveals that graphene oxide is more suitable for the optical initiation than fluorinated graphene (graphene oxide is black, fluorinated graphene is transparent), the reason is that graphene oxide can absorb more energy from the flash lamp. Secondly, Al/GO/GF shows the most intense burning, it reveals the synergistic effect of GO and GF, and also shows that GF has a stronger effect on promoting the of combustion Al/GO. This study shows that GO/GF can greatly promote the combustion of Al particles, Fig. 43.21 shows the synergistic reaction mechanism of GO and GF during the combustion process. Moreover, this study also shows GF is more superior than polytetrafluoroethylene (PTFE) to promote the combustion of Al particles.

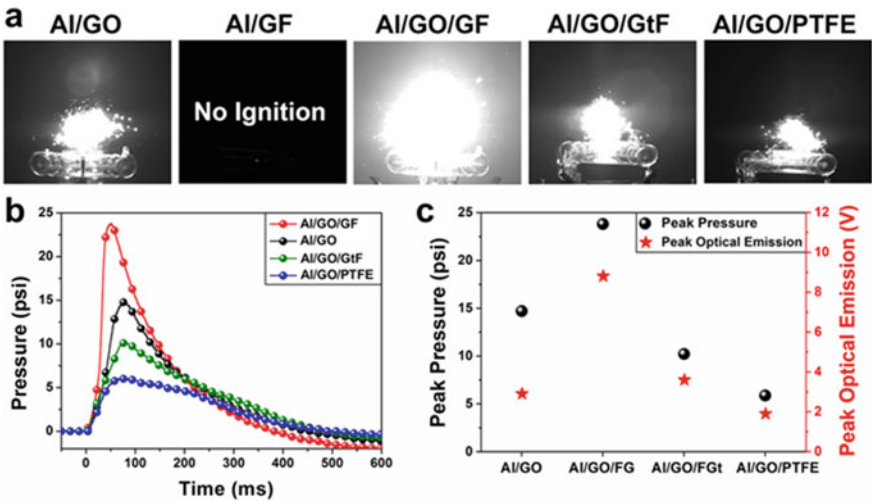

Fig. 43.20 Combustion performance of Al with different additives. **a** Snapshots of the burning of Al/GO (80/20 wt%), Al/GF (80/20 wt%), Al/GO/GF (80/10/10 wt%), Al/GO/GtF (80/10/10 wt%), and Al/GO/PTFE (80/10/10 wt%) composites at 40 **ms**. **b** Traces of the time-resolved pressure release evolution. **c** Summary of the peak values of pressure release and optical emission of different Al composites (except Al/GF). Reprinted with permission from Ref. [47]. Copyright 2020 American Chemical Society

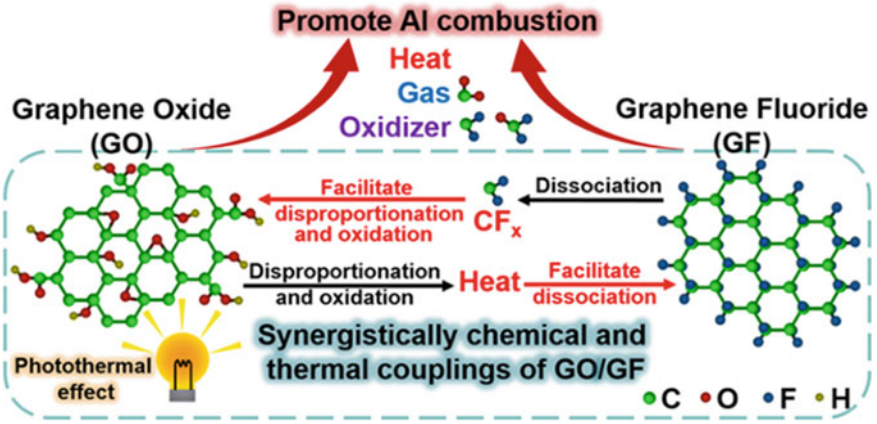

Fig. 43.21 Synergistic reaction mechanism of GO and GF during the combustion of Al with GO and GF and its effects for enhancing the energetic performance of Al. Reprinted with permission from Ref. [47]. Copyright 2020 American Chemical Society

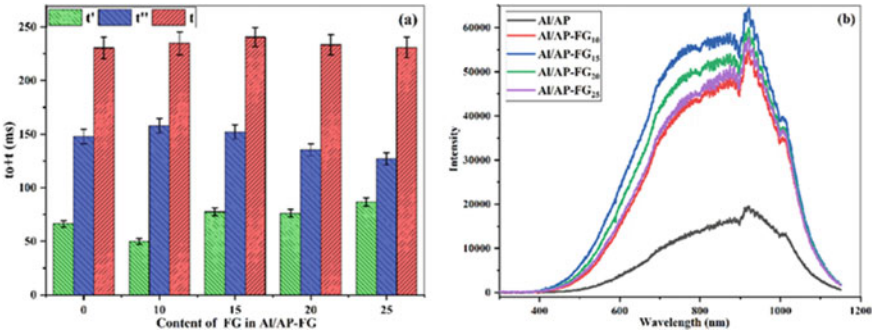

Fig. 43.22 **a** Different burning stages for different composites (t is the combustion duration, t′ is the maximum flame duration, t″ is the stable burning time.). **b** The emission spectra of the maximum combustion intensity. Reprinted from Ref. [49]. Copyright 2021 with permission from Elsevier

Zhu et al. [49] characterized the combustion properties of Al/AP-FG composites with different FG contents. Figure 43.22a is the burning times of these composites at three stages. Through the analysis of different combustion stages, it is found that the higher the content of, the greater the combustion intensity and energy release rate. Figure 43.22b is the emission spectra of the maximum combustion intensity, it shows that fluorinated graphene can greatly promote the combustion of Al/AP. However, fluorinated graphene content is not the higher the better, there is a most suitable proportion-15%. These results show that the introduction of fluorinated graphene can promote the energy release and combustion of Al.

Wang et al. [52] gave the combustion mechanism of KNO_3/B coated with nano-Al or fluorinated graphene through a series of characterization (ignition delay time, flame structure). They show different reaction mechanism. Figure 43.23 is the reaction mechanism of KNO_3/B coated with nano-Al or GF. According to Fig. 43.23a, nano-Al would be reacted with oxygen (or oxidizer) during ignition and it will generate lots of heat, which will induce the ignition of boron. According to Fig. 43.23b, some fluorine-containing groups produced from the thermal decomposition of fluorinated

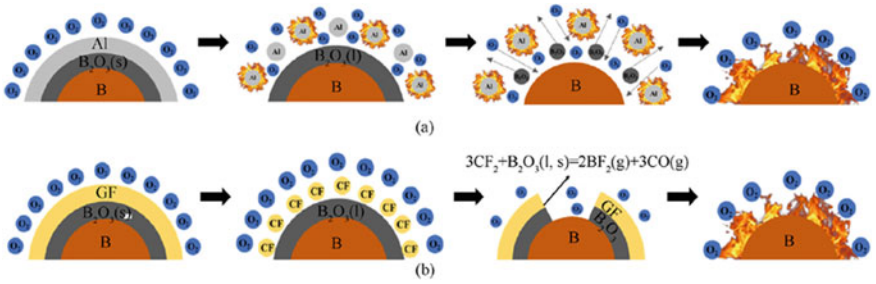

Fig. 43.23 The combustion mechanism of KNO_3/B coated with nano-Al or GF. Reprinted from Ref. [52]

graphene will destroy the oxide shell at low temperature and the subsequent pores will further eliminate the oxide shell. This study not only give two different pathways for promoting the combustion of boron powder, but also reveal the mechanism of fluorinated graphene promoting the combustion of boron powder.

43.6 Conclusions

In this paper, the research progress of fluorinated graphene in energetic materials is reviewed. It is proved that fluorinated graphene has a great prospect in the field of energetic materials. However, the applications of fluorinated graphene in energetic materials still have the following problems:

1. The structure of fluorinated graphene has a great influence on its nature. The preparation of high-quality fluorinated graphene, especially the precise control of fluorinated graphene structure for energetic materials, which needs to be deeply studied.
2. Although the fluorinated graphene-based energetic materials exhibit excellent combustion properties, the nature of the interaction between fluorinated graphene and the matrix (covalent or non-covalent, electrostatic or dispersion) in composites is still unclear.
3. At present, the researches of fluorinated graphene-based energetic materials mainly focus on Al, B composites, and the composites of the third-generation energetic materials (such as RDX, HMX, CL-20) need to be further studied.

In conclusion, deep analysis about the effect of the fluorinated graphene on the thermal decomposition and combustion properties of energetic materials is helpful to realize the wide application of fluorinated graphene in energetic materials and even solid propellants, it is of great practical significance to study the preparation method, theoretical calculation, thermal decomposition mechanism and combustion performance of fluorinated-graphene-based energetic composites.

Acknowledgements This research was funded by the National Natural Science Foundation of China with grant number (21975150).

Conflicts of Interest The authors declare no conflict of interest.

References

1. M. Comet, C. Martin, F. Schnell, D. Spitzer, Nanothermites: a short review. Factsheet for experimenters, present and future challenges. Propellants, Explos., Pyrotech. **44**, 18–36 (2019)
2. R.A. Yetter, G.A. Risha, S.F. Son, Metal particle combustion and nanotechnology. Proc. Combus. Inst. **32**, 1819–1838 (2009)

3. W. Jiang-ning, L. Wei, Z. Wei, C. Jun-bo, S. Xiu-duo, S. Zhi-gang, Effect of aluminum powder content on the burning rate of CL-20/Al-CMDB propellants. Chin. J. Explos. Propellants **41**, 404–407 (2018)
4. M.B. Padwal, D.A. Castaneda, B. Natan, Hypergolic combustion of boron based propellants. Proc. Combus. Inst. **38**, 6703–6711 (2021)
5. W. Ao, Y. Wang, H. Li, J. Xi, J. Liu, J. Zhou, Effect of initial oxide layer on ignition and combustion of boron powder. Propellants Explos. Pyrotech. **39**, 185–191 (2014)
6. Y. Feng, Z. Xia, L. Huang, X. Yan, Experimental investigation on the combustion characteristics of aluminum in air. Acta Astronaut. **129**, 1–7 (2016)
7. X. Liu, J. Gonzales, M. Schoenitz, E.L. Dreizin, Effect of purity and surface modification on stability and oxidation kinetics of boron powders. Thermochim. Acta **652**, 17–23 (2017)
8. X. Li-qun, F. Xue-zhong, W. Han, L. Ji-zhen, T. Qiu-fan, Research progress on the agglomeration phenomenon of aluminum powder in the combustion of aluminized solid propellants. Chin. J. Explos. Propellants **41**(7–15), 25 (2018)
9. L.-B. Li, X. Chen, C.-S. Zhou, M. Zhu, O. Musa, Experimental and numerical investigations of the effect of pressure and oxygen concentration on combustion characteristics of Al/Mg fuel-rich propellants. Appl. Thermal Eng. **167**, 114695 (2020)
10. H.A. Miller, B.S. Kusel, S.T. Danielson, J.W. Neat, E.K. Avjian, S.N. Pierson, S.M. Budy, D.W. Ball, S.T. Iacono, S.C. Kettwich, Metastable nanostructured metallized fluoropolymer composites for energetics. J. Mater. Chem. A **1**, 7050–7058 (2013)
11. T.R. Sippel, S.F. Son, L.J. Groven, Aluminum agglomeration reduction in a composite propellant using tailored Al/PTFE particles. Combust. Flame **161**, 311–321 (2014)
12. C. Huang, H. Yang, Y. Li, Y. Cheng, Characterization of aluminum/poly(vinylidene fluoride) by thermogravimetric analysis, differential scanning calorimetry, and mass spectrometry. Anal. Lett. **48**, 2011–2021 (2015)
13. J. McCollum, M.L. Pantoya, S.T. Iacono, Activating aluminum reactivity with fluoropolymer coatings for improved energetic composite combustion. ACS Appl. Mater. Interfaces **7**, 18742–18749 (2015)
14. K.-L. Chintersingh, M. Schoenitz, E.L. Dreizin, Combustion of boron and boron–iron composite particles in different oxidizers. Combust. Flame **192**, 44–58 (2018)
15. W. He, P.-J. Liu, F. Gong, B. Tao, J. Gu, Z. Yang, Q.-L. Yan, Tuning the reactivity of metastable intermixed composite n-al/ptfe by polydopamine interfacial control. ACS Appl. Mater. Interfaces **10**, 32849–32858 (2018)
16. J.-Y. Lyu, S. Chen, W. He, X.-X. Zhang, D.-Y. Tang, P.-J. Liu, Q.-L. Yan, Fabrication of high-performance graphene oxide doped PVDF/CuO/Al nanocomposites via electrospinning. Chem. Eng. J. **368**, 129–137 (2019)
17. D.W. Kim, K.T. Kim, D.-U. Lee, S.-H. Jung, D.Y. Yang, J. Yu, Influence of poly(vinylidene fluoride) coating layer on exothermic reactivity and stability of fine aluminum particles. Appl. Surface Sci. **551**, 149431 (2021)
18. S.A. Hashim, S. Karmakar, A. Roy, Effects of Ti and Mg particles on combustion characteristics of boron–HTPB-based solid fuels for hybrid gas generator in ducted rocket applications. Acta Astronaut. **160**, 125–137 (2019)
19. K.-L. Chintersingh, M. Schoenitz, E.L. Dreizin, Transition metal catalysts for boron combustion. Combust. Sci. Technol. **193**, 1400–1424 (2021)
20. Z. Li, Y. Wang, Y. Zhang, L. Liu, S. Zhang, CL-20 hosted in graphene foam as a high energy material with low sensitivity. RSC Adv. **5**, 98925–98928 (2015)
21. B. Ye, C. An, Y. Zhang, C. Song, X. Geng, J. Wang, One-step ball milling preparation of nanoscale CL-20/graphene oxide for significantly reduced particle size and sensitivity. Nanoscale Res. Lett. **13**, 42 (2018)
22. X. Zhang, W.M. Hikal, Y. Zhang, S.K. Bhattacharia, L. Li, S. Panditrao, S. Wang, B.L. Weeks, Direct laser initiation and improved thermal stability of nitrocellulose/graphene oxide nanocomposites. Appl. Phys. Lett. **102**, 141905 (2013)
23. C. Zhang, X. Fu, Q. Yan, J. Li, X. Fan, G. Zhang, Study on the thermal decomposition mechanism of graphene oxide functionalized with triaminoguanidine (GO-TAG) by molecular reactive dynamics and experiments. RSC Adv. **9**, 33268–33281 (2019)

24. R.R. Nair, M. Sepioni, I.L. Tsai, O. Lehtinen, J. Keinonen, A.V. Krasheninnikov, T. Thomson, A.K. Geim, I.V. Grigorieva, Spin-half paramagnetism in graphene induced by point defects. Nat. Phys. **8**, 199–202 (2012)
25. F. Karlický, M. Otyepka, Band gaps and optical spectra of chlorographene, fluorographene and graphane from G_0W_0, GW_0 and GW calculations on top of PBE and HSE06 orbitals. J. Chem. Theory Comput. **9**, 4155–4164 (2013)
26. N. Akhtar, G. Anemone, D. Farias, B. Holst, Fluorinated graphene provides long lasting ice inhibition in high humidity. Carbon **141**, 451–456 (2019)
27. W. Lai, D. Xu, X. Wang, Z. Wang, Y. Liu, X. Zhang, X. Liu, Characterization of the thermal/thermal oxidative stability of fluorinated graphene with various structures. Phys. Chem. Chem. Phys **19**, 19442–19451 (2017)
28. R.R. Nair, W. Ren, R. Jalil, I. Riaz, V.G. Kravets, L. Britnell, P. Blake, F. Schedin, A.S. Mayorov, S. Yuan, M.I. Katsnelson, H.-M. Cheng, W. Strupinski, L.G. Bulusheva, A.V. Okotrub, I.V. Grigorieva, A.N. Grigorenko, K.S. Novoselov, A.K. Geim, Fluorographene: a two-dimensional counterpart of teflon. Small **6**, 2877–2884 (2010)
29. R. Zbořil, F. Karlický, A.B. Bourlinos, T.A. Steriotis, A.K. Stubos, V. Georgakilas, K. Šafářová, D. Jančík, C. Trapalis, M. Otyepka, Graphene fluoride: a stable stoichiometric graphene derivative and its chemical conversion to graphene. Small **6**, 2885–2891 (2010)
30. H. Chang, J. Cheng, X. Liu, J. Gao, M. Li, J. Li, X. Tao, F. Ding, Z. Zheng, Facile synthesis of wide-bandgap fluorinated graphene semiconductors. Chem.—A Eur. J. **17**, 8896–8903 (2011)
31. P. Gong, Z. Wang, J. Wang, H. Wang, Z. Li, Z. Fan, Y. Xu, X. Han, S. Yang, One-pot sonochemical preparation of fluorographene and selective tuning of its fluorine coverage. J. Mater. Chem. **22**, 16950–16956 (2012)
32. I.-Y. Jeon, M.J. Ju, J. Xu, H.-J. Choi, J.-M. Seo, M.-J. Kim, I.T. Choi, H.M. Kim, J.C. Kim, J.-J. Lee, H.K. Liu, H.K. Kim, S. Dou, L. Dai, J.-B. Baek, Edge-fluorinated graphene nanoplatelets as high performance electrodes for dye-sensitized solar cells and lithium ion batteries. Adv. Funct. Mater. **25**, 1170–1179 (2015)
33. B.R. Boswell, C.M.F. Mansson, J.M. Cox, Z. Jin, J.A.H. Romaniuk, K.P. Lindquist, L. Cegelski, Y. Xia, S.A. Lopez, N.Z. Burns, Mechanochemical synthesis of an elusive fluorinated polyacetylene. Nat. Chem. **13**, 41–46 (2021)
34. V. Mazánek, O. Jankovský, J. Luxa, D. Sedmidubský, Z. Janoušek, F. Šembera, M. Mikulics, Z. Sofer, Tuning of fluorine content in graphene: towards large-scale production of stoichiometric fluorographene. Nanoscale **7**, 13646–13655 (2015)
35. X. Wang, W. Wang, D. Xu, Y. Liu, W. Lai, X. Liu, Activation effect of porous structure on fluorination of graphene based materials with large specific surface area at mild condition. Carbon **124**, 288–295 (2017)
36. H. Aguilar-Bolados, A. Contreras-Cid, M. Yazdani-Pedram, G. Acosta-Villavicencio, M. Flores, P. Fuentealba, A. Neira-Carrillo, R. Verdejo, M.A. López-Manchado, Synthesis of fluorinated graphene oxide by using an easy one-pot deoxyfluorination reaction. J. Colloid Interface Sci. **524**, 219–226 (2018)
37. M. Jahanshahi, E. Kowsari, V. Haddadi-Asl, M. Khoobi, B. Bazri, M. Aryafard, J.H. Lee, F.B. Kadumudi, S. Talebian, N. Kamaly, M. Mehrali, A. Dolatshahi-Pirouz, An innovative and eco-friendly modality for synthesis of highly fluorinated graphene by an acidic ionic liquid: Making of an efficacious vehicle for anti-cancer drug delivery. Appl. Surface Sci. **515**, 146071 (2020)
38. S. Deng, D. Rhee, W.-K. Lee, S. Che, B. Keisham, V. Berry, T.W. Odom, Graphene wrinkles enable spatially defined chemistry. Nano Lett. **19**, 5640–5646 (2019)
39. J.-Y. Xu, J.-S. Yu, J.-H. Liao, X.-B. Yang, C.-Y. Wu, Y. Wang, L. Wang, C. Xie, L.-B. Luo, Opening the band gap of graphene via fluorination for high-performance dual-mode photodetector application. ACS Appl. Mater. Interfaces **11**, 21702–21710 (2019)
40. X. Wang, Y. Dai, J. Gao, J. Huang, B. Li, C. Fan, J. Yang, X. Liu, High-yield production of highly fluorinated graphene by direct heating fluorination of graphene-oxide. ACS Appl. Mater. Interfaces **5**, 8294–8299 (2013)

41. J.T. Robinson, J.S. Burgess, C.E. Junkermeier, S.C. Badescu, T.L. Reinecke, F.K. Perkins, M.K. Zalalutdniov, J.W. Baldwin, J.C. Culbertson, P.E. Sheehan, E.S. Snow, Properties of fluorinated graphene films. Nano Lett. **10**, 3001–3005 (2010)
42. Z. Wang, J. Wang, Z. Li, P. Gong, X. Liu, L. Zhang, J. Ren, H. Wang, S. Yang, Synthesis of fluorinated graphene with tunable degree of fluorination. Carbon **50**, 5403–5410 (2012)
43. F.-G. Zhao, G. Zhao, X.-H. Liu, C.-W. Ge, J.-T. Wang, B.-L. Li, Q.-G. Wang, W.-S. Li, Q.-Y. Chen, Fluorinated graphene: facile solution preparation and tailorable properties by fluorine-content tuning. J. Mater. Chem. A **2**, 8782–8789 (2014)
44. J. Plšek, K.A. Drogowska, M. Fridrichová, J. Vejpravová, M. Kalbáč, Laser-ablation-assisted SF_6 decomposition for extensive and controlled fluorination of graphene. Carbon **145**, 419–425 (2019)
45. K. Tahara, T. Iwasaki, A. Matsutani, M. Hatano, Effect of radical fluorination on mono- and bi-layer graphene in Ar/F_2 plasma. Appl. Phys. Lett. **101**, 163105 (2012)
46. J. Wang, W. Cao, R. Liu, R. Xu, X. Chen, Graphite fluoride as a new oxidizer to construct nano-Al based reactive material and its combustion performance. Combust. Flame **229**, 111393 (2021)
47. Y. Jiang, S. Deng, S. Hong, S. Tiwari, H. Chen, K.-i Nomura, R.K. Kalia, A. Nakano, P. Vashishta, M.R. Zachariah, X. Zheng, Synergistically chemical and thermal coupling between graphene oxide and graphene fluoride for enhancing aluminum combustion. ACS Appl. Mater. Interfaces **12**, 7451–7458 (2020)
48. A. Wang, S. Bok, C.J. Mathai, R. Thiruvengadathan, C.M. Darr, H. Chen, M.R. Zachariah, K. Gangopadhyay, J.A. McFarland, M.R. Maschmann, S. Gangopadhyay, Synthesis, characterization and nanoenergetic utilizations of fluorine, oxygen co-functionalized graphene by one-step XeF2 exposure. Combust. Flame **215**, 324–332 (2020)
49. B. Zhu, S. Zhang, Y. Sun, Y. Ji, J. Wang, Fluorinated graphene improving thermal reaction and combustion characteristics of nano-aluminum powder. Thermochim. Acta **705**, 179038 (2021)
50. B. Van Devener, J.P.L. Perez, J. Jankovich, S.L. Anderson, Oxide-free, catalyst-coated, fuel-soluble, air-stable boron nanopowder as combined combustion catalyst and high energy density fuel. Energy Fuels **23**, 6111–6120 (2009)
51. T.-K. Liu, I.-M. Shyu, Y.-S. Hsia, Effect of fluorinated graphite on combustion of boron and boron-based fuel-rich propellants. J. Propulsion Power **12**, 26–33 (1996)
52. J. Wang, J. Wang, Y. Mao, R. Peng, F. Nie, The surface activation of boron to improve ignition and combustion characteristic. Def. Technol. (2021)
53. Y. Jiang, A.R. Demko, J. Baek, X. Shi, L. Vallez, R. Ning, X. Zheng, Facilitating laser ignition and combustion of boron with a mixture of graphene oxide and graphite fluoride. Appl. Energy Combust. Sci. **1–4**, 100013 (2020)
54. P. Tang, W. Zhu, Z. Qiao, G. Yang, X. Li, Y. Tang, H. Zhang, Laser-induced energetic material ignition with various fluorinated graphenes: theoretical and experimental studies. Appl. Surface Sci. **570**, 151187 (2021)
55. H. Liu, Q. Jiao, Y. Zhao, H. Li, C. Sun, X. Li, H. Wu, Cu/Fe hydrotalcite derived mixed oxides as new catalyst for thermal decomposition of ammonium perchlorate. Mater. Lett. **64**, 1698–1700 (2010)
56. L. Hai-tao, X. Shuang, S. Liu-fang, W. Yue, P. Ai-min, L. Guang-lan, Thermal decomposition of AP catalyzed by nano ZnO cube and its application in HTPE propellants. Chin. J. Explos. & Propellants **41**, 89–95 (2021)

Chapter 44
Molecular Dynamics Study on Aging Mechanism of HTPB Propellants

Xitong Zhao, Xiaolong Fu, Zhengming Gao, Liping Jiang, Jizhen Li, and Xuezhong Fan

Abstract In order to research the aging mechanism of HTPB propellants, molecular dynamics (MD) simulation method was used to study the aging mechanism of HTPB propellants after aging reaction. The changes of mechanical properties, binding energy, cohesive energy density and other properties of solid propellants were predicted when HMX was decomposed and HTPB was decomposed and oxidative cross-linked. So the aging mechanism of HTPB propellants can be speculated. The results show that during the long-term storage of propellant, HMX molecules will decompose and release gases. The retention of gases will greatly accelerate the aging of the propellant. However, in short-term storage, because HMX decomposition amount is less at room temperature, the effect on the performance is not obvious, so the decomposition of HTPB molecules is the main factor affecting the aging of propellant in short-term storage. The research content has certain guiding significance for the long-term storage of solid propellants.

X. Zhao · X. Fu · L. Jiang · J. Li · X. Fan (✉)
Xi'an Modern Chemistry Research Institute, Xi'an 710065, China
e-mail: xuezhongfan@126.com

X. Zhao
e-mail: zhao_xt204@163.com

X. Fu
e-mail: fuxiaolong204@163.com

L. Jiang
e-mail: jiangliping204@163.com

J. Li
e-mail: jizhenli@126.com

Z. Gao
School of Computer Engineering, Jingchu University of Technology, Jingmen 448000, China
e-mail: gaozming@jcut.edu.cn

A. Gany and X. Fu (eds.), *2021 International Conference on Development and Application of Carbon Nanomaterials in Energetic Materials*, Springer Proceedings in Physics 276,
https://doi.org/10.1007/978-981-19-1774-5_44

44.1 Introduction

Solid propellant is mainly composed of energetic binder, high-energy oxidant, energetic plasticizer, metal particles and some other additives [1]. Hydroxy-terminated polybutadiene (HTPB) composite solid propellant, also known as HTPB propellant, has excellent mechanical properties, high burning rate adjustability and low cost. It is widely used in solid rocket motors [2]. However, in the long-term storage process, due to the influence of environmental temperature and humidity, as well as the instability of HTPB propellant's own components, its internal structure will change, resulting in changes in mechanical properties and binding energy, that is, aging phenomenon, so that it cannot meet the needs of practical use, thus losing its value. Therefore, the research on the aging properties of HTPB propellant has important guiding significance for the long-term storage of solid propellant.

At present, researchers generally combine experiments and test instruments to study the factors, aging mechanism and aging characteristics of propellant aging. Zhang and coworkers [3] studied the mechanical properties of nitrate ester plasticized polyether (NEPE) propellant under different aging degrees. The results show that the decomposition of solid oxidant and the volatilization of plasticizer will destroy the adhesion between solid particles and adhesive, resulting in the decline of mechanical properties. Ding [4] found that the accelerated aging of HTPB propellant at alternating temperature has a high correlation with natural storage. The high temperature accelerated aging experiments show that the higher the storage temperature of solid propellant, the more serious the performance change, that is, the greater the aging rate. During the temperature cycle, the oxidant 1,3,5,7-tetranitro-1,3,5,7-tetrazocane (HMX) and adhesive HTPB in the propellant will undergo thermal decomposition [5], and the autocatalytic effect of HMX will promote the thermal decomposition, resulting in the acceleration of heat release [6]. Therefore, this paper will analyze and study the effect of thermal decomposition of HMX and HTPB on the aging reaction of HTPB propellant.

In the actual environment, HMX and HTPB will not undergo thermal decomposition. Only in the environment of high-temperature storage, HMX will undergo slow decomposition and HTPB will undergo degradation and chain breaking reaction. However, the storage experiment at room temperature requires decades of time, which cannot meet the needs of rapid evaluation. Therefore, researchers need to adopt accelerated aging method. The more commonly used life prediction method is high-temperature accelerated aging method to obtain the aging critical life. The estimated life can be calculated by using the time-temperature superposition principle and Arrhenius equation [7]. In this way, the experimental data equivalent to the long-time low-temperature condition can be measured under the condition of short-time high-temperature.

At the same time, a large number of experimental tests will cause a great waste of manpower and material resources. In recent years, people gradually began to use computer simulation method to study the micro mechanism of propellant, combine macro reaction with micro phenomenon, improve the research efficiency, and provide

prediction and theoretical guidance for the study of aging mechanism of propellants [8, 9]. With the successful application of modern Monte Carlo method in computer simulation, researchers simulated the elastic collision of hard sphere model on this basis, and developed the molecular dynamics method [10–12].

Based on the above analysis, this paper calculates and analyzes the mechanical properties, binding energy and cohesive energy density of HTPB propellant by using the method of molecular dynamics simulation and Materials Studio 8.0 software, and predicts the performance changes of HTPB propellant in the process of high temperature accelerated aging, when HMX decomposition, HTPB molecule degradation, chain breaking and oxidative crosslinking reaction occur. Thus, the aging mechanism of HTPB propellant is inferred.

44.2 Method

44.2.1 Structure of HTPB Propellant Molecular Model

HTPB molecule chain was constructed by MS 8.0 software. The repeating unit was composed of trans-butadiene, cis-butadiene and 1,2-butadiene. The component ratio was 3:1:1, and the single chain molecular weight of HTPB was 1650. The molecular model is shown in Fig. 44.1a. The molecular models of dioctyl sebacate (DOS) and HMX were obtained by querying the Cambridge crystal database (CCDC), as shown in Fig. 44.1b, c. The Geometry Optimization function is used to minimize the energy of HTPB, DOS and HMX molecule respectively. When the energy reaches the minimum, the Amorphous Cell Tools module is used to mix three different molecules

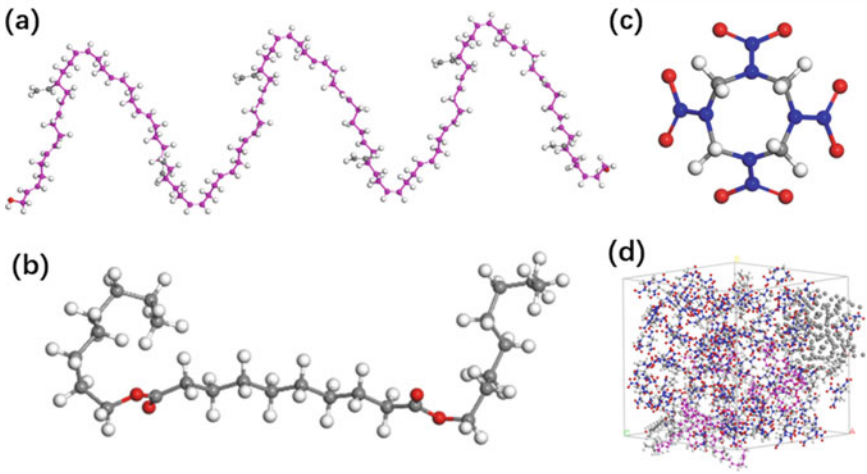

Fig. 44.1 Molecular model of **a** HTPB; **b** DOS; **c** HMX; **d** HTPB propellant

and nano aluminum to build a mixed molecular model. As shown in Fig. 44.1d, the mixture structure includes 2 HTPB molecular chains, 4 DOS molecules, 77 HMX molecules and 1 nano aluminum metal ball model. The content ratio of each component is HTPB: DOS: Al: HMX = 10:5:15:70.

44.2.2 Molecular Dynamics Simulation

After the construction of mixture cell, due to the different arrangement of molecular chains in the cell and the steric effect, there are many different conformations of molecular chains, the internal force of the system is strong and the potential energy of the system does not reach the minimum. Therefore, before molecular dynamics calculation, the structure of the mixed model should be optimized first. Generally, it needs to go through two processes: energy minimization and molecular dynamics optimization, so as to obtain a stable structure with energy minimization.

Firstly, we used the Geometry Optimization function in Forcite module and the Smart Minimization method to optimize the structure. Then, the system was optimized by molecular dynamics way, the dynamics function in Forcite module was selected, the force field was COMPASS [13–15], the Coulomb action and van der Waals force were calculated by Ewald method, and the molecular dynamics was optimized under NPT ensemble, in which the initial temperature was set to 70 °C, the pressure was 0.001 GPa, the temperature control method was Nose, and the pressure regulation method was Parrinello, simulate 100 ps in steps of 0.5 fs. When the temperature variation deviation is less than 10 K and the energy curve is constant or fluctuates slightly up and down along the constant value, it indicates that the structural system meets the balance of temperature and energy at the same time and the structure is stable. After that, further performance calculation and simulation can be carried out.

The mechanical properties, binding energy, cohesive energy density and radial distribution function were calculated by MS 8.0 software. The bond energy of HTPB and HMX were calculated by Gaussian 09 [16] software.

44.3 Result and Discussion

44.3.1 Chain Breaking of HTPB During Propellant Aging

Due to the low hydroxyl content in HTPB, its main chain structure is comparable to that of polybutadiene. The results show that the cracking mechanism of HTPB is similar to that of polybutadiene [8]. When chain breaking occurs, the C-C bond between two secondary carbons is easier to break [17], as shown in Fig. 44.2a.

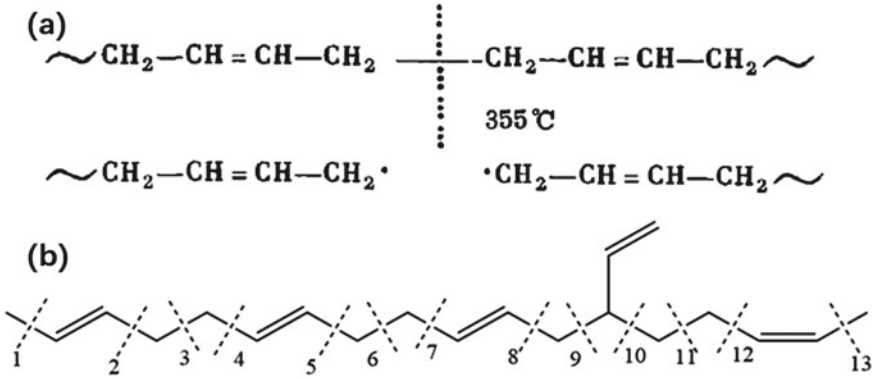

Fig. 44.2 **a** Chain breaking mechanism of HTPB [17]; **b** Chemical bond number of HTPB main chain

Table 44.1 Bond energy in HTPB molecular

Bond	Bond energy (kJ mol^{-1})	Bond	Bond energy (kJ mol^{-1})
1	410.65	8	396.12
2	399.53	9	187.08
3	202.18	10	258.44
4	398.51	11	271.43
5	398.39	12	389.62
6	202.50	13	403.13
7	398.81		

The energy of C-C bonds in HTPB main chain is analyzed. The structural diagram and chemical bond number of repeating unit are shown in Fig. 44.2b. The calculation results are shown in Table 44.1. It can be seen that bond 3, bond 6 and bond 9 have lower bond energy, which is easy to break in the reaction, which is similar to the literature.

According to this chain breaking mechanism, the long-chain HTPB molecule is decomposed into shorter polymer chains, the phenomenon of polymer chain breaking into 2 segments, 4 segments and 8 segments in the aging process is simulated, and then the aging mechanism is judged by calculating the changes of its mechanical properties and binding energy. The aging temperature is 70 °C [18].

44.3.1.1 Mechanical Properties Analysis

Mechanical properties are important properties related to the preparation, processing, production and use of solid propellant. Based on the principle of static analysis, MS program can obtain the atomic internal stress tensor after calculating multiple uniaxial

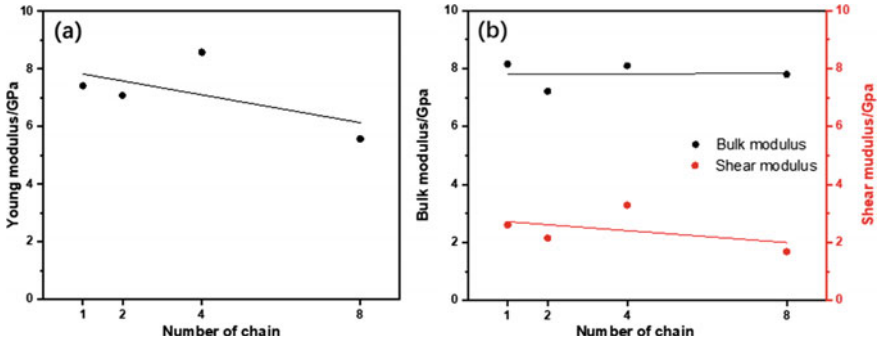

Fig. 44.3 Mechanical modulus curves of solid propellants when HTPB decompose: **a** Young's modulus; **b** Bulk modulus and shear modulus

tension and pure shear, and obtain the elastic coefficient matrix by using the numerical method to obtain the first-order partial derivative of the corresponding stress and strain. Further, other effective isotropic mechanical properties can be obtained, such as shear modulus, bulk modulus and lame constant [19].

The mechanical properties of the mixed molecular model were simulated by Forcite module. The initial model and the mechanical properties of mixed molecules when HTPB molecules are degraded and broken at 70 °C are obtained, as shown in Fig. 44.3.

It can be concluded from the information in the figures that when the HTPB polymer chain in the mixed system breaks into two segments, the mechanical properties of the propellant decrease, which is in line with the change characteristics of the mechanical properties of the propellant during aging. This is because the short polymer chain cannot play the original adhesion, which makes the connection between molecules less stable than that of the long chain, resulting in the deterioration of the mechanical properties of the mixed system. When HTPB molecules break into smaller molecular chains, the mechanical properties do not further decrease, which may be because the smaller molecular chains have smaller energy, which makes the overall energy of the mixed molecules lower and more stable in the macro. On the whole, the fracture of HTPB molecular chain will have a certain impact on the mechanical properties of propellant. Therefore, it can be preliminarily speculated that the decomposition of HTPB molecules into smaller molecular chains will cause propellant aging, which is also consistent with the literature research results.

44.3.1.2 Binding Energy Analysis

Binding energy is a physical quantity that describes the stability of mixed molecules from the perspective of thermodynamics. MS can calculate the bond energy and non-bond energy of each molecule to obtain the total energy of the molecule. Then the binding energy of mixed molecules can be obtained from the total energy of these

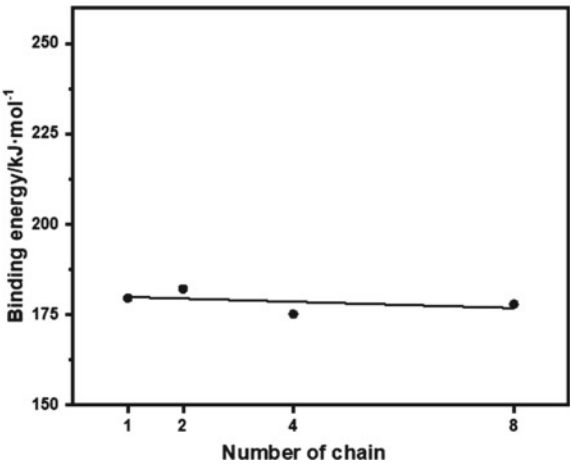

Fig. 44.4 Binding energy curve of solid propellants when HTPB decompose

molecules. The calculation formula of binding energy is as follows:

$$E_{binding} = -E_{inter} = -(E_{AB} - E_A - E_B)$$

where E_{AB} is the total energy of mixture A and B, E_A and E_B are the energy of A and B respectively.

When HTPB molecule decompose, the calculation results of binding energy are shown in Fig. 44.4.

According to the information in the figure, the change of binding energy is consistent with the mechanical properties. When HTPB molecule breaks, the average binding energy in the system will decrease.

44.3.1.3 Cohesive Energy Density Analysis

Cohesive energy density (CED) is a physical quantity to evaluate the magnitude of intermolecular force, which mainly reflects the interaction between groups. In MS software, Forcite module can be directly used to simulate the cohesive energy density of molecules. When HTPB molecule decompose, the calculation results of cohesive energy density are shown in Fig. 44.5.

It can be seen that the variation of cohesive energy density is consistent with the mechanical properties and binding energy calculated before. In the process of HTPB molecular decompose, the change of cohesion energy density is obvious, resulting in the change of intermolecular interaction.

Combined with the above analysis results, in HTPB solid propellant, the decomposition of binder HTPB into shorter molecular chains will cause the aging of propellant. This effect is very obvious in the short-term storage of propellant.

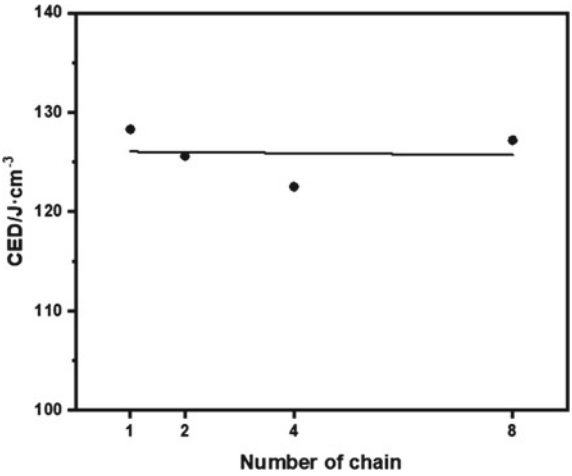

Fig. 44.5 CED curves of solid propellants when HTPB decompose

44.3.1.4 Oxidative Crosslinking of HTPB Molecules

The researchers found that oxidation reaction may occur in the aging process of HTPB propellant, and the oxidation reaction mainly occurs at the C = C double bond in HTPB binder molecules [8]. When the C = C double bond in the propellant is oxidized by the oxidizing substances in the system, the reactions include the cyclization of C = C double bond and the oxidative crosslinking reaction between C = C double bonds. The oxidative crosslinking reaction is shown in Fig. 44.6a.

Therefore, the mixed molecular model of oxidative crosslinking reaction of two HTPB polymer chains can be constructed by MS software, and the mechanical properties, binding energy and cohesive energy density of the mixed system can be calculated. The schematic diagram of the model is shown in Fig. 44.6b. The data comparison between it and the initial structure is shown in Table 44.2.

According to the data in the table, compared with the initial structure, the mechanical modulus of mixed molecules with oxidative crosslinking structure between HTPB has decreased, but the change range is small. The binding energy and cohesive energy density increased, and the change was not violent. It can be concluded that in solid propellant, the oxidative crosslinking reaction of adhesive HTPB will have a certain impact on the mechanical properties of the material and reduce its elastic modulus. From the perspective of thermodynamics, the binding energy of the system increases after oxidative crosslinking. Therefore, oxidative crosslinking reaction will affect the aging reaction of propellant to a certain extent, but it is not the main influencing factor.

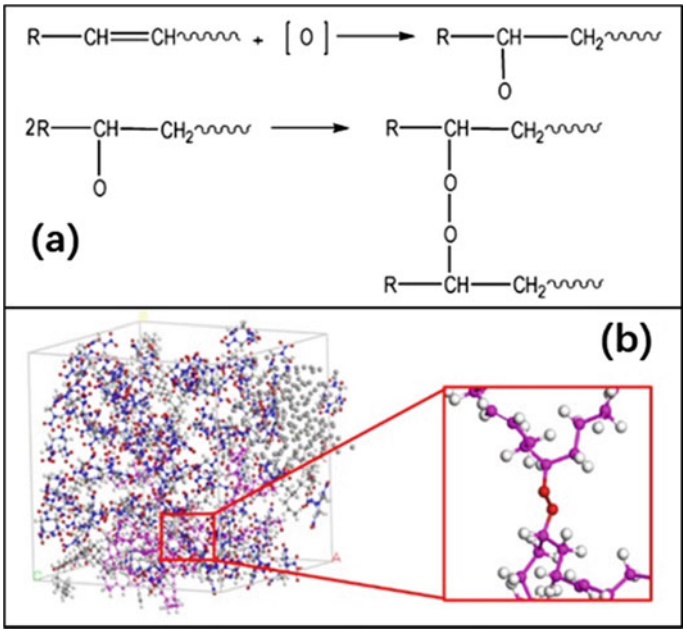

Fig. 44.6 Mechanism [8] and molecular model of HTPB oxidation linking reaction

Table 44.2 Comparison of properties between structures before and after reaction

	Initial structure	Oxidative crosslink
Young modulus (GPa)	8.1122	7.3303
Bulk modulus (GPa)	8.1148	7.9564
Shear modulus (GPa)	2.8321	2.6705
Binding energy (kJ mol^{-1})	179.62	197.24
CED (J cm^{-3})	128.3	126.9

44.3.2 Decomposition of HMX During Propellant Aging

There are many experimental reports on the thermal decomposition mechanism of HMX at atmospheric pressure. The results generally believe that the N-N bond breaking, HONO dissociation, C-N bond breaking and main ring decomposition are the main reaction paths in the process of gas-phase HMX molecular decomposition. N-N bond breaking to generate NO_2 plays a major role in the initial decomposition of single molecules, while the dissociation of HONO and the breaking of C-N bond are more likely to occur in the decomposition of condensed HMX [20]. In

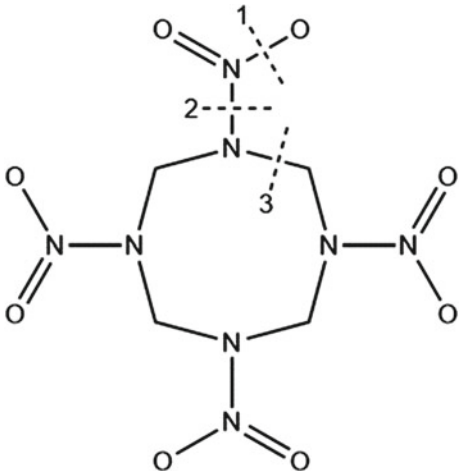

Fig. 44.7 Bond number in HMX molecular

Table 44.3 Bond energy in HMX molecular

Bond	Bond energy (kJ mol^{-1})
1	500.9270215
2	162.859765
3	236.132219

the decomposition process, the intermediate products mainly include H_2CO, N_2O, HONO, HCN, etc. with the progress of the reaction, these intermediate products are further decomposed into final products such as N_2, H_2O, CO and CO_2 [21].

The molecular structure and chemical bond number of HMX are shown in Fig. 44.7, and the calculation results of bond energy are shown in Table 44.3. From the calculation results of bond energy, it can be concluded that the bond energy between N-N bond and C-N bond is relatively low and easy to break, which is consistent with the conclusion of literature research.

We can adjust the molecular composition of the initial mixed molecular model, decompose different numbers of HMX molecules into corresponding gas molecules, and judge the aging mechanism by calculating the changes of their mechanical properties and binding energy.

44.3.2.1 Mechanical Properties Analysis

The mechanical properties of the mixed molecular model were simulated by Forcite module. The mechanical properties after HMX decomposition at 70 °C are obtained, as shown in Fig. 44.9.

It can be concluded from the figure that when HMX decompose during aging, the mechanical properties of propellant will be affected. When HMX decompose into

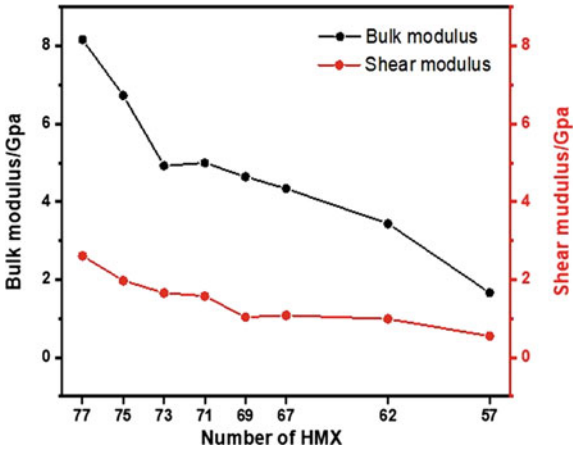

Fig. 44.9 Bulk modulus and shear modulus curves of solid propellants when HMX decompose

corresponding gases, the bulk modulus and shear modulus both decrease with the HMX decomposition. This shows that in solid propellant, when HMX decomposed into gas, the stiffness and hardness of the material are reduced, it is easier to deform and the mechanical properties become worse under the action of external force. This is consistent with the characteristics of propellant aging.

When the solid propellant contains gases, these gas molecules will have a certain impact on the internal structure of the material system, which will change the mechanical properties of the propellant. In order to eliminate the influence of gas on the mechanical properties, the model without gas was simulated. That is, HMX molecules are directly deleted from the system, and the resulting mechanical property changes are shown in Fig. 44.10.

Compared with the data in Fig. 44.9, after removing the gas in the system, the mechanical properties of the propellant system do not change significantly with the decomposition of HMX. After HMX decompose, the mechanical properties decrease,

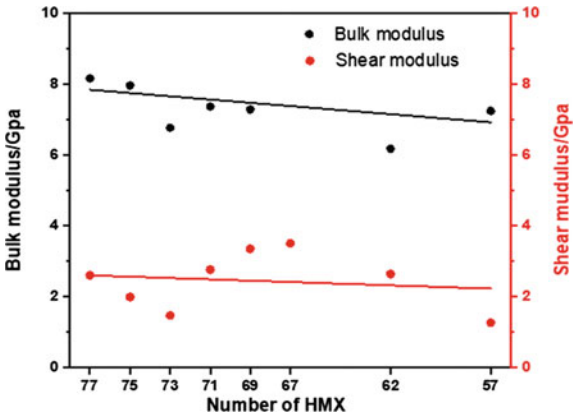

Fig. 44.10 Bulk modulus and shear modulus curves of solid propellants when HMX decompose (without gas)

but the decrease range is not as larger as that in Fig. 44.9. On the whole, the fitted curve is close to a group of straight lines parallel to the x axis. Therefore, it can be inferred that in the aging process of solid propellant, HMX will decompose into corresponding gas molecules over time due to the instability. The change of propellant composition will reduce the mechanical properties of the material, but more importantly, the residue of these gas molecules in the propellant will seriously affect the mechanical properties of the material. Its stiffness and hardness are greatly reduced. These changes are consistent with the characteristics of propellant aging.

Therefore, it can be concluded that the decomposition of HMX in the system, the formation of corresponding gas molecules and retention in the propellant system is one of the reasons for the aging reaction of HTPB solid propellant.

44.3.2.2 Binding Energy Analysis

The binding energy of the system can be obtained by molecular dynamics simulation using Forcite module. However, in the process of HMX decomposition, the total molecular number of the mixed system will also change, so $E'_{binding}$ is introduced, which is defined as:

$$E'_{binding} = E_{binding}/n$$

where n is the number of HMX in the model, and $E'_{binding}$ can be defined as the average binding energy of each HMX molecule [22]. As shown in Fig. 44.11.

It can be concluded that during the aging process of propellant, the average binding energy of the system increases with the decomposition of HMX. From the micro sight, with the decomposition of HMX, the overall energy E_{total} of the system and the total energy E_{HMX} of HMX molecules are increasing, and the increment of E_{HMX} is

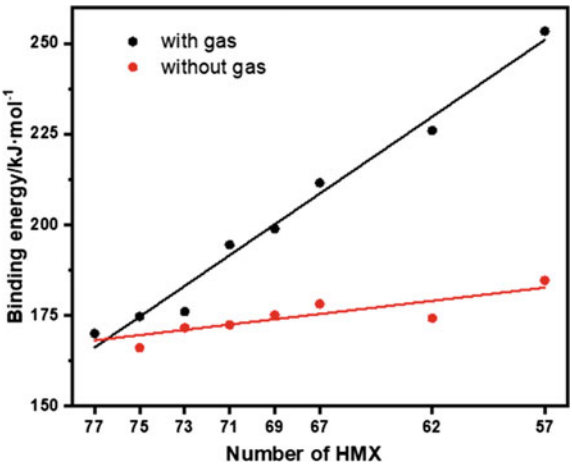

Fig. 44.11 Binding energy curves of solid propellants when HMX decompose

greater than E_{total}, resulting in the increase of overall binding energy. When the gas in the system is no longer retained in the material, the average binding energy also increases, but its increase is significantly lower than that in the presence of gas, which indicates that the gas retention in the material will reduce the overall energy of the system.

44.3.2.3 Cohesive Energy Density Analysis

In order to supplement the effect of HMX decomposition on the aging performance of solid propellant, the cohesive energy density of each mixed system with different HMX content can be simulated and calculated, and the results are shown in Fig. 44.12.

It can be concluded that in the mixed system, with the decomposition of HMX into gas, the cohesive energy density of the mixed system gradually decreases, which means that the mechanical strength and heat resistance of the mixed system are reduced, and the intermolecular interaction is weakened. When the gas in the system increases, the cohesive energy density increases. This result is consistent with the previous calculation results of mechanical properties and binding energy.

Comparing the HMX decomposition data in the propellant with the HTPB degradation chain breaking data, it can be found that the properties of the propellant change more violently under the HMX decomposition, which means that the decomposition of HMX has a more obvious impact on the aging properties of the propellant than the HTPB degradation chain breaking. However, considering that HMX decomposes very slowly at room temperature and has a very limited impact on the aging of propellant in actual storage, the fracture of HTPB molecular chain is still the main factor affecting the aging of propellant.

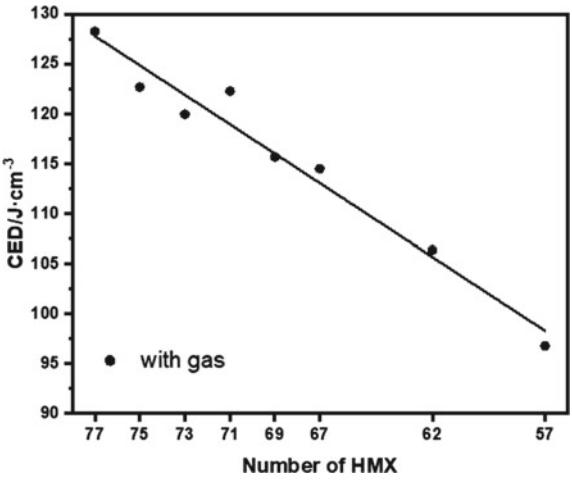

Fig. 44.12 CED curve of solid propellants when HMX decompose

44.4 Conclusion

The aging performance is one of the important properties of solid propellant. The study of aging mechanism has important guiding significance for the long-term storage and safety of propellant. According to the aging mechanism of solid propellant, the properties of HTPB propellant under different aging mechanisms are simulated by molecular dynamics simulation under the condition of high temperature accelerated aging. The main conclusions are as follows:

1. When the adhesive HTPB molecule in the mixed system breaks into a shorter chain, the mechanical properties of the mixed system also become lower. This is because when the HTPB molecular chain breaks into shorter one, the adhesion is restrained. Therefore, the mechanical properties become worse, that is, it causes the aging of the propellant.
2. When the HTPB molecules in the system undergo oxidative crosslinking reaction, the mechanical properties of the propellant decrease significantly, and the binding energy and cohesive energy density decrease at the same time.
3. When HMX in the mixed system decompose into gas, the change of propellant composition will reduce the mechanical properties of the material. More importantly, the retention of these gas molecules in the propellant will seriously affect the mechanical properties of the material, and its stiffness and hardness will be greatly reduced, resulting in the aging of the propellant.

In conclusion, considering the influence of calculation error, it can be inferred that HMX molecules decompose slowly and release gases when heated during the long-term storage of propellant, and the retention of these gases in the system will accelerate the aging of propellant. However, in short-term storage, HMX decomposes slowly at room temperature and has less decomposition amount, which has no obvious impact on the performance of the system. Therefore, the degradation and chain breaking of HTPB molecules is the main factor affecting the aging of propellant during the short-term storage.

References

1. Y. Luo, J. Liu, Research progress of high energy solid propellants. Chin. J. Energ. Mater. **15**(4), 407–410 (2007)
2. L. Fan, S. Hu, Y. Wu et al., Research progress on chemical recognition of aging of HTPB propellant. Chin. J. Explos. Propellants (Huozhayao Xuebao) **40**(04), 8–14 (2017)
3. L. Zhang, S. Heng, Z. Liu et al., Dynamic mechanical properties for aged NEPE propellant. J. Propuls. Technol. **27**(5), 477–480 (2006)
4. B. Ding, X. Zhang, Z. Liu et al., Correlation between alternating temperature accelerated aging and real world storage of HTPB propellant. Chin. J. Energ. Mater. **19**(01), 50–54 (2011)
5. X. Zhang, *Study of Aging Properties and Storage Life Prediction of HTPB Propellant* (National University of Defense Technology, 2009)
6. Z. Tang, L. Yang, X. Qiao et al., On thermal decomposition kinetics and thermal safety of HMX. Chin. J. Energ. Mater. **19**(04), 396–400 (2011)

7. Z. Liu, Y. Shao, X. Ren et al., Mathematical models and its calculations for predicting the life of explosives and propellants. Chin. J. Explos. Propellants (Huozhayao Xuebao) **39**(02), 1–7 (2016)
8. S. Du, H. Qin, J. Yan et al., Molecular simulation of aging mechanism for HTPB propellants. Chin. J. Energ. Mater. **22**(03), 291–294 (2014)
9. Z. Liu, H. Yan, H. Liu et al., (2007) Analysis on the decomposition dechanism of a kind of propellant by quantum chemistry method. Initiat. Pyrotech. **2**, 17–21 (2007)
10. E. Fermi, P. Pasta, S. Ulam, et al., *Studies of the Nonlinear Problems* (Los Alamos Scientific Lab, New Mexico, 1955)
11. B.J. Alder, T.E. Wainwright, Phasw transition for a hard sphere system. J. Chem. Phys. **27**(5), 1208–1209 (1957)
12. C. Zhang, X. Zhao, X. Fu et al., Progress in the application of molecular dynamics simulation in the study of physical and chemical properties of propellant components. Chin. J. Explos. Propellants (Huozhayao Xuebao) **41**(06), 531–542 (2018)
13. H. Sun, P. Ren, J.R. Fried, The COMPASS force field: parameterization and validation for phosphazenes. Comput. Theor. Polym. Sci. **8**(1), 229–246 (1998)
14. S.W. Bunte, H. Sun, Molecular modeling of energetic materials: the parameterization and validation of nitrate esters in the COMPASS force field. J. Phys. Chem. B **104**(11), 2477–2489 (2000)
15. H. Sun, COMPASS: an Ab initio force-field optimized for condensed-phase applications-overview with details on alkane and benzene compounds. J. Phys. Chem. B **102**(38), 7338–7364 (1998)
16. M.J. Frisch, G.W. Trucks, H.B. Schlegel, G.E. Scuseria, M.A. Robb, J.R. Cheeseman, et al., Gaussian 09 Rev. D.01, Wallingford, CT, 2013
17. D. Zhang, T. Du, Thermal decomposition of hydroxyl terminated polybutadiene (HTPB). J. Propuls. Technol. (05), 52–57+79 (1987)
18. J. Cheng, J. Li, X. Hou et al., Aging mechanical properties of HTPB propellant under thermal-mechanical coupled condition. J. Propuls. Technol. **37**(10), 1984–1990 (2016)
19. Y. Fu, S. Hu, Y. Lan et al., Molecular dynamics simulation on the glass transition temperature and mechanical properties of HTPB/plasticizer blends. Atca Chim. Sin. **68**(08), 809–813 (2010)
20. J.P. Lewis, K.R. Glaesemann, K. Vanopdorp et al., Ab initio calculations of reactive pathways for α-octahydro-1,3,5,7-tetranitro-1,3,5,7-tetrazocine (α-HMX). J. Phys. Chem. A **104**(48), 11384–11389 (2000)
21. T. Zhou, Y. Shi, F. Huang, Thermal decomposition mechanism of β-HMX under high pressures via ReaxFF reactive molecular dynamics simulations. Acta Phys. Chim. Sin. **28**(11), 2605–2615 (2012)
22. W. Zhu, X. Wang, J. Xiao et al., Molecular dynamics simulations of AP/HMX composite with a modified force field. J. Hazard. Mater. **167**(1), 810–816 (2009)

Chapter 45
Research Progress on Long Storage Performance of NEPE Propellant

La Shi, Xiaolong Fu, Saiqin Meng, and Jiangning Wang

Abstract The long storage performance of NEPE propellant is an important property concerned by propellant researchers. With the change of long storage time, the fluctuation of propellant performance is an important problem restricting the application of NEPE propellant in military equipment. In this paper, the research progress of long storage performance of NEPE propellant in recent years is reviewed, including aging mechanism, aging performance research methods and life prediction. The results show that the aging reactions of NEPE propellant are mainly divided into nitrate decomposition, binder degradation and post curing reaction. Researchers used computational simulation, spectral method, mechanical method, thermal analysis method, chromatography and other methods to evaluate the long storage performance of NEPE, and based on the above methods to predict the life of NEPE propellant. It is generally considered that the service life of NEPE propellant is about 13–16 years.

45.1 Introduction

Nitrate Ester Plasticized Polyether (NEPE) propellant is plasticized with nitrate ester to make the propellant obtain higher energy, while retaining the high elastic three-dimensional network and giving the propellant excellent mechanical properties. Combining the advantages of the traditional double base propellant, modified double base propellant and composite propellant forms a new type of propellant. NEPE propellant has become the main research subject at home and abroad [1–4].

NEPE propellants will age in the complex storage and use environments, including the degradation of polyethylene glycol (PEG) binding agent, the decomposition,

L. Shi · X. Fu (✉) · S. Meng · J. Wang
Xi'an Modern Chemistry Research Insitute, Xi'an 710065, China
e-mail: fuxiaolong204@163.com

S. Meng
e-mail: msq204@163.com

J. Wang
e-mail: wangjiangning001@sohu.com

A. Gany and X. Fu (eds.), *2021 International Conference on Development and Application of Carbon Nanomaterials in Energetic Materials*, Springer Proceedings in Physics 276,
https://doi.org/10.1007/978-981-19-1774-5_45

diffusion and migration of nitrate esters, the post-curing, and so on. The physical properties, mechanical properties, internal ballistic properties and interface bonding properties of NEPE propellants have undergone significant changes, which seriously affect the use of propellants in the weapons and equipment. For example, the heat released by the thermal decomposition of nitrate esters cannot be quickly dissipated in the propellant grains, and the heat accumulation will cause the temperature of the propellant to rise, which may cause the propellant to ignite spontaneously. The N–O on the nitrate group –ONO– breaks, which causes partial energy loss of the propellant. The thermal decomposition process of the propellant is accompanied by the release of gas. When the generation rate is greater than the outward diffusion rate, the gas accumulation will occur, which may rupture the grain. The migration of the energetic plasticizer will make the propellant to lose the structural integrity, and the interface to take off the stick. The oxidative chain scission of the binders will reduce the relative molecular weight of the binders and the viscosity of the binders, which will directly change the aging performance of NEPE propellant. Stored in a humid environment, the oxidant will absorb moisture and dissolve on the surface, making the filler and the binders interface separating, and the mechanical properties of the propellant will deteriorate rapidly [5]. Traditional experimental methods and phenomenon analysis methods have been relatively mature in the research and application of solid propellant performance. Theoretical calculations, numerical simulations, and simulation models [6–9] can accurately and truly reflect the performance changes of NEPE propellants during long-term storage. This paper classifies and summarizes the current researches on the long-term storage performance of NEPE propellants from the aspects of aging mechanism, aging evaluation methods and life prediction. Finally, the future development and challenges of NEPE propellant long-term storage performance research are analyzed.

45.2 Aging Mechanism

The complexity of the composition of NEPE propellants makes its aging research different from double base propellants and composite propellants. The maximum tensile strength, maximum elongation, stabilizer content, mixed nitrate content, weight loss rate and other parameters are all regular, which can be used as a test indicator for propellant storage. The phase separation between the binder and the plasticizer in NEPE propellant, the aging of the microstructure of the binder mainly lead to the decrease of mechanical properties [10, 11]. PEG will crystallize after low temperature treatment at −20 °C. At the same time, the degree of phase separation increases with the increase of low temperature storage time, the low temperature mechanical properties decrease and the maximum elongation increases steadily [12]. Chain extenders can change the network structure of NEPE propellants, thereby significantly improving the mechanical properties, increasing elongation and decreasing tensile strength [13]. Ammonium perchlorate (AP) will have a strong catalytic effect on the thermal decomposition of the NEPE system,

increase the rate of thermal decomposition, and shorten the time of thermal decomposition [14]. According to the aging mechanism and macro-mechanical properties of NEPE propellant microphase structure, the aging is divided into three stages: nitrate decomposition, binder degradation and post-curing [15, 16].

45.2.1 Nitrate Decomposition Mechanism

One of the reasons for the aging of NEPE propellant is the thermal decomposition of nitrate ester O–NO_2 bond breakage. NO_x is mainly produced by the decomposition of nitrate ester, which can be used as the characteristic gas of aging. The decomposition of nitrate esters will produce H_2O and NO_x free radicals, and the free radicals will counteract the decomposition of nitrate esters. The addition of stabilizers consumes NO_x and can delay the degradation of the propellant. The remaining hydrocarbon structure will also undergo thermal decomposition, producing aldehydes and other combustible components that can be oxidized by NO_2 gas.

The decomposition of nitrate esters is as follows:

$$RONO_2 \rightarrow RO. + .NO_2 \tag{45.1}$$

$$RONO_2 + RO(NO_2) \rightarrow N_2, N_xO, H_2O, H_2, CO_2, CO, C_2H_2O_4, .NO, .NO_2 \tag{45.2}$$

$$NO + O_2 \rightarrow 2NO_2 \tag{45.3}$$

$$NO_2 + NO + H_2O \rightarrow 2HNO_2 \tag{45.4}$$

$$NO_2 + H_2O \rightarrow 2HNO_3 + NO \tag{45.5}$$

During the decomposition of nitrate esters, heat is released to increase the temperature of the propellant. Gas is generated to expand the grain, and the viscosity decreases to change the mechanical properties. Highly active HNO_x is an end product, which will directly lead to the degradation of the binder chain in the interface area. In the experiment, the decomposition temperature of the nitrate ester is higher than the actual use temperature of the propellant, and the NO_x produced by the decomposition will accelerate the degradation of the polyether.

45.2.2 Binder Degradation Mechanism

H_2O is the main factor in the decomposition of the binder polyurethane, leading to the breaking of the binder polymer chain and the destruction of the basic structure of the propellant. When the decomposition reaction of the propellant cannot be inhibited by the stabilizer, the decomposition reaction will continue to decompose until the polymer chains of the binder network structure are completely destroyed and the propellant changes from a softened state to a pulp-like state. The polyurethane binder of NEPE propellant contains ether groups and urethane groups, which decompose as follows:

$$RNHCOOR' + H_2O \overset{H^+ or\ OH^-}{\longrightarrow} RNH_2 + R'OH + CO_2 \uparrow \tag{45.6}$$

$$RNHCONHR' + H_2O \overset{H^+ or\ OH^-}{\longrightarrow} RNH_2 + R'OH + CO_2 \uparrow \tag{45.7}$$

$$RCOOR' \overset{H^+ or\ OH^-}{\longrightarrow} RCOOH + R'OH \tag{45.8}$$

The ether bond of the main chain of tetrahydrofuran epoxypropane copolymer and the carbamate group formed after curing is the lowest link in bond energy. Under the action of the hydrolysate of AP and the low-temperature decomposition product $HClO_4$, the main chain ether bond –C–O–C– generates acid Chain scission is the main degradation reaction of this type of polyurethane propellant.

$$\begin{aligned}&\{HOCH_2CH_2[OCH_2C_2H_5]_n[OCH_2CH_2CH_2CH_2]_m\}OH\\&\quad + RNCO \rightarrow RNHCOOR'\end{aligned} \tag{45.9}$$

In the laser scattering molecular weight spectrum of the degradation product of polyurethane, PEG/multi-functional isocyanate (N-100) binders, the product at the initial stage of the reaction is similar to the PEG molecular mass peak. This proves that the degradation of the binders first occurs in the carbamate structure [17].

In the binder degradation stage, the polyurethane hard molecular chain in NEPE propellant is easy to degrade and break, which is irreversible chemical aging. From the point of view of polymer chain statistics, when the propellant is in a rubbery state, the polymer chain of NEPE propellant can remain unchanged in the uniaxial tensile experiment. Thermodynamically, the ideal tensile strength is:

$$\sigma_b = 3\alpha kT\varepsilon \tag{45.10}$$

σ_b is the tensile strength; α is the number of standard cross-linked network chains per unit volume of the propellant, that is, the cross-linked network concentration; k is Boltzmann's constant; T is the actual temperature; ε is the elongation.

When the degree of microphase separation of the polyurethane hard molecular chain increases, the cross-linked network system increases and the tensile strength increases. At this time, the tensile strength can reflect the concentration of the hard molecular chain. Then, the soft polyurethane molecular chain begins to degrade, the microphase separation is intensified, and the hard molecular chain concentration and tensile strength continue to increase. As the stabilizer content decreases, the nitrate is quickly decomposed. The hard molecular chain is easy to be oxidized and decomposed, its concentration decreases, and the tensile strength appears a second peak. When the stabilizer content is reduced to the point that NO_x cannot be completely consumed and absorbed, the NO_x concentration increases, the thermal degradation and oxidative degradation of the molecular chain intensify, and the macroscopic tensile strength drops rapidly. Under the action of constant strain, the polymer chain unfolds from the collapsed state, the chain is oriented and rearranged, and the molecular chain tends to be oriented in the direction of the force, which increases the elongation of the propellant to a certain extent. In the later stage of aging, the influence of binder aging and interface dehumidification between binder and other fillers is gradually significant. With the occurrence of dehumidification, the physical or chemical adsorption force between the dispersed phase and the continuous phase decreases. And the stress transfer of the entire system Is weakened, so the maximum elongation of the propellant is reduced.

45.2.3 Post Curing Mechanism

Post-curing reaction refers to a curing reaction that has not been completed in the normal curing cycle, but continues to proceed slowly during storage. The decomposition products of nitrate esters, hydroxyl-terminated prepolymers and isocyanates form cross-linked hard molecular chains. And the post-curing reaction is:

$$RNCO + R'OH \rightarrow RNHCOOR' \tag{45.11}$$

As the concentration of hard molecular chains increases, the tensile strength also increases. At the same time, carbamate and carboxyl groups restrict the rotation of the main chain, leading to a decrease in the macroscopic elongation. At the end of the isocyanate reaction in NEPE, the ultimate tensile strength reaches its maximum. Nitrate esters are difficult to decompose at ambient temperature. The post-curing of NEPE propellant only occurs at higher temperatures, and the post-curing time can be ignored in life prediction.

In the polyether polyurethane binders, there are active hydrogen in the carbamate. Under catalyzed conditions, it can further react with isocyanate to form allophanate. When 1,3,5-tri (2-ethylazolidine-1) benzenoic acid adducts cure carboxy-terminated polybutadiene, they will rearrange during storage to produce oxazoline, which continue reacting with the carboxyl group. When the epoxy compound is the curing agent, the curing agent will undergo a homopolymerization reaction.

The cross-linking reaction between isocyanate and multi-functional active hydrogen components increases the cross-link density of the propellant, increases the tensile strength and elastic modulus, and decreases the elongation.

In the observation of phenomena and experimental methods, it is impossible to intuitively quantify the periodic cycles of NEPE propellant aging performance in long-term storage, nor to understand the mechanism behind complex reactions. It is necessary to introduce more advanced instruments, theoretical calculations and computer simulations.

45.3 Aging Assessment Method

The aging of NEPE propellant is caused by a variety of reasons, and it also needs to be characterized by a variety of detection methods. The selected experimental conditions (such as sample preparation, moisture content, loading density, tightness, test temperature, contact area, etc.) will not be fully standardized and will vary from test to test, so the criteria for determining failure are also diverse. It is necessary to decide which test condition can best simulate natural aging according to the situation [18–20].

45.3.1 Calculation Simulation Method

Hou [21] established a meso-particle filling model of NEPE propellant with Abaqus finite element software. He found that AP particles, Al particles and matrix interface dewetting and matrix cracking together led to propellant cracking. Shee [22] used quantum chemistry to derive the molecular electrostatic potential (MESP) that shows the possible positions of the plasticizer and binders interaction. The estimated V_{min} value and their size provide clues for understanding their interaction. There are good correlations between the relative tendency of the interaction energy between the plasticizer and the binders, and the tendency of the corresponding plasticizer to reduce the viscosity of the binders (Fig. 45.1).

Zhang [23] used molecular dynamics (MD) simulation methods to study the adsorption behavior of neutral polymer bonding agent (NPBA) in NEPE propellant, and observed that there was a strong van der Waals force between NPBA and RDX (hexogen), and the High binding energy. The compatibility of NPBA and nitrate plasticizers decreases with the decrease of temperature. At the same time, NPBA can penetrate nitrate plasticizers and adsorb on the surface of RDX to form a dense protective layer, which can prevent nitrate plasticizers damaging the bonding interface. Han [24] used MD method to simulate the bonding unit with cohesive constitutive of particle-matrix bonding. Based on the Kooke-Jeeves inversion optimization algorithm, the NEPE matrix-particle interface bonding energy was obtained as 63.375 J/m^2 through inversion. Comparing the calculated results of the model with

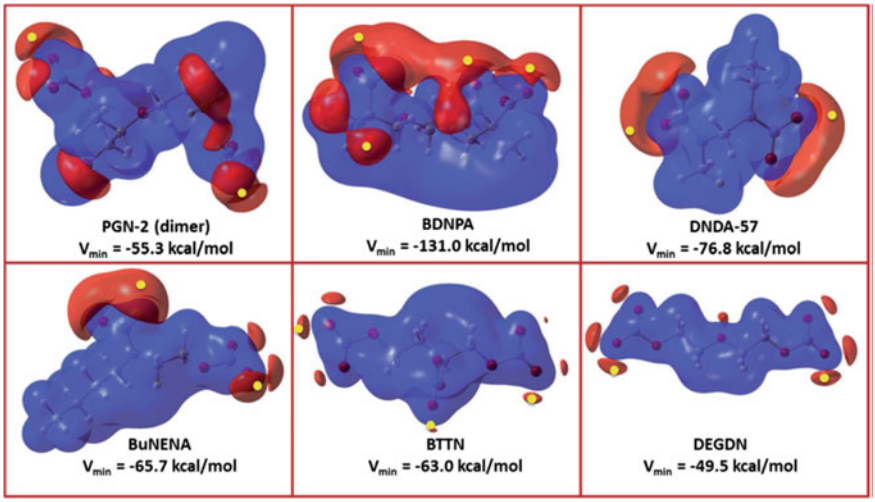

Fig. 45.1 MESP and total V_{min} values of the corresponding samples at B3LYP/6-311$_g$ (D, P) theoretical level of PNG dimer and energetic plasticizer. The yellow dots indicate the position of the V_{min} dots in each sample (red is the electron-rich region, blue is the positive region)

the actual experimental results as shown in Fig. 45.2. It can be found that the simulation curve is more consistent with the experimental results, indicating that the model can be adapted when considering the impact of the NEPE propellant's meso-structure changes on the mechanical properties under external load conditions.

Wang [25] established a MD model for the cooling phase separation of NPBA in an inert solvent, and applied it to the phase separation of a nitrate ester plasticizing solution system improve the composition of the terpolymer during the cooling phase separation process. Zhang [26] used computational programming methods to establish a polyurethane acrylate (PUA) molecular-scale UV curing crosslinking model,

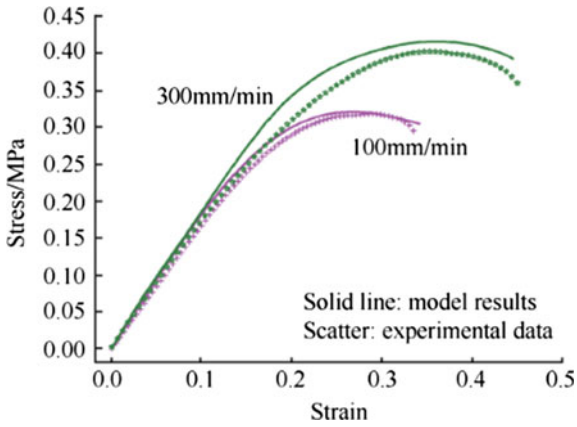

Fig. 45.2 The simulation results are compared with the actual results

and used MD to calculate its mechanical properties, thermal transfer behavior, solubility parameters, radial distribution function, and diffusion coefficient. It is proved that PUA liner has a higher crosslink density, which can effectively prevent the migration of plasticizer.

Li [27] used the dissipative particle dynamics mesoscale simulation method and the new two-sphere shell method to quantitatively characterize the phase separation. She proposed that the phase separation behavior of mesoscale interaction would occur in a macromolecular binder and small molecular plasticizer. The phase separation process of polymer binder and small molecule plasticizer in NEPE propellant is simulated. The method was shown in Fig. 45.3. Two virtual spherical shells or torus: inner ring a and outer ring b. The size and position of the two spherical shells can be changed as required. The simulation is mainly used to track the number changes of blue ion during the phase separation process. Because the chains are entangled with each other, when the phases are separated, the chains will gather in the center of the system, and free particles will accumulate near the wall of the box. At this time, the number of blue particles in the inner spherical shell decreases, while the blue particles in the outer spherical shell b will increase.

Obviously, temperature affects the movement of particles, and the interaction between the binder and the plasticizer is an important factor in the phase separation behavior. As the temperature decreases, the phase separation occurs later and later, but the degree of phase separation gradually increases. Within a certain range, the longer the polymer chain in the simulation system, the earlier the phase separation between polymer and small molecules. But the increase in polymer chain length reduces the degree of phase separation.

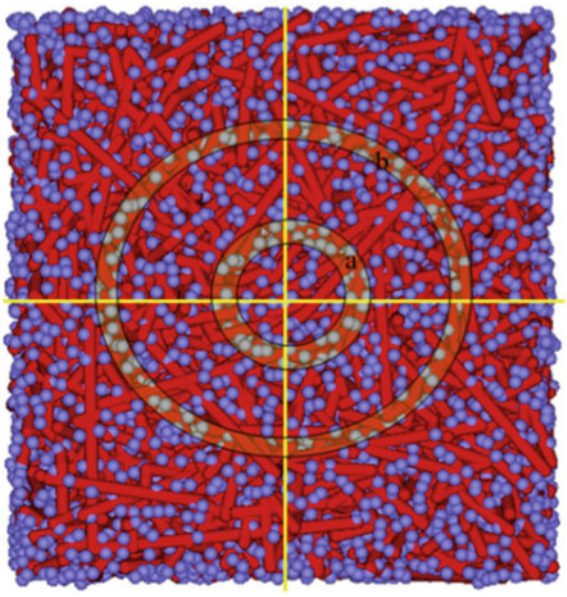

Fig. 45.3 Planar diagram of two spherical shells used in particle calculations

Sui [28] is based on the assumption that the thickness of the shell is constant, the insulating lining is elastic, the branches of the shell can be ignored, the air in the pores of the particles is only used for heat conduction, and the convection can be ignored. A finite element model with symmetrical boundary conditions is established. And the stress response of the drug pellets aged for 20 days at 65 °C, the critical zone is the end of the drug pellets and the inner pore surface. From the point of view of the maximum Von Mises stress, the internal control surface stress is lower than the stress at the end of the grain, so the critical area is the end of the grain. Due to the deformation of the grain, the stress value of the inner hole surface and the end of the grain is relatively high. Due to the different thermal expansion characteristics of the material, the maximum equivalent stress appears on the surface between the grain and the insulating material. The comparison between the stress limit of the propellant and the maximum equivalent stress in the grain shows that both have a downward trend with the increase of time. After a certain period of time, the latter's decline speed increases, resulting in the maximum peak value higher than the grain fracture frequency band. When the relaxation modulus of the propelling column grain drops to 0.7 MPa, the structural integrity will fail.

45.3.2 Spectroscopy

Pang analyzed the microstructure of NEPE propellant through Micro-CT, and studied the chemical composition and distribution of the interface by SEM-EDS, Micro-FTIR, and XPS. He noticed that the curing reaction of the interfacial propellant competes with the cross-reaction of the propellant and the liner. In relation to this, PEG and N-100 are cured to produce C–O–bonded and nitrogen oxide active molecules of carbamate that affect the aging reaction. Liu [29] used 1H quantitative nuclear magnetic resonance method to simultaneously determine the mass ratio and moisture content of the mixture of 1,2,4-butanetriol trinitrate (BTTN) and NG, and verified its accuracy by HPLC. Wu [30] used XPS to analyze the chemical composition and distribution of the NEPE propellant lining interface. He obtained the changes of the main components at various positions before and after aging, and the changes in the binding energy of elements during the interface aging process. He found that the reduction of hydroxyl, nitrogen atom active groups and nitro groups are the main failure reason. Yan [31] performed Fourier infrared spectroscopy qualitative characterization on the accelerated aging NEPE propellant after the tensile strength inflection point appeared, as shown in Fig. 45.4. He obtained the fitting equation between the wavenumber of O–NO_2 the absorption peak 769 cm^{-1}, asymmetric stretching vibration 1639 cm^{-1} and the tensile strength.

$$R_m = 925.207x + 0.3446 \tag{45.12}$$

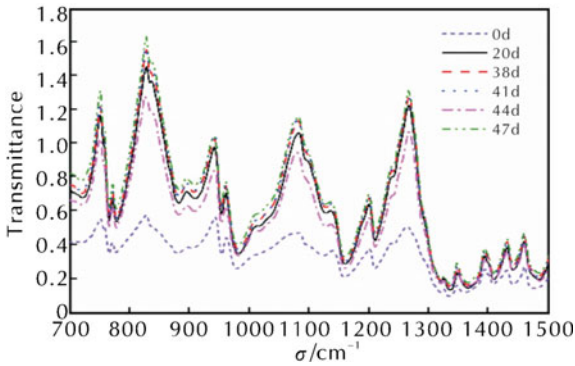

Fig. 45.4 Ir spectra of accelerated aging NEPE propellant at 75°C

where R_m is the tensile strength of the propellant, and x is the sum of the second derivative values of the propellant's infrared spectrum at 769 and 1639 cm^{-1}.

Gui [32] used in-situ diffuse reflectance FT-IR spectroscopy to study the content distribution and curing of chemical groups process dynamics at the interface of NEPE based hydroxy-terminated polybutadiene (HTPB) propellant lining microdomains. During the curing process, the content of –NCO groups hardly increased in the lining area facing the interface, it rose rapidly through the interface layer, and then stabilized in the propellant layer area. But the content of –NH groups went from the lining to the propellant layer gradually increase. In the microscopic area between the liner and the propellant, –C=O decreases rapidly through the interface, and then the propellant area increases slightly. In the early stage of curing, the migration of nitrate ester occurred at the interface between NEPE propellant and liner. In the micro area of the bonding interface, $–O–NO_2$ decreased from the propellant layer to the liner. As shown in Fig. 45.5, the curing kinetics study shows that the secondary reaction model can describe the curing reaction of the bonding interface in the early stage of the curing process. At the same curing temperature, the interface micrometer area lining (point L), the middle point (point l) and the apparent curing reaction rate constant (k) of

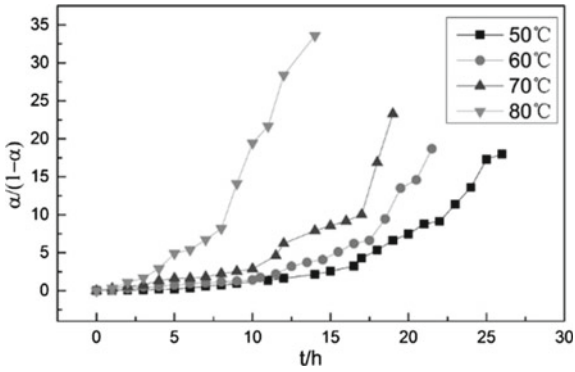

Fig. 45.5 $\alpha/(1-\alpha)$ as a function of curing time

the propellant layer (point P) is $k_L > k_l > k_P$. According to the Arrhenius equation, the apparent activation energies are 39.96, 81.49 and 62.51 kJ·mol^{-1}, respectively.

$\frac{\alpha}{1-\alpha} = kC_0t$, Where α is the degree of curing, t is a certain moment, and k is the rate reaction constant.

Amir [33] used laser-induced breakdown spectroscopy to analyze the thermal aging of composite propellants, and introduced principal component analysis to distinguish different sample spectra. He proved that as the aging time and temperature increase, the chemical structure changes. Zhao [34] observed that the gas phase products of thermal decomposition of NEPE propellant include CO_2, CO, N_2O, HNCO, NO, CH_2O, NO_2, HONO, HCN, ethers, evaporated NG and HMX through infrared spectroscopy. Farley [35, 36] used 532 and 785 nm wavelength Raman spectroscopy to analyze the N-methylp-nitroaniline (MNA) in NEPE propellant aging samples. The computer reduced the fluorescence several times, improved the signal-to-noise ratio of the chemical peak specific to the stabilizer compound and calibrated the data. At last, detect MNA content as low as 0.2% in a few seconds.

45.3.3 Mechanics

Chi [37] analysed the statistical distribution characteristics of the mechanical properties of NEPE propellant during the aging process and the change law of the statistical parameters during the accelerated aging process. He found that the uniaxial tensile test values under the same aging state showed a normal distribution. In the different stage, the mechanical performance parameters have nothing to do with the aging time and temperature, and are normally distributed. Han [38] used the equivalent relationship between time, temperature and damage to predict the long-term relaxation behavior of NEPE propellant based on the uniaxial tensile experiment and cumulative damage model calculation of NEPE propellant. Zhang conducted high-temperature accelerated aging experiments on NEPE propellant, studied the relationship between the mechanical properties of the propellant and chemical stability, and summarized this relationship as a "two-stage". When the nitrate ester decomposition product NO_x consumes the stabilizer, the mechanical properties of the propellant do not change significantly. When the nitrate ester decomposition product reacts to the decomposition of the nitrate ester, the gel content and crosslink density of the polyether system suddenly drop, resulting in The mechanical properties also decline rapidly. Shen [39] used a universal material testing machine to test the mechanical properties of NEPE propellant at different strain rates and temperatures. She concluded that the tensile stress has a linear relationship with the logarithmic strain rate, and the temperature is inversely related to the change of the constant elongation stress and modulus. Wang [40] noticed in the stress relaxation test of NEPE propellant that the test temperature change is inversely related to the change of relaxation modulus. The initial strain increases and the relaxation modulus also increases, and the effect of the loading rate is negligible. Yan used the second-order Gaussian and logarithmic fitting method to establish the correlation model on the basis of uniaxial tensile experiment

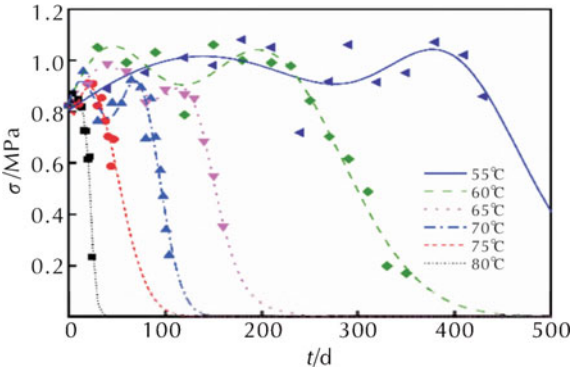

Fig. 45.6 Gaussian fitting curves of tensile strength and aging time at different temperatures

on the aged NEPE propellant. It contained the tensile model during the aging process with the appearance time of the strength inflection point and aging temperature. He was aware that the tensile strength of NEPE propellant fluctuates firstly and then decreases rapidly during the aging process, as shown in Fig. 45.6.

The functional relationship between the inflection point appearance time and the aging temperature is:

$$\lg^2(t) = -0.217T + 18.397 \tag{45.13}$$

Liang [41] analyzed NEPE's mechanical properties, weight loss, adhesion network structure fracture and storage stability to study the laws of accelerated aging. It is obvious that the maximum tensile strength σm shows a good change rule with the increase of storage time. strength is mainly failure in NEPE propellant [42]. With the extension of storage time, the weight loss rate gradually increases, and there is also a strong regularity. The nitrate plasticizer of NEPE propellant undergoes thermal decomposition, and the product will cause the decomposition of the bonded network structure and chain scission, leading to basic structural damage. The thermal decomposition of the propellant is dependent on the heating rate. Sui [28] accelerated the aging of NEPE propellant samples at 65 °C, 70 °C and 75 °C respectively, measured the dynamic mechanical properties of NEPE propellant by dynamic mechanical analysis method, and the strength of the sample by uniaxial tensile test. It is evident that both the relaxation modulus and the strength limit are reduced, and the influence of the change of the relaxation modulus on the completion of the structure is further analyzed.

Gao [43] determined the dynamic mechanical parameters of NEPE propellant samples by a dynamic thermomechanical analyzer, used the principle of frequency-temperature equivalence to translate the frequency spectrum obtained by scanning the frequency at different temperatures, and obtained the rule of the displacement factor changing with the test temperature. In the dynamic mechanical temperature spectrum, the loss modulus of NEPE propellant has only one glass transition peak in the low temperature section. And the polymer chain segment changes from thawing to

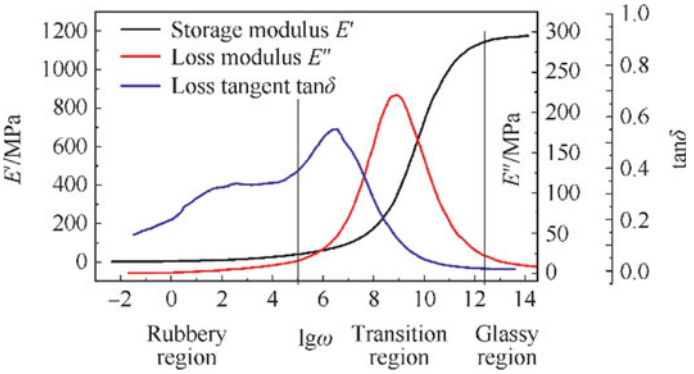

Fig. 45.7 DMA diagram of NEPE at 20 °C

free movement, with overcoming a large friction force, which leads to a large energy loss. When it reaches the maximum value at the glass transition temperature, the glass transition temperature moves to the high temperature direction with the increase of the test frequency. After translation, the dynamic storage modulus, loss modulus and the master curve of loss factor of NEPE propellant are shown in Fig. 45.7 at a reference temperature of 20 °C. It can be known that NEPE propellant has glassy state, glass transition zone and rubbery state from low frequency to high frequency. At lower frequencies, the relaxation characteristics are fully displayed and appear as rubbery. At high frequencies, the relaxation characteristics are not easy to observe, showing In the glass state. When the relaxation time is consistent with the observed world, the loss modulus reaches its peak. In the temperature spectrum and frequency spectrum, the storage modulus, loss modulus and loss factor of high frequency and low temperature section, low frequency and high temperature section are basically equal. When the temperature decreases and the frequency increases, the NEPE propellant exhibits the same mechanics performance.

Xu [44] modified the integral constitutive on the basis the NEPE propellant relaxation test and uniaxial constant velocity tensile test. And he established the accurate prediction of model of the peak stress point in the stress-strain with damage of the non-linear viscosity and elastic constitutive under the Weibull distribution function. Li [45] studied and analyze the mechanical properties and damage process of NEPE propellants under different limiting pressure conditions by a newly designed pressure limiting test machine. And he noticed that the mechanical properties of the propellant materials increase with the increase of different limiting pressures. The maximum tension and the strain rate under various restricted conditions are in a linear logarithmic relationship. The restricted pressure has no obvious effect on the initial elastic modulus. When the mechanical properties of NEPE propellant are changed, the limiting pressure will delay the occurrence and development of damage under tensile load. Based on viscoelastic theory and continuous damage theory, a nonlinear constitutive model of NEPE propellant mechanical response considering the effects of strain rate and confining pressure was established [46].

Nonlinear viscoelastic constitutive model:

$$\sigma = (1 - D(P, \dot{\varepsilon})) \int_0^t E(t - \tau) \frac{\partial \varepsilon}{\partial \tau} dt \tag{45.14}$$

Among them, $D(P, \dot{\varepsilon})$ is the damage variable, σ is the experimental pressure, ε is the tensile stress, $E(t)$ is the relaxation modulus, τ is the integral variable, and t is the time.

By comparing the experimental data fitting curve and the prediction model fitting curve, as shown in Fig. 45.8, the relevant parameter expression is obtained as:

$$k = \left[0.0585 \exp\left(-\frac{P}{0420} + 0.00392\right)\right] \log \dot{\varepsilon} + \frac{0.547}{0.585 + P} + 0.524 \tag{45.15}$$

$$\varepsilon_c = -\frac{0.172}{0.736 + P} + 0.432 \tag{45.16}$$

$$m = \left(-\frac{0.044}{0.475 + P} - 0.033\right) \log \dot{\varepsilon} + 0.465 \exp\left(-\frac{P}{0.593}\right) + 1.062 \tag{45.17}$$

The confining pressure and strain rate have a significant effect on the mechanical response of NEPE propellants. With the increase of confining pressure (from 0 to 5.4 MPa), the maximum tensile stress and ultimate stress gradually become larger. Under the coupling action, the maximum tensile stress and ultimate stress are 2.03 times and 2.19 times that of 0 MPa and 0.00333 s^{-1}, respectively. The initial modulus of elasticity increases slightly with the increase of confining pressure. Therefore, when analyzing the integrity of rocket solid propellant particles, it is necessary to consider the influence of ignition pressurization on the mechanical properties of the grain structure. Under the action of confining pressure, compared with the room

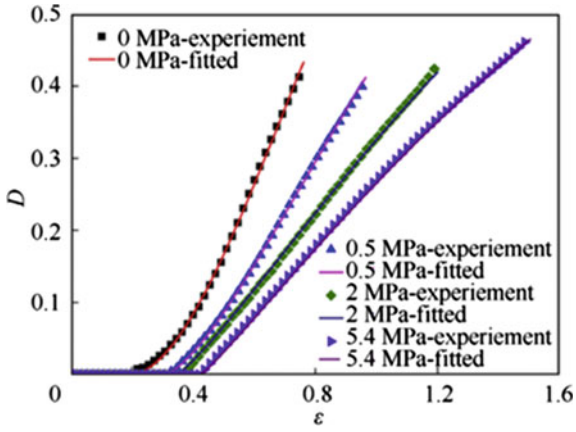

Fig. 45.8 Experimental damage evolution curves and fitting curves were obtained under different confining pressures

pressure, the dehumidification speed is reduced and the dehumidification process is prolonged. The critical strain ε increases with the increase of confining pressure. And the mechanism of the effect of confining pressure on the propellant is to inhibit the internal damage of the propellant Initiation and evolution.

Han conducted stress relaxation tests and uniaxial tensile tests on NEPE propellants at different temperatures and different strain levels. He combined viscoelastic dehumidification criteria, and quantified the microstructure changes and introduced them into the macro viscoelastic constitutive relationship. Then a nonlinear viscoelastic constitutive model of the effect of micro-particle dehumidification on NEPE propellant was established.

$$\sigma_{ij}(t) = \int_0^t 3K(\xi(t) - \zeta)\frac{d\varepsilon_{kk}}{d\zeta}d\zeta \tag{45.18}$$

$$S_{ij}(t) = \int_0^t 2G(\xi(t) - \zeta)\frac{de_{ij}(\zeta)}{d\zeta}d\zeta \tag{45.19}$$

where $\sigma_{ij}(t)$ and $S_{ij}(t)$ are the function of strain tensor decomposition into volume deformation and isobaric distortion with respect to time, e_{ij} is the viscous deviated strain corresponding to the k-th Prony series, and G and K are glassy shear and Bulk modulus.

45.3.4 Thermal Analysis

Zhao [47] studied polyethylene glycol, nitroglycerin, BTTN, stabilizer C_2 and the thermal decomposition mechanism of curing agent in NEPE propellant with a rapid thermal cracking in-situ reaction cell/RSFI-IR. The interaction of components would delay the volatilization and decomposition temperature of nitrate esters, and the decomposition temperature of polyether and stabilizer would advance. The thermal decomposition of NEPE propellant can be divided into three stages. Partial volatilization and initial decomposition, the consumption of stabilizer, the interaction between decomposition products and components, promote the decomposition to accelerate to explosion, and the free radicals generated by the participating substances and decomposition are further decomposed. Researching the thermal decomposition process of NEPE propellant, it is recognized that the decomposition process basically decomposes according to the characteristics of each component. The mutual influence of each component makes the heat transfer and the diffusion of decomposition products hindered. The stabilizer absorbs the NO_x produced by the initial decomposition, and slows down the self-decomposition of the components. Catalysis eventually increases the decomposition temperature. NG, Oktogen (HMX) and RDX are partially gasified

in the thermal decomposition process, and decomposition reaction occurs after most of the ammonium nitrate liquid is liquefied. The content of NO_2, N_2O and HCN gas is relatively large, indicating that the reduction process of N atom plays a major role in the combustion of NEPE propellant.

Pang [48] studied the thermal decomposition behavior and non-isothermal decomposition kinetics of nitrate plasticized polyether NEPE propellant containing ammonium dinitramide (ADN) at 0.1 MPa with DSC, TG, and DTG. At the heating rate of 0.1 MPa and 2.5 K min^{-1}, there are 4 exothermic peaks on the DTG curve, 4 mass loss stages on the TG curve. Nitrate ester evaporates and decomposes in the first stage. ADN decomposes in the second stage. Nitrocellulose and RDX are decomposed in the third stage. And AP is decomposed in the fourth stage. In order to study the thermal decomposition mechanism of the main exothermic reaction stage (main exothermic peak) of the propellant under working pressure and obtain the relevant kinetic parameters (apparent activation energy, refers to the former constant) and the most likely kinetic model function. Mathematical methods were used to process TG-DTG curves under different heating rates, and Ordinary-integral, Mac Callum-Tanner, Šatava-Šesták, Agrawal, Kissinger, Flyn-Wall-Ozawa and other kinetic analysis methods and correction equations were used to modified. Finally, the differential form kinetic model function, apparent activation energy, and exponential constant of the NEPE propellant and the main decomposition reaction of AND were as followings:

$$G(\alpha) = [-\ln(1-\alpha)]^{\frac{2}{3}} \tag{45.20}$$

$$f(\alpha) = \frac{3}{2}(1-\alpha)[-\ln(1-\alpha)]^{\frac{2}{3}} \tag{45.21}$$

$E_a = 143.27\,\text{kJ mol}^{-1}$, $A = 1012.77\,\text{s}^{-1}$.

The main exothermic decomposition reaction kinetic equation is:

$$\frac{d\alpha}{dt} = 10^{12.77}\left(\frac{3}{2}\right)(1-\alpha)[-\ln(1-\alpha)]^{\frac{1}{3}}\exp\left(-1.723\times 10^4/T\right) \tag{45.22}$$

(where α is the conversion degree of the reaction sample, $G(\alpha)$ is the integral model function, $f(\alpha)$ is the differential function model, and T is the temperature at time t) The reaction mechanism of this process can be classified as a chemical reaction.

Sun [49] studied the thermal behavior of NEPE propellant before and after 5 years of natural storage by TG-DSC-MS-FTIR, as shown in Figs. 45.9 and 45.10. The sample has undergone five reaction steps. The breaking of the O–NO_2 bond, the crystal transformation of HMX and the thermal decomposition of plasticizer, HMX and AP, the decomposition process and temperature range of each step remain the same, but the nitrate ester decomposes and evaporates excessively during the later storage period. The figure shows the TG-DSC chart before and after NEPE storage. It can be seen that the aging is divided into five steps. The first step is the evaporation of nitrate. The second step is the $\beta \rightarrow \delta$ crystal form transformation of HMX. The

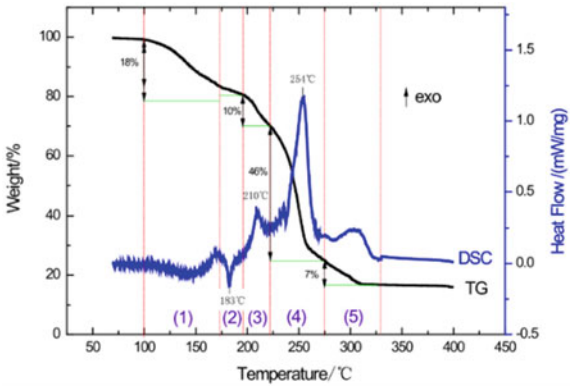

Fig. 45.9 TG-DSC curve of NEPE before storage

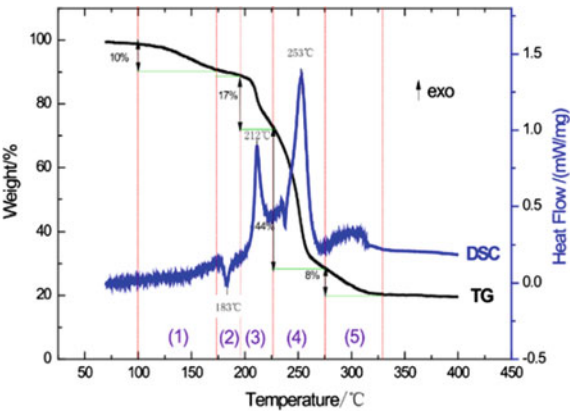

Fig. 45.10 TG-DSC curve of NEPE after storage

third step is the decomposition of nitrate, due to the increase in particle size after sweating and recrystallization of nitrate, which makes it easier to decompose at high temperature. The fourth step is the main decomposition process, which is related to the content of HMX. The necessary endothermic peak and a major exothermic peak. The last step is the decomposition of AP, and the corresponding exothermic peak appears.

The Kissinger, Flynn-Wall-Ozawa, Ordinary integral, Šatava-Šesták, Agrawa methods and correction formulas are used with DSC-TG curves of different heating rates. For nitrate and HMX decomposition processes, n = 2 and n = 3 of the Avramic-Erofeev equation ($G(\alpha) = [-\ln(1-\alpha)]^2$, $G(\alpha) = [-\ln(1-\alpha)]^3$) are used respectively. It is consistent with the calculations of Kissinger and Ozawa better. The kinetic reaction equation before and after storage of nitrate ester is obtained:

$$\frac{d\alpha}{dt} = 10^{14.7}\left(\frac{1}{2}\right)(1-\alpha)[-\ln(1-\alpha)]^{-1}\exp\left(-1.931 \times 10^4/T\right) \qquad (45.23)$$

$$\frac{d\alpha}{dt} = 10^{20.1}\left(\frac{1}{2}\right)(1-\alpha)[-\ln(1-\alpha)]^{-1}\exp\left(-2.514\times 10^4/T\right) \tag{45.24}$$

Kinetic reaction equation before and after HMX storage:

$$\frac{d\alpha}{dt} = 10^{14.5}\left(\frac{1}{3}\right)(1-\alpha)[-\ln(1-\alpha)]^{-2}\exp\left(-2.222\times 10^4/T\right) \tag{45.25}$$

$$\frac{d\alpha}{dt} = 10^{17.0}\left(\frac{1}{3}\right)(1-\alpha)[-\ln(1-\alpha)]^{-2}\exp\left(-2.369\times 10^4/T\right) \tag{45.26}$$

NEPE propellant will produce gas, crystallization and deliquescent during storage, resulting in pores and coarse crystals. Storage cannot change the temperature zone of each process, but it can change certain thermal characteristics. Due to the increase of nitrate particles, its activation energy increases and tends to react in the decomposition stage. The 5 s explosion temperature test results in a lower explosion temperature, indicating a decrease in thermal safety. The calculation of the critical temperature of thermal explosion indicates that the decomposition enthalpy of nitrate is increased, and may lead to heat accumulation. Therefore, the evolution of nitrate esters during storage is the main reason for the aging of NEPE propellants.

Milekhin [50] studied the plasticizer (nitro ether mixture, NG, the evaporation of diethylene glycol dinitrate and triethylene glycol dinitrate) by dynamic thermogravimetry and differential scanning calorimetry. Kissinger, Ozava-Flinn-Wall and Akahira-Sunose methods were used to obtain a series of $V_T(T)$ and $\alpha(T)$ curve to determine kinetic parameters.

The regression equation of the evaporation rate recorded in the experiment is as follows:

$$V_T = \frac{100\left(m_0 - m_f\right)}{m_0^b} \times Z\exp\left(-\frac{E}{RT}\right) \times \left[1 + Zb^{-1}(n-1)\phi(x)\frac{n}{1-n}\right] \tag{45.27}$$

Among them, Z, E, and n are the pre-factors, the activation energy and the reaction order can be obtained by fitting the TGA data curve with Origin, m_0 and m are the initial weight of the sample and the weight at a certain moment, respectively, and m_f is after removing the plasticizer The weight of the residue, $x = -\frac{E}{RT}$, T is the reaction temperature, and b is the heating rate (Table 45.1).

$$\Delta H_v = E - 0.75RT \tag{45.28}$$

$$\Delta H_v = E + 0.5RT \tag{45.29}$$

Table 45.1 Activation energy and heat of evaporation of plasticizer

Calculation methods of the value E	E (kJ mol^{-1})	ΔHv (kJ mol^{-1})	
		$\Delta H_v = E - 0.75RT$	$\Delta H_v = E + 0.5RT$
Ozava-Flinn-Wall	90.20 ± 2.79	88.3 ± 2.8	91.4 ± 2.8
Akahira-Sunose	88.81 ± 2.94	87.0 ± 3.0	901 ± 3.0
Regression	90.80 ± 2.79	88.9 ± 2.8	92.0 ± 2.8
Kissinger	86.36 ± 4.50	84.5 ± 4.5	87.6 ± 4.5
Meaning	89.40 ± 2.8	87.5 ± 2.8	90.6 ± 2.8

The results show that the values of E and ΔH_v are actually the same in the early stage of evaporation. At 298.15 K, $\Delta H_v = 89 \pm 4$ kJ mol^{-1}, which is in good agreement with the literature data on the heat of evaporation of pure nitroglycerin.

45.3.5 Chromatography

Huang [51] analyzed the main migration components of the NEPE propellant insulation layer and lining bonding interface by high performance liquid chromatography (HPLC) and gas chromatography (GC). He found that nitroglycerin (NG) can migrate to the lining and insulation layer. Diisooctyl diacid (DOS) only migrates to the insulating layer and not to the propellant.

Huang [52] determined the migration components of NEPE propellant by HPLC as a basis, and then calculated the apparent activation energy of the migration components with Arrhenius to explain the migration behavior. Wu [53] chose acetonitrile and water as mobile phases, and a UV detector with a wavelength of 200 nm to establish a method for simultaneous determination of the stabilizers MNA and 2-nitrodiphenylamine in NEPE propellant (2-NDPA) content of HPLC. In order to explore the aging mechanism, Wu [54] obtained propellant samples with different aging time periods through 70°C aging storage experiment every 7 days, measured the relative content of MNA, NG and BTTN as characteristic parameters of chemical stability, and studied the stability and correlation with binder network structure. Gel fraction and cross-linking density are detected as characteristic parameters of the binder network structure characteristics. The results show that the MNA content decreases slowly from 0 to 35 days, with a quadratic function relationship with time, and rapidly decreases from 36 to 77 days. The content of NG and BTTN decreases in a cubic function relationship with time. When aging to 56 days, NO_x intensifies the autocatalytic decomposition of nitrate esters, and the chemical stability of the propellant deteriorates. As time goes by, the gel fraction and crosslink density first increase then decrease. After 67 days and 63 days, the decrease rate of gel fraction crosslink density increased respectively. Structural performance aging lags behind chemical stability aging. Network structure parameters decrease logarithmically with MNA content. Nitrate content and gel fraction has a quadratic function relationship and a

cubic function relationship with the crosslink density. In the heat aging process, there are two competing reactions at the same time, one is the post-curing reaction, and the other is the decomposition reaction of the polymer system. In the early stage of aging, the post-curing reaction rate is much greater than the decomposition rate, so the polymer structural parameters get larger. Then the post-curing reaction gradually weakens until it is completely cured. But the network structure is not destroyed by the NO_x free radicals generated by the decomposition of nitrate at that time, because NO_x is mainly absorbed by MNA. In the later stage of the reaction, the decomposition rate of NO_x catalyzed is accelerated by nitrate. The degradation rate of nitrate ester is accelerated, and the increase of NO_x also accelerates the breakage, decomposition and decomposition of the polyether polyurethane molecular chain.

By measuring the characteristic gases (NO_2, NO, CO, and HCl) in the high-temperature accelerated aging experiment, the initial aging stage of NEPE propellant is mainly the volatilization and decomposition of plasticizers, the absorption of NO_x by stabilizers. The additional strain and the decomposition of various components are the main reasons for the changes in gas product content [55]. Mcdonald [36] measured the stabilizer and of dimethyl sulfoxide nitroso/nitro derivatives of NEPE propellant with polyethylene adipate (PGA) and PGA as binders by HPLC and GC. And the resistance of these substances as a function of mass fraction was evaluated. Pang [56] measured the NG, BTTN, cure catalyst triphenylbismuth, and amine stabilizer of NEPE propellant in acetone soaking solution with HPLC, and compared with the standard curve. It can easily and quickly detect the migration of NEPE propellant bonding system components. Yin [57] studied the effect of nitrate migration in NEPE propellant on the bonding performance through high temperature accelerated aging experiments. And she found that the greater the polarity of the lining binders, the more nitrate migration to the lining structure. Gao [58] proposed a new parameter "surface area diffusivity", based on the migration of different solvents to simple polymers. The migration of propellant and liner components at the interface of the insulating layer was measured. The specific surface area diffusivity had nothing to do with the shape of the material.

45.4 Life Prediction

The long storage life of NEPE propellant directly determines whether the propellant can be used safely. Therefore, it is very important to find a suitable method to accurately predict the life of NEPE propellant.

Xiong [59] found the characterization of the aging characteristics of the propellant through the high-temperature accelerated aging test and mechanical property experiment of NEPE propellant, as shown in Fig. 45.11. According to the bimodal characteristics of NEPE, the relationship is established between aging degree and temperature, which combined with kinetics and statistical viewpoints. And the life prediction equation based is established to predict the life of NEPE propellant on Berthlot equation.

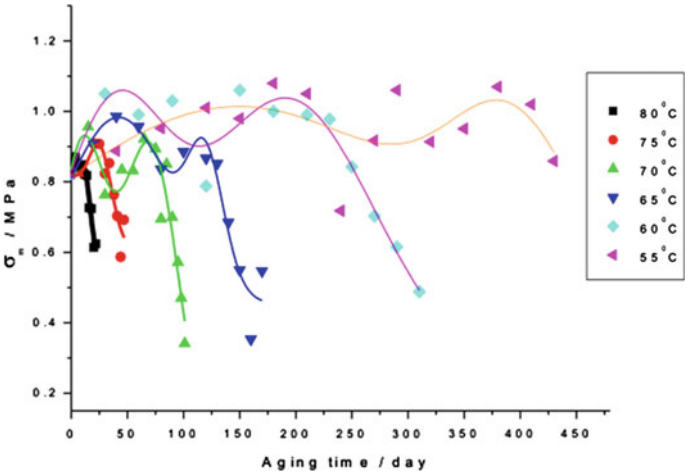

Fig. 45.11 Tensile strength curve of propellant accelerated aging at high temperature

$$\int_{\tau_{\max}}^{\tau_\beta} \frac{1}{f(\alpha)} d\alpha = \int_{\tau_{\max}}^{\tau_\beta} k d\alpha = k\left(\tau_\beta - \tau_{\max}\right) = k\tau_2 \tag{45.30}$$

$$G(\alpha) = k\tau_2 \tag{45.31}$$

$$\ln k = b + aT \tag{45.32}$$

$$\ln \tau_2 = \ln G(\alpha) - b - aT \tag{45.33}$$

$$\ln \tau_2 = C_1 + C_2 T \tag{45.34}$$

where $G(\alpha)$ is the reaction rate, a is the reaction concentration, $f(\alpha)$ is the concentration function, and k is the reaction rate constant, $C_1 = \ln G(\alpha) - b$, $C_2 = -a$.

For example, at 65 °C, the first peak (the peak after curing) is the first center point of the fitting function, and the second peak (the microphase aging peak) is the second center point of the fitting function. The peaks are located at 40.5 days and 123.96 days, respectively. Therefore, the life of NEPE propellant after aging is $\tau_2 = 123.96 - 40.5 = 83.46$ days at 65 °C.

$$\ln \tau_2 = 43.87396 - 0.11651 \times T \tag{45.35}$$

$$\tau_{25^\circ\mathrm{C}} = 9288\, days = 25.5\, years \tag{45.36}$$

T is the aging temperature, τ_2 is the life.

Kong [60] conducted a 10-day high temperature accelerated aging experiment on NEPE propellant samples with 10% constant compressive strain, including CO, NO and HCl gas content detection experiments, and uniaxial tensile experiments on aging samples. He proposed a non-destructive testing life prediction model based on changes in gas content with gray based on data Correlation analysis and singularity correlation analysis, traditional Arrhenius and improved Arrhenius life prediction model.

$$P = P_0 \exp(-Kt) \tag{45.37}$$

$$K = A \exp\left(-\frac{E}{RT}\right) \tag{45.38}$$

Improved model:

$$K = AT^m \exp\left(-\frac{E}{RT}\right) \tag{45.39}$$

$$P = P_0 \exp\left[-\left(AT^m \exp\left(-\frac{E}{RT}\right)\right)t\right] \tag{45.40}$$

$$t = \exp\left(-\ln A + \frac{E}{RT} - m \ln T\right) \ln \frac{P_0}{P} \tag{45.41}$$

Then, four traditional and improved life prediction models are written, which were based on the average mass release of σ_m and CO respectively, and the experimental data are processed as shown in Table 45.2.

Wang [61] accelerated the aging of NEPE propellant at high temperature at 65 °C, 70 °C, 75 °C and 80 °C, then carried out the strength limit test through uniaxial tensile test. He established the microphase structure and macro-mechanical properties of NEPE propellant between the statistical model and got the improved service life prediction equation based on Berthelot equation.

$$\ln \tau_2 = C_1 + C_2 T, C_1 = \ln G(\alpha) - b, C_2 = -a$$

Table 45.2 Estimated storage life (years) of NEPE propellant

Model	25°C	35°C	45°C	55°C	65°C
I	16.09	5.78	2.21	0.90	0.38
II	14.30	3.40	0.88	0.25	0.07
III	15.17	5.16	1.88	0.73	0.30
IV	13.80	3.85	1.16	0.37	0.13

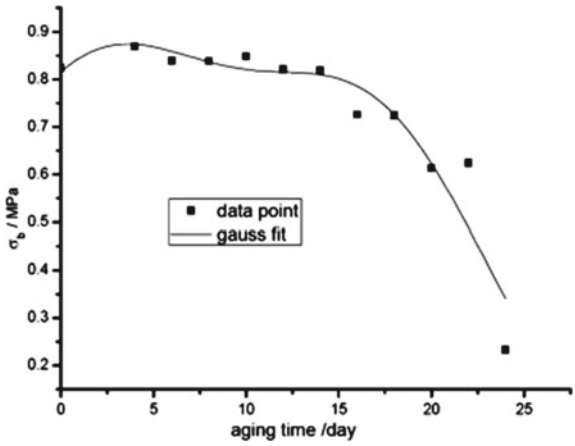

Fig. 45.12 σ_b as a function of aging temperature (80 °C)

where α increases from the initial αu to the maximum αmax is the post-curing stage τ_1, from αmax to the second peak α_β is the microphase aging stage τ_2, and from α_β to αmin in the chemical aging stage is τ_3.

As shown in Fig. 45.12, it is easy to find that the first peak is at 1.96 days and the second peak is at 17.49 days. It's at 80 °C:

$$\tau_2 = 17.49 - 1.96 = 15.53\,days \tag{45.42}$$

The equation can be obtained by fitting:

$$C_1 = 43.87396 \tag{45.43}$$

$$C_2 = -0.11651 \tag{45.44}$$

$$\ln\tau_2 = 43.87396 - 0.11651 \times T \tag{45.45}$$

$$\tau_{25\,^\circ\mathrm{C}} = 9288\,days = 25.5\,years \tag{45.46}$$

Zhang [62] used a DMA to determine the dynamic mechanical properties of NEPE propellant at different temperatures and different aging times. The aging rate was defined by the extreme value of the α relaxation peak of the loss tangent tan δ and the change rate of the vertical displacement factor of the master curve. The inflection point of the aging rate curve is regarded as the critical point of life prediction.

The rate equation is:

$$\mu = \frac{d\left(-\alpha_T^y\right)}{dt} \tag{45.47}$$

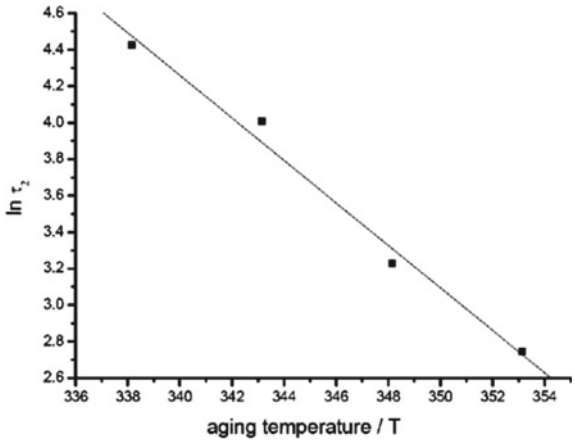

Fig. 45.13 Lnτ2 as a function of aging temperature

The Berthelot equation is $T = a + b.lgt_i$. After linear regression, the old life equations based on the extreme value of the α relaxation peak and the high temperature master curve can be obtained as:

$$T = 103.19 - 20.979 \lg t_i \tag{45.48}$$

$$T = 103.78 - 21.224 \lg t_i \tag{45.49}$$

It can be obtained that the lifetimes at room temperature of 25 °C are 14.6 years and 14.1 years, respectively.

Using the point-slope method, as shown in Fig. 45.13, the life expectancy equation is:

$$\ln \frac{\tau_2}{\tau_1} = \frac{E_a}{R}\left(\frac{1}{T_2} - \frac{1}{T_1}\right) \tag{45.50}$$

where τ is the aging life, E_a can be obtained by fitting the master curve of the relationship between log E' and frequency based on the time–temperature equivalence principle. The 25 °C lifespans are 19.1 years, 18.1 years, 15.3 years, and 14.5 years at 55 °C, 65 °C, 75 °C and 85 °C, respectively.

45.5 Conclusion

Through the analysis of the research progress of NEPE propellant aging in recent years, the following conclusions and prospects are drawn.

1. The aging chemical reaction mechanism of NEPE propellant is complicated. It is necessary to reveal the changes in the microstructure of the propellant during long-term storage, establish the relationship between the microstructure and the macro performance, and explore the correlation between different aging performance parameters, multi-scale and multi-factor to explain the aging phenomenon.
2. Develop analytical instruments for the aging research of solid propellants, and develop fast, non-destructive and accurate technologies for detecting the aging performance of NEPE propellants.
3. On the basis of a sufficient understanding of the aging mechanism and aging performance, construct a suitable aging model to predict the storage life of NEPE propellant, combining experimental verification, theoretical calculation and model prediction.

References

1. W. Xie, Y. Zhao, W. Zhang, Y. Liu, X. Fan, B. Wang, W. He, Q.L. Yan, Sensitivity and stability improvements of NEPE propellants by inclusion of FOX-7. Propellants, Explos., Pyrotech. **43**, 308–314 (2018)
2. H.M. Tan, Development direction of high energy propellant—NEPE propellant. Trans. Beijing Inst. Technol. (S1), 1–7 (1992)
3. H. Zhang, S. Peng, A.M. Pang, Q.W. Cao, Coupling aging behaviors and mechanism between mechanical properties and chemical stability of NEPE propellant. J. Propuls. Technol. **28**(03), 327–332 (2007)
4. H.C. Pei, W.E. Wu, X. Fu, H.F. Qiang, Research progress in molecular simulation of NEPE propellant storage performance. Chem. Propellants Polym. Mater. **13**(03), 26–30 (2015)
5. H.M. Tan, *The Chemistry and Technology of Solid Rocket Propellant* (Transactions of Beijing Institute of Technology, 2015)
6. P.W. Qing, M.L. Wang, R.H. Lu, C.L. Guo, C.L. Huang, Y. Li, X.B. Zhao, S. Peng, Theoretical calculation and numerical simulation of thermal safety on NEPE propellant. Chin. J. Explos. Propellants **42**(6), 602–607 (2019)
7. G. Wang, S.H. Hou, W.M. Wu, H.X. Li, Molecular simulation on selecting curing agent for NEPE propellant based on compatibility. J. Solid Rocket Technol. **38**(05), 684–688 (2015)
8. H.L. Xiao, D.X. Wang, Quantum chemical studies on nitrate esters —trinitroglycerin and mechanisms of its thermal decomposition. Acta Armamentarii **01**, 41–46 (1992)
9. A. Singh, S. Radhakrishnan, R. Vijayalakshmi, M. Talawar, A. Kumar, D. Kumar, Screening of polymer-plasticizer systems for propellant binder applications: an experimental and simulation approach. J. Energ. Mater. **37**, 365–377 (2019)
10. P. van de Witte, P. Dijkstra, J. Van den Berg, J. Feijen, Phase separation processes in polymer solutions in relation to membrane formation. J. Membr. Sci. **117**, 1–31 (1996)
11. K. Nakamae, T. Nishino, S. Asaoka, Microphase separation and surface properties of segmented polyurethane—effect of hard segment content. Int. J. Adhes. Binders **16**, 233–239 (1996)
12. X.P. Zhang, X.B. Zhao, L. Du, J. Zhen, Effect of phase separation on the properties of NEPE propellant. J. Propuls. Technol. **25**(01), 93–94 (2004)
13. X.B. Zhao, X.P. Zhang, J. Zhang, L. Du, Effect of chain extender on the mechanical properties of NEPE propellant. J. Propuls. Technol. **24**(01), 74–79 (2003)
14. Q. Pan, Y. Wang, Z.Q. Chen, F.Q. Zhao, S.W. Li, The thermal decomposition of NEPE propellant (III) thermal decomposition of HMX/RDX/AP-NEPE propellant. Chin. J. Explos. Propellants **26**(03), 45–47 (2003)

15. L.Y. Zhang, S.Y. Heng, Z.R. Liu, L.J. Zhang, P. Yue, Dynamic mechanical properties for aged NEPE propellant. J. Propuls. Technol. **27**(5), 477–480 (2006)
16. X.P. Fan, A prediction on the physical aging life of NEPE-5 propellant. Chin. J. Explos. Propellants **26**, 43–46 (2003)
17. A.M. Pang, X.H. Chi, H.L. Yin, Recent advances on research of binders interfaces between NEPE propellants and HTPB liner. J. Solid Rocket Technol. **41**(02), 181–189 (2018)
18. B. Vogelsanger, Chemical stability, compatibility and shelf life of explosives. CHIMIA Int. J. Chem. **58**, 401–408 (2004)
19. R. Assink, M. Celina, K. Gillen, A. Graham, L. Minier, Polymer aging techniques applied to degradation of a polyurethane propellant binder. Office of Scientific & Technical Information Technical Reports (1999)
20. D. Trache, A.F. Tarchoun, Analytical methods for stability assessment of nitrate esters-based propellants. Crit. Rev. Anal. Chem. **49**, 415–438 (2019)
21. Y.F. Hou, J.S. Xu, Y.J. Gu, Y.J. Gu, C.X. Zhou, Mesoscopic model of cracking process of NEPE propellant based on cohesive zone model. Acta Armamentarh **41**(11), 2206–2215 (2020)
22. S.K. Shee, S.T. Reddy, J. Athar, A.K. Sikder, M. Talawar, S. Banerjee, M.A.S. Khan, Probing the compatibility of energetic binder poly-glycidyl nitrate with energetic plasticizers: thermal, rheological and DFT studies. RSC Adv. **5**, 101297–101308 (2015)
23. P. Zhang, A. Pang, G. Tang, J. Deng, Molecular dynamics simulation study on the mechanism of NPBA enhancing interface strength of NEPE propellant. Appl. Surf. Sci. **493**, 131–138 (2019)
24. L. Han, J.S. Xu, F. T, C.X. Zhou, Research on viscoelastic constitutive model for NEPE composite propellant with meso-mechanics damage due to particle dewetting. J. Propuls. Technol. **38**(08), 1885–1892 (2017)
25. Y. Wang, W. Zhang, K. Xiao, W. Yao, W. Xie, Y. Liu, J. Yang, Y. Chen, Experimental and simulation study of the phase separation of neutral polymeric bonding agent in nitrate ester plasticized polyether propellant and its application. Colloids Surfaces A: Physicochem. Eng. Aspects **610**, 125665 (2021)
26. P. Zhang, J. Yuan, A. Pang, G. Tang, J. Deng, A novel UV-curing liner for NEPE propellant: Insight from molecular simulations. Compos. Part B: Eng. **195**, 108087 (2020)
27. S. Li, Y. Liu, X. Tuo, X. Wang, Mesoscale dynamic simulation on phase separation between plasticizer and binder in NEPE propellants. Polymer **49**, 2775–2780 (2008)
28. X. Sui, N. Wang, Q. Wan, S. Bi, Effects of relaxed modulus on the structure integrity of NEPE propellant grains during high temperature aging. Propellants, Explos., Pyrotech. **35**, 535–539 (2010)
29. K. Liu, M. Wang, M. Xu, Z. Meng, H. Chang, G. Zhang, Z. Chen, L. Zhang, Determination of the component mass ratio and moisture in BTTN/NG nitrate ester mixture simultaneously by qNMR and method validation. Microchem. J. **152**, 104337 (2020)
30. F.J. Wu, S. Peng, X.H. Chi, F.C. Zhong, XPS characterization of NEPE propellant/line bondline. J. Solid Rocket Technol. **32**(02), 192–196 (2009)
31. Z.H. Yan, T. Tao, X. Sui, N.F. Wang, Characterization of tensile strength of NEPE propellant in the aging process. Chin. J. Explos. Propellants **44**(03), 356–360 (2021)
32. D. Gui, Y. Zong, S. Ding, C. Li, Q. Zhang, M. Wang, J. Liu, X. Chi, X. Ma, A. Pang, In–situ characterization and cure kinetics in NEPE propellant/HTPB liner interface by microscopic FT-IR. Propellants, Explos., Pyrotech. **42**, 410–416 (2017)
33. A.H. Farhadian, M.K. Tehrani, M.H. Keshavarz, M. Karimi, S.M.R. Darbani, Relationship between the results of laser-induced breakdown spectroscopy and dynamical mechanical analysis in composite solid propellants during their aging. Appl. Opt. **55**, 4362–4369 (2016)
34. F.Q. Zhao, S.W. Li, Q. Pan, Y. Wang, P. Chen, Y. Gao, Study on thermal decomposition of NEPE propellant(II)—thermal decomposition of HMX/RDX-NEPE propellant. Chin. J. Energ. Mater. **10**(4), 153–156 (2002)
35. C. Farley, A. Kassu, J. Mills, P. Ruffin, M. Curley, S. Sadate-Moualeu, J. Parker, C. Marshall, J. Rice, B. McDonald, Raman spectroscopic analysis of model solid rocket propellant for the detection of stabilizer decay, vol. 11498. International Society for Optics and Photonics. (2020), p. 114980A

36. B. McDonald, C. Marshall, Aging-induced electrical resistance changes in an RDX-loaded nitrate ester propellant with polyglycol adipate (PGA) and polyethylene glycol (PEG) cross-linked binders subject to various thermal and moisture environmental conditions. J. Energ. Mater. **35**, 77–94 (2017)
37. X.H. Chi, S. Peng, F.T. Zhang, G. Yang, Y. Cao, C.Y. Zhao, Effects of aging on statistical mechanical properties distributions of NEPE propellant. J. Solid Rocket Technol. **42**(03), 396–402 (2019)
38. L. Han, X. Chen, J.S. Xu, C.S. Zhou, J.Q. Yu, Research on the time–temperature–damage superposition principle of NEPE propellant. Mech. Time-Depend. Mater. **19**, 581–599 (2015)
39. Y.L. Shen, X. Ren, J.Q. Li, S. Ma, A viscoelastic constitutive model of low smoke NEPE propellant considering strain rate and temperature response. J. Solid Rocket Technol. **42**(03), 314–321 (2019)
40. X.Y. Wang, Q. Tang, W. Li, X.Z. Pan, Study on stress relaxation experiment of NEPE propellant. Chem. Propellants Polym. Mater. **18**(02), 44–47 (2020)
41. Y. Liang, M. Zhang, H. Ren, Q. Jiao, Comprehensive evaluation of the accelerated aging law of NEPE propellants. J. Chem. **2020**, 1–7 (2020)
42. J. An, L. Ding, Y. Liang, Y.L. Zhu, J. Zhou, J.J. Du, K.Y. Wang, Aging properties of NEPE propellant under temperature and pressure loading action. Chin. J. Explos. Propellants **42**(04), 375–379 (2019)
43. Y.B. Gao, X. Chen, J.S. Xu, S.Q. Hu, Dynamic mechanical properties analysis of NEPE propellant. J. Technol. **36**(09), 1410–1415 (2015)
44. Q. Xu, Q.W. Hu, B.L. Sha, B.L. Sha, Viscoelastic constitutive study of NEPE solid propellant with damage. Chin. J. Appl. Mech. **036**(03), 652–657 (2019)
45. H. Li, S.X. Wang, M. Li, J.S. Xu, X.G. Fan, X. Chen, Experimental research on tensile mechanical properties of NEPE propellant under confining pressure. Propellants, Explos., Pyrotech. **45**, 1769–1779 (2020)
46. H. Li, J.S. Xu, J.M. Liu, T.Y. Wang, X. Chen, H.W. Li, Research on the influences of confining pressure and strain rate on NEPE propellant: experimental assessment and constitutive model. Defence Technol. **17**, 1764–1774 (2021)
47. Q. Pan, Y. Wang, Z.Q. Chen, F.Q. Zhao, S.W. Li, Study on the therm aldecom position of NEPE propellant (IV). J. Solid Rocket Technol. **04**, 45–47 (2003)
48. E.G. Yao, F.Q. Zhao, H.X. Gao, S.Y. Xu, R.Z. Hu, H.X. Hao, T. An, Q. Pei, L.B. Xiao, Thermal behavior and non-isothermal decomposition reaction kinetics of aluminum nanopowders coated with an oleic acid/hexogen composite system. Acta Phys. Chim. Sin. **28**, 781–786 (2012)
49. Y. Sun, H. Ren, Q. Jiao, Comparison of thermal behaviors and decomposition kinetics of NEPE propellant before and after storage. J. Therm. Anal. Calorim. **131**, 101–111 (2018)
50. Y.M. Milekhin, A. Koptelov, N. Shishov, I. Koptelov, A. Rogozina, Evaporation of plasticizer from NEPE type propellant. Russ. J. Appl. Chem. **91**, 802–812 (2018)
51. Z.P. Huang, L.M. Tan, Q.W. Cao, X.G. Ma, Quantitative analysis of migrating components in interface of NEPE propellant/liner/insulation. Chin. J. Energ. Mater. **18**(03), 330–334 (2010)
52. Z.P. Huang, H.Y. Nie, Y.Y. Zhang, L.M. Tan, H.L. Yin, X.G. Ma, Migration kinetics and mechanisms of plasticizers, stabilizers at interfaces of NEPE propellant/HTPB liner/EDPM insulation. J. Hazard. Mater. **229**, 251–257 (2012)
53. W.E. Wu, X. Fu, L.T. Ren, H.C. Pei, G. Wang, H.F. Qiang, Determination of stabilizers in NEPE propellant with high performance liquid chromatography. Chem. Propellants Polym. Mater. **13**(06), 87–90 (2015)
54. W.E. Wu, C. Chen, X. Fu, C. Ding, G. Wang, The correlation between chemical stability and binder network structure in NEPE propellant. Propellants, Explos., Pyrotech. **42**, 541–546 (2017)
55. K.H. Dong, L.Z. Kong, L.G. Pei, C.S. Tong, Y.H. Tang, Study on chemical aging properties of NEPE propellant under constant strain. J. Propuls. Technol. **41**(02), 447–454 (2020)
56. A.M. Pang, H.Y. Lie, Z.P. Huang, L.P. Sang, W. Hu, H.L. Yin, X.G. Ma, Q.W. Cao, Determination of Migration Components in the Bonding System of Nitrate Plasticized Polyether Propellant. Hu Bei, CN103207243A,2013-07-17

57. H.L. Yin, D.F. Li, Y. Wang, G.Y. Zhang, Effect of ingredient migration on interface bonding properties of NEPE propellant. J. Solid Rocket Technol. **028**(02), 126–129 (2005)
58. H. Gao, F. Chen, R. Cai, S. Ye, F. Tan, W. Xiong, Y. Yi, W. Hu, The diffusion of components from propellant and liner at the interfaces of EPDM insulation. Propellants, Explos., Pyrotech. **46**, 460–467 (2021)
59. Y. Xiong, X. Sui, N.F. Wang, 27–29 July 2015, Research on NEPE Propellant Life Prediction Model. 51st AIAA/SAE/ASEE Joint Propulsion Conference
60. L.Z. Kong, K.H. Dong, Y.H. Tang, S.G. Lai, Y.H. Qu, Non-destructive storage life prediction of NEPE propellant. Chin. J. Energ. Mater. (2021)
61. N. Wang, Q. Wan, X. Sui, Y. Xiong, Life prediction of NEPE propellants. Propellants, Explos., Pyrotech. **39**, 102–107 (2014)
62. N.Y. Zhang, Z.R. Liu, S.Y. Heng, K.Y. Wang, F. Han, Estimation of life span for NEPE propellant. J. Propuls. Technol. **27**(06), 572–576 (2006)